

Dissertation zur Erlangung des Doktorgrades
der Fakultät für Chemie und Pharmazie
der Ludwig-Maximilians-Universität München

**Systematic Investigations on Ternary Amalgams
of Electropositive Metals:
Preparation, Crystal Structures and
Physical Properties**

Timotheus Hohl

aus Landau i. d. Pfalz, Deutschland

2023

Erklärung

Diese Dissertation wurde im Sinne von § 7 der Promotionsordnung vom 28. November 2011 von Herrn PD Dr. Constantin Hoch betreut.

Eidesstattliche Versicherung

Diese Dissertation wurde eigenständig und ohne unerlaubte Hilfe erarbeitet.

München, 28. Februar 2023

Timotheus Hohl

Dissertation eingereicht am 28.02.2023

1. Gutachter: PD Dr. C. Hoch

2. Gutachter: Prof. Dr. W. Schnick

Mündliche Prüfung am 23.03.2023

νόμωι χροίη, νόμωι γλυκύ, νόμωι πικρό,
ειπώυ, έτεηιδ άτομα και κενόν

Scheinbar ist Farbe, scheinbar Süßigkeit, scheinbar Bitterkeit: wirklich nur Atome und Leeres

Demokrit

Danksagung

Herrn Prof. Dr. Wolfgang Schnick danke ich für die Übernahme des Zweitgutachtens und die Möglichkeit, die Arbeit unter Benutzung seiner Ressourcen anzufertigen.

Den Professoren und Professorinnen Dr. Thomas M. Klapötke, Dr. Silvija Markic, Dr. H.-C. Böttcher und Dr. I. Ivanović-Burmazović danke ich für ihre Bereitschaft, Teil der Prüfungskommission meines Rigorosums zu sein.

Großer Dank gebührt natürlich den Kollegen im Arbeitskreis Hoch. Für notwendigen Schabernack, unvergessliche Memes, erzwungene (aber nicht weniger benötigte) Druckbetankungen, fachliche Diskussionen und Lektionen, und euren unvergleichbaren Humor. Danke an Irina Zaytseva für ihre Inspiration für alles Kreative, an Lukas Nusser für seine ansteckende Begeisterung und Hilfsbereitschaft und an Lucas Balzat für die Unterstützung primitiven Humors.

Danke natürlich auch an meine Praktikanten Lukas Nusser, Jessica Wulfes, Lucas Balzat, Robert Hübsch und Daniel Kraut für ihre Unterstützung und dem Beitrag zu dieser Arbeit. Besonders schön ist es, wenn aus solchen Praktika auch Freundschaften werden.

Ein großes Danke natürlich auch an meine Kooperationspartner: Prof. Dr. Caroline Röhr für ihre Begabung, die kompliziertesten Dinge auf einfache und intuitive Art und Weise zu vermitteln. Bernard Lehmann als Leidensgenossen für tiefgründige Gespräche jeglicher Art. Dr. Martin Etter und Dr. Volodymyr Baran von der Beamline P02.1 am DESY für die Messungen meiner Armada an Pulverproben, ohne welche ich sicher nicht so viele Ergebnisse hätte. Prof. Dr. Stefan Ebbinghaus für die Messungen von magnetischen Suszeptibilitäten und Dr. R. Kremer für die Leitfähigkeitsmessungen.

Wolfgang Wünschheim danke ich für seine schnelle und effektive Hilfe jeglicher technischer Art, und für viele Fachsimpeleien. Dr. Dieter Rau für seine Erläuterungen zu röntgenographischen Messtechniken, Christian Minke für diverse EDX-Spektren. Sandra Albrecht für ICP-Messungen und der gesamten Feinmechanik und Glasbläserei für ihre Bereitschaft, technisch komplexe Lösungen für meine Probleme zu finden.

Den gesamten Arbeitskreismitgliedern der Gruppen Schnick, Johrendt und Lotsch danke ich für die tolle Zusammenarbeit und das positive Arbeitsumfeld; meinen Büropartnern Jennifer Steinadler und Tobias Giftthaler für notwendige Ablenkungen (die sicherlich auch oft genug von mir selbst initiiert wurden), tiefgründige Gespräche über vieles, was fünf Buchstaben hat und viel zu dämliche Witze.

Danke an meine beiden Simons', Marcus, Simone, Maggie, Max, Marie-Helen, Caro, Milica, Melli und Jess.

Die besten kommen zum Schluss... Tino: Danke. Für all Deine Hilfe, Deinen Zuspruch, Dein Vertrauen, und notwendige Tritte. Für Deine vollumfängliche und stets verfügbare Hilfe und dafür, meine Begeisterung an der Chemie aufrecht zu erhalten. Es war mir nicht nur ein innerliches Blumenpflücken. Sondern eine unvergleichliche Freude, meine Doktorarbeit bei Dir anfertigen zu dürfen!

Zuletzt danke ich meiner (erweiterten) Familie, die mich in all den Jahren konsequent unterstützt hat. Ihr habt mich weiter gebracht, als euch bewusst ist. Also Danke an meine Eltern, mein Omiein, Cornelia und Karl-Hermann sowie Michelle und Richard.

Contents

1	Introduction	1
1.1	Historical Aspects	2
1.2	The Polar Metallic Bond	3
1.3	Amalgams of the Less-Noble Metals	4
2	Aims and Scope	11
2.1	Ternary Amalgams	11
2.2	Overview of This Work	11
3	Experimental	13
3.1	General Preparative Methods	14
3.2	Analytical Methods	16
3.3	Utilised Software and Databases.....	19
3.4	Preparative Strategies for Amalgams.....	20
4	Results and Discussion	27
4.1	Structure and Bonding in CsNa ₂ Hg ₁₈ , a New Ternary Amalgam with strong Coulombic Bonding Contributions.....	27
4.2	Ternary Amalgams: Expanding the Structural Variety of the Gd ₁₄ Ag ₅₁ Structure Family	42
4.3	Influence of Disorder on the ‘Bad Metal’ Behaviour in Polar Amalgams.....	61
4.4	The Hg-rich part of the Binary System, K–Hg revised: Synthesis, Crystal and Electronic Structures of KHg ₄ , KHg ₅ and KHg ₈	76
4.5	SrHg _{5.86} – a new binary Sr amalgam	91
4.6	Cyclic Voltammetry as a Tool for the targeted Synthesis of Ternary Amalgams via Electrocrystallisation	98
4.7	The first Be-containing Amalgam?	102
4.8	The ‘Bad Metal’ Behaviour and its Contributing Factors	116
5	Summary	121
5.1	Structure and Bonding in CsNa ₂ Hg ₁₈ , a New Ternary Amalgam with strong Coulombic Bonding Contributions.....	122
5.2	Ternary Amalgams: Expanding the Structural Variety of the Gd ₁₄ Ag ₅₁ Structure Family	123
5.3	Influence of Disorder on the ‘Bad Metal’ Behaviour in Polar Amalgams.....	124
5.4	The Hg-rich part of the Binary System, K–Hg revised: Synthesis, Crystal and Electronic Structures of KHg ₄ , KHg ₅ and KHg ₈	125
5.5	SrHg _{5.86} – a new binary Sr amalgam	126
5.6	Cyclic Voltammetry as a Tool for the targeted Synthesis of Ternary Amalgams via Electrocrystallisation	127
5.7	The first Be-containing Amalgam?	127
5.8	The ‘Bad Metal’ Behaviour and its Contributing Factors	128
6	Outlook	129

7	Appendix	131
8	Miscellaneous	183
8.1	List of Publications	183
8.2	Publications beyond this thesis.....	184
8.3	Conference Contributions and Presentations.....	185
8.4	Deposited Crystallographic data.....	186

1

Introduction

Mercury

Mankind has long been fascinated by mercury. In its pure form, the shiny, silver liquid forms physically perfect mirrors - a property that is still being applied today in liquid-mirror telescopes. It is the only metal liquid at room temperature, and has an unusually high density (13.53 g cm^{-3}). Its high surface tension combined with a low viscosity is being exhibited in the tendency to form droplets of high mobility, which can practically be observed by spilling it on a flat surface.

For chemists, different aspects of the element are more interesting: it can be found in its compounds as linear X—Hg—Hg—X molecular entities containing divalent cationic clusters $[\text{Hg—Hg}]^{2+}$ (found in e.g. Hg_2Cl_2) and monoatomic ions Hg^{2+} (e.g. $\text{Hg}(\text{NO}_3)_2$), mirroring its most common oxidation states +1 and +2. Since mercury forms binary compounds with many elements (see below), its chemistry is extraordinarily diverse.

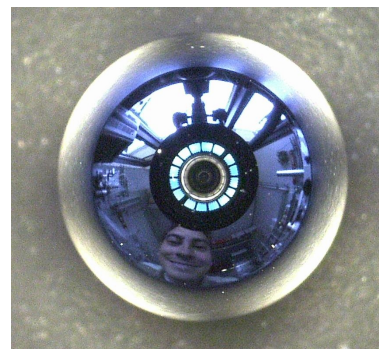


Fig. 1.1: A drop of pure mercury under a light microscope.

Table 1.1: Periodic table of the elements with an emphasis on elements that form compounds with mercury (green). Grey colouring indicates that no compounds with mercury have been observed yet.

H																	He																												
Li	Be											B	C	N	O	F	Ne																												
Na	Mg											Al	Si	P	S	Cl	Ar																												
K	Ca	Sc	Ti	V	Cr	Mn	Fe	Co	Ni	Cu	Zn	Ga	Ge	As	Se	Br	Kr																												
Rb	Sr	Y	Zr	Nb	Mo	Tc	Ru	Rh	Pd	Ag	Cd	In	Sn	Sb	Te	I	Xe																												
Cs	Ba	La	Hf	Ta	W	Re	Os	Ir	Pt	Au	Hg	Tl	Pb	Bi	Po	At	Rn																												
Fr	Ra	Ac	Rf	Db	Sg	Bh	Hs	Mt	Ds	Rg	Uub																																		
<table border="1"> <tbody> <tr> <td>Ce</td><td>Pr</td><td>Nd</td><td>Pm</td><td>Sm</td><td>Eu</td><td>Gd</td><td>Tb</td><td>Dy</td><td>Ho</td><td>Er</td><td>Tm</td><td>Yb</td><td>Lu</td> </tr> <tr> <td>Th</td><td>Pa</td><td>U</td><td>Np</td><td>Pu</td><td>Am</td><td>Cm</td><td>Bk</td><td>Cf</td><td>Es</td><td>Fm</td><td>Md</td><td>No</td><td>Lr</td> </tr> </tbody> </table>																		Ce	Pr	Nd	Pm	Sm	Eu	Gd	Tb	Dy	Ho	Er	Tm	Yb	Lu	Th	Pa	U	Np	Pu	Am	Cm	Bk	Cf	Es	Fm	Md	No	Lr
Ce	Pr	Nd	Pm	Sm	Eu	Gd	Tb	Dy	Ho	Er	Tm	Yb	Lu																																
Th	Pa	U	Np	Pu	Am	Cm	Bk	Cf	Es	Fm	Md	No	Lr																																

Its electron configuration $[\text{Xe}]4f^{14}5d^{10}$ leads to a closed-shell configuration analogous to the noble gases, and is exhibited in its low melting point, a high vapour pressure and the absence of Hg—Hg bonds in its elemental form. Owing to the relativistic effects present in the heavy atoms, its $6s$ electrons are energetically lowered, leading to an approximation of the $5d$ and $6s$ energy levels and to an expansion of the energy gap between the $6s$ and the empty $6p$ states.

This causes not only to the unusual chemical behaviour mentioned above, but also less intuitive consequences such as increased (1st and 2nd) ionisation energies, which in turn influences its electronegativity. This can be observed in the existence of covalent bonding contributions in mercury compounds. Another consequence is that mercury does not form thermodynamically stable anions.

The salts and organometallic compounds of mercury are very toxic (as well as the vapors of the pure element) and their use has therefore been reduced. However, due to the highly unusual properties, it still catches the interest of scientists.

1.1 Historical Aspects



Fig. 1.2: Cinnabar embedded in Quartz (Nevada, USA).

Mercury is one of the oldest known elements, together with gold, silver, copper, iron, lead and sulphur. In nature, it can be found in its elemental form of small droplets together with its ore Cinnabar (HgS). The use of cinnabar dates back to 30 000 BC, where it was used as a component of the pigment ‘Funerary Red’ in paleolithic cave paintings found in Spain.^[1] It was later employed in embalming practices around 7600 – 6000 BC in the Fertile Crescent (Middle East), which is also believed to be the first region on earth where settled farming as a sign of the early development of human society took place.^[2] The use of cinnabar

as the pure pigment named ‘Vermillion’ has been verified to date back to at least 5000 BC,^[3] and has thereafter been used in ancient cultures in South America, Ancient Egypt and China.^[4,5] The first verified intentional usage of elemental mercury was found in Egyptian tombs dating back to 1500 – 1600 BC,^[6] while the first written accounts about the knowledge of the elemental form are found in ancient Greek texts, where Theophrastus also gave documented instructions on how to obtain the metal from its ore.^[7] Since he extracted it “*from native Cinnabar, rubbed with Vinegar in a brass Mortar with a brass Pestle*”, it can be assumed that he also obtained the first copper amalgam.

The process of fire-gilding, which is still being used today for historical and restoration and conservation purposes, dates back to around 15 BC – AD 90 for gilding copper and silver.^[8–10] During this process, gold amalgam is being decomposed by thermal treatment.

During the middle ages, mercury was commonly used for medicinal and alchemical purposes, and its preparation and purification process have been documented by Agricola.^[11,12] A breakthrough relating to the current research area of amalgams was made in 1806 independently by Berzelius and Davy, who performed electrolysis experiments on custom laboratory substances using mercury cathodes and observed the formation of amalgams.^[13,14] This in turn led to the successful discovery and isolation of many alkali and alkaline earth elements: Na, K, Mg (which was first named magnium), Ca, Sr and Ba.

The origin of term ‘*amalgam*’ is still unclear, as related root words exist in Greek (μαλακός, “soft”, Arabic (al-amalgām, “softening ointment, emollient poultice”) and Latin (amalgama, “mercury alloy”). The chemical symbol Hg can be traced back to the Greek term υδραργυρος (*Hydrargyros*, from “quick silver”), yielding today’s element symbol.



Fig. 1.3: Alchemical symbol for mercury.

Not only has mercury been used in numerous applications (e.g. rectifiers and the amalgam process for the production of chlorine and NaOH from brine), but also led to momentous scientific breakthroughs; investigations on mercury vapor were part of the experimental proof for the Bohr model of atoms and its closely related Rydberg constant R , further propelling

the advances in quantum theory as we know it.^[15–17] Additionally, the physical phenomenon of superconductivity was discovered on mercury by H. Kamerlingh-Onnes.^[18] Even until today, the superconductor with the highest critical temperature T_C (under normal pressure) contains mercury ($\text{Hg}_{0.8}\text{Tl}_{0.2}\text{Ba}_2\text{Ca}_2\text{Cu}_3\text{O}_{8.33}$, $T_C = -135^\circ\text{C}$).^[19]

1.2 The Polar Metallic Bond

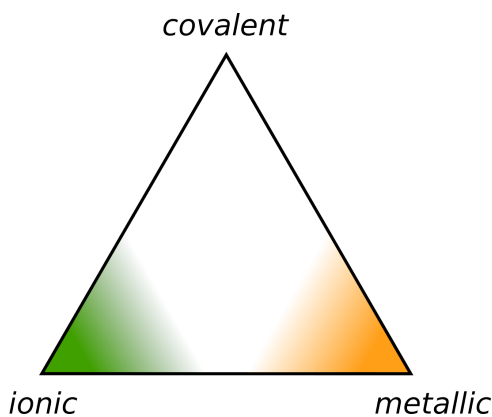


Fig. 1.4: van-Arkel-Ketelaar triangle, showing the three fundamental bonding types. For emphasis, the metallic and ionic bond regions are highlighted.^[20,21]

During the scope of this work, however, it will be used to emphasise the gradual transition between a metallic and ionic bond. An intuitive approach for the concept of is the visualisation of different bonding has been made by van Arkel-Ketelaar^[20,21] triangles (cf. Fig. 1.4), where the vertices represent the three fundamental bonds in chemistry: Ionic, covalent and metallic. Typical representatives thereof are widely given by CsF, F_2 and Sn or Li, respectively. Along the edges of the triangles, compounds comprising bonding contributions from both vertices can be found. For example, typical half metals like Te or As can be sorted between the covalent and the metallic bond,^[22] while representatives of the polar covalent bond (e.g. BF_3 , CF_4 or NF_3) can be located between the covalent and ionic bond.^[22,23]

To account for deeper understanding of chemical bonds through the use of modern computational methods, the proposed triangle has been modified numerously.^[24] A common denominator in these triangles is the fact that electronegativity differences $\Delta\chi$ and average electronegativities χ are being used as a reference points. It is debatable if this manner of use is exact as well as concise, since many compounds combine aspects of all three bonding types, which then makes a precise, quantified positioning of a given compound difficult to achieve. In this regard, the van Arkel-Ketelaar triangle represents a considerably oversimplified picture of the true bonding contributions in many areas of science. Nevertheless, for an intuitive understanding about the combination of different bonding aspects and for educational purposes, it represents a valuable, easy graph.

Considering the physical properties, polar metals often exhibit ‘bad metal’ behaviour. Macroscopically, this can be observed by an overall metallic behaviour, but unusually high specific resistivities combined with a non-linear temperature dependence thereof. The electric conductivity σ depends on the lifetime τ of the electron wave between two scattering events. These events are caused by phononic or lattice vibrations, which are temperature-dependent, and disorder. The latter can be introduced by macroscopic anomalies such as strain or mechanical deformation of the sample, structural defects such as under- or mixed occupancy, impurities of the sample as well as the existence of Coulombic (partial-)charges. Additional, but direct influences on the conductivity are the free electron concentration n , the effective electron (or

hole) mass m^* , as well as the elementary charge q . This is summarised in the following equation:

$$\sigma = \frac{nq^2\tau}{m^*} \quad (1.1)$$

The linear temperature dependence of conductivity can be attributed to the increase of the scattering rates of electrons on phonons. Because a minimum lifetime limit τ_{\min} must exist (following Heisenberg's uncertainty principle), a lower limit for the value of metallic conductivity exists: the Mott-Ioffe-Regel limit σ_{MIR} .^[25] Since metals with conductivities lower than this limit would then have non-physically high scattering rates, they should in theory be insulators. Most metals will melt before reaching this limit. However, compounds with pronounced 'bad metal' behaviour not only reach, but can exceed this limit.^[26–28]

1.3 Amalgams of the Less-Noble Metals

Amalgams of the less noble metals serve as ideal candidates for the systematic investigation of the polar metal bond. Due to a combination of low electron affinity of mercury and high differences of electronegativities (ΔEN), a significant, yet incomplete electron transfer is present in these compounds. A high ΔEN is necessary to induce a high electron transfer from the electropositive to the electronegative partner. If the electron affinity of the electronegative partner is high, cations and anions are formed. If, however, the electron affinity is low, a partial electron transfer with no anion formation and a polar metallic bond results. The lattice energy of intermetallic amalgams is so low that thermodynamically unfavourable mercuride anions cannot be stabilised, yet a certain amount of negative charge is allowed for an individual Hg atom in crystalline amalgams.

In their crystal structures, this is represented by the formation of Hg sublattices $[\text{Hg}_n]^{\delta-}$, where negative partial charges are delocalised. These contain spacial voids, in which the (partial) positive charges are contained at the less noble metal position. This leads to overall metallic structures, containing ionic contributions through separated (partial) charges (cf. Fig. 1.5). Therefore, different aspects present themselves on a structural level: on the one hand, ionic contributions are emphasised by the formation of coordination polyhedra. On the other hand, a distinctive tendency towards the formation of closed packaging occurs.

The structural variety of amalgams is extremely rich, and many examples for amalgams of the less noble metals exist. Amalgams of the alkali and alkaline earth metals have extensively been studied, inspired by their unique structural chemistry and diversity. In Table 1.3, all reported Hg-rich representatives are summarised. A graphical representation including the Hg: M ratio and coordination environments is given in Fig. 4.28 in Chapter 4.4.

Because of systematic investigations of applying amalgam formation for the separation of the lanthanoid metals, some of their respective amalgams have been characterised as well.^[30,31] Recently, research interest on amalgams has somewhat decreased, owing to the sophisticated preparative chemistry, their complex structural motifs and the toxicity of mercury. Due to the constant development and implementation of modern X-ray diffraction methods, their structural elucidation is becoming easier.

Regarding their structural motifs, amalgams of alkali and alkaline earth metals show a distinct trend: the dimension of the Hg sublattice is dependent on the content of mercury. In $\alpha\text{-Na}_3\text{Hg}$,

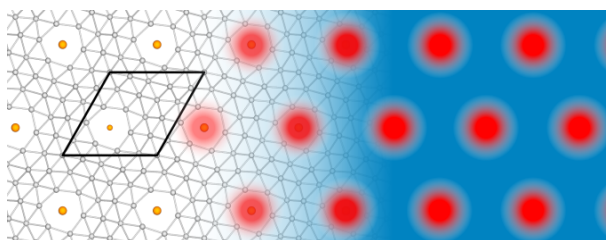


Fig. 1.5: Visualisation of the Coulombic charge separation (blue: δ^- , red: δ^+) in amalgams. The net consists of a Hg sublattice (grey), with incorporated Yb atoms (orange).^[29]

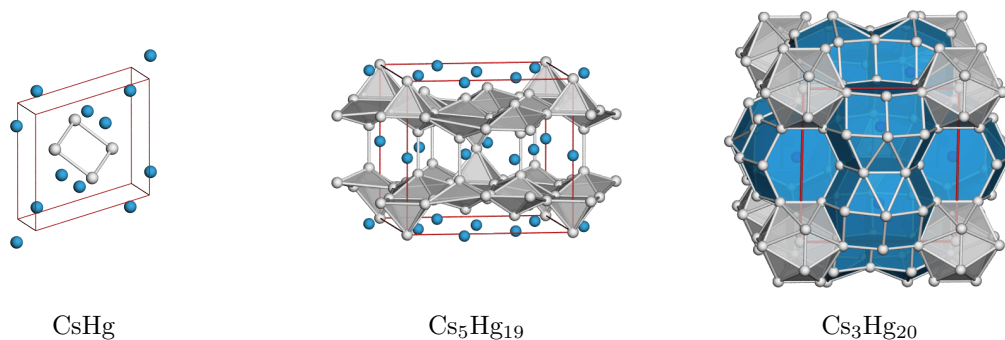


Fig. 1.6: Crystal structures of selected Cs amalgams with increasing Hg:Cs ratio. Emphasised is the growing connectivity of the Hg network. Hg: grey, Cs: blue.

a CsCl type structure exists, forming ‘isolated’ mercury anions.^[33] Small, cluster-like polyhedra in the form of $[\text{Hg}_4]^{\delta-}$ squares or $[\text{Hg}_8]^{\delta-}$ cubes can be found in CsHg and $\text{Rb}_{15}\text{Hg}_{16}$.^[40–42] With increasing Hg content, sheets and chains may form, as has been observed e.g. in $A\text{Hg}_2$ (with $A = \text{Rb}, \text{Cs}$) and $A_2\text{Hg}_7$ (with $A = \text{K}, \text{Rb}$).^[44,48] When even more mercury is added, mercury forms extended, negatively polarised sublattices with embedded atoms of the less noble metals (e.g. $M\text{Hg}_{11}$ for $M = \text{K}, \text{Rb}, \text{Ca}, \text{Sr}, \text{Ba}$ or $\text{Cs}_2\text{Hg}_{27}$).^[62–64]

References

- [1] P. Bueno-Ramírez, R. Barroso-Bermejo, R. de Balbín-Behrmann, Funerary red (cinnabar versus ochre) and megalithic rituals in the central Iberian peninsula: The hypogean necropolis of Valle de las Higueras, Huecas, Toledo, Spain, *Bull. Soc. Prehist. Franc.* **2019**, *T116*, No. 1, 73–94, <https://www.jstor.org/stable/26910786>.
- [2] J. Martín-Gil, F. Martín-Gil, G. D. de Castro, P. Zapatero-Magdaleno, F. Sarabia-Herrero, The first known use of vermilion, *Experientia* **1995**, *51*, 759–761, DOI: [10.1007/bf01922425](https://doi.org/10.1007/bf01922425).
- [3] Y. Goren, A. Goring-Morris, I. Segal, The Technology of Skull Modelling in the Pre-Pottery Neolithic B (PPNB): Regional Variability, the Relation of Technology and Iconography and their Archaeological Implications, *J. Archaeolog. Sci.* **2001**, *28*, 671–690, DOI: [10.1006/jasc.1999.0573](https://doi.org/10.1006/jasc.1999.0573).
- [4] M. E. Weeks, *Discovery of the Elements*, 6th ed., (Ed.: H. M. Leicester), Wiley-VCH, Easton (PA), USA, **1960**, pp. 47–52.
- [5] I. Shimada, J. A. Griffin, Objetos de metales preciosos del Sicán medio, *Investigación y ciencia* **1994**, *213*, 54–61, <https://www.investigacionyciencia.es/revistas/investigacion-y-ciencia/mscara-preincaica-84/objetos-de-metales-preciosos-del-sican-medio-5443>.
- [6] J. M. Stillman, *The Story of Early Chemistry*, 1st ed., D. Appleton and Co., New York City (NY), USA, **1924**, pp. 2–7.
- [7] J. Hill, Theophrastus, *Theophrastus’s History of Stones*, 2nd ed., printed for the author, London, UK, **1774**, pp. 227–235.
- [8] J. M. Riddle, Dioscorides, *De Materia Medica*, 1st ed., The Ohio State University, Columbus (OH), USA, **1952**.
- [9] H. Rackham, Pliny, *Natural History, Book XXXIV*, 1st ed., Harvard University Press., Harvard (MA), USA, **1952**.
- [10] F. Granger, Vitruvius, *De architectum, VII*, 1st ed., Harvard University Press., Harvard (MA), USA, **1934**.
- [11] A. Greenberg, *From alchemy to chemistry in picture and story*, 1st ed., Wiley-Interscience, New Jersey (NY), USA, **2007**.
- [12] H. C. Hoover, H. L. Hoover, Agricola, *De Re Metallica*, 1st ed., Dover Publications, Mineola (NY), USA, **1950**.

Table 1.3: Summary of all reported alkali, alkaline earth and rare earth metal amalgams including their respective space group and Literature, sorted by increasing Hg content. Compounds highlighted in green are presented in this work. For reasons of clarity, the rare earth metals are not differentiated individually.

Hg : M	Sum formula	Li	Na	K	Rb	Cs	Be	Mg	Ca	Sr	Ba	RE	SG	Lit.
	MHg	■						■					$Pm\bar{3}m$	[32–37]
1	NaHg		■										$Cmcm$	[33, 38]
	MHg			■		■							$P\bar{1}$	[39–41]
1.06	Rb ₁₅ Hg ₁₆				■								$I4_1/a$	[42]
1.4	K ₅ Hg ₇		■	■									$Pbcm$	[43]
	MHg ₂		■	■	■	■							$P6/mmm$	[38]
2	MHg ₂			■	■	■							$Imma$	[34, 38, 44]
	MHg ₂							■	■			■	$P\bar{3}m1$	[31, 35]
	MHg ₂												$P6/mmm$	[45]
2.25	Ca ₄ Hg ₉								■	■			$I4/mcm$	[46]
3	MHg ₃	■										■	$P6_3/mmc$	[45, 47]
3.5	M ₂ Hg ₇			■	■	■							$P\bar{3}m1$	[48]
3.6	K ₃ Hg ₁₁			■	■	■							$Immm$	[49]
3.8	M ₅ Hg ₁₉				■	■	■						$I4/m$	[49, 50]
4	KHg ₄			■									$Cmcm$	—
4.09	M ₁₁ Hg ₄₅											■	$F\bar{4}3m$	[51]
4.43	M ₇ Hg ₃₁			■	■	■							$P6/mmm$	[49, 52]
4.46	M ₁₃ Hg ₅₈									■	■	■	$P6_3/mmc$	[36, 53]
4.73	Na ₁₁ Hg ₅₂		■										$P\bar{6}$	[54]
4.91	M ₁₁ Hg ₅₄								■	■			$P\bar{6}$	[29, 55]
5	KHg ₅			■									$P2_1/c$	—
5.15	Ba ₂₀ Hg ₁₀₃										■		$F\bar{4}3m$	[56]
5.5	Eu ₁₀ Hg ₅₅											■	$P\bar{6}$	[57]
5.86	SrHg _{5.86}									■			$Pnma$	—
6	MHg ₆			■	■						■	■	$Pnma$	[58, 59]
6.5	MHg _{6.5}											■	n.a.	[60]
6.6	M ₃ Hg ₂₀				■	■	■						$Pm\bar{3}n$	[49]
8	SrHg ₈									■			$Pnma$	[61]
	KHg ₈			■									$P\bar{1}$	—
11	MHg ₁₁			■	■	■			■	■	■		$Pm\bar{3}m$	[62, 63]
13.5	Cs ₂ Hg ₂₇					■							$Im\bar{3}$	[64]

- [13] J. J. Berzelius, *Föreläsningar i Djurkemi*, 1st ed., Dover Publications, Stockholm, Sweden, **1950**.
- [14] H. Davy, I. The Bakerian Lecture, on some chemical agencies of electricity, *Phil. Trans. R. Soc.* **1807**, *97*, 1–56, DOI: [10.1098/rstl.1807.0001](https://doi.org/10.1098/rstl.1807.0001).
- [15] J. Franck, G. Hertz, Über Zusammenstöße zwischen Elektronen und den Molekülen des Quecksilberdampfes und die Ionisierungsspannung desselben, *Phys. Bl.* **1967**, *23*, 294–301, DOI: [10.1002/phbl.19670230702](https://doi.org/10.1002/phbl.19670230702).
- [16] N. Bohr, I. On the constitution of atoms and molecules, *Philos. Mag. Series 6* **1913**, *26*, 1–25, DOI: [10.1080/14786441308634955](https://doi.org/10.1080/14786441308634955).
- [17] J. Rydberg, Recherches sur la constitution des spectres d'émission des éléments chimiques, *Kongliga Svenska Vetenskaps-Akademiens Handlingar* **1889**, *23*, 1–155, DOI: [10.1080/14786441308634955](https://doi.org/10.1080/14786441308634955).

- [18] H. Kamerlingh-Onnes, Further experiments with liquid helium. C. On the change of electric resistance of pure metals at very low temperatures, etc. IV. The resistance of pure mercury at helium temperatures., *Comm. Phys. Lab. Univ. Leiden* **1911**, 120b.
- [19] P. Dai, B. Chakoumakos, G. Sun, K. Wong, Y. Xin, D. Lu, Synthesis and neutron powder diffraction study of the superconductor $\text{HgBa}_2\text{Ca}_2\text{Cu}_3\text{O}_{8+\delta}$ by Tl substitution., *Phys. C* **1995**, 243, DOI: [10.1016/0921-4534\(94\)02461-8](https://doi.org/10.1016/0921-4534(94)02461-8).
- [20] A. E. van Arkel, *Molecules and Crystals*, 1st ed., Butterworths, London, UK, **1949**.
- [21] J. A. Ketelaar, *Chemical Constitution*, 2nd ed., Elsevier, Amsterdam, Niederlande, **1958**.
- [22] W. B. Jensen, A Quantitative van Arkel Diagram, *J. Chem. Educ.* **1995**, 72, 395, DOI: [10.1021/ed072p395](https://doi.org/10.1021/ed072p395).
- [23] L. C. Allen, Extension and completion of the periodic table, *J. Am. Chem. Soc.* **1992**, 114, 1510–1511, DOI: [10.1021/ja00030a073](https://doi.org/10.1021/ja00030a073).
- [24] T. L. Meek, L. D. Garner, Electronegativity and the Bond triangle, *J. Chem. Educ.* **2005**, 82, 325, DOI: [10.1021/ed082p325](https://doi.org/10.1021/ed082p325).
- [25] A. F. Ioffe, A. R. Regel, Non-crystalline, amorphous and liquid electronic semiconductors, *Prog. Semicond.* **1960**, 4, 237–291.
- [26] O. Gunnarsson, M. Calandra, J. E. Han, Saturation of Electrical Resistivity, *Rev. Mod. Phys.* **2003**, 75, 1085–1099, DOI: [10.1103/RevModPhys.75.1085](https://doi.org/10.1103/RevModPhys.75.1085).
- [27] R. Jaramillo, S. Ha, D. Silevitch, S. Ramanathan, Origins of bad-metal conductivity and the insulator–metal transition in the rare-earth nickelates, *Nat. Phys.* **2014**, 10, 304–307, DOI: [10.1038/nphys2907](https://doi.org/10.1038/nphys2907).
- [28] N. E. Hussey, K. Takenaka, H. Takagi, Universality of the Mott–Ioffe–Regel limit in metals, *Philos. Mag.* **2004**, 84, 2847–2864, DOI: [10.1080/14786430410001716944](https://doi.org/10.1080/14786430410001716944).
- [29] F. Tambornino, C. Hoch, The simplest representative of a complex series: the Hg-rich amalgam $\text{Yb}_{11}\text{Hg}_{54}$, *Z. Kristallogr.* **2017**, 232, 557–565, DOI: [10.1515/zkri-2016-2036](https://doi.org/10.1515/zkri-2016-2036).
- [30] J. W. Neckers, H. C. Kremers, Observations on the rare earths, XXVIII. The separation of cerium, *J. Am. Chem. Soc.* **1928**, 50, 955–958, DOI: [10.1021/ja01391a004](https://doi.org/10.1021/ja01391a004).
- [31] A. Iandelli, R. Ferro, La struttura cristallina dei composti LaHg , CeHg , PrHg , NdHg , *Atti Accad. Naz. Lincei Rend. Classe Sci. Fis. Mat. Nat.* **1951**, 10, 48–52.
- [32] E. Zintl, G. Brauer, Über die Valenzelektronenregel und die Atomradien unedler Metalle in Legierungen, *Z. Phys. Chem.* **1933**, 20B, 245–271, DOI: [10.1515/zpch-1933-2023](https://doi.org/10.1515/zpch-1933-2023).
- [33] H.-J. Deiseroth, A. Stupperich, R. Pankaluoto, N. E. Christensen, NaHg : A variant of the cesium-chloride structure structural relations and electronic structure, *Z. Anorg. Allg. Chem.* **1991**, 597, 41–50, DOI: [10.1002/zaac.19915970107](https://doi.org/10.1002/zaac.19915970107).
- [34] E. J. Duwell, N. C. Baenziger, The crystal structures of KHg and KHg_2 , *Acta Crystallogr.* **1955**, 8, 705–710, DOI: [10.1107/S0365110X55002168](https://doi.org/10.1107/S0365110X55002168).
- [35] G. Bruzzone, F. Merlo, The Calcium-Mercury System, *J. Less-Common Met.* **1973**, 32, 237–241, DOI: [10.1016/0022-5088\(73\)90091-X](https://doi.org/10.1016/0022-5088(73)90091-X).
- [36] G. Bruzzone, F. Merlo, The Strontium-Mercury System, *J. Less-Common Met.* **1974**, 35, 153–157, DOI: [10.1016/0022-5088\(74\)90154-4](https://doi.org/10.1016/0022-5088(74)90154-4).
- [37] G. Brauer, W. Haucke, Kristallstruktur der intermetallischen Phasen MgAu und MgHg , *Z. Phys. Chem.* **1936**, 33B, 304–310, DOI: [10.1515/zpch-1936-3327](https://doi.org/10.1515/zpch-1936-3327).
- [38] J. W. Nielsen, N. C. Baenziger, The Crystal Structures of NaHg_2 , NaHg and Na_3Hg_2 , *Acta Crystallogr.* **1954**, 7, 277–282, DOI: [10.1107/S0365110X54000783](https://doi.org/10.1107/S0365110X54000783).
- [39] E. Biehl, H.-J. Deiseroth, Crystal structure of potassiumamalgam, KHg , *Z. Kristallogr. - Cryst. Mater.* **1996**, 211, 630, DOI: [10.1524/zkri.1996.211.9.630](https://doi.org/10.1524/zkri.1996.211.9.630).
- [40] H.-J. Deiseroth, A. Strunck, Square Hg_4 Clusters in the Compound CsHg , *Angew. Chem. Int. Ed.* **1987**, 26, 687–688, DOI: [10.1002/anie.198706871](https://doi.org/10.1002/anie.198706871).

- [41] H.-J. Deiseroth, A. Strunck, W. Bauhofer, CsHg, eine ungewöhnliche Variante der CsCl-Struktur Darstellung, Kristallstruktur und physikalische Eigenschaften, *Z. Anorg. Allg. Chem.* **1989**, 575, 31–38, DOI: [10.1002/zaac.19895750106](https://doi.org/10.1002/zaac.19895750106).
- [42] H.-J. Deiseroth, A. Strunck, W. Bauhofer, Hg₈ (“Mercubane”) Clusters in Rb₁₅Hg₁₆, *Angew. Chem. Int. Ed.* **1989**, 28, 1251–1252, DOI: [10.1002/anie.198912511](https://doi.org/10.1002/anie.198912511).
- [43] E. J. Duwell, N. C. Baenziger, The crystal structure of K₅Hg₇, *Acta Cryst.* **1960**, 13, 476–479, DOI: [10.1107/S0365110X60001126](https://doi.org/10.1107/S0365110X60001126).
- [44] H.-J. Deiseroth, A. Strunck, W. Bauhofer, RbHg₂ und CsHg₂, Darstellung, Kristallstruktur, elektrische Leitfähigkeit, *Z. Anorg. Allg. Chem.* **1988**, 558, 128–136, DOI: [10.1002/zaac.19885580112](https://doi.org/10.1002/zaac.19885580112).
- [45] A. Iandelli, A. Palenzona, Su alcuni composti intermetallici dell'europio con zinco, cadmio e mercurio, *Atti Accad. Naz. Lincei Rend. Cl. Sci. Fis. Mater. Nat.* **1964**, 37, 165–168.
- [46] M. Pušelj, Z. Ban, Ternäre Gamma-Messing-Phasen in den Systemen Calcium-M^{IB(II B)}-Quecksilber, *Z. Naturforsch. B* **1980**, 35, 1594–1595, DOI: [10.1515/znb-1980-1225](https://doi.org/10.1515/znb-1980-1225).
- [47] F. Tambornino, *Electrolytic Synthesis and Structural Chemistry of Intermetallic Phases with Polar Metal-Metal Bonding*, Dissertation, LMU München, **2016**.
- [48] E. Biehl, H.-J. Deiseroth, K₂Hg₇ und Rb₂Hg₇, zwei Vertreter eines neuen Strukturtyps binärer intermetallischer Verbindungen, *Z. Anorg. Allg. Chem.* **1999**, 625, 1337–1342, DOI: [10.1002/\(SICI\)1521-3749\(199908\)625:8<1337::AID-ZAAC1337>3.0.CO;2-W](https://doi.org/10.1002/(SICI)1521-3749(199908)625:8<1337::AID-ZAAC1337>3.0.CO;2-W).
- [49] E. Todorov, S. C. Sevov, *J. Solid State Chem.* **2000**, 149, 419–427, DOI: [10.1006/jssc.1999.8569](https://doi.org/10.1006/jssc.1999.8569).
- [50] E. Biehl, H.-J. Deiseroth, Rb₅Hg₁₉: Eine neue, geordnete Defektvariante des BaAl₄-Strukturtyps, *Z. Anorg. Allg. Chem.* **1999**, 625, 389–394, DOI: [10.1002/\(SICI\)1521-3749\(199903\)625:3<389::AID-ZAAC389>3.0.CO;2-9](https://doi.org/10.1002/(SICI)1521-3749(199903)625:3<389::AID-ZAAC389>3.0.CO;2-9).
- [51] F. Merlo, M. L. Fornasini, Crystal Structure of the R₁₁Hg₄₅ compounds (R = La, Ce, Pr, Nd, Sm, Gd, U), *J. Alloys Compd.* **1979**, 64, 221–231, DOI: [10.1016/0022-5088\(79\)90173-5](https://doi.org/10.1016/0022-5088(79)90173-5).
- [52] G. Bruzzone, F. Merlo, The Barium-Mercury System, *J. Less-Common Met.* **1975**, 39, 271–276, DOI: [10.1016/0022-5088\(75\)90201-5](https://doi.org/10.1016/0022-5088(75)90201-5).
- [53] G. Bruzzone, F. Merlo, The Lanthanum-Mercury System, *J. Less-Common Met.* **1976**, 44, 259–265, DOI: [10.1016/0022-5088\(76\)90140-5](https://doi.org/10.1016/0022-5088(76)90140-5).
- [54] C. Hoch, A. Simon, Na₁₁Hg₅₂: Complexity in a Polar Metal, *Angew. Chem. Int. Ed.* **2012**, 51, 3262–3265, DOI: [10.1002/anie.201108064](https://doi.org/10.1002/anie.201108064).
- [55] A. V. Tkachuk, A. Mar, Alkaline-Earth Metal Mercury Intermetallics, A_{11-x}Hg_{54+x} (A = Ca, Sr), *Inorg. Chem.* **2008**, 47, 1313–1318, DOI: [10.1021/ic7015148](https://doi.org/10.1021/ic7015148).
- [56] M. Wendorff, C. Röhr, The new complex barium mercuride Ba₂₀Hg₁₀₃ and its ternary zinc and cadmium variants, *Z. Naturforsch. B.* **2012**, 67, 893–906, DOI: [10.5560/znb.2012-0186](https://doi.org/10.5560/znb.2012-0186).
- [57] F. Tambornino, C. Hoch, The Mercury-richest Europium Amalgam Eu₁₀Hg₅₅, *Z. Anorg. Allg. Chem.* **2015**, 641, 537–542, DOI: [10.1002/zaac.201400561](https://doi.org/10.1002/zaac.201400561).
- [58] F. Tambornino, C. Hoch, Bad metal behaviour in the new Hg-rich amalgam KHg₆ with polar metallic bonding, *J. Alloys Compd.* **2015**, 618, 299–304, DOI: [10.1016/j.jallcom.2014.08.173](https://doi.org/10.1016/j.jallcom.2014.08.173).
- [59] M. Wendorff, C. Röhr, The new barium mercuride BaHg₆ and ternary indium and gallium derivatives, *J. Alloys Compd.* **2013**, 546, 320–328, DOI: [10.1016/j.jallcom.2012.07.101](https://doi.org/10.1016/j.jallcom.2012.07.101).
- [60] T. B. Massalski, H. Okamoto, P. R. Subramanian, L. K. (Hrsg.), *Binary Alloy Phase Diagrams*, 2nd ed., ASM International, Materials Park (OH), USA, **1990**.
- [61] A. V. Tkachuk, A. Mar, In search of the elusive amalgam SrHg₈: a mercury-rich intermetallic compound with augmented pentagonal prisms, *Dalton Trans.* **2010**, 39, 7132–7135, DOI: [10.1039/C0DT00304B](https://doi.org/10.1039/C0DT00304B).
- [62] E. Biehl, H.-J. Deiseroth, Darstellung, Strukturchemie und Magnetismus der Amalgame MHg₁₁ (M: K, Rb, Ba, Sr), *Z. Anorg. Allg. Chem.* **1999**, 625, 1073–1080, DOI: [10.1002/\(SICI\)1521-3749\(199907\)625:7<1073::AID-ZAAC1073>3.0.CO;2-V](https://doi.org/10.1002/(SICI)1521-3749(199907)625:7<1073::AID-ZAAC1073>3.0.CO;2-V).
- [63] M. Pušelj, Z. Ban, Beitrag zur Kenntnis des Systems Quecksilber-Calcium, *Croat. Chem. Acta* **1978**, 51, 75–79.

- [64] C. Hoch, A. Simon, $\text{Cs}_2\text{Hg}_{27}$, das quecksilberreichste Amalgam – ein naher Verwandter der Bergman-Phasen, *Z. Anorg. Allg. Chem.* **2008**, *634*, 853–856, DOI: [10.1002/zaac.200700535](https://doi.org/10.1002/zaac.200700535).

2

Aims & Scope

2.1 Ternary Amalgams

While binary amalgams have been studied extensively, only scarce knowledge exists about ternary representatives. No systematic studies with this regard have been conducted, and the only examples for ternary amalgams with two different electropositive metals so far are $\text{NaK}_{29}\text{Hg}_{48}$,^[1] Li_2MgHg ^[2] and $\text{Li}_6M_{17}\text{Hg}_9$ ^[3] ($M = \text{Ca}, \text{Sr}, \text{Yb}$). Introducing a second less noble metals into the crystal structure should yield a higher variety of parameters that influence not only their crystal structure, but local electronic structures as well. Keeping this in mind, different aspects for these investigations are of interest:

1. Structural variety, where different results can be expected in the form of:
 - new structures with unique structure types
 - mixed crystals of binary, isotypic structures (solid solutions)
 - coloured variants of binary structures (i.e. different ordered occupancies of crystallographic positions by the less noble metals)
 - substitutional mixed crystals by the statistical inclusion of an atom M^{II} into a binary structure of M^{I} , where an isotypic binary structure of M^{II} is unknown
2. The influence of different aspects of the crystal structures on the ‘bad metal’ behaviour

This work will highlight synthetic approaches, structural characterisations of new binary and ternary amalgams, investigations of the electronic structures and the physicochemical properties as well as the resulting estimation of the quantitative influence of the parameters on the ‘bad metal’ behaviour.

2.2 Overview of This Work

Since literature on the practical aspects of amalgam preparation is still scarce, a compilation of all employed and newly developed techniques is given in Chapter 3, while detailed experimental descriptions can be found in Chapter 7. In Chapter 4, the main results are presented in the form of peer-reviewed publications together with several still unpublished manuscripts already submitted or in preparation for imminent submission.

Chapter 4.1 describes the synthesis and characterisation of a new ternary amalgam comprising two alkali metals with a unique structure type: $\text{CsNa}_2\text{Hg}_{18}$. Calculations of the electronic structure as well as resistivity measurements are discussed to yield more insight into structure-property relations.

The combination of different ‘coloring’ variants of amalgams and the resulting impact on the still growing family of amalgams belonging to the $\text{Gd}_{14}\text{Ag}_{51}$ structure family is shown in Chapter 4.2.

The introduction of disorder in the form of solid solutions as well as substitutional mixed crystals on the examples of $\text{K}_{1-x}\text{Rb}_x\text{Hg}_{11}$ ($x = 0.472(7)$) and $\text{Cs}_{3-x}\text{Ca}_x\text{Hg}_{20}$ ($x = 0.20(3)$) together with

calculations of the electronic structures, physicochemical measurements and implications for the degree of influence on the overall behaviour of polar metals is emphasised in Chapter 4.3.

The discovery of three new binary amalgams – KHg_4 , KHg_5 and KHg_8 – and the thermochemical reinvestigation via a combination of DSC (Differential Scanning Calorimetry) and powder diffraction experiments as the base for the redesign of the Hg-rich part of the K–Hg phase diagram is presented in Chapter 4.4.

Additional results include the discovery, structural characterisation and electronic considerations of $\text{SrHg}_{5.86}$ (Chapter 4.5) and preliminary results on experimental developments for the synthesis of ternary amalgams via electrochemical methods on the basis of cyclic voltammetry (Chapter 4.6) as well as renewed efforts for the synthesis of a Be-containing amalgam (Chapter 4.7).

In Chapter 4.8, the obtained results are put into perspective regarding relative quantification of the contributing factors for ‘bad metal’ behaviour in amalgams.

A comprehensive summary for the different results obtained is given in Chapter 5, while Chapter 6 compiles propositions for future endeavours in this research area.

In Chapter 7, detailed descriptions of the experiments performed during this thesis, obtained powder diffraction and DSC as well as additional crystallographic data can be found.

Chapter 8 contains a list of all publications, contributions to conferences and talks, deposited crystallographic data and the CV.

References

- [1] H.-J. Deiseroth, E. Biehl, $\text{NaK}_{29}\text{Hg}_{48}$: A Contradiction to or an Extension of Theoretical Concepts to Rationalize the Structures of Complex Intermetallics?, *J. Solid State Chem.* **1999**, *147*, 177–184, DOI: [10.1006/jssc.1999.8209](https://doi.org/10.1006/jssc.1999.8209).
- [2] H. Pauly, A. Weiss, H. Witte, Kubisch flächenzentrierte Legierungen der Zusammensetzung Li_2MgX mit raumzentrierter Unterstruktur, *Z. Metallkd.* **1968**, *59*, 414–418.
- [3] A. V. Tkachuk, A. Mar, $\text{Li}_6\text{A}_{17}\text{Hg}_9$ (A=Ca, Sr, Yb): Intermetallic Compounds of Mercury with a Zeolite-Like Topology of Cubic Networks, *Chem. Eur. J.* **1993**, *15*, 10348–10351, DOI: [10.1002/chem.200902250](https://doi.org/10.1002/chem.200902250).

3

Experimental

Utilised Chemicals

All used chemicals are listed in the following table, including their respective purities and manufacturers.

Table 3.1: Compound, purity and manufacturer. * = dried over CaH₂ and distilled before use, ¹ = for starting materials, ² = for syntheses.

Compound	purity	manufacturer
Ar	99.999 %	Air Liquide
Ba	99.50 %	SMT Metalle Wimmer
Be	99.5 %	Alfa Aesar
Ca	99.99 %	Sigma-Aldrich
CaI ₂ · 6 DMF	recrystallised	own manufacturing (see Ch. 7.2, p. 138)
Cs	doubly distilled	MPI-FKF Stuttgart
CsI	99.9 %	Alfa Aesar
Diamond	polycrystalline powder, ≤ 1 μm	Sigma-Aldrich
Decamethylferrocene	97 %, sublimated	Sigma-Aldrich
Eu	99.99 %	Smart Elements
Hg	doubly distilled	not specified (see Ch. 3.1.3, p. 14)
HI	57 wt.% in H ₂ O	Sigma-Aldrich
HNO ₃ conc.	technical grade	in-house chemical
I ₂	99.5 %	Acros Organics
K	doubly distilled	MPI-FKF Stuttgart
KI	recrystallised	Alfa-Aesar
MgI ₂ · 6 DMF	recrystallised	own manufacturing (see Ch. 7.2, p. 137)
Magnesium ¹	99 %	Riedel-de Haën
Magnesium ²	99.99 %	Smart Elements
Na ¹	99.9 %	Sigma-Aldrich
Na ²	doubly distilled	MPI-FKF Stuttgart
NaI · 3 DMF	recrystallised	own manufacturing
NH ₃ (gas)	99.998 %	Air Liquide
N,N-Dimethylformamid (DMF)*	≥ 98 %	Sigma Aldrich
Rb	doubly distilled	MPI-FKF Stuttgart
RbI	99.8 %	Alfa Aesar
Sr	dist.	SMT Metalle Wimmer
SrI ₂ · 7 DMF	recrystallised	own manufacturing (see Ch. 7.2, p. 138)
Tetrabutylammonium perchlorate	electrochemical grade	Alfa Aesar
Toluene	technical grade	in-house chemical
Yb	99.99 %	Smart Elements

3.1 General Preparative Methods

3.1.1 Glovebox and Vacuum-/Inert-Gas-Apparatus

Unless stated otherwise, all preparations of experiments and samples were handled in a glovebox (UNILab, MBRAUN Inertgas-Systeme GmbH, Garching, Germany) under Argon atmosphere ($O_2 \leq 0.1$ ppm, $H_2O \leq 0.1$ ppm). For this purpose, Ar was purified by streaming over a combination of a BTS catalyst and molecular sieve (4 Å).

Where needed, experiments in glassware were handled with a Schlenk apparatus, where pressures with $p \leq 1 \times 10^{-3}$ mbar could be achieved. The Argon used in this apparatus was purified by streaming over an array of columns filled with KOH, silica gel, molecular sieve 3 Å, P_4O_{10} , and a titanium sponge ($\vartheta = 780$ °C).

3.1.2 Niobium-/Tantalum Crucibles and Arc-welding Apparatus

Experiments for the syntheses of ternary amalgams at elevated temperatures were performed in sealed Ta or Nb crucibles made of tubings of their respective metal (inner diameter 9 mm, wall thickness 0.5 mm, PLANSEE, Reutte, Austria). After filling with the metals, these crucibles were closed by selfmade lids of the same metal by using a screw press. In this step, it was necessary to make sure that no metals are inside the joints of the crucible and the lid. Before usage, all crucibles were heated under vacuum in a high frequency oven ($\vartheta = 1500$ °C) to remove the oxide layer.

After filling, the crucibles were welded shut with an arc-welding installation under Argon. In order to minimise evaporation of the starting materials, the welding process was done in small increments and under sufficient cooling. The crucibles were then transferred into reaction tubes made of glass (or quartz if $\vartheta \geq 400$ °C) and the pressure reduced ($p \approx 10^{-2}$ mbar) in order to avoid splintering of the glass due to the heating process.

3.1.3 Purification of Mercury

Mercury was collected from residues of pressure valves or was donated from other working groups or the waste disposal service. Because of the unclear state of purity it was cleaned following a universal procedure. The only impurity that is removed unsatisfactorily by this procedure is gold. A further description of the process together with a recycling protocol for Hg containing waste is given in Chapter 4.3.

CAUTION! When handling mercury, all preparative work should be done over a nonbreakable (plastic) container for the collection of spilled mercury. Additionally, all glassware should be cleaned with half concentrated nitric acid. Wastes should be disposed of separately.



Fig. 3.1: Running distillation of Mercury as performed during the scope of this work.

For initial removal of solid contaminants, mercury was filtered twice over a folded filter with a small hole at the tip. Afterwards, the same volume of half concentrated nitric acid was added to dissolve all other metals less noble than Hg. The two-phase mixture was vigorously mixed using a prismatic stir bar to ensure sufficient contact between the two phases. After the appearance of a white solid was observed, the reaction was stopped by diluting with generous amounts of distilled water. After decanting, the mercury was repeatedly rinsed with distilled

water to remove excess (dissolved) salts, while residual water was removed using lintless paper

towels. It was then filtered two more times using folded filters, followed by distillation at 250 °C under dynamic vacuum. All tapered joints had to be secured thoroughly with steel joint clips, while the whole apparatus had to be supported by multiple clamps due to its weight.

3.1.4 Synthesis of Anhydrous BeI₂

Beryllium iodide was used as starting compound for all experiments targeting to the synthesis of a beryllium amalgam. The synthesis procedure was taken from literature and adapted in a way that (under)graduate students were able to safely apply it as a routine experiment. An in-depth description of this process together with further processing and products of BeI₂ within the electrocrystallisation experiments can be found in Chapter 4.7.

CAUTION! Beryllium and its compounds are regarded as toxic and carcinogenic. Because the biochemical mechanisms that cause beryllium associated diseases are still unknown, special (safety) precautions are strongly advised.^[1] The setup for the synthesis of BeI₂ is depicted on the right. The procedure is a slightly modified version of the one reported by Wood and Brenner^[2] and included in Brauer's Handbook.^[3] This modular setup facilitates the multi-gram scale of high-purity BeI₂ by combining synthesis and purification process in a one-step fashion, while also avoiding excess waste (contrary to syntheses inside sealed quartz tubes). A sufficient amount of Be metal was loaded into a corundum crucible inside a quartz tube, which was then connected to a 100mL Schlenk flask. The apparatus was dried by evacuation ($\leq 1 \times 10^{-3}$ mbar), and thoroughly heated (oven: 300 °C for 1 h, connector and Schlenk flask with a hot-air gun for 15 min at 300 °C). Valve I was closed, the Schlenk flask disconnected under reverse Ar flow, and 2.0 g (7.9 mmol) I₂ beads were added. After cooling with liquid N₂, pressure was reduced to $\leq 1 \times 10^{-3}$ mbar.

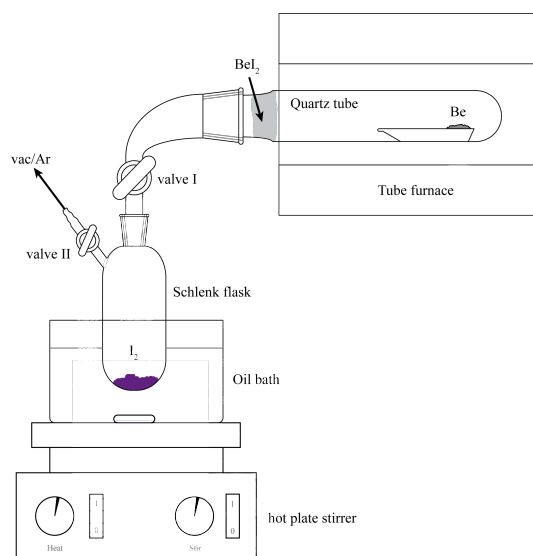


Fig. 3.2: Setup for the synthesis of BeI₂.



Fig. 3.3: Colourless crystals of BeI₂ are forming at the cooler part of the quartz tube.

Valve I was opened and the oven temperature increased to 650 °C. Subsequently, the temperature of the oil bath was set to 250 °C. At the same time, static vacuum was enabled by closing valve II, and, to avoid resublimation of I₂, the oil bath and connector were mantled with aluminum foil. The synthesis was stopped when the atmosphere in the system appeared colourless again, indicating quantitative Iodine consumption. The apparatus was reduced to $\leq 1 \times 10^{-3}$ mbar, valve I closed, and the quartz tube with connector attached transferred into the glove box for opening and storage of BeI₂. The colourless, needle-shaped crystals of BeI₂ (see Fig. 3.3, left), which formed at the colder part of the quartz tube can be scratched off quite easily. If necessary, an additional distillation step was performed by loading the quartz tube with BeI₂, reducing the pressure for 1 h to $\leq 1 \times 10^{-3}$ mbar and then increasing the oven temperature to 650 °C. **Analysis:** Via pXRD, the distilled BeI₂ was identified as phase-pure β -BeI₂ (see Fig. 7.87, p. 168).

3.1.5 Synthesis of Anhydrous DMF Complexes of Alkaline Earth Metal Iodides

For cyclic voltammetry and electrocrystallisation experiments, DMF complexes of the respective metal iodides were used. To ensure anhydrous conditions, all syntheses were performed using inert gas techniques. Metal iodides are beneficial starting compounds for electrochemical experiments for several reasons: (1) they show high solubility in DMF, (2) the formation of iodine or triiodide at the anode is a visible indicator for the onset of the electrochemical reaction, (3) the iodides or the iodide solvates can easily be prepared and purified in one-pot reactions.

Metal iodide solvates can be synthesised as follows: (1) dissolve the pure metal in stoichiometric amounts of concentrated HI (in the case of Mg) in DMF or add stoichiometric amounts of concentrated HI to a suspension of the respective carbonate (used for Sr and Ca) in DMF, (2) remove remaining solids with a Schlenk frit, (3) connect a Dean-Stark apparatus, add a small amount of toluene and remove the toluene/water azeotropic mixture by distillation and (4) optional evaporation of large surplus solvent if necessary, cooling and filtration via Schlenk frit and subsequent drying under vacuum. Detailed descriptions for the synthesis of $\text{MgI}_2 \cdot 6 \text{DMF}$, $\text{CaI}_2 \cdot 6 \text{DMF}$ and $\text{SrI}_2 \cdot 7 \text{DMF}$ can be found in Chapter 7, p. 137–138. The process has also been described in detail in literature.^[4]

3.2 Analytical Methods

3.2.1 Powder X-ray Diffraction (pXRD)

Representative portions of the samples were ground using an agate mortar inside a glovebox, filled into glass capillaries (HILGENBERG, Malsfeld, Germany; special glass No. 10, inner diameter 0.3–0.5 mm) and sealed with birch tar. Owing to the high absorption coefficients of amalgams, samples were optically diluted with diamond powder (volume ratio ranging from 1:1 to 1:50, depending on the sample). The diffraction experiments were carried out on a Stadi P (STOE & CIE., Darmstadt, Germany; Mo- $K_{\alpha 1}$ -radiation, $\lambda = 0.7093 \text{ \AA}$, Ge(111) monochromator; Si as external standard) with parafocussing DEBYE-SCHERRER geometry and a MYTHENII detector (DECTRIS LTD., Baden-Daettwil, Switzerland). Towards the end of this work, the radiation was changed to Ag- $K_{\alpha 1}$ ($\lambda = 0.5594075 \text{ \AA}$). Samples measured with this wavelength are labelled accordingly in the respective diffractogram.

Measurements were performed at room temperature, for optimisation of signal-to-noise ratio multiple scans without background correction were added. Obtained diffractograms were compared to data from literature or automatically generated reflection intensities from single-crystal data. The used software is listed in Ch. 3.3.

On selected samples, powder diffraction measurements were conducted at a Synchrotron (PETRA III, Beamline P02.1, DESY, Hamburg, Germany) during the Rapid Access Program 2021A under proposal ID RAAt-20010291. The samples were prepared as described before and irradiated for 300 s ($\lambda = 0.20735 \text{ \AA}$). An area detector VAREX XRD 4343CT (150×150 μm pixel size, 2880×2880 total pixel area, CsI scintillator directly deposited on amorphous Si-photodiodes) was used to collect intensities. Data integration and analysis software is specified in Ch. 3.3.

3.2.2 Single Crystal X-ray Diffractometry (SCXRD)

Crystalline, air- and moisture-sensitive samples were retrieved from the reaction containers in a glovebox and transferred into paraffin oil dried over potassium. Appropriate crystals were selected under a microscope (Leica MZ6, LEICA, 4.0-fold magnification) and then transferred into flame-narrowed capillaries (HILGENBERG, Malsfeld, Germany; special glass No. 10, inner

diameter 0.1–0.3 mm) filled with the same oil. Afterwards, the capillaries were sealed with birch tar and mounted on brass pins.

Measurements were carried out on two different diffractometers: Device 1 was an IPDS-1 (STOE & CIE., Darmstadt, Germany; fine-focus sealed X-ray tube, Ag- K_{α} -radiation, $\lambda = 0.56087 \text{ \AA}$, graphite monochromator) equipped with an imaging plate detector. Device 2 was a type D8 Quest diffractometer (BRUKER Corp., Billerica (MA), USA) with an air-cooled micro-focus X-ray tube $I\mu S$, (PHOTONII CMOS detector; Mo- K_{α} -radiation, $\lambda = 0.7107 \text{ \AA}$, Goebel mirror optics).

3.2.3 Differential Scanning Calorimetry (DSC)

Thermal analysis was performed with a simultaneous TG-DTA/DSC device (STA 449 F5 Jupiter, NETZSCH, Selb, Germany). Measurements were done under reverse Ar flow. Crucibles were self-made using Ta/Nb tubings (length = 20 mm, inner diameter 5 mm, wall thickness 0.5 mm, WHS SONDERMETALLE e.K., Grünsfeld, Germany), where the base was made of the same metal and attached using a screw press and subsequent arc-welding. The crucibles were then filled with the sample ($m = 10\text{--}80 \text{ mg}$) and closed with flat pliers. The seam was then sealed by arc-welding.

For every measurement, a reference measurement was performed with Ar-filled crucibles and the same temperature program as the final measurement. Details on the temperature programs are described at the respective diagram.

3.2.4 Magnetic Susceptibility

Magnetic measurements were performed by M. Sc. Martin Weidemann using a VSM (Vibrating Sample Magnetometer) on a PPMS (Physical Property Measurement System, QUANTUM DESIGN Inc., San Diego (CA), USA) in a temperature range of 1.9–300 K with a magnetic field of $\pm 15 \text{ Oe}$. Samples were placed in capsules self-made made of PFEP, which were then fixated on a brass holder. Data was collected with the MultiVu software.^[5] On selected samples, measurements were conducted by Prof. S. G. Ebbinghaus using the ADMS option of a PPMS QUANTUM DESIGN Inc., San Diego (CA), USA) with the same self-made capsules made of PFEP. The magnetic field was set to 100 Oe, and the temperature was decreased from 6 K to 2 K.

3.2.5 Electric Conductivity

Temperature dependent electric conductivity measurements between 2 and 296 K were performed by Dr. Reinhard Kremer (MPI FKF, Stuttgart, Germany) with the ac-resistivity option of a physical property measurement system (PPMS, Quantum Design) on cold-pressed sample pellets (thickness approx. 0.5 mm to 1 mm) with the van-der-Pauw technique using currents between 1 mA and 100 mA. Electrical contacts (contact resistance below a few Ohm) were applied in an Argon filled glove box using silver paint. After rapid mounting of the sample, the PPMS cryostat was evacuated to high vacuum ($\leq 10^{-5} \text{ mbar}$) and immediately cooled down rapidly to liquid He temperatures. At low temperatures approximately 10 mbar ^4He exchange was charged to the cryostat and subsequently the resistance measurement was done by raising the temperature to room temperature.

3.2.6 X-ray Spectroscopy (EDX)

For the analysis of the chemical composition, selected samples were analysed with energy-dispersive X-ray spectroscopy (EDX). For this purpose, samples were mounted on a Al carrier

with an adhesive conducting carbon foil. The measurements were carried out by Mr. Christian Minke on a scanning electron microscope (JEOL JSM-6500F (JEOL Ltd., Akashima, Japan) equipped with an X-Mas 80 SSD (OXFORD INSTRUMENTS, Abingford, U.K.) energy-dispersive X-ray (EDX) detector on several particles with an acceleration voltage of 20 kV.

3.2.7 Elemental Analysis (ICP-AES)

ICP-AES was used for the analysis of all elements except for halides, C, H, N and O. For this purpose, the sample was wet-chemically solubilised and inserted into an Ar plasma (10 000 K). Position and intensity of the spectral lines are used to derive the quantitative and qualitative composition, while the error is $\leq 5\%$. Measurements were conducted on a VARIAN VISTA RL CCD. A comprehensive list of spectral lines used for the analysis can be found in Table 3.2. If multiple wavelengths were used, an arithmetic mean was calculated. Measurements were performed by Ms. J. Obel or Ms. S. Albrecht.

Table 3.2: Overview of the analysed elements and their respective emission wavelengths.

Element	λ [nm]	Element	λ [nm]
Al	396.152	Cu	324.754
Be	313.107	Mg	279.553
Ca	396.847	Si	288.158
Na	589.592	Hg	194.164

3.2.8 Cyclic Voltammetry (CV)

Cyclic voltammetry was performed in a specially devised apparatus (see Fig. 4.54), which enables electrochemical measurements in an air- and moisture-free atmosphere. A silver wire immersed in supporting electrolyte solution was used as a pseudo-reference electrode (RE), while contact to the electrolyte solution was enabled through a pore 4 size glass frit, platinum rods were used as electrodes (counter electrode CE, diameter = 2 mm, working electrode WE, diameter = 1.5 mm). The potentiostat used was a Autolab PGSTAT101 (Deutsche METROHM GmbH & Co. KG, Filderstadt, Germany).

3.2.9 Quantum Mechanical Calculations

Quantum mechanical calculations were performed with the program suite Wien2K.^[6] This program utilises the APW+lo (Augmented Plane Waves + Local Orbitals) method, which considers all electrons with a full potential approach. Models which include all electrons are being considered as standard for the precision of solid state DFT (density functional theory) and yield the most dependable values for a given functional, as long as numerical accuracy is achieved through the employed basis sets and sufficiently dense k-meshes.^[7,8] This is particularly useful for calculations involving heavy elements such as mercury to account for relativistic effects and f-electrons, which are exhibiting unusual behaviour.

Calculations were either performed on a local PC (64 bit operating system (Linux Mint 20 Cinnamon) with a quad-core processor (Intel Core i-7500 CPU @ 4 x 3.40GHz) equipped with 24 GB RAM) or done by the group of Prof. J. Minar (University of West Bohemia, Plzeň, Czech Republic) if mixed or underoccupancy existed in the considered material. If not stated otherwise, exchange correlations were calculated with the standard PBE-GGA functional,^[9] which was chosen due to its high accuracy for numerous compounds/elements, while its wide-spread usage enables comparability with other calculations from literature.^[10] Convergence criteria were chosen for energy convergence ≤ 0.0001 eV and charge distance ≤ 0.00001 eV.

In the case of calculations of the electronic structures of amalgams with mixed occupancies (cf. Chapter 4.3), the fully relativistic Korringa-Kohn-Rostoker (KKR) Green function method as implemented in the sprkk code was employed.^[11,12] The Vosko, Wilk and Nusair local density approximation (VWN-LDA)^[13] was used to approximate the exchange-correlation part of the

potential as well as the atomic sphere approximation. The KKR code allows for a treatment of mixed occupied crystallographic positions without the construction of a virtual fully ordered supercell model as approximation to the averaged and purely statistically disordered crystal structure (CPA approximation)^[11] which was used for the mixed crystal $\text{K}_{0.5}\text{Rb}_{0.5}\text{Hg}_{11}$ and $\text{Cs}_{2.8}\text{Ca}_{0.2}\text{Hg}_{20}$. The electronic density of states (DOS) was calculated on the basis of the crystallographic structure model without allowing for a structure relaxation. The energy integrals were evaluated by contour integration on a semicircular path within the complex energy plane, using a Gaussian mesh of 32 points. For multipole expansion of the Green's function we used a cutoff $\ell_{max} = 3$ to obtain reliable results. Once the Green's function components have been determined, the charge density can be obtained via the k-space integration over the Brillouin zone (BZ). Self-consistent calculations were performed using a grid of $24 \times 24 \times 24$ points in the full BZ. Structure constant matrix k-dependent convergence parameters were set manually to $\text{ETA} = 2.0$, $\text{RMAX} = 2.0$ and $\text{GMAX} = 2.0$.

Total and partial density of states (tDOS and pDOS) were determined with the modified tetrahedon method.^[6]

3.3 Utilised Software and Databases

3.3.1 Single Crystal X-ray Diffraction

- data collection, integration and absorption correction (D8 Quest): APEX3^[14]
- data collection, integration and absorption correction (IPDS 1): XAREA,^[15] XRED,^[16] XSHAPE^[17]
- structure solution: SHELXS-97^[18]
- structure refinement: SHELXL-97^[18]
- absorption correction, symmetry analysis, etc.: PLATON^[19]
- structure visualisation: DRAWXTL^[20]

3.3.2 Powder X-ray Diffraction

- diffractometer control and data collection (STOE): WINXPOW^[21]
- data analysis (STOE): WINXPOW^[22]
- data integration (Synchrotron): DIOPTAS^[23]
- Rietveld refinements: GSAS-II,^[24] TOPAS^[25]
- graphical representation: XMGrace^[26]

3.3.3 DSC

- data collection and processing: NETZSCH Proteus^[27]
- graphical representation: XMGrace^[26]

3.3.4 Cyclic Voltammetry

- device control and data collection: NOVA^[28]
- data analysis: ORIGINPRO^[29]
- graphical representation: XMGrace^[26]

3.3.5 Databases

- Inorganic Crystal Structure Database (ICSD)^[30]
- Pearson's Crystal Data - Crystal Structure Database for Inorganic Compounds^[31]

3.3.6 Other Software

- 2D graph generation: XMGrace^[26]
- Complexity analysis: CRYSTIT^[32]
- Preparation of graphics and setups: INKSCAPE^[33]
- L^AT_EX-Editor: OVERLEAF

3.4 Preparative Strategies for Amalgams

3.4.1 Established Preparative Strategies

From stoichiometric mixtures of the elements

The simplest preparative strategy consists of weighing the elements in the desired stoichiometric amounts into an ampule, sealing it and subject it to a dedicated temperature treatment. This is advantageous for all congruently melting amalgams and has successfully been performed for e.g. NaHg₂,^[34] SrHg^[35] or YbHg.^[36] In some cases, especially low reaction temperatures allow for a simple setup, in which the elements are filled in a Schlenk tube and are heated to a homogeneous melt with a heat gun. This has proven to be suitable for e.g. Rb₃Hg₂₀ (see Fig. 3.4). Caution has to be applied when mixing alkali metals with mercury. This is generally very exothermic and has to be performed very slowly in order to prevent evaporation of mercury.

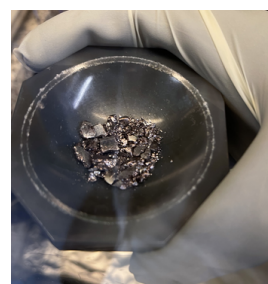


Fig. 3.4: Violet, crystalline solid of Rb₃Hg₂₀.

From the elements, by quenching and tempering

Many amalgams do not melt congruently, and therefore cannot be obtained by slow cooling of a melt. In many cases, rapid quenching of a melt with desired stoichiometric composition and subsequent tempering just below the peritectic decomposition temperature, sometimes for several months, has proven successful.^[37–41]

From the elements, employing a Hg surplus

Refluxing the electropositive metal with a surplus of mercury (e.g. ratios of M : Hg = 1 : 20) in vertical glass ampoules, where only the lower part is heated in a furnace and the upper part is cooled in air was suitable for the preparation of Hg-rich lanthanoid metal amalgams such as RE_{11+x}Hg_{55-x} or RE_{11+x}Hg_{45-x}.^[42] The ampoules had a constriction in the middle which allowed to distill off the surplus mercury after the synthesis and separating it from the remaining solid amalgam by sealing off the ampule at the constriction.

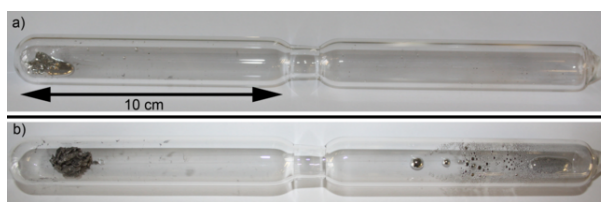


Fig. 3.5: Glass ampoules for the synthesis of RE_{11+x}Hg_{55-x}. (a, top): rare earth metal with Hg, sealed under vacuum. (b, bottom): product (left) and surplus Hg (right) after distillation. The constriction (middle) enables the isolation of the product via flame sealing.

3.4.2 New Preparative Strategies

From the elements, the ‘cryogenic method’

To avoid extreme heating during the mixing of alkali or alkaline earth elements with mercury, which would be sufficient to destroy especially Hg-rich amalgams due to their very low decomposition temperatures, a new method was developed. It shows to be generally very helpful for the Hg-richest amalgams and was employed for e.g. KHg_{11} and RbHg_{11} , which have decomposition temperatures of ca. 70°C . They can be obtained as phasepure material in gram scale by adding Hg in a dropwise manner under reverse flow onto the cooled ($\vartheta = -78^\circ\text{C}$, with a dry ice/acetone mixture) alkali metal. The mixture is then allowed to slowly thaw to RT in the cooling bath.

Electrocrystallisation

Isothermal electrocrystallisation has proven a generally appropriate way to prepare Hg-rich amalgams even with lowest thermal decomposition temperatures in high yield and high crystallinity. The process has been reported before^[43] and is being adapted now for ternary amalgams. The details of the process are presented in the following:

In order to perform electrochemical syntheses, a specially devised apparatus for isothermal electrocrystallisation was used (see Fig. 3.6). This apparatus enables the electrosynthesis of tempered solutions of salts of less-noble metals in polar, aprotic solvents under inert gas conditions. In the electrolysis apparatus, anodic and cathodic region are separated with a glass frit.

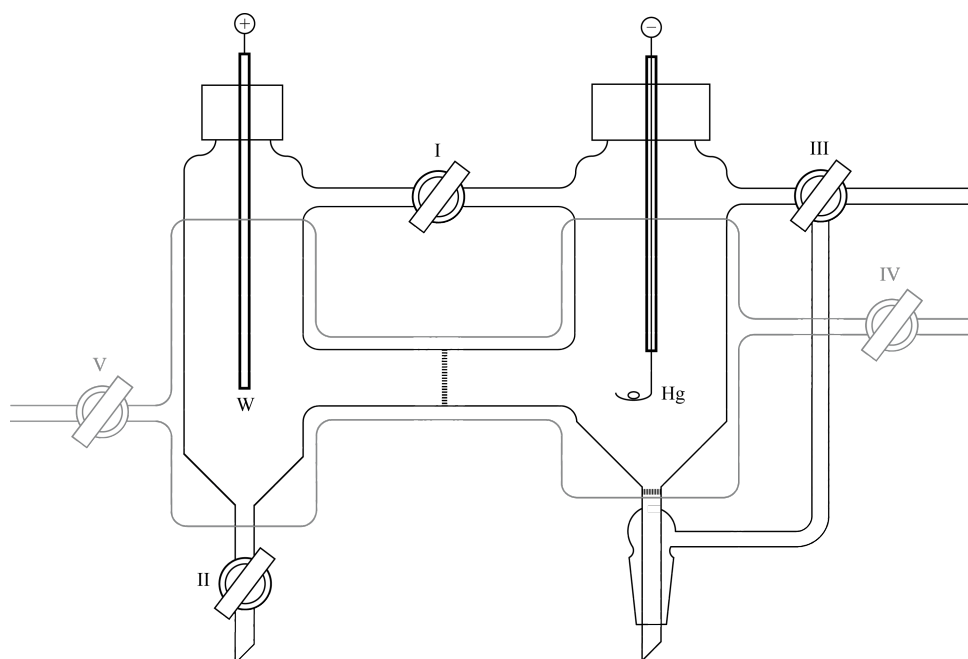


Fig. 3.6: Apparatus for performing anhydrous electrolysis used in this work.

The valve **I** (NS 14) enables a pressure equilibration between the two half cells, while valve **II**, which is attached to the anodic half cell, serves as a drainage for the electrolyte or solvent. Both half cells possess glass screw threads at the top, which can be connected with screw caps (for evacuation) or the desired electrodes (for electrolysis). The flow of inert gas or vacuum can be switched via valve **III**. Additionally, the cathodic half cell contains a glass frit and an inner NS14 glass joint with a lateral pressure balance. At the level of the amalgamated copper spoon, another inner NS14 glass joint serves as an access point for the direct manipulation of the spoon, as well as sample recovery (due to the non-usage, not depicted). The temperature

of the synthesis can be controlled via connection of a cryostat or thermostat to valves **IV** and **V**, which give access to the cooling jacket (highlighted in grey). A tungsten rod (**W**) serves as the cathode, while the anode is made of an amalgamated copper spoon (**Hg**). For this purpose, a copper spoon was immersed in half-concentrated nitric acid, which contained small amounts of dissolved mercury. The spoon was rinsed multiple times with distilled water, carefully dried with a paper towel. It was then attached to a crocodile clip connected to a platinum wire, which was in turn connected to the d.c. source (Voltage Transformer Type L30/5 BA, ZENTRO ELEKTRONIK GMBH, Bad Wildbad, Germany; Ela-precision, max. load voltage 10 V, max. load current 5 A).

If not stated otherwise, all electrolyses were performed as described in the following paragraph. Before each usage, the glass apparatus was cleaned in a *i*-PrOH/KOH-bath and subsequently in a HCl-bath ($c = 0.1 \text{ mol L}^{-1}$), afterwards dried in a drying oven at 105°C and stored there until the experiment. Assembly and connecting to the Schlenk system was performed while the apparatus was still hot. It was then evacuated ($p \leq 1 \times 10^{-3} \text{ mbar}$) and flooded with Argon three times. Under reverse Ar flow, the anodic chamber was filled with the respective freshly prepared metal iodide solution ($c = 0.1 \text{ mol L}^{-1}$). The electrodes were inserted and sealed using quickfits, connected with the voltage source via crocodile clips and the experiment was then started.

Electrocrystallisation of BeI_2 in liquid NH_3

A dedicated apparatus for the isothermal electrocrystallisation has been developed especially for the synthesis of beryllium amalgam. This is also presented with more detail in Chapter 4.7.

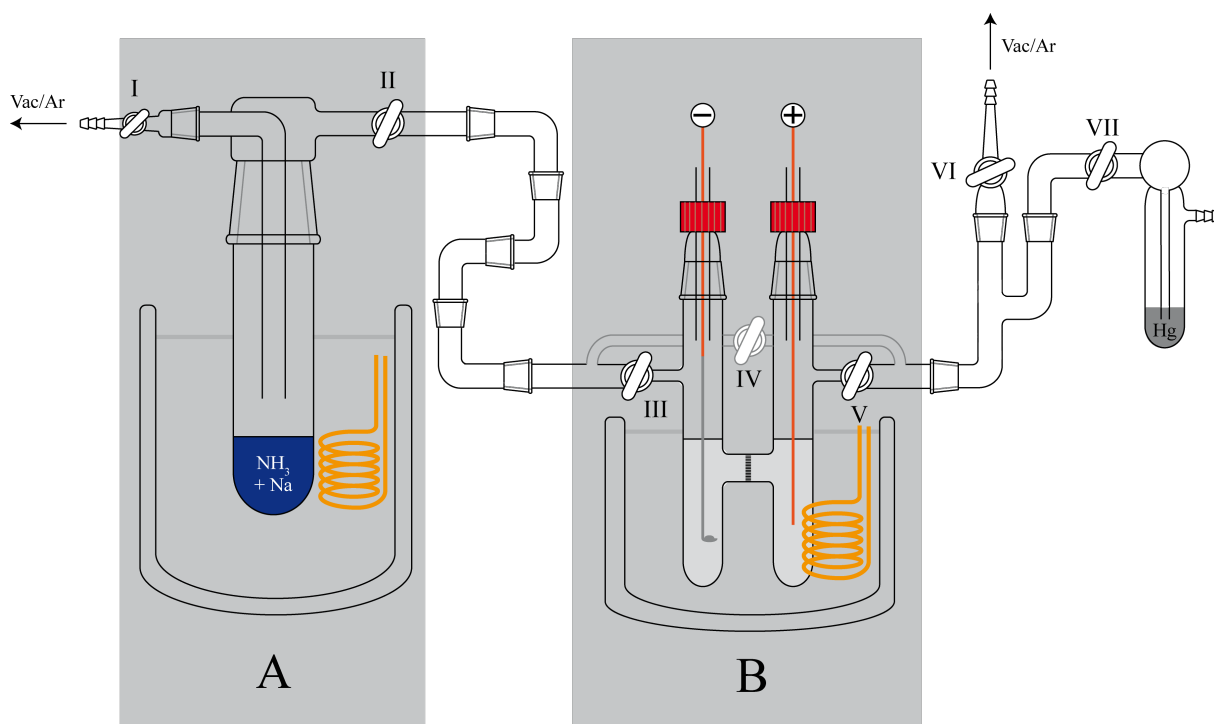


Fig. 3.7: Apparatus for performing the electrolysis of BeI_2 in liquid ammonia.

CAUTION: The greatest danger of the setup is posed by the outage of the cryostat, which in turn leads to a buildup of high pressure from liquid ammonia. Therefore, the usage of pressure relief valves (in this setup filled with mercury) is absolutely required. Furthermore, Beryllium

and its compounds are regarded as toxic and carcinogenic. Because the biochemical mechanisms that cause beryllium associated diseases are still unknown, special (safety) precautions are strongly advised.^[1]

The setup shown in Fig. 3.7 comprises a cooling trap (**A**) and an electrolysis chamber (**B**). Via valve **I** the cooling trap was evacuated. Prior to synthesis, it was filled with elemental Na inside the glovebox (approx. 1 cm³). Via valve **VI** the electrolysis chamber was evacuated. It was loaded with 2.1 g BeI₂ inside the glovebox, attached to the setup and kept under Ar until the start of the electrolysis. Afterwards, the rest of the setup was evacuated ($\leq 1 \times 10^{-3}$ mbar) and flushed with Ar thrice (Valves **IV** and **VI** open, the rest closed). Valve **VI** was closed, valves **I**, **II** and **III** opened and the cooling trap A used for drying the NH₃ and serving as reservoir was flushed with NH₃. Condensation was started after 5 min with the cryostat temperature set to -65 °C. After a sufficient amount (150 mL) of cornflower blue electride was visible, NH₃ flow was stopped, valves **III** and **V** were opened, the temperature of the cryostat for the electrolysis chamber set to -60 °C, while the temperature of the cooling bath A was increased to -35 °C. This enables a distillation of completely dry ammonia. To avoid possible loss of electrolyte through evaporation/boiling of NH₃, a sufficient amount (approx. 50 mL of freshly dried NH₃ was kept in the cooling trap. The electrodes were self-made of Cu wire, with an amalgamated Cu spoon filled with a small amount of elemental Hg attached to the cathode.

After decreasing the temperature of the electrolysis chamber to -37 °C to account for evaporation through heat generation of the electric current, the experiment was started (terminal voltage 5 V, after 15 min 10 V). In total, electrolysis was performed over 17 h. A formation of a crystalline, metallic solid was observed at the cathode spoon. The system was carefully allowed to warm up to RT and the electrolysis chamber evacuated.

Analysis: Via pXRD, the obtained solid was identified as Cu₇Hg₆ (see Fig. 7.91, p. 168). Furthermore, it was discovered that the Cu originated from the anode, which was replaced with tungsten for the following experiment.

To inhibit the formation of Cu₇Hg₆, the copper cathode was replaced by a tungsten rod (0.75 mm), which was in turn flame-sealed in a glass tube. Furthermore, an additional Hg pressure release and a one-way valve was integrated in the apparatus between the valves **II** and **III** in order to allow for parallel condensation of NH₃ without interruption of the electrosynthesis. The electrolysis lasted for 44 hours in total, after which the system was slowly warmed up to RT and evacuated for removal of residual ammonia. A silver-black, crystalline solid was obtained.

Analysis: All attempts for the analysis were unsuccessful. The obtained compound disintegrated when ground in an agate mortar, resulting in elemental mercury droplets. Isolation of single crystals was also not possible, since the crystals rapidly dissolved in either freshly dried paraffin oil as well as dried perfluorinated paraffin oil.

3.4.3 A screening strategy to identify promising systems for ternary amalgams

Combining three elements sometimes results in the formation of at least one ternary compound, in other cases, only binary products are formed. When attempting to study a large number of ternary systems systematically for the presence of ternary compounds, a rapid and easy screening procedure of all available systems is needed in order to identify the most promising candidate systems. The systems which have to be considered for the systematic studies on ternary amalgams of the less-noble metals comprise the 5 alkali (Li–Cs), 5 alkaline earth (Be–Ba) and 16 lanthanoid metals (Sc, Y, La–Lu, without Pm) and their combinations. This results in 676 ternary amalgam system candidates. For many of the respective binary systems, amalgam crystal structures or even the phase diagrams are available. This enables a fast screening by a combination of thermoanalytical and powder X-ray diffraction experiments.

For the ternary systems, samples with compositions $M^I : M^{II} : \text{Hg} = 1 : 1 : 10$ were weighed into small tantalum ampules and analysed with DSC measurements (see Chapter 3.2.3). The detected signals were compared to the reported phase diagrams and the samples resulting from the DSC runs were subsequently analysed with X-ray powder diffraction. The systems which showed DSC signals not belonging to binary phases and showing unindexed powder patterns were regarded as prime candidates for subsequent detailed studies of phase formations. As highlighted in Fig. 3.8, the screening experiments are valuable; this particular example lead to the synthesis and structural characterisation of the new ternary amalgam $\text{Yb}_{10.7}\text{Sr}_{0.3}\text{Hg}_{54}$ (cf. Chapter 4.2).

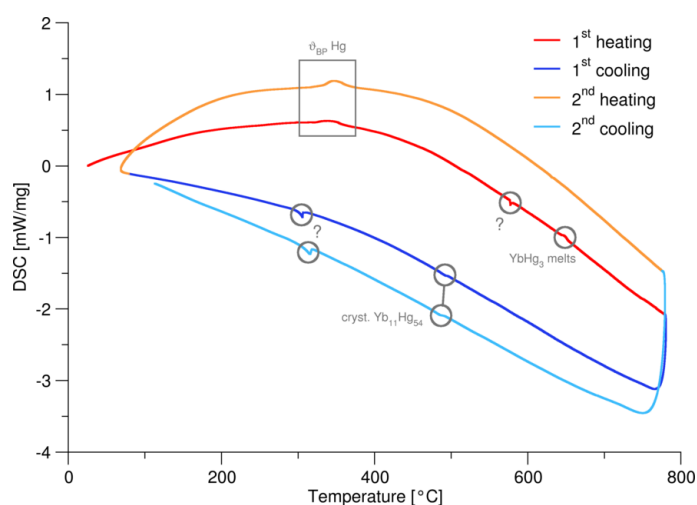


Fig. 3.8: Exemplary DSC screening measurement in the Sr–Yb–Hg system. Direct assignment of the DSC signals was possible for the boiling of Hg, melting of YbHg_3 and the formation of $\text{Yb}_{11}\text{Hg}_{54}$. The existence of additional DSC signals indicates the formation of ternary phases.

References

- [1] D. Naglav, M. R. Buchner, G. Bendt, F. Kraus, S. Schulz, Off the Beaten Track - A Hitchhiker's Guide to Beryllium Chemistry, *Angew. Chem. Int. Ed.* **2016**, *55*, 10562–10576, DOI: 10.1002/anie.201601809.
- [2] G. B. Wood, A. Brenner, Electrodeposition of Metals from Organic Solutions, *J. Electrochem. Soc.* **1957**, *11*, 29–37, DOI: 10.1149/1.2428491.
- [3] G. Brauer, *Handbook of Preparative Inorganic Chemistry*, Vol. 1, 2nd ed., Academic Press, New York (NY), USA, **1963**, pp. 892–893.
- [4] C. Hoch, Syntheses and crystal structures of solvate complexes of alkaline earth and lanthanoid metal iodides with *N,N*-dimethylformamide, *Z. Kristallogr.* **2020**, *235*, 401–411, DOI: 0.1515/zkri-2020-0071.
- [5] *MULTIVU*, QUANTUM DESIGN Inc., San Diego (CA), USA, version 1.5.11, **2013**.
- [6] P. Blaha, K. Schwarz, F. Tran, R. Laskowski, G. Madsen, L. Marks, WIEN2k: An APW+lo program for calculating the properties of solids, *J. Chem. Phys.* **2020**, *152*, 074101, DOI: 10.1063/1.5143061.

- [7] K. Lejaeghere, G. Bihlmayer, T. Björkman, P. Blaha, S. Blügel, V. Blum, D. Caliste, I. E. Castelli, S. J. Clark, A. Dal Corso, S. de Gironcoli, T. Deutsch, J. K. Dewhurst, I. Di Marco, C. Draxl, M. Dułak, O. Eriksson, J. A. Flores-Livas, K. F. Garrity, L. Genovese, P. Giannozzi, M. Giantomassi, S. Goedecker, X. Gonze, O. Grånäs, E. K. U. Gross, A. Gulans, F. Gygi, D. R. Hamann, P. J. Hasnip, N. A. W. Holzwarth, D. Iuşan, D. B. Jochym, F. Jollet, D. Jones, G. Kresse, K. Koepernik, E. Küçükbenli, Y. O. Kvashnin, I. L. M. Locht, S. Lubeck, M. Marsman, M. Marzari, U. Nitzsche, L. Nordström, T. Ozaki, L. Paulatto, C. J. Pickard, W. Poelmans, M. I. J. Probert, K. Refson, M. Richter, G.-M. Rignanese, S. Saha, M. Scheffler, M. Schlipf, K. Schwarz, S. Sharma, F. Tavazza, P. Thunström, A. Tkatchenko, M. Torrent, D. Vanderbilt, M. J. van Setten, V. Van Speybroeck, J. M. Wills, J. R. Yates, G.-X. Zhang, S. Cottenier, Reproducibility in density functional theory calculations of solids, *Science* **2016**, *351*, 1415, DOI: [10.1126/science.aad3000](https://doi.org/10.1126/science.aad3000).
- [8] P. Haas, F. Tran, P. Blaha, Calculation of the lattice constant of solids with semilocal functionals, *Phys. Rev. B* **2009**, *79*, 085104, DOI: [10.1103/PhysRevB.79.085104](https://doi.org/10.1103/PhysRevB.79.085104).
- [9] J. P. Perdew, K. Burke, M. Enzerhof, Generalized Gradient Approximation Made Simple, *Phys. Rev. Lett.* **1996**, *77*, 3865–3868, DOI: [10.1103/PhysRevLett.77.3865](https://doi.org/10.1103/PhysRevLett.77.3865).
- [10] G. I. Csonka, J. P. Perdew, A. Ruzsinszky, P. H. T. Philipsen, S. Lebègue, J. Paier, O. A. Vydrov, J. G. Ángyán, Assessing the performance of recent density functionals for bulk solids, *Phys. Rev. B* **2009**, *79*, 155107, DOI: [10.1103/PhysRevB.79.155107](https://doi.org/10.1103/PhysRevB.79.155107).
- [11] H. Ebert, D. Ködderitzsch, J. Minár, Calculating condensed matter properties using the KKR-Green's function method—recent developments and applications, *J. Rep. Prog. Phys.* **2011**, *74*, 096501, DOI: [10.1088/0034-4885/74/9/096501](https://doi.org/10.1088/0034-4885/74/9/096501).
- [12] H. Ebert, M. Battocletti, D. Banea, S. Bornemann, J. Braun, S. Chadov, M. Deng, H. Freyer, T. Huhne, D. Ködderitzsch, M. Kosuth, S. Lowitzer, S. Mankovsky, J. Minár, A. Perlov, V. Popescu, O. Sipr, C. Zecha, The Munich SPR-KKR Package, version 7.7, **2012**.
- [13] H. S. Vosko, L. Wilk, M. Nusair, Accurate spin-dependent electron liquid correlation energies for local spin density calculations: a critical analysis, *Can. J. Phys.* **1980**, *58*, 1200–1211, DOI: [10.1139/p80-159](https://doi.org/10.1139/p80-159).
- [14] APEX3, BRUKER AXS GmbH, Karlsruhe, Deutschland, version 2018.1-0, **2018**.
- [15] IPDS CONTROL SOFTWARE X-AREA, STOE & Cie. GmbH, Darmstadt, Deutschland, version 1.39, **2006**.
- [16] X-RED, STOE & Cie. GmbH, Darmstadt, Deutschland, version 1.3.1, **2005**.
- [17] X-SHAPE, STOE & Cie. GmbH, Darmstadt, Deutschland, version 2.0.7, **2005**.
- [18] G. M. Sheldrick, A short history of SHELX, *Acta Crystallogr.* **2008**, *A64*, 112–122, DOI: [10.1107/S0108767307043930](https://doi.org/10.1107/S0108767307043930).
- [19] A. L. Spek, Structure validation in chemical crystallography, *Acta Crystallogr.* **2009**, *D65*, 148, DOI: [10.1107/S090744490804362X](https://doi.org/10.1107/S090744490804362X).
- [20] L. W. Finger, M. Kroeker, B. H. Toby, DRAWxtl, an open-source computer program to produce crystal structure drawings, *J. Appl. Crystallogr.* **2007**, *40*, 188–192, DOI: [10.1107/S0021889806051557](https://doi.org/10.1107/S0021889806051557).
- [21] WINXPOW, STOE & Cie. GmbH, Darmstadt, Deutschland, version 2.9.9, **2007**.
- [22] WINXPOW, STOE & Cie. GmbH, Darmstadt, Deutschland, version 2.12, **2007**.
- [23] C. Prescher, V. B. Prakapenka, DIOPTAS: a program for reduction of two-dimensional X-ray diffraction data and data exploration, *High Press. Res.* **2015**, *35*, 223–230, DOI: [10.1080/08957959.2015.1059835](https://doi.org/10.1080/08957959.2015.1059835).
- [24] B. H. Toby, R. B. Von Dreele, GSAS-II: the genesis of a modern open-source all purpose crystallography software package, *J. Appl. Crystallogr.* **2013**, *46*, 544–549, DOI: [10.1107/S0021889813003531](https://doi.org/10.1107/S0021889813003531).
- [25] A. A. Coelho, TOPAS and TOPAS-Academic: an optimization program integrating computer algebra and crystallographic objects written in C++, *J. Appl. Cryst.* **2018**, *51*, 210–218, DOI: [10.1107/S1600576718000183](https://doi.org/10.1107/S1600576718000183).
- [26] XMGRACE, Grace Development Team - E. Stambulchik, Rehovot, Israel, version 5.1.25, **2015**.

- [27] *NETZSCH PROTEUS THERMAL ANALYSIS*, NETZSCH Gerätebau GmbH, Selb, Deutschland, version 6.1.0, **2017**.
- [28] *NOVA*, METROHM AUTOLAB & B.V., Utrecht, Niederlande, version 2.1.5, **2021**.
- [29] *ORIGINPRO 2019B*, ORIGINLAB, Northampton, MA, USA, version 9.6.5.169, **2019**.
- [30] Inorganic Crystal Structure Database, FIZ Karlsruhe, version 2012-1, <https://icsd.fiz-karlsruhe.de>.
- [31] *PEARSON'S CRYSTAL DATA*, K. Cenzual, P. Villars, ASM International N.V., Materials Park (OH), USA, **2016**.
- [32] C. Kaußler, G. Kieslich, crystIT: complexity and configurational entropy of crystal structures via information theory, *J. Appl. Crystallogr.* **2021**, *54*, 306–316, DOI: [10.1107/S1600576720016386](https://doi.org/10.1107/S1600576720016386).
- [33] *INKSCAPE*, Open Source Software licensed under GPL, Inkscape development team, version 1.1.2, **2021**.
- [34] J. W. Nielsen, N. C. Baenziger, The Crystal Structures of NaHg₂, NaHg and Na₃Hg₂, *Acta Crystallogr.* **1954**, *7*, 277–282, DOI: [10.1107/S0365110X54000783](https://doi.org/10.1107/S0365110X54000783).
- [35] G. Bruzzone, F. Merlo, The Strontium-Mercury System, *J. Less-Common Met.* **1974**, *35*, 153–157, DOI: [10.1016/0022-5088\(74\)90154-4](https://doi.org/10.1016/0022-5088(74)90154-4).
- [36] A. Iandelli, A. Palenzona, Atomic size of rare earths in intermetallic compounds. MX compounds of CsCl type, *J. Less-Common Met.* **1965**, *9*, 1–6.
- [37] H.-J. Deiseroth, Discrete and extended metal clusters in alloys with mercury and other group 12 elements. In *Molecular Clusters of the Main Group Elements*, (Eds.: M. Driess, H. Nöth), Wiley-VCH, Weinheim, Germany, **2004**, pp. 169–187.
- [38] E. Biehl, H.-J. Deiseroth, Darstellung, Strukturchemie und Magnetismus der Amalgame MHg₁₁ (M: K, Rb, Ba, Sr), *Z. Anorg. Allg. Chem.* **1999**, *625*, 1073–1080, DOI: [10.1002/\(SICI\)1521-3749\(199907\)625:7<1073::AID-ZAAC1073>3.0.CO;2-V](https://doi.org/10.1002/(SICI)1521-3749(199907)625:7<1073::AID-ZAAC1073>3.0.CO;2-V).
- [39] E. Biehl, H.-J. Deiseroth, Rb₅Hg₁₉: Eine neue, geordnete Defektvariante des BaAl₄-Strukturtyps, *Z. Anorg. Allg. Chem.* **1999**, *625*, 389–394, DOI: [10.1002/\(SICI\)1521-3749\(199903\)625:3<389::AID-ZAAC389>3.0.CO;2-9](https://doi.org/10.1002/(SICI)1521-3749(199903)625:3<389::AID-ZAAC389>3.0.CO;2-9).
- [40] H.-J. Deiseroth, A. Strunck, W. Bauhofer, CsHg, eine ungewöhnliche Variante der CsCl-Struktur Darstellung, Kristallstruktur und physikalische Eigenschaften, *Z. Anorg. Allg. Chem.* **1989**, *575*, 31–38, DOI: [10.1002/zaac.19895750106](https://doi.org/10.1002/zaac.19895750106).
- [41] H.-J. Deiseroth, A. Stupperich, R. Pankaluoto, N. E. Christensen, NaHg: A variant of the cesium-chloride structure structural relations and electronic structure, *Z. Anorg. Allg. Chem.* **1991**, *597*, 41–50, DOI: [zaac.19915970107](https://doi.org/10.1002/zaac.19915970107).
- [42] F. Tambornino, *Electrolytic Synthesis and Structural Chemistry of Intermetallic Phases with Polar Metal-Metal Bonding*, Dissertation, LMU München, **2016**.
- [43] F. Tambornino, J. Sappl, F. Pultar, T. M. Cong, S. Hübner, T. Giftthaler, C. Hoch, Electrocrystallization - a synthetic method for intermetallic phases with polar metal-metal bonding, *Inorg. Chem.* **2016**, *55*, 11551–11559, DOI: [10.1021/acs.inorgchem.6b02068](https://doi.org/10.1021/acs.inorgchem.6b02068).

4

Results & Discussion

4.1 Structure and Bonding in CsNa₂Hg₁₈, a New Ternary Amalgam with strong Coulombic Bonding Contributions

Timotheus Hohl¹, Frank Tambornino² and Constantin Hoch^{1,*}

* Correspondence: constantin.hoch@cup.uni-muenchen.de; Tel.: +49-89-2180-77421

¹ Department Chemie, LMU München, Butenandtstraße 5-13(D), D-81377 München, Germany; timotheus.hohl@cup.uni-muenchen.de; constantin.hoch@cup.uni-muenchen.de

² Fachbereich Chemie, Universität Marburg, Hans-Meerwein-Straße 4, D-35032 Marburg, Germany; frank.tambornino@chemie.uni-marburg.de

published in: *Crystals* **2022**, *12*, 1679.

DOI: [10.3390/cryst12111679](https://doi.org/10.3390/cryst12111679)

Reprinted in a slightly adapted version from *Crystals*. Copyright 2022 by the authors, licensee MDPI, Basel, Switzerland. This article is an open article distributed under the terms and conditions of the Creative Commons Attribution license (<http://creativecommons.org/licenses/by/4.0/>). Full text available under <https://doi.org/10.3390/cryst12111679>.

4.1.1 Abstract

The new ternary amalgam CsNa₂Hg₁₈ was synthesised from the elements in an unconventional low-temperature procedure. It crystallises in an own tetragonal structure type (space group *I4/mmm*, $a = 7.3054(7)$ and $c = 20.046$ Å) and combines ionic and metallic bonding contributions. In the crystal structure, Cs and Na atoms are embedded in a Hg scaffold with highly covalent Hg–Hg bonding. The alkali metal atoms are coordinated exclusively by Hg atoms in unusual environments with coordination numbers CN = 24 for Cs and CN = 16 for Na. Polar amalgams are suitable model systems for studying the parameters influencing the ‘bad metal’ behaviour in polar intermetallic phases. We present structural studies on the basis of powder and single crystal diffraction data together with measurements of the specific resistivity and DFT calculations of the electronic structure. For CsNa₂Hg₁₈, a high specific resistivity can be observed, but the Ioffe-Regel saturation of the resistivity is much less expressed than in other polar amalgams.

4.1.2 Introduction

The number of preparative and structural studies on binary amalgams of the less noble metals is considerable.^[1,2] Their structural chemistry is extremely rich, owing to the versatile bonding characteristics of negatively polarised Hg^{δ-}. As Hg has a thermodynamically unfavourable electron affinity and does for example not form an anion in the gas phase,^[3] a Zintl-analogous

anion Hg^- is unknown, yet a certain negative partial charge can be stabilised in the crystal lattice. This partial charge increases with the Hg content of the amalgams as the unfavourable electron density can be better delocalised over a larger number of Hg atoms. A hypothetical Hg^- would have the electron configuration $[\text{Xe}]4f^{14}5d^{10}6s^26p^1$, and for this reason, p - p σ interactions can be expected. Mixing of s and p (and d) states is to a certain extent hampered by spin-orbit coupling and relativistic effects, which make the structural chemistry of amalgams so unique. A versatile mixture of metallic, ionic and covalent bonding contributions occurs, depending on the amount of Hg present in the amalgams, on the quotients of the atomic radii and on the extent of the electron transfer. In Hg-poor amalgams, isolated Hg atoms occur, but with rising Hg content, soon Hg–Hg bonding is found. In some amalgams, $[\text{Hg}_4]$ square groups are present with 90° interatomic angles as an expression of the abovementioned p - p σ bonding situation.^[4–6] Further, $[\text{Hg}_8]$ cubes or ladders of $[\text{Hg}_4]$ squares are known.^[7,8] In Hg-rich amalgams, more and more d participation leads to complex networks, and the $[\text{Hg}_{12}]$ icosahedron is one of the predominant structural motifs. In this case, the close relation of $\text{Hg}^{\delta-}$ to the electron-deficient p^1 metals and their structures becomes evident.

A second frequent structural feature contrasting the covalent Hg–Hg interactions is the tendency of the polar amalgams to form coordination polyhedra of Hg atoms (‘anions’) around the less noble metal atoms (‘cations’). This, of course, is more pronounced in Hg-rich amalgams for reasons of stoichiometry, but also in Hg-poor amalgams, the tendency to avoid cation-cation contacts becomes evident. Hg coordinated polyhedra around the electropositive metal atoms vary depending on the atomic sizes from $[\text{MHg}_8]$ (e.g. in HgMn ^[9] with $r_{\text{Mn}}/r_{\text{Hg}} = 0.9$) to $[\text{MHg}_{24}]$ (e.g. in the title compound $\text{CsNa}_2\text{Hg}_{18}$ with $r_{\text{Cs}}/r_{\text{Hg}} = 1.7$). As Hg is a medium to small-sized metal atom ($r_{\text{Hg}}^{\text{met}} = 150$ pm),^[10] an atomic radii quotient $r_{\text{M}}/r_{\text{Hg}}$ of roughly 1 is a common case. Therefore, in Hg-rich amalgams, coordination numbers CN of ≥ 12 occur frequently, and (anti-)cuboctahedra $[\text{MHg}_{12}]$, icosahedra $[\text{MHg}_{12}]$, Frank–Kasper polyhedra $[\text{MHg}_{14–16}]$ are common structural motifs.

The third structural motif often found in amalgams of less noble metals is the tendency to form closest sphere packings or structural cut-outs thereof. The large structure family of amalgams of $\text{Ag}_{14}\text{Gd}_{54}$ -related structures shows the tendency toward formation of an hcp lattice very clearly.^[11,12] The structures of other amalgams can be rationalised as arrangements of more or less close-packed nets; others show arrangements of octahedra and tetrahedra as motifs from closest sphere packings. In all of these cases, the metal atomic radius quotient is close to 1.

These three structural motifs – covalent Hg networks, coordination polyhedra $[\text{MHg}_n]$ and variations of closest sphere packings – often occur at the same time, and it is, to a certain extent, arbitrary which aspect is emphasised in the respective structural description. A structural discussion focussing on ionic polarity and electron transfer from the less noble metal on Hg may utilise the more ‘ionic picture’ of coordination polyhedra while a more ‘intermetallic picture’ may focus on the sphere packing aspects. Emphasising the electronic configuration of the Hg atoms may afford for the ‘covalent picture’, highlighting the Hg network with Hg–Hg bonding. In many cases, all three aspects are shown for a given amalgam structure.

In contrast to the manifold studies on binary amalgams, knowledge on ternary amalgams is scarce. The only examples for ternary amalgams containing two less noble metals simultaneously are $\text{NaK}_{29}\text{Hg}_{48}$,^[13] Li_2MgHg ,^[14] $\text{Li}_6\text{Ca}_{17}\text{Hg}_9$, $\text{Li}_6\text{Sr}_{17}\text{Hg}_9$ and $\text{Li}_6\text{Yb}_{17}\text{Hg}_9$.^[15] Other amalgams with participation of transition metals next to less noble metals also are known. All structurally characterised ternary amalgams with participation of at least one less noble metal are compiled in Table 4.1.

Table 4.1: Ternary amalgams described in the literature containing at least one less noble (= alkali, alkaline earth or lanthanoid) metal. Data are compiled from Pearson's Crystal Data.^[16]

Phase	space group	struct. type	Lit.	Phase	space group	struct. type	Lit.
Ternary amalgams with alkali metals							
Li ₂ MgHg	<i>Fm</i> 3 <i>m</i>	Cu ₂ MnAl	[14]	KAsHg	<i>P</i> 6 ₃ / <i>m</i> <i>m</i> <i>c</i>	BeZrSi	[17]
Li ₂ GeHg	<i>Fm</i> 3 <i>m</i>	Cu ₂ MnAl	[18]	KSbHg	<i>P</i> 6 ₃ / <i>m</i> <i>m</i> <i>c</i>	BeZrSi	[17]
Li ₆ Ca ₁₇ Hg ₉	<i>Im</i> 3 <i>m</i>	own	[15]	KC ₄ Hg	<i>F</i> ddd	own	[19]
Li ₆ Sr ₁₇ Hg ₉	<i>Im</i> 3 <i>m</i>	Li ₆ Ca ₁₇ Hg ₉	[15]	K ₄ Ge _{21.3} Hg _{1.7}	<i>Pm</i> 3 <i>n</i>	Na ₄ Si ₂₃	[20]
Li ₆ Yb ₁₇ Hg ₉	<i>Im</i> 3 <i>m</i>	Li ₆ Ca ₁₇ Hg ₉	[15]	K ₄ Ge _{21.4} Hg _{1.6}	<i>Pm</i> 3 <i>n</i>	Na ₄ Si ₂₃	[20]
LiTl _{0.5} Hg _{0.5}	<i>Pm</i> 3 <i>m</i>	CsCl	[21]	K ₄ Sn ₂₁ Hg ₂	<i>Pm</i> 3 <i>n</i>	Na ₄ Si ₂₃	[22]
Na ₂ SnHg	<i>F</i> 43 <i>m</i>	Li ₂ AgSb	[23]	K ₈ In ₁₀ Hg	<i>P</i> 6 ₃ / <i>m</i>	own	[24]
Na ₂ PbHg	<i>F</i> 43 <i>m</i>	Li ₂ AgSb	[23]	Rb ₄ Ge _{21.3} Hg _{1.7}	<i>Pm</i> 3 <i>n</i>	Na ₄ Si ₂₃	[20]
Na ₅ Sn _{9.6} Hg _{2.4}	<i>Pbcn</i>	own	[25]	Rb ₄ Ge _{21.5} Hg _{1.5}	<i>Pm</i> 3 <i>n</i>	Na ₄ Si ₂₃	[20]
NaTl _{0.5} Hg _{0.5}	<i>F</i> d3 <i>m</i>	NaTl	[26]	Rb ₄ Sn ₂₁ Hg ₂	<i>Pm</i> 3 <i>n</i>	Na ₄ Si ₂₃	[22]
Na _{2.1} C ₆₀ Hg _{0.2}	<i>Pa</i> 3	own	[27]	Cs ₄ Sn ₂₁ Hg ₂	<i>Pm</i> 3 <i>n</i>	Na ₄ Si ₂₃	[22]
Na ₂ C ₆₀ Hg _{0.2}	<i>Pa</i> 3	Na ₂ RbC ₆₀	[27]				
NaK ₂₉ Hg ₄₈	<i>Pm</i> 3 <i>n</i>	own	[13]				
Ternary amalgams with alkaline earth metals							
MgLi ₂ Hg	<i>Fm</i> 3 <i>m</i>	Cu ₂ MnAl	[14]	BaGa _{0.8} Hg _{5.2}	<i>Cmcm</i>	own	[28]
Mg ₂₁ Ga ₅ Hg ₃	<i>I</i> 4 ₁ / <i>a</i>	Pt ₈ Al ₂₁	[29]	BaGa _{1.9} Hg _{2.1}	<i>I</i> 4 ₁ / <i>amd</i>	own	[28]
Mg ₂ Au _{0.5} Hg _{0.5}	<i>Pnma</i>	Co ₂ Si	[30]	Ba ₃ Ga _{0.2} Hg _{10.8}	<i>Pm</i> mmn	Ba ₃ ZnHg ₁₀	[28]
MgAu _{0.67} Hg _{0.33}	<i>Pm</i> 3 <i>m</i>	CsCl	[30]	BaIn _{1.1} Hg _{0.9}	<i>Imma</i>	KHg ₂	[31]
Mg ₃ Au _{0.7} Hg _{0.3}	<i>P</i> 6 ₃ / <i>m</i> <i>m</i> <i>c</i>	Na ₃ As	[30]	BaIn _{1.7} Hg _{2.3}	<i>I</i> 4/ <i>mmm</i>	BaAl ₄	[28]
Ca ₁₇ Li ₆ Hg ₉	<i>Im</i> 3 <i>m</i>	own	[15]	BaIn _{2.8} Hg _{8.2}	<i>Pm</i> 3 <i>m</i>	BaHg ₁₁	[32]
CaSn _{0.7} Hg _{1.3}	<i>P</i> 6/ <i>mmm</i>	UHg ₂	[33]	BaIn _{1.2} Hg _{4.8}	<i>Pnma</i>	BaHg ₆	[34]
BaHgSn	<i>P</i> 6 ₃ <i>mc</i>	LiGaGe	[33]	BaIn _{3.1} Hg _{3.9}	<i>C</i> mmm	own	[32]
CaPbHg	<i>P</i> 6 ₃ / <i>m</i> <i>m</i> <i>c</i>	BeZrSi	[33]	Ba ₃ InHg ₁₀	<i>I</i> mmm	La ₃ Al ₁₁	[28]
Ca ₄ Zn _{4.5} Hg _{4.5}	<i>P</i> 43 <i>m</i>	Cu ₉ Al ₄	[35]	BaTl ₂ Hg ₂	<i>P</i> 4 ₂ / <i>m</i> <i>nm</i>	own	[36]
Ca ₄ Cu _{4.5} Hg _{4.5}	<i>P</i> 43 <i>m</i>	Cu ₉ Al ₄	[35]	BaTl _{3.2} Hg _{0.8}	<i>C</i> 2 ₁ / <i>m</i>	EuIn ₄	[36]
Ca ₄ Au _{4.5} Hg _{4.5}	<i>P</i> 43 <i>m</i>	Cu ₉ Al ₄	[35]	Ba ₄ Ge ₁₉ Hg ₄	<i>Pm</i> 3 <i>n</i>	Na ₄ Si ₂₃	[37]
SrSnHg	<i>P</i> 6 ₃ <i>mc</i>	LiGaGe	[33]	BaSnHg	<i>P</i> 6 ₃ / <i>m</i> <i>m</i> <i>c</i>	BeZrSi	[33]
SrPbHg	<i>P</i> 6 ₃ <i>mc</i>	LiGaGe	[33]	BaPbHg	<i>Imma</i>	KHg ₂	[33]
SrTl ₂ Hg ₂	<i>P</i> 4 ₂ / <i>m</i> <i>nm</i>	BaTl ₂ Hg ₂	[36]	Ba ₃ ZnHg ₁₀	<i>Pm</i> mmn	own	[38]
Sr ₁₇ Li ₆ Hg ₉	<i>Im</i> 3 <i>m</i>	Ca ₁₇ Li ₆ Hg ₉	[15]	BaZn _{0.6} Hg _{3.4}	<i>I</i> 43 <i>d</i>	own	[38]
Sr ₃ In _{10.3} Hg _{0.7}	<i>I</i> mmm	La ₃ Al ₁₁	[39]	Ba ₂₀ Zn ₅ Hg ₉	<i>F</i> 43 <i>m</i>	own	[40]
SrIn _{3.4} Hg _{0.6}	<i>C</i> 2/ <i>m</i>	EuIn ₄	[39]	Ba ₃ CdHg ₁₀	<i>I</i> mmm	La ₃ Al ₁₁	[28]
SrIn _{1.3} Hg _{2.7}	<i>C</i> 2/ <i>m</i>	EuIn ₄	[39]	Ba ₂₀ Cd ₄ Hg ₉	<i>F</i> 43 <i>m</i>	own	[40]
SrIn _{0.9} Hg _{3.0}	<i>C</i> 2/ <i>m</i>	EuIn ₄	[39]				
SrIn _{1.3} Hg _{1.8}	<i>C</i> 2/ <i>m</i>	SrIn _{1.2} Hg _{1.3}	[39]				
SrIn _{3.0} Hg _{1.0}	<i>I</i> 4/ <i>mmm</i>	CeAl ₂ Ga ₂	[39]				
SrIn _{2.8} Hg _{1.2}	<i>I</i> 4/ <i>mmm</i>	CeAl ₂ Ga ₂	[39]				
SrIn ₂ Hg ₂	<i>I</i> 4/ <i>mmm</i>	CeAl ₂ Ga ₂	[39]				
Ternary amalgams with lanthanoid metals							
CePdHg	<i>P</i> 62 <i>m</i>	ZrNiAl	[41]	EuSnHg	<i>P</i> 6 ₃ <i>mc</i>	LiGaGe	[33]
PrPdHg	<i>P</i> 62 <i>m</i>	ZrNiAl	[41]	EuPbHg	<i>P</i> 6 ₃ <i>mc</i>	LiGaGe	[33]
Pr ₆ Fe ₁₃ Hg	<i>I</i> 4/ <i>m</i> <i>cm</i>	Pr ₆ Fe ₁₃ Ge	[42]	GdPdHg	<i>P</i> 62 <i>m</i>	ZrNiAl	[41]
Nd ₆ Fe ₁₃ Hg	<i>I</i> 4/ <i>m</i> <i>cm</i>	Pr ₆ Fe ₁₃ Ge	[42]	YbSnHg	<i>P</i> 6 ₃ <i>mc</i>	LiGaGe	[33]
SmPdHg	<i>P</i> 62 <i>m</i>	ZrNiAl	[41]	YbPbHg	<i>P</i> 6 ₃ / <i>m</i> <i>m</i> <i>c</i>	BeZrSi	[33]
				Yb ₁₇ Li ₆ Hg ₉	<i>Im</i> 3 <i>m</i>	Li ₆ Ca ₁₇ Hg ₉	[15]

Ternary amalgams are only reported in the Hg-poor region $M:\text{Hg} \leq 1:2.5$. The Hg-richest phases have the composition $A_3B\text{Hg}_{10}$. For the abovementioned reasons, we attempt, for the first time, a systematic study on ternary Hg-rich amalgams of less noble metals. As Hg shows high reactivity towards a large number of metallic elements, the outcome of a study designated to ternary amalgams can be expected to be rich. CsNa₂Hg₁₈ is an example for a ternary amalgam with high ionic bonding contributions, and it adopts a new structure type with an unprecedented Hg network.

4.1.3 Results and Discussion

Crystal Structure of CsNa₂Hg₁₈

The first single crystals of CsNa₂Hg₁₈ were observed in a sample with the initial weighed ratio of Cs:Na = 1:1 and a large Hg surplus. The new amalgam was found with Cs₃Hg₂₀ as only impurity. An optimised synthesis yielded phase-pure material (see Fig. 4.7), details are given in section 4.1.4 (p. 36).

CsNa₂Hg₁₈ crystallises in a new structure type with tetragonal symmetry in space group *I4/mmm*. Its crystal structure is built from one Cs, one Na and three crystallographically independent Hg positions. For basic crystallographic data and for details on data collection and handling see Table 4.2 (right). The structure of this new Hg-rich amalgam can be described with several different concepts, which is a common finding for Hg-rich amalgams^[11,46,47] and reflects the interplay of metallic and ionic bonding on the structural level.

A more ionic structural picture results from the description of the crystal structure using coordination polyhedra of the ‘anionic’ Hg atoms around the ‘cations’ Cs1 and Na1 (for fractional atomic coordinates, site symmetries and isotropic thermal displacement parameters see Table 4.3, anisotropic displacement parameters are compiled in Table 4.4). This representation of the crystal structure of CsNa₂Hg₁₈ is shown in Fig. 4.1, center and right. The next neighbouring atoms of both Cs1 and Na1 are only Hg atoms with a clear separation of the interatomic distances (see Table 4.5) from the next shell of atoms. For the large atom Cs1 a 24-vertex polyhedron [CsHg₂₄] with site symmetry *4/mmm* is found. It is a rhombicuboctahedron consisting of 18 square and 8 triangular faces. The point symmetry of the ideal Archimedean polyhedron would be *m $\bar{3}$ m*, however, the tetragonal distortion in this crystal structure is quite small, see Fig. 4.1, top right. All Hg–Hg distances range between 2.844(1) and 3.062(1) Å and are well in the range of Hg–Hg distances observed in other Hg-rich amalgams. The Cs–Hg interatomic distances are rather large in comparison with those found for other Cs amalgams (see Fig. 4.4), which can be attributed to the unusually large coordination number.

Table 4.2: Crystallographic data and details on single crystal data collection, structure solution and refinement for CsNa₂Hg₁₈. Data collection was performed at room temperature. All standard deviations are given in parentheses in units of the last digit.

Composition	CsNa ₂ Hg ₁₈
Crystal system	tetragonal
Space group	<i>I4/mmm</i> , No. 139
Lattice parameters <i>a</i> , <i>c</i> [Å]	7.3054(7), 20.046(3)
<i>V</i> [Å ³]	1069.8(3)
<i>Z</i>	2
Density (X-ray) [g · cm ⁻³]	11.76
Diffractometer	STOE IPDS 1
	AgK _α radiation,
	λ = 0.56086 Å
Absorption coeff. μ [mm ⁻¹]	71.24
θ range [°]	2.34 – 26.24
Index range	–9 ≤ <i>h</i> , <i>k</i> ≤ 9, –27 ≤ <i>l</i> ≤ 27
No. of collected refl.	5786
No. of independent refl.	448
No. of indep. refl. (<i>I</i> ≥ 2σ(<i>I</i>))	363
<i>R</i> _{int}	0.1694
<i>R</i> _σ	0.0571
<i>F</i> (000)	3034
Corrections	Lorentz, polarisation, absorption effects
Absorption correction	numerical, indexed crystal faces [43, 44]
Structure solution	direct methods [45]
Structure refinement	full-matrix least-squares on <i>F</i> ² [45]
No. of L.S. parameters	21
Goof	1.015
<i>R</i> values (<i>I</i> ≥ 2σ(<i>I</i>))	<i>R</i> 1 = 0.0325, <i>wR</i> 2 = 0.0649
<i>R</i> values (all data)	<i>R</i> 1 = 0.0453, <i>wR</i> 2 = 0.0679
Res. ρ(e ⁻) min/max [e ⁻ · Å ⁻³]	–3.108 / +2.331
Extinction coefficient	0.0029(2)
CCDC deposition No.	2031829

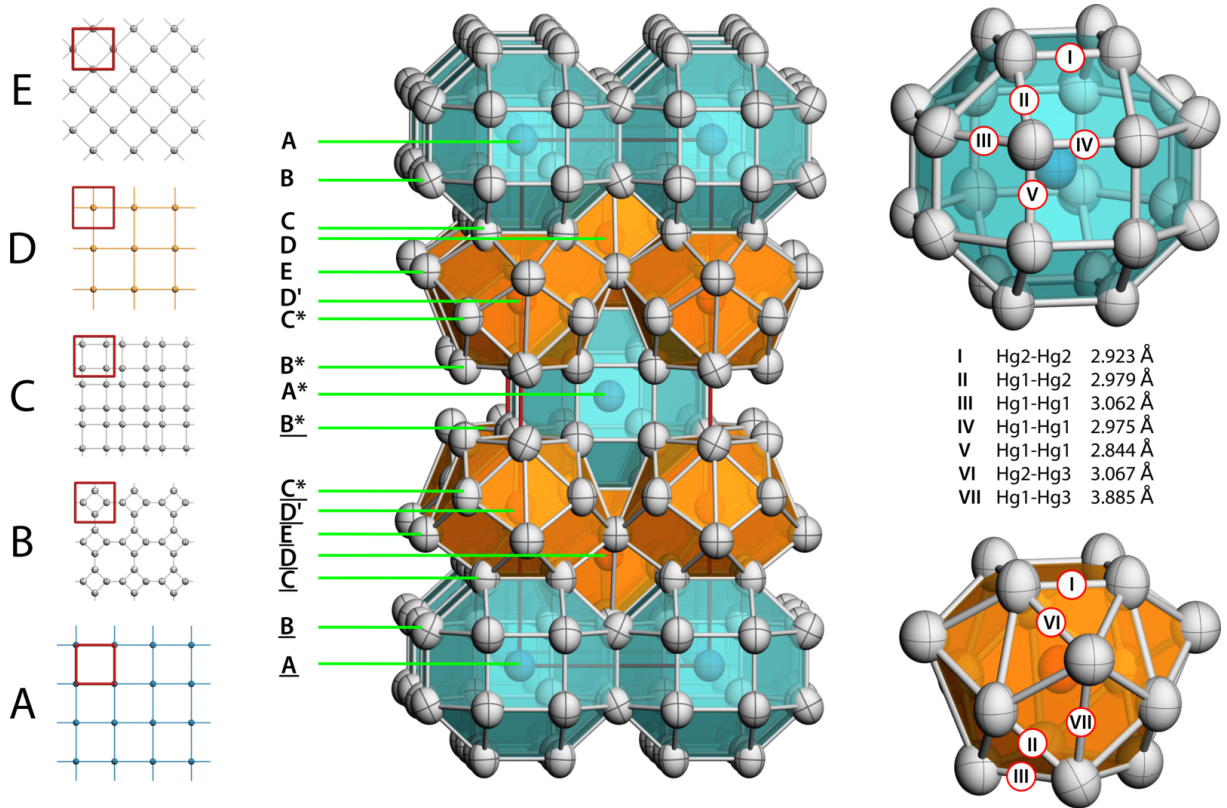


Fig. 4.1: Crystal structure of $\text{CsNa}_2\text{Hg}_{18}$. **Center:** unit cell with polyhedra representation for Cs1 and Na1. Hg: grey, Cs: blue, Na: orange. Polyhedra around Cs1 are drawn in light blue, polyhedra around Na1 in orange. The crystallographic c axis points upwards, the unit cell is marked in red. For all atoms ellipsoids are shown on a 99% probability level. **Left:** Net representation with net A (Cs atoms) at $z = 0$, net B (Hg1 atoms) at $z \approx 0.07$, net C (Hg2 atoms) at $z \approx 0.17$, net D (Na atoms) at $z \approx 0.20$ and net E (Hg3 atoms) at $z = 1/4$. The stacking sequence marked next to the unit cell is coded with nets X and X' being related by rotation around the c axis by 45° , X and X* related by the body centering and X and \bar{X} related by the horizontal mirror plane at height $z = 1/2$. **Right:** coordination polyhedra around Cs1 (top) and around Na1 (bottom).

Table 4.3: Standardised fractional atomic coordinates^[48] and equivalent isotropic displacement parameters [\AA^2] for $\text{CsNa}_2\text{Hg}_{18}$ as a result from single crystal structure refinement. The equivalent isotropic displacement parameter is defined as 1/3 of the trace of the anisotropic displacement tensor. All standard deviations are given in parentheses in units of the last digit.

Atom	Wyckoff Letter	Site Symmetry	x	y	z	U_{equiv}
Cs1	$2a$	$4/mmm$	0	0	0	0.0325(6)
Na1	$4e$	$4mm$	0	0	0.3002(7)	0.033(3)
Hg1	$16n$	$.m.$	0	0.29638(11)	0.42906(3)	0.0405(3)
Hg2	$16m$	$..m$	0.20003(6)	x	0.17161(4)	0.0380(3)
Hg3	$4d$	$4m2$	0	1/2	1/4	0.0409(4)

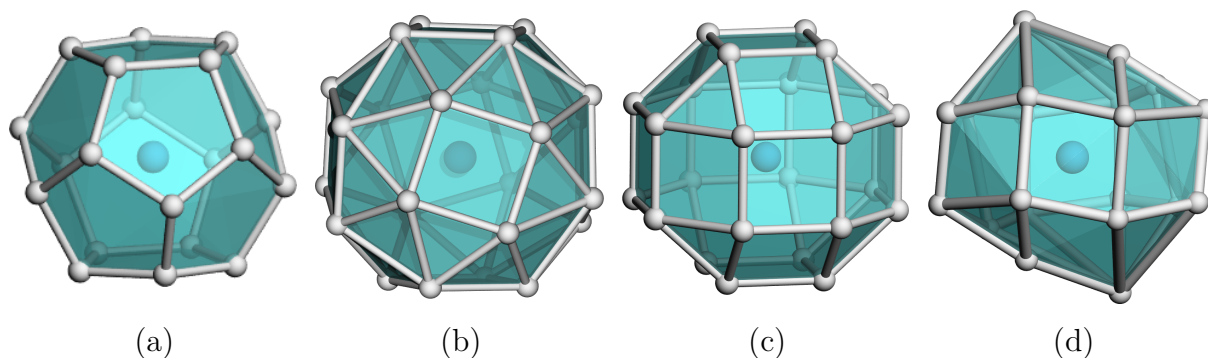


Fig. 4.2: Polyhedra for coordination number 24: (a) truncated hexagonal trapezohedron occurring in clathrates of type I, (b) snub cube as found in the NaZn_{13} structure type, (c) rhombicuboctahedron in $\text{CsNa}_2\text{Hg}_{18}$, (d) intermediate step between (b and c) as observed in the crystal structure of CsIn_{12} .

The coordination number 24 and the rhombicuboctahedron as coordination polyhedron are quite rare in structural chemistry. *Pearson's Crystal Data Base*^[16] lists 2299 entries for crystal structures in which at least one atomic site has $\text{CN} = 24$. The largest number corresponds to structures with partial occupied atomic positions, such as CaF_2 - or α - AgI -related structures, where unreasonably short distances between atoms occur. In structures with fully occupied $[\text{AB}_{24}]$ coordination spheres two major groups can be distinguished: 468 of them belonging to the group of clathrates Type I containing truncated hexagonal trapezohedra $[\text{NaSi}_{24}]$, and 125 entries are phases crystallising in the NaZn_{13} structure type where the Na position atoms are coordinated in snub cubes $[\text{NaZn}_{24}]$. These two polyhedra are shown in Fig. 4.2 and are the most prominent for atoms having coordination number 24. The rhombicuboctahedron has (to our knowledge) not been observed yet. However, rotation of the square faces of a snub cube by 28.7° results in a rhombicuboctahedron, and an intermediate polyhedron with a rotation of only 8.7° was already found in CsIn_{12} .^[49]

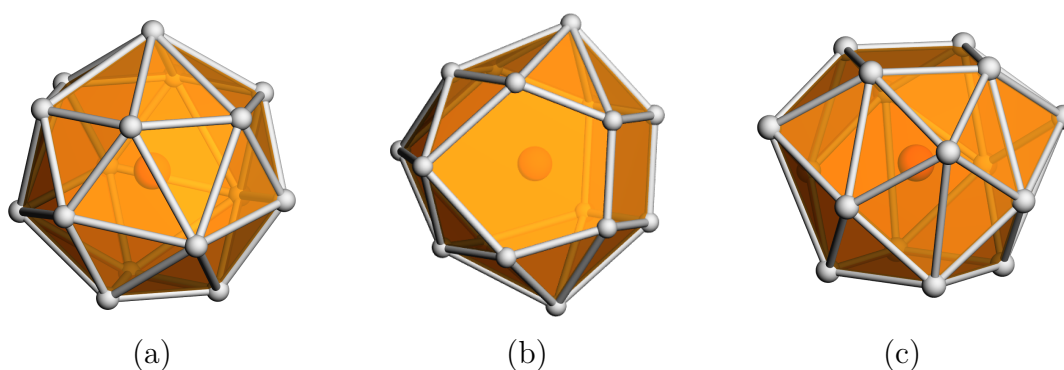


Fig. 4.3: Polyhedra for coordination number 16: (a) Frank-Kasper-type polyhedron (fourcapped truncated tetrahedron) as found in e.g. MgCu_2 -type structures, (b) fourcapped hexagonal prism, realised in many AlB_2 -type structures, (c) snub square antiprism in $\text{CsNa}_2\text{Hg}_{18}$.

The $[\text{NaHg}_{16}]$ coordination polyhedron shown in Fig. 4.1 on the lower right can be described as a snub square antiprism (Johnson solid No. J_{85}). Its ideal point symmetry (D_{4d}) is reduced to $C_{4v} = 4mm$. The Hg–Hg distances in this polyhedron are well within the range of commonly observed interatomic distances within Hg-rich amalgams. The Na–Hg interatomic distances are well in agreement with those found in other Na amalgams, see Fig. 4.4. Here again, the coordination polyhedron is an uncommon one: for coordination number 16 (8644 entries in *Pearson's Crystal Data Base*) there are several polyhedra, see Fig. 4.3. The by far most frequent one with 7005 entries is the 16-vertex Frank-Kasper polyhedron (fourcapped truncated tetrahedron)

Phase	$d_{\text{Na-Hg}}^{\text{min}}$	$d_{\text{Na-Hg}}^{\text{max}}$	CN	Ref.
α -Na ₃ Hg	313	354	9-11	[50]
Na ₈ Hg ₃	315	343	11-13	[51]
Na ₃ Hg ₂	313	338	12-14	[6]
NaHg	315	338	12-14	[8]
NaHg ₂	332	332	14	[6]
β -Na ₃ Hg	332	384	14	[50]
Na ₁₁ Hg ₅₂	315	376	14-16	[11]
CsNa ₂ Hg ₁₈	315	379	16	

Phase	$d_{\text{Cs-Hg}}^{\text{min}}$	$d_{\text{Cs-Hg}}^{\text{max}}$	CN	Ref.
CsHg ₂	374	404	12	[52]
CsHg	382	423	15-16	[5]
Cs ₅ Hg ₁₉	368	415	17-18	[53]
Cs ₃ Hg ₂₀	386	407	20	[53]
Cs ₂ Hg ₂₇	375	408	20	[54]
CsNa ₂ Hg ₁₈	401	419	24	

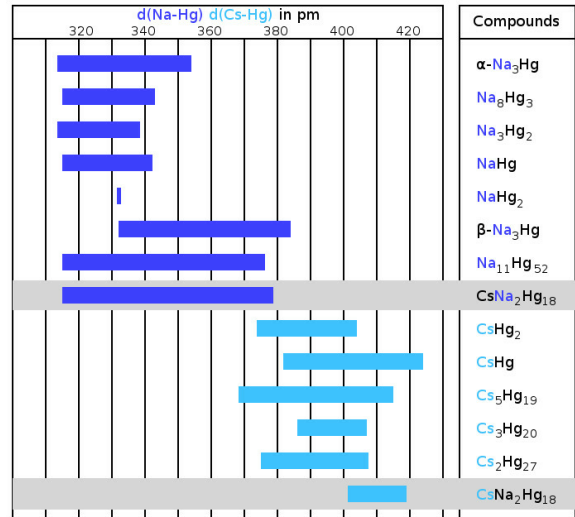


Fig. 4.4: Na–Hg and Cs–Hg interatomic distances (in pm) and coordination numbers vs. Hg in CsNa₂Hg₁₈ in comparison to those found in literature for binary Na and Cs amalgams.

which occurs e.g. in the MgCu₂-type structures, followed by a fourcapped hexagonal prism occurring in AlB₂-related structures. The snub square antiprism observed here seems to be a rather exotic solution for the realisation of coordination number 16, see Fig. 4.3. The cation topology can be described in a packing with a defect-ThCr₂Si₂ topology in the sense of Th□₂Si₂.

An alternative visualisation of the crystal structure of CsNa₂Hg₁₈ is a net representation. This type of structure description is common for Frank–Kasper phases. The crystal structure can be subdivided in perfectly flat nets perpendicular to the tetragonal *c* axis of the unit cell. To construct the whole crystal structure, five nets are necessary (see Fig. 4.1). At height $z = 0$ as square planar net from Cs atoms on (0,0,0) is located, followed on both sides by net type B, yielding a 4.8.8 pattern of squares and octagons of Hg(1) atoms at height $z \approx 0.07$. Two of these nets form a Cs-centered octagonal prism and a set of empty [Hg₈] cubes. Net type C is located at height $z \approx 0.17$ and consists only of Hg(2) atoms forming a net of large and small squares with rectangles between them. The small squares augment the Cs-centered octagonal prisms to rhombicuboctahedra, while the large squares form the bases of the [NaHg₁₆] snub square antiprisms. Net type D consists only of Na(1) atoms forming a square net at height $z \approx 0.20$. Net type E consists of Hg(2) and Hg(3) atoms in a square arrangement at height $z = 1/4$. Stacking of the five simple net types (taking rotations and inversions into account) is realised in a complex periodicity given in Fig. 4.1.

Emphasising the covalent nature of the Hg sublattice would lead to a structural description in analogy of other 3D networks such as clathrates, zeolites or MOFs. The 3D network topology of the Hg atoms only can be analysed with e.g. the software package ToposPro.^[55] The connection pattern of the Hg network in CsNa₂Hg₁₈ yields a new 3D network topology with the point symbol $\{3^2.4^7.5^6\}4\{3^5.4^8.5^8\}4\{3^8.4^{12}.5^8\}$.

Table 4.4: Coefficients of the anisotropic displacement tensor [\AA^2] for CsNa₂Hg₁₈. U_{ij} is defined as $U_{ij} = \exp(-2\pi^2[U_{11}(ha^*)^2 + \dots + 2U_{21}hka^*b^*])$. All standard deviations are given in parentheses in units of the last digit.

Atom	U_{11}	U_{22}	U_{33}	U_{23}	U_{13}	U_{12}
Cs1	0.0322(8)	$= U_{11}$	0.0331(13)	0	0	0
Na1	0.030(4)	$= U_{11}$	0.038(7)	0	0	0

continued on the next page

Atom	U_{11}	U_{22}	U_{33}	U_{23}	U_{13}	U_{12}
Hg1	0.0365(4)	0.0479(4)	0.0370(4)	-0.0032(3)	0	0
Hg2	0.0337(3)	= U_{11}	0.0465(4)	0.0047(2)	= U_{23}	-0.0018(2)
Hg3	0.0397(5)	= U_{11}	0.0432(7)	0	0	0

Table 4.5: Selected interatomic distances (and their frequencies) in $\text{CsNa}_2\text{Hg}_{18}$ in Å. All standard deviations are given in parentheses in units of the last digit. The Hg–Hg bond labels are the same as in Fig. 4.1.

Atom 1	Atom 2	Distance	Label	Atom 1	Atom 2	Distance	Label
Cs1	Hg2	4.0132(9) ($8\times$)		Hg2	Hg2	2.9226(10) ($2\times$)	I
	Hg1	4.1925(5) ($16\times$)			Hg1	2.9792(8) ($2\times$)	II
Na1	Hg2	3.150(3) ($4\times$)		Hg3	Hg3	3.0670(5) ($2\times$)	VI
	Hg2	3.304(11) ($4\times$)			Na1	3.150(3) ($1\times$)	
	Hg1	3.370(11) ($4\times$)			Na1	3.304(11) ($1\times$)	
Hg1	Hg3	3.789(4) ($4\times$)		Hg2	Hg2	3.3079(15) ($1\times$)	
	Hg1	2.8443(14) ($1\times$)	V		Cs1	4.0132(9) ($1\times$)	
	Hg1	2.9759(16) ($1\times$)	IV		Hg3	Hg2	3.0670(5) ($8\times$)
Hg2	2.9792(8) ($2\times$)	II	Na1	3.789(4) ($4\times$)			
Hg1	3.0621(12) ($2\times$)	III	Hg1	3.8854(9) ($4\times$)		VII	
Na1	3.370(11) ($1\times$)						
Cs1	4.1925(5) ($2\times$)						

Chemical bonding in $\text{CsNa}_2\text{Hg}_{18}$

From DFT calculations, information on polarity of the bonding inside amalgams in the sense of high Coulombic contributions to the metallic bonding cannot directly be derived, however, there exist several typical indications for a disturbance of the conduction electrons by strong local electric fields caused by ionic bonding contributions. The DOS and pDOS plots are shown in Fig. 4.5 (right). The individual pDOS curves are multiplied with a factor taking into account their respective site multiplicities.

At the Fermi level, the density of states has a pronounced local minimum, yet it is non-zero. This is one of the characteristic features of a metal with relatively low charge carrier concentration. The partial densities of states for the alkali metals also is non-zero, however, with a pronounced minimum at the Fermi level. This can be interpreted as partial electron transfer, resulting in partially positively charged atoms in the sense of $\text{Cs}^{\delta+}(\text{Na}^{\delta+})_2[\text{Hg}_{18}]^{\delta-}$. As the local minima in the pDOS of Na and Cs are not very pronounced, one can assume δ , the overall polarity, to not be very large. The respective partial negative charge is distributed rather evenly over all atomic sites of the Hg lattice, according to the calculated Bader charges (see Table 4.6). The differences in charge distribution (Hg3 has a slightly lower partial charge than Hg1 and Hg2) may be the result of longer Hg3–Na contacts (see Table 4.5).

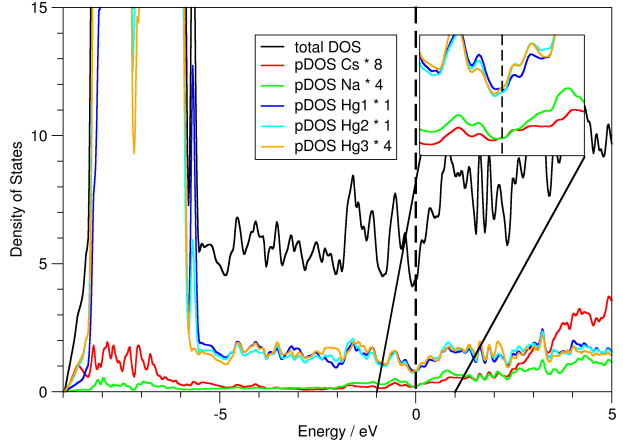


Fig. 4.5: Density of states (DOS) and partial density of states (pDOS) curves for $\text{CsNa}_2\text{Hg}_{18}$ and the individual atomic sites therein. The Fermi energy is marked as dashed vertical line. The region ± 1 eV around the Fermi energy is magnified in the inset.

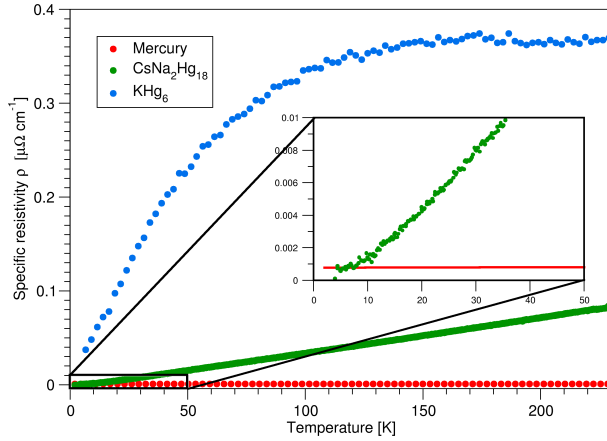


Fig. 4.6: Specific resistivity of $\text{CsNa}_2\text{Hg}_{18}$ (green) versus temperature, in comparison to the specific resistivities of pure mercury (red) and KHg_6 (blue).

The electron density on the bond critical points is very low for the Hg–Na and Hg–Cs contacts and significantly higher for the Hg–Hg contacts, indicating ionic Hg–alkali metal and covalent Hg–Hg interactions. The rather uniform electron density distribution amongst Hg atoms can be seen not only in the Bader charges but also in the very similar pDOS curves in the region around E_F for all three crystallographically different Hg sites. Another typical feature in the DOS curves of Hg-rich amalgams with high polarity is the broad range of energy over which d , s and p -states are spread. This mixing is common for systems with predominantly covalent Hg–Hg interactions.

The specific resistivity of $\text{CsNa}_2\text{Hg}_{18}$ is shown in Fig. 4.6 and reflects the macroscopic aspects of the electronic situation. The ‘bad metal’ behaviour,^[56] consisting of high specific resistivity with steep temperature dependence is present. However, a typical deviation from linear temperature dependence and a low Ioffe-Regel limit^[57] cannot be discerned up to room temperature. For comparison, the specific resistivities of elemental Hg and the amalgam KHg_6 ^[46] with equal $A:\text{Hg}$ ratio are shown. From the band structure calculations, a relatively small polarity was seen, and the lower extent of ‘bad metal’ behaviour visible in the specific resistivity plot corroborates this finding. From direct comparison it can be assumed that parameters additional to the Hg content of an amalgam contribute to the macroscopic physical behaviour, such as e.g. phononic contributions, structural complexity or defects.

Table 4.6: Details of the calculation of the electronic structure of $\text{Cs}_2\text{NaHg}_{18}$ together with Bader charges and bond critical points. The Hg–Hg bond labels are the same as in Fig. 4.1.

Calculation details			
R_{mt} (all atoms)			132.3 pm (2.5 a.u.)
$R_{mt} \cdot K_{max}$			8.0
k-points/BZ			1000
k-points/IBZ			99
Monkhorst-Pack grid			$10 \times 10 \times 10$
Bader charges			
	Na		+0.819
	Cs		+0.763
	Hg1		−0.113
	Hg2		−0.169
	Hg3		−0.074
Bond critical points			
ρ_{BCP} ($e^- \text{Å}^{-3}$)	Bond	dist. (Å)	label
0.0312	Cs–Hg1	4.1925(5)	
0.0395	Cs–Hg2	4.0132(9)	
0.0581	Na–Hg2	3.150(3)	
0.0488	Na–Hg2	3.304(11)	
0.3041	Hg1–Hg1	2.8443(14)	V
0.2414	Hg1–Hg1	2.9759(16)	IV
0.2429	Hg1–Hg2	2.9792(8)	II
0.2081	Hg1–Hg1	3.0621(12)	III
0.2670	Hg2–Hg2	2.9226(10)	I
0.2061	Hg2–Hg3	3.0670(5)	VI

4.1.4 Materials and Methods

Synthesis

Due to the high sensitivity of the alkali metals and also the reaction products, all experiments were carried out under inert gas conditions, either inside an argon-filled glove box ($p(\text{H}_2\text{O})$ and $p(\text{O}_2) < 0.1$ ppm) or with the use of a Schlenk apparatus (vacuum/argon). Prior to the preparation of the amalgams, mercury was cleaned by filtration, subsequent stirring in half-concentrated HNO_3 to dissolve incorporated less noble metallic impurities and organic adhesions, and then distilled twice in vacuum.

For the synthesis of $\text{CsNa}_2\text{Hg}_{18}$, metallic sodium (distilled twice, MPI FKF Stuttgart, Germany) and cesium (donated by Kriminalpolizei Heilbronn, Germany) were mixed with elemental mercury and heated in glass tubes. First single crystals were taken from a sample containing 975.0 mg (7.3 mmol) Cs, 162.0 mg (7.0 mmol) Na and 11.79 g (58.8 mmol) Hg which were mixed under ice cooling in a Schlenk tube. The reaction of the alkali metals with elemental Hg is very exothermic. The mixture was heated with an hot air gun to 300°C until a homogeneous melt was obtained and cooled slowly to room temperature. The mass was crushed and a powder diffraction pattern showed the presence of $\text{Cs}_3\text{Hg}_{20}$ together with NaHg_2 as only impurities. This powder was subsequently mixed with additional 5 g (49.9 mmol) of Hg and the mixture tempered at 105°C for 5 months. Afterwards, surplus Hg was filtered off with a frit under argon atmosphere. The solid contained well-crystallised cuboid specimens of $\text{CsNa}_2\text{Hg}_{18}$.

In a second synthesis attempt, a stoichiometric mixture of the elements, heated to 300°C , quenched on ice and tempered at 105°C for 2 weeks, yielded $\text{CsNa}_2\text{Hg}_{18}$ as the main phase, containing 6.3 at.-% of $\text{Cs}_3\text{Hg}_{20}$.

In an optimised synthesis, 217.3 mg (9.45 mmol) Na and 624.4 mg (4.70 mmol) Cs were mixed in a Schlenk tube and cooled to -78°C with a dry ice cooling bath. The stoichiometric amount of 17.071 g (85.1 mmol) Hg was added slowly and dropwise. The mixture was allowed to thaw together with the cooling bath to room temperature over night. The resulting product showed no impurity lines in the powder diagrams. After synthesis, the sample containers were transferred to a glove box and small portions of the air- and moisture- sensitive samples were brought to air under potassium-dried paraffin oil for optical inspection and crystal preparation for diffraction experiments.

Powder diffractometry

For powder diffraction experiments, representative parts of the product of an optimised synthesis were ground in an agate mortar inside an argon-filled glove box. In order to obtain fine powder from the slightly ductile sample, diamond powder (Sigma Aldrich, synthetic monocrystalline powder, $< 1\ \mu\text{m}$, dried by heating in vacuum) was added in an approximate volume ratio of amalgam : diamond = 1 : 20. The powder then was melt-sealed in thin-walled glass capillaries (Spezialglas No. 10, Hilgenberg, Malsfeld, Germany, $\varnothing = 0.5\ \text{mm}$) and mounted and centered on the goniometer of a Stadi P diffractometer system (Stoe & Cie, Darmstadt, Germany, equipped with $\text{Mo-K}_{\alpha 1}$ radiation, curved Ge monochromator and a MYTHEN

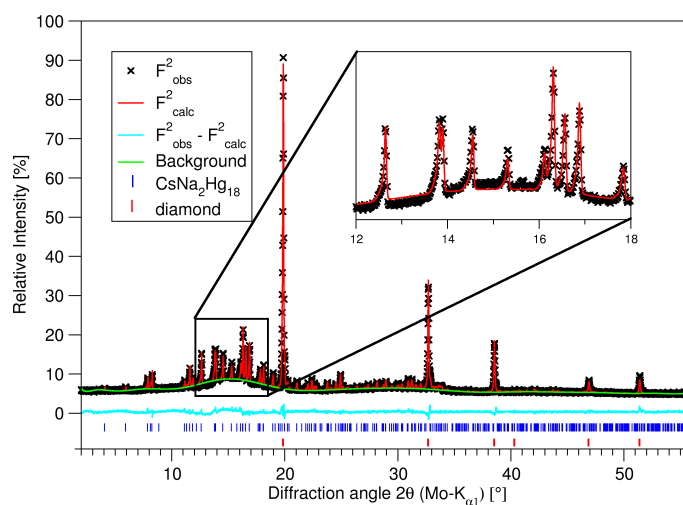


Fig. 4.7: Rietveld refinement on a sample of phase-pure $\text{CsNa}_2\text{Hg}_{18}$, diluted with diamond powder. For details on the refinement, see Table 4.7.

radiation, curved Ge monochromator and a MYTHEN

2K strip detector, Dectris, Baden-Dättwil, Switzerland). Data collection was performed in parafocusing Debye–Scherrer geometry. Multiple ranges were collected successively and added afterwards in order to optimise the signal-to-noise ratio. The powder diffraction pattern was used for a Rietveld refinement; see Fig. 4.7 and Table 4.7. Therefinement was performed with the program package Topas,^[58] taking the single crystal structure model as the starting value. The background was modeled by a shifted Chebyshev function with 20 parameters; the profiles were modeled based on instrument and sample parameters (fundamental parameter approach).

Single crystal diffractometry

Crystals of CsNa₂Hg₁₈ were found as cuboids with a metallic luster. Suitable specimens were selected under a binocular and sealed in glass capillaries ($\varnothing = 0.2$ mm) filled with paraffin oil dried over potassium sand prior to use. The capillaries were mounted and centered on the one-circle goniometer of an IPDS1 diffractometer system (Stoe & Cie, Darmstadt, Germany, Ag-K α radiation) in a general orientation. This was checked by evaluating the orientation matrix obtained from the indexing of 25 orientation frames and eventually twisting the crystal orientation with the angular slides of the goniometer head. Data collection in φ mode was performed for the accessible part of at least one-half of the Ewald sphere ($\varphi_{max} = 200^\circ$). After data collection and Lorentz and polarisation correction, the crystal shape was measured, and the faces indexed. The shape was optimised on the basis of the intensity distribution,^[43] and a numerical absorption correction was performed on this basis.^[44] The result was compared to absorption corrections performed by other algorithms (semi-empirical on the basis of multiple recorded reflections or numerical on the basis of uncorrected crystal faces^[59,60]). The high absorption coefficients, even in Ag-K α radiation, affords meticulous checks on data collection parameters as well as the outcome of the absorption correction processes. However, data quality is often hampered, as becomes visible from the unusual ratio of $R1$ and $wR2$ or high values for R_{int} and R_σ , see Table 4.2. This is often the case when dealing with sensitive amalgam crystals due to a superficial thin coating of the crystals with a film of liquid mercury. This film is either the result of decomposition or is a consequence of the synthesis from a mixture with excess Hg that cannot be separated entirely from the temperature-sensitive crystals by distillation or centrifugation. Taking this highly absorbing but diffusely diffracting liquid Hg film into account during absorption correction is only possible to a certain, sometimes unsatisfactory, degree.

Table 4.7: Crystallographic data and details on a Rietveld refinement of a phase-pure sample of CsNa₂Hg₁₈ as a result of an optimised synthesis. For a graphical representation of the refinement, see Fig. 4.7. Refinement was performed with the Topas suite.^[58] Below: refined fractional coordinates. In order to reach full convergence, all atoms were refined with identical values for B_{eq} of 2.39(9) pm². Standard deviations are given in units of the last digits in parentheses.

Crystal system	tetragonal		
Space group	$I4/mmm$, No. 139		
Lattice parameters a, c [Å]	7.3169(3), 20.058(1)		
V [Å ³]	1073.9(1)		
Z	2		
Calc. density [g · cm ⁻³]	11.719(1)		
Radiation/wavelength [Å]	Mo-K α 1, 0.70932		
Step size [°]	0.015		
Data points	3600		
Diffractometer	STOE Stadi P		
Detector	Dectris MYTHEN 2K		
Sample geometry	capillary ($\varnothing = 0.5$ mm)		
ϑ range [°]	1.0–28.0		
Refined parameters	35		
Background function	shifted Chebyshev		
Background parameters	20		
Peak shape function	fundamental parameter approach		
R_P [%]	1.521		
R_{wP} [%]	2.020		
R_{F2} [%]	1.220		
R_{Bragg} [%]	1.557		
GooF on χ^2	1.656		
Atom	x	y	z
Cs1	0	0	0
Na1	0	0	0.309(3)
Hg1	0	0.2956(5)	0.4291(2)
Hg2	0.1987(3)	x	0.1720(2)
Hg3	0	1/2	1/4

DFT calculations

Based on the crystal structure DFT calculations of the electronic structure, Bader charges^[61] of the atomic positions were performed with the Wien2K package.^[62] The full-potential linear augmented plane wave FP-LAPW was used, based on the exchange and correlation functional with generalised gradient approximation (GGA-PBE).^[63] Muffin-tin radii were assumed to 132.3 pm (2.5 a.u.) and the number of basis functions was calculated by the value of $R_{\text{mt}} \cdot K_{\text{max}} = 8.0$, with K_{max} as the largest k vector. Cutoff energies used were $E_{\text{max}}^{\text{pot}} = 196$ eV (potential) and $E_{\text{max}}^{\text{wf}} = 139$ eV (interstitial PW).

4.1.5 Conclusion

Ternary amalgams containing two different electropositive metals can belong to three basic types: (1) They can form solid solutions $A_{1-x}B_x\text{Hg}_n$ in the case that there are two isostructural binary amalgams $A\text{Hg}_n$ and $B\text{Hg}_n$. This has been observed for $\text{K}_{1-x}\text{Rb}_x\text{Hg}_{11}$ or for $\text{Rb}_{3-x}\text{Cs}_x\text{Hg}_{20}$.^[64] (2) They can form ternary ordering variants of binary structure types, which has been observed with amalgams belonging to the $\text{Gd}_{14}\text{Ag}_{51}$ structure family, such as $\text{Yb}_{10.5}\text{Sr}_{0.5}\text{Hg}_{54}$ or $\text{Ca}_5\text{Eu}_9\text{Hg}_{51}$.^[65] (3) Finally, fully new structure types can emerge, as is shown here in the case of $\text{CsNa}_2\text{Hg}_{18}$. From the current state of our systematic studies on ternary amalgams, we see that this is by far the rarest of the three cases. All ternary amalgams show typical structural features and physical properties of polar intermetallic phases, as are already found for the binary amalgams. Enlarging the number of individual amalgam phases by transitioning from binary to ternary amalgams allows for comparative studies and for the identification of common parameters influencing the extent of ‘bad metal’ behaviour. In the future, this knowledge may be transferred from the model system of amalgams to further polar intermetallics in order to deliberately tailor physical properties crucial for thermoelectric, catalytic, electronic or magnetic applications.

References

- [1] H.-J. Deiseroth, Discrete and extended metal clusters in alloys with mercury and other group 12 elements. In *Molecular Clusters of the Main Group Elements*, (Eds.: M. Driess, H. Nöth), Wiley-VCH, Weinheim, Germany, **2004**, pp. 169–187.
- [2] M. Wendorff, C. Röhr, Alkaline-earth tri-mercurides $A^{\text{II}}\text{Hg}_3$ ($A^{\text{II}} = \text{Ca}, \text{Sr}, \text{Ba}$): Binary intermetallic compounds with a common and a new structure type, *Z. Kristallogr.* **2018**, *233*, 515–529, DOI: [10.1515/zkri-2018-2054](https://doi.org/10.1515/zkri-2018-2054).
- [3] J. H. Simons, R. P. Seward, Slow Electron Scattering and the Apparent Electron Affinity of Mercury, *J. Chem. Phys.* **1938**, *6*, 790–794, DOI: [10.1063/1.1750172](https://doi.org/10.1063/1.1750172).
- [4] E. Biehl, H.-J. Deiseroth, Crystal structure of potassiumamalgam, KHg , *Z. Kristallogr. - Cryst. Mater.* **1996**, *211*, 630, DOI: [10.1524/zkri.1996.211.9.630](https://doi.org/10.1524/zkri.1996.211.9.630).
- [5] H.-J. Deiseroth, A. Strunck, W. Bauhofer, CsHg , eine ungewöhnliche Variante der CsCl -Struktur Darstellung, Kristallstruktur und physikalische Eigenschaften, *Z. Anorg. Allg. Chem.* **1989**, *575*, 31–38, DOI: [10.1002/zaac.19895750106](https://doi.org/10.1002/zaac.19895750106).
- [6] J. W. Nielsen, N. C. Baenziger, The Crystal Structures of NaHg_2 , NaHg and Na_3Hg_2 , *Acta Crystallogr.* **1954**, *7*, 277–282, DOI: [10.1107/S0365110X54000783](https://doi.org/10.1107/S0365110X54000783).
- [7] H.-J. Deiseroth, A. Strunck, W. Bauhofer, Hg_8 (“Mercubane”) Clusters in $\text{Rb}_{15}\text{Hg}_{16}$, *Angew. Chem. Int. Ed.* **1989**, *28*, 1251–1252, DOI: [10.1002/anie.198912511](https://doi.org/10.1002/anie.198912511).
- [8] H.-J. Deiseroth, A. Stupperich, R. Pankaluoto, N. E. Christensen, NaHg : A variant of the cesium-chloride structure structural relations and electronic structure, *Z. Anorg. Allg. Chem.* **1991**, *597*, 41–50, DOI: [zaac.19915970107](https://doi.org/10.1002/zaac.19915970107).

- [9] F. Lihl, Über den Aufbau des Systems Quecksilber-Mangan, *Monatsh. Chem.* **1955**, *86*, 186–190, DOI: [10.1007/BF00899290](https://doi.org/10.1007/BF00899290).
- [10] J. C. Slater, Atomic Radii in Crystals, *J. Chem. Phys.* **1964**, *41*, DOI: [10.1063/1.1725697](https://doi.org/10.1063/1.1725697).
- [11] C. Hoch, A. Simon, Na₁₁Hg₅₂: Complexity in a Polar Metal, *Angew. Chem. Int. Ed.* **2012**, *51*, 3262–3265, DOI: [10.1002/anie.201108064](https://doi.org/10.1002/anie.201108064).
- [12] F. Tambornino, J. Sappl, C. Hoch, The Gd₁₄Ag₅₁ structure type and its relation to some complex amalgam structures, *J. Alloys Compd.* **2015**, *618*, 326–335, DOI: [10.1016/j.jallcom.2014.08.017](https://doi.org/10.1016/j.jallcom.2014.08.017).
- [13] H.-J. Deiseroth, E. Biehl, NaK₂₉Hg₄₈: A Contradiction to or an Extension of Theoretical Concepts to Rationalize the Structures of Complex Intermetallics?, *J. Solid State Chem.* **1999**, *147*, 177–184, DOI: [10.1006/jssc.1999.8209](https://doi.org/10.1006/jssc.1999.8209).
- [14] H. Pauly, A. Weiss, H. Witte, Kubisch flächenzentrierte Legierungen der Zusammensetzung Li₂MgX mit raumzentrierter Unterstruktur, *Z. Metallkd.* **1968**, *59*, 414–418.
- [15] A. V. Tkachuk, A. Mar, Li₆A₁₇Hg₉ (A=Ca, Sr, Yb): Intermetallic Compounds of Mercury with a Zeolite-Like Topology of Cubic Networks, *Chem. Eur. J.* **1993**, *15*, 10348–10351, DOI: [10.1002/chem.200902250](https://doi.org/10.1002/chem.200902250).
- [16] PEARSON'S CRYSTAL DATA, K. Cenzual, P. Villars, ASM International N.V., Materials Park (OH), USA, **2016**.
- [17] R. Vogel, H. U. Schuster, KHgAs (Sb) und KZnAs – Ternäre Verbindungen mit modifizierter Ni₂In-Struktur, *Z. Naturforsch.* **1980**, *B 35*, 114–116, DOI: [10.1515/znb-1980-0127](https://doi.org/10.1515/znb-1980-0127).
- [18] H.-U. Schuster, Ternäre Lithiumverbindungen vom Typ Li₂MeGe (Me = Zn, Cd, Hg), *Z. Anorg. Allg. Chem.* **1969**, *370*, 149–159, DOI: [10.1002/zaac.19693700307](https://doi.org/10.1002/zaac.19693700307).
- [19] P. Lagrange, M. E. Makrini, A. Hérold, structure cristalline du mercurographite KHgC₄, *Rev. Chim. Minér.* **1983**, *20*, 229–246.
- [20] A. Kaltzoglou, S. Ponou, T. Fässler, A₄Ge₉ (A = K, Rb as Precursors for Hg-Substituted Clathrate-I Synthesis: Crystal Structure of A₈Hg₃Ge₄₃, *Eur. J. Inorg. Chem.* **2008**, 4507–4510, DOI: [10.1002/ejic.200800631](https://doi.org/10.1002/ejic.200800631).
- [21] H. Pauly, A. Weiss, H. Witte, Phasenbreite und Valenzelektronenkonzentration (VEK) in den ternären kubischen Zintlphasen vom NaTl-Typ, *Z. Metallkd.* **1968**, *59*, 554–558, DOI: [10.1515/ijmr-1968-590706](https://doi.org/10.1515/ijmr-1968-590706).
- [22] A. Kaltzoglou, S. Pounou, T. Fässler, Synthesis and Crystal Structure of Mercury-Substituted Type-I Clathrates A₈Hg₄Sn₄₂ (A = K, Rb, Cs), *Eur. J. Inorg. Chem.* **2008**, *538*, 538–542, DOI: [10.1002/ejic.200700854](https://doi.org/10.1002/ejic.200700854).
- [23] S. Matthes, H.-U. Schuster, Ternäre Natriumphasen mit Cadmium bzw. Quecksilber und Zinn bzw. Blei, *Z. Naturforsch.* **1980**, *35b*, 778–780, DOI: [10.1515/znb-1980-0632](https://doi.org/10.1515/znb-1980-0632).
- [24] S. C. Sevov, J. E. Ostenson, J. D. Corbett, K₈In₁₀Hg: A Zintl Phase with isolated In₁₀ clusters, *J. Alloys Compd.* **1993**, *202*, 289–294, DOI: [10.1016/0925-8388\(93\)90551-W](https://doi.org/10.1016/0925-8388(93)90551-W).
- [25] S. Ponou, S. J. Kim, T. Fässler, Synthesis and Characterization of Na₅M_{2+x}Sn_{10-x} (x ≈ 0.5, M = Zn, Hg) - A Doped Tetrahedral Framework Structure, *J. Am. Chem. Soc.* **2009**, *131*, 10246–10252, DOI: [10.1021/ja902664c](https://doi.org/10.1021/ja902664c).
- [26] P. C. Schmidt, W. Baden, N. Weiden, A. Weiss, The Intermetallic System NaHg_{1-x}Tl_x. X-Ray Investigations and Measurements of the Knight Shift of Na, Hg, and Tl, *Phys. Status Solidi A.* **1985**, *92*, 205–212, DOI: [10.1002/pssa.2210920119](https://doi.org/10.1002/pssa.2210920119).
- [27] J. M. Fox, P. F. Henry, M. J. Rosseinsky, Na_{2+x}Hg_yC₆₀: Post-transition metal intercalation chemistry of a C₆₀ host, *Chem. Commun.* **1996**, 2299–2300, DOI: [10.1039/CC9960002299](https://doi.org/10.1039/CC9960002299).
- [28] M. Wendorff, C. Röhr, Barium Triel Mercurides Ba_M_xHg_{4-x} and Ba₃M_xHg_{11-x} (M = Ga, In, Cd), *Z. Naturforsch. B.* **2013**, *68*, 307–322, DOI: [10.5560/znb.2013-3084](https://doi.org/10.5560/znb.2013-3084).
- [29] L. Zheng, Y. Feng, R. Wang, Y. Chen, Crystal structure and properties of the new ternary compound Mg₂₁Ga₅Hg₃, *Intermetallics* **2009**, *17*, 873–877, DOI: [10.1016/j.intermet.2008.10.007](https://doi.org/10.1016/j.intermet.2008.10.007).

- [30] J. L. C. Daams, J. H. N. Van Vucht, Contribution to the system Mg-Au-Hg, *Philips J. Res.* **1984**, *39*, 275–292.
- [31] J. C. Dai, J. D. Corbett, Substitution of Au or Hg into BaTl₂ and BaIn₂. New Ternary Examples of Smaller CeCu₂-Type Intermetallic Phases, *Inorg. Chem.* **2006**, *45*, 2104–2111, DOI: [10.1021/ic051891k](https://doi.org/10.1021/ic051891k).
- [32] M. Wendorff, C. Röhr, The New Hg-rich Barium Indium Mercurides BaIn_xHg_{7-x} (x=3.1) and BaIn_xHg_{11-x} (x=0-2.8). Synthesis, crystal and electronic structure, *J. Solid State Chem.* **2013**, *203*, 297–303, DOI: [0.1016/j.jssc.2013.04.042](https://doi.org/10.1016/j.jssc.2013.04.042).
- [33] F. Merlo, M. Pani, M. L. Fornasini, RMX compounds formed by alkaline earths, europium and ytterbium. III. Ternary Phases with M ≡ Mg, Hg and X ≡ Si, Ge, Sn, Pb, *J. Alloys Compd.* **1993**, *196*, 145–148, DOI: [10.1016/0925-8388\(93\)90585-B](https://doi.org/10.1016/0925-8388(93)90585-B).
- [34] M. Wendorff, C. Röhr, The new barium mercuride BaHg₆ and ternary indium and gallium derivatives, *J. Alloys Compd.* **2013**, *546*, 320–328, DOI: [10.1016/j.jallcom.2012.07.101](https://doi.org/10.1016/j.jallcom.2012.07.101).
- [35] M. Pušelj, Z. Ban, Ternäre Gamma-Messing-Phasen in den Systemen Calcium-M^{IB(II B)}-Quecksilber, *Z. Naturforsch. B* **1980**, *35*, 1594–1595, DOI: [10.1515/znb-1980-1225](https://doi.org/10.1515/znb-1980-1225).
- [36] J.-C. Dai, S. Gupta, J. D. Corbett, Synthesis, Structure, and Bonding of BaTl₄. Size Effects on Encapsulation of Cations in Electron-Poor Metal Networks, *Inorg. Chem.* **2011**, *50*, 238–244, DOI: [10.1021/ic1018828](https://doi.org/10.1021/ic1018828).
- [37] N. O. Melnychenko, Solid solution based clathrate Ba₈Ge₄₃(₃)₃ (₃ = vacancy) with transition elements, *Nauk. Visn. Uzhhorod. Univ. Ser. Khim.* **2013**, *30*, 46–49.
- [38] M. Schwarz, M. Wendorff, C. Röhr, The new barium zinc mercurides Ba₃ZnHg₁₀ and BaZn_{0.6}Hg_{3.4} - Synthesis, crystal and electronic structure, *J. Solid State Chem.* **2012**, *196*, 416–424, DOI: [10.1016/j.jssc.2012.06.047](https://doi.org/10.1016/j.jssc.2012.06.047).
- [39] M. Wendorff, C. Röhr, Strontium-Metallide im Bereich des Schnitts SrIn₄ – SrHg₄, *Z. Naturforsch.* **2014**, *69b*, 388–408, DOI: [10.5560/znb.2014-4007](https://doi.org/10.5560/znb.2014-4007).
- [40] M. Wendorff, C. Röhr, The new complex barium mercuride Ba₂₀Hg₁₀₃ and its ternary zinc and cadmium variants, *Z. Naturforsch. B.* **2012**, *67*, 893–906, DOI: [10.5560/znb.2012-0186](https://doi.org/10.5560/znb.2012-0186).
- [41] A. Iandelli, The structure of some ternary intermetallic compounds of the rare earths, *J. Alloys Compd.* **1994**, *203*, 137–138, DOI: [10.1016/0925-8388\(94\)90724-2](https://doi.org/10.1016/0925-8388(94)90724-2).
- [42] F. Weitzer, A. Leithe-Jasper, P. Rogl, A. Rainbacher, G. Wiesinger, W. Steiner, J. Friedl, F. E. Wagner, Magnetism of ternary compounds RE₆Fe₁₃X; RE=Pr, Nd; X=Cu, Ag, Au, Zn, Cd and Hg, *J. Appl. Phys.* **1994**, *75*, 7745–7751, DOI: [10.1063/1.356606](https://doi.org/10.1063/1.356606).
- [43] X-SHAPE, STOE & Cie. GmbH, Darmstadt, Deutschland, version 2.0.7, **2005**.
- [44] X-RED, STOE & Cie. GmbH, Darmstadt, Deutschland, version 1.3.1, **2005**.
- [45] G. M. Sheldrick, A short history of SHELX, *Acta Crystallogr.* **2008**, *A64*, 112–122, DOI: [10.1107/S0108767307043930](https://doi.org/10.1107/S0108767307043930).
- [46] F. Tambornino, C. Hoch, Bad metal behaviour in the new Hg-rich amalgam KHg₆ with polar metallic bonding, *J. Alloys Compd.* **2015**, *618*, 299–304, DOI: [10.1016/j.jallcom.2014.08.173](https://doi.org/10.1016/j.jallcom.2014.08.173).
- [47] F. Tambornino, K. Schwärzer, C. Hoch, Synthesis and characterization of La_{11+x}Hg_{45-x} and RE₁₁Hg_{45.5} (RE = Sm, Nd) as hettotypes of the Sm₁₁Cd₄₅ structure type, *Inorg. Chem.* **2016**, *242*, 162–169, DOI: [10.1016/j.jssc.2016.07.001](https://doi.org/10.1016/j.jssc.2016.07.001).
- [48] L. M. Gelato, E. Parthé, Structure Tidy – a computer program to standardize crystal structure data, *J. Appl. Crystallogr.* **1987**, *20*, 139–143, DOI: [10.1107/S0021889887086965](https://doi.org/10.1107/S0021889887086965).
- [49] F. Tambornino, J. Sappl, F. Pultar, T. M. Cong, S. Hübner, T. Giftthaler, C. Hoch, Electrocrystallization - a synthetic method for intermetallic phases with polar metal-metal bonding, *Inorg. Chem.* **2016**, *55*, 11551–11559, DOI: [10.1021/acs.inorgchem.6b02068](https://doi.org/10.1021/acs.inorgchem.6b02068).
- [50] H.-J. Deiseroth, D. Toelstede, Na₃Hg: Das natriumreichste Amalgam im System Natrium-Quecksilber, *Z. Anorg. Allg. Chem.* **1992**, *615*, 43–48, DOI: [10.1002/zaac.19926150909](https://doi.org/10.1002/zaac.19926150909).
- [51] H.-J. Deiseroth, D. Toelstede, Na₈Hg₃: ein alkalimetallreiches Amalgam mit isolierten Quecksilberanionen?, *Acta Crystallogr.* **1970**, *A26*, 437–439, DOI: [10.1107/S0567739470001122](https://doi.org/10.1107/S0567739470001122).

- [52] H.-J. Deiseroth, A. Strunck, W. Bauhofer, RbHg₂ und CsHg₂, Darstellung, Kristallstruktur, elektrische Leitfähigkeit, *Z. Anorg. Allg. Chem.* **1988**, 558, 128–136, DOI: [10.1002/zaac.19885580112](https://doi.org/10.1002/zaac.19885580112).
- [53] E. Todorov, S. C. Sevov, *J. Solid State Chem.* **2000**, 149, 419–427, DOI: [10.1006/jssc.1999.8569](https://doi.org/10.1006/jssc.1999.8569).
- [54] C. Hoch, A. Simon, Cs₂Hg₂₇, das quecksilberreichste Amalgam – ein naher Verwandter der Bergman-Phasen, *Z. Anorg. Allg. Chem.* **2008**, 634, 853–856, DOI: [10.1002/zaac.200700535](https://doi.org/10.1002/zaac.200700535).
- [55] V. A. Blatov, A. P. Shevchenko, D. M. Proserpio, Applied Topological Analysis of Crystal Structures with the Program Package ToposPro, *Cryst. Growth Des.* **2014**, 14, 3576–3586, DOI: [10.1021/cg500498k](https://doi.org/10.1021/cg500498k).
- [56] O. Gunnarsson, M. Calandra, J. E. Han, Saturation of electrical resistivity, *Rev. Mod. Phys.* **2003**, 75, 1085–1099, DOI: [10.1103/RevModPhys.75.1085](https://doi.org/10.1103/RevModPhys.75.1085).
- [57] A. F. Ioffe, A. R. Regel, Non-crystalline, amorphous and liquid electronic semiconductors, *Prog. Semicond.* **1960**, 4, 237–291.
- [58] A. A. Coelho, TOPAS and TOPAS-Academic: an optimization program integrating computer algebra and crystallographic objects written in C++, *J. Appl. Cryst.* **2018**, 51, 210–218, DOI: [10.1107/S1600576718000183](https://doi.org/10.1107/S1600576718000183).
- [59] A. L. Spek, Structure validation in chemical crystallography, *Acta Crystallogr.* **2009**, D65, 148, DOI: [10.1107/S090744490804362X](https://doi.org/10.1107/S090744490804362X).
- [60] N. W. Alcock, Crystal measurements for absorption correction, *Z. Anorg. Allg. Chem.* **1990**, 587, 103–109, DOI: [10.1002/zaac.19905870112](https://doi.org/10.1002/zaac.19905870112).
- [61] R. F. W. Bader, A quantum theory of molecular structure and its applications, *Chem. Rev.* **1991**, 91, 893–928, DOI: [10.1021/cr00005a013](https://doi.org/10.1021/cr00005a013).
- [62] P. Blaha, K. Schwarz, F. Tran, R. Laskowski, G. Madsen, L. Marks, WIEN2k: An APW+lo program for calculating the properties of solids, *J. Chem. Phys.* **2020**, 152, 074101, DOI: [10.1063/1.5143061](https://doi.org/10.1063/1.5143061).
- [63] J. P. Perdew, K. Burke, M. Enzerhof, Generalized Gradient Approximation Made Simple, *Phys. Rev. Lett.* **1996**, 77, 3865–3868, DOI: [10.1103/PhysRevLett.77.3865](https://doi.org/10.1103/PhysRevLett.77.3865).
- [64] T. Hohl, R. K. Kremer, S. G. Ebbinghaus, S. A. Khan, J. Minár, C. Hoch, Influence of Disorder on the Bad Metal Behavior in Polar Amalgams, *Inorg. Chem.* **2023**, DOI: [10.1021/acs.inorgchem.2c04430](https://doi.org/10.1021/acs.inorgchem.2c04430).
- [65] T. Hohl, L. Nusser, J. Wulfes, C. Hoch, Ternary Amalgams: Expanding the structural variety of the Gd₁₄Ag₅₁ family, *submitted to: Z. Kristallogr.* **2023**.

4.2 Ternary Amalgams: Expanding the Structural Variety of the $\text{Gd}_{14}\text{Ag}_{51}$ Structure Family

Timotheus Hohl¹, Lukas Nusser¹, Jessica Wulfes² and Constantin Hoch^{1,*}

* Correspondence: constantin.hoch@cup.uni-muenchen.de; Tel.: +49-89-2180-77421

¹ Department Chemie, Ludwig-Maximilians-Universität München

² Institut für Physikalische Chemie, CAU Kiel

published in: *Z. Kristallogr.* **2023**, in print.

DOI: [10.1515/zkri-2023-0007](https://doi.org/10.1515/zkri-2023-0007)

Reprinted (adapted) from *Zeitschrift für Kristallographie - Crystalline Materials*. Copyright 2023 De Gruyter.

4.2.1 Abstract

In intermetallic chemistry, the $\text{Ag}_{14}\text{Gd}_{51}$ structure type is rather common and has many amalgam representatives. Up to today, binary amalgams of this type have been described for $M = \text{Na}, \text{Ca}, \text{Sr}, \text{Eu}, \text{Yb}$, and the structure family still is growing. $\text{Yb}_{11}\text{Hg}_{54}$ is the only representative with a fully ordered crystal structure, and all other representatives

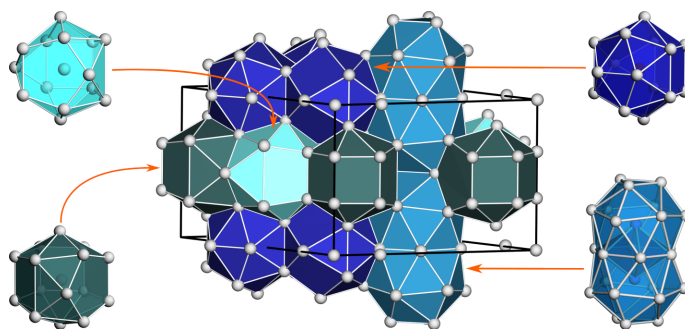


exhibit individual disorder phenomena or patterns. The diversity of disorder phenomena in this structural family is unique. In order to shed a light on the underlying reasons for this unexpected structural complexity, we compare the available literature structure models with three new ternary variants, $\text{Yb}_{10.7}\text{Sr}_{0.3}\text{Hg}_{54}$, $\text{Ca}_{4.5}\text{Eu}_{6.5}\text{Hg}_{54}$ and $\text{Ca}_{6.9}\text{Na}_{4.1}\text{Hg}_{54}$ (all in space group type $P\bar{6}$, $a = 13.5811(11)$, $13.5406(8)$ and $13.564(5)$ Å, $c = 9.7948(12)$, 9.7149 and $9.810(7)$ Å for $\text{Yb}_{10.7}\text{Sr}_{0.3}\text{Hg}_{54}$, $\text{Ca}_{4.5}\text{Eu}_{6.5}\text{Hg}_{54}$ and $\text{Ca}_{6.9}\text{Na}_{4.1}\text{Hg}_{54}$, respectively). Their crystal structures have been examined in detail on the basis of both single crystal and powder X-ray diffraction data. Each of the three new amalgams exhibits its own set of disorder phenomena that is again different from those of the respective binary variants.

The synopsis of the crystal structures and their individual disorder phenomena indicates that the reason for the disorder phenomena cannot be found only by analyzing geometric details such as atomic radii quotients or coordination polyhedral volumina, and additional electronic reasons must be assumed.

4.2.2 Introduction

The combination of strong local Coulomb fields caused by a considerable but incomplete electron transfer from a less electronegative to a more electronegative component together with overall metallic behaviour is indicative for polar intermetallics and results in combination of physical properties interesting for e.g. thermoelectric materials. Due to the complicated bonding situation, the structural diversity of amalgams of the less-noble metals is extremely rich. They serve as model systems for investigation of the polar metallic bond, Due to the unfavourable electron affinity of Hg,^[1] the electron transfer in all amalgams of less electronegative metals is incomplete, and the resulting negative partial charge will be delocalized over the existing Hg network. The

ability to delocalize the partial charges increases with the size of the Hg sublattice, which in turn is dependent on the Hg content. Therefore, Hg-rich amalgams serve as ideal candidates for the investigation of polar metals with especially large ionic contributions. Among them, a large number with compositions close to $M\text{Hg}_{\sim 5}$ have been reported. They belong to the $\text{Gd}_{14}\text{Ag}_{51}$ structure family, together with a large number of other, Hg-free intermetallic compounds (see Table 4.8). The amalgams have a common basic structure, but each compound shows distinct disorder or superstructure patterns. The only representative of the less-noble amalgams in this structure family without any disorder is $\text{Yb}_{11}\text{Hg}_{54}$.^[2] While the precise structural elucidation has been made easier by modern X-ray methods, the reasons for these disorder phenomena are still unclear. We have synthesized ternary amalgam structures with two different less electronegative metals and analyzed their crystal structures. Increasing the number of individual representatives helps in discerning patterns and trends and to identify parameters which are responsible for the realisation of the different individual disorder phenomena. By choosing the right combination of two different less electronegative metals, a differentiation between electronic and geometric effects can succeed.

Table 4.8: List of known compounds belonging to the $\text{Gd}_{14}\text{Ag}_{51}$ structure family. Data are compiled from Pearson's Crystal Data.^[3]

Compound	Lit.	Compound	Lit.	Compound	Lit.	Compound	Lit.
Binary variants							
$\text{Dy}_{14}\text{Ag}_{51}$	[4]	$\text{Er}_{14}\text{Ag}_{51}$	[5]	$\text{Gd}_{14}\text{Ag}_{51}$	[5]	$\text{Ho}_{14}\text{Ag}_{51}$	[5]
$\text{La}_{14}\text{Ag}_{51}$	[5]	$\text{Nd}_{14}\text{Ag}_{51}$	[6]	$\text{Pr}_{14}\text{Ag}_{51}$	[6]	$\text{Pu}_{141}\text{Ag}_{51}$	[7]
$\text{Sm}_{14}\text{Ag}_{51}$	[5]	$\text{Tb}_{14}\text{Ag}_{51}$	[4]	$\text{Y}_{14}\text{Ag}_{514}$	[5]	$\text{Cu}_{14}\text{Au}_{51}$	[5]
$\text{Gd}_{14}\text{Au}_{51}$	[8]	$\text{Ho}_{14}\text{Au}_{51}$	[8]	$\text{La}_{14}\text{Au}_{51}$	[6]	$\text{Nd}_{14}\text{Au}_{51}$	[6]
$\text{Pr}_{14}\text{Au}_{51}$	[6]	$\text{Pu}_{14}\text{Au}_{51}$	[9]	$\text{Sm}_{14}\text{Au}_{51}$	[8]	$\text{Tb}_{14}\text{Au}_{51}$	[8]
$\text{Th}_{14}\text{Au}_{51}$	[10]	$\text{U}_{14}\text{Au}_{51}$	[11]	$\text{Ca}_{14}\text{Cd}_{51}$	[12]	$\text{Eu}_{14}\text{Cd}_{51}$	[13]
$\text{Yb}_{14}\text{Cd}_{51}$	[13]	$\text{Hf}_{14}\text{Cu}_{51}$	[14]	$\text{Th}_{14}\text{Cu}_{51}$	[15]	$\text{Y}_{14}\text{Cu}_{53}$	[16]
$\text{Zr}_{14}\text{Cu}_{51}$	[14]	$\text{Ca}_{10.9}\text{Hg}_{54.1}$	[17]	$\text{Eu}_{10}\text{Hg}_{55}$	[18]	$\text{Na}_{11}\text{Hg}_{52}$	[19]
$\text{Sr}_{10.5}\text{Hg}_{54.5}$	[17]	$\text{Yb}_{11}\text{Hg}_{54}$	[2]				
Ternary variants							
$\text{Er}_{14}\text{Ag}_{48}\text{Sn}_3$	[20]	$\text{Gd}_{14}\text{Ag}_{36.4}\text{Ga}_{14.6}$	[21]	$\text{Tb}_{14}\text{Ag}_{32.3}\text{Ga}_{7.8}$	[22]	$\text{Gd}_{13.5}\text{Ag}_{49.2}\text{Sn}_{2.3}$	[23]
$\text{La}_{14}\text{Ag}_{48.8}\text{Mg}_{2.2}$	[24]	$\text{La}_{10.1}\text{Sn}_{3.9}\text{Ag}_{51}$	[25]	$\text{Pr}_{14}\text{Ag}_{47.8}\text{Sn}_{3.2}$	[26]	$\text{Ca}_{14}\text{Au}_{46}\text{Sn}_5$	[27]
$\text{U}_{14}\text{Au}_{42}\text{Cu}_9$	[28]	$\text{Er}_{14}\text{Au}_{34.1}\text{Ga}_{16.9}$	[29]	$\text{Tm}_{14}\text{Au}_{34.4}\text{Ga}_{16.6}$	[29]	$\text{Pr}_{14}\text{Au}_{42.5}\text{Sn}_{8.5}$	[30]
$\text{Dy}_{14}\text{Cu}_{44.5}\text{Ga}_{6.5}$	[31]	$\text{Gd}_{14}\text{Cu}_{48}\text{Ga}_3$	[32]	$\text{Ho}_{14}\text{Cu}_{44.5}\text{Ga}_{6.5}$	[33]	$\text{Lu}_{14}\text{Cu}_{41}\text{Ga}_{10}$	[34]
$\text{Sc}_{14}\text{Cu}_{37}\text{Ga}_{14}$	[35]	$\text{Sm}_{14}\text{Cu}_{46}\text{Ga}_5$	[36]	$\text{Tb}_{14}\text{Cu}_{48}\text{Ga}_3$	[32]	$\text{Y}_{14}\text{Cu}_{44.5}\text{Ga}_{6.5}$	[37]
$\text{Y}_{11.7}\text{Zr}_{2.3}\text{Cu}_{51}$	[38]						

4.2.3 Experimental

Synthesis

Considering the high sensitivity of the starting materials and the reaction products, all experiments were performed under inert gas conditions; either in an argon-filled glove box ($p(\text{H}_2\text{O})$ and $p(\text{O}_2) < 0.1$ ppm) or with the use of Schlenk apparatus (vacuum/argon). Prior to usage, Mercury was purified by filtration, subsequent stirring with half-concentrated HNO_3 to dissolve impurities of less noble metals, and then double distillation in vacuum.

For the synthesis of $\text{Yb}_{10.7}\text{Sr}_{0.3}\text{Hg}_{54}$, 76.0 mg (0.44 mmol) Yb (99.999 %, Smart Elements, dendritic pieces), 37.2 mg (0.42 mmol) Sr (99.99%, Sigma Aldrich, dendritic pieces) and 888.8 mg (4.43 mmol) Hg were filled into a Ta crucible and sealed by arc-welding. The crucible was then heated to 1073 K with 100 K h^{-1} , kept at this temperature for 12 h and then rapidly cooled with ice water.

$\text{Ca}_{4.5}\text{Eu}_{6.5}\text{Hg}_{54}$ was synthesised by weighing 37.5 mg (0.94 mmol) Ca (Sigma-Aldrich, 99.99 %, dendritic pieces), 136.7 mg (0.90 mmol) Eu (99.99 %, Smart Elements, dendritic pieces) and 1.847 g (9.21 mmol) Hg into a Ta crucible and sealing via arc-welding. It was then heated to

1073 K, kept at this temperature for 24 h, cooled with 0.5 K h^{-1} to 923 K and rapidly cooled to room temperature with ice water.

For the synthesis of $\text{Ca}_{6.9}\text{Na}_{4.1}\text{Hg}_{54}$, 25.5 mg (0.61 mmol) Ca, 14.1 mg (0.61 mmol) Na (distilled twice, MPI FKF Stuttgart, Germany) and 1.961 g (9.78 mmol) Hg were filled into a Ta crucible and welded shut. With 50 K h^{-1} , the reaction mixture was heated to 573°C , kept at this temperature for four months and then rapidly cooled to room temperature with ice water.

Single Crystal Analysis

Portions of the reaction products were transferred from the glove box under dried paraffin oil. Typically, amalgams of the $\text{Gd}_{14}\text{Ag}_{51}$ structure type form prismatic to needle-like crystals. Suitable single crystals were selected with a binocular and mounted in glass capillaries ($\varnothing = 0.2 \text{ mm}$) filled with potassium-dried paraffin oil. The capillaries were mounted and centered either on the one-circle goniometer of an IPDS-1 diffractometer system (Stoe & Cie, Darmstadt, Germany, Ag- $\text{K}\alpha$ radiation) in a general orientation to avoid systematic loss of reflections with high l indices, or on a D8 Quest diffractometer system (Bruker AXS, Karlsruhe, Germany) with microfocussed Mo- $\text{K}\alpha$ radiation, Göbel mirror optics and a Photon II CMOS detector. The orientation was validated by evaluating the orientation matrix obtained from orientation images and adjusting the angular slides of the goniometer head.

Data were collected in φ mode for the accessible part of at least one half of the Ewald sphere ($\varphi_{max} = 200^\circ$). After collection of the data and Lorentz and polarization correction, the crystal shape was measured and the faces indexed. The shape was then optimized on the basis of the intensity distribution,^[39] and the subsequent numerical absorption correction was carefully performed on this basis.^[40] Since refinement taking the $\text{Ca}_{11}\text{Hg}_{54}$ model as starting values did not lead to converging results, structure solution and refinement of $\text{Ca}_{4.5}\text{Eu}_{6.5}\text{Hg}_{54}$ were performed anew in space group $P\bar{6}$, yielding four mixed atomic positions for the less noble metals and 16 for mercury. $\text{Yb}_{10.7}\text{Sr}_{0.3}\text{Hg}_{54}$ was refined starting from the structure model of $\text{Yb}_{11}\text{Hg}_{54}$. Each crystallographic position was carefully checked for mixed and/or underoccupancy. Single crystal data sets for $\text{Yb}_{10.7}\text{Sr}_{0.3}\text{Hg}_{54}$ were collected from several crystals, and the refined mixed occupation patterns as well as the refined atomic fractions were equal within the error margin. One crystal proved to be the binary amalgam $\text{Sr}_{10.7}\text{Hg}_{54.3}$ [17], identified by its singular disorder pattern and slightly but significantly larger lattice parameters. Crystallographic data and data collection and handling details for $\text{Yb}_{10.7}\text{Sr}_{0.3}\text{Hg}_{54}$ and $\text{Ca}_{4.5}\text{Eu}_{6.5}\text{Hg}_{54}$ are listed in Tables 4.9 and 4.11. For the latter, powder diffraction data and Rietveld refinements thereof were used for further validation of the results obtained from single crystal data, resulting in only slightly different occupancy factors (see Table 4.15).

The crystal quality of the ternary Ca-Na-Amalgam was insufficient for single crystal measurements, and the structure was determined by Rietveld refinement of powder diffraction data obtained by Synchrotron radiation.

Powder diffraction and Rietveld refinement

For X-ray powder diffraction experiments, powder samples of the Ca-Eu amalgam and Ca-Na amalgam were prepared inside an argon-filled glovebox. The samples were ground in an agate mortar, in both cases with the addition of ca. 50 vol.-% diamond powder (Sigma Aldrich, synthetic monocrystalline powder, $< 1 \mu\text{m}$) in order to account for their ductility and high absorption coefficients. The samples were then filled in glass capillaries (inner dia. 0.5 mm, Hilgenberg, Malsfeld, Germany) and flame-sealed with birch tar. The samples were investigated with synchrotron radiation ($\lambda = 0.20735 \text{ \AA}$, PETRA III, Beamline P02.1, DESY, Hamburg, Germany) equipped with a VAREX XRD 4343CT Flat Panel Detector (2880×2880 pixels, $150 \times 150 \mu\text{m}$ pixel size) and LaB_6 (NIST 660c) as an external standard. Data were integrated with the DIOPITAS software package.^[41] Rietveld refinement was performed with the GSAS-II software.^[42] Results of the Rietveld refinements of $\text{Ca}_{6.9}\text{Na}_{4.1}\text{Hg}_{54}$ and $\text{Ca}_{4.5}\text{Eu}_{6.5}\text{Hg}_{54}$ are listed in Table 4.10 and

4.12. For the Ca-Eu amalgam, the model derived from single crystal structure refinement used as starting values, while for the Ca-Na amalgam, the model of the Ca amalgam was employed. As a result of the high parameter to data ratio, all standard deviations of all least-squares parameters were obtained as penultimate results, while the final refinement excluded all background parameters as well as atomic positions and isotropic displacement factors in order to reach convergence.

The powder diffractograms collected under the same circumstances from a identically prepared sample of the Sr-Yb amalgam yielded only very unsatisfying Rietveld refinement results. The underlying reason is the presence of the binary amalgam $\text{Sr}_{10.7}\text{Hg}_{54.3}$ [Mar]. This phase shows a very similar diffraction pattern with only slightly diverging lattice parameters. A simultaneous refinement of both phases was not successful, as the presence of the binary amalgam leads only leads to a broadening of the reflections, even at high diffraction angles (see Figure 4.10 and inset). Therefore, we had to rely on single crystal data for the refinement of the structural details of $\text{Yb}_{10.7}\text{Sr}_{0.3}\text{Hg}_{54}$.

4.2.4 Results

The crystal structures of $\text{Ca}_{6.9}\text{Na}_{4.1}\text{Hg}_{54}$, $\text{Ca}_{4.5}\text{Eu}_{6.5}\text{Hg}_{54}$ and $\text{Yb}_{10.7}\text{Sr}_{0.3}\text{Hg}_{54}$ represent hettotypes of the $\text{Gd}_{14}\text{Ag}_{51}$ aristotype structure and crystallize in the hexagonal space-group type $P\bar{6}$. In all three crystal structures, four different coordination polyhedra around the less noble metal positions are present, with coordination numbers between 14 and 16. Accordingly, there are four crystallographically independent atomic sites for the less noble metal atoms, while the number of crystallographic Hg positions is 14 (Sr-Yb and Ca-Na amalgam) or 16 (Ca-Eu amalgam). The disorder phenomena observed for all amalgams in this structural family affect only few crystallographic positions: the four M positions can show mixed occupation with Hg (this is the case in Eu amalgam) or with two less electronegative metals (in the Ca, the Sr, the Na-Ca, the Eu-Ca and the Yb-Sr amalgam), and only some Hg positions can show either mixed occupation with a less electronegative metal (in the Na amalgam) or underoccupation in combination with split positions (this occurs in the Eu and the Ca-Eu amalgam). In addition, superstructures can occur: the unit cells of the Na and the Na-Ca amalgams are $3 \times 3 \times 1$ supercells of the original $\text{Gd}_{14}\text{Ag}_{51}$ unit cell, retaining the space group type $P\bar{6}$. When a measure for structural complexity is calculated following the concept given by Krivovichev,^[43] it becomes clear that the overall structural complexity is only marginally increased by introducing mixed or split positions, but increases drastically when lowering symmetry (by descending from $P6/m$ to $P\bar{6}$ or by increasing the cell volume in a supercell).^[2]

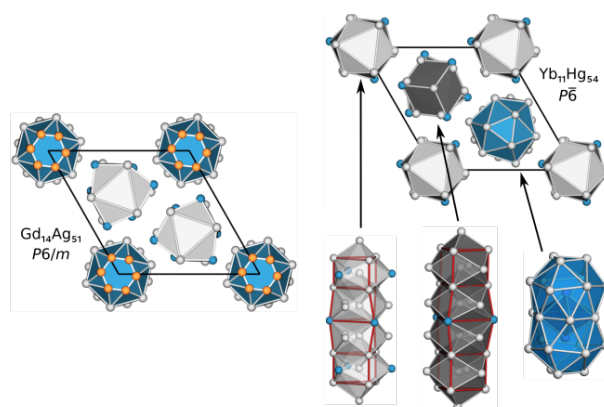


Fig. 4.8: Comparison of the crystal structure of $\text{Yb}_{11}\text{Hg}_{54}$ (right) to the $\text{Gd}_{14}\text{Ag}_{51}$ aristotype (left). Yb/Gd and its surrounding interpenetrating Frank-Kasper type coordination polyhedra (cp) are depicted in blue, while Hg/Ag and its cp's are coloured in grey. Mutually exclusive Ag positions in the $\text{Gd}_{14}\text{Ag}_{51}$ structure are depicted in orange. The color differentiation (light/dark grey) of the cp's around Hg1–Hg4 highlights the loss of symmetry.

$\text{Yb}_{11}\text{Hg}_{54}$ - the common denominator

So far, the binary amalgam $\text{Yb}_{11}\text{Hg}_{54}$ is the only representative with a fully ordered crystal structure. It contains four crystallographically independent sites for Yb, and fourteen for Hg and has been described extensively by F. Tambornino.^[2] The relation to the $\text{Gd}_{14}\text{Ag}_{51}$ aristotype is shown in Fig. 4.8.

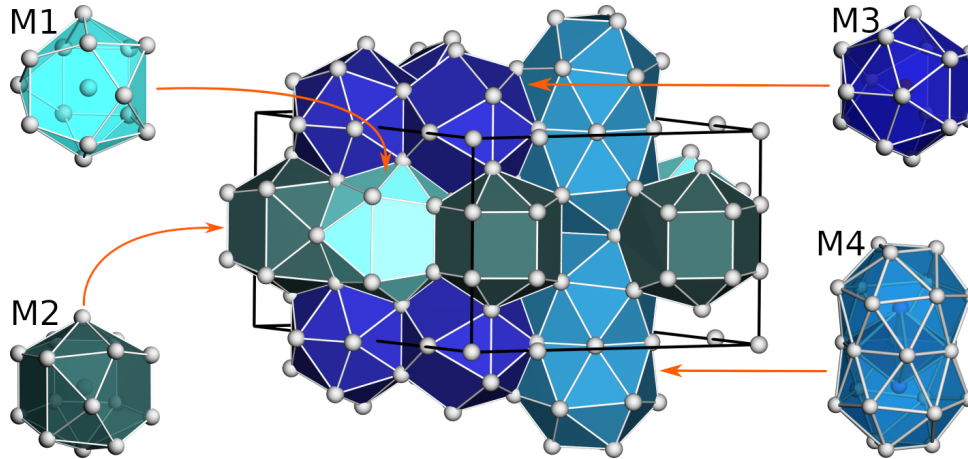


Fig. 4.9: Crystal structure of $\text{Yb}_{11}\text{Hg}_{54}$, with the emphasis on the coordination polyhedra (cp's) around the Yb positions (middle), the unit cell is marked in black. top left (M1): irregular four-capped pentagonal prism (CN = 14) around Yb1; lower left (M2): irregular tricapped hexagonal prism (CN = 15) around Yb2; top right (M3): irregular fivecapped pentagonal prism (CN = 15) around Yb3; lower right (M4): interpenetrating Frank-Kasper polyhedra (CN = 16) around Yb4.

For the consideration of the amalgam structures, however, a different approach emphasising the coordination polyhedra around the less noble metal atomic positions is more intuitive. This approach is visualized in Fig. 4.9. Four different polyhedra for the different crystallographic positions of Yb are needed: the polyhedron around Yb1 (M1) can be derived from a fourcapped pentagonal prism, type (M2) around Yb2 is a tricapped hexagonal prism, type (M3) around Yb3 is a fivecapped pentagonal prism, and type M4 around Yb4 forms pairs of interpenetrating Frank-Kasper polyhedra. While this representation is not space-filling, it is most suitable for the comprehensive description and comparison of the crystal structures.

Yb_{10.7}Sr_{0.3}Hg₅₄

Table 4.9: Crystallographic data and details on single crystal data collection, structure solution and refinement for Yb_{10.7}Sr_{0.3}Hg₅₄. All standard deviations are given in parentheses in the units of the last digit.

Refined Composition	Yb _{10.71(6)} Sr _{0.29(6)} Hg ₅₄	R_{int}	0.1694
Crystal system	hexagonal	R_{σ}	0.0764
Space group	$P\bar{6}$, No. 174	$F(000)$	2072
Lattice parameters a, c [Å]	13.5379(12), 9.7488(12),	Corrections	Lorentz, Polarisation, Absorption
V [Å ³]	1547.3(4)	Absorption correction	numerical, indexed crystal faces [44]
Z	1	Structure solution	direct methods [45]
Density (X-ray) [g · cm ⁻³]	13.62	Structure refinement	full-matrix least-squares
Diffractometer	Bruker D8 Quest		on F^2 [45]
	MoK α radiation,	No. of L.S. parameters	112
	Göbel optics	Goof	1.115
Absorption coeff. μ [mm ⁻¹]	149.4	R values ($I \geq 2\sigma(I)$)	$R1 = 0.0594$,
ϑ range [°]	10.35–56.56		$wR2 = 0.1429$
Index range	$0 \leq h \leq 15$,	R values (all data)	$R1 = 0.0648$,
	$0 \leq k \leq 15$,		$wR2 = 0.1451$
	$0 \leq l \leq 12$	Res. $\rho(e^-)$ min/max [$e^- \text{Å}^{-3}$]	-5.37 / +5.17
No. of collected refl.	75124	Extinction coefficient	0.00064(9)
No. of independent refl.	1281	CCDC deposition No.	2240995
No. of indep. refl. ($I \geq 2\sigma(I)$)	1211		

For the determination of the structure of the ternary Sr-Yb amalgam, the fully ordered model of Yb₁₁Hg₅₄ was used as starting values. No additional atomic positions for Hg were found, while thermal displacement ellipsoids in combination with the distances to Hg and free refinement of the occupation factors indicated a mixed occupation of the Yb position with Sr. For validation, it was then cross-checked with mixed occupation with Hg instead of Sr. Details on the structure solution and refinement are listed in Table 4.9, fractional atomic coordinates, occupancies and equivalent isotropic displacement parameters are listed in Table 4.15 (middle).

The new ternary Sr-Yb amalgam represents the most simple disorder pattern: only one of the four different atomic positions for the electropositive metals (M4, inside the Frank-Kasper type polyhedron with CN = 16) shows mixed occupancy: 86% Yb and 14% Sr. The atomic positions M1–M3 are fully occupied by Yb. As the volumes of the coordination polyhedra (calculated with Vesta,^[46] see Table 4.14) increase with the respective coordination numbers, it seems reasonable to find Sr only in the largest coordination polyhedron M4 due to the difference in atomic radii of Sr and Yb ($r_{\text{Sr}}^{\text{met}} = 249$ pm, $r_{\text{Yb}}^{\text{met}} = 226$ pm^[47]). The observed M–Hg distances (3.222(8)–3.574(9) Å) are in good agreement with reported values (Yb₁₁Hg₅₄: 3.197–3.51 Å, Sr_{10.5}Hg_{54.5}: 3.336–3.570 Å),^[2,17] see also Table 4.13 and Fig. 4.14. While Rietveld refinement of a bulk powder sample did not lead to convergence, it can be seen in the powder diffractogram that the theoretical patterns calculated for the ternary amalgam model and for the binary Yb amalgam can be discerned (see Fig. 4.10). The uptake of the observed small quantity of Sr in the Yb amalgam therefore can be regarded as the maximum allowed amount.

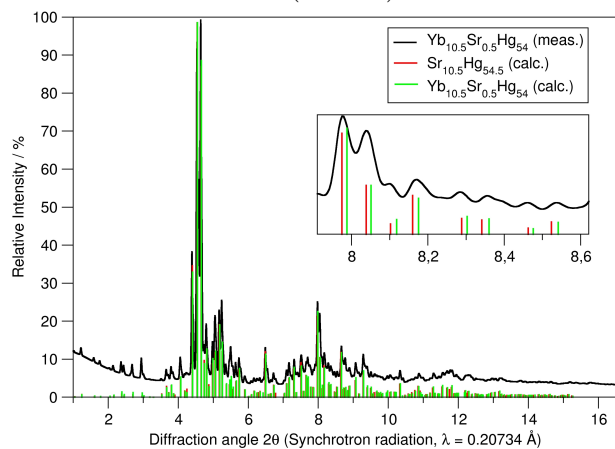


Fig. 4.10: Powder diffractogram of a bulk sample of Yb_{10.7}Sr_{0.3}Hg₅₄ (black) in comparison to theoretical diffraction patterns calculated from the single crystal structure models of the binary strontium amalgam Sr_{10.5}Hg_{54.5} [17] (red) and the new ternary variant Yb_{10.5}Sr_{0.5}Hg₅₄ (green). The inset shows an enlarged cutout emphasizing the close proximity of the reflections of the binary and the ternary amalgams.

Ca_{6.9}Na_{4.1}Hg₅₄

Crystallographic data obtained on the basis of a Rietveld refinement of Ca_{6.9}Na_{4.1}Hg₅₄ are listed in Table 4.10, the atomic positions and the occupancy factors are listed in Table 4.15. A graphical representation of the refinement results is shown in Fig. 4.11. Since the structure was determined by Rietveld refinement starting from the literature Ca_{14-x}Hg_{51+x} single crystal model,^[17] only isotropic displacement parameters could be calculated. The observed M–Hg distances (3.06–3.68 Å) are within the range of the distances present in the binary amalgams (3.20–3.531 Å) for Ca_{10.9}Hg_{54.1}, 3.15–3.78 Å for Na₁₁Hg₅₂),^[17,19] see Table 4.13 and Fig 4.14.

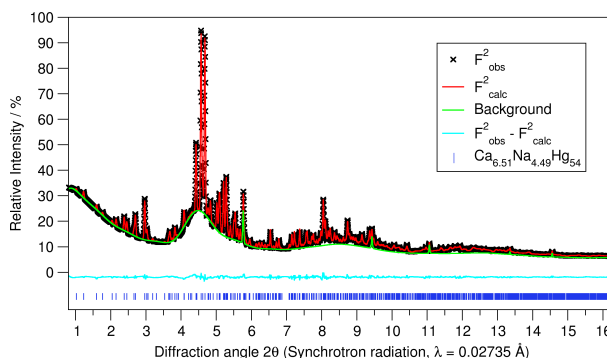


Fig. 4.11: Graphical representation of the Rietveld refinement of Ca_{6.9}Na_{4.1}Hg₅₄. The difference plot indicates no existence of additional crystalline phases, while the pronounced diffuse background originates from excess elemental Mercury.

Table 4.10: Basic crystallographic data and details on data collection treatment as a result of a Rietveld refinement for Ca_{6.9}Na_{4.1}Hg₅₄. All standard deviations are given in parentheses in the units of the last digit.

Refined composition	Ca_{6.9(1)}Na_{4.1(1)}Hg₅₄	Final L.S. Parameter shift	0.072
Crystal system	hexagonal	2θ range [°]	0.002–17.23
Space group	$P\bar{6}$ (No. 174)	Sample geometry	capillary (∅ = 0.5 mm)
Lattice parameters [Å]	$a = 13.546(5)$ $c = 9.810(7)$	Refined parameters	80
V [Å ³]	1558.8(16)	Background function	cosine
Z	1	Background parameters	35
Calc. density [g cm ⁻³]	12.76	Peak shape function	Finger-Cox-Jephcoat
Radiation	Synchrotron, $\lambda = 0.20735$ Å	R_p %	1.22
Data points	4129	R_{wp} %	1.67
Detector	Varex XRD 4343CT flat panel detector	R_{F2} %	0.25
		R_{Bragg} %	2.73
		GooF on on χ^2	6.79
		CCDC deposition No.	2240996

The ternary Ca-Na amalgam Ca_{6.9}Na_{4.1}Hg₅₄ ($P\bar{6}$, $a = 13.546(5)$, $c = 9.810(7)$ Å) exhibits a new disorder phenomenon, uncommon to all other crystal structures in this field: while the crystallographic site M1 is occupied only by Ca, the sites M2–M4 are occupied by a mixture of Ca and Na, and each site exhibits a different Ca : Na ratio (see Table 4.15). The ratio of Ca : Na follows no obvious pattern: For the atomic positions M2 and M3 with the same coordination number CN = 15, the occupancy is almost reversed (80% Na / 20% Ca for M2, 15% Na / 85% Ca for M3), and in the larger polyhedron M4 the sodium fraction is higher as the Ca fraction (61% Na and 39% Ca). The observed disorder phenomena cannot be derived as a combination of the disorder phenomena of the respective binary amalgams – the binary Ca amalgam contains only one disordered crystallographic site (M4, mixed occupancy by Ca and Hg), the Na amalgam has a 3×3×1 superstructure with one Hg site showing mixed occupancy by Na and Hg. Since the metallic radii of Na, Ca and Hg are rather similar ($r_{Na}^{met} = 227$ pm, ($r_{Ca}^{met} = 231$ pm, ($r_{Hg}^{met} = 223$ pm^[47]), one would expect the same mixing fraction for all atomic positions if only geometric considerations were applicable.

Ca_{4.5}Eu_{6.5}Hg₅₄

The structure of the ternary Ca-Eu amalgam was first solved and refined from single crystal X-ray diffraction data (see Table 4.11 for details), however, a closer evaluation of precession images and data statistics revealed that the crystal quality was insufficient for a concise picture. The reflections in the $0kl$ and $hk0$ plane are well defined, the ones in $h0l$ revealed high-intensity smeared profiles (see Fig. 4.12), indicating an intergrowth of poorly oriented crystal specimens. This is in agreement with the observation that the crystals grow as needles and tend to form agglomerations. Nevertheless, data quality was sufficient to derive a preliminary structure model. Rietveld refinement from powder diffraction (see Fig. 4.13) was performed subsequently with the parameters from the single crystal model as starting values. The refinement results are listed in Table 4.12, fractional atomic coordinates as well as occupancy factors for both single crystal data and results from the Rietveld refinement are compiled in Table 4.15. It is noteworthy that the details of the structural disorder from the single crystal, albeit with low significance, are very close from those derived from the bulk powder diagram. This observation has been made in the course of many amalgam studies and indicates that the overall variance of the disorder phenomena is small over a large ensemble of individual crystals.

Table 4.11: Crystallographic data and details on single crystal data collection, structure solution and refinement for Ca_{4.9}Eu_{6.1}Hg₅₄. All standard deviations are given in parentheses in the units of the last digit.

Refined composition	Ca _{4.9(5)} Eu _{6.1(5)} Hg ₅₄
Crystal system	hexagonal
Space group	$P\bar{6}$ (No. 174)
Lattice parameters (Å)	$a = 13.546(5)$ $c = 9.810(7)$
V (Å ³)	1558.8(16)
Z	1
Calc. density (g cm ⁻³)	12.755
Diffractometer	STOE IPDS 1
	AgK α radiation, $\lambda = 0.56087$ Å
Data collection temperature (K)	295(2)
Absorption coefficient μ (mm ⁻¹)	75.939
2θ range (°)	3.28–42.00
Indexing range	$-17 \leq h, k \leq 17$ $-12 \leq l \leq 12$
No. of observed data	14130
No. of independent data	2424
No. of independent data with $I \geq 2\sigma(I)$	1895
R_{int}	0.2066
R_{σ}	0.1041
$F(000)$	4798
Corrections	Lorentz, polarisation, absorption effects
Absorption correction	numerical, indexed crystal faces [39, 40]
Structure solution	direct methods [45]
Structure refinement	full-matrix least-squares on F^2 [45]
No. of L.S. parameters	124
Goof	1.189
R values ($I \geq 2\sigma(I)$)	$R1 = 0.1016,$ $wR2 = 0.2330$
R values (all data)	$R1 = 0.1273,$ $wR2 = 0.2447$
Res. $\rho(e^-)$ min/max ($e^- \text{Å}^{-3}$)	$-9.086/+9.480$
Extinction coefficient	0.00011(2)

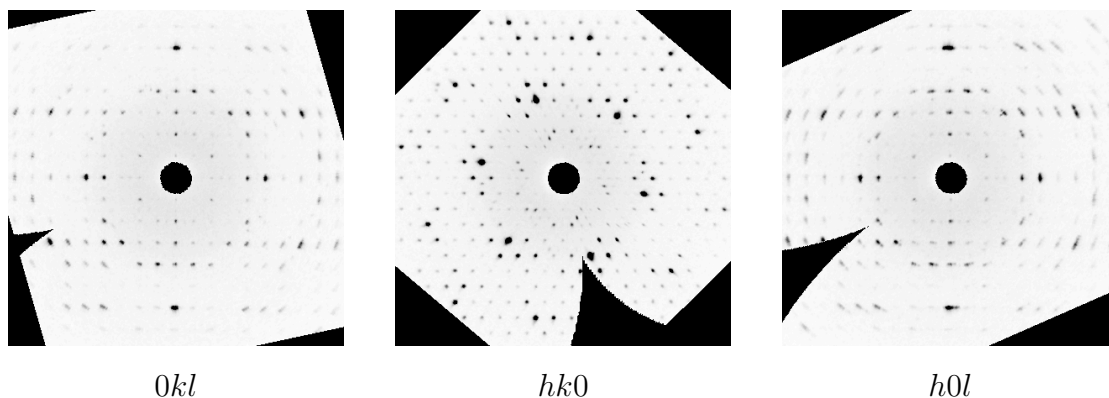


Fig. 4.12: Reciprocal lattice sections calculated from the single crystal data collection of $\text{Ca}_{4.5}\text{Eu}_{6.5}\text{Hg}_{54}$. Left: $0kl$, middle: $hk0$, right: $h0l$.

In the crystal structure of $\text{Ca}_{4.5}\text{Eu}_{6.5}\text{Hg}_{54}$, again a new disorder pattern is found. While the specific disorder pattern again cannot be derived by combining those of the binary amalgams, it can be regarded as a bridge between them: In analogy to $\text{Eu}_{10}\text{Hg}_{55}$, 16 sites for Hg exist, while a chain along c of mutually exclusive Hg split positions with a 87:13 ratio occurs. This has only been observed for the binary Eu amalgam so far. In addition, all four crystallographic positions for the electropositive metals, M1–M4, exhibit an individual mixed Ca/Eu occupancy. The ternary Ca–Eu amalgam thus shows the highest degree of disorder within the family of the $\text{Gd}_{14}\text{Ag}_{51}$ -type amalgams so far.

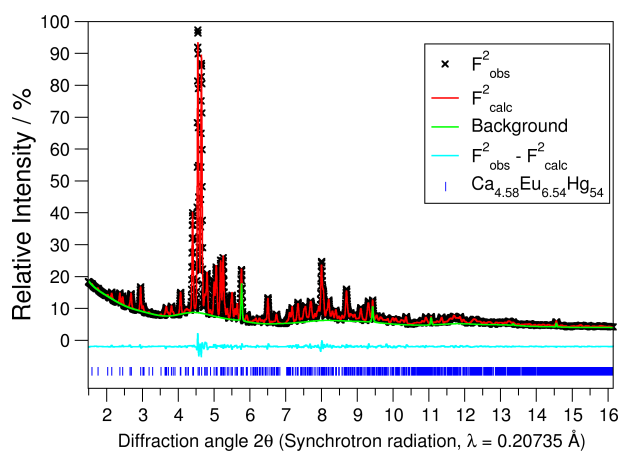
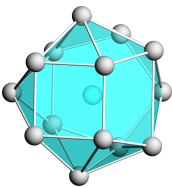
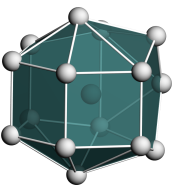
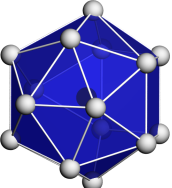
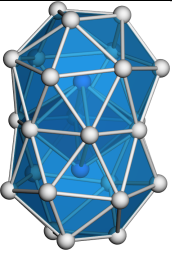
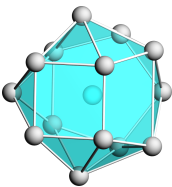
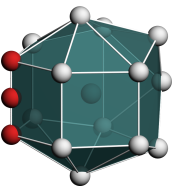
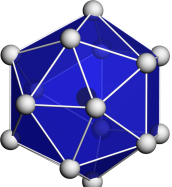
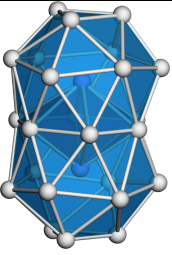
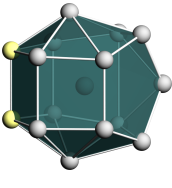
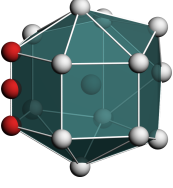
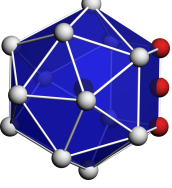
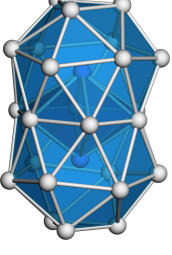


Fig. 4.13: Graphical representation of the Rietveld refinement of $\text{Ca}_{4.5}\text{Eu}_{6.5}\text{Hg}_{54}$. The difference plot indicates no existence of additional crystalline phases, while the pronounced diffuse background originates from excess elemental mercury. For crystallographic details see Table 4.12.

Table 4.12: Basic crystallographic data and details on data collection treatment as a result of a Rietveld refinement of $\text{Ca}_{4.5}\text{Eu}_{6.5}\text{Hg}_{54}$. All standard deviations are given in parentheses in the units of the last digit.

Refined composition	$\text{Ca}_{4.5(3)}\text{Eu}_{6.5(3)}\text{Hg}_{54}$	Final L.S. parameter shift	0.0566
Crystal system	hexagonal	2θ range [°]	0.002–17.23
Space group	$P\bar{6}$ (No. 174)	Sample geometry	capillary ($\varnothing = 0.5$ mm)
Lattice parameters [Å]	$a = 13.5406(8)$ $c = 9.7149(2)$	Refined parameters	51
V [Å ³]	1542.56(10)	Background function	cosine
Z	1	Background parameters	30
Calc. density [g cm ⁻³]	12.918	Peak shape function	Finger-Cox-Jephcoat
Radiation	Synchrotron, $\lambda = 0.20735$ Å	R_p %	1.73
Data points	4129	R_{wp} %	2.45
Detector	Varex XRD 4343CT flat panel detector	R_{F2} %	0.26
		R_{Bragg} %	2.46
		GooF on on χ^2	9.33
		CCDC deposition No.	2240997

Table 4.13: Comparison of the coordination polyhedra of the known binary and new ternary amalgams belonging to the $\text{Ag}_{14}\text{Gd}_{51}$ structure family around the less noble metal positions M1–4. Color codes are analogous with Fig. 4.9. Special or additional Hg positions are highlighted in yellow and red.

	M1	M2	M3	M4
				
CN	14	15	15	16
$\text{Yb}_{11}\text{Hg}_{54}$	all positions fully occupied by Yb			
$\text{Ca}_{10.9}\text{Hg}_{54.1}$	100% Ca	100% Ca	100% Ca	96% Ca 4% Hg
$\text{Sr}_{10.5}\text{Hg}_{54.5}$	100% Sr	100% Sr	100% Sr	74% Sr 26% Hg
$\text{Yb}_{10.7}\text{Sr}_{0.3}\text{Hg}_{54}$	100% Yb	100% Yb	100% Yb	86% Yb 14% Sr
$\text{Ca}_{6.9}\text{Na}_{4.1}\text{Hg}_{54}$	100% Ca	24% Ca 76% Na	84% Ca 16% Na	32% Ca 68% Na
				
CN	14	15 (+1)	15	16
$\text{Ca}_{4.5}\text{Eu}_{6.5}\text{Hg}_{54}$	36% Eu 64% Ca	79% Eu 21% Ca	57% Eu 43% Ca	66% Eu 34% Ca
	+ mutually exclusive Hg positions along <i>c</i> (red), but different occupation than $\text{Eu}_{10}\text{Hg}_{55}$			
				
CN	15	15 (+1)	15 (+1)	16
$\text{Eu}_{10}\text{Hg}_{55}$	100% Eu additional Hg site (yellow)	100% Eu	100% Eu	55% Eu 45% Hg
	+ mutually exclusive Hg positions along <i>c</i> (red)			

4.2.5 Conclusions

The amalgams belonging to the $\text{Gd}_{14}\text{Ag}_{51}$ structure family show a surprising variety in structural disorder phenomena. Each representative has its own pattern of mixed occupations and/or split positions, and it is unclear which parameters influence the structural details. To discern patterns and to eventually attribute the underlying parameters, we have successfully enlarged the number of representatives of the respective amalgams by creating ternary members with two different electropositive metals. Yet, their number is still too small to give a concluding discussion, but it becomes clear that geometric factors play an important, but not the only role. Electronic reasons additionally have to be taken into account.

There is evidence for a correlation between the size of the four different coordination polyhedra M1–M4 for the ‘cation’ positions and the observed mixed occupation phenomena. As the M1 site with CN = 14 has the smallest, M2 and M3 with CN = 15 very similar intermediate and M4 with CN = 16 the largest volume (see Fig. 4.15 and Table 4.14), larger atoms such as Sr prefer occupation of the M4 site when competing with a smaller ‘cation’. The volume of the polyhedra here gives a better picture for the evaluation of geometric preferences rather than the shortest contacts M–Hg, see Table 4.14.

The radii of the electropositive metals^[47] are increasing in the following sequence with Sr being considerably larger than the others:

$$r_{\text{Yb}}=226 \text{ pm} \xrightarrow{\Delta=1} r_{\text{Na}}=227 \text{ pm} \xrightarrow{\Delta=4} r_{\text{Ca}}=231 \text{ pm} \xrightarrow{\Delta=2} r_{\text{Eu}}=233 \text{ pm} \xrightarrow{\Delta=16} r_{\text{Sr}}=249 \text{ pm}$$

The smaller metals Yb, Na, Ca and Eu show a preference for the occupation of the smaller polyhedra rather than the largest M4 site. When comparing the ternary amalgams with Ca/Na, Yb/Sr or Ca/Eu, this tendency may explain the mixed occupations with the larger atom preferred on the M4 and the smaller atoms occupying the smaller M1–M3 sites. Also the quotients of mixing on these sites follows the radius quotients to a wide extent. The individual occupations of the four sites M1–M4 for all reported amalgams is compiled in Table 4.13. The correlation between atomic size and prevalence for the occupation of the M1–M4 polyhedra can be seen in Fig. 4.15. The linear interpolations of the radius volume correlations for CN = 14, 15 and 16 show a parallel progression and a constant difference of $\approx 10 \text{ \AA}^3$. The strongest scattered values belong to the Ca amalgam (too low values) and the Eu and Ca-Eu amalgams as well as the Yb-Sr amalgam. There are some contradictions to a simple geometric rule which can be held responsible for this scattering: (1) The occupation ratios in the ternary Na-Ca amalgam do not follow the geometrical reasons, however, the atomic sizes do not differ considerably to make this a strong argument against geometric reasons. (2) In the binary amalgams of Ca, Sr and Eu a mixed occupation occurs on the M4 position, and it is together with Hg. As Hg is even smaller ($r_{\text{Hg}} = 223 \text{ pm}$), there cannot be a geometrical reason. (3) In the ternary Yb-Sr amalgam, where the atomic size difference is maximal, the M4 position is occupied by 86% Yb and only 14% Sr. (4) In the ternary Ca-Eu amalgam the M2 site is occupied by a higher ratio of Eu than Ca (79%/21%) despite Ca being the smaller atom. A respective underoccupation of mixing with

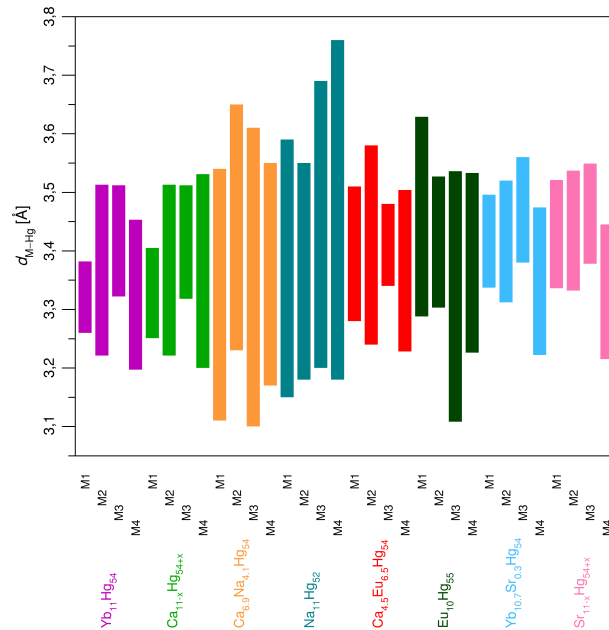


Fig. 4.14: Compilation of the M–Hg distances in all reported and the three new binary amalgams within the $\text{Gd}_{14}\text{Ag}_{51}$ structure family.

Hg in the binary Eu amalgam is not observed. (5) The occurrence of a set of mutually exclusive Hg split positions (each forming an equidistant Hg chain) in the Eu and the Ca-Eu amalgam cannot be explained from packing effects or atomic size ratios. The first three aspects may be resolved by assuming that the volume of the M4 polyhedron is already too large, even for the largest atom Sr. Therefore, a partial occupation with Hg can be explained as Hg despite its size is stabilized by the strong covalent Hg–Hg contributions. Also the Coulombic repulsion of the ‘cations’ in direct vicinity of the centers of the two interpenetrating M4 polyhedra may play a role here. This also could explain the higher percentage of Na in the M4 polyhedron of the Na-Ca amalgam. The electron transfer from alkali metals generally is smaller than from alkaline earth metals in amalgams (The melting points of alkaline earth amalgams generally is several hundred °C higher than the respective alkali amalgams, indicating higher ionic bonding contributions). Therefore the partial positive charge on Ca is higher than on Na, and occupation of this site with prevalently Na reduces Coulombic repulsion.

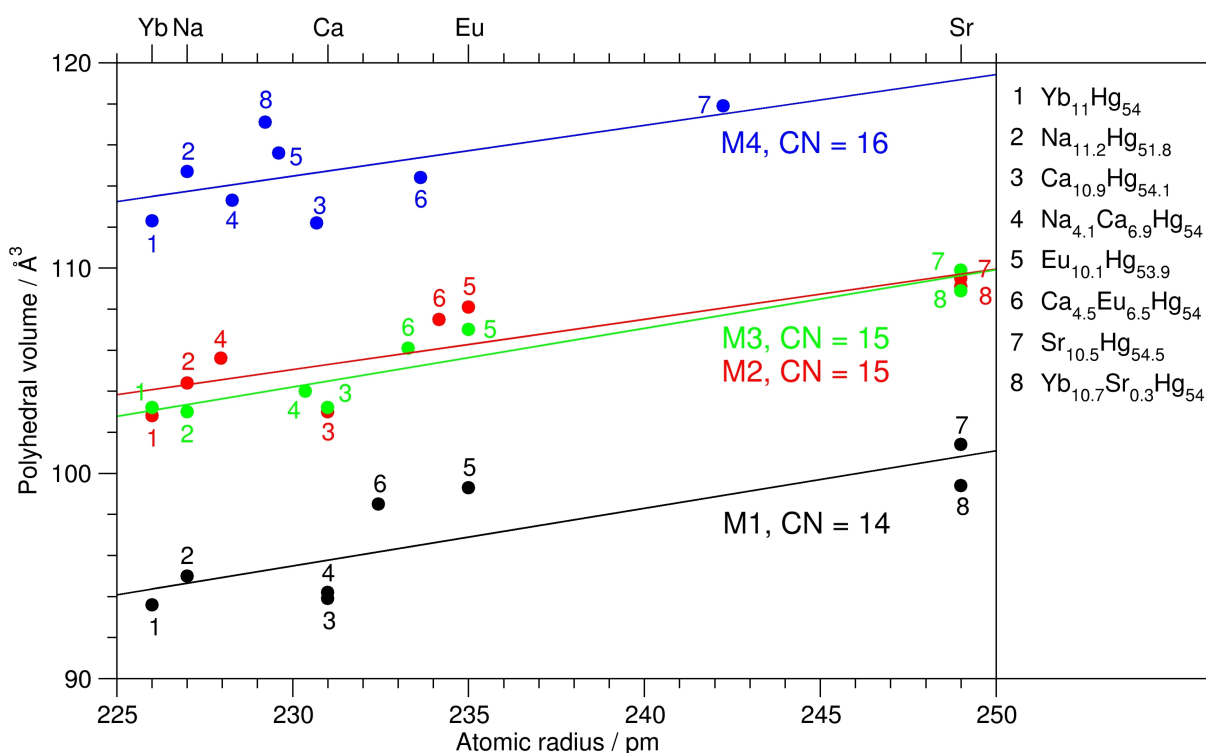


Fig. 4.15: Correlation of the volumina of the four different coordination polyhedra M1 (black), M2 (red), M3 (green) and M4 (blue) of the electropositive metals in the amalgams belonging to the Gd₁₄Ag₅₁ family with the metal atom radii.^[47] For amalgams with mixed occupations, the weighted mean radii are given according to the respective occupancies on the individual crystallographic sites (see Table 4.13). The data point numbers refer to the individual amalgams, see legend on the right.

In addition to the clearly apparent geometric aspects electronic reasons have to be taken into account. Strong local Coulombic fields within the highly polar amalgams with respect to charge repulsion in neighbored polyhedra or, in the case of the two interpenetrating M4 polyhedra, between directly adjacent metal positions will influence the occupation pattern. This, however, cannot account for all disorder phenomena, e.g. the Hg split positions. Details of the electronic structures would help evaluating the effects of local disorder on the overall energy of the amalgam system. Detailed and high-level calculations of the electronic structures are hampered by the extraordinarily high level of structural complexity in these compounds.

Table 4.14: Comparison of the polyhedral volumina^[46] of the Gd₁₄Ag₅₁-type amalgams around the electropositive metal positions M1-4 in Å³ together with the minimal M–Hg distances in pm. The values for Na₁₁Hg₅₂ are averaged over all topologically equivalent positions of the 3×3×1 superstructure.

Yb ₁₁ Hg ₅₄	V	93.6	102.8	103.2	112.3
	d_{\min}	326	322	332	320
Na ₁₁ Hg ₅₂	V	95.0	104.4	103.0	114.7
	d_{\min}	320	321	321	320
Ca _{10.9} Hg _{54.1}	V	93.9	103.0	103.2	112.2
	d_{\min}	325	322	332	320
Eu ₁₀ Hg ₅₅	V	99.3	108.1	107.0	115.6
	d_{\min}	329	330	311	323
Sr _{10.5} Hg _{54.5}	V	101.4	109.5	109.9	117.9
	d_{\min}	334	333	338	326
Ca _{6.9} Na _{4.1} Hg ₅₄	V	94.2	105.6	104.0	113.3
	d_{\min}	311	323	310	317
Ca _{4.5} Eu _{6.5} Hg ₅₄	V	98.5	107.5	106.1	114.4
	d_{\min}	328	324	334	323
Yb _{10.7} Sr _{0.3} Hg ₅₄	V	99.4	109.1	108.9	117.1
	d_{\min}	334	331	338	322

A further increase of the number of amalgam representatives of the Gd₁₄Ag₅₁ structure family is feasible by creating ternary members with two different electropositive metals. In the future, we will study the differences in polarity in the sense of the electron transfer $M^{\delta+}[\text{Hg}_n]^{\delta-}$ in individual members of this class of amalgams and its influence on macroscopic properties, such as electric conductivity. Together with an evaluation of the charge carrier concentration, accessible by Hall effect measurements, this may help to get further insights in the role of electronic effects on the crystal structures. The fascination about the richness and diversity of disorder phenomena and their adjustment for each individual representative of this structural family will remain.

Acknowledgements

We acknowledge DESY (Hamburg, Germany), a member of the Helmholtz Association HGF, for the provision of experimental facilities. Parts of this research were carried out at PETRA III, beamline P02.1 within the rapid access program 2021A under proposal ID RAAt-20010291. Financial support by the Deutsche Forschungsgemeinschaft within the project with No. 429690805 is also gratefully acknowledged.

Table 4.15: Standardised^[48] fractional atomic coordinates, Wyckoff numbers, site symmetry, occupation factors and isotropic displacement parameters $U_{\text{iso/equiv}}$ [\AA^2] for $\text{Yb}_{10.7}\text{Sr}_{0.3}\text{Hg}_{54}$ (top), $\text{Ca}_{6.9}\text{Na}_{4.1}\text{Hg}_{54}$ (middle) and $\text{Ca}_{4.5}\text{Eu}_{6.5}\text{Hg}_{54}$ (bottom). Standard deviations in units of the last digit are given in parentheses. In case of the Ca-Eu-Amalgam, both occupancy factors are provided, with data from the single crystal refinement in parentheses.

Atom	occ.	Wyck.	x	y	z	$U_{\text{iso/equiv}}$
$\text{Yb}_{10.7}\text{Sr}_{0.3}\text{Hg}_{54}$						
Yb1	1	3 <i>k</i>	0.4624(4)	0.0581(5)	1/2	0.0403(11)
Yb2	1	3 <i>k</i>	0.2048(6)	0.2544(6)	1/2	0.060(2)
Yb3	1	3 <i>j</i>	0.4317(5)	0.3084(5)	0	0.0462(12)
Yb41	0.71(6)	2 <i>h</i>	1/3	2/3	0.2007(5)	0.023(2)
Sr41	0.29(6)	2 <i>h</i>	1/3	2/3	0.2007(5)	0.023(2)
Hg1	1	6 <i>l</i>	0.4496(2)	0.2787(2)	0.3455(3)	0.0234(5)
Hg2	1	6 <i>l</i>	0.2383(2)	0.0502(2)	0.3387(3)	0.0309(7)
Hg3	1	6 <i>l</i>	0.1779(3)	0.2039(2)	0.1670(3)	0.0329(6)
Hg4	1	6 <i>l</i>	0.4612(2)	0.1048(2)	0.1624(3)	0.0255(6)
Hg5	1	6 <i>l</i>	0.1394(2)	0.4138(2)	0.2909(3)	0.0289(6)
Hg6	1	6 <i>l</i>	0.3919(2)	0.4491(2)	0.2625(3)	0.0231(5)
Hg7	1	3 <i>k</i>	0.3440(4)	0.5465(3)	1/2	0.0319(9)
Hg8	1	3 <i>j</i>	0.2369(3)	0.0244(4)	0	0.0339(9)
Hg9	1	3 <i>j</i>	0.2505(3)	0.4177(3)	0	0.0306(8)
Hg10	1	3 <i>j</i>	0.1044(3)	0.5092(3)	0	0.0280(8)
Hg11	1	2 <i>i</i>	2/3	1/3	0.1616(5)	0.0290(10)
Hg12	1	1 <i>f</i>	2/3	1/3	1/2	0.0242(12)
Hg13	1	2 <i>g</i>	0	0	0.3435(5)	0.0279(10)
Hg14	1	1 <i>a</i>	0	0	0	0.0381(12)
$\text{Ca}_{6.9}\text{Na}_{4.1}\text{Hg}_{54}$						
Ca1	1	3 <i>k</i>	0.491(4)	0.063(4)	1/2	0.0073(8)
Ca2	0.24(11)	3 <i>k</i>	0.195(6)	0.251(5)	1/2	0.0073(8)
Na2	0.76(11)	3 <i>k</i>	0.195(6)	0.251(5)	1/2	0.0073(8)
Ca3	0.84(12)	3 <i>j</i>	0.410(3)	0.307(3)	0	0.0073(8)
Na3	0.16(12)	3 <i>j</i>	0.410(3)	0.307(3)	0	0.0073(8)
Ca4	0.32(12)	2 <i>h</i>	1/3	2/3	0.186(6)	0.012(2)
Na4	0.68(12)	2 <i>h</i>	1/3	2/3	0.186(6)	0.012(2)
Hg1	1	6 <i>l</i>	0.4505(4)	0.2784(4)	0.3433(7)	0.0089(3)
Hg2	1	6 <i>l</i>	0.2394(4)	0.0439(4)	0.3461(5)	0.0089(3)
Hg3	1	6 <i>l</i>	0.1814(4)	0.2017(4)	0.1710(7)	0.0089(3)
Hg4	1	6 <i>l</i>	0.4610(5)	0.1027(5)	0.1654(8)	0.0089(3)
Hg5	1	6 <i>l</i>	0.1443(5)	0.4229(5)	0.2950(5)	0.0089(3)
Hg6	1	6 <i>l</i>	0.3935(5)	0.4466(4)	0.2597(6)	0.0089(3)
Hg7	1	3 <i>k</i>	0.3511(8)	0.5490(7)	1/2	0.0073(8)
Hg8	1	3 <i>j</i>	0.2377(6)	0.0307(7)	0	0.0073(8)
Hg9	1	3 <i>j</i>	0.2424(7)	0.4070(7)	0	0.0073(8)
Hg10	1	3 <i>j</i>	0.1035(7)	0.5109(7)	0	0.0073(8)
Hg11	1	2 <i>i</i>	2/3	1/3	0.1558(12)	0.012(2)
Hg12	1	2 <i>g</i>	0	0	0.3467(11)	0.012(2)
Hg13	1	1 <i>f</i>	2/3	1/3	1/2	0.021(4)
Hg14	1	1 <i>a</i>	0	0	0	0.021(4)
$\text{Ca}_{4.5}\text{Eu}_{6.5}\text{Hg}_{54}$						
Eu1	0.57(3) (0.41(5))	3 <i>j</i>	0.594(2)	0.0531(15)	0	0.0318(9)
Ca1	0.43(3) (0.59(5))	3 <i>j</i>	0.594(2)	0.0531(15)	0	0.0318(9)
Eu2	0.79(3) (0.83(6))	3 <i>j</i>	0.0495(15)	0.2599(12)	0	0.0318(9)
Ca2	0.21(3) (0.17(6))	3 <i>j</i>	0.0495(15)	0.2599(12)	0	0.0318(9)
Eu3	0.36(3) (0.26(5))	3 <i>k</i>	0.431(2)	0.121(2)	1/2	0.0318(9)
Ca3	0.64(3) (0.74(5))	3 <i>k</i>	0.431(2)	0.121(2)	1/2	0.0318(9)
Eu4	0.66(3) (0.78(6))	2 <i>h</i>	1/3	2/3	0.3031(16)	0.004(5)
Ca4	0.34(3) (0.22(6))	2 <i>h</i>	1/3	2/3	0.3031(16)	0.004(5)

continued on the next page

Atom	occ.	Wyck.	x	y	z	$U_{\text{iso/equiv}}$
Hg1	1	6l	0.0253(6)	0.2073(6)	0.3331(9)	0.041(2)
Hg2	1	6l	0.0553(4)	0.4515(4)	0.2395(7)	0.0198(14)
Hg3	1	6l	0.2346(4)	0.1866(4)	0.1586(7)	0.020(2)
Hg4	1	6l	0.2732(6)	0.4161(6)	0.2068(6)	0.030(2)
Hg5	1	6l	0.4521(5)	0.1711(6)	0.1544(7)	0.021(2)
Hg6	1	6l	0.4574(5)	0.3503(6)	0.3370(8)	0.026(2)
Hg7	1	3k	0.1012(9)	0.5914(10)	$\frac{1}{2}$	0.0318(9)
Hg8	1	3k	0.1633(9)	0.4183(8)	$\frac{1}{2}$	0.0318(9)
Hg9	1	3k	0.2349(8)	0.2112(7)	$\frac{1}{2}$	0.0318(9)
Hg10	1	3j	0.2076(8)	0.5446(8)	0	0.0318(9)
Hg11	1	2i	$\frac{2}{3}$	$\frac{1}{3}$	0.341(2)	0.041(4)
Hg12	1	1e	$\frac{2}{3}$	$\frac{1}{3}$	0	0.033(3)
Hg13	0.87(11) (0.71(2))	2g	0	0	0.1560(13)	0.033(3)
Hg14	0.131(11) (0.29(2))	1a	0	0	0	0.033(3)
Hg15	0.87(11) (0.71(2))	1b	0	0	$\frac{1}{2}$	0.033(3)
Hg16	0.131(11) (0.29(2))	2g	0	0	0.326(11)	0.033(3)

Table 4.16: Coefficients U_{ij} of the anisotropic displacement parameters for $\text{Yb}_{10.7}\text{Sr}_{0.3}\text{Hg}_{54}$ (top) and $\text{Ca}_{4.9}\text{Eu}_{6.1}\text{Hg}_{54}$ (bottom) in [\AA^2]. U_{ij} is defined as: $U_{ij} = \exp[-2\pi^2(U_{11}(ha^*)^2 + \dots + 2U_{21}hka^*b^*)]$. Standard deviations in units of the last digit are given in parentheses.

Atom	U_{11}	U_{22}	U_{33}	U_{23}	U_{13}	U_{12}
$\text{Yb}_{10.7}\text{Sr}_{0.3}\text{Hg}_{54}$						
Yb1	0.039(2)	0.043(3)	0.043(3)	0	0	0.023(2)
Yb2	0.063(4)	0.059(4)	0.053(4)	0	0	0.028(3)
Yb3	0.052(3)	= U_{11}	0.042(3)	0	0	0.032(3)
Yb41	0.023(2)	= U_{11}	0.024(3)	0	0	0.0114(12)
Sr41	0.023(2)	= U_{11}	0.024(3)	0	0	0.0114(12)
Hg1	0.0274(12)	0.0229(12)	0.0228(11)	-0.0002(8)	0.0010(9)	0.0147(10)
Hg2	0.0240(12)	0.0255(13)	0.0451(17)	-0.0030(10)	0.0005(11)	0.0138(10)
Hg3	0.0330(14)	0.0333(14)	0.0237(13)	0.0006(9)	0.0010(10)	0.0101(11)
Hg4	0.0321(14)	0.0229(12)	0.0228(13)	0.0004(9)	0.0027(10)	0.0148(10)
Hg5	0.0208(11)	0.0293(12)	0.0362(14)	0.0096(11)	0.0046(10)	0.0122(10)
Hg6	0.0271(12)	0.0264(12)	0.0196(11)	-0.0007(8)	0.0006(8)	0.0163(10)
Hg7	0.054(2)	0.029(2)	0.022(2)	0	0	0.028(2)
Hg8	0.023(2)	0.032(2)	0.041(2)	0	0	0.010(2)
Hg9	0.028(2)	0.034(2)	0.034(2)	0	0	0.019(2)
Hg10	0.025(2)	0.031(2)	0.029(2)	0	0	0.016(2)
Hg11	0.0272(14)	0.0272(14)	0.033(3)	0	0	0.0136(7)
Hg12	0.021(2)	= U_{11}	0.031(3)	0	0	0.0103(8)
Hg13	0.0243(13)	= U_{11}	0.030(5)	0	0	0.0122(6)
Hg14	0.035(2)	= U_{11}	0.040(9)	0	0	0.0177(11)
$\text{Ca}_{4.9}\text{Eu}_{6.1}\text{Hg}_{54}$						
Eu1	0.002(6)	0.007(6)	0.017(7)	0	0	-0.014(4)
Ca1	0.002(6)	0.007(6)	0.017(7)	0	0	-0.014(4)
Eu2	0.019(5)	0.012(4)	0.049(6)	0	0	0.007(3)
Ca2	0.019(5)	0.012(4)	0.049(6)	0	0	0.007(3)
Eu3	0.035(11)	0.017(9)	0.008(8)	0	0	-0.006(7)
Ca3	0.035(11)	0.017(9)	0.008(8)	0	0	-0.006(7)
Eu4	0.028(5)	= U_{11}	0.080(11)	0	0	0.014(2)
Ca4	0.028(5)	= U_{11}	0.080(11)	0	0	0.014(2)
Hg1	0.057(3)	0.027(2)	0.042(3)	0.008(2)	-0.011(3)	-0.007(2)
Hg2	0.0107(15)	0.035(2)	0.032(2)	-0.0020(18)	0.0012(16)	0.0067(15)
Hg3	0.028(2)	0.0176(18)	0.059(3)	0.000(2)	0.003(2)	0.0141(16)
Hg4	0.031(2)	0.036(2)	0.067(3)	-0.022(2)	-0.024(2)	0.0315(19)

continued on the next page

Atom	U_{11}	U_{22}	U_{33}	U_{23}	U_{13}	U_{12}
Hg5	0.0179(17)	0.0132(15)	0.0266(19)	-0.0019(14)	0.0003(15)	0.0030(13)
Hg6	0.024(2)	0.049(3)	0.037(3)	-0.010(2)	-0.0057(18)	0.031(2)
Hg7	0.016(2)	0.026(3)	0.042(3)	0	0	0.002(2)
Hg8	0.021(3)	0.035(3)	0.044(4)	0	0	0.006(2)
Hg9	0.077(6)	0.045(5)	0.074(7)	0	0	0.034(5)
Hg10	0.035(3)	0.037(4)	0.040(4)	0	0	-0.009(3)
Hg11	0.0106(16)	= U_{11}	0.040(4)	0	0	0.0053(8)
Hg12	0.007(2)	= U_{11}	0.033(5)	0	0	0.0034(10)
Hg13	0.020(3)	= U_{11}	0.044(7)	0	0	0.0102(16)
Hg14	0.015(10)	= U_{11}	0.08(4)	0	0	0.008(5)
Hg15	0.037(6)	= U_{11}	0.086(17)	0	0	0.019(3)
Hg16	0.014(7)	= U_{11}	0.055(19)	0	0	0.007(4)

Table 4.17: Selected interatomic distances (and their frequencies) around the less noble metal positions $M1-M4$ for the new ternary amalgams $\text{Yb}_{10.7}\text{Sr}_{0.3}\text{Hg}_{54}$ (left), $\text{Ca}_{6.9}\text{Na}_{4.1}\text{Hg}_{54}$ (center) and $\text{Ca}_{4.5}\text{Eu}_{6.5}\text{Hg}_{54}$ (right) in Å. Standard deviations in units of the last digit are given in parentheses.

$\text{Yb}_{10.7}\text{Sr}_{0.3}\text{Hg}_{54}$			$\text{Ca}_{6.9}\text{Na}_{4.1}\text{Hg}_{54}$			$\text{Ca}_{4.5}\text{Eu}_{6.5}\text{Hg}_{54}$						
Atom 1	Atom 2	distance	Atom 1	Atom 2	distance	Atom 1	Atom 2	distance				
Yb1	Hg5	3.313(5) (2x)	Ca1	Hg1	3.11(3) (2x)	Ca1/Eu1	Hg4	3.28(3) (2x)				
	Hg14	3.351(5)		Hg13	3.17(4)		Hg2	3.29(2) (2x)				
	Hg6	3.332(4) (2x)		Hg6	3.18(4) (2x)		Hg6	3.357(9) (2x)				
	Hg4	3.353(3) (2x)		Hg4	3.321(15) (2x)		Hg5	3.38(3) (2x)				
	Hg2	3.372(5) (2x)		Hg7	3.33(6)		Hg5	3.40(3) (2x)				
	Hg1	3.396(5) (2x)		Hg5	3.45(3) (2x)		Hg12	3.41(3)				
	Hg1	3.426(5) (2x)		Hg1	3.49(5) (2x)		Hg5	3.48(2) (2x)				
Yb2	Hg7	3.469(7)	Ca2/Na2	Hg2	3.54(4) (2x)	Ca2/Eu2	Hg10	3.51(3)				
	Hg3	3.300(3) (2x)		Hg2	3.228(5) (2x)		Hg13	3.24(2)				
	Hg2	3.393(6) (2x)		Hg3	3.248(6) (2x)		Hg1	3.297(10) (2x)				
	Hg5	3.402(7) (2x)		Hg5	3.301(7) (2x)		Hg10	3.345(17)				
	Hg7	3.425(8)		Hg12	3.419(4) (2x)		Hg4	3.358(14) (2x)				
	Hg2	3.478(7) (2x)		Hg7	3.434(8)		Hg3	3.414(14) (2x)				
	Hg6	3.471(6) (2x)		Hg2	3.515(6) (2x)		Hg2	3.46(2) (2x)				
Yb3	Hg15	3.511(7) (2x)	Ca3/Na3	Hg6	3.524(5) (2x)	Ca3/Eu3	Hg5	3.48(3) (2x)				
	Hg1	3.503(7) (2x)		Hg1	3.650(6) (2x)		Hg3	3.48(3) (2x)				
	Yb4/Sr4	Yb4/Sr4		Hg4	3.371(6) (2x)		Ca4/Na4	Hg9	3.06(5)	Ca4/Eu4	Hg14	3.58(2) (2x)
				Hg3	3.405(6) (2x)			Hg3	3.10(3) (2x)		Hg6	3.34(3) (2x)
				Hg6	3.390(4) (2x)			Hg6	3.15(3) (2x)		Hg2	3.35(2) (2x)
				Hg8	3.406(7)			Hg8	3.30(3)		Hg1	3.35(3) (2x)
				Hg4	3.394(6) (2x)			Hg10	3.36(4)		Hg8	3.37(3)
Hg1			3.415(3) (2x)	Hg1	3.437(14) (2x)	Hg5		3.409(9) (2x)				
Hg12			3.412(6)	Hg4	3.49(3) (2x)	Hg11		3.41(2) (2x)				
Yb4/Sr4	Yb4/Sr4	Hg9	3.440(7)	Hg4	3.49(3) (2x)	Hg9	3.43(4)					
		Hg10	3.51(7)	Hg4	3.61(4) (2x)	Hg6	3.45(3) (2x)					
		Hg5	3.225(3) (3x)	Hg11	3.68(4) (2x)	Hg7	3.48(4)					
		Hg10	3.372(4) (3x)	Hg5	3.168(8)	Hg4	3.228(9) (3x)					
		Hg7	3.379(5) (3x)	Hg5	3.169(5)	Hg7	3.335(13) (3x)					
		Hg6	3.464(2) (3x)	Hg5	3.169(7)	Hg10	3.448(12) (3x)					
		Hg9	3.559(4) (3x)	Hg10	3.265(8)	Hg2	3.487(5) (3x)					
		Yb4/Sr4	Yb4/Sr4	Yb4/Sr4	Hg10	3.265(6)	Hg10	3.265(6)	Hg8	3.504(10) (3x)		
					Hg10	3.266(10)	Hg10	3.266(10)	Ca4/Eu4	3.69(3)		
					Hg7	3.498(6)	Hg7	3.498(6)				
					Hg7	3.498(4)	Hg7	3.498(4)				
					Hg7	3.498(6)	Hg7	3.498(6)				
					Hg6	3.510(7)	Hg6	3.510(7)				
					Hg6	3.510(4)	Hg6	3.510(4)				
Hg6	3.511(7)				Hg6	3.511(7)						
Hg9	3.548(10)				Hg9	3.548(10)						
Hg9	3.548(10)				Hg9	3.548(10)						
Hg9	3.549(8)	Hg9	3.549(8)									
		Ca4/Na4	3.58(10)									

References

- [1] J. H. Simons, R. P. Seward, Slow Electron Scattering and the Apparent Electron Affinity of Mercury, *J. Chem. Phys.* **1938**, *6*, 790–794, DOI: [10.1063/1.1750172](https://doi.org/10.1063/1.1750172).
- [2] F. Tambornino, C. Hoch, The simplest representative of a complex series: the Hg-rich amalgam Yb₁₁Hg₅₄, *Z. Kristallogr.* **2017**, *232*, 557–565, DOI: [10.1515/zkri-2016-2036](https://doi.org/10.1515/zkri-2016-2036).
- [3] PEARSON'S CRYSTAL DATA, K. Cenzual, P. Villars, ASM International N.V., Materials Park (OH), USA, **2016**.
- [4] O. D. McMasters, K. A. Gschneidner, R. F. Venteicher, Crystallography of the silver-rich rare-earth-silver intermetallic compounds, *Acta Crystallogr.* **1970**, *B26*, 1224–1229, DOI: [10.1107/S0567740870003928](https://doi.org/10.1107/S0567740870003928).
- [5] S. Steeb, D. Godel, C. Löhr, On the structure of the compounds Ag₃RE (RE = Y, La, Ce, Sm, Gd, Dy, Ho, Er), *J. Less-Common Met.* **1968**, *15*, 137–141, DOI: [10.1016/0022-5088\(68\)90047-7](https://doi.org/10.1016/0022-5088(68)90047-7).
- [6] C. Donolato, S. Steeb, Structures of the compounds Au₃La, Au₃Ce, Au₃Pr, Au₃Nd, Ag₃Pr, and Ag₃Nd, *J. Less-Common Met.* **1969**, *18*, 312–313, DOI: [10.1016/0022-5088\(69\)90170-2](https://doi.org/10.1016/0022-5088(69)90170-2).
- [7] O. J. C. Runnalls, The crystal structures of some intermetallic compounds of plutonium, *Can. J. Chem.* **1956**, *34*, 133–145, DOI: [10.1139/v56-017](https://doi.org/10.1139/v56-017).
- [8] O. D. McMasters, K. A. Gschneidner, G. Bruzzone, A. Palenzona, Stoichiometry, crystal structures and melting points of the lanthanide-gold alloys, *J. Less-Common Met.* **1971**, *25*, 135–160, DOI: [10.1016/0022-5088\(71\)90125-1](https://doi.org/10.1016/0022-5088(71)90125-1).
- [9] V. I. Kutaitsev, N. T. Chebotarev, M. A. Andrianov, V. N. Konev, I. G. Lebedev, V. I. Bagrova, A. V. Beznosikova, A. A. Kruglov, P. N. Petrov, E. S. Smotritskaya, Phase diagrams of plutonium with metals of groups IIA, IVA, VIII, and IB., *Sov. At. Energy* **1967**, *23*, 1279–1287, DOI: [10.1007/BF01162033](https://doi.org/10.1007/BF01162033).
- [10] A. Palenzona, S. Cirafici, The Th–Au phase diagram, *J. Less-Common Met.* **1986**, *124*, 245–249, DOI: [10.1016/0022-5088\(86\)90497-2](https://doi.org/10.1016/0022-5088(86)90497-2).
- [11] A. Dommann, F. Hulliger, On the structure types of UAu₂ and U₁₄Au₅₁, *J. Less-Common Met.* **1988**, *141*, 261–273, DOI: [10.1016/0022-5088\(88\)90412-2](https://doi.org/10.1016/0022-5088(88)90412-2).
- [12] G. Bruzzone, The Ca–Cd and Ba–Cd systems, *Gazz. Chim. Ital.* **1972**, *102*, 234–242.
- [13] A. Palenzona, The Ytterbium-Cadmium system, *J. Less-Common Met.* **1971**, *25*, 367–372, DOI: [10.1016/0022-5088\(71\)90179-2](https://doi.org/10.1016/0022-5088(71)90179-2).
- [14] J.-P. Gabathuler, P. White, E. Parthé, Zr₁₄Cu₅₁ and Hf₁₄Cu₅₁ with GdAg_{3.6} structure type, *Acta Crystallogr.* **1975**, *B31*, 608–610, DOI: [10.1107/S0567740875003378](https://doi.org/10.1107/S0567740875003378).
- [15] B. Berlin, Formation of the intermediate phases of the system thorium-copper in liquid sodium, *J. Less-Common Met.* **1972**, *29*, 334–348, DOI: [10.1016/0022-5088\(72\)90198-1](https://doi.org/10.1016/0022-5088(72)90198-1).
- [16] N. N. Belyavina, V. Y. Markiv, O. I. Nakochenka, Reinvestigation of the Y–Cu–Ga system at 700 °C, *J. Alloys Compd.* **2012**, *541*, 288–296, DOI: [10.1016/j.jallcom.2012.07.034](https://doi.org/10.1016/j.jallcom.2012.07.034).
- [17] A. V. Tkachuk, A. Mar, Alkaline-Earth Metal Mercury Intermetallics, A_{11-x}Hg_{54+x} (A = Ca, Sr), *Inorg. Chem.* **2008**, *47*, 1313–1318, DOI: [10.1021/ic7015148](https://doi.org/10.1021/ic7015148).
- [18] F. Tambornino, C. Hoch, The Mercury-richest Europium Amalgam Eu₁₀Hg₅₅, *Z. Anorg. Allg. Chem.* **2015**, *641*, 537–542, DOI: [10.1002/zaac.201400561](https://doi.org/10.1002/zaac.201400561).
- [19] C. Hoch, A. Simon, Na₁₁Hg₅₂: Complexity in a Polar Metal, *Angew. Chem. Int. Ed.* **2012**, *51*, 3262–3265, DOI: [10.1002/anie.201108064](https://doi.org/10.1002/anie.201108064).
- [20] J. Liang, C. Liao, C. Yin, Y. Han, L. Q. Nong, S. Xie, Interaction of the components in the Ag–Er–Sn system at 400 °C, *J. Alloys Compd.* **2010**, *502*, 68–73, DOI: [10.1016/j.jallcom.2010.04.148](https://doi.org/10.1016/j.jallcom.2010.04.148).
- [21] R. V. Gumeniuk, I. B. Taras, Y. B. Kuzma, The interactions between the components in the Gd–Ag–Ga system, *J. Alloys Compd.* **2006**, *416*, 131–134, DOI: [10.1016/j.jallcom.2005.08.038](https://doi.org/10.1016/j.jallcom.2005.08.038).
- [22] R. V. Gumeniuk, B. M. Stel'makhovych, Y. B. Kuzma, The Tb–Ag–Ga system, *J. Alloys Compd.* **2003**, *352*, 128–133, DOI: [10.1016/S0925-8388\(02\)01160-X](https://doi.org/10.1016/S0925-8388(02)01160-X).

- [23] J. L. Liang, Y. Du, Y. Y. Tang, C. Z. Liao, J. L. Meng, H. H. Xu, Phase equilibria of the Ag–Gd–Sn ternary system at 400 °C, *J. Alloys Compd.* **2009**, *481*, 264–269, DOI: [10.1016/j.jallcom.2009.03.175](https://doi.org/10.1016/j.jallcom.2009.03.175).
- [24] S. D. Negri, P. G. Solokha, V. V. Pavlyuk, A. Saccone, The isothermal section of the La–Ag–Mg phase diagram at 400 °C, *Intermetallics* **2011**, *19*, 671–681, DOI: [10.1016/j.intermet.2011.01.007](https://doi.org/10.1016/j.intermet.2011.01.007).
- [25] J. Liang, C. Liao, Y. Du, Y. Tang, Y. Han, Y. He, S. Liu, The isothermal section of the Ag–La–Sn system at 400 °C, *J. Alloys Compd.* **2010**, *493*, 122–1271, DOI: [10.1016/j.jallcom.2009.12.087](https://doi.org/10.1016/j.jallcom.2009.12.087).
- [26] D. Mazzone, P. Riani, G. Zanicchi, R. Marazza, R. Ferro, The isothermal section at 400 °C of the Pr–Ag–Sn ternary system, *Intermetallics* **2002**, *10*, 801–809, DOI: [10.1016/S0966-9795\(02\)00056-0](https://doi.org/10.1016/S0966-9795(02)00056-0).
- [27] Q. Lin, J. D. Corbett, Ca₁₄Au₄₆Sn₅: A "colored" Gd₁₄Ag₅₁-type structure containing columns of well-differentiated hexagonal gold stars, *Inorg. Chem.* **2011**, *50*, 1808–1815, DOI: [10.1021/ic102243c](https://doi.org/10.1021/ic102243c).
- [28] M. Kontani, T. Nishioka, Y. Hamaguchi, H. Matsui, H. A. Katori, T. Goto, Magnetic properties of Binary and Pseudobinary U–Au Heavy Fermion Systems, *J. Phys. Soc. Jpn.* **1994**, *63*, 3421–3430, DOI: [10.1143/JPSJ.63.3421](https://doi.org/10.1143/JPSJ.63.3421).
- [29] Y. V. Verbovytsky, New ternary phases from the R–Au–Ga systems (R = Gd–Tm), *Chem. Met. Alloys* **2014**, *7*, 42–55, DOI: [10.30970/cma7.0268](https://doi.org/10.30970/cma7.0268).
- [30] D. Mazzone, R. Marazza, P. Riani, G. Zanicchi, G. Cacciamani, M. L. Fornasini, P. Manfrinetti, The isothermal section at 600 °C of the Pr–Au–Sn phase diagram, *Calphad* **2009**, *33*, 31–43, DOI: [10.1016/j.calphad.2008.09.017](https://doi.org/10.1016/j.calphad.2008.09.017).
- [31] V. Y. Markiv, I. P. Shevchenko, N. N. Belyavina, P. P. Kuz'menko, Phase equilibria (500 °C) in the Dy–Cu–Ga system and new compounds with the BaAl₄-type structure and its derivatives in the RE–Cu–Ga systems, *Dopov. Akad. Nauk Ukr. RSR* **1985**, *A7*, 76–81.
- [32] R. V. Gumenyuk, Y. B. Kuz'ma, Crystal Structure of Gd₁₄Cu₄₈Ga₃ and Tb₁₄Cu₄₈Ga₃, *Inorg. Mater.* **2007**, *43*, 135–137, DOI: [10.1134/S0020168507020070](https://doi.org/10.1134/S0020168507020070).
- [33] I. P. Shevchenko, V. Y. Markiv, Y. P. Yarmolyuk, Y. Grin, A. O. Fedorchuk, Phase equilibria and crystalline structure of compounds in the system Ho–Cu–Ga, *Russ. Metall.* **1989**, *1*, 219–222.
- [34] V. Y. Markiv, I. P. Shevchenko, N. N. Belyavina, Phase equilibria and crystalline structure of a compound in the Lu–Cu–Ga system, *Russ. Metall.* **1989**, *2*, 201–206.
- [35] V. Y. Markiv, I. P. Shevchenko, N. N. Belyavina, Crystal structure of some ternary compounds in the system Sc–Cu–Ga., *Russ. Metall.* **1984**, *5*, 227–230.
- [36] V. Y. Markiv, I. P. Shevchenko, N. N. Belyavina, P. P. Kuz'menko, Crystal structure of phases in the Sm–Cu–Ga system, *Dopov. Akad. Nauk Ukr. RSR* **1986**, *A11*, 78–81.
- [37] V. Y. Markiv, I. P. Shevchenko, N. N. Belyavina, P. P. Kuz'menko, Phase equilibria in the Cu-rich part of the Y–Cu–Ga system at 800 °C, *Dopov. Akad. Nauk Ukr. RSR* **1985**, *A7*, 76–81.
- [38] P. Myronenko, O. R. Myakush, V. S. Babizhetskii, B. Y. Kotur, Phase equilibria in Y–Zr–Cu system at 870 K, *Visn. Lviv. Derzh. Univ. Ser. Chim.* **2011**, *52*, 22–26.
- [39] X-SHAPE, STOE & Cie. GmbH, Darmstadt, Deutschland, version 2.0.7, **2005**.
- [40] X-RED, STOE & Cie. GmbH, Darmstadt, Deutschland, version 1.3.1, **2005**.
- [41] C. Prescher, V. B. Prakapenka, DIOPTAS: a program for reduction of two-dimensional X-ray diffraction data and data exploration, *High Press. Res.* **2015**, *35*, 223–230, DOI: [10.1080/08957959.2015.1059835](https://doi.org/10.1080/08957959.2015.1059835).
- [42] B. H. Toby, R. B. Von Dreele, GSAS-II: the genesis of a modern open-source all purpose crystallography software package, *J. Appl. Crystallogr.* **2013**, *46*, 544–549, DOI: [10.1107/S0021889813003531](https://doi.org/10.1107/S0021889813003531).
- [43] S. Krivovichev, Topological complexity of crystal structures: quantitative approach, *Acta Crystallogr.* **2012**, *A68*, 393–398, DOI: [10.1107/S0108767312012044](https://doi.org/10.1107/S0108767312012044).
- [44] APEX3, BRUKER AXS GmbH, Karlsruhe, Deutschland, version 2018.1-0, **2018**.
- [45] G. M. Sheldrick, A short history of SHELX, *Acta Crystallogr.* **2008**, *A64*, 112–122, DOI: [10.1107/S0108767307043930](https://doi.org/10.1107/S0108767307043930).

- [46] K. Momma, F. Izumi, Vesta 3 for three-dimensional visualization of crystal, volumetric and morphology data, *J. Appl. Cryst.* **2011**, *44*, 1272–1276, DOI: [10.1107/S0021889811038970](https://doi.org/10.1107/S0021889811038970).
- [47] M. W. H. (ed.), *CRC Handbook of Chemistry and Physics*, 97th ed., CRC Press, Boca Raton (FL), USA, **2017**.
- [48] L. M. Gelato, E. Parthé, Structure Tidy – a computer program to standardize crystal structure data, *J. Appl. Crystallogr.* **1987**, *20*, 139–143, DOI: [10.1107/S0021889887086965](https://doi.org/10.1107/S0021889887086965).

4.3 Influence of Disorder on the ‘Bad Metal’ Behaviour in Polar Amalgams

Timotheus Hohl[†], Reinhard K. Kremer[‡], Stefan G. Ebbinghaus[¶], Saleem A. Khan[§], Ján Minár[§] and Constantin Hoch^{†,*}

* Correspondence: constantin.hoch@cup.uni-muenchen.de; Tel.: +49-89-2180-77421

[†] Department Chemie, Ludwig-Maximilians-Universität München

[‡] Max-Planck-Institut für Festkörperforschung Stuttgart

[¶] Institut für Chemie, Martin-Luther-Universität Halle-Wittenberg

[§] New Technologies - Research Center, University of West Bohemia, Pilsen, Czech Republic

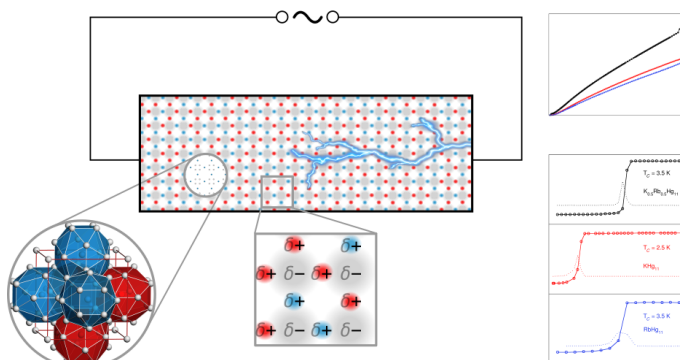
Published in: *Inorg. Chem.* **2023**, 62(9), 3965–3975.

DOI: [10.1021/acs.inorgchem.2c04430](https://doi.org/10.1021/acs.inorgchem.2c04430)

Reprinted with permission from Inorganic Chemistry. Copyright 2023 American Chemical Society.

4.3.1 Abstract

The two new ternary amalgams $K_{1-x}Rb_xHg_{11}$ ($x = 0.472(7)$) and $Cs_{3-x}Ca_xHg_{20}$ ($x = 0.20(3)$) represent two different examples how to create ternary compounds from binaries by statistical atom substitution. $K_{1-x}Rb_xHg_{11}$ is a Vegard-type mixed crystal of the isostructural binaries KHg_{11} and $RbHg_{11}$ (cubic, space group $Pm\bar{3}m$, No. 221, $a = 9.69143(3)$ Å, Rietveld refinement), whereas $Cs_{3-x}Ca_xHg_{20}$ is a substitution variant of the Rb_3Hg_{20} structure type (cubic, space group $Pm\bar{3}n$, No. 223, $a = 10.89553(14)$ Å, Rietveld refinement) for which a fully substituted isostructural binary Ca phase is unknown. In $K_{1-x}Rb_xHg_{11}$, the valence electron concentration (VEC) is not changed by the substitution, whereas in $Cs_{3-x}Ca_xHg_{20}$ the VEC increases with the Ca content. Amalgams of electropositive metals form polar metal bonds and show ‘bad metal’ properties. By thermal analysis, magnetic susceptibility and resistivity measurements and DFT calculations of the electronic structures we investigate the effect of the structural disorder introduced by creating mixed atom occupation on the physical properties of the new two polar amalgam systems.



4.3.2 Introduction

Polar intermetallic phases combine metal-bonding with ionic, often covalent bonding contributions.^[1,2] The latter originate from the large electronegativity difference between the constituents of the intermetallic phases. In contrast to Zintl phases, the electron transition from the electropositive to the electronegative constituent remains a partial one, so that overall metallic behaviour is retained. This interplay of ionic and metal bonding contributions makes polar very interesting intermetallics, from the theoretical point of view, but also the physical properties resulting from the unconventional bonding situation have attracted special attention. The unusual metallic properties of polar intermetallic phases have been summarised under the term

‘bad metal’ behaviour^[3,4] and have gained high interest, e.g. with respect to thermoelectric applications,^[5–7] and their unusual magnetic, electric, optic, caloric and catalytic properties, which make them promising candidates in many fields of applications.

‘Bad metal’ behaviour results from a low free electron concentration combined with very small mean free electron paths.^[8] ‘Bad metals’ show an overall relatively high electrical resistivity, and the increase with temperature is linear with a very steep slope only in the low temperature regime. At higher temperatures the resistivity tends to saturate, typically at values of few hundred $\mu\Omega\text{cm}$. The electron concentration can be reduced by localisation in covalent bonds or by Coulombic fields. The mean free path of the electrons is determined by scattering due to electron-phonon interaction, crystal defects and impurities. In ordinary metals, the mean free paths are in the range of several hundred atomic distances,^[9] and disorder phenomena such as doping, mixed crystal formation, local structural distortions, domain sizes, have large influence on the specific resistivity. In ‘bad metals’, however, the mean free paths are much smaller, and, contrary to the original assumption by Ioffe and Regel, they can even be shorter than the interatomic distances.^[10,11] The influence of microscopic disorder thus may be much smaller but still has to be taken into account. In order to identify the relevance of structural disorder, we investigated two newly synthesised differently disordered amalgams and compare them with their fully ordered representatives. Amalgams are ideal candidates for the study of polar intermetallic phases, and this has been exemplified on a number of examples.^[12–14]

The isostructural amalgams KHg_{11} and RbHg_{11} ^[15] and their Vegard-type solid solution $\text{K}_{1-x}\text{Rb}_x\text{Hg}_{11}$ with $x = 0.472(7)$ and the mixed crystal $\text{Cs}_{3-x}\text{Ca}_x\text{Hg}_{20}$ ($x = 0.20(3)$) serve as case examples to study the influence of statistical mixed occupancy and its influence on properties like metallic resistivity, superconductivity, electronic structure and thermal stability. A statistical mixture of element constituents can be regarded as the extreme case for a high concentration of defects or impurities with the associated local lattice distortions.

The structures within the two families $M\text{Hg}_{11}$ ^[15] and $M_3\text{Hg}_{20}$ ^[16] are of equal polarity and have equal structural complexity. For the two compounds both parameters are very similar and therefore in a first approximation the influence of the disorder phenomena on the physical properties of the materials can be favourably studied.

Within the systems $M\text{Hg}_{11}$ and $M_3\text{Hg}_{20}$ two different kinds of mixed crystal series can be expected, allowing to study two different aspects: $M\text{Hg}_{11}$ with $M = \text{K}$ and Rb form the complete mixed quasi-binary series $\text{K}_{1-x}\text{Rb}_x\text{Hg}_{11}$ with purely statistical Rb – Cs occupation on only one high symmetry crystallographic position. This enables to study of the influence of statistical disorder of two atoms with different radii ($r_{\text{K}}^{\text{Slater}} = 220 \text{ pm}$, $r_{\text{Rb}}^{\text{Slater}} = 235 \text{ pm}$ ^[17]) without changing the valence electron concentration (VEC). In $\text{Cs}_3\text{Hg}_{20}$ we were able to partially substitute Ca for Cs , resulting in a compounds with composition $\text{Cs}_{3-x}\text{Ca}_x\text{Hg}_{20}$ ($x \approx 0.2$). In this example, again structural disorder by statistical occupancy is present, and both the atomic radii ($r_{\text{Cs}}^{\text{Slater}} = 260 \text{ pm}$, $r_{\text{Ca}}^{\text{Slater}} = 180 \text{ pm}$) and the VEC differ.

Here, we report on the crystal structure, the thermal stability, electronic structure calculations, specific resistivity, and superconductivity of the mixed crystals $\text{K}_{1-x}\text{Rb}_x\text{Hg}_{11}$ ($x = 0.472(7)$, henceforth referred to as $\text{K}_{0.5}\text{Rb}_{0.5}\text{Hg}_{11}$), and $\text{Cs}_{3-x}\text{Ca}_x\text{Hg}_{20}$ ($x = 0.20(3)$, henceforth referred to as $\text{Cs}_{2.8}\text{Ca}_{0.2}\text{Hg}_{20}$), and compare them with their respective fully ordered binary phases.

4.3.3 Materials and Methods

Hazards and risks

Dealing with the elemental alkali metals exhibits some risks due to their high reactivity towards air and moisture. All experimental work has to be performed under strict exclusion of atmosphere, requiring a well-maintained glove box and/or a suitable Schlenk apparatus in order to prevent deterioration of the starting materials. Disposing of alkali metal residuals is best per-

formed by hydrolysing them in a Schlenk tube under streaming inert gas by dropwise addition of ethanol. The Schlenk tube may be externally cooled with an ice bath when the reaction is too vivid. Isopropanol or other alcohols are strongly deprecated as the respective alcoholates are poorly soluble in their alcohols so that an alkali metal core coated by alcoholate remains for days and then reacts when hydrolysing the alcohol solution, sometimes leading to ignition of the alcohol and subsequently severe burns.

Experiments with elemental mercury can be easily performed at virtually no risk when taking into account two simple rules. Firstly, mercury has a very high density. The sheer weight of mercury is surprising, even for an experienced chemist, and simple experimental techniques, such as e.g. pipetting, are challenging. Therefore, in all experiments a non-breakable (plastic) tray has to be put under the working equipment in order to collect eventually spilled mercury droplets. Plastic or thin-walled glass bottles cannot be used for storage, and the volume has to be adjusted to the container – 1 L of mercury weighs 13.7 kg. Secondly, mercury vapours, if inhaled constantly over a long period, to chronic intoxication. The vapour pressure of mercury at room temperature and normal pressure is already sufficient to cause severe effects. Therefore all work with elemental mercury has to be performed under a fume hood, in a glove box or under Schlenk conditions.

Reacting alkali metals with mercury has to be done with extreme care as the reactions are highly exothermic. This is almost independent of the alkali metal to mercury ratio and varies slightly with the alkali metals. The reaction enthalpy can be as high as to evaporate a considerable portion of the mercury. Therefore slow addition of mercury to the alkali metal under external cooling is preferred. Bringing a dry ice cooled alkali metal mixture together with solid mercury and slowly bringing the mixture to room temperature is an extremal example for this strategy. Another way for leading an isothermal reaction is electrocrystallisation as presented before.^[18] For reactions below ca. 300 °C, normal laboratory glass ware is fitting as the alkali metals are very rapidly being consumed by the mercury and the amalgams do not deteriorate silicatic container materials. For reactions at higher temperatures or long-time tempering, metal ampules have to be used. Due to the high vapour pressure of mercury at elevated temperatures the ampules have to be sealed.

Alkali metal amalgams are very sensitive materials, reacting with traces of moisture or air within seconds. Most amalgams react vividly when poured into water, but without ignition. Sometimes, formation of colloidal mercury is observed instead of the formation of small, silver mercury droplets. Colloidal mercury is a dark grey suspension, sometimes stable for days without accumulating into droplets. These suspensions should be disposed of immediately by addition of half-concentrated HNO₃. In all other cases, the mercury from hydrolysed amalgams can easily be recycled.

Mercury can be recycled without substantial loss by the following procedure. Mercury waste of any form can be collected and dissolved in half-concentrated HNO₃. The clear solution is then diluted by at least factor 10. An excess of coarse copper turnings or pieces of copper foil is added to the solution. Immediately, mercury precipitates on the copper metal surface. With very high Hg concentrations, Hg droplets or a puddle of the metal collects at the bottom of the container. The amalgamated copper is then separated from the solution which now is vitually mercury-free, washed with water and dried and subsequently filled into a glass flask. The collected mercury does not contain any metallic impurities which are less noble than copper. The mercury is distilled off the copper at ca. 120 °C and a pressure of ca. 10⁻³ mbar. It is already of high purity and can either be used directly or further be purified. The copper turnings can be reused and the HNO₃ solution contains Cu²⁺ and less noble metals as the only contaminations.

Chemicals

Mercury was purified by stirring the crude metal with half-concentrated HNO₃ to remove less noble and organic impurities. The mercury then was washed and passed through a paper filter

with a pinhole to remove solid impurities. Subsequently, it was doubly distilled in vacuum. The alkali metals were donations from Max Planck Institut für Festkörperforschung (Stuttgart, Germany) in the form of doubly distilled metals sealed in glass ampules under argon. Caesium was donated by Kriminalpolizei Heilbronn (Germany) and came in sealed glass ampules under argon.

Calcium was used as purchased from Smart Elements (Wien, Austria) in the form of dendritic sublimate with a purity of at least 99.9%.

Synthesis

$\text{K}_{0.5}\text{Rb}_{0.5}\text{Hg}_{11}$ was synthesised by slowly adding 11.23 g (56.0 mmol) Hg to a mixture of 273.3 mg (7.0 mmol) K and 598.3 mg (7.0 mmol) Rb in a glass Schlenk tube under argon atmosphere. The mixture was then carefully heated with a heatgun until forming a homogeneous liquid phase (ca. 320–330 °C). Subsequently, it was allowed to cool to room temperature within estimated 30 min. The resulting homogenous crystalline solid was identified as a mixture of $\text{Rb}_7\text{Hg}_{31}$ ^[16] and a yet unknown phase. Subsequently, the obtained solid was ground to a fine powder and another 23.54 g (117.4 mmol) Hg were added, resulting in a nominal composition of $\text{K}:\text{Rb}:\text{Hg} = 1:1:24.8$. The mixture was annealed at 105 °C for 28 days and cooled to room temperature by taking the ampule from the furnace. The metallic product consisted of $\text{K}_{0.5}\text{Rb}_{0.5}\text{Hg}_{11}$ as the only solid phase with a slight excess of elemental mercury, see Fig. 4.16.

$\text{Cs}_{2.8}\text{Ca}_{0.2}\text{Hg}_{20}$ was synthesised by reacting a mixture of 45.1 mg (1.13 mmol) Ca, 149.5 mg (1.13 mmol) Cs and 1.805 g (9.30 mmol) Hg in a tantalum crucible, which was closed by arc welding. The crucible was heated to 300 °C (rate: 50 K h⁻¹) and held at this temperature for 8 weeks, after which it was cooled to room temperature by turning off the oven. The phase pure product consisted of $\text{Cs}_{2.8}\text{Ca}_{0.2}\text{Hg}_{20}$ (see Fig. 4.17).

KHg_{11} and RbHg_{11} were obtained by cooling the alkali metals (180–480 mg) with an acetone/dry ice cooling agent, and adding stoichiometric amounts of Hg dropwise under vigorous reverse flow of inert gas. After warming the system slowly up to room temperature, the product was identified as phase-pure KHg_{11} and RbHg_{11} . When the dry ice cooling is not applied, a mixture of KHg_6 ^[13] and KHg_{11} is obtained.

$\text{Cs}_3\text{Hg}_{20}$ was synthesised by dropwise adding 4.56 g (22.7 mmol) Hg to 452.0 mg (3.4 mmol) Cs in a glass Schlenk flask. The mixture was homogenised by slight shaking while heating with a heat gun until a homogeneous melt was achieved (approx. 300 °C) and allowed to cool to room temperature within estimated 30 min. By X-ray powder diffraction, the obtained product was identified as $\text{Cs}_3\text{Hg}_{20}$ with minor traces of $\text{Cs}_5\text{Hg}_{19}$.^[16]

Purity of the amalgams was only checked on the X-ray level. EDX spectroscopy is not feasible because of the high reactivity of the samples and lack of a trustable airlock system in order to transfer the samples into the electron microscope. ICP-OES was performed on the amalgams but only reflects the weighing stoichiometry and the absence of impurity elements.

Powder diffraction and Rietveld refinement

In all cases, the amalgam samples showed no single crystals of suitable quality for single crystal X-ray diffraction experiments, even after several attempts to improve the crystal quality by Ostwald ripening procedures. From other amalgam systems, e.g. from the $\text{Gd}_{14}\text{Ag}_{51}$ structure family, we have multiple examples indicating that the refinement of disorder phenomena on data from different single crystals of one sample and from Rietveld refinement of powder samples representing a larger cross section do not show significant deviations. We have observed no signs for any ordering phenomena on a more complex or local level, however, the real structure ordering necessary on an atomic level would have to be studied by e.g. electron diffraction. The high sensitivity of the samples has impeded such studies so far.

For X-ray powder diffraction investigations, the samples were prepared in an argon-filled glove-box. 50vol.-% of diamond powder was added to effectively crush the ductile samples and to

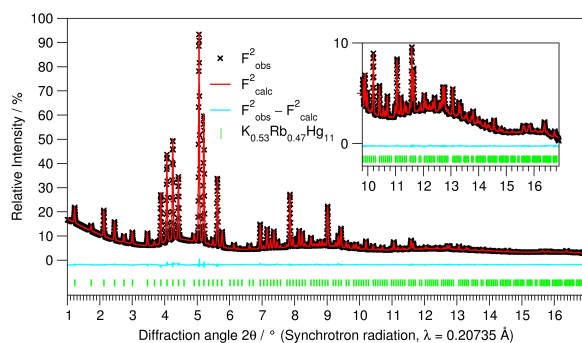


Fig. 4.16: Graphical representation of the Rietveld refinement of the X-ray powder diffractogram of $\text{K}_{0.53}\text{Rb}_{0.47}\text{Hg}_{11}$. The diffraction pattern shows no additional crystalline phases, while the diffuse contributions to the background intensity can be ascribed to elemental mercury. The inset shows the magnified high-angle region of the diffractogram.

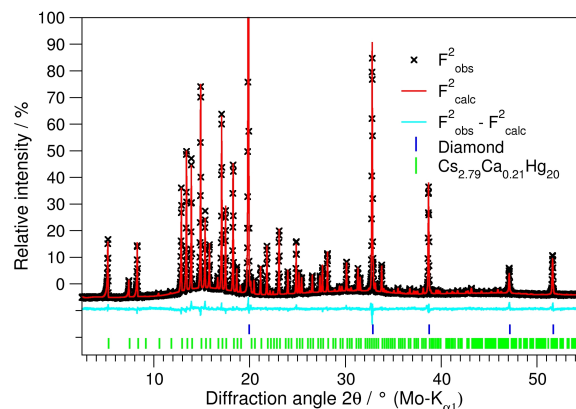


Fig. 4.17: Rietveld refinement of $\text{Cs}_{2.8}\text{Ca}_{0.2}\text{Hg}_{20}$, mixed with 50 vol.-% of diamond powder. No additional crystalline phases are visible in the X-ray powder diffraction pattern. The strongest reflection, originating from diamond powder, is cut off to highlight more details of the amalgam pattern.

reduce X-ray absorption. The powders were filled in glass capillaries (inner diameter 0.5 mm, Hilgenberg, Malsfeld, Germany), which were sealed with birch tar.

Table 4.18: Crystallographic data and details on data collection and treatment resulting from the Rietveld refinements of the X-ray powder diffractograms of $\text{K}_{0.5}\text{Rb}_{0.5}\text{Hg}_{11}$ and $\text{Cs}_{2.8}\text{Ca}_{0.2}\text{Hg}_{20}$.

Refined composition		$\text{K}_{0.528(7)}\text{Rb}_{0.472(7)}\text{Hg}_{11}$	$\text{Cs}_{2.81(3)}\text{Ca}_{0.20(3)}\text{Hg}_{20}$
Crystal system		— cubic —	
Space group		$Pm\bar{3}m$ (No. 221)	$Pm\bar{3}n$ (No. 223)
Formula units	<i>Z</i>	3	2
Lattice parameters [\AA , \AA^3]	<i>a</i>	9.69143(3)	10.89553(14)
	<i>V</i>	910.256(8)	1293.44(5)
Radiation		Synchrotron	Mo-K α 1
Wavelength [\AA]	λ	0.20735	0.709317
Refinement software		GSAS-II[19]	TOPAS[20]
Data range [$^\circ$]	2θ	1–16.6	2.5–55.0
Step size [$^\circ$]	$\Delta 2\theta$	0.04174	0.015
Abs. coeff. [mm^{-1}]	μ	140.555	120.227
Data points		4152	3501
Background function		cosine	shifted Chebyshev
No. of independent parameters		63	57
Thereof: background parameters		36	21
<i>R</i> values [%]	<i>R_P</i>	0.774	0.884
	<i>R_{WP}</i>	1.201	1.248
	<i>R_{exp}</i>	0.255	0.745
	<i>R_{Bragg}</i>	1.17	1.62
Goof [χ^2]		4.744	1.675

$\text{K}_{0.5}\text{Rb}_{0.5}\text{Hg}_{11}$ was characterised with synchrotron radiation ($\lambda = 0.20735 \text{ \AA}$, PETRA III, Beamline P02.1, DESY, Hamburg, Germany) employing a VAREX XRD 4343CT Flat Panel Detector (2880 \times 2880 pixels, 150 \times 150 μm pixel size). The diffraction data were integrated using the DIPTAS package.^[21] Rietveld refinements were carried out with the GSAS-II software.^[19] The published crystal structure data RbHg_{11} ^[15] were used as starting parameters for the refinement. The refined structure parameters are given in Table 4.20, essential crystallographic data and details on data collection and refinement are summarised in Table 4.18. A graphical representation of the Rietveld refined diffraction pattern is presented in Fig. 4.16 (right). No superstructure reflections are discernable in the difference plot. Selected interatomic distances are compiled in Table 4.22.

$\text{Cs}_{2.8}\text{Ca}_{0.2}\text{Hg}_{20}$ was characterised using a STADI P diffractometer (Mo- $K_{\alpha 1}$ -radiation, $\lambda = 0.7093 \text{ \AA}$, parafocussing Debye-Scherrer geometry, Stoe & Cie GmbH, Darmstadt, Germany) equipped with a Ge(111) monochromator and a MYTHENII detector (Dectris, Baden-Daettwil, Switzerland). Rietveld profile refinements were performed with the TOPAS software applying a fundamental parameter approach.^[20] Starting parameters for the refinement were taken from the literature structure model for $\text{Cs}_3\text{Hg}_{20}$.^[16] The refined structure data are summarised in Table 4.21, relevant crystallographic data and details of the data collection and refinement are collected in Table 4.18 (below). A graphical representation of the Rietveld refinement is shown in Fig. 4.17 (left). Selected interatomic distances are compiled in Table 4.22.

Thermal Analysis

The phases KHg_{11} , RbHg_{11} , $\text{K}_{0.5}\text{Rb}_{0.5}\text{Hg}_{11}$, $\text{Cs}_3\text{Hg}_{20}$, and $\text{Cs}_{2.8}\text{Ca}_{0.2}\text{Hg}_{20}$ were investigated by differential scanning calorimetry (DSC). 30–60 mg of the sample were filled into small tantalum ampules (\varnothing : 5 mm) which were cold welded using pliers and a vise. To improve the footing and the thermal contact, the ampules were placed in Pt crucibles. The measurements were performed under streaming Argon (20 mL min^{-1}) using a STA 449 F5 Jupiter setup (Netzsch, Selb, Germany) equipped with a type S thermocouple. Data were collected by performing three cycles of heating to $150 \text{ }^\circ\text{C}$ and cooling at a rate of 5 K min^{-1} . Data processing was performed with the Netzsch software package Proteus.^[22]

Specific Resistivity

Temperature dependent measurements of the specific resistivity between 2 and 296 K were performed with the ac-resistivity (typically 19 Hz) option of a Physical Property Measurement System (PPMS Quantum Design Inc., San Diego (CA), USA) with currents between 1 and 100 mA on cold-pressed sample discs (thickness approx. 0.5 mm to 1 mm) employing the van-der-Pauw technique. Thin gold wires were attached to the discs by silver paint in an Argon filled glove box. After rapid transferring under inert gas and mounting of the sample, the PPMS cryostat was immediately evacuated to high vacuum ($\leq 10^{-5}$ mbar) while cooling rapidly to liquid He temperature. At low temperatures approximately 5 mbar of ^4He exchange gas was charged to the cryostat and subsequently the resistance was measured by slowly raising the temperature to room temperature. In some cases deterioration of the electrical contacts was observed at about 250 K, most probably due to corrosion of the contacts by metallic Hg, released from the samples surface due to hydrolysis with residual moisture. The results of the resistance measurements are depicted in Fig. 4.23.

Susceptibility Measurements

Magnetic measurements on KHg_{11} between 1.9 K and 300 K with a magnetic field of ± 15 Oe were performed using a VSM (Vibrating Sample Magnetometer) installed in a Physical Property Measurement System (PPMS, Quantum Design Inc., San Diego (CA), USA). Samples were placed in capsules made of PFEP, which were then fixed to a brass holder. Data were collected with the MultiVu software.^[23] RbHg_{11} and $\text{K}_{0.5}\text{Rb}_{0.5}\text{Hg}_{11}$ were investigated using the ACMS option of a PPMS. The magnetic field was set to 100 Oe, the temperature was decreased from 6 to 2 K at a rate of 0.05 K min^{-1} and data points were recorded every 0.2 K for RbHg_{11} and 0.1 K for $\text{K}_{0.5}\text{Rb}_{0.5}\text{Hg}_{11}$, respectively. To check for a possible thermal hysteresis, both samples were afterwards measured accordingly during warming up to 6 K.

Band structure calculations

The electronic structures calculation were performed employing the fully relativistic Korringa-Kohn-Rostoker (KKR) Green function method as implemented in the sprkk code.^[24,25] The Vosko, Wilk and Nusair local density approximation (VWN-LDA)^[26] was used to approximate

the exchange-correlation part of the potential as well as the atomic sphere approximation. The KKR code allows for a treatment of mixed occupied crystallographic positions without the construction of a virtual fully ordered supercell model as approximation to the averaged and purely statistically disordered crystal structure (CPA approximation)^[24] which was used for the mixed crystal $K_{0.5}Rb_{0.5}Hg_{11}$ and $Cs_{2.8}Ca_{0.2}Hg_{20}$. The electronic density of states (DOS) was calculated on the basis of the crystallographic structure model without allowing for a structure relaxation. The energy integrals were evaluated by contour integration on a semicircular path within the complex energy plane, using a Gaussian mesh of 32 points. For multipole expansion of the Green's function we used a cutoff $\ell_{max} = 3$ to obtain reliable results. Once the Green's function components have been determined, the charge density can be obtained via the k-space integration over the Brillouin zone (BZ). Self-consistent calculations were performed using a grid of $24 \times 24 \times 24$ points in the full BZ. Structure constant matrix k-dependent convergence parameters were set manually to $ETA = 2.0$, $RMAX = 2.0$ and $GMAX = 2.0$.

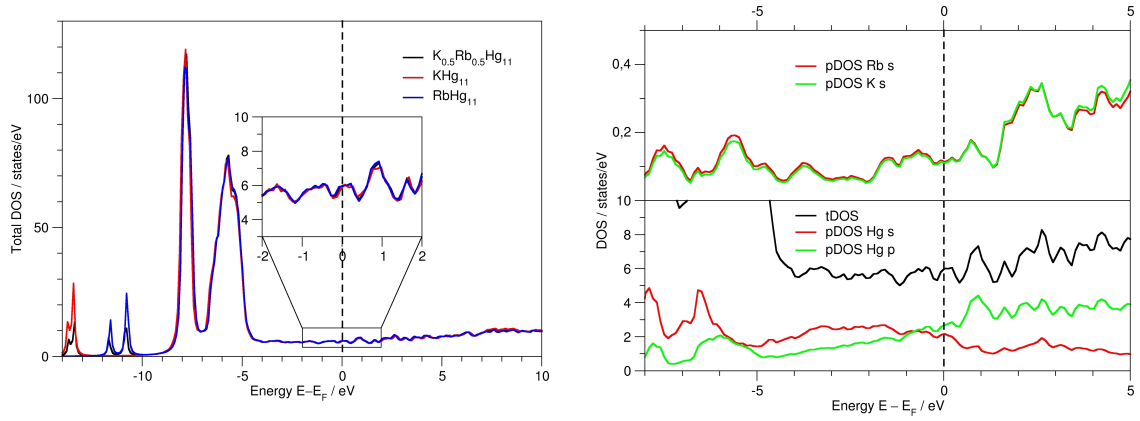


Fig. 4.18: Left: Total density of states (DOS) for KHg₁₁ (red), RbHg₁₁ (blue) and K_{0.5}Rb_{0.5}Hg₁₁ (black). The Fermi level is depicted by the dashed line. The inset magnifies the DOS directly around the Fermi energy. **Right:** partial DOS curves for Rb and K *s* states and for Hg *s* and *p* states in K_{0.5}Rb_{0.5}Hg₁₁.

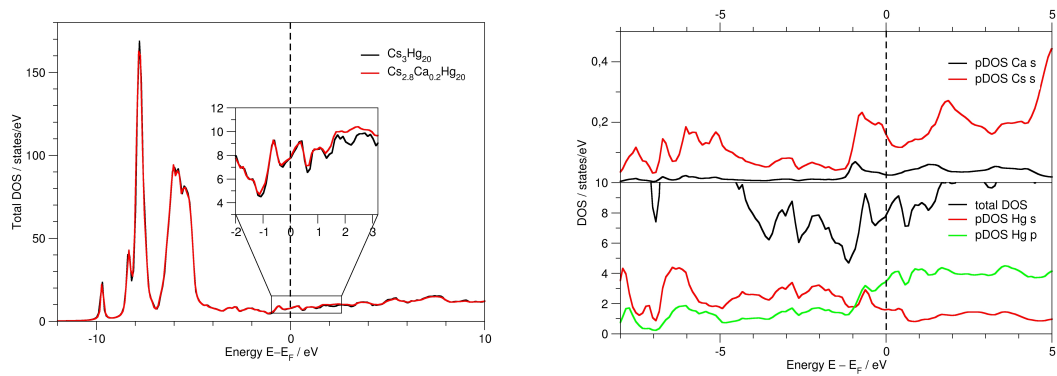


Fig. 4.19: Left: Plot of the density of states (DOS) for Cs₃Hg₂₀ (black) and for Cs_{2.8}Ca_{0.2}Hg₂₀ (red). **Right:** partial DOS (black) *s* contributions of Ca and Cs and partial DOS *s* and *p* contributions for Hg.

4.3.4 Results and Discussion

$K_{0.5}Rb_{0.5}Hg_{11}$

Rubidium and potassium form several isotopic Hg-rich amalgams, for example M_2Hg_7 , M_7Hg_{32} and MHg_{11} .^[15,16,27] The crystal structure of the quasi-binary compound $K_{0.5}Rb_{0.5}Hg_{11}$ is isotopic to the respective binary amalgams (space group $Pm\bar{3}m$, $a = 9.69143(3)$ Å). A comparison of the lattice parameters is shown in Table 4.19, while additional crystallographic data are compiled in Table 4.20. The crystal structure of MHg_{11} (see Fig. 4.20, right) has been discussed in detail^[15] with respect to different aspects: (a) $[MHg_{20}]$ coordination polyhedra forming four-capped tetragonal hexagonal prisms together with a single Hg atom arrange with a Cu_3Au topology, (b) a combination of $[Hg@Hg_{12}]$ cuboctahedra, $[Hg_4]$ squares and $[Hg_8]$ cubes with interstitial M atoms form a $Y_3TaNi_{6+x}Al_{26}$ topology, and (c) a description by multi-layered endohedral $[Hg@Hg_{12}Hg_{32}A_{12}]$ polyhedra sets. In this work, due to its simplicity, the foremost view is chosen for the visualisation of the structure (cf. Fig. 4.20). In the solid solution of $K_{0.5}Rb_{0.5}Hg_{11}$, the single crystallographic site occupied by the alkali metal shows mixed occupation with 47.2(7) % K and 52.8(7) % Rb (cf. Table 4.20) as obtained from Rietveld refinements. The deviation from the initial composition may indicate a slight inhomogeneity of the sample. The formation of a Vegard-type mixed crystal can be expected as the atomic radii of K and Rb differ only by ca. 6% (220 pm for K and 235 pm for Rb, respectively).^[17]

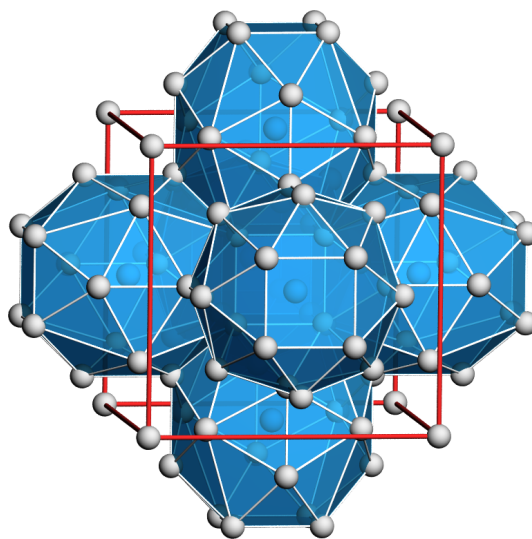


Fig. 4.20: Crystal structure of MHg_{11} ($M = K, Rb$). Mercury atoms are shown in grey, the blue polyhedra are centered by M atoms.

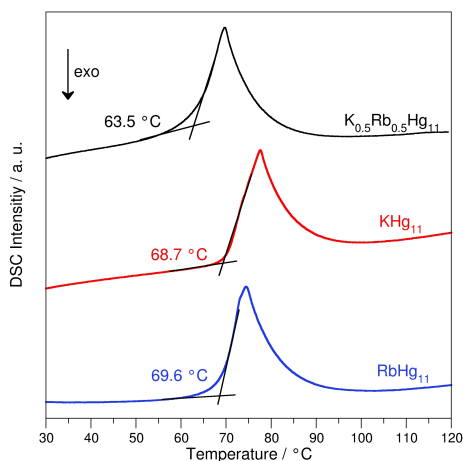


Fig. 4.21: DSC measurements (heating curves) of $RbHg_{11}$ (blue), KHg_{11} (red) and $K_{0.5}Rb_{0.5}Hg_{11}$ (black).

The partial DOS reveals the considerable contributions from alkali metal s at the Fermi energy. As expected, mixing of two alkali metals on the single crystallographic position does not alter the electron count, and the only discernible differences in the DOS appear in the energy range between -10 and -14 eV, where the p states for the alkali metals are either at lower (K) or slightly higher (Rb) energies and consequently at both energy regions for the mixed crystal. Structural disorder does not inflict the electronic situation here

According to the thermal analysis, KHg_{11} melts at $68.7^\circ C$ and $RbHg_{11}$ at $69.6^\circ C$, whereas the solid solution phase $K_{0.5}Rb_{0.5}Hg_{11}$ melts at $63.5^\circ C$ (see Fig. 4.21, left). The reduction of the melting temperature for the solid solution is consistent with other observations for intermetallic solid solutions^[28] and with theoretical considerations based on the Landau theory^[29] and can be ascribed to local strain. As the atomic radii do not differ that much, the local strain is low and the melting point reduction is small but nonetheless significant and larger than the difference of the melting points of the two binary compounds. Powder diffraction analyses of the samples before and after DSC measurements (see Fig. 4.24) confirm that the composition has not changed, indicating congruent melting.

The calculated density of states for $K_{0.5}Rb_{0.5}Hg_{11}$ (see Fig. 4.18) does not significantly differ from those calcu-

as the VEC is not changed. Alkali metal s states considerably contribute to the DOS at the Fermi level.

In Fig. 4.22 (right), the susceptibility measurements of $\text{K}_{0.5}\text{Rb}_{0.5}\text{Hg}_{11}$, KHg_{11} and RbHg_{11} are shown. All samples are superconductors with transition temperatures below that of pure Hg (4.15 K).^[30] While KHg_{11} and RbHg_{11} exhibit critical temperatures at 2.5 and 3.5 K. The transition temperature of $\text{K}_{0.5}\text{Rb}_{0.5}\text{Hg}_{11}$ is very close to that of RbHg_{11} .

As shown in Fig. 4.23, the comparison of the electrical resistivities of KHg_{11} , RbHg_{11} and $\text{K}_{0.5}\text{Rb}_{0.5}\text{Hg}_{11}$ supports the assumption that the mean free path plays an important role. All three isostructural amalgams have a low concentration of free charge carriers because of high Coulomb contributions, and the specific resistivities of the binary compounds are very similar. The steeper slope and the significantly higher deviation from linear temperature behaviour for $\text{K}_{0.5}\text{Rb}_{0.5}\text{Hg}_{11}$ must be ascribed to the structural disorder reducing the mean free path and more pronounced scattering.

The detailed study of $\text{K}_{0.5}\text{Rb}_{0.5}\text{Hg}_{11}$ and the comparison with the two fully ordered binary amalgams gives strong evidence for the influence of structural disorder on the macroscopic properties. Both specific resistivity and superconductivity are modified, and as the electronic situations in the binary and the ternary isostructural amalgams remains unchanged, the influence must be mainly ascribed to the structural disorder, reducing the mean free paths and enhance electron scattering. The Vegard-type solid solution $\text{K}_{0.5}\text{Rb}_{0.5}\text{Hg}_{11}$ shows to be an ideal candidate to study statistical disorder, which is in accordance with the lowering of the congruent melting point with respect to the fully ordered binary compounds. No other parameters but the introduction of structural disorder therefore can be discerned causing the changes in the physical properties.

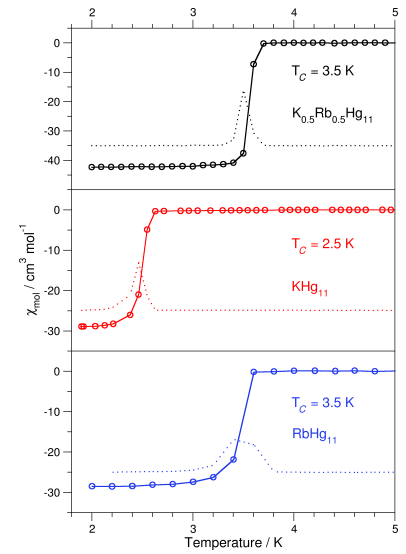


Fig. 4.22: Magnetic susceptibility measurements of $\text{K}_{0.5}\text{Rb}_{0.5}\text{Hg}_{11}$ (top), KHg_{11} (center) and RbHg_{11} (bottom). First derivatives are depicted with dotted lines. All samples are superconductors below their respective critical temperatures (T_C).

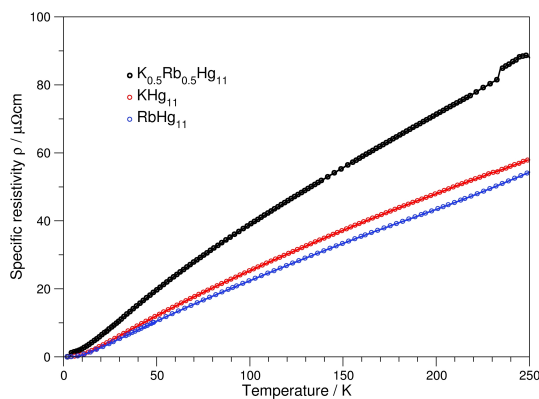


Fig. 4.23: Temperature dependence of the electrical resistivities of RbHg_{11} (blue), KHg_{11} (red) and $\text{K}_{0.5}\text{Rb}_{0.5}\text{Hg}_{11}$ (black) in comparison with the resistivities of the binary amalgams. The ternary solid solution exhibits a more pronounced ‘bad metal’ behaviour.

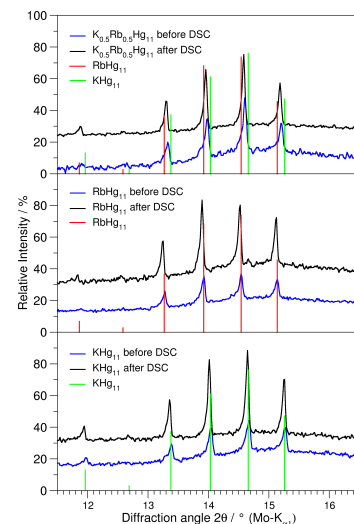


Fig. 4.24: Comparison of the X-ray powder diffractograms of samples of KHg_{11} , RbHg_{11} and $\text{K}_{0.5}\text{Rb}_{0.5}\text{Hg}_{11}$ before and after the DSC measurements. The calculated diffraction peak positions for KHg_{11} and RbHg_{11} are given as vertical bars.

$\text{Cs}_{2.8}\text{Ca}_{0.2}\text{Hg}_{20}$

The mixed crystal $\text{Cs}_{2.8}\text{Ca}_{0.2}\text{Hg}_{20}$ differs in several aspects from that of $\text{K}_{0.5}\text{Rb}_{0.5}\text{Hg}_{11}$. Whereas the K-Rb amalgam represents a solid solution where the VEC is not altered by the substitution and only structural disorder is introduced, in the Cs-Ca amalgam, in addition to moderate structural disorder the electron concentration is also modified by replacing an alkaline with an earth alkaline metal. In the case of $\text{Cs}_{2.8}\text{Ca}_{0.2}\text{Hg}_{20}$, no respective isotypic binary mercury-rich boundary phase $\text{Ca}_3\text{Hg}_{20}$ is known so far. The mercury-richest Ca amalgams with a Hg:Ca ratio > 2 are CaHg_3 ^[31] and $\text{Ca}_{10.5}\text{Hg}_{54.5}$ ^[32]. The new ternary amalgam $\text{Cs}_{2.8}\text{Ca}_{0.2}\text{Hg}_{20}$ is isotypic to $\text{Cs}_3\text{Hg}_{20}$, with only minor differences of the lattice parameters (cf. Table 4.19). Its crystal structure can be described as a Cr_3Si -type arrangement built from Hg-centered $[\text{Hg}@\text{Hg}_{12}]$ icosahedra and twice-capped antiprismatic hexarhombic dodecahedra $[\text{CsHg}_{20}]$ centered by Cs/Ca atoms occupying a single crystallographic site (see Fig. 4.25, right). The arrangement is closely related to the clathrate type I structure. The single Cs site is statistically occupied by only 6.5(9)% Ca (cf. Table 4.21) which represents the maximum accepted Ca substitution, as a 1:1 Ca:Cs ratio was provided in the synthesis mixture. The given occupancies were derived from Rietveld refinements of X-ray powder diffraction patterns and can be considered as average value of the bulk sample. No single crystal specimens could be analysed, and a concentration variation could not be discerned. The existence of a full solid solution $\text{Cs}_{3-x}\text{Ca}_x\text{Hg}_{20}$ is unlikely due to the substantial change of the valence electron concentration ranging from VEC = 1.87 for $x = 0$ to 2.0 for $x = 1$. For the mixed crystal $\text{Cs}_{2.8}\text{Ca}_{0.2}\text{Hg}_{20}$ the minute change in the VEC = 1.89 still appears to be tolerable.

Thermal analysis shows that while $\text{Cs}_3\text{Hg}_{20}$ already melts at 151.5 °C, its substituted variant $\text{Cs}_{2.8}\text{Ca}_{0.2}\text{Hg}_{20}$ melts at 165.5 °C (see Fig. 4.26, right). As may be expected, $\text{K}_{0.5}\text{Rb}_{0.5}\text{Hg}_{11}$, exhibits a melting temperature reduced from those of the two isotypic binary phases. This different behaviour can be understood since in $\text{Cs}_{2.8}\text{Ca}_{0.2}\text{Hg}_{20}$ the electron transfer δ in $M^{\delta+}[\text{Hg}_n]^{\delta-}$ is higher for $M =$ alkaline earth metal than for $M =$ alkali metal. In addition, the Ca incorporation increases the lattice energy through higher Coulombic contributions. Generally, alkaline earth metal amalgams have melting points several hundred degrees higher than alkali metal amalgams.^[31] The small amount of Ca incorporation apparently leads to a noticeable increase of the lattice energy overcompensating for the local strain effects which tend to decrease the melting temperature of $\text{K}_{0.5}\text{Rb}_{0.5}\text{Hg}_{11}$.

The calculated electronic structure (see Fig. 4.19) reveals that the Ca incorporation into $\text{Cs}_3\text{Hg}_{20}$ does not inflict the total density of states, especially the total density of states (tDOS) close to the Fermi level remains unchanged. These states are predominantly of Hg s and p character and belong to the metallic cluster framework. Cs and Ca s states, nevertheless, both contribute to the DOS at the Fermi level. No indication is found for a structural instability that may be

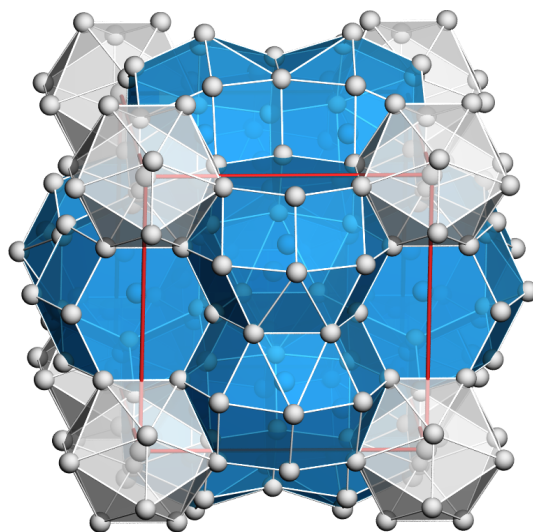


Fig. 4.25: Crystal structure of $M_3\text{Hg}_{20}$ ($M = \text{Cs}, \text{Rb}$). Blue polyhedra are centered by M atoms, while the grey icosahedra are centered by Hg.

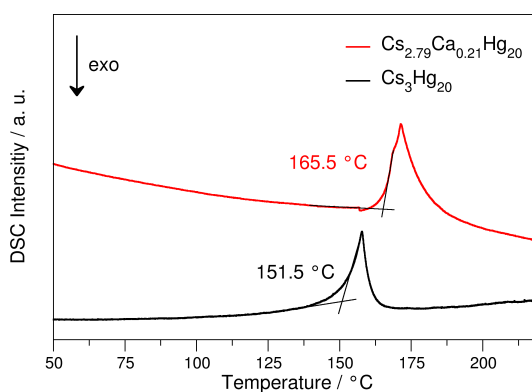


Fig. 4.26: DSC measurements of $\text{Cs}_3\text{Hg}_{20}$ (black) and $\text{Cs}_{2.8}\text{Ca}_{0.2}\text{Hg}_{20}$ (red).

expected for higher electron concentration. In close vicinity of E_F , no pronounced minima or maxima are seen. An increase of electron density would lead to an increase of energy by filling predominantly Hg p states, and this might be the limiting factor for the structural stability of the mixed crystal $\text{Cs}_{1-x}\text{Ca}_x\text{Hg}_{20}$. With higher electron concentrations other amalgams with comparable Ca:Hg ratios, such as $\text{Ca}_{10.5}\text{Hg}_{54.5}$, compete.

We were unable to collect reliable data for the thermal behaviour of the specific resistivity and for the susceptibility of $\text{Cs}_{2.8}\text{Ca}_{0.2}\text{Hg}_{20}$, however, the electronic structure calculations suggest a behaviour comparable to that of $\text{K}_{0.5}\text{Rb}_{0.5}\text{Hg}_{11}$. There are no drastic changes in the DOS despite the small changes in VEC, so the disorder phenomena should be the dominant factor and may lead to a more pronounced ‘bad metal’ behaviour also for $\text{Cs}_{2.8}\text{Ca}_{0.2}\text{Hg}_{20}$.

The situation in the ternary substitution variant $\text{Cs}_{2.8}\text{Ca}_{0.2}\text{Hg}_{20}$ is slightly different from the one in the mixed crystal $\text{K}_{0.5}\text{Rb}_{0.5}\text{Hg}_{11}$ where the structural disorder is not combined with a change in the VEC. Already the increased melting point in $\text{Cs}_{2.8}\text{Ca}_{0.2}\text{Hg}_{20}$ indicates that the overall bonding situation is altered by substituting the monovalent alkali metal by a divalent alkaline earth metal. The change in the electronic situation is a very delicate one: Formally the valence electron concentration changes from 1.87 in $\text{Cs}_3\text{Hg}_{20}$ to 1.89 in $\text{Cs}_{2.8}\text{Ca}_{0.2}\text{Hg}_{20}$, and only very slight details in the partial DOS are noticeable. This slight increase of the electron concentration appears to be still acceptable by the structure, whereas for $x > 0.2$ the enhanced electron concentration may be the electronic reason why no complete solid solution and no binary Ca representative of this structure type exists.

4.3.5 Conclusions

Introducing structural disorder has an influence on the physical properties of polar intermetallic phases. By comparison of the properties of the Vegard-type mixed crystal $\text{K}_{0.5}\text{Rb}_{0.5}\text{Hg}_{11}$ with those of the fully ordered isotypic binary phases KHg_{11} and RbHg_{11} it is possible to study this influence in detail. By doing the same with the substitutional mixed crystal $\text{Cs}_{2.8}\text{Ca}_{0.2}\text{Hg}_{20}$ where together with structural disorder the VEC changes, the relative sizes of structural and electronic effects on the property changes can be estimated. This is especially of interest for polar intermetallic phases with their special electronic situations caused by the combination of low free electron concentrations and very small mean free paths. The physical properties resulting from the ‘bad metal’ behaviour are of interest for new materials with respect to e.g. energy transformation and energy storage. It is therefore of interest for chemists and material scientists to get knowledge about ways to deliberately tailor those physical properties by parameters accessible to the preparative chemist. Free electron concentration and mean free path can be influenced in several ways, and introducing of structural disorder is one of them.

Our experimental and theoretical results indicate that structural disorder indeed is a parameter influencing the ‘bad metal’ behaviour in polar intermetallics. Structural disorder, however, is not the most determining factor, as a comparison with other amalgams and their metallic properties

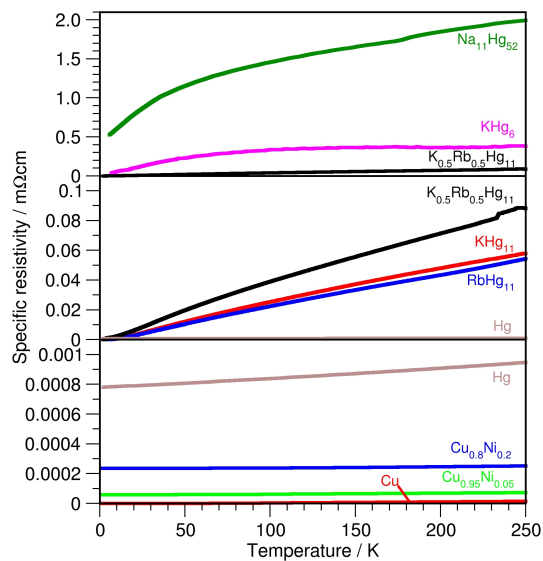


Fig. 4.27: A comprehensive overview over the temperature dependency of the specific resistivities of some metals and amalgams. Bottom: comparison of the resistivities of pure copper (red), copper with 5% Ni (green), copper with 20% Ni (blue)^[33] and Hg (grey).^[34] Center: the resistivity of Hg (grey) in comparison to the ones of KHg_{11} (red), RbHg_{11} (blue) and $\text{K}_{0.5}\text{Rb}_{0.5}\text{Hg}_{11}$ (black). Top: resistivities of the amalgams $\text{K}_{0.5}\text{Rb}_{0.5}\text{Hg}_{11}$ (black), KHg_6 (magenta)^[13] and $\text{Na}_{11}\text{Hg}_{52}$ (green).^[12] Note the different orders of magnitude for the three sets.

shows (see Fig. 4.27). It indicates that a much more important influence on the macroscopic properties is the degree of electron transfer from the electropositive metal onto the Hg sublattice, corresponding to the Coulombic polarity. The ionic contributions, electron localisation and the presence of strong scattering centers in the crystal lattice, dominate the metallic properties of amalgams over the influence of disorder phenomena. Also covalent bonding contributions lead to localisation of electrons, and so the detailed electronic situation of the Hg sublattice plays an important role. Other contributions may be the degree of structural complexity (high-symmetrical and simple amalgams tend to be better metals than those with large translation periods and low symmetry). We plan future work on the contributions of these parameters to the overall behaviour of polar intermetallic phases, again on the case study examples of Hg-rich amalgams of electropositive metals. The gained insights, however, can directly be transferred onto other intermetallic systems with higher interest for application materials.

Table 4.19: Comparison of lattice parameters, melting temperatures and critical temperatures for the two mixed crystal amalgams and their respective binary relatives.

	KHg₁₁	K_{0.5}Rb_{0.5}Hg₁₁	RbHg₁₁	Cs₃Hg₂₀	Cs_{2.8}Ca_{0.2}Hg₂₀
a [Å]	9.6300(10) [15]	9.69143(3)	9.7070(10) [15]	10.9130(10) [16]	10.89553(14)
V [Å ³]	893.0600 [15]	910.257(8)	914.6505 [15]	1299.6706 [16]	1293.44(5)
occ. [%]	100	52.8(7) K 47.2(7) Rb	100	100	93.5(9) Cs 6.5(9) Ca
T_{melt} [°C]	68.7	62.9	69.6	151.5	165.5
T_C [K]	2.5	3.5	3.5	—	—

4.3.6 Acknowledgments

We thank Prof. Dr. Florian Kraus for the provision of suitable sample containers for the susceptibility measurements. We acknowledge Dr. Martin Etter from DESY (Hamburg, Germany), a member of the Helmholtz Association HGF, for the provision of experimental facilities. Parts of this research were carried out at PETRA III, beamline P02.1 within the rapid access program 2021A under proposal ID RAAt-20010291. Financial support by the Deutsche Forschungsgemeinschaft within the project with No. 429690805 is gratefully acknowledged. We also acknowledge the support from University of West Bohemia, New Technologies - Research Center's group members for the calculations and the funding for the cooperation from Computational and Experimental Design of Advanced Materials with New Functionalities (CEDAMNF; grant CZ.02.1.01/0.0/0.0/15_003/0000358) of the Ministry of Education, Youth and Sports (Czech Republic).

Table 4.20: Standardised^[35] fractional atomic coordinates, Wyckoff positions, site symmetry, occupation factors and isotropic displacement parameters [Å²] for K_{0.5}Rb_{0.5}Hg₁₁. Standard deviations are given in parentheses.

Atom	Wyckoff Letter	Site Symmetry	x	y	z	U_{equiv}	occ.
K(1)	3d	4/ <i>mm.m</i>	0	0	1/2	0.0356(13)	0.472(7)
Rb(1)	3d	4/ <i>mm.m</i>	0	0	1/2	0.0356(13)	0.528(7)
Hg(1)	1b	<i>m</i> $\bar{3}m$	1/2	1/2	1/2	0.0583(6)	1
Hg(2)	8g	.3 <i>m</i>	0.15387(4)	0.15387(4)	0.15387(4)	0.0610(3)	1
Hg(3)	12j	<i>m.m</i> 2	0.26771(4)	1/2	0.26771(4)	0.0552(2)	1
Hg(4)	12i	<i>m.m</i> 2	0.34560(4)	0.34560(4)	0	0.0570(2)	1

Table 4.21: Standardised^[35] fractional atomic coordinates, Wyckoff positions, site symmetry, occupation factors and isotropic displacement parameters [\AA^2] for $\text{Cs}_{2.8}\text{Ca}_{0.2}\text{Hg}_{20}$. Standard deviations are given in parentheses.

Atom	Wyckoff Letter	Site Symmetry	x	y	z	U_{equiv}	occ.
Cs(1)	6d	$\bar{4}m.2$	1/4	1/2	0	0.0342(14)	0.935(9)
Ca(1)	6d	$\bar{4}m.2$	1/4	1/2	0	0.0342(14)	0.065(9)
Hg(1)	2a	$m\bar{3}$.	0	0	0	0.0494(14)	1
Hg(2)	6c	$\bar{4}m.2$	1/4	0	1/2	0.0570(14)	1
Hg(3)	8e	.32	1/4	1/4	1/4	0.0570(14)	1
Hg(4)	24k	$m..$	0.25970(11)	0.13474(11)	0	0.0532(14)	1

Table 4.22: Selected interatomic distances [\AA] and respective frequencies for $\text{K}_{0.5}\text{Rb}_{0.5}\text{Hg}_{11}$ and $\text{Cs}_{2.8}\text{Ca}_{0.2}\text{Hg}_{20}$.

$\text{K}_{0.5}\text{Rb}_{0.5}\text{Hg}_{11}$					$\text{Cs}_{2.8}\text{Ca}_{0.2}\text{Hg}_{20}$				
atom 1	–	atom 2	distance	freq.	atom 1	–	atom 2	distance	freq.
K1/Rb1	–	Hg4	3.6575(13)	4x	Cs1/Ca1	–	Hg3	3.85215(6)	4x
	–	Hg3	3.6668(12)	8x		–	Hg4	3.85215(6)	4x
	–	Hg2	3.9625(15)	8x		–	Hg2	3.988(5)	4x
Hg1	–	Hg4	3.1954(13)	12x	–	Hg2	4.060(4)	8x	
	–	Hg2	2.979(3)	3x	Hg1	–	Hg2	3.172(5)	12x
Hg2	–	Hg3	3.019(2)	3x	Hg2	–	Hg4	2.920(5)	1x
	–	K1	3.9625(15)	3x	–	Hg2	2.922(9)	1x	
	–	Hg3	2.999(3)	2x	–	Hg3	3.004(2)	2x	
	–	Hg2	3.019(2)	2x	–	Hg1	3.172(5)	1x	
Hg3	–	Hg4	3.0846(13)	4x	–	Cs1	3.988(5)	1x	
	–	Hg3	3.0846(13)	4x	–	Cs1	4.030(4)	1x	
	–	Hg4	3.1954(13)	4x	Hg3	–	Hg2	3.004(2)	6x
	–	K1	3.6668(12)	1x	–	Cs1	3.85215(6)	3x	
Hg4	–	Hg2	2.920(5)	4x	Hg4	–	Hg2	2.920(5)	4x
	–	Cs1	3.85215(6)	3x	–	Cs1	3.85215(6)	3x	
	–	Cs1	3.85215(6)	3x					

RESULTS AND DISCUSSION

References

- [1] J. D. Corbett, Explanatory Synthesis: The Fascinating and Diverse Chemistry of Polar Intermetallic Phases, *Inorg. Chem.* **2010**, *49*, 13–28, DOI: [10.1021/ic901305g](https://doi.org/10.1021/ic901305g).
- [2] F. C. Gladisch, S. Steinberg, Revealing Tendencies in the Electronic Structures of Polar Intermetallic Compounds, *Crystals* **2018**, *8*, 80, DOI: [10.3390/cryst8020080](https://doi.org/10.3390/cryst8020080).
- [3] V. J. Emery, S. A. Kivelson, Superconductivity in Bad Metals, *Phys. Rev. Lett.* **1995**, *74*, 3253–3256, DOI: [10.1103/PhysRevLett.74.3253](https://doi.org/10.1103/PhysRevLett.74.3253).
- [4] A. F. Gebard, S. B. Arnason, Bad-metal behavior: exotic physics or a consequence of microstructure?, *J. Supercond.* **1995**, *74*, 3253–3256, DOI: [10.1023/A:1007714813001](https://doi.org/10.1023/A:1007714813001).
- [5] D. M. R. (ed.), *Thermoelectrics Handbook*, CRC Press, Boca Raton (FL), USA, **2005**.
- [6] M. Christensen, S. Johnsen, B. B. Iversen, Thermoelectric clathrates of type I, *Dalton Trans.* **2009**, *39*, 978–992, DOI: [10.1039/B916400F](https://doi.org/10.1039/B916400F).
- [7] S. M. Kauzlarich, K. P. Devlin, C. J. Perez, Zintl phases for thermoelectric applications. In *Thermoelectric Energy Conversion*, (Ed.: R. Funahashi), Woodhead Publishing, Duxford, UK, **2021**, pp. 157–182.
- [8] A. F. Ioffe, A. R. Regel, Non-crystalline, amorphous and liquid electronic semiconductors, *Prog. Semicond.* **1960**, *4*, 237–291.
- [9] D. Gall, Electron mean free path in elemental metals, *J. Appl. Phys.* **2016**, *119*, 085101, DOI: [10.1063/1.4942216](https://doi.org/10.1063/1.4942216).
- [10] O. Gunnarsson, M. Calandra, J. E. Han, Saturation of Electrical Resistivity, *Rev. Mod. Phys.* **2003**, *75*, 1085–1099, DOI: [10.1103/RevModPhys.75.1085](https://doi.org/10.1103/RevModPhys.75.1085).

- [11] E. H. Sondheimer, The mean free path of electrons in metals, *Adv. Phys.* **2001**, *50*, 499–537, DOI: [10.1080/00018730110102187](https://doi.org/10.1080/00018730110102187).
- [12] C. Hoch, A. Simon, Na₁₁Hg₅₂: Complexity in a Polar Metal, *Angew. Chem. Int. Ed.* **2012**, *51*, 3262–3265, DOI: [10.1002/anie.201108064](https://doi.org/10.1002/anie.201108064).
- [13] F. Tambornino, C. Hoch, Bad metal behaviour in the new Hg-rich amalgam KHg₆ with polar metallic bonding, *J. Alloys Compd.* **2015**, *618*, 299–304, DOI: [10.1016/j.jallcom.2014.08.173](https://doi.org/10.1016/j.jallcom.2014.08.173).
- [14] T. Hohl, F. Tambornino, C. Hoch, Structure and Bonding in CsNa₂Hg₁₈, a New Ternary Amalgam with Strong Coulombic Bonding Contributions, *Crystals* **2022**, *12*, 1679, DOI: <https://doi.org/10.3390/cryst12111679>.
- [15] E. Biehl, H.-J. Deiseroth, Darstellung, Strukturchemie und Magnetismus der Amalgame MHg₁₁ (M: K, Rb, Ba, Sr), *Z. Anorg. Allg. Chem.* **1999**, *625*, 1073–1080, DOI: [10.1002/\(SICI\)1521-3749\(199907\)625:7<1073::AID-ZAAC1073>3.0.CO;2-V](https://doi.org/10.1002/(SICI)1521-3749(199907)625:7<1073::AID-ZAAC1073>3.0.CO;2-V).
- [16] E. Todorov, S. C. Sevov, *J. Solid State Chem.* **2000**, *149*, 419–427, DOI: [10.1006/jssc.1999.8569](https://doi.org/10.1006/jssc.1999.8569).
- [17] J. C. Slater, Atomic Radii in Crystals, *J. Chem. Phys.* **1964**, *41*, DOI: [10.1063/1.1725697](https://doi.org/10.1063/1.1725697).
- [18] F. Tambornino, J. Sappl, F. Pultar, T. M. Cong, S. Hübner, T. Giftthaler, C. Hoch, Electrocrystallization - a synthetic method for intermetallic phases with polar metal-metal bonding, *Inorg. Chem.* **2016**, *55*, 11551–11559, DOI: [10.1021/acs.inorgchem.6b02068](https://doi.org/10.1021/acs.inorgchem.6b02068).
- [19] B. H. Toby, R. B. Von Dreele, GSAS-II: the genesis of a modern open-source all purpose crystallography software package, *J. Appl. Crystallogr.* **2013**, *46*, 544–549, DOI: [10.1107/S0021889813003531](https://doi.org/10.1107/S0021889813003531).
- [20] A. A. Coelho, TOPAS and TOPAS-Academic: an optimization program integrating computer algebra and crystallographic objects written in C++, *J. Appl. Cryst.* **2018**, *51*, 210–218, DOI: [10.1107/S1600576718000183](https://doi.org/10.1107/S1600576718000183).
- [21] C. Prescher, V. B. Prakapenka, DIOPTAS: a program for reduction of two-dimensional X-ray diffraction data and data exploration, *High Press. Res.* **2015**, *35*, 223–230, DOI: [10.1080/08957959.2015.1059835](https://doi.org/10.1080/08957959.2015.1059835).
- [22] NETZSCH PROTEUS THERMAL ANALYSIS, NETZSCH Gerätebau GmbH, Selb, Deutschland, version 6.1.0, **2017**.
- [23] MULTIVU, QUANTUM DESIGN Inc., San Diego (CA), USA, version 1.5.11, **2013**.
- [24] H. Ebert, D. Ködderitzsch, J. Minár, Calculating condensed matter properties using the KKR-Green's function method—recent developments and applications, *J. Rep. Prog. Phys.* **2011**, *74*, 096501, DOI: [10.1088/0034-4885/74/9/096501](https://doi.org/10.1088/0034-4885/74/9/096501).
- [25] H. Ebert, M. Bottoni, D. Benea, S. Bornemann, J. Braun, S. Chadov, M. Deng, H. Freyer, T. Hühne, D. Ködderitzsch, M. Kosuth, S. Lowitzer, S. Mankovsky, J. Minár, A. Perlov, V. Popescu, O. Sipr, C. Zecha, The Munich SPR-KKR Package, version 7.7, **2012**.
- [26] H. S. Vosko, L. Wilk, M. Nusair, Accurate spin-dependent electron liquid correlation energies for local spin density calculations: a critical analysis, *Can. J. Phys.* **1980**, *58*, 1200–1211, DOI: [10.1139/p80-159](https://doi.org/10.1139/p80-159).
- [27] E. Biehl, H.-J. Deiseroth, K₂Hg₇ und Rb₂Hg₇, zwei Vertreter eines neuen Strukturtyps binärer intermetallischer Verbindungen, *Z. Anorg. Allg. Chem.* **1999**, *625*, 1337–1342, DOI: [10.1002/\(SICI\)1521-3749\(199908\)625:8<1337::AID-ZAAC1337>3.0.CO;2-W](https://doi.org/10.1002/(SICI)1521-3749(199908)625:8<1337::AID-ZAAC1337>3.0.CO;2-W).
- [28] P. Yi, M. Falk, T. Weihs, Intermetallic formation at deeply supercooled Ni/Al multilayer interfaces: A molecular dynamics study, *J. Appl. Phys.* **2018**, *124*, 165303, DOI: [10.1139/p80-159](https://doi.org/10.1139/p80-159).
- [29] H. Li, M. Li, A theory for polymorphic melting in binary solid solutions, *J. Mat. Res.* **2011**, *26*, 997–1005, DOI: [10.1557/jmr.2011.55](https://doi.org/10.1557/jmr.2011.55).
- [30] E. Maxwell, Isotope Effect in the Superconductivity of Mercury, *Phys. Rev.* **1950**, *78*, 477, DOI: [DOI10.1103/PhysRev.78.477](https://doi.org/10.1103/PhysRev.78.477).
- [31] M. Wendorff, C. Röhr, Alkaline-earth tri-mercurides A^{II}Hg₃ (A^{II} = Ca, Sr, Ba): Binary intermetallic compounds with a common and a new structure type, *Z. Kristallogr.* **2018**, *233*, 515–529, DOI: [10.1515/zkri-2018-2054](https://doi.org/10.1515/zkri-2018-2054).

- [32] A. V. Tkachuk, A. Mar, Alkaline-Earth Metal Mercury Intermetallics, $A_{11-x}Hg_{54+x}$ ($A = Ca, Sr$), *Inorg. Chem.* **2008**, *47*, 1313–1318, DOI: [10.1021/ic7015148](https://doi.org/10.1021/ic7015148).
- [33] Y. C. Hu, M. W. Ackerman, K. Y. Wu, T. N. Havill, R. H. Bogaard, A. R. Matula, S. G. Oh, H. M. James, Electrical Resistivity of Ten Selected Binary Alloy Systems, *J. Phys. Chem. Ref. Data* **1983**, *12*, 183–322, DOI: [10.1063/1.555684](https://doi.org/10.1063/1.555684).
- [34] M. W. H. (ed.), *CRC Handbook of Chemistry and Physics*, 97th ed., CRC Press, Boca Raton (FL), USA, **2017**.
- [35] L. M. Gelato, E. Parthé, Structure Tidy – a computer program to standardize crystal structure data, *J. Appl. Crystallogr.* **1987**, *20*, 139–143, DOI: [10.1107/S0021889887086965](https://doi.org/10.1107/S0021889887086965).

4.4 The Hg-rich part of the Binary System, K–Hg revised: Synthesis, Crystal and Electronic Structures of KHg_4 , KHg_5 and KHg_8

Timotheus Hohl¹, Constantin Hoch¹, Marco Wendorff² and Caroline Röhr^{2,*}

* Correspondence: caroline@ruby.chemie.uni-freiburg.de; Tel.: +49-761-203-6343

¹ Department Chemie, Ludwig-Maximilians-Universität München

² Institut für Anorganische und Analytische Chemie, Albert-Ludwigs-Universität Freiburg

Manuscript in preparation for: *Inorg. Chem.* **2023**.

The Manuscript is currently in preparation in cooperation with C. Röhr. KHg_5 and KHg_4 were first discovered in her group. She is performing the structural descriptions and electronic calculations for KHg_4 and KHg_5 in depth. Characterisation, structural description, electronic calculations and discussion thereof as well as thermoanalysis and the subsequent redesign of the K–Hg phase diagram were conducted by T. Hohl.

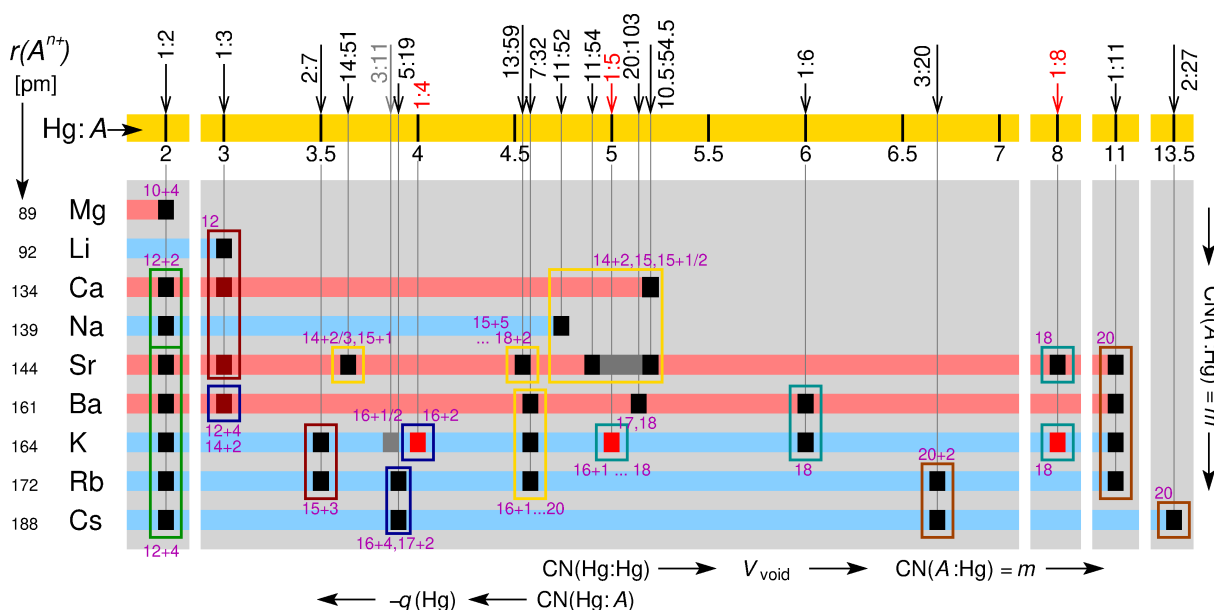


Fig. 4.28: Reported Hg-rich mercurides of alkali/alkaline-earth elements. The new compounds are shown in red. Arrows indicate increasing values, coordination numbers are included in violet. The figure was provided by C. Röhr and slightly adapted from a previous work.^[1]

4.4.1 Introduction

Mercury-rich amalgams of the less noble metals serve as ideal candidates for the investigation of polar metallic bonds. Due to the interplay of covalent, ionic and metallic bonding contributions, these compounds exhibit a broad structural variety, as well as unusual physicochemical properties (e.g. low electrical conductivity),^[2,3] which originates from the incomplete electron transfer from the less noble metal to mercury. Although most systems have been thoroughly studied, new compounds can still be found, as is apparent in the recent discovery of KHg_6 , BaHg_6 and SrHg_8 .^[4-6]

In the phase diagram of K–Hg, many representatives can be found; a comprehensive list of reported binary K–Hg phases with Hg : K \geq 2, including their structural features is compiled in Table 4.23.

Table 4.23: Summary of the reported K amalgams with Hg : K ratio \geq 2 together with their space groups and structural features.

Compound	Space group	Structural features	Literature
KHg ₂	<i>P6/mmm</i>	AlB ₂ structure type	[7]
K ₂ Hg ₇	<i>P$\bar{3}$m1</i>	<i>trans</i> -connected chains of distorted cubes	[8]
K ₃ Hg ₁₁	<i>Immm</i>	defect BaAl ₄ structure type	[9]
K ₇ Hg ₃₁	<i>P6/mmm</i>	Ba ₇ Cd ₃₁ structure type	[9]
KHg ₆	<i>Pnma</i>	BaHg ₆ structure type	[4]
KHg ₁₁	<i>Pm$\bar{3}$m</i>	BaHg ₁₁ structure type	[10]

4.4.2 Experimental

Single crystals of KHg₈ were serendipitously obtained by adding 4.9868 g (24.86 mmol) Hg slowly and dropwise onto 219.4 mg (5.55 mmol) K at -78°C , resulting in a K to Hg ratio of 7 : 31 to validate the existence of the binary potassium amalgam K₇Hg₃₁. The mixture was allowed to thaw to RT inside the cooling bath over night. Xenomorphic, silver metallic crystalline fragments were isolated under potassium-dried paraffin oil using a binocular and fixated inside a flame-sealed glass capillary. Orientation images yielded a triclinic metric with $a = 6.3001(17)$, $b = 8.9723(19)$ and $c = 12.637(3)$ Å. A careful comparison to reported binary potassium amalgams yielded no accordance, and a full measurement was subsequently performed. The final data collection was done on a one-circle diffractometer device (IPDS 1, Stoe & Cie, Darmstadt, Germany, graphite-monochromatized Ag-K α radiation, image plate detector system) in φ scan geometry with $\Delta\varphi = 1.5^\circ$ and $0 \leq \varphi \leq 199.5^\circ$ and subsequently corrected for Lorentz-, polarisation and absorption effects.^[11–13] The absence of any systematic absence conditions indicated two possible space groups for the refinement: *P1* and *P $\bar{1}$* . Wilson statistics indicated a non-centrosymmetric symmetry, so the structure solution was performed in *P1*. Due to better *R*-values however, the final refinement was done in spacegroup *P $\bar{1}$* . For the absorption correction, the crystal shape originating from the indexed faces was optimised on the basis of the intensity distribution,^[13] and numerical absorption correction was performed.^[12] All details on the results of the data collection, structure solution and refinement are listed in Table 4.24 (right), while fractional atomic coordinates and isotropic displacement parameters are compiled in Table 4.27. Anisotropic displacement parameters are shown in Table 4.28, and selected interatomic distances in Table 4.29.

KHg₄ and KHg₅ were obtained from stoichiometric melts of the elements. Details on single crystal diffraction experiments will be provided by C. Röhr. Results of data collection, structure solution and refinements are summarised in Table 4.24, and their fractional atomic coordinates and isotropic displacement parameters can be found in Table 4.27. Anisotropic displacement parameters are listed in Table 4.28, while selected interatomic distances can be found in Table 4.29.

Table 4.24: Crystallographic data and selected details on data collection, structure solution and refinement of KHg₄, KHg₅ and KHg₈. Data collection was performed at room temperature. All standard deviations are given in parentheses in units of the last digit.

	KHg ₄	KHg ₅	KHg ₈
Crystal system	orthorhombic	monoclinic	triclinic
Space group	<i>Cmcm</i> (No. 63)	<i>P2₁/c</i> (No. 14)	<i>P$\bar{1}$</i> (No. 2)

continued on the next page

		KHg ₄	KHg ₅	KHg ₈
Lattice parameters [\AA , $^\circ$]	<i>a</i>	9.374(3)	11.4832(10)	6.3001(17)
	<i>b</i>	8.735(3)	17.5862(15)	8.9723(19)
	<i>c</i>	6.456(2)	10.3152(9)	12.637(3)
	α			99.30(3)
	β		116.6871(11)	91.34(3)
	γ			98.36(3)
<i>V</i> [\AA^3]		528.7(3)	1861.2(3)	696.7(3)
<i>Z</i>		4	12	3
Density (X-ray) [$\text{g} \cdot \text{cm}^{-3}$]		10.572	11.156	11.755
Diffractometer		BRUKER APEX Quazar		STOE IPDS 1
Radiation		Mo-K α		AgK α
	λ	0.7107 \AA		0.56087 \AA
Absorption coeff. μ [mm^{-1}]		116.402	123.823	72.230
ϑ range [$^\circ$]		3.188–29.974	1.985–27.496	2.414–19.99
Index range		$-13 \leq h \leq 12$,	$-14 \leq h \leq 14$,	$-16 \leq h \leq 16$,
		$-12 \leq k \leq 12$,	$-22 \leq k \leq 22$,	$-6 \leq k \leq 6$,
		$-9 \leq l \leq 9$	$-13 \leq l \leq 13$	$-12 \leq l \leq 12$
No. of collected refl.		3784	33794	5546
No. of independent refl.		439	4272	2546
No. of indep. refl. ($I \geq 2\sigma(I)$)		397	3936	1385
R_{int}		0.0622	0.0653	0.1032
R_σ		0.0368	0.0433	0.1553
$F(000)$		1356	5028	1977
Corrections		Lorentz, Polarisation, Absorption (numerical)[12–14]		
Structure solution		direct methods [15]		
Structure refinement		full-matrix least-squares on F^2 [15]		
No. of L.S. parameters		17	164	125
GooF		1.356	1.376	0.852
R values ($I \geq 2\sigma(I)$)	<i>R1</i>	0.0491	0.1017	0.0583,
	<i>wR2</i>	0.1386	0.2692	0.1151
R values (all data)	<i>R1</i>	0.0527	0.1060	0.1161,
	<i>wR2</i>	0.1413	0.2704	0.1276
Extinction coefficient		0.00042(18)	0.000025(8)	0.0097(4)
Res. $\rho(\text{e}^-)$ min/max [$\text{e}^- \text{\AA}^{-3}$]		-4.917 / +5.894	-10.130 / +10.904	-3.319 / +3.653

4.4.3 Crystal structures

The crystal structure of KHg₄

KHg₄ crystallises in a new structure type in the orthorhombic crystal system (space group $Cmcm$, No. 63, $a = 9.374(3) \text{\AA}$, $b = 8.735(3) \text{\AA}$, $c = 6.456(2) \text{\AA}$). It contains one crystallographic position for K, and two for Hg. The structure can be described via different approaches. A viewpoint which highlights the space filling combination of interpenetrating $[\text{K}@\text{Hg}_{16}+\text{K}_2]$ and trigonal prismatic $[\text{Hg}_6]$ polyhedra is visualised in Fig. 4.29 (right). The cation coordination polyhedra (ccp's) around potassium can be derived by substituting two Hg–Hg dumbbells of an elongated triangular bicupola (Johnson Solid No. J_{35}) with K (cf. Fig. 4.30). These ccp then form corrugated, interpenetrating chains along c . This coordination polyhedron has previously not been encountered in amalgams.

While the coordination number 18 has been observed in many binary amalgams (i.e. KHg₆,^[4] BaHg₆,^[5] Ba₂₀Hg₁₀₃,^[16] SrHg₈^[6]), the coordination pattern 16+2 has not been encountered so far, the ccp within the literature structures are exclusively $M\text{Hg}_{18}$ polyhedra.

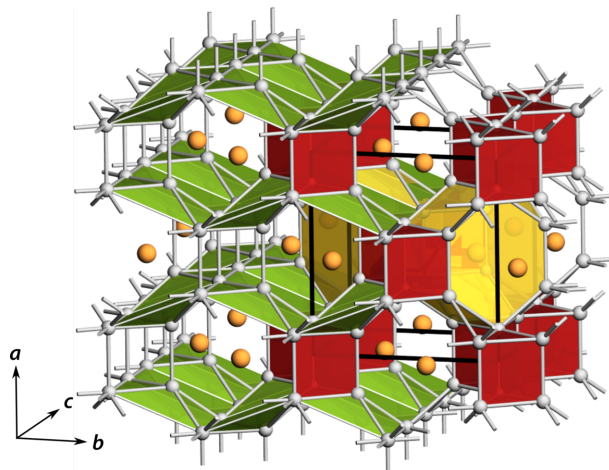


Fig. 4.29: Polyhedral representation of the crystal structure of KHg₄. On the right side, the space-filling combination of ccps of K (yellow) and Hg₆ prisms is highlighted, while the green Hg₅ pyramids emphasise the relation to other Hg-rich amalgams. Hg: grey, K: orange, unit cell: black.

The K–Hg distances in KHg_4 range from 3.428(2) to 3.846(2) Å, which is well within distances reported in the literature (cf. Fig. 4.39). However, if the overall coordination sphere is considered, an additional K–K contact exists (4.286(9) Å). These K atoms serve as the center of the next ccp, resulting in a corrugated chain of interpenetrating polyhedra. This contact is smaller than the sum of the metallic radius ($\sum r_{\text{K}}^{\text{met}} = 4.698 \text{ Å}^{[17]}$), but even larger than the sum of its ionic radii ($\sum r_{\text{K}^+} = 2.66 \text{ Å}^{[18]}$), emphasising the complicated bonding situation comprised of ionic and metallic contributions.

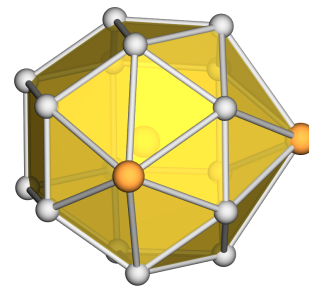


Fig. 4.30: Coordination polyhedron around K in KHg_4 . Hg: grey, K: orange.

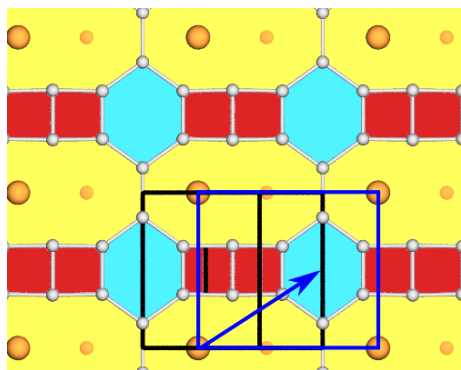


Fig. 4.31: Net representation of KHg_4 parallel to $(1\bar{1}0)$. Yellow: merged KHg_8 octagons, blue: Hg_6 hexagons inside the ccp, red: Hg_4 squares representing the faces of the Hg_6 prisms. Unit cell: black, Hg: grey, K: orange. The direction of the stacking shift is indicated by an arrow.

The crystal structure of KHg_5

KHg_5 also crystallises a new structure type in the monoclinic crystal system (space group $P2_1/c$, No. 14, $a = 11.4832(10) \text{ Å}$, $b = 17.5862(15) \text{ Å}$, $c = 10.3152(9) \text{ Å}$, $\beta = 116.6781(11)^\circ$). In its unit cell, three crystallographically independent positions for potassium, and fifteen for Hg are present. Again, two different approaches can be utilised to describe the crystal structure. The emphasis on coordination polyhedra yields three ccp's for K: (1) the ccp around K3 is best described by a 5:8:5 polyhedron as already described for the crystal structures of and KHg_6 .^[4] Here, it is slightly distorted and has point symmetry 1 (in KHg_6 : *m*).^[4] The polyhedra around K1 and K2 can not be described independent from each other, since their coordination environments overlap. In these dumbbells best denoted by the interpenetration of a (17+1)-fold (or 5:7+1:5) coordination formed by 17 Hg atoms as well as K2 surrounding K1, and a 16+1-fold (or 5:6+1:5) coordination around K2, comprised of 16 Hg atoms as well as K1. Both coordination polyhedra have not been observed before, and the 17-fold coordination is a rather unique motif (as is later discussed in the case of KHg_8 as well). The interatomic distances support this observation: K1–Hg distances are found between 3.441(15) and 4.069(16) Å (reported values for

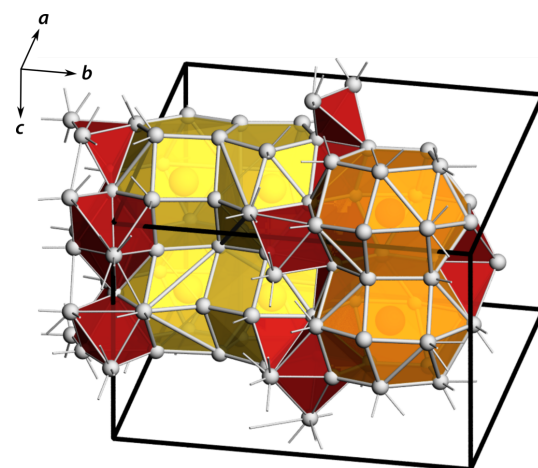


Fig. 4.32: Polyhedral representation of the crystal structure of KHg_5 . Different types of ccp (K1/K2: yellow, K3: orange) as well as Hg_4 tetrahedra and Hg_6 octahedra (red) are emphasised. Hg: grey, K: orange, unit cell: black.

CN = 18 are 3.457–4.080 Å^[4]), while K2–Hg and K3–Hg distances are between 3.354(15) and 3.989(16) Å (K2) as well as 3.421(14) and 3.849(14) Å (K3). The observed K2–Hg3 distance is the shortest found in Hg-rich potassium amalgams so far. Additionally, K–K distances of 4.23(2) Å can be found as a result of the interpenetrating polyhedra. The different coordination polyhedra around K are presented in Fig. 4.33. For space-filling of the unit cell, a combination of Hg₄ tetrahedra and Hg₆ must be added. These are visualised in Fig. 4.32 as red polyhedra.

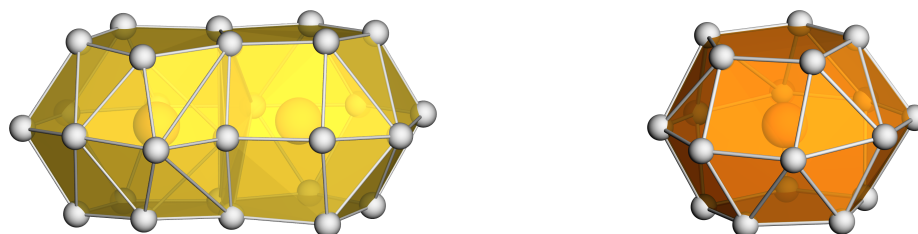


Fig. 4.33: From left to right: coordination polyhedra around K1/K2 (yellow) and K1 (right, orange). Hg: grey, K: orange.

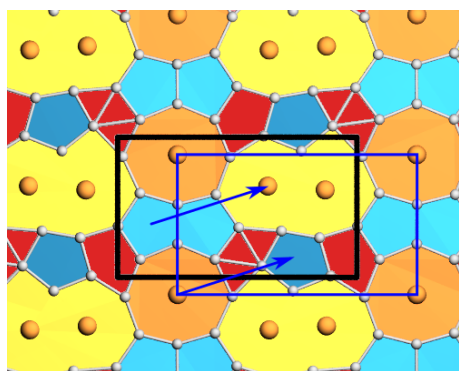


Fig. 4.34: Net representation of KHg₅ perpendicular to *c*. Yellow: merged KHg₈ octagons around K2/K3, orange: octagons around K1, light blue: Hg₅ pentagons at the top of the ccp, red: space-filling Hg_{*x*} polyhedra. Unit cell: black, Hg: grey, K: orange. The direction of the stacking shift is indicated by arrows.

A facile visualisation of the crystal structure is given in Fig. 4.34 (left), where the net representation is shown. The nets, perpendicular to the crystallographic *c*-axis, consist of octagons (orange), which represents the ‘equatorial plane’ in the ccp of K1, for which the top and bottom planes are built by the dark blue pentagons. The yellow polygons however, can not be unambiguously named. The best approach would be a merged K₂Hg₁₁ polygon, where two heptagons are overlapping. They represent the equatorial planes dumbbell-shaped interpenetrating polyhedra pictured above, and are capped by the light blue, slightly distorted pentagons. The positioning of the next layer is indicated by the arrows, while the stacking can best be denoted as a ...*ABA'B'*... order, where the ' indicates a rotation of 180° due to the glide plane *c*. Again, voids are left, which can be assigned to a Hg sublattice (red), following the trend of the enlargement of the Hg network with respect to the one in KHg₄.

The crystal structure of KHg_8

As well as KHg_4 and KHg_5 , KHg_8 crystallises in a new structure type, belonging to the triclinic crystal system (space group $P\bar{1}$, No.2, $a = 6.3001(17) \text{ \AA}$, $b = 8.9723(19) \text{ \AA}$, $c = 12.637(3) \text{ \AA}$, $\alpha = 99.30(3)^\circ$, $\beta = 91.34(3)^\circ$, $\gamma = 98.36(3)^\circ$). Its unit cell is comprised of two atomic positions for K (of which one shows inversion symmetry), and twelve for Hg. Again, two representations are valuable for understanding the crystal structure. Applying a more ionic picture yields two different types of coordination polyhedra: literature-known KHg_{18} polyhedra (5:8:5 coordination with CN = 18) around K1 as well as irregular KHg_{17} (CN = 17) polyhedra around K2. This polyhedron around K2 exhibits a previously unencountered coordination environment: on one side, its regular-shaped pentagon (face-sharing with the ccp around K1), followed by a 7-fold coordination, and then again a pentagon, although heavily distorted. The unusual coordination number results in a high degree of distortion; in order to compensate for the loss of one vertex, the position of one Hg atom is changed in a manner that leads to a widened pentagon (or envelope-like shape), and can be interpreted as a 5:7:4+1 fashion. The direct contact of these KHg_{17} polyhedra leads to spatial constriction, resulting in the observed distortion. A reason for this distortion might be found if the remaining space of the unit cell is also being considered: the insertion of an additional Hg position (while also lacking surplus volume for it) would lead to the destabilisation of the overall crystal lattice. In turn, a more stable coordination environments will be formed (i.e. KHg_{20} polyhedra in KHg_{11} ^[10]). This is in good agreement with all experimental observations: KHg_{11} was obtained in every attempt for the phase-pure synthesis of this amalgam.

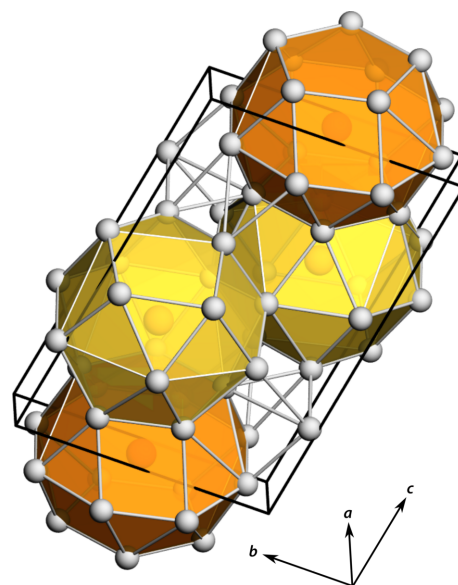


Fig. 4.35: Polyhedral representation of the crystal structure of KHg_8 . For reasons of clarity, only ccp's (K1: orange, K2: yellow) are emphasised. Hg: grey, K1/2: dark/light orange, unit cell: black.

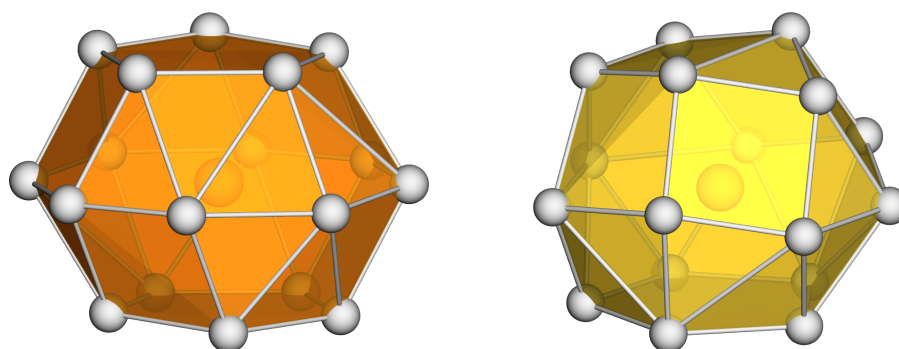


Fig. 4.36: left: 5:8:5 coordination polyhedron around K1. right: irregular ccp around K2 with CN = 17. K: orange, Hg: grey.

The observed K–Hg distances in KHg_8 for the different polyhedra reflect their coordination environment: for K1 (CN = 18), they range between 3.476(2) and 3.977(4) \AA and are only slightly smaller than the comparable literature values (KHg_{18} in KHg_6 : 3.457(8)–4.239(13) \AA ^[4]). The polyhedron around K2 with CN = 17 reflects this, its largest K–Hg distances are smaller than the K1–Hg distances (3.481(7)–3.841(9) \AA). A comparison of K–Hg distances can be found in Fig. 4.39. The Hg–Hg distances (2.918(3)–3.484(3) \AA) reflect the strong Hg–Hg interactions in this structure.

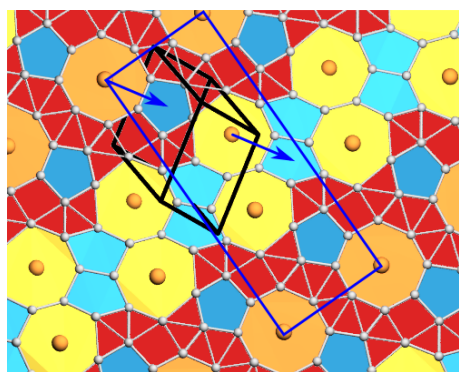


Fig. 4.37: Net representation of KHg_8 . Orange: octagons around K2, yellow: edge-sharing KHg_8 heptagons around K1, light blue: Hg_5 envelope-shaped pentagons in the ccp of K1, dark blue: pentagons in the ccp's of both ccp's, red: space-filling Hg_x polyhedra. Unit cell: black, Hg: grey, K: orange. The direction of the stacking shift is indicated by arrows.

In order to draw a space-filling picture of the polyhedra, a multitude of different Hg_x polyhedra would be necessary. Since visualisation of the polyhedral representation only gets less comprehensible, it is not shown. Instead, a focus on the net representation (see Fig. 4.37, left) proves to be worthwhile.

In these nets, octagons around K1, heptagons around K2, pentagons (or extended rectangles) serving as the 'upper/lower' planes of the ccp's as well as a number of triangular 'voids' built by Hg. The stacking order in this crystal structure follows the pattern $\dots\text{ABB}'\text{A}'\dots$, mirroring the only existing symmetry element $\bar{1}$ in the center of the unit cell. It can also be seen that the higher coordination number (8, around K1) is being stabilised by the surrounding Hg-lattice, while the lower one (7, around K2) tends to form 'bigger' substructures via edge-sharing dumbbells (yellow). Again, it should be pointed out that these nets are not perfect planes, which becomes clear if the 'caps' of the irregular polyhedra around K1 are considered: their envelope-shaped appearance makes an even plane impossible to construct.

General trends

As shown, crystal structures of Hg-rich amalgams can be described via two intuitive approaches: the stacking of covalent Hg nets (bigger polygons are centered by the less noble metal), or the space-filling combination of ccp's and different (irregular) polyhedra only consisting of Hg. With an increase of the Hg content, the crystal structures are exhibiting more complex structural motifs. The Hg-rings around the less noble metal grow bigger and move away from each other, which affords for more complicated patterns of Hg around the polyhedra in order to fill residual space. At the same time, the 'interstitial' Hg aims to form a network close to its crystal structure, which manifests in the formation of increasingly complicated combinations of polygons (or polyhedra) of decreasing symmetry. While this pattern is not completely linear or proportional, it is certainly a fitting approximation and a valuable tool for understanding the variety of the crystal structures present in amalgams in general and can be observed in the examples of the $\text{KHg}_4 - \text{KHg}_8$ region. The following Figure 4.38 highlights the coordination patterns of the nets present in the known binary potassium compounds.

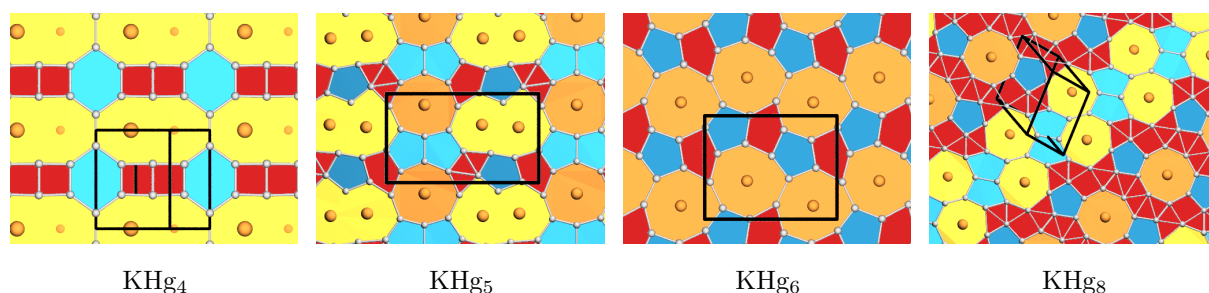


Fig. 4.38: Net representation of selected binary potassium amalgams with increasing Hg content. Unit cell: black, Hg atoms: grey, K atoms: orange. Octagons are depicted in orange, merged octagons or heptagons in yellow, capping penta- or hexagons in blue, while interstitial polygons are depicted in red.

Phase	$d_{\text{K-Hg}}^{\text{min}}$	$d_{\text{K-Hg}}^{\text{max}}$	CN	Ref.
K_2Hg_7	3.560	3.993	15 + 3	[8]
KHg_4	3.428	3.846	16 + 2	this work
K_7Hg_{32}	3.419	4.009	16 + 1 - 20	[9]
KHg_5	3.354	4.069	16 + 1 - 18	this work
KHg_6	3.457	4.080	18	[4]
KHg_8	3.476	3.814	17 - 18	this work
KHg_{11}	3.649	3.944	20	[10]

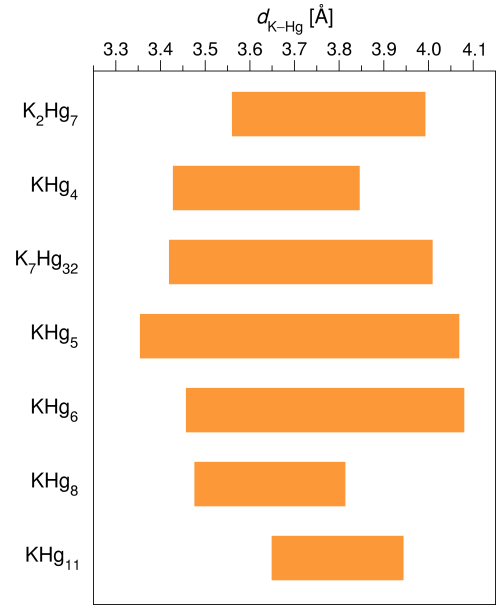


Fig. 4.39: K-Hg interatomic distances [Å] and coordination numbers of Hg-rich potassium amalgams found in this work compared to literature-known representatives. Results presented in this work are highlighted in blue.

4.4.4 Electronic structures

Electronic structure calculations were performed with the Wien2K program package,^[19] applying the full-potential linear augmented plane wave (FP-LAPW) method. The exchange and correlation contribution was described by the functional of Perdew, Burke and Enzerhof (PBE) with a generalised gradient approximation (GGA).^[20] Muffin-tin radii were set to 132.3 pm (2.5 a.u.), while the number of basis functions was determined by the value of $R_{\text{mt}} \cdot K_{\text{max}} = 8$ with K_{max} being the largest k vector. The separation energy was set to -6 Ry. 980 k points in the Brillouin zone (490 thereof in the irreducible Brillouin zone) were calculated via a $14 \times 10 \times 7$ Monkhorst-Pack grid. Cutoff energies used were $E_{\text{max}}^{\text{pot}} = 163$ eV (potential) and $E_{\text{max}}^{\text{wf}} = 139$ eV (interstitial PW). Charge distribution for the individual atoms was calculated via analysis of the electron density map by calculation of heights and positions of the bond critical points (saddle points).^[21]

The DOS and pDOS plots are shown in Fig. 4.40 (right). To compensate for the multiplicity of the atomic position of K1, its absolute values were divided by the factor two. No pronounced minimum at the Fermi level exists, which would indicate the existence of (pseudo-)band gaps. This underlines the overall metallic behaviour of the structure and is in accordance with calculations of the electronic structures of similar amalgams (e.g. KHg_6 ,^[4] SrHg_8 ^[6]). However, very small local maxima between -0.5 and -2 eV exist for some

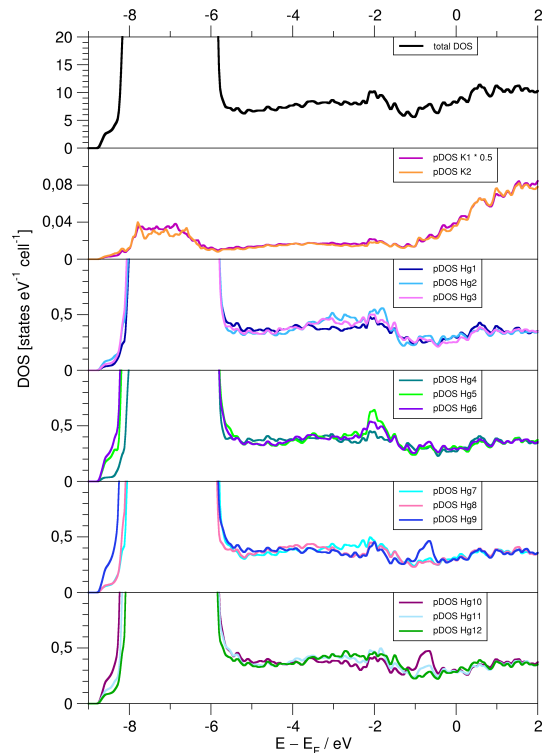


Fig. 4.40: Calculated total density of states (tDOS) together with the partial states (pDOS) of KHg_8 in the range from -9 to 2 eV relative to E_{F} .

Hg positions, highlighting the different partial charge distributions. Contributions of K1 and K2 below the fermi level originate mostly from *p*-states, but some *s*-state contributions still exist, emphasising the incomplete electron transfer from K to the Hg network. The Hg contributions to the electronic structure is a mix of *s*- and *p*-states, accenting the interplay of different bonding contributions. Bader charges have been calculated as well, yielding +0.78 and +0.77 for K1 and K2, respectively, while charges distributed over the Hg network range between -0.06 and -0.14 . Again, the obtained results are in good agreement with literature-known values.

Table 4.26: Bader charges calculated on the basis of the results of electronic calculations of KHg_s with the Wien2K^[19] program package.

K1	+0.78	Hg1	-0.06	Hg4	-0.14	Hg7	-0.10	Hg10	-0.09
K2	+0.77	Hg2	-0.06	Hg5	-0.06	Hg8	-0.10	Hg11	-0.10
		Hg3	-0.12	Hg6	-0.09	Hg9	-0.12	Hg12	-0.12

4.4.5 Redetermination of the K–Hg phase diagram

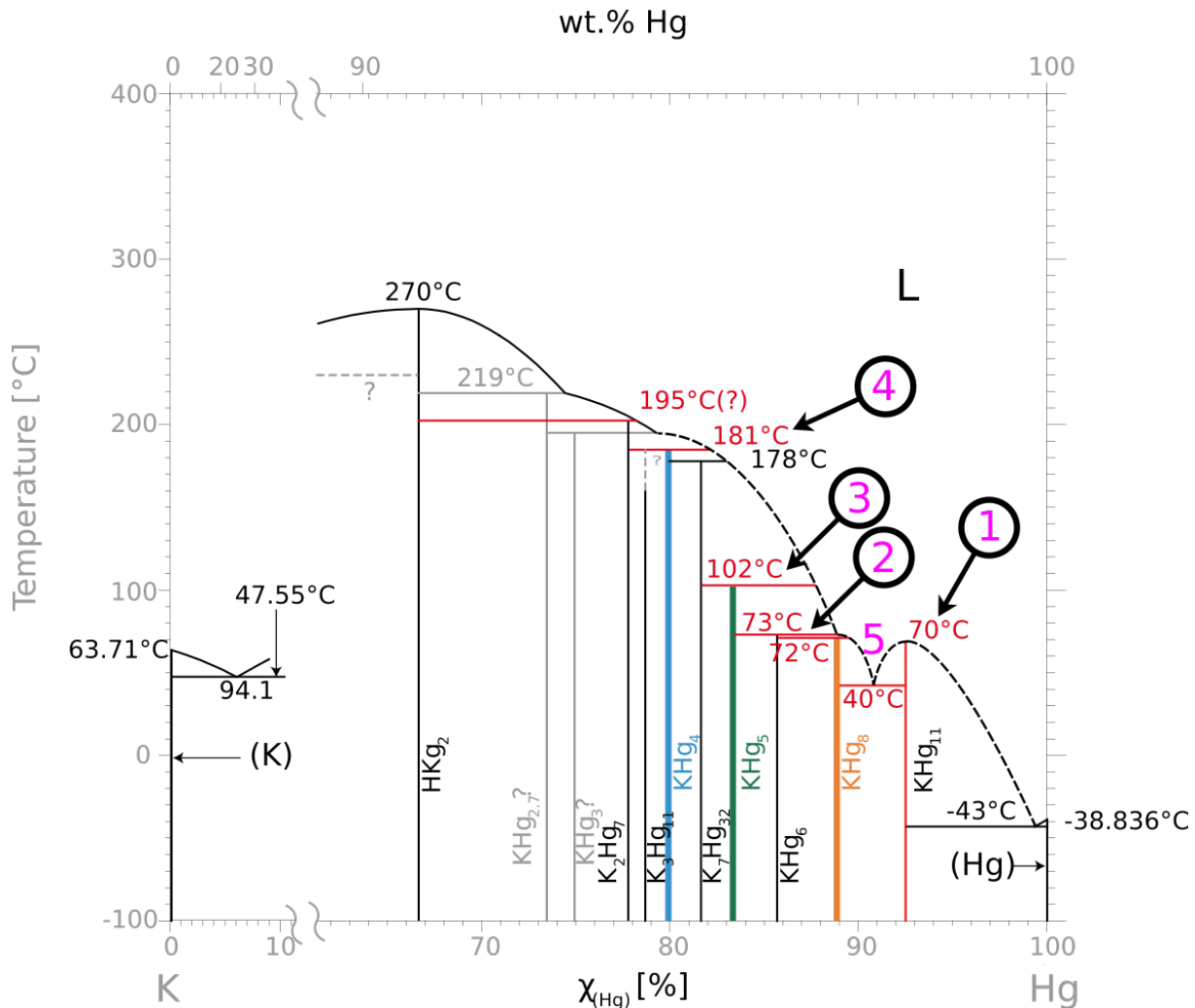


Fig. 4.41: The Hg-rich part of the revised K–Hg phase diagram. Red: reassessed data, grey: not reproducible, blue: KHg₄, green: KHg₅, orange: KHg₈. 1: KHg₁₁ (cf. Fig. 4.42 and 4.43), 2: KHg₈ (cf. Fig. 4.44 and 4.45), 3: KHg₅ (cf. Fig. 4.46), 4: KHg₄ (cf. Fig. 4.47). Number 5 is the eutectic, which can also be seen in Fig. 4.42.

For the investigation of the newly found binaries in relation to the K–Hg phase diagram (see above), numerous samples have been analysed via Differential Scanning Calorimetry (DSC). For this purpose, about 30–80 mg of the sample were transferred in either tantalum ($\vartheta \geq 250^\circ\text{C}$) or stainless steel crucibles ($\vartheta \leq 250^\circ\text{C}$). The former were welded shut using the arc-welding technique, while the latter were sealed using a dedicated press. The samples were heated under constant (20 mL min^{-1}) Ar flow with heating/cooling rates of 5 K min^{-1} . Since the exact constitution of the phases might change during one heating/cooling cycle, the measurements consisted of four cycles. Before and after the DSC measurements, the constituting phases were identified with X-ray powder diffraction (where possible). Data are being provided in Fig. 4.42–4.46.

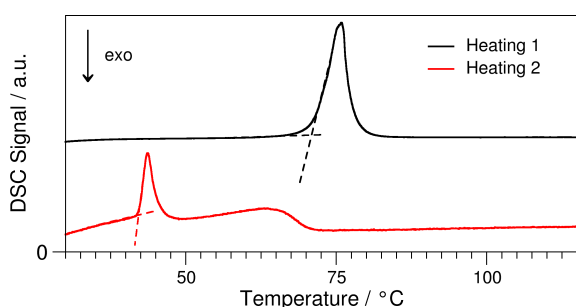


Fig. 4.42: DSC measurement of a sample consisting of KHg_{11} with data from the first (black) and second heating cycle (red). The endothermic signal in the second cycle belongs to the eutectic between KHg_8 and KHg_{11} .

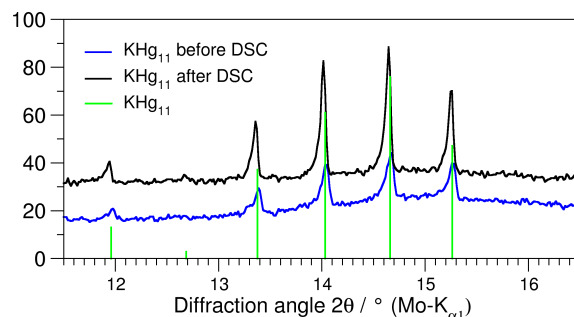


Fig. 4.43: Powder diffractogram of KHg_{11} ^[10] (green) before (black) and after (blue) DSC measurements.

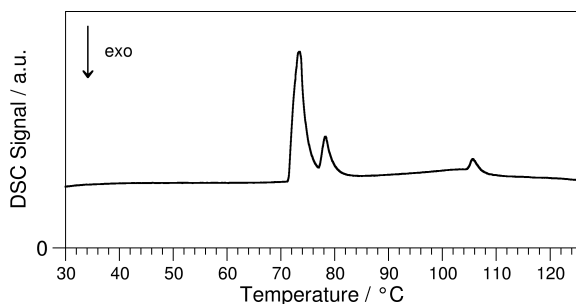


Fig. 4.44: DSC measurement of a sample consisting majorly of KHg_8 .

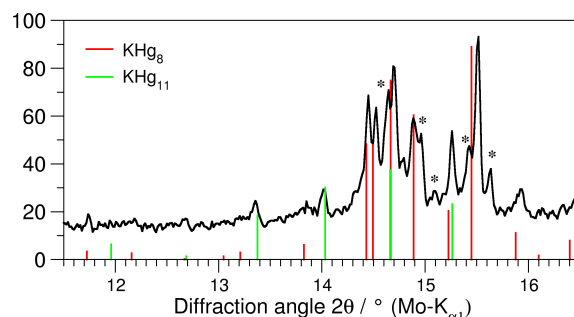


Fig. 4.45: Powder diffractogram from Exp. TH124-4 (black) before the DSC measurement. Red: KHg_8 , green: KHg_{11} ^[10] Reflection intensities marked with an * cannot be assigned to known binaries.

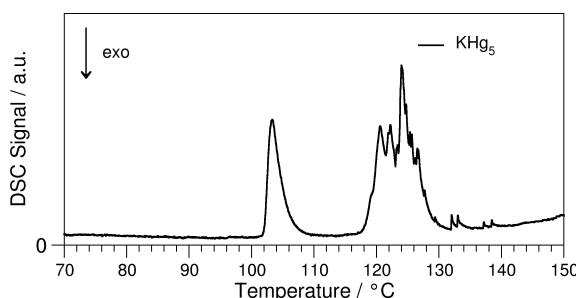


Fig. 4.46: DSC measurement of a sample consisting of KHg_5 .

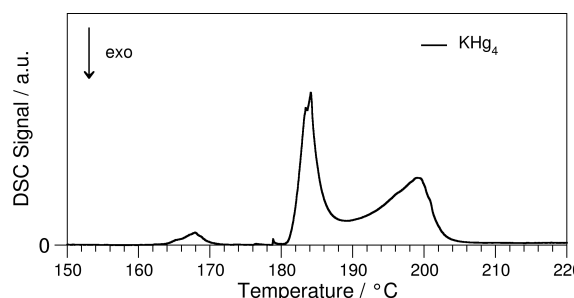


Fig. 4.47: DSC measurement of a sample consisting of KHg_4 .

Table 4.27: Standardised fractional atomic coordinates,^[22] occupancy factors, site symmetry and isotropic displacement parameters [\AA^2] for KHg_8 . U_{eq} is defined as 1/3 of the trace of the orthogonalised U_{ij} tensor. Standard deviations in units of the last digit are given in parentheses. The additional

Atom	Wyckoff Letter	Site Symmetry	x	y	z	U_{equiv}
KHg_4						
K1	4c	$m2m$	0.0000	0.3386(7)	0.2500	0.0187(11)
Hg1	8g	$..m$	0.34561(6)	0.21041(9)	0.2500	0.0198(4)
Hg2	8e	2..	0.15937(7)	0.0000	0.0000	0.0199(4)
KHg_5						
K1	4e	1	0.3762(14)	0.2500(9)	0.0632(16)	0.017(3)
K2	4e	1	0.8758(13)	0.3668(9)	0.0637(15)	0.015(3)
K3	4e	1	0.1526(15)	0.6268(8)	0.4548(17)	0.017(3)
Hg1	4e	1	0.0221(2)	0.25099(16)	0.3861(3)	0.0177(5)
Hg2	4e	1	0.7378(2)	0.25008(16)	0.2435(3)	0.0163(5)
Hg3	4e	1	0.5972(3)	0.23289(18)	0.4230(3)	0.0205(6)
Hg4	4e	1	0.3583(3)	0.03108(17)	0.0391(3)	0.0215(6)
Hg5	4e	1	0.3618(3)	0.47859(17)	0.0674(3)	0.0191(6)
Hg6	4e	1	0.1004(3)	0.09319(16)	0.4225(3)	0.0174(6)
Hg7	4e	1	0.0911(3)	0.41093(16)	0.4242(3)	0.0186(6)
Hg8	4e	1	0.6280(3)	0.09437(17)	0.2023(3)	0.0184(6)
Hg9	4e	1	0.6271(3)	0.40675(17)	0.1710(3)	0.0208(6)
Hg10	4e	1	0.1359(3)	0.50207(16)	0.1924(3)	0.0192(6)
Hg11	4e	1	0.1451(3)	0.00586(16)	0.1985(3)	0.0194(6)
Hg12	4e	1	0.4198(3)	0.10182(17)	0.3348(3)	0.0234(6)
Hg13	4e	1	0.4912(3)	0.38924(17)	0.3671(3)	0.0224(6)
Hg14	4e	1	0.1699(3)	0.18379(17)	0.2100(3)	0.0212(6)
Hg15	4e	1	0.2174(3)	0.34337(17)	0.2347(3)	0.0222(6)
KHg_8						
K1	1e	$\bar{1}$	$\frac{1}{2}$	$\frac{1}{2}$	0	0.033(3)
K2	2i	1	0.2324(12)	0.7228(11)	0.3738(7)	0.035(2)
Hg1	2i	1	0.0114(3)	0.4460(3)	0.1397(2)	0.0741(8)
Hg2	2i	1	0.0372(3)	0.0294(3)	0.24827(18)	0.0554(6)
Hg3	2i	1	0.0748(6)	0.7430(4)	0.0867(2)	0.0960(10)
Hg4	2i	1	0.1046(3)	0.6686(3)	0.63559(15)	0.0513(5)
Hg5	2i	1	0.2040(3)	0.0673(2)	0.55914(17)	0.0513(5)
Hg6	2i	1	0.2215(3)	0.1167(3)	0.03718(18)	0.0575(6)
Hg7	2i	1	0.2878(4)	0.3571(5)	0.7410(2)	0.1000(12)
Hg8	2i	1	0.2924(3)	0.3977(2)	0.50584(18)	0.0522(5)
Hg9	2i	1	0.3778(5)	0.3667(3)	0.2521(2)	0.0816(8)
Hg10	2i	1	0.4782(3)	0.1129(2)	0.36674(17)	0.0508(5)
Hg11	2i	1	0.4831(6)	0.1297(3)	0.8368(3)	0.1060(12)
Hg12	2i	1	0.6852(3)	0.1756(3)	0.12221(19)	0.0592(6)

Table 4.28: Coefficients of the anisotropic displacement parameters [\AA^2] for KHg_8 . U_{ij} is defined as $U_{ij} = \exp(-2\pi^2[U_{11}(ha^*)^2 + \dots + 2U_{21}hka^*b^*])$. Standard deviations in units of the last digit are given in parentheses.

Atom	U_{11}	U_{22}	U_{33}	U_{23}	U_{13}	U_{12}
KHg_4						
K1	0.025(2)	0.013(3)	0.018(3)	0.000	0.000	0.000
Hg1	0.0199(5)	0.0181(6)	0.0215(5)	0.000	0.000	0.0003(2)
Hg2	0.0238(5)	0.0182(6)	0.0178(5)	-0.0001(2)	0.000	0.000

continued on the next page

Atom	U_{11}	U_{22}	U_{33}	U_{23}	U_{13}	U_{12}
KHg₅						
K1	0.013(6)	0.022(7)	0.018(7)	-0.007(6)	0.009(5)	0.004(6)
K2	0.006(6)	0.027(8)	0.008(6)	0.004(6)	0.000(5)	0.005(5)
K3B	0.023(7)	0.005(6)	0.027(8)	-0.009(5)	0.015(6)	-0.001(5)
Hg1	0.0135(11)	0.0188(12)	0.0219(13)	0.0036(10)	0.0089(10)	0.0018(10)
Hg2	0.0134(11)	0.0207(12)	0.0170(12)	0.0002(10)	0.0089(9)	0.0000(10)
Hg3	0.0132(12)	0.0331(16)	0.0172(12)	0.0006(11)	0.0085(10)	-0.0007(11)
Hg4	0.0137(12)	0.0222(14)	0.0260(14)	0.0012(11)	0.0066(11)	-0.0011(10)
Hg5	0.0120(12)	0.0245(14)	0.0225(13)	-0.0053(11)	0.0094(10)	0.0012(10)
Hg6	0.0155(12)	0.0200(13)	0.0201(12)	0.0007(10)	0.0113(10)	0.0029(10)
Hg7	0.0194(13)	0.0206(13)	0.0194(13)	-0.0029(10)	0.0120(11)	-0.0025(10)
Hg8	0.0138(12)	0.0228(13)	0.0206(13)	-0.0014(10)	0.0096(10)	-0.0030(10)
Hg9	0.0143(12)	0.0231(14)	0.0247(14)	0.0021(11)	0.0085(11)	-0.0003(10)
Hg10	0.0216(13)	0.0165(12)	0.0215(13)	-0.0002(10)	0.0115(11)	-0.0009(10)
Hg11	0.0228(13)	0.0198(13)	0.0196(13)	0.0015(10)	0.0131(11)	0.0028(11)
Hg12	0.0319(16)	0.0174(13)	0.0282(15)	-0.0018(11)	0.0198(13)	-0.0014(11)
Hg13	0.0213(14)	0.0222(14)	0.0268(14)	-0.0024(11)	0.0134(12)	-0.0022(11)
Hg14	0.0205(13)	0.0244(14)	0.0215(13)	-0.0036(11)	0.0117(11)	-0.0101(11)
Hg15	0.0213(13)	0.0227(14)	0.0244(14)	0.0039(11)	0.0119(11)	0.0066(11)
KHg₈						
K1	0.033(6)	0.030(7)	0.036(7)	-0.005(5)	-0.001(5)	0.011(5)
K2	0.030(4)	0.043(5)	0.033(5)	0.005(4)	0.007(3)	0.014(4)
Hg1	0.0555(12)	0.0919(19)	0.0613(14)	-0.0110(13)	0.0135(9)	-0.0093(11)
Hg2	0.0566(11)	0.0525(13)	0.0582(13)	0.0084(10)	0.0042(9)	0.0125(9)
Hg3	0.141(3)	0.107(2)	0.0563(15)	0.0095(15)	0.0084(15)	0.075(2)
Hg4	0.0525(10)	0.0614(13)	0.0386(10)	0.0052(9)	0.0062(8)	0.0072(8)
Hg5	0.0446(9)	0.0479(12)	0.0575(12)	-0.0068(9)	0.0030(8)	0.0121(8)
Hg6	0.0676(12)	0.0525(13)	0.0547(12)	0.0094(10)	0.0099(9)	0.0152(9)
Hg7	0.0436(10)	0.194(3)	0.0492(13)	-0.0382(16)	-0.0050(9)	0.0397(14)
Hg8	0.0494(10)	0.0548(13)	0.0572(12)	0.0200(9)	0.0046(8)	0.0116(8)
Hg9	0.144(2)	0.0657(17)	0.0540(13)	0.0234(12)	0.0353(14)	0.0600(15)
Hg10	0.0607(11)	0.0424(11)	0.0500(11)	0.0090(9)	0.0001(8)	0.0088(8)
Hg11	0.180(3)	0.0488(15)	0.0775(18)	-0.0027(13)	0.0677(19)	-0.0170(16)
Hg12	0.0681(13)	0.0460(12)	0.0633(14)	0.0082(10)	0.0071(10)	0.0081(9)

Table 4.29: Selected interatomic distances (and their frequencies) and their labels in KHg_s in Å. All standard deviations are given in parentheses in units of the last digit.

Atom 1	Atom 2	Distance	Atom 1	Atom 2	Distance
KHg₄					
K1	Hg1	3.428(2) (2×)	Hg1	Hg1	2.8947(15)
	Hg1	3.556(5) (2×)		Hg2	3.0010(10) (2×)
	Hg1	3.5636(12) (4×)		Hg2	3.0052(10) (2×)
	Hg2	3.686(5) (4×)		Hg1	3.7567(12)
	Hg2	3.846(2) (4×)		Hg1	3.7567(11)
					Hg2
			Hg2	3.2282(10) (2×)	
KHg₅					
K1	Hg3	3.441(15)	Hg2	Hg8	2.965(4)
	Hg3	3.453(14)		Hg3	2.969(4)
	Hg15	3.457(15)		Hg3	2.972(4)
	Hg15	3.470(14)	Hg3	Hg9	2.986(4)
	Hg14	3.532(15)		Hg12	2.937(4)
	Hg14	3.534(16)		Hg13	2.957(4)
	Hg1	3.633(14)	Hg4	Hg9	3.450(4)
	Hg12	3.691(17)		Hg8	3.459(4)
	Hg12	3.696(17)		Hg7	2.931(4)
	Hg2	3.711(14)		Hg13	2.940(4)
	Hg13	3.721(15)		Hg8	2.997(4)

continued on the next page

Atom 1	Atom 2	Distance	Atom 1	Atom 2	Distance	
K2	Hg8	3.766(15)		Hg12	3.068(4)	
	Hg13	3.773(14)		Hg13	3.142(4)	
	Hg9	3.777(16)		Hg8	3.383(4)	
	Hg4	3.857(16)		Hg10	3.383(4)	
	Hg6	3.951(15)		Hg11	3.537(4)	
	Hg5	4.025(16)		Hg15	3.576(4)	
	Hg7	4.069(16)		Hg9	3.647(4)	
	Hg3	3.354(15)		Hg4	3.847(6)	
	Hg10	3.463(15)		Hg5	3.993(4)	
	Hg7	3.506(14)	Hg5	Hg6	2.967(4)	
	Hg15	3.529(14)		Hg9	3.016(4)	
	Hg11	3.548(15)		Hg8	3.091(4)	
	Hg6	3.555(15)		Hg12	3.105(4)	
	Hg9	3.566(14)		Hg12	3.120(4)	
	Hg10	3.575(15)		Hg13	3.180(4)	
	Hg2	3.578(15)		Hg9	3.227(4)	
	Hg8	3.596(14)		Hg10	3.400(4)	
	Hg2	3.598(15)		Hg11	3.499(4)	
	Hg1	3.607(14)		Hg15	3.735(4)	
	K3	Hg1	3.637(15)	Hg6	Hg10	2.906(4)
Hg5		3.654(15)		Hg11	3.004(4)	
Hg5		3.989(16)		Hg15	3.088(4)	
Hg10		3.421(14)		Hg14	3.091(4)	
Hg14		3.457(16)		Hg10	3.116(4)	
Hg11		3.459(16)	Hg7	Hg11	2.944(4)	
Hg4		3.493(15)		Hg11	2.992(4)	
Hg2		3.527(14)		Hg10	3.107(4)	
Hg3		3.561(15)		Hg14	3.144(4)	
Hg2		3.574(16)		Hg15	3.144(4)	
Hg9		3.588(17)	Hg8	Hg10	2.919(4)	
Hg7		3.601(15)		Hg13	3.102(4)	
Hg8		3.601(15)		Hg12	3.245(4)	
Hg13		3.666(16)		Hg13	3.810(4)	
Hg6		3.712(16)	Hg9	Hg11	2.920(4)	
Hg11		3.722(15)		Hg13	3.076(4)	
Hg1	3.781(14)		Hg12	3.210(4)		
Hg1	3.850(16)		Hg12	3.469(4)		
Hg1	Hg7	3.849(14)	Hg10	Hg15	2.914(4)	
	Hg6	2.889(4)		Hg10	3.792(6)	
	Hg7	2.901(4)		Hg11	3.866(4)	
	Hg2	2.916(4)	Hg11	Hg14	3.139(4)	
	Hg14	3.204(4)		Hg12	3.285(4)	
	Hg14	3.217(4)		Hg15	2.923(4)	
	Hg15	3.641(4)	Hg14	Hg15	2.848(4)	
	Hg15	3.671(4)				
	KHg₈					
	K1	Hg8	3.476(2) (2×)	Hg3	Hg4	2.969(3)
Hg9		3.595(2) (2×)		Hg7	3.045(3)	
Hg11		3.602(3) (2×)		Hg4	3.105(3)	
Hg12		3.640(2) (2×)		Hg9	3.237(3)	
Hg5		3.732(2) (2×)		Hg6	3.310(3)	
Hg10		3.767(3) (2×)		Hg12	3.379(3)	
Hg9		3.768(3) (2×)	Hg4	Hg4	2.992(4)	
Hg6		3.818(2) (2×)		Hg8	3.053(3)	
Hg10		3.977(4) (2×)		Hg12	3.238(3)	
K2		Hg8	3.481(7)		Hg7	3.241(3)
	Hg8	3.501(8)	Hg5	Hg10	2.950(3)	
	Hg3	3.515(8)		Hg6	3.032(3)	
	Hg11	3.567(8)		Hg11	3.061(3)	
	Hg12	3.569(9)		Hg6	3.174(3)	
	Hg1	3.592(8)		Hg5	3.256(4)	
	Hg1	3.596(8)		Hg12	3.263(3)	
	Hg7	3.632(9)		Hg9	3.484(3)	
	Hg9	3.646(8)	Hg6	Hg9	2.918(3)	
	Hg4	3.646(9)		Hg11	2.922(3)	
	Hg7	3.690(8)		Hg12	3.097(3)	
	Hg4	3.701(7)		Hg10	3.206(4)	
	Hg2	3.729(9)		Hg7	3.478(3)	
	Hg4	3.760(8)	Hg7	Hg12	3.021(3)	
	Hg1	3.778(7)		Hg11	3.129(3)	

continued on the next page

Atom 1	Atom 2	Distance	Atom 1	Atom 2	Distance
Hg1	Hg10	3.780(8)	Hg8	Hg11	2.932(5)
	Hg3	3.814(9)		Hg12	3.000(5)
	Hg1	2.938(3)		Hg9	3.030(3)
	Hg7	2.973(3)		Hg10	3.320(4)
	Hg7	3.063(3)		Hg9	Hg10
Hg2	3.075(3)	Hg12	2.916(4)		
Hg4	3.121(3)	Hg10	3.073(3)		
Hg2	Hg8	3.152(3)	Hg10	Hg11	2.931(5)
	Hg10	3.055(3)			
	Hg7	3.061(3)			
	Hg5	3.104(3)			
	Hg3	3.125(3)			
	Hg6	3.244(3)			
	Hg12	3.440(4)			
	Hg11	3.452(4)			

References

- [1] M. Wendorff, C. Röhr, Alkaline-earth tri-mercurides $A^{II}Hg_3$ ($A^{II} = Ca, Sr, Ba$): Binary intermetallic compounds with a common and a new structure type, *Z. Kristallogr.* **2018**, *233*, 515–529, DOI: [10.1515/zkri-2018-2054](https://doi.org/10.1515/zkri-2018-2054).
- [2] V. J. Emery, S. A. Kivelson, Superconductivity in Bad Metals, *Phys. Rev. Lett.* **1995**, *74*, 3253–3256, DOI: [10.1103/PhysRevLett.74.3253](https://doi.org/10.1103/PhysRevLett.74.3253).
- [3] A. F. Gebard, S. B. Arnason, Bad-metal behavior: exotic physics or a consequence of microstructure?, *J. Supercond.* **1995**, *74*, 3253–3256, DOI: [10.1023/A:1007714813001](https://doi.org/10.1023/A:1007714813001).
- [4] F. Tambornino, C. Hoch, Bad metal behaviour in the new Hg-rich amalgam KHg_6 with polar metallic bonding, *J. Alloys Compd.* **2015**, *618*, 299–304, DOI: [10.1016/j.jallcom.2014.08.173](https://doi.org/10.1016/j.jallcom.2014.08.173).
- [5] M. Wendorff, C. Röhr, The new barium mercuride $BaHg_6$ and ternary indium and gallium derivatives, *J. Alloys Compd.* **2013**, *546*, 320–328, DOI: [10.1016/j.jallcom.2012.07.101](https://doi.org/10.1016/j.jallcom.2012.07.101).
- [6] A. V. Tkachuk, A. Mar, In search of the elusive amalgam $SrHg_3$: a mercury-rich intermetallic compound with augmented pentagonal prisms, *Dalton Trans.* **2010**, *39*, 7132–7135, DOI: [10.1039/C0DT00304B](https://doi.org/10.1039/C0DT00304B).
- [7] E. J. Duwell, N. C. Baenziger, The crystal structures of KHg and KHg_2 , *Acta Crystallogr.* **1955**, *8*, 705–710, DOI: [10.1107/S0365110X55002168](https://doi.org/10.1107/S0365110X55002168).
- [8] E. Biehl, H.-J. Deiseroth, K_2Hg_7 und Rb_2Hg_7 , zwei Vertreter eines neuen Strukturtyps binärer intermetallischer Verbindungen, *Z. Anorg. Allg. Chem.* **1999**, *625*, 1337–1342, DOI: [10.1002/\(SICI\)1521-3749\(199908\)625:8<1337::AID-ZAAC1337>3.0.CO;2-W](https://doi.org/10.1002/(SICI)1521-3749(199908)625:8<1337::AID-ZAAC1337>3.0.CO;2-W).
- [9] E. Todorov, S. C. Sevov, *J. Solid State Chem.* **2000**, *149*, 419–427, DOI: [10.1006/jssc.1999.8569](https://doi.org/10.1006/jssc.1999.8569).
- [10] E. Biehl, H.-J. Deiseroth, Darstellung, Strukturchemie und Magnetismus der Amalgame MHg_{11} (M: K, Rb, Ba, Sr), *Z. Anorg. Allg. Chem.* **1999**, *625*, 1073–1080, DOI: [10.1002/\(SICI\)1521-3749\(199907\)625:7<1073::AID-ZAAC1073>3.0.CO;2-V](https://doi.org/10.1002/(SICI)1521-3749(199907)625:7<1073::AID-ZAAC1073>3.0.CO;2-V).
- [11] IPDS CONTROL SOFTWARE X-AREA, STOE & Cie. GmbH, Darmstadt, Deutschland, version 1.39, **2006**.
- [12] X-RED, STOE & Cie. GmbH, Darmstadt, Deutschland, version 1.3.1, **2005**.
- [13] X-SHAPE, STOE & Cie. GmbH, Darmstadt, Deutschland, version 2.0.7, **2005**.
- [14] SADABS, Bruker AXS Inc. (Madison, WI, USA), version 2.03, **2018**.
- [15] G. M. Sheldrick, A short history of SHELX, *Acta Crystallogr.* **2008**, *A64*, 112–122, DOI: [10.1107/S0108767307043930](https://doi.org/10.1107/S0108767307043930).
- [16] M. Wendorff, C. Röhr, The new complex barium mercuride $Ba_{20}Hg_{103}$ and its ternary zinc and cadmium variants, *Z. Naturforsch. B.* **2012**, *67*, 893–906, DOI: [10.5560/znb.2012-0186](https://doi.org/10.5560/znb.2012-0186).
- [17] L. Pauling, Atomic Radii and Interatomic Distances in Metals, *J. Am. Chem. Soc.* **1947**, *69*, 542–553, DOI: [10.1021/ja01195a024](https://doi.org/10.1021/ja01195a024).

- [18] J. C. Slater, Atomic Radii in Crystals, *J. Chem. Phys.* **1964**, *41*, DOI: [10.1063/1.1725697](https://doi.org/10.1063/1.1725697).
- [19] P. Blaha, K. Schwarz, F. Tran, R. Laskowski, G. Madsen, L. Marks, WIEN2k: An APW+lo program for calculating the properties of solids, *J. Chem. Phys.* **2020**, *152*, 074101, DOI: [10.1063/1.5143061](https://doi.org/10.1063/1.5143061).
- [20] J. P. Perdew, K. Burke, M. Enzerhof, Generalized Gradient Approximation Made Simple, *Phys. Rev. Lett.* **1996**, *77*, 3865–3868, DOI: [10.1103/PhysRevLett.77.3865](https://doi.org/10.1103/PhysRevLett.77.3865).
- [21] R. F. W. Bader, A quantum theory of molecular structure and its applications, *Chem. Rev.* **1991**, *91*, 893–928, DOI: [10.1021/cr00005a013](https://doi.org/10.1021/cr00005a013).
- [22] L. M. Gelato, E. Parthé, Structure Tidy – a computer program to standardize crystal structure data, *J. Appl. Crystallogr.* **1987**, *20*, 139–143, DOI: [10.1107/S0021889887086965](https://doi.org/10.1107/S0021889887086965).

4.5 SrHg_{5.86} – a new binary Sr amalgam

Unpublished results

4.5.1 Introduction

In the phase diagram of Sr–Hg, five types of Hg-rich amalgams with a Hg:Sr ratio ≥ 2 can be found (cf. Fig. 4.48, right): SrHg₂^[3] (CeCu₂ structure type), SrHg₃^[4] (Ni₃Sn type), Sr_{14-x}Hg_{51+x}^[3,5,6] (Gd₁₄Ag₅₁ structure family), SrHg₈^[2] (unique) and SrHg₁₁^[7] (BaHg₁₁ type). The existence of SrHg₁₃ and Sr₂Hg₉ is questionable, they have not been encountered so far. It stands to reason that additional phases in the Hg-rich region around SrHg_{~6} region have previously been overlooked, since the heavier homologue Ba also has a representative of the composition BaHg₆.^[8]

4.5.2 Experimental

In an attempt to synthesise a ternary Na–Sr amalgam, 10.2 mg (0.444 mmol) Na, 38.7 mg (0.442 mmol) Sr and 1.9529 g (9.82 mmol) Hg were filled into a Ta crucible and closed via arc-welding. With 50 K h⁻¹, the reaction mixture was heated to 200 °C, kept at this temperature for 24 h and then cooled to RT with 5 K h⁻¹.

Analysis: Via pXRD, only Na₁₁Hg₅₂ could be identified (see Fig. 7.114, p. 172).

Due to the systematic non-linear shift of all Bragg signals in the diffraction pattern and the rather unusual shape of the obtained silver metallic crystals (needles and trigonal platelets), single crystal diffraction experiments on an IPDS 1 diffractometer equipped with Ag-K α ($\lambda = 0.56087 \text{ \AA}$) were performed. Multiple orientation measurements of the trigonal-shaped crystals yielded the hexagonal metrics of the binary sodium amalgam Na₁₁Hg₅₂. This is rather surprising, since it was observed in all previous experiments that specimens of this amalgam appear to have a hexagonal, rod-like habitus.

Consequently, the needle-shaped crystals were investigated with care. Orientation measurements yielded an orthorhombic metric with $a = 13.521$, $b = 5.007$ and $c = 10.389 \text{ \AA}$. Comparison to known binary amalgams of Ca, Na and Sr yielded no accordance, hence a full measurement of the single crystal was performed. Final data collection was performed on a one-circle diffractometer system (IPDS 1, Stoe & Cie, Darmstadt, Germany, image plate detector, graphite monochromator, Ag-K α radiation) in φ scan geometry with $\Delta\varphi = 1.4^\circ$ and $0 \leq \varphi \leq 219.8^\circ$ and subsequently corrected for Lorentz-, polarisation and absorption effects.^[9–11] The systematic absences for $0kl : k + l = 2n$ and $hk0 : h = 2n$ indicated two possible space groups for the refinement: $Pna2_1$ and $Pnma$. Wilson statistics were inconclusive, which is why the latter space group was used for the structure solution and final refinement. For the absorption correction, the crystal shape originating from the indexed faces was optimised on the basis of the intensity distribution,^[11] and numerical absorption correction was performed.^[10] All details on the results of the data collection, structure solution and refinement are listed in Table 4.30 (right), while fractional atomic coordinates and isotropic displacement parameters are compiled in Table 4.31.

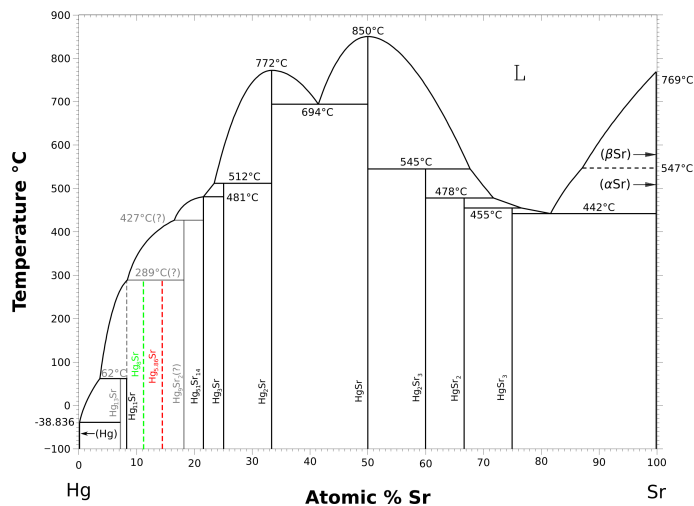


Fig. 4.48: Adapted^[1] phase diagram of the system Sr–Hg. SrHg₈^[2] (green) as well as the new SrHg_{5.86} (red) have been included. Unconfirmed data are coloured in gray.

Anisotropic displacement parameters are shown in Table 4.32, and selected interatomic distances in Table 4.33.

Table 4.30: Crystallographic data and details on single crystal data collection, structure solution and refinement for SrHg_{5.86}. Data collection was performed at room temperature. All standard deviations are given in parentheses in units of the last digit.

Composition	SrHg _{5.86}	No. of indep. refl. ($I \geq 2\sigma(I)$)	442
Crystal system	orthorhombic	R_{int}	0.1694
Space group	$Pnma$, No. 62	R_{σ}	0.0764
Lattice parameters a, b, c [Å]	13.5123(11), 5.007(2), 10.389(4)	$F(000)$	2072
V [Å ³]	702.9(5)	Corrections	Lorentz, Polarisation, Absorption (multi-scan) [12]
Z	4	Structure solution	direct methods [13]
Density (X-ray) [g · cm ⁻³]	12.202	Structure refinement	full-matrix least-squares on F^2 [13]
Diffractometer	STOE IPDS 1	No. of L.S. parameters	44
	AgK α radiation, $\lambda = 0.56087$ Å	GooF	0.875
Absorption coeff. μ [mm ⁻¹]	75.434	R values ($I \geq 2\sigma(I)$)	$R1 = 0.0361$, $wR2 = 0.0654$
ϑ range [°]	1.95–19.99	R values (all data)	$R1 = 0.1672$, $wR2 = 0.0734$
Index range	$-16 \leq h \leq 16$, $-6 \leq k \leq 6$, $-12 \leq l \leq 12$	Res. $\rho(e^-)$ min/max [e ⁻ Å ⁻³]	-2.320 / +2.676
No. of collected refl.	5409	Extinction coefficient	0.000010(2)
No. of independent refl.	656		

4.5.3 Results

Crystal Structure

SrHg_{5.86} crystallises isotypic to BaHg₆^[8] and KHg₆^[14] in the orthorhombic crystal system (space group $Pnma$, No. 62, $a = 13.5123(11)$, $b = 5.007(2)$, $c = 10.389(4)$ Å). Its crystal structure consists of only one atomic position for Sr, and six for Hg. One Hg position (Hg2) is not fully occupied, a structural exception when compared to the known $M\text{Hg}_6$ ($M = \text{K}, \text{Ba}$) compounds. The structure can be built by stacking layers of Hg nets consisting of five- and eight-membered rings with the Schläfli notation $(5^2.8)_2(5.8^2)$ (see Fig. 4.49, right). Within these layers, strong covalent bonds Hg–Hg bonds (2.837–3.132 Å, range I) can be found, while the Hg–Hg bonds between adjacent layers are slightly longer (2.917–3.375 Å, range II) and therefore weaker (cf. Table 4.33).

The eight-membered rings are centered by Sr, and the nets are stacked along [010] in an ... ABA ... sequence. In these nets, one type of distorted octagon (dark blue) is present, which is in turn capped above and below by a pentagon (light blue), resulting in a 5 : 8 : 5 coordination sphere (CN = 18). The second - highly distorted - pentagon (red) is not part of the coordination sphere, but occupies the gaps of the non space-filling packing of the SrHg_{18-x} polyhedron (blue). These gaps can be filled by stacking of face-sharing Hg₆ octahedra in an interpenetrating cluster-like fashion. The clusters share a high similarity with the ones encountered in Cs₁₁O₃, without the central atom O inside the octahedra. However, one small gap in the crystal structure remains, and can be filled with Hg₄ tetrahedra (green). Its faces are not apparent in the nets, but can be seen as a direct consequence of the 2₁ screw axis in this space group. A detailed view of the relation of the nets to the structure is shown in Fig. 4.50 (below), while the different polyhedra with their respective bond types and constituting atoms are highlighted in Fig. 4.51.

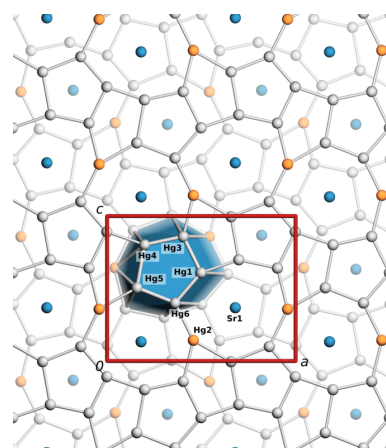


Fig. 4.49: Formation of the SrHg_{18-x} polyhedra (blue) as a result of the stacking of the nets parallel to the ac plane, projection along [010]. Sr: blue, Hg1–5: grey, Hg6: orange, unit cell: red. The nets lie at $y = \frac{1}{4}$ and $y = \frac{3}{4}$, respectively.

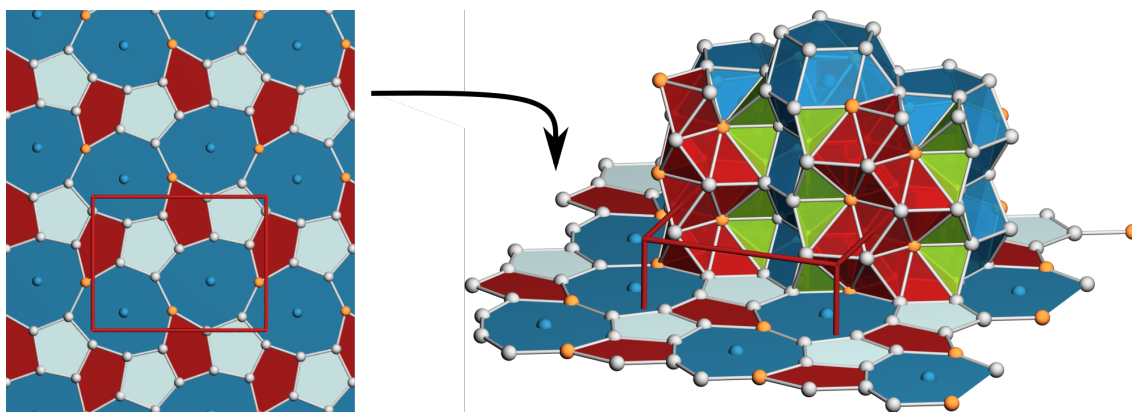


Fig. 4.50: **Left:** net representation of $\text{SrHg}_{5.86}$, with the projection along $[010]$. SrHg_8 octagons are coloured in dark blue, Hg_5 pentagons belonging to the coordination sphere light blue, space-filling Hg_5 pentagons in red. **Right:** SrHg_{18} polyhedra: dark blue, Hg_6 octahedra: red, Hg_4 tetrahedra: green. In both pictures, Sr atoms are coloured in blue, $\text{Hg}_1/\text{Hg}_3\text{--Hg}_6$ in grey, Hg_2 in orange and the unit cell in red.

So far, the coordination pattern 5:8:5 has been encountered in other binary amalgams as well: KHg_4 , KHg_5 , KHg_6 , KHg_8 , BaHg_6 and SrHg_8 .^[2,8,14,15] Analogous to the findings in the KHg_{4-8} range, the voids (red) in these nets increase with rising Hg content, yielding an increasing structural complexity. However, none of these known amalgams exhibit any sign of underoccupation of the Hg positions.

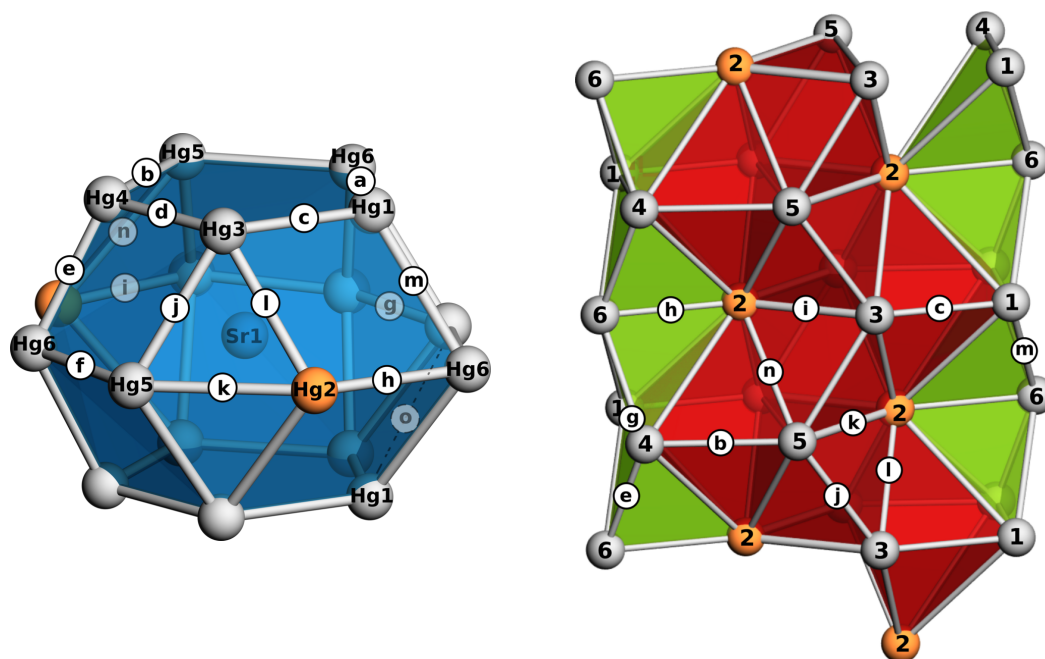


Fig. 4.51: **Left:** 5:8:5 coordination polyhedron around Sr in $\text{SrHg}_{5.86}$. **Right:** space-filling Hg polyhedra in $\text{SrHg}_{5.86}$. Red: Hg_6 octahedra, green: Hg_4 tetrahedra. In both pictures, labeling of atoms and bonds is analogous to Fig. 4.49 and 4.50, as well as Table 4.33.

Calculations of the electronic structure

Electronic structure calculations were performed with the Wien2K program package,^[16] applying the full-potential linear augmented plane wave (FP-LAPW) method. The exchange and correlation contribution was described by the functional of Perdew, Burke and Enzerhof (PBE) with a generalised gradient approximation (GGA).^[17] Muffin-tin radii were set to 132.3 pm (2.5 a.u.), while the number of basis functions was determined by the value of $R_{\text{mt}} \cdot K_{\text{max}} = 8$ with K_{max} being the largest k vector. The separation energy was set to -6 Ry. 816 k points in the Brillouin zone (108 thereof in the irreducible Brillouin zone) were calculated via a $6 \times 17 \times 8$ Monkhorst-Pack grid. Cutoff energies used were $E_{\text{max}}^{\text{pot}} = 190$ eV (potential) and $E_{\text{max}}^{\text{wf}} = 218$ eV (interstitial PW). Charge distribution for the individual atoms was calculated via analysis of the electron density map by calculation of heights and positions of the bond critical points (saddle points).^[18] Further details and selected results of the calculations are compiled in Table 4.34. It is crucial to note that since the Wien2K program package does not allow for under- or mixed occupancy, the calculations were performed for the fully ordered model with the nominal sum formula SrHg_6 .

The overall electronic behaviour is similar to other Hg-rich amalgams; between -9 and -6 eV, pronounced s - and p -state mixing of Hg occurs. This can be observed in the crystal structure by the formation of extensive Hg networks. The contributions of Sr to this network are relatively weak, and originate mostly from p -states. Since the electron transfer from Sr to Hg is incomplete (as seen in the Bader charge analysis), the s -states still contribute at the Fermi level.

4.5.4 Discussion

A small, but significant detail seems to stand out: when the data calculated for the fully ordered model are compared to the data known for the isotypic compound BaHg_6 , the Bader charge of Sr is 8 % higher than Ba (+1.41 vs. +1.30^[8]). This stands in contrast to their respective electronegativities: Sr has a slightly higher electronegativity than Ba ($\chi_{\text{Sr}} = 0.95$ vs. $\chi_{\text{Ba}} = 0.89$ ^[19]), which would then indicate a lower, or at least the same, partial charge. This might be the reason why the atomic position of Hg2 exhibits a slightly lower occupancy; it is the Hg position with the highest Hg coordination number (details of the Hg coordination polyhedra have already been extensively studied for BaHg_6 ^[8]), i.e. the ‘most metallic’ position. This is being supported by the fact that this crystallographic site is also the one where a substitution of Hg takes place the ternary $\text{BaHg}_{6-x}\text{M}_x$ ($M = \text{In}, \text{Ga}$).^[8] A comparison of electronic structure calculations comparing the fully ordered model to the obtained model from single crystal data would be ideal, but is not within the scope of this work.

From a crystallographic point of view, $\text{SrHg}_{5.86}$ is a useful link in the overall behaviour of the structural relation: if the nets are considered, the coordination polyhedron around Sr is being enlarged to a certain upper limit (which seems to be an octagon), after which surplus Hg fills the remaining space with increasingly complex polyhedra combinations. Fig. 4.53 (below) visualises this trend.

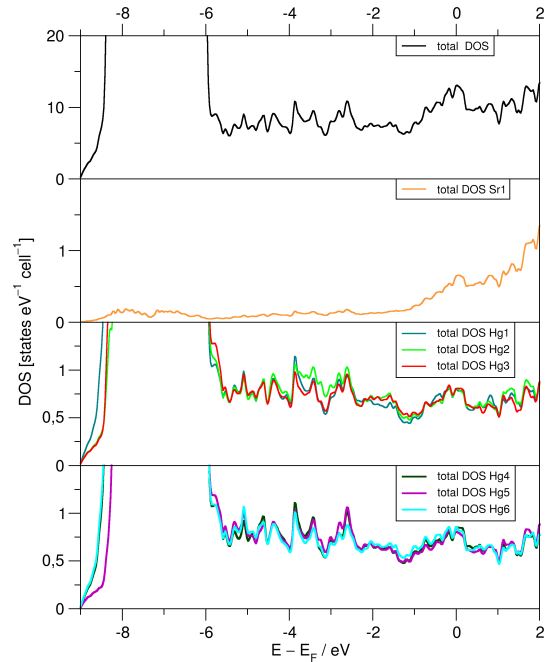


Fig. 4.52: Calculated total density of states (tDOS) together with the partial states (pDOS) of SrHg_6 in the range from -9 to 2 eV relative to E_F .

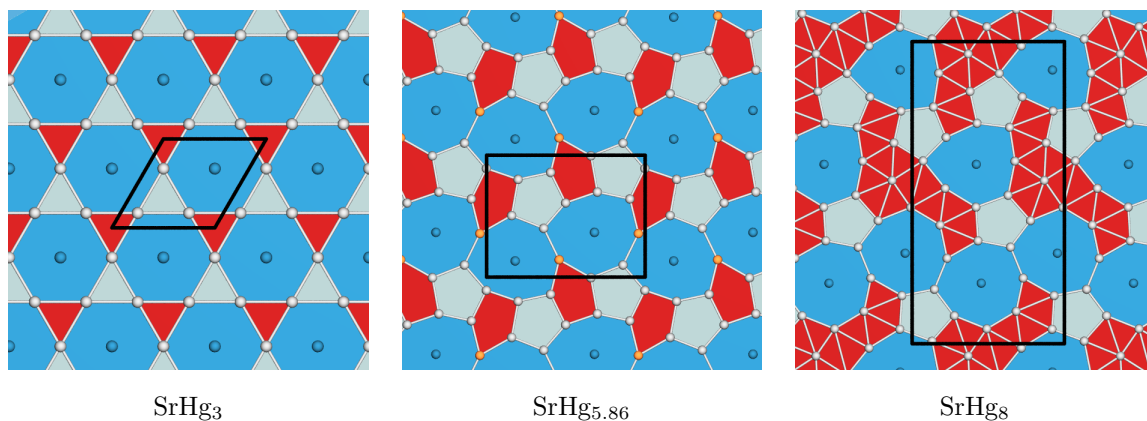


Fig. 4.53: Net representation of selected binary Sr amalgams with increasing Hg content. Unit cell: black, Sr atoms: blue (underoccupied Hg2 in SrHg_{5.86}: orange), Hg atoms: grey. Planes of the coordination polyhedra around are depicted in blue, while residual space filled by the Hg network is coloured in red.

4.5.5 Conclusion

SrHg_{5.86} is a promising new system for the investigation of polar metal behaviour via Hg-rich amalgams, neatly complementing the binary phase diagram. So far, the crystal data and the electronic structure is in high accordance to other literature known examples within the same structure family - BaHg₆ and KHg₆.^[8,14] Unfortunately, specimens of this compound have only been found in one synthesis, all other thermochemical synthesis attempts have been unfruitful. Suggestions for future synthetic attempts are being discussed in Chapter 6.

Table 4.31: Standardised fractional atomic coordinates,^[20] occupancy factors, site symmetry and isotropic displacement parameters [\AA^2] for SrHg_{5.86}. U_{eq} is defined as 1/3 of the trace of the orthogonalised U_{ij} tensor. Standard deviations in units of the last digit are given in parentheses.

Atom	Occupancy factor	Wyckoff Letter	Site Symmetry	x	y	z	U_{equiv}
Sr1	1	4c	.m.	0.3199(2)	$\frac{1}{4}$	0.6326(3)	0.0232(6)
Hg1	1	4c	.m.	0.00177(11)	$\frac{1}{4}$	0.10884(14)	0.0330(4)
Hg2	0.863(10)	4c	.m.	0.04259(14)	$\frac{1}{4}$	0.64250(18)	0.0385(8)
Hg3	1	4c	.m.	0.09638(14)	$\frac{1}{4}$	0.35887(16)	0.0446(4)
Hg4	1	4c	.m.	0.30172(12)	$\frac{1}{4}$	0.27815(16)	0.0386(4)
Hg5	1	4c	.m.	0.34238(12)	$\frac{1}{4}$	0.00495(19)	0.0442(4)
Hg6	1	4c	.m.	0.63977(13)	$\frac{1}{4}$	0.59953(15)	0.0370(4)

Table 4.32: Coefficients of the anisotropic displacement tensor [\AA^2] for SrHg_{5.86}. U_{ij} is defined as $U_{ij} = \exp - 2\pi^2 [U_{11}(ha^*)^2 + \dots + 2U_{21}hka^*b^*]$. All standard deviations are given in parentheses in units of the last digit.

Atom	U_{11}	U_{22}	U_{33}	U_{23}	U_{13}	U_{12}
Sr1	0.0268(16)	0.0167(14)	0.0260(14)	0	0.0052(10)	0
Hg1	0.0200(7)	0.0316(9)	0.0474(8)	0	-0.0004(6)	0
Hg2	0.0361(12)	0.0452(15)	0.0343(11)	0	-0.0044(7)	0
Hg3	0.0589(12)	0.0353(10)	0.0397(9)	0	0.0072(8)	0
Hg4	0.0452(9)	0.0234(9)	0.0471(9)	0	-0.0218(7)	0
Hg5	0.0406(8)	0.0365(11)	0.0554(10)	0	0.0143(7)	0
Hg6	0.0599(11)	0.0218(9)	0.0292(8)	0	-0.0050(6)	0

Table 4.33: Selected interatomic distances (and their frequencies) and their labels in SrHg_{5.86} in Å. All standard deviations are given in parentheses in units of the last digit. The Hg–Hg bond labels are the same as in Fig. 4.51, while the range indicates the position of the bond (I: within net parallel to the *ac* plane, II: bond connecting the nets).

Atom 1	Atom 2	Distance	Atom 1	Atom 2	Distance	label	range	
Sr1	Hg4	3.355(2) (2×)	Hg1	Hg6	2.857(2)	a	I	
	Hg1	3.483(2) (2×)		Hg3	2.895(3)	c	I	
	Hg1	3.511(3)		Hg4	2.947(2)	g	I	
	Hg6	3.518(3) (2×)		Hg6	3.1519(18) (2×)	m	II	
	Hg5	3.583(3) (2×)		Hg1	3.374(2) (2×)	o	II	
	Hg3	3.616(3) (2×)		Hg2	Hg6	2.984(3)	h	I
	Hg4	3.690(4)			Hg3	3.035(3)	i	I
	Hg6	3.697(4)			Hg5	3.109(3)	k	I
	Hg2	3.749(4)			Hg3	3.130(2) (2×)	l	II
	Hg2	3.809(4)			Hg5	3.275(2) (2×)	n	I
	Hg5	3.880(4)			Hg3	Hg4	2.898(3)	d
	Hg3	4.149(4)		Hg5		3.0422(18) (2×)	j	II
Hg6	4.335(4)	Hg4	Hg5	2.891(3)		b	I	
			Hg6	2.9168(15) (2×)	e	II		
			Hg5	2.945(3)	f	I		

Table 4.34: Details of the electronic structure calculations of the fully ordered SrHg₆.

		label	dist. [Å]	ρ_{BCP} e[-10^{-6}Å^{-3}]
Crystal data	Table 4.30	a	2.857	0.3025
R _{mt} (all atoms)	132.3 pm (2.5 a.u.)	b	2.892	0.2856
R _{mt} ·K _{max}	8.0	c	2.896	0.2831
k-points / BZ	816	d	2.898	0.2788
k-points / IBZ	108	e	2.917	0.2709
Monkhorst-Pack-Grid	6×17×8	f	2.946	0.2585
DOS plot	Fig. 4.52	g	2.947	0.2554
Bader charges	Sr	h	2.985	0.2380
	Hg1	i	3.035	0.2178
	Hg2	j	3.042	0.2152
	Hg3	k	3.110	0.1927
	Hg4	l	3.130	0.1837
	Hg5	m	3.154	0.1817
	Hg6			

References

- [1] T. B. Massalski, H. Okamoto, P. R. Subramanian, L. K. (Hrsg.), *Binary Alloy Phase Diagrams*, 2nd ed., ASM International, Materials Park (OH), USA, **1990**.
- [2] A. V. Tkachuk, A. Mar, In search of the elusive amalgam SrHg₈: a mercury-rich intermetallic compound with augmented pentagonal prisms, *Dalton Trans.* **2010**, 39, 7132–7135, DOI: [10.1039/C0DT00304B](https://doi.org/10.1039/C0DT00304B).
- [3] G. Bruzzone, F. Merlo, The Strontium-Mercury System, *J. Less-Common Met.* **1974**, 35, 153–157, DOI: [10.1016/0022-5088\(74\)90154-4](https://doi.org/10.1016/0022-5088(74)90154-4).
- [4] M. Wendorff, C. Röhr, Alkaline-earth tri-mercurides A^{II}Hg₃ (A^{II} = Ca, Sr, Ba): Binary intermetallic compounds with a common and a new structure type, *Z. Kristallogr.* **2018**, 233, 515–529, DOI: [10.1515/zkri-2018-2054](https://doi.org/10.1515/zkri-2018-2054).
- [5] A. V. Tkachuk, A. Mar, Alkaline-Earth Metal Mercury Intermetallics, A_{11-x}Hg_{54+x} (A = Ca, Sr), *Inorg. Chem.* **2008**, 47, 1313–1318, DOI: [10.1021/ic7015148](https://doi.org/10.1021/ic7015148).
- [6] M. Wendorff, C. Röhr, New giant (pseudo)hexagonal structures of intermetallic compounds Sr(Cd/Hg/Zn)_{~5}, *Z. Kristallogr. Suppl.* **2016**, 36, 80, DOI: [10.1515/9783110476620](https://doi.org/10.1515/9783110476620).

- [7] E. Biehl, H.-J. Deiseroth, Darstellung, Strukturchemie und Magnetismus der Amalgame MHg₁₁ (M: K, Rb, Ba, Sr), *Z. Anorg. Allg. Chem.* **1999**, *625*, 1073–1080, DOI: [10.1002/\(SICI\)1521-3749\(199907\)625:7<1073::AID-ZAAC1073>3.0.CO;2-V](https://doi.org/10.1002/(SICI)1521-3749(199907)625:7<1073::AID-ZAAC1073>3.0.CO;2-V).
- [8] M. Wendorff, C. Röhr, The new barium mercuride BaHg₆ and ternary indium and gallium derivatives, *J. Alloys Compd.* **2013**, *546*, 320–328, DOI: [10.1016/j.jallcom.2012.07.101](https://doi.org/10.1016/j.jallcom.2012.07.101).
- [9] IPDS CONTROL SOFTWARE X-AREA, STOE & Cie. GmbH, Darmstadt, Deutschland, version 1.39, **2006**.
- [10] X-RED, STOE & Cie. GmbH, Darmstadt, Deutschland, version 1.3.1, **2005**.
- [11] X-SHAPE, STOE & Cie. GmbH, Darmstadt, Deutschland, version 2.0.7, **2005**.
- [12] SADABS, Bruker AXS Inc. (Madison, WI, USA), version 2.03, **2018**.
- [13] G. M. Sheldrick, A short history of SHELX, *Acta Crystallogr.* **2008**, *A64*, 112–122, DOI: [10.1107/S0108767307043930](https://doi.org/10.1107/S0108767307043930).
- [14] F. Tambornino, C. Hoch, Bad metal behaviour in the new Hg-rich amalgam KHg₆ with polar metallic bonding, *J. Alloys Compd.* **2015**, *618*, 299–304, DOI: [10.1016/j.jallcom.2014.08.173](https://doi.org/10.1016/j.jallcom.2014.08.173).
- [15] T. Hohl, C. Hoch, M. Wendorff, C. Röhr, manuscript in preparation.
- [16] P. Blaha, K. Schwarz, F. Tran, R. Laskowski, G. Madsen, L. Marks, WIEN2k: An APW+lo program for calculating the properties of solids, *J. Chem. Phys.* **2020**, *152*, 074101, DOI: [10.1063/1.5143061](https://doi.org/10.1063/1.5143061).
- [17] J. P. Perdew, K. Burke, M. Enzerhof, Generalized Gradient Approximation Made Simple, *Phys. Rev. Lett.* **1996**, *77*, 3865–3868, DOI: [10.1103/PhysRevLett.77.3865](https://doi.org/10.1103/PhysRevLett.77.3865).
- [18] R. F. W. Bader, A quantum theory of molecular structure and its applications, *Chem. Rev.* **1991**, *91*, 893–928, DOI: [10.1021/cr00005a013](https://doi.org/10.1021/cr00005a013).
- [19] A. L. Allred, Electronegativity values from thermochemical data, *J. Inorg. Nucl. Chem.* **1961**, *17*, 215–221, DOI: [10.1016/0022-1902\(61\)80142-5](https://doi.org/10.1016/0022-1902(61)80142-5).
- [20] E. Parthé, L. M. Gelato, The standardization of inorganic crystal-structure data, *Acta Crystallogr.* **1984**, *A40*, 169–183, DOI: [10.1107/S0108767384000416](https://doi.org/10.1107/S0108767384000416).

4.6 Cyclic Voltammetry as a Tool for the targeted Synthesis of Ternary Amalgams via Electrocrystallisation

Unpublished results

For the synthesis of Hg-rich amalgams, the electrocrystallisation of metal iodides in DMF has proven to be a valuable and facile preparative tool.^[1–4] By modulation of the temperature with respect to the corresponding phase diagram, the desired compounds can be obtained in a multigram scale, while also avoiding the need for common solid-state techniques (i.e. arc-welding in metal ampoules) and unwanted byproducts.

So far, however, this experimental approach has only been successfully employed for the targeted synthesis of binary amalgams. First experiments indicate that ternary amalgams can be synthesised as well.^[3] The electrocrystallisation of a 50:50 (Vol.) electrolyte comprised of saturated NaI/KI solutions in DMF yielded a compound containing Na as well as K. The complete crystal structure is not solved in all aspects (main structural features have been determined), and the synthetic approach was rather difficult to reproduce.

For the targeted synthesis of ternary amalgams, the preparative method contains a main obstacle: the simultaneous deposition of two different metals from solution. Walther Nernst first discovered and formulated the relationship between electrode potential and concentration of an electrolyte:^[5]

$$E = E^0 + \frac{RT}{z_e F} \ln \left(\frac{a_{ox}}{a_{red}} \right) \quad (4.1)$$

From this equation, it becomes clear that the defining parameter for the reduction potential is the concentration of the ion. If two different ions are considered, a simultaneous reduction takes place when their respective reduction potentials are equal. Consequently, this can be achieved by modulating the concentration. But since (standard) reduction potentials for metals have so far been determined mostly for standard conditions, their investigation in respect to their application in the aforementioned synthetic approach is necessary.

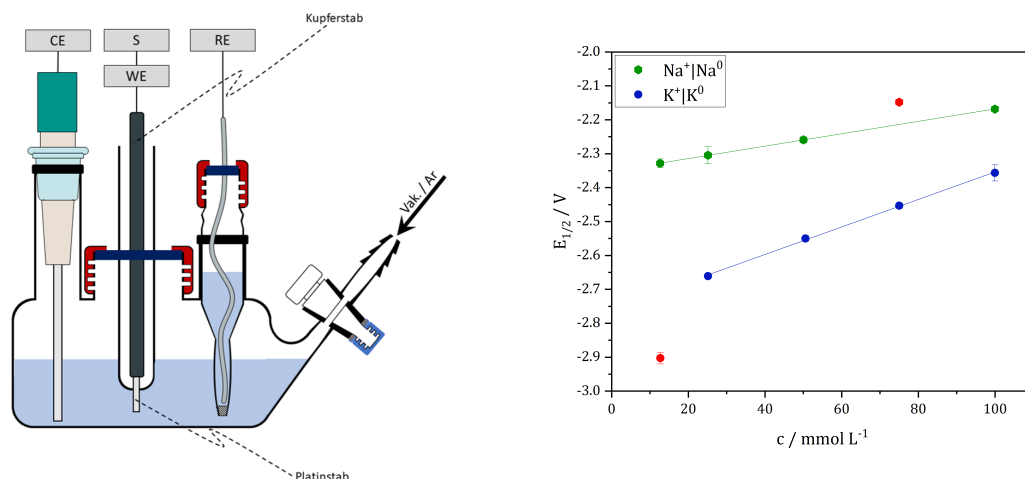


Fig. 4.54: **Left:** Custom-built Schlenk apparatus for CV measurements. RE = reference electrode, WE = working electrode, CE = counter electrode, S = sense. **Right:** obtained concentration- dependent halfwave potentials for the reduction of Na^+ (green) and K^+ (blue) including their fits. Red values were omitted for further calculations.

For this purpose, cyclic voltammetry (CV) is the tool of choice, since it enables the concentration-dependent determination of oxidation/reduction potentials of ions present in the electrolyte. A custom-built apparatus (see Fig. 4.54, left) has been made to ensure inert-gas conditions. In

this apparatus, platinum electrodes serve as working (WE) and counter electrodes (CE), while a silver wire serves as a pseudo-reference electrode. As an internal reference, ferrocene was added to the electrolyte solution, while a constant electrical conductivity was ensured by using $[\text{NBu}_4]\text{ClO}_4$ as supporting electrolyte.

Using a potentiostat, multiple measurements with varying scan rates were performed for concentrations between 13 mM and 100 mM. The determined correlation between concentration and reduction potential is visualised in Fig. 4.54 (right). From the obtained values, a reasonable ion concentration comparable to the overall ion concentration in the CV measurements was devised, and the concentrations of NaI:KI were then calculated to 115 mM:112 mM (the respective halfway potential $E_{1/2} = -1.92$ V). The electrosynthesis was then performed with the apparatus described in Ch. 3.4.2, while the potentiostat provided the electrochemical potential. Over 24 h, the potential was gradually increased from -1.2 V to -2.5 V in 60 min intervals. Details on all CV measurements as well as the electrosynthesis can be obtained from the F-Bericht of R. Hübsch.

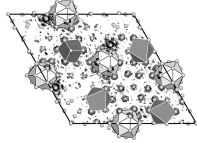
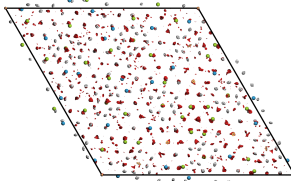
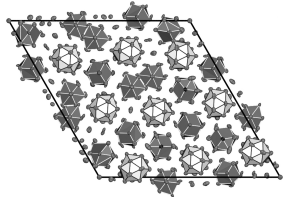
The obtained crystalline solid was then investigated using pXRD. It became clear that while the overall metric of the diffraction pattern shows a close resemblance to the one of $\text{Na}_{11}\text{Hg}_{52}$, intensities at lower diffraction angles can not be accounted for by the model (see Fig. 7.115, p. 172). After multiple attempts to obtain single crystal diffraction data, the crystal quality was deemed insufficient. The sample was then diluted with a minimal amount of elemental Hg, heated to 60°C (for 1 min) and stored for about six months. Investigation with a microscope showed that needle-shaped specimens with a length of several millimeters have grown (see Fig. 4.55, right). Several subsequent attempts for the refinement of the crystal structure have been made, employing different X-ray sources (Ag vs. Mo-K_α -radiation) and low-temperature measurements. But so far, all obtained data sets were insufficient. However, a preliminary model could be derived from one specimen. Details on structure determination and refinement can be seen in Table 4.36. As indicated by the R -values as well as the residual electron density, the model is still incomplete. What can be determined, however, is the fact that the metric is the one of $\text{Na}_{11}\text{Hg}_{52}$ and that a variety of permutations of disorder (i.e. Na/K, Na/Hg mixed occupancy as well as underoccupancy of K) is present. The metric is different from the results of the previous results of F. Tambornino, where the a and b axes are only two thirds of the corresponding axes of $\text{Na}_{11}\text{Hg}_{52}$.^[6]

So far, the refined model contains 99 positions for Hg, 7 for Na (3 thereof underoccupied), 11 for K (one thereof underoccupied), 3 with mixed occupancy by Na/Hg and 1 with mixed occupancy of K/Na. In contrast, $\text{Na}_{11}\text{Hg}_{52}$ contains 101 positions for Hg, 30 for Na and one with mixed occupancy of Na/Hg. A comprehensive overview comparing the main structural features and the preliminary results is given in Table 4.35 (below).



Fig. 4.55: Obtained crystals from THR003 after Ostwald ripening.

Table 4.35: Comparison of the obtained crystal structure (middle) with the known binary amalgam $\text{Na}_{11}\text{Hg}_{52}$ ^[2] (right) as well as data from the dataset obtained by F. Tambornino^[6] (left). All unit cells are projections along c .

			
nominal sum formula	$\text{Na}_{11-x}\text{K}_x\text{Hg}_{52}$ ^[6]	$\text{Na}_{2.5}\text{K}_{3.9}\text{Hg}_{52}$	$\text{Na}_{11}\text{Hg}_{52}$ ^[2]
crystal system, space gr.		hexagonal, $P\bar{6}$ (No. 174), all structures	
a [Å]	26.13	39.74	39.70
c [Å]	9.60	9.73	9.68
superstructure	$2 \times 2 \times 1$	$3 \times 3 \times 1$	$3 \times 3 \times 1$
atomic positions (total)	50 ($Z = 2$)	123	132
Hg	46	99	101
Hg/Na (mixed occ.)	n.a.	3	1
Na	n.a.	7	30
Na/K (mixed occ.)	n.a.	1	—
K	n.a.	11(+1)	—
K (underocc.)	n.a.	1	—

A first comparison of the obtained crystal data to the powder diffractogram (see Fig. 4.56, right) shows that while the preliminary model is not yet complete, it points in the right direction, since reflection data at low angles are being described significantly better than by the $\text{Na}_{11}\text{Hg}_{52}$ model. The results clearly show that the principal method of CV is a valuable and accessible tool for the successful synthesis of ternary amalgams via electrocrystallisation. Furthermore, the indicators for two different structures that are related to the $\text{Gd}_{14}\text{Ag}_{51}$ structure family give an impression for the vast and often underestimated potential of this synthetic route.

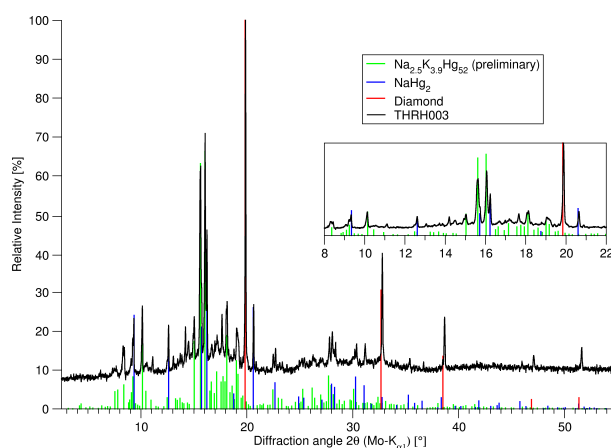


Fig. 4.56: Powder diffractogram of THR003 (black) in comparison to the preliminary model generated from the crystal data (green). Diamond^[7] (red) is used for optical dilution of the sample, while NaHg_2 ^[8] (blue) is still present as a byproduct.

Table 4.36: Crystallographic data and details on single crystal data collection, structure solution and refinement for the preliminary model of $\text{Na}_{2.5}\text{K}_{3.9}\text{Hg}_{52}$. Data collection was performed at room temperature. All standard deviations are given in parentheses in units of the last digit.

Composition	$\text{Na}_{2.5}\text{K}_{3.9}\text{Hg}_{52}$	R_{int}	0.4565
Crystal system	hexagonal	R_σ	0.1966
Space group	$P\bar{6}$, No. 174	$F(000)$	38929
Lattice parameters a, c [Å]	39.736(11), 9.728(3)	Corrections	Lorentz, Polarisation, Absorption (multi-scan) [9]
V [Å ³]	13302(7)	Structure solution	direct methods [10]
Z	1	Structure refinement	full-matrix least-squares on F^2 [10]
Density (X-ray) [$\text{g} \cdot \text{cm}^{-3}$]	12.103	No. of L.S. parameters	838
Diffractometer	Bruker D8 Quest	Goof	1.126
	MoK α radiation, $\lambda = 0.71073$ Å	R values ($I \geq 2\sigma(I)$)	$R1 = 0.1245$, $wR1 = 0.3048$
Absorption coeff. μ [mm^{-1}]	134.834	R values (all data)	$R1 = 0.1672$, $wR2 = 0.3407$
ϑ range [°]	2.05 – 24.00		
Index range	$-45 \leq h, k \leq 45$, $-11 \leq l \leq 11$		

continued on the next page

No. of collected refl.	261375	Res. $\rho(e^-)$ min/max [$e^- \text{Å}^{-3}$]	-6.832 / +12.957
No. of independent refl.	14857	Extinction coefficient	0.000010(2)
No. of indep. refl. ($I \geq 2\sigma(I)$)	10493		

References

- [1] F. Tambornino, J. Sappl, F. Pultar, T. M. Cong, S. Hübner, T. Giftthaler, C. Hoch, ElectrocrySTALLIZATION - a synthetic method for intermetallic phases with polar metal-metal bonding, *Inorg. Chem.* **2016**, *55*, 11551–11559, DOI: [10.1021/acs.inorgchem.6b02068](https://doi.org/10.1021/acs.inorgchem.6b02068).
- [2] C. Hoch, A. Simon, Na₁₁Hg₅₂: Complexity in a Polar Metal, *Angew. Chem. Int. Ed.* **2012**, *51*, 3262–3265, DOI: [10.1002/anie.201108064](https://doi.org/10.1002/anie.201108064).
- [3] F. Tambornino, C. Hoch, Bad metal behaviour in the new Hg-rich amalgam KHg₆ with polar metallic bonding, *J. Alloys Compd.* **2015**, *618*, 299–304, DOI: [10.1016/j.jallcom.2014.08.173](https://doi.org/10.1016/j.jallcom.2014.08.173).
- [4] C. Hoch, A. Simon, Cs₂Hg₂₇, das quecksilberreichste Amalgam – ein naher Verwandter der Bergman-Phasen, *Z. Anorg. Allg. Chem.* **2008**, *634*, 853–856, DOI: [10.1002/zaac.200700535](https://doi.org/10.1002/zaac.200700535).
- [5] W. Nernst, Die elektromotorische Wirksamkeit der Ionen, *Z. Phys. Chem.* **1889**, *4U*, 129–181, DOI: [10.1515/zpch-1889-0412](https://doi.org/10.1515/zpch-1889-0412).
- [6] F. Tambornino, C. Hoch, The simplest representative of a complex series: the Hg-rich amalgam Yb₁₁Hg₅₄, *Z. Kristallogr.* **2017**, *232*, 557–565, DOI: [10.1515/zkri-2016-2036](https://doi.org/10.1515/zkri-2016-2036).
- [7] W. H. Bragg, W. L. Bragg, The structure of the diamond, *Proc. Royal Soc. London* **1913**, *89*, 277–291, DOI: [10.1098/rspa.1913.0084](https://doi.org/10.1098/rspa.1913.0084).
- [8] J. W. Nielsen, N. C. Baenziger, The Crystal Structures of NaHg₂, NaHg and Na₃Hg₂, *Acta Crystallogr.* **1954**, *7*, 277–282, DOI: [10.1107/S0365110X54000783](https://doi.org/10.1107/S0365110X54000783).
- [9] SADABS, Bruker AXS Inc. (Madison, WI, USA), version 2.03, **2018**.
- [10] G. M. Sheldrick, A short history of SHELX, *Acta Crystallogr.* **2008**, *A64*, 112–122, DOI: [10.1107/S0108767307043930](https://doi.org/10.1107/S0108767307043930).

4.7 The first Be-containing Amalgam?

Unpublished results

So far, no Be amalgam has been successfully synthesised. The conventional solid state synthesis is not an option: applying Tamman's rule of thumb (two thirds of the melting temperatures of the higher melting compound; $\vartheta_{\text{melt}}(\text{Be}) = 1287^\circ\text{C}$) would yield a reaction temperature of $\vartheta = 767^\circ\text{C}$. At this temperature, Hg is already evaporated ($\vartheta_{\text{BP}}(\text{Hg}) = 365.7^\circ\text{C}$). If the trivial synthesis of Li and Mg amalgams as well as the existence of other alkali or alkaline earth amalgams are taken into account,^[1,2] a facile route for the synthesis of a Be amalgam should in theory be feasible. The diagonal relationship with Al, which is completely miscible with Hg, would suggest a similar behaviour for Be. Additionally, the existence of Be-Pt (PtBe₅, PtBe₁₂)^[3,4] and Be-Au (AuBe, AuBe₂, AuBe₅ and AuBe₁₂)^[3-6] intermetallics further indicates the potential existence of a Be amalgam.

4.7.1 Preparative attempts towards Be amalgams

High-pressure synthesis from the elements

In order to avoid the evaporation of Hg at temperatures as high as to activate Be metal, both elements were attempted to react at high pressure (4 GPa) and high temperature (800 °C) in a multi-anvil pressure setup. After cooling to room temperature and pressure release, the elements were regained.

Thermal decomposition of precursor complexes

Subsequently, syntheses via thermal composition of suitable precursor complexes were tried. These precursors should combine several characteristics:

- good crystallinity
- thermally decomposable without residue
- complex ligands should be reducing agents (preferably anionic with terminal O or N atoms) to facilitate the reduction of the central metal atom

Promising candidates with these properties are oxalate, ethylenediamine and guanidin.

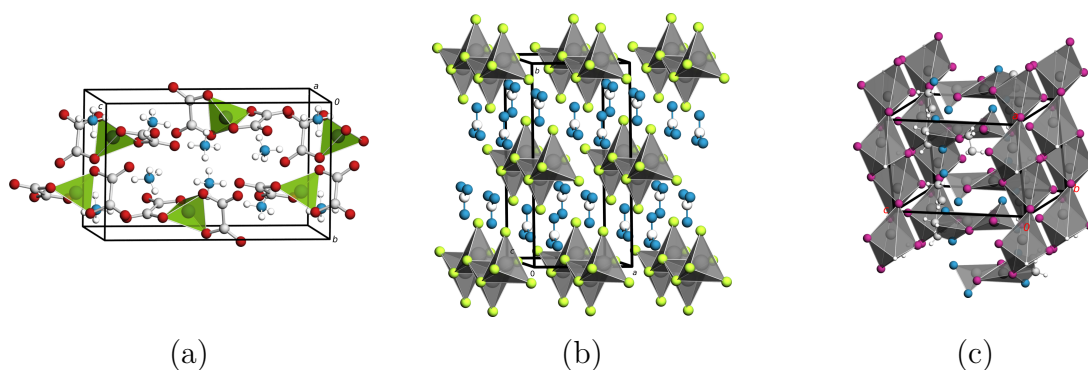


Fig. 4.57: (a) Crystal structure of $[\text{NH}_4]_2[\text{Be}(\text{C}_2\text{O}_4)_2]$. Be: dark green, N: blue, C: light grey, O: red, H: white. The tetrahedral coordination of Be is emphasised in green. (b) Crystal structure of $[(\text{Gdn})][\text{HgCl}_3]$. Hg: grey, Cl: neon green, N: blue, C: light grey. The distorted $[\text{HgCl}_5]$ trigonal bipyramids are connected via edges, resulting in chains along the *c*-axis. (c) Crystal structure of $[(\text{Hg}(\text{en}))_2\text{I}_3][\text{HgI}_3]$. Hg: dark grey, I: violet, N: blue, C: light grey, H: white. The distorted $[\text{HgCl}_5]$ trigonal bipyramids are connected via edges, resulting in chains along the *c*-axis.

While the synthesis of a Be amalgam via precursors was ultimately unsuccessful, several new Hg and Be compounds were isolated and characterised: $(\text{NH}_4)[\text{Be}(\text{C}_2\text{O}_4)_2]$, $[(\text{Hg}(\text{en}))_2\text{I}_3][\text{HgI}_3]$ and $(\text{Gdn})[\text{HgCl}_3]$ (all depicted in Fig. 4.57).

It was observed that thermal treatment of these precursor complexes leads to the formation of elemental Hg and BeO. It seems that this synthetic route will not yield to the formation of a Be amalgam.

Electrocrystallisation from Be-containing solutions

Following the procedure of dissolving the metal iodide in DMF and electrolysing this solution with a Hg cathode, a successful route for a large number of different amalgams, did not lead to a result here. The reason is a very high overvoltage necessary for the deposition for Be from a DMF solvate complex present in solution, higher than the decomposition voltage of the solvent. Be^{2+} forms extremely stable complexes with O-donor ligands, so the solvent DMF had to be changed to a new one which (a) is capable of dissolving Be salts and (b) forms solvates of Be^{2+} which are much less stable than the ones of DMF. Therefore, solvents with N or S as donor atoms were tested, and a number of Be solvate complexes could be prepared and characterised. The results of these experiments is presented in the publication in the next paragraph. However, no Be amalgam could be obtained from the electrolysis of the respective solvate complexes in their solvents, mostly due to the low decomposition voltages of the solvents. The electrocrystallisation of BeI_2 in *N*-methylimidazole (NMIM) and *N,N*-Dimethylthioformamide (Thio-DMF) lead to the formation of Cu_7Hg_6 .^[7]

4.7.2 Synthesis and Crystal Structures of β -[Be(DMF)₄]I₂, [Be(Pyr)₄]I₂, [Be(NMP)₄]I₂ and [BeI₂(Lut)₂]

Timotheus Hohl¹, Torben Sinn¹ and Constantin Hoch^{1,*}

* Correspondence: constantin.hoch@cup.uni-muenchen.de; Tel.: +49-89-2180-77421

¹ Department Chemie, Ludwig-Maximilians-Universität München

published in: *Z. Naturforsch.* **2020**, 75b, 509–516.

DOI: [10.1515/znb-2020-0035](https://doi.org/10.1515/znb-2020-0035)

Reprinted (adapted) with permission from Zeitschrift für Naturforschung. Copyright 2020 De Gruyter.

Abstract

Four solvent complexes of beryllium iodide were prepared by dissolving BeI₂ in N,N-dimethyl formamide (DMF), pyridine (Pyr), *N*-methyl pyrrolidone (NMP) and 2,6-dimethyl pyridine (2,6-lutidine, Lut). Their crystal structures were established from single crystal X-ray diffraction. For [Be(DMF)₄]I₂ a new modification is reported (monoclinic, space group $P2_1/c$, $a = 12.491(2)$, $b = 11.593(2)$, $c = 15.310(3)$ Å, $\beta = 94.7073(6)^\circ$). In [Be(Pyr)₄]I₂ (monoclinic, space group $C2/c$, $a = 17.8799(13)$, $b = 7.6174(5)$, $c = 18.2611(14)$ Å, $\beta = 113.508(4)^\circ$) and [Be(NMP)₄]I₂ (orthorhombic, space group $Pbca$, $a = 13.941(5)$, $b = 15.754(3)$, $c = 24.634(7)$ Å) homoleptic tetrahedral complex cations are formed, while the sterically demanding solvent ligand Lut yields a neutral complex with covalently bound iodine ligands [Be(Lut)₂]I₂ (monoclinic, space group $P2_1/c$, $a = 7.8492(9)$, $b = 24.265(3)$, $c = 27.037(3)$ Å, $\beta = 97.076(3)^\circ$). Their electrochemical stability with respect to their application as beryllium electrolytes for deposition of beryllium from solution is discussed.

Introduction

Amalgams of alkali and earth alkaline metals are exceptionally suited model systems for the investigation of polar metal-metal bonding. Our group has synthesized and characterized various of these amalgams via isothermal electrocrystallisation.^[15–20] Iodides of the less noble metals, dissolved in an aprotic, polar solvent are used for this synthetic approach as electrolyte. Besides several beneficial aspects of the iodides, they serve as good indicators for the reaction progress because of the anodic oxidation of I[−] to I₃[−] which appears brown in polar solvents and therefore enables a simple visual evaluation of the electrochemical reaction. Today, many amalgams with high Coulombic polarity arising from electronegativity differences between mercury as noble metal and alkali, earth alkaline or lanthanoid metals as less noble components, are known.^[21,22] However, one of the most interesting systems, Be–Hg, still remains unknown.^[23] The lack of phases known in the binary system Be–Hg seems to be caused in a simple preparative hindrance: as beryllium affords activation temperatures which are so high that mercury already evaporates before reaction takes place, amalgam

Table 4.37: Comparison of known Be-solvate complexes with (poly-)iodide anions, sorted by their respective interatomic distances. Compounds introduced in this work are highlighted in grey. (Me-Im: *N*-methylimidazole, DIC: diisopropylcarbodiimide, TMU: *N,N*-tetramethylurea)

Compound	ligand atom	$d_{\text{Be-Donor}}$ [Å]	Lit.
[Be(Me-Im) ₄]I ₂	N	1.703(3)	[8]
[Be(Pyr) ₄] ₂ (I ₃) ₂ (I ₄)	N	1.723(8)–1.738(8)	[9]
[Be(Pyr) ₄]I ₂	N	1.734(3)–1.735(3)	
[Be(DIC) ₄](I ₃) ₂	N	1.734(6)	[10]
[BeI ₂ (Lut) ₂]	N	1.77(1)–1.81(1)	
β -[Be(DMF) ₄]I ₂	O	1.57(2)–1.64(2)	
[Be(NMP) ₄]I ₂	O	1.58(1)–1.64(2)	
α -[Be(DMF) ₄]I ₂	O	1.594(8)–1.636(9)	[11]
[BeI ₂ (DMF) ₂]	O	1.601(7)–1.606(7)	[12]
[BeI(DMF) ₃]	O	1.611(4)–1.620(6)	[12]
[Be(TMU) ₄](I ₃) ₂	O	1.625(5)	[13]
[BeI ₂ (OEt ₂) ₂]	O	1.650(4)–1.657(4)	[14]

temperatures which are so high that mercury already evaporates before reaction takes place, amalgam

formation directly from the elements is not feasible. An electrochemical approach at low temperatures by electrodeposition of beryllium from solution onto a reactive mercury cathode may be a promising alternative route. Initial experiments showed that while BeI_2 easily dissolves in DMF, the $[\text{Be}(\text{DMF})_4]^{2+}$ cation is apparently too stable: the voltage needed for releasing the beryllium at the cathode is higher than the electrochemical stability range of the solvent. For this reason new, relatively labile complexes of BeI_2 , where the ligand also serves as the solvent, have to be found and characterized.

Since beryllium is the least investigated non-radioactive element, data on beryllium coordination compounds are scarce. Additionally, due to preparative restrictions – minor amounts of water present in solvents lead to the violent formation of hydrogen halides from beryllium halides, while beryllium hydroxide precipitates – coordination compounds of beryllium where the solvents also serve as the ligand, have not been investigated thoroughly. The majority of knowledge about beryllium solvate complexes and beryllium complexes with organic ligands has been reviewed by Dehnicke and Neumüller in 2008.^[24] Most interestingly, some compounds prepared from beryllium iodide also contain polyiodide anions, pointing to unidentified oxidation processes (see Table 4.37).

In this work, we present three new beryllium solvate complexes $[\text{Be}(\text{Solv})_4]\text{I}_2$ with *N,N*-dimethyl formamide, pyridine and *N*-methyl pyrrolidone as well as a new $[\text{BeI}_2(\text{Solv})_2]$ complex with 2,6-lutidine. It is interesting to find that the DMF complex was recently crystallized and characterized by Müller and Buchner^[25] in a different structure and after thorough comparison of their crystallographic data with ours we come to the conclusion that this compound forms two different modifications.

Table 4.39: Crystallographic data and selected details on data collection, structure solution and refinement of β - $[\text{Be}(\text{DMF})_4]\text{I}_2$ (**1**), $[\text{Be}(\text{Pyr})_4]\text{I}_2$ (**2**), $[\text{Be}(\text{NMP})_4]\text{I}_2$ (**3**) and $[\text{BeI}_2(\text{Lut})_2]$ (**4**).

	β - $[\text{Be}(\text{DMF})_4]\text{I}_2$	$[\text{Be}(\text{Pyr})_4]\text{I}_2$	$[\text{Be}(\text{NMP})_4]\text{I}_2$	$[\text{BeI}_2(\text{Lut})_2]$
Refined composition	$\text{BeI}_2(\text{NOC}_3\text{H}_7)_4$	$\text{BeI}_2(\text{NC}_5\text{H}_5)_4$	$\text{BeI}_2(\text{NOC}_5\text{H}_9)_4$	$\text{BeI}_2(\text{NC}_7\text{H}_9)_2$
Crystal system	monoclinic	monoclinic	orthorhombic	monoclinic
Space group	$P2_1/c$ (No. 14)	$C2/c$ (No. 15)	$Pbca$ (No. 61)	$P2_1/c$ (No. 14)
<i>a</i> [Å]	12.491(2)	17.8799(13)	13.941(5)	7.8492(9)
<i>b</i> [Å]	11.593(2)	7.6174(5)	15.754(3)	24.265(3)
<i>c</i> [Å]	15.310(3)	18.2611(14)	24.634(7)	27.037(3)
β [°]	94.7073(6)	113.508(4)	90	97.076(3)
Volume [Å ³]	2209.7(7)	2280.7(3)	5410(3)	5110.3(10)
<i>Z</i>	4	4	8	12
Calculated density [g · cm ⁻³]	1.67	1.69	1.62	1.86
Diffractometer	BRUKER D8 Venture, Goebel mirror, rotating anode	BRUKER D8 Quest, graphite-monochromatized	STOE IPDS-I	BRUKER D8 Quest, Goebel mirror, microfocus tube
Radiation type			Mo-K α	
<i>T</i> [K]	109.0(2)	293(2)	293(2)	293(2)
μ [mm ⁻¹]	2.9	2.8	2.4	3.7
Data range ϑ [°]	3.196–27.500	2.995–32.497	2.119–24.998	2.427–24.999
Index range	$-16 \leq h \leq 16$, $-15 \leq k \leq 15$, $-19 \leq l \leq 19$	$-26 \leq h \leq 26$, $-11 \leq k \leq 11$, $-27 \leq l \leq 27$	$-16 \leq h \leq 13$, $-18 \leq k \leq 17$, $-29 \leq l \leq 29$	$-9 \leq h \leq 9$, $-28 \leq k \leq 28$, $-32 \leq l \leq 32$
No. of observed refl.	48049	34309	18470	134227
No. of independent refl.	5058	3994	4757	8997
Thereof with ($I \geq 2\sigma(I)$)	4875	3392	1094	7057
<i>F</i> (000) [e]	1080	1112	2608	2712
Corrections		Polarization, Lorentz, Absorption (numerical) [26, 27]		
Structure solution		direct methods [28]		
Structure refinement		full-matrix least squares on F^2 [28]		
No. of L.S. parameters	217	124	281	515
Goof on F^2	1.090	1.060	0.354	1.080
<i>R1/wR2</i> (for $I \geq 2\sigma(I)$)	0.0176 / 0.0427	0.0346 / 0.0762	0.0263 / 0.0373	0.0457 / 0.0817
<i>R1/wR2</i> (all data)	0.0186 / 0.0432	0.0428 / 0.0795	0.1473 / 0.0428	0.0620 / 0.0855
Res. $\rho(e^-)$ min/max [e ⁻ Å ⁻³]	/-0.70/+1.51	-0.82 / +1.18	-0.22 / +0.31	-1.03 / +0.78
CCDC deposition No.	1983410	1983413	1983411	1983412

Results and Discussion

Details on data collection, crystallographic data, structure solution and refinement are given in Table 4.39. Standardized atomic coordinates^[29] and isotropic displacement parameters can be found in Tables 7.1–7.8 in the Appendix, as well as the anisotropic displacement parameters. Selected interatomic distances and angles can be found in Table 4.40. Projections of the unit cells together with depictions of single complex units are shown in Fig. 4.58.

Table 4.40: Selected interatomic distances [Å] and angles [°] of (1), (2), (3) and (4) as well as the sums of covalent radii ($\Sigma(r_{\text{cov}})$) and ($\Sigma(r_{\text{ionic}})$), respectively.^[30,31] Standard deviations in units of the last digit are given in parentheses.

	$d(\text{Be-O})$	$d(\text{Be-N})$	$d(\text{Be-I})$	$\angle(\text{O-Be-O})$	$\angle(\text{N-Be-N})$	$\angle(\text{I-Be-I})$
1	1.572(2) -1.64(2)	—	—	106.2(9) -113.2(9)	—	—
2	—	1.734(3) -1.735(3)	—	—	103.9(2) -113.33(7)	—
3	1.58(1) -1.64(2)	—	—	103.0(8) 113.1(8)	—	—
4	—	1.77(1) -1.81(1)	2.46(1) -2.522(9)	—	107.1(6) -108.3(5)	2.46(1) -2.522(9)
$\Sigma(r_{\text{cov}})$	1.65	1.73	2.35	—	—	—
$\Sigma(r_{\text{ionic}})$	1.62	1.73	2.47	—	—	—

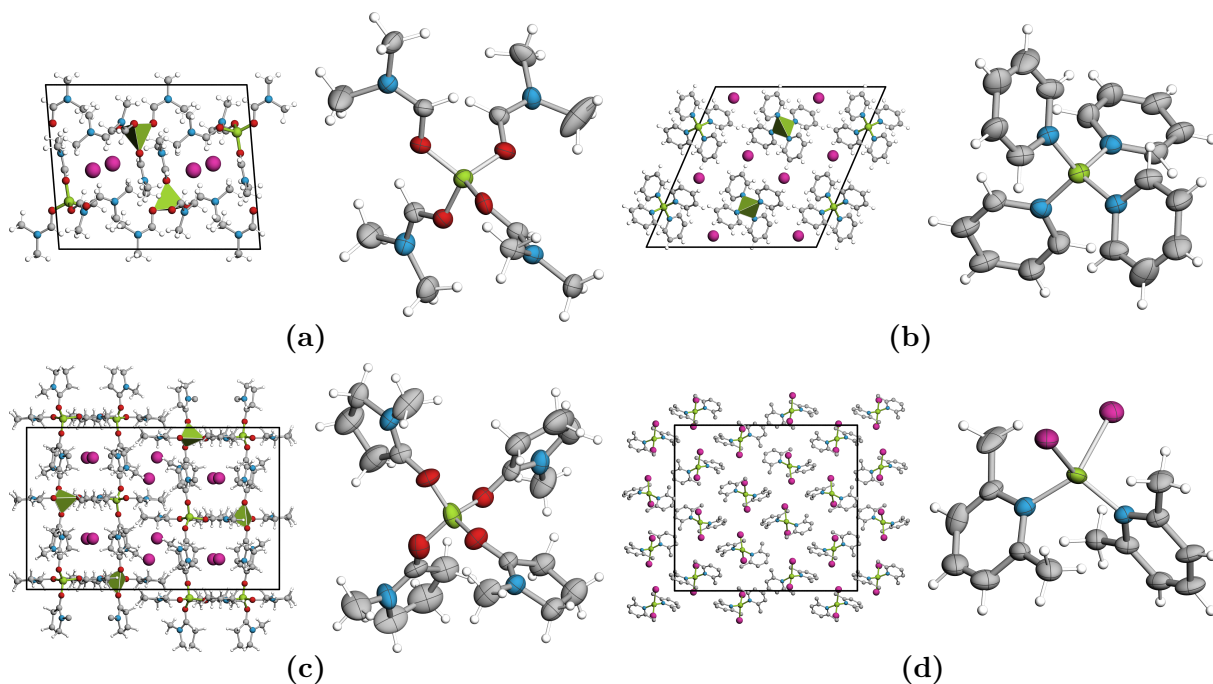


Fig. 4.58: Crystal structures of (a) β -[Be(DMF)₄]I₂, (b) [Be(Pyr)₄]I₂, (c) [Be(NMP)₄]I₂ and (d) [BeI₂(Lut)₂]. For all compounds projections of the unit cells [(a,b): along 010, (c,d): along 100] are given together with one single complex cation or molecule [Be(L)₄]. All ellipsoids are drawn at a 50% probability level. Be: green, O: red, N: blue, I: violet, C: grey, H: white, program DrawXTL.^[32]

β -tetrakis(*N,N*-dimethylformamide)beryllium(II) iodide (**1**) forms colorless, bisphenoidal and deliquescent crystals. Specimens suitable for data collections were selected under a polarization microscope and sealed in capillaries filled with dried paraffin oil to prevent hydrolysis. From the collected intensities of one half of the Ewald sphere the monoclinic metrics together with the extinction conditions $h0l$ only observed for $l = 2n$ and $0k0$ only observed for $k = 2n$ pointed

unambiguously towards space group $P2_1/c$ in which structure solution was performed successfully. All non-H atom positions were taken from structure solution and refined subsequently with anisotropic displacement parameters. The H atom positions were fixed geometrically.

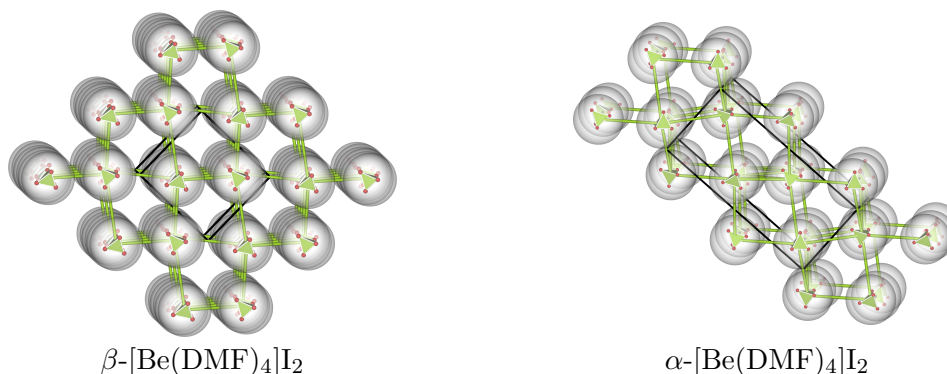


Fig. 4.59: Comparison of the packing topologies in the two modifications of $\text{Be}(\text{DMF})_4\text{I}_2$; **left:** $\beta\text{-}[\text{Be}(\text{DMF})_4]\text{I}_2$, **right:** $\alpha\text{-}[\text{Be}(\text{DMF})_4]\text{I}_2$.^[12] Shown are spheres of arbitrary radii depicting the $[\text{Be}(\text{DMF})_4]$ complex cationic units with the central $[\text{BeO}_4]$ tetrahedral cores highlighted as green tetrahedra. In both modifications the complex cations form a distorted cubic primitive packing, however, degree of distortion and orientation of the respective single $[\text{BeO}_4]$ units show differences.

Müller and Buchner recently published a crystal structure for $[\text{Be}(\text{DMF})_4]\text{I}_2$.^[12] The structure model is presented in the same space group type, however, in the $P2_1/n$ setting and the relations of the cell dimensions for our modification and the literature structure in their respective different settings are compiled in Table 4.41. A graphical comparison of the two structure models is given in Fig. 4.59. It becomes clear that the best comparison in lattice metrics can be made between our setting in $P2_1/c$ and the one given in literature in $P2_1/a$. Then, the a parameter in the literature model is virtually the doubled a parameter of our cell, the b and c parameters are about the same in both models, however, being significantly smaller. This together with the fact that changing axes a and c changes the $P2_1/c$ setting to $P2_1/a$ but not to $P2_1/n$ and together with the absence of any intensities in our diffraction images giving rise to an axis doubling shows that $[\text{Be}(\text{DMF})_4]\text{I}_2$ truly forms two different modifications. Their respective molar volumes differ by a small but significant amount: the one for our modification is larger by about 1%, probably founded in the different measurement temperatures. Since crystallizations were performed from saturated solutions, different temperatures can be taken as reason for the formation of the different modifications. As our crystals were measured at 109 K and the literature measurement was performed at 100 K, we chose the assignment of β as the HT phase to our structure model and α as the LT phase to the literature model.

The local geometric details within the complex cations do not differ significantly between the two modifications. We observe Be–O distances between 1.57(2) and 1.64(2) Å, which are the shortest ones in the available literature to our knowledge, and the range for Be–O distances in $\alpha\text{-}[\text{Be}(\text{DMF})_4]\text{I}_2$ with 1.601(5)–1.634(6) Å is in very good agreement. Also the O–Be–O angles (106.2(9)–113.2(9)° in our model and 107.3(5)–113.0(5)° in $\alpha\text{-}[\text{Be}(\text{DMF})_4]\text{I}_2$) do not differ signifi-

Table 4.41: Comparison of different settings of the unit cells of the two modifications of $\text{Be}(\text{DMF})_4\text{I}_2$: ours (left) and the literature model by Müller and Buchner (right).^[12] Transformation of our model in $P2_1/c$ to $P2_1/n$ was performed to give comparable unit cell dimensions. Best comparable metrics are highlighted in bold.

	$\beta\text{-}[\text{Be}(\text{DMF})_4]\text{I}_2$		$\alpha\text{-}[\text{Be}(\text{DMF})_4]\text{I}_2$		
	$P2_1/c$	$P2_1/n$	$P2_1/c$	$P2_1/n$	$P2_1/a$
a	12.491	12.491	15.296	30.493	25.270
b	11.593	11.593	11.371	11.371	11.371
c	15.310	19.039	25.270	15.293	15.296
β	94.71	126.12	94.25	124.27	94.25
V	2210	2210	4383	4383	4383
Z	4	4	8	8	8
V_{molar}	552.5	552.5	547.9	547.9	547.9

cantly. Overall, the energetic differences between the two modifications must be very small. It is therefore difficult to impossible to study this phase transformation with differential thermoanalytic measurements due to low temperature and very small enthalpic effects. The phase transition can be assumed to be of higher order (displacive) due to the observed minor changes in the local complex geometric parameters, and a group-subgroup relation between the two models may be realized within a *klassengleiche* transition of index 2 from the $P2_1/c$ aristotype structure to the hettotype $P2_1/a$ structure with doubling of the a axis.

A data set of a single crystal of tetrakis(pyridine)beryllium(II) iodide (**2**) was successfully solved and refined in space group $C2/c$ (No. 15), as indicated by the monoclinic metric, the extinction conditions hkl only observed for $k+l = 2n$ and $h0l$ only observed for $l = 2n$, and the $E^2 - 1$ value statistics pointing towards centrosymmetry. The crystal structure shows one crystallographically independent Be atom tetrahedrally coordinated by four N atoms of the pyridine ligands with Be–N distances ranging from 1.734(3) to 1.735(3) Å. These distances are similar to those reported for the compounds $[\text{Be}(\text{Pyr})_4]_2(\text{I}_3)_2(\text{I}_4)$ ^[9] and $[\text{Be}(\text{DIC})_4](\text{I}_3)_2$.^[10] The N–Be–N angles range from 103.9(2) to 113.33(7)° which deviates from the ideal tetrahedral angle by only 5.1%.

The tetrahedral complex units $[\text{Be}(\text{Pyr})_4]^{2+}$ are packed in a hcp topology, see Fig. 4.60. The unit cell metrics indicate very low distortion and therefore small deviation of the individual complex cations from spherical behavior: a and c parameters are very similar and the monoclinic angle is rather close to 120°, the b parameter is about half of a and c , and finally $C3/c$ is a subgroup of $P6_3/mmc$, the space group of the hcp packing.

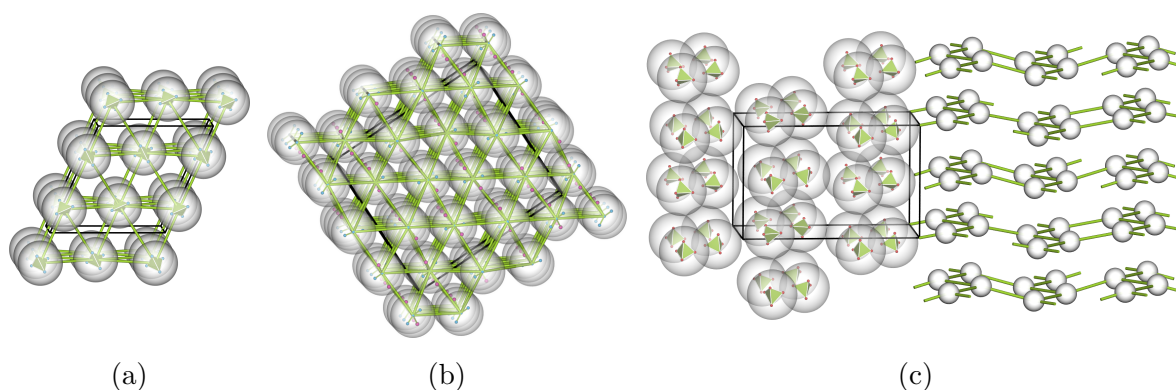


Fig. 4.60: Packing topologies of the complex units $[\text{Be}(\text{L})_4]$ in (a) $\text{Be}(\text{Pyr})_4\text{I}_2$, (b) $\text{Be}(\text{Lut})_2\text{I}_2$ and (c) $\text{Be}(\text{NMP})_4\text{I}_2$. Spheres of arbitrary radii depict the $[\text{Be}(\text{L})_4]$ complex units with the central $[\text{Be}(\text{N}/\text{O})_4]$ tetrahedral cores indicated as green tetrahedra in (a) and (c). Whereas in (a) and (b) hcp packing can be found, (c) may best be described as a flattened arsenic-type packing.

Yellow crystals of tetrakis-(*N*-methylpyrrolidone)beryllium(II) iodide (**3**) yielded a data set which could be solved and refined in space group $Pbca$ (No. 61), as indicated by the characteristic absence conditions together with the orthorhombic metric and the $E^2 - 1$ statistics pointing towards centrosymmetry. The crystal structure shows one crystallographically independent Be atom which is tetrahedrally coordinated by four O atoms of the NMP ligands. The Be–O distances range from 1.58(1) to 1.64(2) Å which is very close to the distances observed in (1). The packing of the tetrahedral $[\text{Be}(\text{NMP})_4]$ cationic units follows a more complicated topology here. As can be seen in Fig. 4.60, slightly puckered honeycomb layers are stacked along the b direction, resulting in a packing topology that can be described as a flattened arsenic-type structure.

The data set obtained from a pale orange, platelet-shaped single crystal of bis(2,6-lutidine)diiodo beryllium(II) was indexed with a monoclinic metric and showed the extinction conditions unambiguously pointing towards space group $P2_1/c$ in which it could be solved and refined. There are three topologically identical but crystallographically independent complexes $[\text{BeI}_2(\text{Lut})_2]$ units

present in the unit cell, differing only slightly in the respective ligand orientations. Symmetry checking did not lead to higher metric symmetry, lattice centering or reduction of the unit cell. In all the complex units the Be atom is tetrahedrally coordinated by two I atoms and two N atoms of the 2,6-lutidine ligands with the Be–N distances between 1.77(1) and 1.81(1) Å. While the angles N–Be–N (108.3(5)°) and I–Be–I (103.5(3)°) are relatively close to the ideal tetrahedral angle, the N–Be–I angles range between 94.6 and 129.9(5)°, showing a considerable distortion of the coordination tetrahedron, together with the large difference between the Be–I and Be–N distances. The individual [BeI₂(Lut)₂] units are stacked in a hcp topology with the hexagonal layers oriented perpendicular to the stacking direction [210], see Fig. 4.60.

Experimental Section

Caution! Beryllium and its compounds are regarded as toxic and carcinogenic. Because the biochemical mechanisms that cause beryllium-associated diseases are still unknown, special (safety) precautions are strongly advised.^[33]

Synthesis of BeI₂

A slightly modified version of the procedure reported by Wood and Brenner^[34] and included in Brauer's Handbook^[35] was used to prepare BeI₂ in a multigram scale from the elements. The apparatus shown in Fig. 4.61 (right) was loaded with beryllium metal (99.5%, Sigma-Aldrich) in a corundum crucible inside a quartz tube, which was connected to a Schlenk flask via a connecting valve I. After thorough heating at 500 °C under vacuum for about 12 h in order to establish anhydrous conditions, the system was allowed to cool under inert gas (Ar). Under reverse flow, I₂ beads (99.5%, Acros Organics) were inserted into the Schlenk flask. Experiments showed that the amount of Be used is not crucial while the amount of iodine is important due to its partial pressure. For our setup, we recommend not using more than 2.0 g I₂ (7.9 mmol) in order to enable the reaction product to distill off and thus ensuring an ongoing reaction. While cooling the iodine-containing flask with liquid nitrogen, the system was once more evacuated until a sufficiently low pressure (10⁻³ mbar) could be established. The reaction was then carried out under vacuum while maintaining a temperature of 650 °C for the tube furnace and 250 °C for the oil bath. The temperature of 480 °C given in literature is too low. The reaction must be performed above the boiling temperature of BeI₂ (590 °C^[36]) so that the reaction product is separated from the beryllium metal and condenses as white crystals in the colder part of the quartz tube. To avoid resublimation of iodine crystals in the connector, it was mantled with aluminum foil. The synthesis was stopped when the atmosphere in the system appeared colorless again, indicating complete iodine consumption. The Schlenk flask was disconnected, the quartz tube with the connector still attached filled with inert gas and then transferred into the glove box for opening and storing of BeI₂. Purity was checked by powder diffractometry (see Fig 7.128).

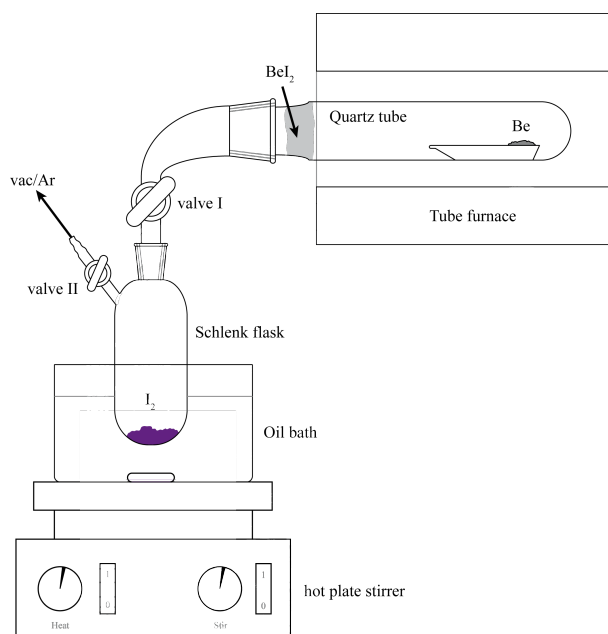


Fig. 4.61: Schematic illustration of the reaction apparatus for the synthesis of BeI₂.

While cooling the iodine-containing flask with liquid nitrogen, the system was once more evacuated until a sufficiently low pressure (10⁻³ mbar) could be established. The reaction was then carried out under vacuum while maintaining a temperature of 650 °C for the tube furnace and 250 °C for the oil bath. The temperature of 480 °C given in literature is too low. The reaction must be performed above the boiling temperature of BeI₂ (590 °C^[36]) so that the reaction product is separated from the beryllium metal and condenses as white crystals in the colder part of the quartz tube. To avoid resublimation of iodine crystals in the connector, it was mantled with aluminum foil. The synthesis was stopped when the atmosphere in the system appeared colorless again, indicating complete iodine consumption. The Schlenk flask was disconnected, the quartz tube with the connector still attached filled with inert gas and then transferred into the glove box for opening and storing of BeI₂. Purity was checked by powder diffractometry (see Fig 7.128).

A similar experimental approach, although inside a sealed quartz ampule, was recently suggested by Müller et al.^[25] Our approach not only combines the synthesis and the purification process while avoiding excess quartz waste in a single step and a relatively simple system, but

furthermore enables a continuous synthesis through exchanging the Schlenk flask with fresh I_2 . Additionally, the amount of Be metal used is of no consequence for the success of the synthesis, which simplifies the process even further.

Purification of solvents

The solvents were freshly distilled under Ar atmosphere and stored using a 3 Å molecular sieve. NMP and 2,6-lutidine were dried over KOH, while DMF and pyridine were dried using CaH_2 . Beryllium iodide dissolves highly exothermic in DMF, pyridine and NMP. Special caution is advised for DMF: the high solvation enthalpy may decompose the solvent and therefore calls for intense cooling. In 2,6-lutidine, BeI_2 dissolves only in minor amounts, therefore thermal treatment and removal of excess solid is needed. After reducing the solutions *in vacuo* and optional storage at cooler temperatures for about 10 days in case of 2,6-lutidine, crystals were obtained and characterized.

Synthesis of 1

Due to the solvation enthalpy of BeI_2 with DMF which is so high that decomposition of DMF occurs when it is added dropwise to solid BeI_2 , reaction of BeI_2 with DMF has to be performed slowly and under cooling. 2.174 g BeI_2 (10.33 mmol) were inserted into a Schlenk flask filled with argon and connected to a second Schlenk flask filled with 50 ml DMF. In order to establish equilibrium conditions, the apparatus was left in this state for 24 h. During that time, a volumetric increase of the solid was observed indicating the formation of a solvate by slow diffusion of DMF vapor. To enable slow solvation, BeI_2 then was cooled with ice, while the DMF was heated to 100 °C. This led to the complete dissolution of BeI_2 , resulting in a light orange liquid. After concentrating the solution *in vacuo*, bisphenoidal colorless crystals formed.

Synthesis of 2

2.046 g BeI_2 (7.78 mmol) were inserted into a Schlenk flask filled with argon and connected to a second Schlenk flask filled with 50 mL pyridine. The same procedure as described for DMF was performed. This led to the partial dissolution of BeI_2 , resulting in a light yellow liquid containing a colorless solid. A small portion of the liquid was concentrated *in vacuo* until crystal formation occurred.

Synthesis of 3

To 697.9 mg BeI_2 (2.66 mmol), cooled with liquid nitrogen, 55 mL of NMP were added. After warming to room temperature, a yellow liquid was obtained, from which a sample was concentrated *in vacuo* until crystallization occurred.

Synthesis of 4

To 19.0 mg BeI_2 (0.70 mmol), cooled with ice, 2.0 mL 2,6-lutidine (17.3 mmol) were added. After heating the suspension to 100 °C for one hour, undissolved BeI_2 was removed using a Schlenk frit. The remaining liquid was stored at 5 °C for 10 days, after which the formation of light orange platelets was observed.

Single crystal X-ray diffraction

Single crystals suitable for X-ray investigations were selected under a binocular with polarization filter and sealed in paraffin-filled glass capillaries with an inner diameter of 0.1 mm. Crystals of (**1**) were centered on a three-circle goniometer of a diffractometer system D8 Venture (BRUKER AXS GmbH, Karlsruhe, Germany) equipped with a CCD detector, a rotating anode and a Goebel mirror using $Mo-K_\alpha$ radiation. Data collection was performed at 109 K in a nitrogen cooling stream. Crystals of the products (**2**) and (**3**) were centered on a one-circle goniometer of a diffractometer system IPDS-1 (STOE & CIE., Darmstadt, Germany) equipped with an imaging

plate detector and graphite-monochromatized Mo-K α radiation.

A crystal of (**3**) was mounted in a non-arbitrary orientation on the one-circle goniometer, leading to systematically unobserved regions of the Ewald sphere. This may explain the uncommonly low value of GooF (see Table 4.39). Crystals of product (**4**) were centered on a three-circle goniometer of a diffractometer system D8 Quest (BRUKER AXS GmbH, Karlsruhe, Germany) equipped with a CCD detector, a microfocus tube and a Goebel mirror using Mo-K α radiation. For all products, data from half of the Ewald sphere were collected and subsequently corrected for Lorentz, polarization and absorption effects.^[26,27,37] In all refinements, the H atomic positions were generated geometrically and coupled to their adjoining C atoms using a riding model. CCDC entries 1983410 (**1**), 1983413 (**2**), 1983411 (**3**) and 1983412 (**4**) contain the supplementary crystallographic data for this paper. These data can be obtained free of charge from The Cambridge Crystallographic Data Centre via www.ccdc.cam.ac.uk/data_request/cif.

Conclusion

Electrocrystallisation experiments employing solutions of all four complexes with their respective ligand serving as solvent showed that all of the synthesized compounds appear to be of high inertness and no beryllium amalgam was obtained. In these experiments, a mercury cathode, tungsten anode and a voltage of 3.0 V were used at room temperature. Further details on the practical details can be found in our corresponding article concerning electrocrystallisation.^[15] A crucial parameter of a successful electrocrystallisation is the lability of the metal-solvent complex. If the lability of the complex is too low an overvoltage is needed to release the metal during electrolysis. In those cases where this overvoltage is higher than the decomposition potential of the solvent, an electrolytic deposition of the metal cannot be observed. Lability of a complex is a consequence of the metal-donor interaction. Since the nature of the Be-donor bond is generally not discussed in literature on beryllium complexes with organic ligands, it seems that this is a non-trivial topic. Comparing ionic and covalent radii sums^[30,31] lead to no further judgement regarding the nature of the Be-N or the Be-O bond in our complexes can be made due to their very small, if even existent differences (see Tab. 4.40). In order to make a qualified estimation of the degree of covalency in the Be-donor bonds in these complexes and therefore to give an estimation of their lability, quantum mechanical calculations and bonding analyses with Bader charge distributions or analysis of the electron localizability indicator (ELI) seem promising but are not within the scope of this work.

Acknowledgment

We thank the Deutsche Forschungsgemeinschaft (German Research Foundation, DFG) for their financial support of this project.

Electrocrystallisation in liquid Ammonia

Since all attempts from ‘regular’ solvents were unfruitful with regard to the successful synthesis of a Be amalgam, other systems had to be considered. The electrochemical reduction of Be on an industrial scale to obtain a high-purity metal is performed as a fused-salt electrolysis of BeCl_2 (in LiCl at 500 °C or NaCl at 350 °C) or BeF_2 (in LiCl or KCl at 500 °C).^[38] Because of the energy-intensive processes owing to the elevated temperatures, numerous experimental approaches for the electrodeposition of elemental Be were explored, and summarised in detail by Wood and Brenner.^[34] The most promising results were found for a 3 M $\text{Be}(\text{Me})_2$ + 2.3 M BeCl_2 solution in diethyl ether. However, the need for the synthesis of the starting material quickly ruled out this approach. Another promising synthetic route was proposed in 1931 by H. S. Booth and G. G. Torrey,^[39] and in contrast to many other syntheses, confirmed in 1959 by I. A. Menzies et al.^[40]

Based on these findings, a new attempt for the electrochemical synthesis of a Be amalgam was made. The experimental details can be found in Chapter 3.4.2 (p. 22). Since the electrocrystallisation calls for a liquid Mercury cathode, the synthesis temperature must be above its crystallisation temperature ($\vartheta_{\text{melt}}(\text{Hg}) = -38.83\text{ °C}$), but below the boiling point of ammonia ($\vartheta_{\text{bp}}(\text{NH}_3) = -33\text{ °C}$). Consequently, the solubility of BeI_2 in liquid NH_3 was tested in a preliminary experiment and was confirmed, it dissolves readily at -52 °C in concentrations sufficient for the subsequent electrocrystallisation experiments ($c \approx 1\text{ mol L}^{-1}$), forming a colourless solution (see right image). It was already discovered in 1899 by P. Lebeau^[41] that Beryllium iodide has a good solubility in liquid ammonia (“*En chauffant légèrement, il se produit une nouvelle absorption d’ammoniac et la substance fond, cristallisant par refroidissement.*”), but the exact concentrations and temperatures were not published. He even described the formation of a complex salt of the nominal composition $2\text{GlI}_3 \cdot 3\text{AzH}_3$ ($\text{Gl} = \text{Be}$, from the term *Glucinium*, $\text{AzH}_3 = \text{NH}_3$, from *Azote*), which was only recently confirmed and characterised as $[\text{Be}(\text{NH}_3)_4]\text{I}_2$.^[42]



Fig. 4.62: Colorless solution of BeI_2 in liquid ammonia at -52 °C .



Fig. 4.63: Left: Mercury cathode during the first electrocrystallisation experiment of BeI_2 in liquid NH_3 . As can be seen, the spoon appears to have a shiny and smooth surface, showing the liquid state of the elemental Hg. The light blue colour indicates the formation of the $[\text{Cu}(\text{NH}_3)_4]^{2+}$ complex. Right: corroded Cu anode from the electrocrystallisation.

In the first attempt, a copper rod served as an anode. During the experiment, it was observed that the electrolyte has changed colour: the previously colourless solution has turned slightly blue (see Fig. 4.63, right). This colour indicates the presence of Cu^{2+} in the system, which then forms the characteristically blue $[\text{Cu}(\text{NH}_3)_4]^{2+}$ complex. A crystalline, metallic solid was obtained, but was identified as Cu_7Hg_6 (cf. Fig. 7.91, p. 168). ICP-OES measurements were performed and confirmed these findings. While the standard electrode potentials E° for aqueous systems ($E^\circ(\text{Be}^{2+}) = -1.487\text{ V}$, $E^\circ(\text{Cu}^{2+}) = 0.344\text{ V}$)^[43] imply that the reduction of Be^{2+} should be favoured over the oxidation of Cu and its subsequent reduction to form a copper amalgam, they have rarely been determined in non-aqueous systems, so the reason for the favoured galvanic corrosion might simply lie in their vastly different

standard potentials in liquid ammonia.

In a subsequent synthesis, a tungsten rod was used as anode, to avoid the formation of a copper amalgam. Electrolysis was performed for 44 hours in total, and after removal of the copper spoon from the apparatus, a silver-black, crystalline solid was obtained. However, all attempts to analyse the compound were unsuccessful: if ground in a mortar for powder diffraction analysis, the compound decomposed, yielding elemental Hg droplets. Inspection of the crystalline specimens was performed after transfer out of the glovebox under potassium-dried paraffin oil. The compound decomposed within minutes, building a spongy, colourless solid (most probably from $\text{Be}(\text{OH})_2$) and elemental Hg droplets. All attempts to isolate crystals for single crystal X-ray diffraction experiments were unsuccessful, since the obtained product decomposed even in flame-sealed glass capillaries. A final, conclusive analysis was not possible within the scope of this work, but the results so far have been quite promising, and future efforts should be made. Hopefully, the very elusive Be-amalgam will then be unambiguously identified: the experimental findings indicate that a Be amalgam can be prepared by electrolysis of a solution of BeI_2 in liquid NH_3 at a temperature between -39 and -33° on a mercury cathode using a W anode. The amalgam most probably is not only very sensitive towards moisture and air, but also seems to be stable only below room temperature.

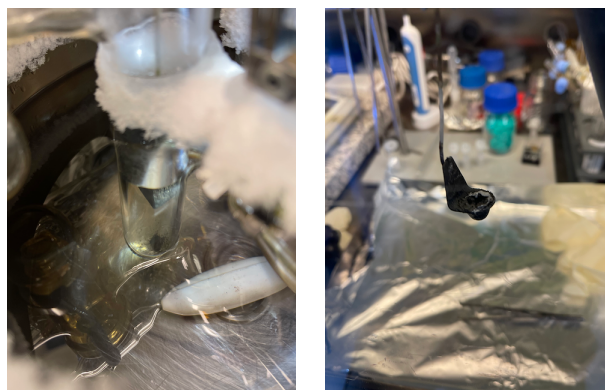


Fig. 4.64: **Left:** Mercury cathode during the second electrocrystallisation experiment of BeI_2 in liquid NH_3 . The amalgamated copper spoon shows visible crystallinity. **Right:** Extracted cathode after performed electrocrystallisation.

References

- [1] A. Jose, G. S. K. Rao, Preparation of Lithium Amalgam, *J. Chem. Educ.* **1970**, *47*, 277, DOI: [10.1021/ed047p277](https://doi.org/10.1021/ed047p277).
- [2] H. Fleck, L. L. Basset, Magnesiumamalgam, ein neues Reagens zur Reduction in neutraler Lösung, *Fresenius Z. Anal. Chem.* **1898**, *37*, 322, DOI: [10.1007/BF01461685](https://doi.org/10.1007/BF01461685).
- [3] L. Misch, Die Kristallstruktur des AuBe_5 und PdBe_5 und ihre Beziehung zur kubischen AB_2 -Struktur, *Metallwirtsch. Metallwiss. Metalltech.* **1935**, *14*, 897–899.
- [4] F. W. von Batchelder, R. F. Raeuchle, The tetragonal $M\text{Be}_{12}$ structure of silver, palladium, platinum and gold, *Acta Crystallogr.* **1958**, *11*, 122, DOI: [10.1107/S0365110X58000323](https://doi.org/10.1107/S0365110X58000323).
- [5] B. D. Cullity, The Crystal Structure of AuBe , *Trans. Am. Inst. Min. Metall. Pet. Eng.* **1947**, *171*, 396–400.
- [6] M. H. Müller, L. H. Schwartz, S. S. Sidhu. In Annual Pittsburgh Diffraction Conference, *Vol. 16*, (Ed.: T. P. D. Society), **1958**, p. 43.
- [7] H. J. Bernhardt, K. Schmetzer, Belendorffite, a new copper amalgam dimorphous with kolymite, *M. Jb. Miner. Mh.* **1992**, *1*, 21–28.
- [8] B. Neumüller, K. Dehnicke, N-Methylimidazolkomplexe des Berylliums: $[\text{Be}(\text{Me-Im})_4]\text{I}_2$ und $[\text{Be}_3(\mu\text{-OH}_3(\text{Me-Im})_6)\text{Cl}_3]$, *Z. Anorg. Allg. Chem.* **2010**, *636*, 1516–1521, DOI: [10.1002/zaac.201000100](https://doi.org/10.1002/zaac.201000100).
- [9] B. Neumüller, K. Dehnicke, Tetrapyridin-Beryllium-Polyiodid. Synthese und Kristallstruktur von $[\text{Be}(\text{Py})_4]_2(\text{I}_3)_2(\text{I}_4)$, *Z. Anorg. Allg. Chem.* **2010**, *636*, 515–517, DOI: [10.1002/zaac.200900481](https://doi.org/10.1002/zaac.200900481).
- [10] B. Neumüller, K. Dehnicke, Tetra(diisopropylcarbodiimid-N)-Beryllium-bis-Triiodid und 1,3-Diisopropyl-2,4-bis(isopropylimino)-1,3-Diazetid, *Z. Anorg. Allg. Chem.* **2010**, *636*, 1767–1771, DOI: [10.1002/zaac.201000026](https://doi.org/10.1002/zaac.201000026).

- [11] C. Hoch, Syntheses and crystal structures of solvate complexes of alkaline earth and lanthanoid metal iodides with N,N-dimethylformamide, *Z. Kristallogr. - Cryst. Mater.* **2020**, *235*, 401–411, DOI: [10.1515/zkri-2020-0071](https://doi.org/10.1515/zkri-2020-0071).
- [12] M. Müller, M. R. Buchner, Solution Behavior of Beryllium Halides in Dimethylformamide, *Inorg. Chem.* **2019**, *58*, 13276–13284, DOI: [10.1021/acs.inorgchem.9b02139](https://doi.org/10.1021/acs.inorgchem.9b02139).
- [13] B. Neumüller, K. Dehnicke, Tetra(*N,N'*-tetramethylharnstoff)-Beryllium-Triiodid, [Be(TM_H)₄](I₃)₂, *Z. Anorg. Allg. Chem.* **2010**, *636*, 962–965, DOI: [10.1002/zaac.200900541](https://doi.org/10.1002/zaac.200900541).
- [14] C. Jones, A. Stasch, Crystal Structure of [BeI₂(OEt₂)₂] (OEt₂ = diethyl ether), *X-Ray Struct. Anal. Online* **2007**, *23*, x115–x116, DOI: [10.2116/analscix.23.x115](https://doi.org/10.2116/analscix.23.x115).
- [15] F. Tambornino, J. Sappl, F. Pultar, T. M. Cong, S. Hübner, T. Giftthaler, C. Hoch, ElectrocrySTALLIZATION - a synthetic method for intermetallic phases with polar metal-metal bonding, *Inorg. Chem.* **2016**, *55*, 11551–11559, DOI: [10.1021/acs.inorgchem.6b02068](https://doi.org/10.1021/acs.inorgchem.6b02068).
- [16] C. Hoch, A. Simon, Tetramethylammoniumamalgam, [N(CH₃)₄]Hg₈, *Z. Anorg. Allg. Chem.* **2006**, *632*, 2288–2294, DOI: [10.1002/zaac.200600163](https://doi.org/10.1002/zaac.200600163).
- [17] C. Hoch, A. Simon, Cs₂Hg₂₇, das quecksilberreichste Amalgam – ein naher Verwandter der Bergman-Phasen, *Z. Anorg. Allg. Chem.* **2008**, *634*, 853–856, DOI: [10.1002/zaac.200700535](https://doi.org/10.1002/zaac.200700535).
- [18] F. Tambornino, C. Hoch, Bad metal behaviour in the new Hg-rich amalgam KHg₆ with polar metallic bonding, *J. Alloys Compd.* **2015**, *618*, 299–304, DOI: [10.1016/j.jallcom.2014.08.173](https://doi.org/10.1016/j.jallcom.2014.08.173).
- [19] F. Tambornino, C. Hoch, The Mercury-richest Europium Amalgam Eu₁₀Hg₅₅, *Z. Anorg. Allg. Chem.* **2015**, *641*, 537–542, DOI: [10.1002/zaac.201400561](https://doi.org/10.1002/zaac.201400561).
- [20] F. Tambornino, C. Hoch, The simplest representative of a complex series: the Hg-rich amalgam Yb₁₁Hg₅₄, *Z. Kristallogr.* **2017**, *232*, 557–565, DOI: [10.1515/zkri-2016-2036](https://doi.org/10.1515/zkri-2016-2036).
- [21] M. Wendorff, C. Röhr, Alkaline-earth tri-mercurides A^{II}Hg₃ (A^{II} = Ca, Sr, Ba): Binary intermetallic compounds with a common and a new structure type, *Z. Kristallogr.* **2018**, *233*, 515–529, DOI: [10.1515/zkri-2018-2054](https://doi.org/10.1515/zkri-2018-2054).
- [22] H.-J. Deiseroth, Discrete and extended metal clusters in alloys with mercury and other group 12 elements. In *Molecular Clusters of the Main Group Elements*, (Eds.: M. Driess, H. Nöth), Wiley-VCH, Weinheim, Germany, **2004**, pp. 169–187.
- [23] T. B. Massalski, H. Okamoto, P. R. Subramanian, L. K. (Hrsg.), *Binary Alloy Phase Diagrams*, 2nd ed., ASM International, Materials Park (OH), USA, **1990**.
- [24] B. Neumüller, W. Petz, K. Dehnicke, Dimethylsulfoxid-Komplexe von Beryllium(II)-chlorid. Kristallstrukturen von [Be(OSMe₂)₄]Cl₂, [Be(OSMe₂)₃(H₂O)]Cl₂ und [Be(OSMe₂)₂(H₂O)₂]Cl₂, *Z. Anorg. Allg. Chem.* **2008**, *634*, 662–668, DOI: [10.1002/zaac.200700524](https://doi.org/10.1002/zaac.200700524).
- [25] M. Müller, F. Pielhofer, M. R. Buchner, A facile synthesis for BeCl₂, BeBr₂ and BeI₂, *Dalton Trans.* **2018**, *47*, 12506–12510, DOI: [10.1039/C8DT01756E](https://doi.org/10.1039/C8DT01756E).
- [26] X-RED, STOE & Cie. GmbH, Darmstadt, Deutschland, version 1.3.1, **2005**.
- [27] X-SHAPE, STOE & Cie. GmbH, Darmstadt, Deutschland, version 2.0.7, **2005**.
- [28] G. M. Sheldrick, A short history of SHELX, *Acta Crystallogr.* **2008**, *A64*, 112–122, DOI: [10.1107/S0108767307043930](https://doi.org/10.1107/S0108767307043930).
- [29] L. M. Gelato, E. Parthé, Structure Tidy – a computer program to standardize crystal structure data, *J. Appl. Crystallogr.* **1987**, *20*, 139–143, DOI: [10.1107/S0021889887086965](https://doi.org/10.1107/S0021889887086965).
- [30] P. Pyykkö, M. Atsumi, Molecular Single-Bond Covalent Radii for Elements 1–118, *Chem. Eur. J.* **2008**, *15*, 186–197, DOI: [10.1002/chem.200800987](https://doi.org/10.1002/chem.200800987).
- [31] R. D. Shannon, Revised effective ionic radii and systematic studies of interatomic distances in halides and chalcogenides, *Acta Crystallogr.* **1976**, *A32*, 751–767, DOI: [10.1107/S0567739476001551](https://doi.org/10.1107/S0567739476001551).
- [32] L. W. Finger, M. Kroeker, B. H. Toby, DRAWxtl, an open-source computer program to produce crystal structure drawings, *J. Appl. Crystallogr.* **2007**, *40*, 188–192, DOI: [10.1107/S0021889806051557](https://doi.org/10.1107/S0021889806051557).
- [33] D. Naglav, M. R. Buchner, G. Bendt, F. Kraus, S. Schulz, Off the Beaten Track - A Hitchhiker's Guide to Beryllium Chemistry, *Angew. Chem. Int. Ed.* **2016**, *55*, 10562–10576, DOI: [10.1002/anie.201601809](https://doi.org/10.1002/anie.201601809).

- [34] G. B. Wood, A. Brenner, Electrodeposition of Metals from Organic Solutions, *J. Electrochem. Soc.* **1957**, *11*, 29–37, DOI: [10.1149/1.2428491](https://doi.org/10.1149/1.2428491).
- [35] G. Brauer, *Handbook of Preparative Inorganic Chemistry*, Vol. 1, 2nd ed., Academic Press, New York (NY), USA, **1963**, pp. 892–893.
- [36] D. L. Perry, S. L. P. (Eds.), *Handbook of inorganic compounds*, CRC Press, New York (NY), USA, **1963**, p. 63.
- [37] APEX3, BRUKER AXS GmbH, Karlsruhe, Deutschland, version 2018.1-0, **2018**.
- [38] K. A. Walsh, Chapter 7.11 Electrorefining of Beryllium. In *Beryllium Chemistry and Processing*, (Eds.: E. E. Vidal, A. Goldberg, E. N. C. Dalder, D. L. Olson, B. Mishra), ASM International, Materials Park (OH), USA, **2009**, pp. 90–91.
- [39] H. S. Booth, G. G. Torrey, Contributions to the Chemistry of Beryllium, III. Electrolysis of Solutions of Beryllium Compounds in Liquid Ammonia, *J. Phys. Chem.* **1931**, *35*, 3111–3120, DOI: [10.1021/j150329a002](https://doi.org/10.1021/j150329a002).
- [40] I. A. Menzies, D. L. Hill, L. W. Owen, The electrodeposition of beryllium from non-aqueous solutions, *J. Less-Common Met.* **1959**, *1*, 321–330, DOI: [10.1016/0022-5088\(59\)90009-8](https://doi.org/10.1016/0022-5088(59)90009-8).
- [41] P. Lebeau, Recherches sur le glucinium et ses composés, *Ann. Chim. Phys.* **1899**, *7(T16)*, 457–502, <https://gallica.bnf.fr/ark:/12148/bpt6k34916d/f455.item>.
- [42] M. Müller, M. R. Buchner, Preparation and crystal structures of the beryllium amines $[\text{Be}(\text{NH}_3)_4]\text{X}_2$ ($\text{X} = \text{Br}, \text{I}, \text{CN}, \text{SCN}, \text{N}_3$) and $\text{Be}(\text{NH}_3)_2\text{X}'_2$ ($\text{X}' = \text{Cl}, \text{Br}$), *Chem. Commun.* **2019**, *55*, 13649–13652, DOI: [10.1039/C9CC07712J](https://doi.org/10.1039/C9CC07712J).
- [43] P. Vanýsek, Electrochemical Series. In *ASM Handbook, Volume 13B*, (Eds.: S. D. Cramer, B. S. Covino), ASM International, Materials Park (OH), USA, **2005**.

4.8 The ‘Bad Metal’ Behaviour and its Contributing Factors

‘Bad metal’ behaviour as an indication of high polarity in an intermetallic phase has been observed in several binary amalgams so far. Increasing the number of representatives by the targeted synthesis of ternary amalgams facilitates the identification of several parameters that are decisive for the specific ‘bad metal’ behaviour of an individual amalgam through the comparison of multiple, different examples. The identification of these parameters and the estimation of their relative impact is necessary in order to understand the underlying structure-property relations and deliberately tune the properties of polar intermetallics by preparative means. We were able to detect the decisive parameters for ‘bad metal’ behaviour and discuss them in this subchapter.

The ‘bad metal’ behaviour of amalgams is caused by multiple factors, which can not always be fully separated. These factors are:

- Polarity in the sense of the electron transfer δ in $M^{\delta+}[\text{Hg}_n]^{\delta-}$
- Structural Complexity
- Structural Disorder

Measurements of the specific resistivity ρ , which have been performed for the structurally unique $\text{CsNa}_2\text{Hg}_{18}$ (Chapter 4.1) and the solid solution $\text{K}_{1-x}\text{Rb}_x\text{Hg}_{11}$ (Chapter 4.3) as well as for several literature-known amalgams, are the most direct approach for the quantification of the ‘bad metal’ behaviour.

4.8.1 Structural Disorder

The introduction of disorder can be implemented in the form of statistical mixed occupancy in otherwise isostructural compounds. This way, other factors (e.g. structural complexity or valence electron concentration) become negligible, and the direct influence of disorder on the overall structure can be considered in an isolated manner. KHg_{11} and RbHg_{11} show a very similar behaviour, while for $\text{K}_{1-x}\text{Rb}_x\text{Hg}_{11}$, the slope appears steeper. This proves that the influence of disorder has no influence on the lower limit of the conductivity ρ_{min} , while the influence on the non-linear temperature dependence becomes more pronounced, resulting in a reduced mean free path length and more scattering events.

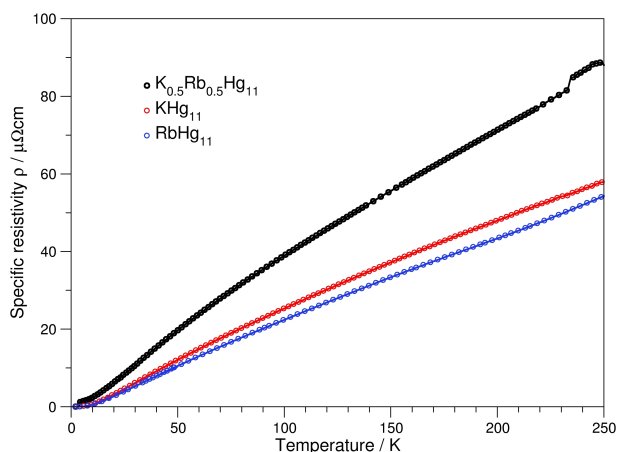


Fig. 4.65: Specific resistivities ρ of the isostructural amalgams KHg_{11} (red), RbHg_{11} (blue) and the mixed crystal $\text{K}_{1-x}\text{Rb}_x\text{Hg}_{11}$ (black).

4.8.2 Polarity

In order to estimate the electron transfer between the less noble metal and mercury, electronic calculations of ‘Bader charges’ can be made. Bader charges, which are based on the AIM (atoms in molecules)^[1] concept, are calculated as results of a topological analysis of molecular and atomic electron densities and included in most modern *ab initio* quantum chemical calculation methods (such as Wien2K).^[2] The obtained results should not be taken as absolute values, since they

only represent a spatial charge state. The reason for this is found in the AIM theory, where the calculations are being made only in a geometric fashion. A three-dimensional space for one atom is assigned, and the overall electron density integrated, which then lacks the appropriate inclusion of covalent or metallic bonding contributions.

Bader charges have been calculated for amalgams Li_3Hg , LiHg , LiHg_3 , NaHg_2 , KHg_6 , KHg_{11} and $\text{CsNa}_2\text{Hg}_{18}$ (see. Tables 4.42 and 4.43). For these, temperature-dependent resistivity measurements were performed. Details for the calculations are summarised in the table below. For maximum comparability, all parameters were the same, while the number of k-points in the Brillouin zone was chosen to be as close as possible.

Table 4.42: Details of the electronic structure calculations for Li_3Hg , LiHg , NaHg_2 and LiHg_3 with an emphasis on Bader charges. Multiplicities of the atoms are given in the parentheses.

Compound Ref.	Li_3Hg [3]		LiHg [3]		NaHg_2 [4]		LiHg_3 [3]	
R_{mt} (all atoms)	132.3 pm (2.5 a.u.)							
$R_{\text{mt}} \cdot K_{\text{max}}$	8.0							
k-points / BZ	1000		1000		972		990	
k-points / IBZ	47		35		84		72	
Monkhorst-Pack-Grid	$10 \times 10 \times 10$		$10 \times 10 \times 10$		$9 \times 9 \times 12$		$9 \times 9 \times 10$	
Bader charges	Li1 (4)	+0.82	Li1 (1)	+0.85	Na1 (1)	+0.79	Li1 (2)	+0.87
	Li2 (8)	+0.83	Hg1 (1)	-0.85	Hg1 (2)	-0.39	Hg1 (6)	-0.29
	Hg1 (4)	-0.82						

Table 4.43: Details of the electronic structure calculations for KHg_6 , KHg_{11} and $\text{CsNa}_2\text{Hg}_{18}$ with an emphasis on Bader charges. Multiplicities (given in the parentheses) are factored into the final charge.

Compound Ref.	KHg_6 [5]		$\text{CsNa}_2\text{Hg}_{18}$ Tab. 4.2		KHg_{11} [6]	
R_{mt} (all atoms)	132.3 pm (2.5 a.u.)					
$R_{\text{mt}} \cdot K_{\text{max}}$	8.0					
k-points / BZ	816		1000		1000	
k-points / IBZ	108		99		35	
Monkhorst-Pack-Grid	$6 \times 17 \times 8$		$10 \times 10 \times 10$		$10 \times 10 \times 10$	
Bader charges	K1 (4)	+0.77	Na1 (4)	+0.82	K1 (3)	+0.78
	Hg1 (4)	-0.09	Cs1 (2)	+0.76	Hg1 (1)	-0.04
	Hg2 (4)	-0.11	Hg1 (16)	-0.11	Hg2 (8)	-0.08
	Hg3 (4)	-0.16	Hg2 (16)	-0.17	Hg3 (12)	-0.09
	Hg4 (4)	-0.15	Hg3 (4)	-0.07	Hg4 (12)	-0.05
	Hg5 (4)	-0.12		+0.82		
Hg6 (4)	-0.14		+0.82			

While absolute values are not appropriate for the quantification of the polarity, the calculations can be useful since they mirror the overall increase of partial electron transfer with higher Hg contents. It can also be seen that the calculated values behave in accordance with the respective electronegativities of the less-noble metals. However, when resistivity measurements of the different Li amalgams are being compared (see Fig. 4.66, right), the differences in their calculated Bader charges fails to explain the significantly different behaviour. NMR investigations (Knight shift) combined with pDOS calculations conducted by F. Tambornino^[3] showed that these approaches are not only more precise, but can – at least to a certain extent – explain the observed behaviour. This also emphasises that

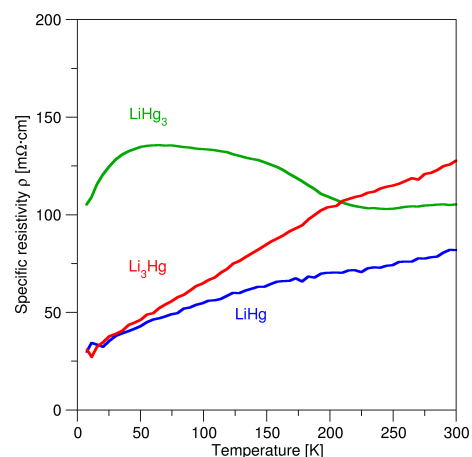


Fig. 4.66: Specific resistivities ρ of Li_3Hg (red), LiHg (blue) and LiHg_3 (green).

the calculation of the Bader charges can give a broad estimate, but fails to describe the quantitative polarity of the amalgam.

If resistivity measurements of two compounds with an equal Hg content and similar Bader charges (i.e. KHg_6 and $\text{CsNa}_2\text{Hg}_{18}$, see Fig. 4.67) are compared, the difference in their respective partial charges can not explain their significantly different physical behaviour. While the existing data indicates that the influence of polarity on the ‘bad metal’ behaviour is in the order of several magnitudes, the structural complexity has to be taken into account as well.

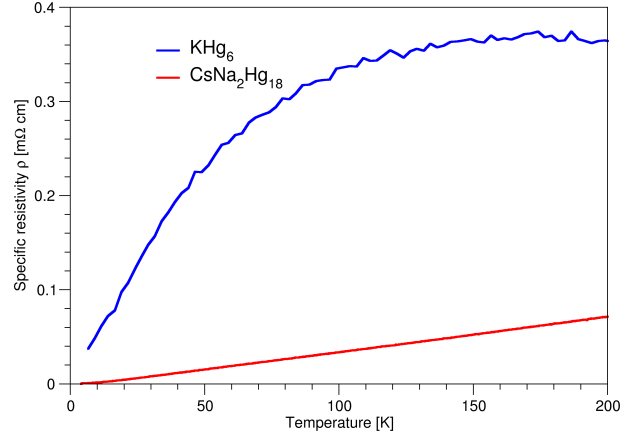


Fig. 4.67: Specific resistivities ρ of KHg_6 (blue) and $\text{CsNa}_2\text{Hg}_{18}$ (red).

4.8.3 Structural Complexity

It is clear that the complexity of the crystal structures in amalgams correlates with their ‘bad metal’ behaviour. However, the broad termination of ‘complex’ crystal structures often encountered in literature is not precise enough. A mathematical approach is found by the definition of complexity measures.^[7,8] These are based on a numerical approach, where structural information is transformed and applied within information theory concepts. This concept then treats the total crystal structure as a graph, containing vertices/nodes (atoms) and edges/links (bonds). The structural information content I_G of a given crystal structure is calculated as the sum of the probabilities of atoms present in a crystallographic orbit of the structure. This information content in [bits/atom] can then be multiplied by the number of atoms per unit cell, yielding $I_{G,total}$ in [bits/unit cell]. Normalisation can be made by as well, leading to the dimensionless $I_{G,norm}$ between 0 and 1. Different approaches can be made when comparing different structures. For structures with a similar composition, a comparison of the information density ($\rho_{inf} = I_{G,total}/V$ seems appropriate, since it accounts for the differences of their unit cells as a consequence of the size differences of their constituting atoms. If different compositions are being considered, their complexities should be compared with focus on either I_G or $I_{G,total}$.

In the following table, the information content of the selected structures is compiled.

Table 4.44: Calculations of the information content in KHg_6 ,^[5] $\text{CsNa}_2\text{Hg}_{18}$, KHg_{11} ,^[6] RbHg_{11} ,^[6] $\text{K}_{1-x}\text{Rb}_x\text{Hg}_{11}$, LiHg ,^[3] LiHg_3 ^[3] and $\text{Na}_{11}\text{Hg}_{52}$.^[9] They were performed with the program package CrystIT.^[10]

	I_G [bits/atom]	$I_{G,total}$ [bits/unit cell]	$I_{G,norm}$	ρ_{inf} [bits/Å ⁻³]
KHg_6	2.81	78.6	0.584	0.106
$\text{CsNa}_2\text{Hg}_{18}$	1.92	40.23	0.436	0.075
KHg_{11}	1.98	71.32	0.383	0.079
RbHg_{11}	1.98	71.32	0.383	0.078
$\text{K}_{1-x}\text{Rb}_x\text{Hg}_{11}$	2.06	74.31	0.399	0.081
LiHg	1.00	2.00	1.00	0.056
LiHg_3	0.811	6.49	0.27	0.040
$\text{Na}_{11}\text{Hg}_{52}$	6.95	3939.03	0.759	0.298

From these values, it becomes clear that the structural complexity clearly has an influence on the ‘bad metal’ behaviour. The comparison of the calculated values explains why the conductivity of the solid solution $K_{1-x}Rb_xHg_{11}$ has a steeper slope, and also why the specific resistivity of $CsNa_2Hg_{18}$ is smaller than the one of KHg_6 . It highlights the reason why $Na_{11}Hg_{52}$ exhibits higher resistivities than either KHg_6 and $CsNa_2Hg_{18}$ (cf. Fig. 4.68). On the other hand, it fails to comprehend the unusually high resistivities measured for the Li-amalgams.

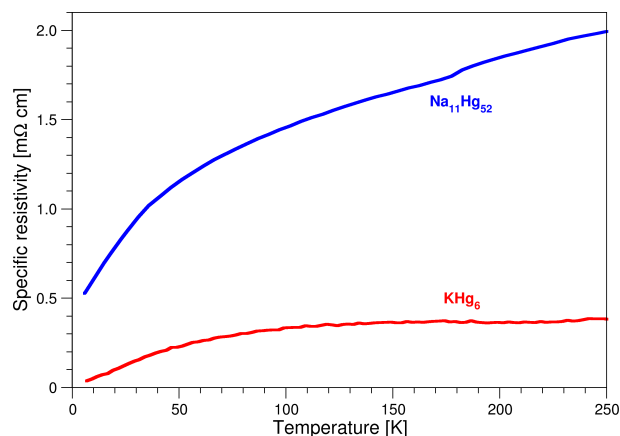


Fig. 4.68: Specific resistivities ρ of KHg_6 (red) and $Na_{11}Hg_{52}$ (blue).

4.8.4 A Qualitative Scale

Based on these comparison, the contributing factors for the ‘bad metal’ behaviour of amalgams can now for the first time be put in qualitative relation to each other. It seems that the that the factor with the highest impact is the polarity, as discussed on the examples of the Li amalgams. This also correlates – to a certain degree – with the Hg content.

Fig. 4.69 (below) compares the specific resistivities of different amalgams previously discussed, as well as those of regular metals.

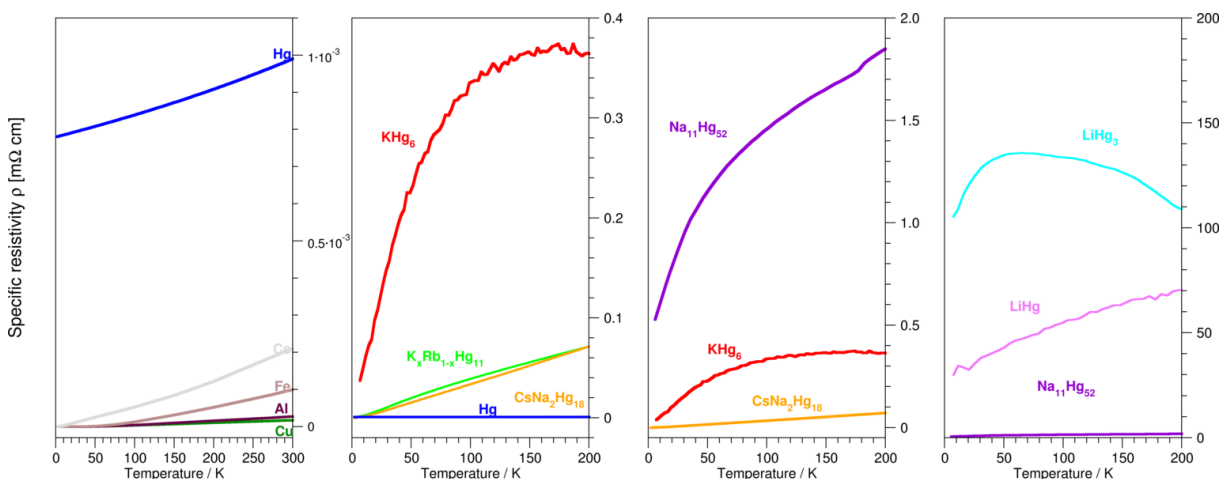


Fig. 4.69: Visualisation of the increasing ‘bad metal’ behaviour in selected amalgams for the relative quantification of the influencing parameters.

Lesser contributions seem to originate from the structural complexity of the amalgams, which is discernible by the comparison of $CsNa_2Hg_{18}$ vs. KHg_6 vs. $Na_{11}Hg_{52}$. So far, the smallest influence seems to be the introduction of disorder, which has been shown in Fig. 4.65.

This can be summarised on a relative scale:



Fig. 4.70: Relative scale for the contribution of the different parameters disorder, structural complexity and degree of electron transfer $\delta^{+/-}$.

References

- [1] R. F. W. Bader, A quantum theory of molecular structure and its applications, *Chem. Rev.* **1991**, *91*, 893–928, DOI: [10.1021/cr00005a013](https://doi.org/10.1021/cr00005a013).
- [2] P. Blaha, K. Schwarz, F. Tran, R. Laskowski, G. Madsen, L. Marks, WIEN2k: An APW+lo program for calculating the properties of solids, *J. Chem. Phys.* **2020**, *152*, 074101, DOI: [10.1063/1.5143061](https://doi.org/10.1063/1.5143061).
- [3] F. Tambornino, *Electrolytic Synthesis and Structural Chemistry of Intermetallic Phases with Polar Metal-Metal Bonding*, Dissertation, LMU München, **2016**.
- [4] J. W. Nielsen, N. C. Baenziger, The Crystal Structures of NaHg₂, NaHg and Na₃Hg₂, *Acta Crystallogr.* **1954**, *7*, 277–282, DOI: [10.1107/S0365110X54000783](https://doi.org/10.1107/S0365110X54000783).
- [5] F. Tambornino, C. Hoch, Bad metal behaviour in the new Hg-rich amalgam KHg₆ with polar metallic bonding, *J. Alloys Compd.* **2015**, *618*, 299–304, DOI: [10.1016/j.jallcom.2014.08.173](https://doi.org/10.1016/j.jallcom.2014.08.173).
- [6] E. Biehl, H.-J. Deiseroth, Darstellung, Strukturchemie und Magnetismus der Amalgame MHg₁₁ (M: K, Rb, Ba, Sr), *Z. Anorg. Allg. Chem.* **1999**, *625*, 1073–1080, DOI: [10.1002/\(SICI\)1521-3749\(199907\)625:7<1073::AID-ZAAC1073>3.0.CO;2-V](https://doi.org/10.1002/(SICI)1521-3749(199907)625:7<1073::AID-ZAAC1073>3.0.CO;2-V).
- [7] S. Krivovichev, Topological complexity of crystal structures: quantitative approach, *Acta Crystallogr.* **2012**, *A68*, 393–398, DOI: [10.1107/S0108767312012044](https://doi.org/10.1107/S0108767312012044).
- [8] S. Krivovichev, Which Inorganic Structures are the Most Complex?, *Angew. Chem. Int. Ed.* **2014**, *53*, 654–661, DOI: [10.1002/anie.201304374](https://doi.org/10.1002/anie.201304374).
- [9] C. Hoch, A. Simon, Na₁₁Hg₅₂: Complexity in a Polar Metal, *Angew. Chem. Int. Ed.* **2012**, *51*, 3262–3265, DOI: [10.1002/anie.201108064](https://doi.org/10.1002/anie.201108064).
- [10] C. Kaußler, G. Kieslich, crystIT: complexity and configurational entropy of crystal structures via information theory, *J. Appl. Crystallogr.* **2021**, *54*, 306–316, DOI: [10.1107/S1600576720016386](https://doi.org/10.1107/S1600576720016386).

5

Summary

Overview

The primary objective of this work was the first systematic study of ternary amalgams containing two different electropositive metals. For this purpose, the huge number of possible candidate systems was first screened by a combination of thermoanalytical measurements and powder X-ray diffraction. The existing methods for the preparation of amalgams had to be adapted to new conditions, and new synthetic routes were established.

The new ternary amalgams were characterised by modern X-ray diffraction techniques, employing single crystal measurements as well as powder diffraction with laboratory and synchrotron radiation. Four different possibilities for ternary amalgams can be expected: (1) new structure types, (2) solid solutions of isotypic binary amalgams, (3) colouring variants of binary structure types and (4) substitutional mixed crystals. For all four cases, examples could be established.

Additionally, the ‘bad metal’ behaviour for a number of amalgams was characterised with a combination of measurements of the specific resistivity, superconductivity, thermal stability and calculations of the electronic structures. With the help of the new ternary amalgams and their comparison to reported and additional new binary compounds, it was for the first time possible to establish the relevant parameters which control the ‘bad metal’ behaviour: structural disorder, structural complexity and the degree of polarity in terms of electron transfer from the electropositive metal to mercury. The interplay is complex, however, and their relative contributions on the overall behaviour could be estimated by chosen examples. Through this, it is now possible to perform targeted experiments in order to deliberately tune the physical properties of amalgams and other polar intermetallics with higher relevance for future applications.

Against this background, summaries of the previous (published and unpublished) results are given in the following.

5.1 Structure and Bonding in $\text{CsNa}_2\text{Hg}_{18}$, a New Ternary Amalgam with strong Coulombic Bonding Contributions

published in: *Crystals* 2022, 12(11), 1679.

Access via: DOI: [10.3390/cryst12111679](https://doi.org/10.3390/cryst12111679)

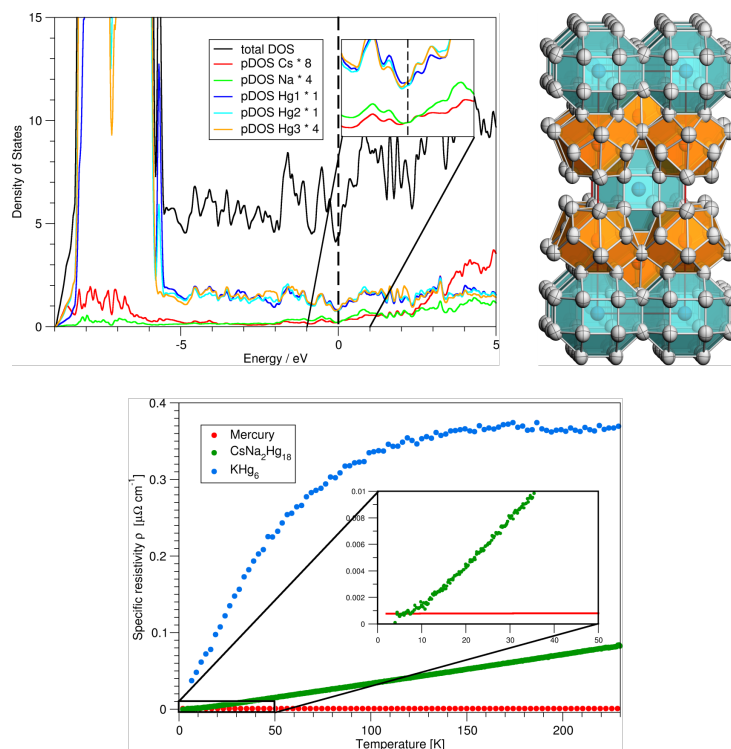


Fig. 5.1: Visualisation of the crystal structure of $\text{CsNa}_2\text{Hg}_{18}$ (top right; Hg: grey, Na: orange, Cs: turquoise), the results of the electronic structure calculations (top left) and comparison of the specific resistivity ρ to KHg_6 and elemental Hg (bottom).

In Chapter 4.1, the synthesis of the new Hg-rich ternary amalgam $\text{CsNa}_2\text{Hg}_{18}$ is discussed. It is a representative of ternary amalgams with a new structure type in the sense of the classification in 5. Via a newly developed synthetic approach – the combination of the elements at temperatures below their crystallisation point and slow thawing to ambient temperatures – it was possible to obtain the first ternary Na-Cs amalgam as a phase-pure product. It crystallises in well-shaped cuboid specimens with a silver-metallic luster and exhibits a tetragonal metric (space group $I4/mmm$, No. 139, $a = 7.3054(7) \text{ \AA}$, $c = 20.046(3) \text{ \AA}$) in a unique structure type. Its structure can be described via the stacking of five nets or alternatively via the packing of two different, hitherto unreported coordination polyhedra: Na is surrounded by a $[\text{NaHg}_{16}]$ snub square antiprism, Cs is surrounded by a $[\text{CsHg}_{20}]$ rhombicuboctahedron. Both descriptions emphasise the unusual bonding situation present in amalgams as an interplay of covalent Hg networks, Coulombic charge distribution and overall metallic properties. Specific resistivity measurements as well as electronic structure calculations have been performed. The different contributions of the s - and p -states to the band structure highlight the interplay of covalent and metallic bonding contributions, while the calculations of the Bader charges determines the degree of the charge transfer from the less noble metals to the Hg network, yielding a further indicator towards the ‘polarity’ of the bonding situation prevalent in this amalgam. The ‘bad metal’ behaviour is surprisingly less pronounced than in other amalgams with a ratio $M : \text{Hg} = 1 : 6$ or with comparable structural complexity.

5.2 Ternary Amalgams: Expanding the Structural Variety of the $Gd_{14}Ag_{51}$ Structure Family

published in: *Z. Krist.* **2023**. in print.

Access via: DOI: [10.1515/zkri-2023-0007](https://doi.org/10.1515/zkri-2023-0007)

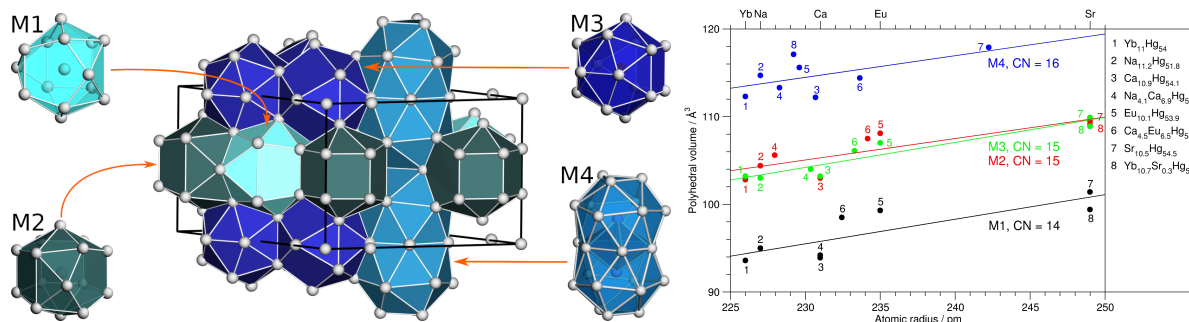


Fig. 5.2: Graphical representation of the different coordination polyhedra of the $Gd_{14}Ag_{51}$ structure family in amalgams (left), and a comparison of atomic radii and polyhedra volumina of the newly discovered ternary variants $Yb_{10.7}Sr_{0.3}Hg_{54}$, $Ca_{4.5}Eu_{6.5}Hg_{54}$ and $Ca_{6.9}Na_{4.1}Hg_{54}$ with the binary representatives (right).

In Chapter 4.2, the structural investigation of the three ternary amalgams $Yb_{10.7}Sr_{0.3}Hg_{54}$, $Ca_{4.5}Eu_{6.5}Hg_{54}$ and $Ca_{6.9}Na_{4.1}Hg_{54}$ is discussed. They represent the first ternary structural variants of the amalgams of the $Gd_{14}Ag_{51}$ structure family, where the known binary amalgams are distinguished by individual disorder phenomena in their crystal structures (except for the Yb amalgam $Yb_{11}Hg_{54}$).^[1–4]

The presented ternary amalgams are derivatives of the binary hettotypes, but the combination of different structural disorder phenomena has not been observed before and cannot be obtained by addition of the ones existing in the binaries. They can therefore be interpreted as representatives of ‘coloured’ variants of the respective binary amalgams.

All three ternary compounds crystallise in the hexagonal space group $P\bar{6}$ (with $a = 3.5811(11)$, $13.5406(8)$ and $13.564(5)$ \AA , $c = 9.7948(12)$, 9.7149 and $9.810(7)$ \AA for the Yb-Sr, Ca-Eu and Ca-Na amalgam, respectively). The individual disorder phenomena concern the four crystallographic positions of the less noble metals, M1–M4. In the Yb-Sr amalgam, the polyhedra M1–M3 are fully occupied by Yb, while only M4 exhibits mixed occupancy of Yb and Sr. In the Ca-Na amalgam, M1 is fully occupied by Ca, all other ccp’s are showing mixed occupancies of Ca and Na. And lastly, in the Ca-Eu amalgam, not only do all polyhedra show different mixed occupancies of Ca and Eu, but also mutually exclusive Hg split positions along the c axis can be observed.

It was shown that in the amalgams, the comparison of the metallic radii with the polyhedra volume of the cation coordination polyhedra (ccp) leads to the conclusion that geometric considerations can only partially explain the appearing disorder phenomena. Electronic contributions will therefore have to be taken into account as well.

In comparison to the reported members of the structure family, the three new ternary amalgams give a direct insight into the role of geometric and electronic parameters on structural complexity as the determining factors of ‘bad metal’ behaviour.

5.3 Influence of Disorder on the ‘Bad Metal’ Behaviour in Polar Amalgams

Published in: *Inorg. Chem.* **2023**, *62*(9), 3965–3975.

Access via: DOI: [10.1021/acs.inorgchem.2c04430](https://doi.org/10.1021/acs.inorgchem.2c04430)

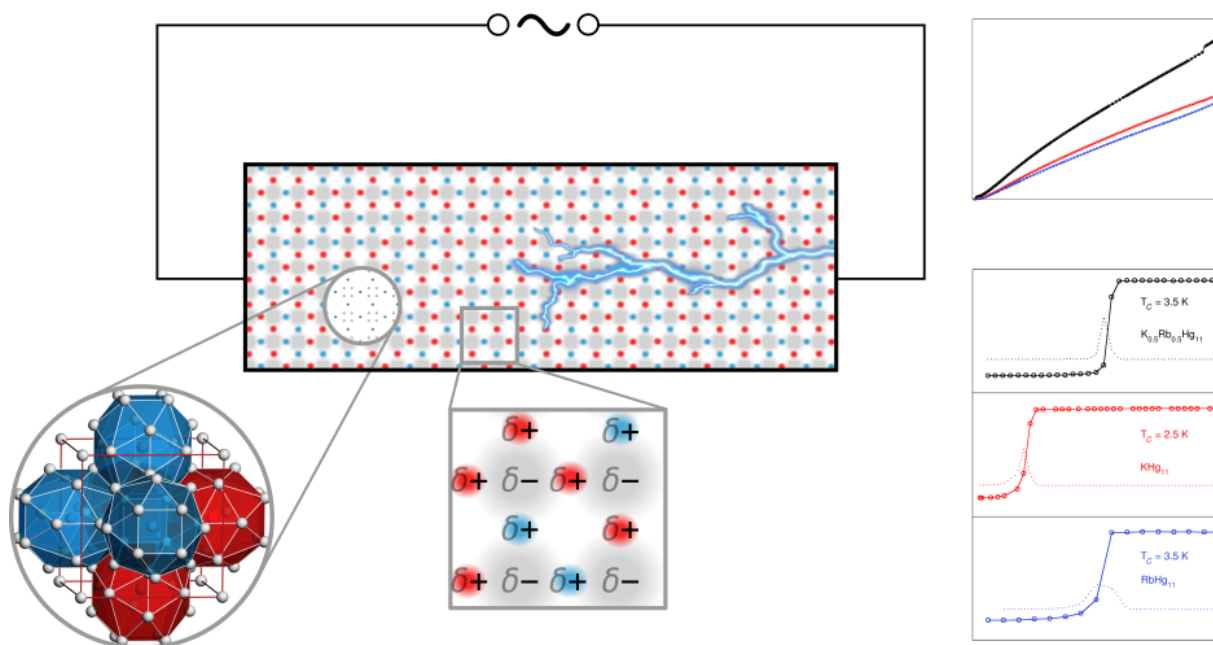


Fig. 5.3: Visualisation of the Vegard-type solid solution of $K_{1-x}Rb_xHg_{11}$, as well as specific resistivity (top right) and magnetic susceptibility measurements (bottom right).

In Chapter 4.3, the influence of structural disorder on the ‘bad metal’ behaviour of polar amalgams is discussed on the basis of two different types of mixed crystals, represented by two newly synthesised ternary amalgams. The first compound, $K_{1-x}Rb_xHg_{11}$ (with $x = 0.472(2)$, cubic, space group $Pm\bar{3}m$, $a = 9.69143(3)$ Å, Rietveld refinement from synchrotron powder diffraction data), a Vegard-type mixed crystal (or solid solution) contains disorder in the sense that the single crystallographic position of the less-noble metal atom (Rb or K) in the isotypic structures of the $BaHg_{11}$ structure type exhibits a statistically mixed occupancy, mirroring the original weighing scheme. In the second compound, $Cs_{3-x}Ca_xHg_{20}$ (with $x = 0.20(3)$, cubic, space group $Pm\bar{3}m$, $a = 10.89553(14)$ Å, Rietveld refinement from X-ray powder diffraction data), disorder can be observed by the introduction of about 6% Ca on the single crystallographic position for Cs. This compound represents an example of a substitutional mixed crystal, since no isotypic structure of the Rb_3Hg_{20} type has been found for Ca.

The investigation of their physicochemical properties (i.e. specific resistivity and magnetic susceptibility), thermoanalysis and the calculation of electronic structures have been performed. By comparison of the specific resistivities and the calculated electronic structures, it can be shown that structural disorder has a significant, but rather minor effect on the ‘bad metal’ behaviour.

5.4 The Hg-rich part of the Binary System, K–Hg revised: Synthesis, Crystal and Electronic Structures of KHg_4 , KHg_5 and KHg_8

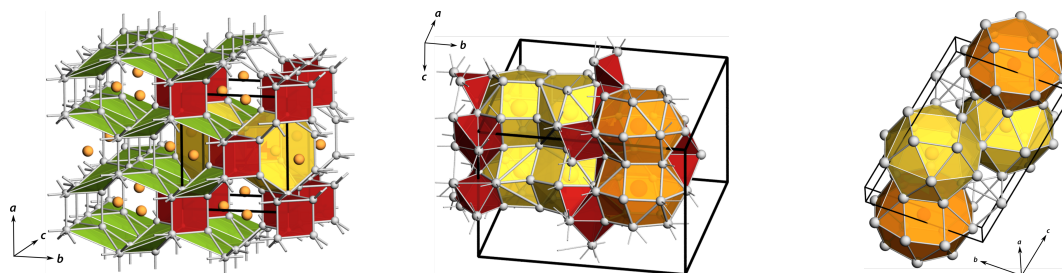


Fig. 5.4: Crystal structures of the new binary potassium amalgams KHg_4 (left), KHg_5 (middle) and KHg_8 (right). Cation coordination polyhedra around K are coloured in yellow/orange, polyhedra by Hg in red and green. Hg: grey, unit cell: black.

The synthesis and structural characterisation of three new Hg-rich binary potassium amalgams is reported. Each structure crystallises in a new structure type (KHg_4 : orthorhombic, space group $Cmcm$ (No. 63), $a = 9.374(3)$, $b = 8.735(3)$, $c = 6.456(2)$ Å; KHg_5 : monoclinic, space group $P2_1/c$ (No. 14), $a = 11.4832(10)$, $b = 17.5862(15)$, $c = 10.3152(9)$ Å, $\beta = 116.6871(11)^\circ$ and KHg_8 : triclinic, space group $P\bar{1}$ (No. 2), $a = 6.3001(17)$, $b = 8.9723(19)$, $c = 12.637(3)$ Å, $\alpha = 99.30(3)$, $\beta = 91.34(3)$, $\gamma = 98.36(3)^\circ$, respectively). In all structures, previously unobserved cationic coordination environments with CN = 16+2 (KHg_4), 17+1/18+1 (KHg_5) and 18 (KHg_8) are present. The trend of higher coordination numbers can also be visualised by net representation of the amalgams:

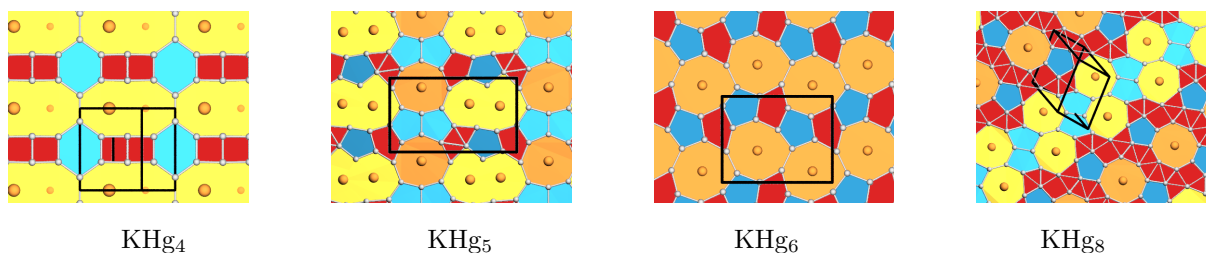


Fig. 5.6: Net representation of selected binary potassium amalgams with increasing Hg content. Unit cell: black, Hg atoms: grey, K atoms: orange. Octagons are depicted in orange, merged octagons or heptagons in yellow, capping penta- or hexagons in blue, while interstitial polygons are depicted in red.

Electronic calculations emphasise the partial electron transfer from the less noble alkali metal to the Hg network. Based on the combination of thermoanalysis and powder diffraction experiments, the Hg-rich part of the binary K–Hg phase diagram was revised, again indicating the impact of new preparation techniques on a deeper understanding of phase formation and phase relations.

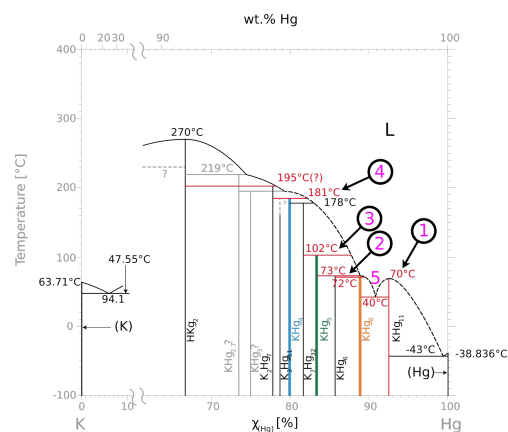


Fig. 5.5: Revised K–Hg phase diagram with an emphasis on the Hg-rich part of the system. Newly assigned data as well as points of interest are colour-differentiated.

5.5 SrHg_{5.86} – a new binary Sr amalgam

The synthesis and crystal structure determination of the new binary Sr-amalgam SrHg_{5.86} is reported. Starting from a ternary weighing stoichiometry (Na:Sr:Hg = 1:1:22), needle-shaped specimens of the title compound were isolated, next to trigonal platelets of Na₁₁Hg₅₂. The structure with an orthorhombic unit cell (space group *Pnma*, No. 62, $a = 13.5123(11)$ Å, $b = 5.007(2)$ Å, $c = 10.389(4)$ Å) is isotypic to other known binary amalgams with this M :Hg ratio (BaHg₆, KHg₆).^[5,6] Due to an underoccupancy of one of the six crystallographic sites for Hg, this amalgam is best described with the nominal sum formula SrHg_{6-x}.

In order to find a reason of this underoccupancy, electronic calculations of the fully ordered model (SrHg₆) were performed. While the exact reason for the lower occupancy of the one atomic Hg site could not be taken directly from details of the DOS, the calculation of the Bader charges for the fully ordered model revealed an significantly higher charge for the alkaline earth atom than in the isotypical BaHg₆. Together with the fact that this position exhibits the highest number of Hg atoms in its coordination sphere (i.e. the most metallic position where high coulombic partial charges are unfavourable), this corroborates the need for the underoccupancy.

This study highlights again how new preparative approaches can yield new phases in well-studied systems. The example of SrHg_{6-x} is a very instructive model for the direct interplay of structural disorder and electronic structure.

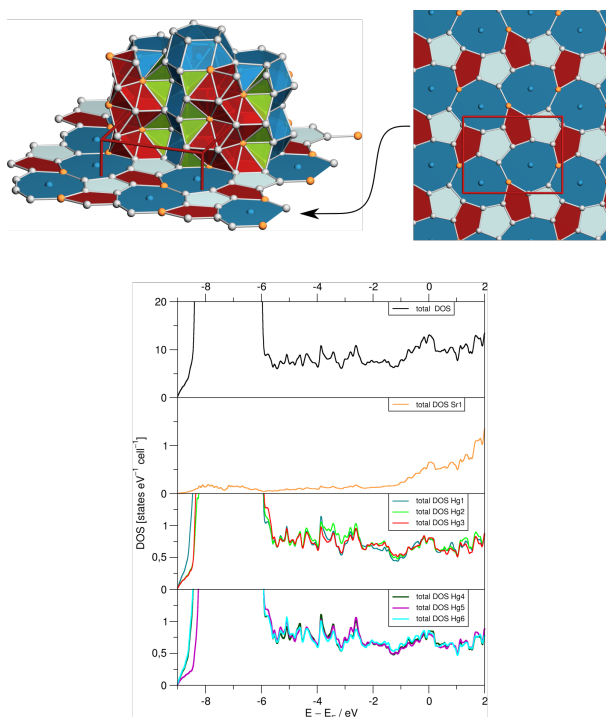


Fig. 5.7: Visualisation of the crystal structure of SrHg_{5.86} by the stacking of nets (top right) or polyhedra (top left) and the electronic structure calculation results for the fully ordered model SrHg₆. (bottom)

5.6 Cyclic Voltammetry as a Tool for the targeted Synthesis of Ternary Amalgams via Electrocrystallisation

Due to the different reduction potential of metals, synthesis of ternary amalgams via electrocrystallisation is difficult. But since their potentials depend on concentration, they can be adjusted. During the scope of this thesis, first attempts for the determination of concentration-dependent reduction potentials of Na^+ and K^+ have been performed on their iodides in DMF via cyclic voltammetry (CV). Based on these data, an electrocrystallisation experiment with a mixture of NaI/KI was performed. Via X-ray diffraction experiments on powder samples and single crystals, the (preliminarily determined) crystal structure represents a new member of the $\text{Gd}_{14}\text{Ag}_{51}$ structure family with close relation to the crystal structure of $\text{Na}_{11}\text{Hg}_{52}$, but with manifold and new disorder phenomena. By this, it was proven that the electrocrystallisation method, once developed for the synthesis of binary amalgams, can in principle be adapted so that it is equally useful for the synthesis of ternary amalgams.

5.7 The first Be-containing Amalgam?

Parts published in: *Z. Naturforsch.* **2020**, *75b*, 509–516.

Access via: DOI: [10.1515/znb-2020-0035](https://doi.org/10.1515/znb-2020-0035)

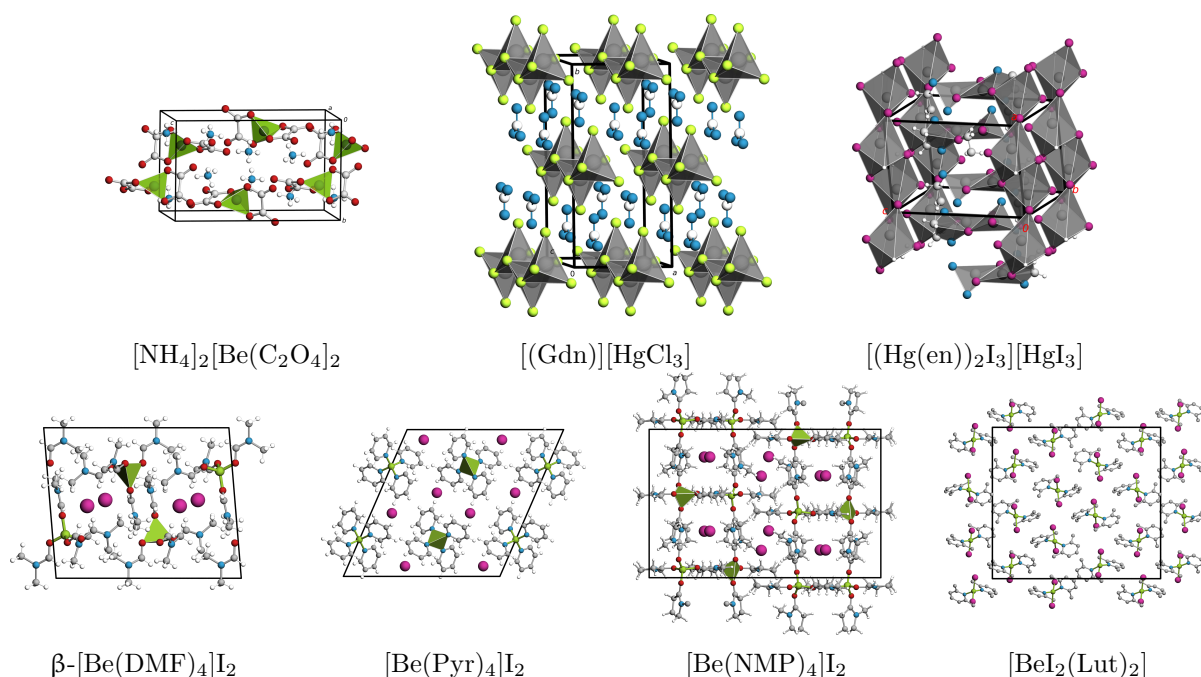


Fig. 5.8: Crystal structures of new complex salts of Be and Hg discovered within the Bachelor thesis (top row) and new solvate complexes of Be (bottom row).

The thermochemical approach via decomposition of precursor complexes did not yield any promising results, and neither did electrocrystallisation experiments in ‘classical’ organic solvents. While the experimental attempts yielded several new complex salts of mercury and beryllium (see Chapter 4.7), advanced experimental techniques were tested. So far, the electrolysis of BeI_2 in liquid ammonia seems the most promising approach. Reproducibly, a metallic, crystalline product was obtained and most probably represents the first beryllium amalgam. However, its extreme sensitivity made characterisation via X-ray diffraction experiments unsuccessful within the scope of this work.

5.8 The ‘Bad Metal’ Behaviour and its Contributing Factors

Three main parameters are contributing for the observed ‘bad metal’ behaviour in amalgams:

- Polarity in the sense of the electron transfer δ in $M^{\delta+}[\text{Hg}_n]^{\delta-}$
- Structural complexity
- Structural disorder

Through comparison of the ‘bad metal’ behaviour in amalgams synthesised in this work with already reported phases, these variables can thus be analysed independently of each other. While a clear separation of these parameters is not always possible, they can now be sorted on a relative scale, particularities have been discussed in Chapter 4.8.

For the first time, these parameters can not only be identified, but also put in a qualitative scale based on our results. There are indications that the degree of polarity (i.e. the exact partial charge) has the biggest influence on the ‘bad metal’ behaviour in amalgams, followed by structural complexity. The smallest impact seems to be contributed by the introduction of structural disorder, since this in turn has small consequences on the structural complexity.



Fig. 5.9: Relative scale for the contribution of the different parameters disorder, structural complexity and degree of electron transfer $\delta^{+/-}$.

Since we have shown that these parameters can be directly influenced by chemical means (Hg content, choice of the electropositive metal, formation of mixed crystals, etc.), the deliberate tailoring of the ‘bad metal’ behaviour in polar intermetallics appears to be feasible in the nearer future.

References

- [1] A. V. Tkachuk, A. Mar, Alkaline-Earth Metal Mercury Intermetallics, $A_{11-x}\text{Hg}_{54+x}$ ($A = \text{Ca}, \text{Sr}$), *Inorg. Chem.* **2008**, *47*, 1313–1318, DOI: [10.1021/ic7015148](https://doi.org/10.1021/ic7015148).
- [2] C. Hoch, A. Simon, $\text{Na}_{11}\text{Hg}_{52}$: Complexity in a Polar Metal, *Angew. Chem. Int. Ed.* **2012**, *51*, 3262–3265, DOI: [10.1002/anie.201108064](https://doi.org/10.1002/anie.201108064).
- [3] F. Tambornino, C. Hoch, The Mercury-richest Europium Amalgam $\text{Eu}_{10}\text{Hg}_{55}$, *Z. Anorg. Allg. Chem.* **2015**, *641*, 537–542, DOI: [10.1002/zaac.201400561](https://doi.org/10.1002/zaac.201400561).
- [4] F. Tambornino, C. Hoch, The simplest representative of a complex series: the Hg-rich amalgam $\text{Yb}_{11}\text{Hg}_{54}$, *Z. Kristallogr.* **2017**, *232*, 557–565, DOI: [10.1515/zkri-2016-2036](https://doi.org/10.1515/zkri-2016-2036).
- [5] M. Wendorff, C. Röhr, The new barium mercuride BaHg_6 and ternary indium and gallium derivatives, *J. Alloys Compd.* **2013**, *546*, 320–328, DOI: [10.1016/j.jallcom.2012.07.101](https://doi.org/10.1016/j.jallcom.2012.07.101).
- [6] F. Tambornino, C. Hoch, Bad metal behaviour in the new Hg-rich amalgam KHg_6 with polar metallic bonding, *J. Alloys Compd.* **2015**, *618*, 299–304, DOI: [10.1016/j.jallcom.2014.08.173](https://doi.org/10.1016/j.jallcom.2014.08.173).

6

Outlook

The first systematic approach to synthesis, structural and physicochemical characterisation of ternary amalgams with two different electropositive metals has proven to be fruitful. The initial screening of promising systems was designed in a way that ternary phases with high formation enthalpies were favourably detected. This can be taken as a starting point for further investigations going more into detail and reveal new phases with more delicate formation conditions. For those phases, the newly developed preparation routes can be applied.

Especially the electrochemical synthesis shows a high potential. The determination of the exact reduction potentials, which then serve as the basis for the calculation of necessary concentrations for the simultaneous electrocrystallisation experiments, is crucial. Since the electrodes used are hand-made, experiments with standard electrodes, as well as the usage of a standard reference electrode instead of a pseudo-reference electrode should guarantee reliable, reproducible results. Furthermore, the current apparatus for the electrocrystallisations should be modified in a manner that allows for the inclusion of such a standard reference electrode in order to enable the precise observation and direct manipulation of the overall potential of the system.

The revision of binary systems with the aid of new preparative strategies will be lucrative. As shown on the examples of the new binary amalgams of Sr and K, the reported binary phase diagrams of amalgams of the less noble metals are still incomplete. Through the combination of thermoanalysis and X-ray powder diffraction, newly found phases can be integrated into the phase diagrams. As a first step, the phase-pure syntheses of the Hg-rich compounds $\text{SrHg}_{5.86}$ and KHg_8 for the determination of their physical properties should be performed. A new preparative procedure for the screening of the Hg-rich part of a binary system has already been developed for the investigation of the K–Hg system and is depicted in Fig. 7.1 (p. 141). The idea is to put a large amount of the Hg-richest amalgam on a coarse glass frit and slowly heat until the amalgam undergoes a peritectic decomposition. The Hg-rich melt is then separated via the frit while the remaining Hg-poorer amalgam can be analysed. Then, it is reheated until the next peritectic decomposition, and this process is continued until the first congruently melting phase is reached. This typically has a composition $M\text{Hg}$ or $M\text{Hg}_2$. A complementary access to new phases would be a modified electrocrystallisation procedure: The exact weight of the Hg used on the amalgamated copper spoon has to be determined, and the amount of available e.g. K^+ in the electrolyte limited accordingly – the electrolysis stops automatically if one of the metals has been completely depleted. The temperature of the electrocrystallisation has to be kept above the decomposition temperature of the Hg-richer amalgam, ideally only by 1 °C. The composition of the final product is then limited by the ‘weighing scheme’ and should in theory allow for the crystallisation of KHg_8 .

Following the example of the Vegard-type mixed crystal series $K_{1-x}Rb_xHg_{11}$ in Chapter 4.3, several other solid solutions should be of interest according to pairs of isotypic binary amalgams with M atoms with radius quotients close to 1. Table 6.1 (right) shows potential systems where the formation of solid solutions seems possible. Indicators for the presence of solid solutions in the shown system so far exists for the system $Cs_{5-x}Rb_xHg_{19}$ (TH011-1, TH074, TH083), but attempts of confirmation via Rietveld refinement on the basis of Synchrotron powder data have been unsuccessful so far. These systems would allow further investigation of the influence of structural disorder on the ‘bad metal’ behaviour with negligible contributions by structural complexity or differences in polarity.

Table 6.1: Comparison of isotypic binary amalgams for future investigations, sorted by increasing Hg content (with $Hg:M \geq 2$) and atomic number within the same main group. Li, Be, Na and Mg are omitted. Gray indicates the same nominal sum formula, but a diverging crystal structure.

	K	Rb	Cs	Ca	Sr	Ba
MHg_3						
M_2Hg_7						
M_5Hg_{19}						
M_7Hg_{31}						
$MHg_{\sim 6}$						
M_3Hg_{20}						
MHg_{11}						

As additional and complementary tools for the characterisation of the ‘bad metal’ behaviour, solid state NMR measurements on ^{119}Hg can be of great value, since they allow for the exact quantification of the electron transfer and hence a quantification of the polarity in amalgams. Initial, very promising experiments have been performed on the series of Li amalgams. A supplementary method for the quantification of polarity is the measurement of the Hall coefficient. This allows for the quantification of the free charge carrier concentration, an additional parameter influencing the ‘bad metal’ behaviour which has so far been neglected. A screening of reported and new amalgams with this respect is necessary for a more detailed insight. Extensive electronic calculations will have to be performed for the binary and ternary representatives of the $Gd_{14}Ag_{51}$ structure family as well, since this might give additional insight about the underlying reasons for the observed disorder patterns in their crystal structures. These analyses should be performed on selected, literature-known amalgams as well.

Lastly, the electrocrystallisation experiment of BeI_2 in liquid ammonia should be repeated, but with modifications: (1) the electrode should be washed with liquid ammonia to remove excess Be salts and (2) reattempting the isolation of single crystals directly from the apparatus without interrupting the cold chain. This way, the verification of the existence as well as the structural characterisation of the elusive Be amalgam is in direct reach.

Based on the results of this work, the qualitative influence of the factors influencing the ‘bad metal’ behaviour could be discovered. Through systematic preparative efforts and complementing quantum-mechanical calculations, we are confident that the last steps in the unraveling of the structure-property relations in polar metals can soon be taken, enabling a targeted design of substances with the desired physical properties.

7

Appendix

7.1 Crystallographic Data

7.1.1 β -[Be(DMF)₄]I₂

Table 7.1: Standardised fractional atomic coordinates^[1] and equivalent isotropic displacement parameters [\AA^2] for β -[Be(DMF)₄]I₂ (**1**). The equivalent isotropic displacement parameter is defined as 1/3 of the trace of the anisotropic displacement tensor. Standard deviations in units of the last digit are given in parentheses.

Atom	<i>x</i>	<i>y</i>	<i>z</i>	<i>U</i> _{equiv}
Be1	0.2113(2)	0.2429(2)	0.43116(15)	0.0220(4)
I1	0.01991(2)	0.89923(2)	0.30024(2)	0.03073(5)
I2	0.56530(2)	0.24838(2)	0.35936(2)	0.02567(4)
O1	0.26570(10)	0.31616(11)	0.01930(8)	0.0247(3)
N1	0.41223(12)	0.37744(13)	0.10217(10)	0.0238(3)
C11	0.36530(15)	0.33584(15)	0.02959(11)	0.0235(3)
H11	0.4071	0.3200	-0.0165	0.028
C12	0.3531(2)	0.4046(2)	0.17809(11)	0.0284(4)
H12A	0.3610	0.4851	0.1917	0.043
H12B	0.3810	0.3596	0.2274	0.043
H12C	0.2784	0.3870	0.1650	0.043
C13	0.5279(2)	0.4018(2)	0.11020(14)	0.0327(4)
H13A	0.5588	0.3767	0.0581	0.049
H13B	0.5612	0.3613	0.1600	0.049
H13C	0.5392	0.4832	0.1178	0.049
O2	0.23849(10)	0.16597(11)	0.34789(8)	0.0246(3)
N2	0.21126(13)	0.11475(13)	0.20537(10)	0.0260(3)
C21	0.18095(15)	0.16202(15)	0.27631(11)	0.0229(3)
H21	0.1128	0.1948	0.2741	0.027
C22	0.1353(2)	0.1054(2)	0.12827(12)	0.0366(5)
H22A	0.0981	0.0330	0.1295	0.055
H22B	0.1734	0.1095	0.0764	0.055
H22C	0.0844	0.1675	0.1281	0.055
C23	0.3137(2)	0.0586(3)	0.20359(19)	0.0698(10)
H23A	0.3636	0.0916	0.2477	0.105
H23B	0.3401	0.0689	0.1470	0.105
H23C	0.3057	-0.0223	0.2149	0.105
O3	0.08361(10)	0.25676(11)	0.43881(8)	0.0231(3)
N3	0.08416(12)	0.69135(13)	0.04881(10)	0.0230(3)
C31	0.01652(14)	0.1755(2)	0.44017(11)	0.0243(3)
H31	0.0406	0.1004	0.4329	0.029
C32	0.1586(2)	0.5947(2)	0.04325(15)	0.0328(4)
H32A	0.1255	0.5253	0.0623	0.049
H32B	0.2230	0.6096	0.0801	0.049
H32C	0.1760	0.5857	-0.0163	0.049
C33	0.1249(2)	0.8061(2)	0.0348(2)	0.0533(7)
H33A	0.0876	0.8606	0.0685	0.080
H33B	0.1139	0.8252	-0.0262	0.080
H33C	0.2003	0.8085	0.0530	0.080
O4	0.26221(10)	0.37102(11)	0.42331(8)	0.0244(3)

continued on the next page

Atom	<i>x</i>	<i>y</i>	<i>z</i>	<i>U_{equiv}</i>
N4	0.27335(13)	0.54643(14)	0.36165(10)	0.0265(3)
C41	0.22179(15)	0.4517(2)	0.37686(11)	0.0234(3)
H41	0.1517	0.4434	0.3521	0.028
C42	0.2210(2)	0.6394(2)	0.3093(2)	0.0438(5)
H42A	0.1497	0.6160	0.2885	0.066
H42B	0.2617	0.6559	0.2602	0.066
H42C	0.2173	0.7073	0.3448	0.066
C43	0.6156(2)	0.0644(2)	0.10402(15)	0.0379(5)
H43A	0.6141	0.1081	0.0507	0.057
H43B	0.5779	0.1059	0.1463	0.057
H43C	0.5816	-0.0089	0.0925	0.057

Table 7.2: Coefficients of the anisotropic displacement parameters [\AA^2] for β -[Be(DMF)₄]₂ (**1**). U_{ij} is defined as $U_{ij} = \exp -2\pi^2 [U_{11}(ha^*)^2 + \dots + 2U_{21}hka^*b^*]$. Standard deviations in units of the last digit are given in parentheses.

Atom	U_{11}	U_{22}	U_{33}	U_{23}	U_{13}	U_{12}
Be1	0.0229(11)	0.0238(11)	0.0187(10)	0	-0.0017(8)	-0.0006(8)
I1	0.03377(7)	0.02479(7)	0.03230(7)	-0.00043(5)	-0.00536(5)	-0.00294(5)
I2	0.02199(6)	0.02735(7)	0.02774(7)	0.00586(4)	0.00255(4)	0.00226(4)
O1	0.0253(6)	0.0293(7)	0.0189(6)	-0.0042(5)	-0.0022(5)	0.0017(5)
N1	0.0263(8)	0.0240(7)	0.0203(7)	-0.0026(6)	-0.0028(6)	0.0023(6)
C11	0.0278(9)	0.0230(8)	0.0193(7)	-0.0012(6)	-0.0003(6)	0.0031(7)
C12	0.0365(10)	0.0306(10)	0.0173(8)	-0.0046(7)	-0.0023(7)	0.0061(8)
C13	0.0274(9)	0.0371(11)	0.0324(10)	-0.0058(8)	-0.0053(8)	-0.0034(8)
O2	0.0252(6)	0.0276(7)	0.0205(6)	-0.0037(5)	-0.0023(5)	0.0022(5)
N2	0.0353(8)	0.0223(7)	0.0202(7)	-0.0006(6)	0.0018(6)	0.0038(6)
C21	0.0264(8)	0.0217(8)	0.0204(8)	0.0013(6)	0.0007(6)	0.0012(7)
C22	0.0554(13)	0.0359(11)	0.0174(8)	-0.0021(8)	-0.0027(8)	0.0040(10)
C23	0.059(2)	0.103(3)	0.0457(14)	-0.029(2)	-0.0072(12)	0.049(2)
O3	0.0236(6)	0.0259(6)	0.0195(6)	-0.0010(5)	-0.0006(5)	-0.0013(5)
N3	0.0231(7)	0.0239(7)	0.0216(7)	-0.0006(6)	-0.0007(5)	-0.0007(6)
C31	0.0240(8)	0.0236(8)	0.0246(8)	-0.0035(7)	-0.0028(7)	0.0013(7)
C32	0.0243(9)	0.0308(10)	0.0425(11)	-0.0002(8)	-0.0030(8)	0.0039(8)
C33	0.0318(11)	0.0284(11)	0.101(2)	0.0083(13)	0.0159(13)	-0.0052(9)
O4	0.0270(6)	0.0237(6)	0.0218(6)	0.0003(5)	-0.0020(5)	-0.0038(5)
N4	0.0304(8)	0.0221(7)	0.0278(7)	-0.0016(6)	0.0074(6)	0.0007(6)
C41	0.0254(8)	0.0255(9)	0.0199(8)	-0.0023(7)	0.0048(6)	0.0006(7)
C42	0.0458(13)	0.0304(11)	0.0562(14)	0.0147(10)	0.0103(11)	0.0062(10)
C43	0.0366(11)	0.0305(10)	0.0459(12)	0.0025(9)	0.0003(9)	0.0114(9)

7.1.2 [Be(Pyr)₄]₂

Table 7.3: Standardised fractional atomic coordinates^[4] and equivalent isotropic displacement parameters [\AA^2] for [Be(Pyr)₄]₂ (**2**). The equivalent isotropic displacement parameter is defined as 1/3 of the trace of the anisotropic displacement tensor. Standard deviations in units of the last digit are given in parentheses.

Atom	<i>x</i>	<i>y</i>	<i>z</i>	<i>U_{equiv}</i>
I1	0.36534(2)	0.19194(2)	0.43023(2)	0.05936(10)
Be1	0	0.5327(5)	$\frac{1}{4}$	0.0373(6)
N1	0.05573(9)	0.3922(2)	0.21623(9)	0.0391(3)
C11	0.01539(14)	0.2853(3)	0.15407(14)	0.0507(5)
H11	-0.0409	0.2971	0.1278	0.061
C12	0.0544(2)	0.1595(4)	0.1282(2)	0.0612(6)
H12	0.0248	0.0874	0.0852	0.073
C13	0.1372(2)	0.1413(4)	0.1661(2)	0.0591(6)
H13	0.1645	0.0573	0.1491	0.071

continued on the next page

Atom	<i>x</i>	<i>y</i>	<i>z</i>	<i>U_{equiv}</i>
C14	0.17946(15)	0.2488(4)	0.2296(2)	0.0575(6)
H14	0.2358	0.2389	0.2562	0.069
C15	0.13685(12)	0.3721(3)	0.25328(12)	0.0465(4)
H15	0.1655	0.4440	0.2966	0.056
N2	0.43534(10)	0.1700(2)	0.17618(10)	0.0392(3)
C21	0.3864(2)	0.2785(3)	0.19701(15)	0.0522(5)
H21	0.3888	0.2737	0.2488	0.063
C22	0.3796(2)	0.2959(5)	0.0464(2)	0.0752(9)
H22	0.3782	0.3004	-0.0050	0.090
C23	0.3302(2)	0.4043(4)	0.0674(2)	0.0667(7)
H23	0.2951	0.4828	0.0307	0.080
C24	0.3337(2)	0.3944(4)	0.1439(2)	0.0635(6)
H24	0.3006	0.4660	0.1595	0.076
C25	0.43141(15)	0.1800(3)	0.10157(14)	0.0536(5)
H25	0.4644	0.1069	0.0864	0.064

Table 7.4: Coefficients of the anisotropic displacement parameters [\AA^2] for $[\text{Be}(\text{Pyr})_4]\text{I}_2$ (**2**). U_{ij} is defined as $U_{ij} = \exp[-2\pi^2(U_{11}(ha^*)^2 + \dots + 2U_{21}hka^*b^*)]$. Standard deviations in units of the last digit are given in parentheses.

Atom	U_{11}	U_{22}	U_{33}	U_{23}	U_{13}	U_{12}
I1	0.05528(12)	0.06351(13)	0.04890(12)	0.00295(7)	0.00981(7)	-0.01271(7)
Be1	0.0348(14)	0.045(2)	0.0320(14)	0	0.0127(11)	0
N1	0.0362(7)	0.0459(8)	0.0336(7)	-0.0012(6)	0.0122(6)	0.0021(6)
C11	0.0433(10)	0.0597(13)	0.0430(10)	-0.0100(9)	0.0107(8)	0.0029(9)
C12	0.0717(16)	0.0595(14)	0.0494(12)	-0.0151(10)	0.0208(11)	0.0046(12)
C13	0.0692(15)	0.0595(13)	0.0526(12)	0.0056(11)	0.0286(12)	0.0237(12)
C14	0.0463(11)	0.0681(14)	0.0548(13)	0.0082(11)	0.0166(10)	0.0194(11)
C15	0.0384(9)	0.0568(11)	0.0396(9)	0.0008(8)	0.0108(7)	0.0044(8)
N2	0.0407(8)	0.0426(8)	0.0343(7)	0.0020(6)	0.0151(6)	0.0034(6)
C21	0.0586(12)	0.0546(12)	0.0454(11)	0.0005(9)	0.0228(10)	0.0133(10)
C22	0.078(2)	0.104(2)	0.0451(12)	0.0295(14)	0.0265(13)	0.027(2)
C23	0.0629(14)	0.0642(15)	0.0614(15)	0.0212(12)	0.0124(12)	0.0148(12)
C24	0.0677(15)	0.0544(13)	0.0653(15)	0.0024(11)	0.0233(12)	0.0219(12)
C25	0.0522(11)	0.0732(15)	0.0399(10)	0.0110(10)	0.0230(9)	0.0156(10)

7.1.3 $[\text{Be}(\text{NMP})_4]\text{I}_2$

Table 7.5: Standardised fractional atomic coordinates^[1] and equivalent isotropic displacement parameters [\AA^2] for $[\text{Be}(\text{NMP})_4]\text{I}_2$ (**3**). The equivalent isotropic displacement parameter is defined as 1/3 of the trace of the anisotropic displacement tensor. Standard deviations in units of the last digit are given in parentheses.

Atom	<i>x</i>	<i>y</i>	<i>z</i>	<i>U_{equiv}</i>
I1	0.36534(2)	0.19194(2)	0.43023(2)	0.05936(10)
Be1	0	0.5327(5)	$\frac{1}{4}$	0.0373(6)
N1	0.05573(9)	0.3922(2)	0.21623(9)	0.0391(3)
C11	0.01539(14)	0.2853(3)	0.15407(14)	0.0507(5)
H11	-0.0409	0.2971	0.1278	0.061
C12	0.0544(2)	0.1595(4)	0.1282(2)	0.0612(6)
H12	0.0248	0.0874	0.0852	0.073
C13	0.1372(2)	0.1413(4)	0.1661(2)	0.0591(6)
H13	0.1645	0.0573	0.1491	0.071
C14	0.17946(15)	0.2488(4)	0.2296(2)	0.0575(6)
H14	0.2358	0.2389	0.2562	0.069
C15	0.13685(12)	0.3721(3)	0.25328(12)	0.0465(4)
H15	0.1655	0.4440	0.2966	0.056
N2	0.43534(10)	0.1700(2)	0.17618(10)	0.0392(3)

continued on the next page

Atom	<i>x</i>	<i>y</i>	<i>z</i>	<i>U_{equiv}</i>
C21	0.3864(2)	0.2785(3)	0.19701(15)	0.0522(5)
H21	0.3888	0.2737	0.2488	0.063
C22	0.3796(2)	0.2959(5)	0.0464(2)	0.0752(9)
H22	0.3782	0.3004	-0.0050	0.090
C23	0.3302(2)	0.4043(4)	0.0674(2)	0.0667(7)
H23	0.2951	0.4828	0.0307	0.080
C24	0.3337(2)	0.3944(4)	0.1439(2)	0.0635(6)
H24	0.3006	0.4660	0.1595	0.076
C25	0.43141(15)	0.1800(3)	0.10157(14)	0.0536(5)
H25	0.4644	0.1069	0.0864	0.064

Table 7.6: Coefficients of the anisotropic displacement parameters [\AA^2] for $[\text{Be}(\text{NMP})_4]\text{I}_2$ (**3**). U_{ij} is defined as $U_{ij} = \exp -2\pi^2[U_{11}(ha^*)^2 + \dots + 2U_{21}hka^*b^*]$. Standard deviations in units of the last digit are given in parentheses.

Atom	U_{11}	U_{22}	U_{33}	U_{23}	U_{13}	U_{12}
I1	0.05528(12)	0.06351(13)	0.04890(12)	0.00295(7)	0.00981(7)	-0.01271(7)
Be1	0.0348(14)	0.045(2)	0.0320(14)	0	0.0127(11)	0
N1	0.0362(7)	0.0459(8)	0.0336(7)	-0.0012(6)	0.0122(6)	0.0021(6)
C11	0.0433(10)	0.0597(13)	0.0430(10)	-0.0100(9)	0.0107(8)	0.0029(9)
C12	0.0717(16)	0.0595(14)	0.0494(12)	-0.0151(10)	0.0208(11)	0.0046(12)
C13	0.0692(15)	0.0595(13)	0.0526(12)	0.0056(11)	0.0286(12)	0.0237(12)
C14	0.0463(11)	0.0681(14)	0.0548(13)	0.0082(11)	0.0166(10)	0.0194(11)
C15	0.0384(9)	0.0568(11)	0.0396(9)	0.0008(8)	0.0108(7)	0.0044(8)
N2	0.0407(8)	0.0426(8)	0.0343(7)	0.0020(6)	0.0151(6)	0.0034(6)
C21	0.0586(12)	0.0546(12)	0.0454(11)	0.0005(9)	0.0228(10)	0.0133(10)
C22	0.078(2)	0.104(2)	0.0451(12)	0.0295(14)	0.0265(13)	0.027(2)
C23	0.0629(14)	0.0642(15)	0.0614(15)	0.0212(12)	0.0124(12)	0.0148(12)
C24	0.0677(15)	0.0544(13)	0.0653(15)	0.0024(11)	0.0233(12)	0.0219(12)
C25	0.0522(11)	0.0732(15)	0.0399(10)	0.0110(10)	0.0230(9)	0.0156(10)

7.1.4 $[\text{BeI}_2(\text{Lut})_2]$

Table 7.7: Standardised fractional atomic coordinates^[1] and equivalent isotropic displacement parameters [\AA^2] for $[\text{BeI}_2(\text{Lut})_2]$ (**4**). The equivalent isotropic displacement parameter is defined as 1/3 of the trace of the anisotropic displacement tensor. Standard deviations in units of the last digit are given in parentheses.

Atom	<i>x</i>	<i>y</i>	<i>z</i>	<i>U_{equiv}</i>
I11	0.18598(6)	0.66146(2)	0.64007(2)	0.04604(13)
I12	0.05949(6)	0.81734(2)	0.62201(2)	0.04988(14)
Be1	0.3141(11)	0.7531(4)	0.6293(3)	0.037(2)
N11	0.4836(7)	0.7462(2)	0.6792(2)	0.0362(13)
C111	0.6353(9)	0.7224(3)	0.6700(3)	0.040(2)
C112	-0.2261(9)	0.7192(3)	0.7071(3)	0.047(2)
H112	-0.1224	0.7047	0.6998	0.056
C113	-0.2405(10)	0.7372(3)	0.7541(3)	0.055(2)
H113	-0.1475	0.7352	0.7790	0.066
C114	0.3948(10)	0.2582(3)	0.7358(3)	0.047(2)
H114	0.4088	0.2698	0.7037	0.057
C115	0.4711(8)	0.7621(3)	0.7263(2)	0.0353(15)
C11A	0.6568(10)	0.6976(3)	0.6203(3)	0.055(2)
H11A	0.7710	0.6831	0.6211	0.083
H11B	0.5751	0.6684	0.6130	0.083
H11C	0.6382	0.7254	0.5949	0.083
C11B	0.3023(11)	0.7834(4)	0.7391(3)	0.063(2)
H11D	0.3131	0.7931	0.7738	0.095
H11E	0.2697	0.8155	0.7193	0.095

continued on the next page

Atom	<i>x</i>	<i>y</i>	<i>z</i>	<i>U_{equiv}</i>
H11F	0.2161	0.7555	0.7323	0.095
N12	0.4008(7)	0.7814(2)	0.5772(2)	0.0369(13)
C121	0.5024(9)	0.8270(3)	0.5842(3)	0.047(2)
C122	-0.4263(13)	0.8500(5)	0.5446(4)	0.083(3)
H122	-0.3561	0.8809	0.5498	0.100
C123	0.5422(15)	0.6720(5)	0.9983(4)	0.095(4)
H123	0.5916	0.6565	0.9720	0.113
C124	0.4379(12)	0.7168(4)	0.9904(3)	
H124	0.4157	0.7323	0.9588	0.085
C125	0.3656(9)	0.7611(3)	0.5301(3)	0.047(2)
C12A	0.5420(10)	0.8533(3)	0.6343(3)	0.055(2)
H12A	0.6148	0.8847	0.6318	0.083
H12B	0.4371	0.8649	0.6460	0.083
H12C	0.5994	0.8271	0.6573	0.083
C12B	0.2427(13)	0.7151(4)	0.5205(3)	0.073(3)
H12D	0.2316	0.7056	0.4858	0.110
H12E	0.2839	0.6838	0.5401	0.110
H12F	0.1329	0.7261	0.5293	0.110
I21	0.15835(6)	0.67878(2)	0.85467(2)	0.04949(14)
I22	0.28315(7)	0.52344(2)	0.87034(2)	0.05114(14)
Be2	0.0280(12)	0.5868(4)	0.8603(3)	0.040(2)
N21	-0.0716(7)	0.5579(3)	0.9112(2)	0.0431(14)
C211	-0.1722(10)	0.5128(3)	0.9024(3)	0.053(2)
C212	0.7401(11)	0.4909(4)	0.9398(4)	0.071(3)
C213	0.2440(12)	0.4857(5)	1.0145(4)	0.081(3)
H213	0.3083	0.4989	0.9903	0.098
C214	0.1350(12)	0.4435(4)	1.0041(3)	0.065(3)
H214	0.1173	0.4289	0.9720	0.078
C215	-0.0486(10)	0.5785(3)	0.9585(3)	0.054(2)
C21A	-0.1928(11)	0.4847(3)	0.8517(3)	0.062(2)
H21A	-0.2681	0.4537	0.8523	0.094
H21B	-0.2405	0.5104	0.8267	0.094
H21C	-0.0826	0.4725	0.8441	0.094
C21B	0.0718(14)	0.6244(4)	0.9702(3)	0.080(3)
H21D	0.0743	0.6342	1.0046	0.120
H21E	0.1846	0.6133	0.9639	0.120
H21F	0.0352	0.6555	0.9497	0.120
N22	-0.1352(7)	0.5936(2)	0.8087(2)	0.0374(13)
C221	-0.2933(9)	0.6148(3)	0.8157(3)	0.042(2)
C222	0.5709(10)	0.6143(3)	0.7782(3)	0.056(2)
H222	0.4647	0.6280	0.7842	0.067
C223	0.5921(12)	0.5937(3)	0.7319(4)	0.066(3)
H223	0.4998	0.5913	0.7068	0.079
C224	0.7544(11)	0.5764(3)	0.7235(3)	0.055(2)
H224	0.7733	0.5647	0.6919	0.066
C225	-0.1123(10)	0.5765(3)	0.7616(2)	0.041(2)
C22A	-0.3170(10)	0.6403(4)	0.8639(3)	0.060(2)
H22A	-0.2123	0.6376	0.8862	0.090
H22B	-0.3470	0.6785	0.8588	0.090
H22C	-0.4073	0.6216	0.8781	0.090
C22B	0.0616(11)	0.5594(4)	0.7513(3)	0.061(2)
H22D	0.0573	0.5486	0.7171	0.091
H22E	0.1399	0.5896	0.7579	0.091
H22F	0.0999	0.5288	0.7724	0.091
I31	0.49758(6)	0.50821(2)	0.60296(2)	0.04983(14)
I32	0.58904(7)	0.34833(3)	0.61768(2)	0.0600(2)
Be3	0.3579(11)	0.4176(4)	0.6117(3)	0.0352(19)
N31	0.1906(7)	0.4261(2)	0.5623(2)	0.0331(12)
C311	0.2017(9)	0.4058(3)	0.5155(2)	0.0399(16)
C312	-0.0601(10)	0.5957(3)	0.5202(3)	0.051(2)

continued on the next page

Atom	<i>x</i>	<i>y</i>	<i>z</i>	<i>U_{equiv}</i>
H312	-0.0695	0.6110	0.5513	0.061
C313	0.0919(10)	0.5751(3)	0.5103(3)	0.057(2)
H313	0.1887	0.5777	0.5338	0.069
C314	0.8984(9)	0.4495(3)	0.5345(3)	0.051(2)
H314	0.7962	0.4657	0.5411	0.061
C315	0.0407(8)	0.4505(3)	0.5704(3)	0.039(2)
C31A	0.3697(11)	0.3856(4)	0.5026(3)	0.063(2)
H31A	0.3561	0.3728	0.4687	0.094
H31B	0.4519	0.4150	0.5062	0.094
H31C	0.4095	0.3558	0.5244	0.094
C31B	0.0253(9)	0.4812(3)	0.6176(3)	0.050(2)
H31D	-0.0891	0.4955	0.6168	0.073
H31E	0.0492	0.4567	0.6455	0.073
H31F	0.1060	0.5111	0.6209	0.073
N32	0.2627(7)	0.3959(2)	0.6657(2)	0.0388(13)
C321	0.3042(10)	0.4182(3)	0.7126(2)	0.048(2)
C322	0.2047(12)	0.4068(3)	0.7496(3)	0.061(2)
H322	0.2321	0.4227	0.7808	0.073
C323	-0.0667(11)	0.8726(4)	0.7586(3)	0.065(2)
H323	0.0052	0.8673	0.7341	0.078
C324	1.0363(10)	0.3466(3)	0.6973(3)	0.056(2)
H324	0.9479	0.3209	0.6922	0.067
C325	0.1348(8)	0.3575(3)	0.6594(3)	0.040(2)
C32A	0.4599(13)	0.4528(4)	0.7224(3)	0.085(3)
H32A	0.5129	0.4564	0.6924	0.127
H32B	0.4288	0.4887	0.7334	0.127
H32C	0.5391	0.4359	0.7478	0.127
C32B	0.1011(10)	0.3237(3)	0.6134(3)	0.059(2)
H32D	0.0065	0.2993	0.6163	0.088
H32E	0.0735	0.3475	0.5852	0.088
H32F	0.2014	0.3025	0.6091	0.088

Table 7.8: Coefficients of the anisotropic displacement parameters [\AA^2] for $[\text{BeI}_2(\text{Lut})_2]$ (4). U_{ij} is defined as $U_{ij} = \exp -2\pi^2[U_{11}(ha^*)^2 + \dots + 2U_{21}hka^*b^*]$. Standard deviations in units of the last digit are given in parentheses.

Atom	U_{11}	U_{22}	U_{33}	U_{23}	U_{13}	U_{12}
I11	0.0433(3)	0.0428(3)	0.0510(3)	-0.0007(2)	0.0018(2)	-0.0047(2)
I12	0.0429(3)	0.0546(3)	0.0526(3)	0.0033(2)	0.0074(2)	0.0107(2)
Be1	0.025(4)	0.054(6)	0.032(4)	-0.007(4)	0	0.002(4)
N11	0.033(3)	0.040(3)	0.035(3)	-0.003(2)	$= -U_{23}$	-0.006(2)
C111	0.035(4)	0.039(4)	0.045(4)	0.004(3)	0.003(3)	$= U_{13}$
C112	0.032(4)	0.047(4)	0.059(5)	-0.001(4)	-0.001(3)	0.002(3)
C113	0.050(5)	0.052(5)	0.055(5)	0.003(4)	-0.018(4)	-0.007(4)
C114	0.056(5)	0.049(4)	0.034(4)	0.006(3)	$= -U_{23}$	0.003(4)
C115	0.038(4)	0.036(4)	0.031(3)	-0.009(3)	0.003(3)	-0.001(3)
C11A	0.046(5)	0.071(6)	0.052(5)	-0.011(4)	0.018(4)	0.014(4)
C11B	0.059(5)	0.095(7)	0.037(4)	-0.013(4)	0.009(4)	0.013(5)
N12	0.030(3)	0.043(3)	0.038(3)	0.003(3)	0.002(2)	0.001(2)
C121	0.039(4)	0.049(4)	0.054(5)	0.010(4)	0.011(3)	-0.006(3)
C122	0.073(7)	0.100(8)	0.081(7)	0.020(6)	0.023(5)	-0.029(6)
C123	0.108(9)	0.123(10)	0.059(6)	-0.030(6)	0.035(6)	0.023(8)
C124	0.083(7)	0.091(7)	0.041(5)	-0.009(5)	0.019(5)	-0.002(6)
C125	0.041(4)	0.062(5)	0.039(4)	-0.001(4)	0.004(3)	0.008(4)
C12A	0.055(5)	0.048(5)	0.060(5)	0.004(4)	-0.003(4)	-0.019(4)
C12B	0.094(7)	0.091(7)	0.035(4)	-0.013(4)	0.005(4)	-0.026(6)
I21	0.0432(3)	0.0404(3)	0.0625(3)	-0.0003(2)	-0.0027(2)	-0.0016(2)
I22	0.0475(3)	0.0545(3)	0.0514(3)	0.0038(2)	0.0058(2)	0.0163(2)
Be2	0.039(5)	0.042(5)	0.037(5)	-0.001(4)	0.001(4)	$= U_{13}$

continued on the next page

Atom	U_{11}	U_{22}	U_{33}	U_{23}	U_{13}	U_{12}
N21	0.042(3)	0.052(4)	0.036(3)	0.006(3)	0.006(3)	0.014(3)
C211	0.046(4)	0.056(5)	0.055(5)	0.017(4)	0.003(4)	0.011(4)
C212	0.049(5)	0.083(7)	0.082(7)	0.042(6)	0.005(5)	-0.004(5)
C213	0.048(5)	0.141(10)	0.057(6)	0.041(6)	0.017(4)	0.020(6)
C214	0.056(6)	0.102(8)	0.040(5)	0.014(5)	0.015(4)	0.034(5)
C215	0.056(5)	0.065(5)	0.041(4)	0	0.007(4)	0.018(4)
C21A	0.067(6)	0.050(5)	0.069(6)	0.006(4)	0.002(4)	-0.013(4)
C21B	0.112(8)	0.082(7)	0.044(5)	-0.021(5)	0.007(5)	-0.004(6)
N22	0.039(3)	0.035(3)	0.037(3)	0.001(2)	0	-0.003(2)
C221	0.034(4)	0.037(4)	0.053(4)	0.002(3)	= U_{23}	0
C222	0.039(4)	0.056(5)	0.070(6)	0.004(4)	-0.007(4)	-0.008(4)
C223	0.058(6)	0.055(5)	0.076(6)	0.006(5)	-0.027(5)	-0.012(4)
C224	0.075(6)	0.044(4)	0.042(4)	-0.001(3)	-0.009(4)	-0.010(4)
C225	0.052(4)	0.035(4)	0.036(4)	0.005(3)	-0.003(3)	0.001(3)
C22A	0.042(5)	0.073(6)	0.065(5)	-0.001(4)	0.011(4)	0.018(4)
C22B	0.068(6)	0.075(6)	0.040(4)	0.001(4)	0.011(4)	0.015(5)
I31	0.0432(3)	0.0507(3)	0.0547(3)	-0.0006(2)	0.0026(2)	-0.0098(2)
I32	0.0503(3)	0.0754(4)	0.0547(3)	0.0148(3)	0.0086(2)	0.0242(3)
Be3	0.039(5)	0.043(5)	0.024(4)	-0.005(4)	0.007(4)	-0.004(4)
N31	0.033(3)	0.035(3)	0.031(3)	0.001(2)	0	-0.003(2)
C311	0.048(4)	0.037(4)	0.034(4)	0.001(3)	0	-0.002(3)
C312	0.063(5)	0.046(4)	0.036(4)	-0.002(3)	-0.018(4)	-0.007(4)
C313	0.045(5)	0.058(5)	0.063(5)	-0.001(4)	-0.021(4)	-0.013(4)
C314	0.031(4)	0.047(4)	0.071(5)	0.011(4)	-0.006(4)	-0.004(3)
C315	0.031(4)	0.039(4)	0.048(4)	0.008(3)	0.004(3)	-0.003(3)
C31A	0.077(6)	0.077(6)	0.035(4)	-0.010(4)	0.013(4)	0.012(5)
C31B	0.040(4)	0.057(5)	0.049(4)	0.006(4)	0.004(3)	0.008(4)
N32	0.036(3)	0.044(3)	0.035(3)	0.002(3)	0.001(2)	-0.003(3)
C321	0.068(5)	0.047(4)	0.029(4)	0.002(3)	0.006(3)	-0.007(4)
C322	0.094(7)	0.057(5)	0.034(4)	0.007(4)	0.015(4)	0.020(5)
C323	0.060(6)	0.086(7)	0.053(5)	-0.014(5)	0.023(4)	-0.007(5)
C324	0.046(5)	0.062(5)	0.062(5)	0.017(4)	0.015(4)	-0.004(4)
C325	0.034(4)	0.042(4)	0.044(4)	0.008(3)	0.002(3)	0
C32A	0.112(8)	0.105(8)	0.034(4)	-0.014(5)	-0.003(5)	-0.058(7)
C32B	0.053(5)	0.059(5)	0.062(5)	-0.003(4)	0	-0.021(4)

7.2 Detailed Compilation of all performed Experiments

Unless stated otherwise, all following experiments and their further handling were performed inside a glovebox.

MgI₂ · 6 DMF (TH017)

To 30 mL HI(aq) (57 wt.%), Mg was added until no further reaction was observed. To ensure a quantitative reaction, a small amount of excess Mg was added and the solution stored for at least twelve hours. The solution was then filtered and reduced under vacuum until crystallisation was observed. The obtained crystalline solid was then completely dissolved in the minimum amount of DMF. A Dean-Stark apparatus was connected, the setup rinsed with Ar for 15 min, 5 mL Toluene added and then heated until boiling. In sum, 30 mL of condensate were removed, afterwards the solution was reduced under vacuum to ca. 30 mL. After cooling to 4 °C, colorless crystalline solid was obtained and filtered in a Schlenk frit under Ar gas. Lastly, the obtained product was dried thoroughly under vacuum. Due to the high sensitivity of the compound towards air and moisture, it was subsequently stored in the glovebox.

Analysis: Via pXRD the obtained product was identified as pure MgI₂ · 6 DMF (see Fig. 7.18, p. 156).

CaI₂ · 6 DMF (THRH - CaI₂ · 6 DMF)

To a suspension of 13.5 g (135 mmol) CaCO₃ in 200 mL DMF, 42 mL HI(aq) (57 wt.%) were slowly added. 25 mL Toluene were added, and a Dean-Stark apparatus was connected. The system was rinsed with N₂ for 15 min, and the temperature of the oil bath gradually increased to 180 °C. In total, approx. 100 mL solvent were removed, and the solution was cooled with an ice bath for crystallisation. The colourless crystals were isolated with a Schlenk frit and dried thoroughly under vacuum. Due to the high sensitivity of the compound towards air and moisture, it was subsequently stored in the glovebox.

Analysis: Via pXRD the obtained product was identified as pure CaI₂ · 6 DMF (see Fig. 7.112, p. 172).

SrI₂ · 7 DMF (THRH - SrI₂ · 7 DMF)

(20.0 g, 135 mmol) SrCO₃ were mixed in 200 mL DMF. Under stirring, 36 mL HI(aq) (57 wt.%) were slowly added. The solution was stirred at room temperature for 1 hr. Residual solid was removed by vacuum filtration with a Schlenk frit. 20 mL Toluene were added to the clear, light yellow solution. A Dean-Stark apparatus was connected, the setup rinsed with N₂ for 15 min and then heated until boiling. The temperature of the oil bath was stepwise increased to 170 °C, and in total 50 mL solvent removed. The solution was reduced in vacuum (60 °C, 20–26 mbar) by approx. 40 mL. After cooling to 4 °C over night, the crystalline product was isolated with a Schlenk frit and washed once with ice-cold DMF (20 mL). The product was then dried under vacuum and transferred into the glovebox for storage and further usage.

Analysis: Via pXRD the obtained product was identified as pure SrI₂ · 7 DMF (see Fig. 7.113, p. 172).

7.2.1 Synthesis of Binary Amalgams - Starting Materials

CsHg₂ (TH080)

In a 100 mL Schlenk flask, 7.512 g (37.5 mmol) Hg were slowly added to 2.4885 g (18.7 mmol) Cs. While lightly shaking, the reaction mixture was homogenised by melting with a hot-air gun (300 °C) and allowed to cool to RT. The obtained product served as starting material for TH082 and TH083 (see p. 146 and 146).

Analysis: The obtained product was identified via pXRD as a mixture of CsHg₂ and Cs₅Hg₁₉ (see p. 165, Fig. 7.69).

Cs₃Hg₂₀ (TH076, TH079)

TH076: In a 100 mL Schlenk flask, 9.10 g (45.3 mmol) Hg were slowly added to 954.6 mg (7.2 mmol) Cs. Under light shaking, the reaction mixture was homogenised by melting with a hot-air gun (300 °C) and the melt was allowed to cool to RT. The obtained solid was used in TH077 (see p. 146) and TH078 (see p. 146).

Analysis: Due to experiment design, the obtained product was analysed via pXRD together with TH075 (Rb₃Hg₂₀). As can be seen, the only Cs amalgam synthesised was Cs₃Hg₂₀ (see Fig. 7.66, p. 164).

TH079: To 452.0 mg (3.4 mmol) Cs, 4.56 g (22.7 mmol) Hg were slowly added inside a 100 mL Schlenk flask. The obtained solid was molten with a hot-air gun (300 °C) while lightly shaking. Afterwards, the melt was allowed to cool to RT.

Analysis: Via pXRD analysis, the obtained product could be identified as phase-pure Cs₃Hg₂₀ (see Fig. 7.68, p. 165).

KHg₂ (TH121)

To 889.1 mg (22.74 mmol) K 9.1172 g (45.45 mmol) Hg were carefully added. Under light shaking, the reaction mixture was homogenised by melting with a hot air gun (470 °C), after which it was allowed to cool to RT.

Analysis: Via pXRD, the obtained violet, crystalline solid was identified as KHg₂ and trace amounts of a yet unknown phase (see Fig. 7.95, p. 169).

KHg₁₁ (TH110, TH122)

TH110: In a 100mL Schlenk flask 181.1 mg (4.63 mmol) K were cooled to –78 °C with an acetone/dry ice mixture. Under Ar reverse flow, 10.2281 g (50.99 mmol) Hg were slowly added dropwise. Over night, the reaction mixture was left inside the cooling agent and slowly thawed to RT.

Analysis: The obtained silver crystalline solid was identified as phase-pure KHg₁₁ (see Fig. 7.85, p. 167).

TH122: TH122 was performed the same way as TH110, the only changes were the amounts of metal used: 800 mg (20.5 mmol) K, 49.0 g (244.3 mmol) Hg.

Analysis: The obtained silver crystalline solid was identified as phase-pure KHg₁₁ (see Fig. 7.96, p. 169).

RbHg₂ (TH081)

In a 100mL Schlenk flask, 8.2438 g (41.4 mmol) Hg were slowly added to 1.7563 g (20.6 mmol) Rb. The reaction mixture was homogenised by lightly shaking and melting with a hot-air gun (300 °C) and then allowed to cool off to RT. The obtained crystalline, lightly violet metal was used in TH082 and TH83 (see p. 146).

Analysis: The product was identified as RbHg₂ with minor impurities originating from Rb₅Hg₁₉ (see p. 165, Fig. 7.70).

Rb₃Hg₂₀ (TH075)

In a 100mL Schlenk flask, 9.399 g (46.96 mmol) Hg were carefully added to 600.8 mg (7.0 mmol) Rb and the reaction mixture homogenised by melting with a hot-air gun at 300 °C under light shaking. The obtained crystalline solid was used in TH077 (see p. 146) and TH078 (see p. 146).

Analysis: Due to experiment design, the obtained product was analysed via pXRD together with TH076 (Cs₃Hg₂₀). As can be seen, the only Rb amalgam synthesised was Rb₃Hg₂₀ (see Fig. 7.66, p. 164).

Rb₇Hg₃₁ (TH115)

In a 50mL Schlenk flask, 450.6 mg (5.27 mmol) Rb were cooled to –78 °C with an acetone/dry ice mixture. Under reverse Ar flow, 4.6879 g (23.37 mmol) Hg were slowly added dropwise. The mixture was then allowed to slowly thaw to RT together with the cooling bath.

Analysis: The obtained crystalline solid was identified as a mixture of Rb₃Hg₂₀ and Rb₅Hg₁₉ (see Fig. 7.90, p. 168).

RbHg₈ (TH109)

In a 50mL Schlenk flask, 504.6 mg (5.30 mmol) Rb were cooled to –78 °C with an acetone/dry ice mixture. Under reverse Ar flow, 9.4917 g (47.52 mmol) Hg were slowly added dropwise. The mixture was then allowed to slowly thaw to RT together with the cooling bath.

Analysis: The obtained solid was identified as phase-pure RbHg₁₁ (see Fig. 7.84, p. 167).

RbHg₁₁ (TH111)

In a 100 mL Schlenk flask, 474.1 mg (5.55 mmol) Rb were cooled to $-78\text{ }^{\circ}\text{C}$ with an acetone/dry ice mixture. Under reverse Ar flow, 12.2349 g (60.99 mmol) Hg were slowly added dropwise. While staying in the cooling agent, the mixture was allowed to slowly thaw to RT over night.

Analysis: The obtained solid was identified as phase-pure RbHg₁₁ (see Fig. 7.86, p. 168).

7.2.2 Electrocrystallisation Experiments**7.2.2.1 Preliminary Tests****Electrolysis of 0.1 M KI/NaI in DMF (TH002)**

A freshly prepared equimolar solution of 5 mmol NaI and 5 mmol KI in 100 mL DMF was electrolysed for 48 h with a terminal voltage of 3 V. A formation of silver crystals was observed.

Analysis: An isolated single crystal was investigated with SCXRD. Since orienting measurements yielded the cell metric of the known Na amalgam Na₁₁Hg₅₂,^[2] further analysis was not performed.

Electrolysis of Na-containing Hg in 0.1 M KI (TH003)

In a first step, NaHg₂ was prepared by carefully adding 4.73 g (23.6 mmol) Hg to 270 mg (11.7 mmol) Na in the glovebox in a 50 mL Schlenk flask. Outside the glovebox, the reaction mixture was homogenised by melting with a hot-air gun at $300\text{ }^{\circ}\text{C}$ under light shaking. The obtained silver-metallic solid was then thoroughly ground and further 16.55 g (82.5 mmol) Hg were added. After tempering the reaction mixture for 10 h at $50\text{ }^{\circ}\text{C}$ in an oil bath, the solid residue was removed with a Schlenk frit. Analysis via ICP-AES determined the Sodium content at 0.7%.

The electrolysis was performed with a 0.1 M solution of KI in DMF, where the amalgamated copper spoon was filled with the prepared sodium-containing mercury. Electrolysis was performed over 48 h with a terminal voltage of 3 V. A significant formation of crystals was observed.

Analysis: Via SCXRD, an isolated single crystal was investigated. Orienting measurements yielded the cell metric of the known KHg₁₁,^[3] therefore further analysis was not performed.

Electrolysis of Na-containing Hg in 0.1 M CsI (TH005, TH006, TH007)

TH005: The experiment was performed analogous to TH003, but a solution of 0.1 M CsI in DMF was used. After 24 h (terminal voltage: 3 V) crystal formation was observed, but rapidly dissolved within seconds after turning off the voltage source.

TH006: The experiment TH005 was repeated, but with a slightly smaller amount of Hg. After 7 days (terminal voltage 3 V) no crystal formation was observed.

TH007: The electrolysis was repeated analogous to TH005, with no change of outcome.

7.2.2.2 Syntheses**Elektrolysis of 0.1 M MgI₂ in DMF (TH018)**

A freshly prepared solution of 5 mmol MgI₂ in 100 mL DMF was electrolysed for 48 h (terminal voltage 3 V). The formation of silver-metallic crystals occurred.

Analysis: Via pXRD, the obtained solid was identified as MgHg₂ (see Fig. 7.19, p. 156).

Solubility of BeI₂ in liquid NH₃ (TH113)

For validation purposes considering the feasibility of an electrosynthesis, BeI₂ was tried to dissolve in liquid ammonia. The apparatus used is analogous to the one depicted in Fig. 3.7, but

instead of an electrolysis chamber in (B) with a cryostat, a quartz tube and a common Dewar with an *i*-PrOH/dry ice mixture was used and the temperature gradually increased via addition of more solvent. The rest of the procedure (condensation onto elemental Na and distillation of NH₃) was performed as described in Chapter 3.4.2. 100 mg BeI₂ (1.90 mmol) were filled into the quartz tube together with a stir bar. It was observed that BeI₂ could be dissolved completely in about 3 mL at -52 °C, which yields a solubility of at least 0.63 mol L⁻¹. The whole apparatus was allowed to warm up to RT over night and then evacuated to $\leq 1 \times 10^{-3}$ mbar.

Analysis: After evaporation, colourless, needle-shaped crystals were obtained. Via pXRD, they were identified as Be(NH₃)₄I₂ (see Fig. 7.88, p. 168).

Electrolysis 0.1 M KI at 75 °C (TH127)

A solution of 0.1 mol L⁻¹ KI in DMF was electrolysed at 75 °C (setting of Thermostat: 78 °C) with a starting current of 3 V. After 16 h, the current was increased to 5 V. The formation of small amounts of a crystalline metallic solid was observed, and the current further increased to 8 V. After additional 48 h, the synthesis was stopped.

Analysis: Via pXRD, the obtained solid was identified as KHg₆ and small amounts of an unknown compound (see. Fig. 7.106, p. 171).

7.2.3 Thermochemical Experiments

7.2.3.1 Syntheses in Binary Systems

K₇Hg₃₁ (TH114)

In a 100 mL Schlenk flask, 219.4 mg (5.55 mmol) K were cooled to -78 °C with an acetone/dry ice mixture. Under reverse Ar flow, 4.9868 g (24.86 mmol) Hg dropwise added. While staying in the cooling agent, the mixture was allowed to slowly thaw to RT over night.

Analysis: An isolated single crystal was identified as the new potassium amalgam KHg₈ (see Chapter 4.4, p. 76), while pXRD analysis identified the product as a mixture of KHg₄ and KHg₅ (see Fig. 7.89, p. 168).

KHg₈ (TH118, TH119, TH124, TH125, TH126, TH128)

TH118: In a 100 mL Schlenk flask 249.7 mg (6.39 mmol) K were cooled to -78 °C with an acetone/dry ice mixture. Under reverse Ar flow, 10.2479 g (51.09 mmol) Hg were dropwise added. While staying in the cooling agent, the mixture thawed to RT over night.

Analysis: The obtained solid was identified as a mixture of KHg₆ and KHg₁₁ with minimal amounts of KHg₈ (see Fig. 7.92, p. 169).

TH119: In a quartz flask, 9.7347 g (48.53 mmol) Hg were added dropwise to 237.3 mg (6.07 mmol) K. With a hot-air gun at 200 °C the reaction mixture was homogenised under light shaking, and rapidly cooled in ice water.

Analysis: The obtained solid was identified as a mixture of KHg₆ and KHg₁₁, with traces of KHg₈ (see Fig. 7.93, p. 169).

TH124: To 859.4 mg (21.98 mmol, 1.0 eq.) K, 48.4542 g (241.60 mmol) Hg were dropwise added under acetone/dry ice cooling. The mixture was allowed to thaw to RT over night. The crystalline solid was thoroughly ground and further 192.7 mg (4.93 mmol) K were added to reach a stoichiometry of KHg₉. pXRD identified the mixture as pure KHg₁₁ (TH124; see Fig. 7.97, p. 169). After heating to 60 °C and cooling to RT, the composition was still identified as KHg₁₁ (TH124-2; Fig. 7.98, p. 170). Additional Ostwald ripening (TH124-3) still yielded KHg₁₁



Fig. 7.1: Special Schlenk frit for the separation of liquid and solid components in at elevated temperatures under inert conditions.

(TH124-3; Fig. 7.99, p. 170). 47.2626 g of TH124-2 were ground and mixed with 105.6 mg (2.70 mmol) K, transferred into a specially devised Schlenk-frit (see Fig. 7.1), stored for 7 days at 69 °C and the obtained solid characterised via pXRD. As can be seen, the solid contains KHg_{11} as well as KHg_8 (TH124-4; see Fig. 7.100, p. 170). It was then kept at 70 °C for three months.

Analysis: Via pXRD the obtained solid was identified as KHg_{11} (see Fig. 7.101, p. 170).

TH125: To 600.2 mg (15.35 mmol, 1.0 eq.) K, 18.414 g (92.14 mmol, 6.0 eq.) Hg were added under reverse Ar flow while cooling in an acetone/dry ice bath. Over night, the mixture was allowed to thaw to RT in the cooling agent. The solid was characterised via pXRD as KHg_6 (see Fig. 7.102, p. 170). 15.9360 g (1.0 eq.) of TH125 were thoroughly ground, and 5.1595 g (0.33 eq.) Hg were dropwise added. After each drop, the mixture was carefully ground. **Analysis:** Via pXRD the obtained solid was identified as KHg_{11} (see Fig. 7.103, p. 170).

TH126: To 625.0 mg (15.99 mmol, 1.0 eq.) K, 19.2487 g (95.96 mmol, 6.0 eq.) Hg were added under Ar reverse flow while cooling in an acetone/dry ice bath. The mixture was allowed to thaw to RT over night while staying in the cooling agent. Via pXRD, it was identified as a mixture of KHg_6 and KHg_{11} (see Fig. 7.2.3.1, p. 142). 7.2477 g (1.0 eq.) of TH126 were thoroughly ground, and further 2.3422 g (0.33 eq.) Hg were slowly added.

Analysis: The obtained product was identified as a mixture of KHg_{11} and KHg_6 (see Fig. 7.105, p. 171).

TH128: 119.4 mg (3.05 mmol) K and 4.8997 g (24.43 mmol) Hg were weighed into a Ta crucible and welded shut. With a heating rate of 5 K min^{-1} , the crucible was heated to 300 °C and kept at this temperature for 24 h, after which it was rapidly cooled off with ice water. Analysis via pXRD identified the obtained product as a mixture of KHg_6 and KHg_{11} (see Fig. 7.107, p. 171). Ca. 2.4 g of TH128 were then thoroughly ground and transferred into a Schlenk flask for Ostwald ripening (30 min intervals at 45 °C for 30 days). The product obtained was identified as a mixture of KHg_6 and KHg_{11} (see Fig. 7.108, p. 171). The remaining solid from TH128 was pressed into pills (diameter = 10 mm) and treated with the same Ostwald ripening process. It was identified as a mixture of KHg_6 and KHg_{11} (see Fig. 7.109, p. 171).

SrHg_{5.86} (TH120)

TH120: In a quartz flask, 9.2999 g (46.36 mmol) Hg were added dropwise to 693.7 mg (7.92 mmol) Sr. For homogenisation, the mixture was molten with a hot-air gun at 650 °C for approx. 10 min, and rapidly cooled in ice water.

Analysis: Via pXRD, the obtained metallic solid was identified as a mixture of $\text{SrHg}_{5.86}$, $\text{Sr}_{10.5}\text{Hg}_{54.5}$, and SrHg_8 (see Fig. 7.94, p. 169).

7.2.3.2 Syntheses in Ternary Systems

Na–K–Hg (TH010)

TH010: In a 100 mL Schlenk flask 11.23 g (56.0 mmol) Hg were dropwise added under reverse Ar flow to 160.9 mg (7.0 mmol) Na and 273.3 mg (7.0 mmol) K. With a hot-air gun (300 °C), the reaction mixture was melted while lightly shaking, and allowed to cool to RT. The obtained solid was identified as a mixture of NaHg_2 , $\text{Na}_{11}\text{Hg}_{52}$ and KHg_5 (see Fig. 7.10, p. 155). After thorough grounding, additional 15.0 g (74.8 mmol) Hg were dropwise added left at 105 °C for several weeks. The mixture was allowed to cool to RT in a sand bath, and excess mercury removed with a Schlenk frit.

Analysis: The obtained solid was identified as KHg_{11} (see Fig. 7.11, p. 155).

Na–Rb–Hg (TH004, TH061, TH084, TH086, TH087)

TH004: In a 100mL Schlenk flask 11.23 g (56.0 mmol) Hg were slowly added to 160.9 mg (7.0 mmol) Na and 598.3 mg (7.0 mmol) Rb. With a hot-air gun (300 °C), the reaction mixture was melted while lightly shaking, and allowed to cool to RT. The obtained solid was identified as a mixture of $\text{Rb}_3\text{Hg}_{20}$ and NaHg_2 (see Fig. 7.4, p. 154). After thorough grinding, additional 11.23 g (56.0 mmol) Hg were added dropwise and the reaction mixture was kept at 105 °C for five months. With a Schlenk frit, a crystalline solid was isolated.

Analysis: The obtained solid was identified as $\text{Na}_{11}\text{Hg}_{52}$, with a slight shift towards higher diffraction angles (see Fig. 7.5, p. 154).

TH061: To improve the crystal quality of TH004-2, Ostwald ripening (35 °C/RT) was performed.

Analysis: Analysis via SCXRD yielded mixed occupancy of some Na positions of the $\text{Na}_{11}\text{Hg}_{52}$ structure. Due to standard deviations higher than the occupancy factors, no final structure model was determined.

TH084: In a Quartz flask, 39.245 g (195.65 mmol) Hg were dropwise added to 160.1 mg (6.96 mmol) Na and 589.9 mg (6.90 mmol) Rb. The reaction mixture was homogenised by melting with a hot-air gun at 300 °C under light shaking and then rapidly cooled in an ice bath. The reaction mixture was then divided into TH086 and TH087.

Analysis: The obtained suspension was identified as a mixture of Hg, $\text{Na}_{11}\text{Hg}_{52}$ and RbHg_{11} (see Fig. 7.73, p. 165).

TH086: Approx. half of TH084 were transferred into a 10mL Schlenk flask, after which they were treated via Ostwald ripening (80 ± 5 °C, ca. 100 cycles).

Analysis: Via pXRD, only RbHg_{11} was found as a product (see Fig. 7.75, p. 166).

TH087: Approx. half of TH084 was transferred into a 10mL Schlenk flask and then treated via Ostwald ripening (50 ± 5 °C).

Analysis: Via pXRD, only RbHg_{11} was found as a product (see Fig. 7.76, p. 166).

Na–Cs–Hg (TH001, TH040–043, TH072, TH096, TH130)

TH001: In a 100mL Schlenk flask, 11.79 g (58.8 mmol) Hg were dropwise added under reverse Ar flow to 975.0 mg (7.34 mmol) Cs and 162 mg (7.04 mmol) Na. The reaction mixture was homogenised by slightly shaking the mixture while melting with a hot air gun (300 °C). The obtained solid was identified as a mixture of NaHg_2 and $\text{Cs}_3\text{Hg}_{20}$ (see Fig. 7.2, p. 154). After thorough grinding, further 10.0 g (49.9 mmol) Hg were added and the mixture was kept in a drying oven (105 °C). Cube-shaped crystals were then isolated with a Schlenk frit.

Analysis: The obtained single crystals were identified as a new ternary amalgam, $\text{CsNa}_2\text{Hg}_{18}$ (see Ch. 4.1, p. 27). Furthermore, pXRD analysis showed that the majority of the obtained solid was $\text{CsNa}_2\text{Hg}_{18}$ with impurities by $\text{Cs}_3\text{Hg}_{20}$ (see Fig. 7.3, p. 154).

TH040: 257.8 mg (11.2 mmol) Na, 745.1 mg (5.6 mmol) Cs and 8.9971 g (44.9 mmol) Hg were weighed into a 100mL Schlenk flask. The released heat was so intense that a boiling retardation took place. The reaction mixture was then disposed of.

TH041: 257.8 mg (11.2 mmol) Na and 745.1 mg (5.6 mmol) Cs were weighed into a 100mL Schlenk flask and 8.9971 g (44.9 mmol) Hg slowly added. The reaction mixture was then homogenised under light shaking while melting with a hot air gun (350 °C) and allowed to cool of to RT. Afterwards, the experiment was stored in a drying oven (105 °C).

Analysis: After seven and fourteen days the reaction mixture was analysed via pXRD. It was discovered that after 14 days, the reaction was almost finished, with $\text{Cs}_3\text{Hg}_{20}$ as a byproduct (see Fig. 7.41, p. 160). DSC measurements showed two reversible processes (see p. 174, Fig. 7.124), thus Ostwald ripening at 60 °C was performed (see TH072).

TH042: For DSC measurements, 182.0 mg (7.92 mmol, 10 mol-%) Na and 526.1 mg (3.96 mmol, 2.5 mol-%) Cs were weighed into a 100mL Schlenk flask. While cooling with an ice bath, 14.292 g (71.25 mmol, 87.5 mol-%) Hg were dropwise added. The reaction mixture was then homogenised with a hot air gun (400 °C) while lightly shaking and allowed to cool to RT.

Analysis: Via pXRD, the obtained product was identified as mostly CsNa₂Hg₁₈, with minor impurities from Na₁₁Hg₅₂ (see Fig. 7.42, p. 160)

TH043: For DSC measurements, 53.3 mg (2.31 mmol, 4.4 mol-%) Na and 395.5 mg (2.98 mmol, 5.6 mol-%) Cs were weighed into a 100mL Schlenk flask. While cooling with an ice bath, 9.5411 g (47.62 mmol, 90.0 mol-%) Hg were dropwise added. The reaction mixture was then homogenised with a hot air gun (400 °C) while lightly shaking and allowed to cool to RT.

Analysis: Via pXRD, the obtained product was identified as mostly CsNa₂Hg₁₈, with minor impurities of Cs₃Hg₂₀ and Na₁₁Hg₅₂ (see Fig. 7.43, p. 160)

TH072: The solid obtained in TH041 was tempered at 60 °C. To enable Ostwald ripening, the oven was not closed off completely in order to facilitate regular heating and cooling. Tempering took place over the course of six weeks.

Analysis: Rietveld analysis showed that the product contained CsNa₂Hg₁₈, with XX-at% Cs₃Hg₂₀ as byproduct (see Fig. 7.64, p. 164).

TH096: In order to synthesise phase-pure Cs₂CsHg₁₈, 271.3 mg (3.45 mmol) Na and 624.4 mg (4.70 mmol) Cs were weighed into a 100mL Schlenk flask. The liquid mixture was then cooled to -78 °C with an acetone/dry ice mixture. 17.0708 g (85.10 mmol) Hg were added dropwise, and the mixture allowed to slowly warm up to RT by leaving it in the cooling bath.

Analysis: Rietveld analysis confirmed that the obtained product is phase-pure CsNa₂Hg₁₈ (see Fig. 4.7 and Table 4.7, p. 36).

TH130: Because of the results of the DSC measurement of TH096 (see Fig. 7.127, p. 174), about 15 g of TH096 were put onto a special Schlenk frit, heated to 130 °C for 24 h and then filtered using vacuum. **Analysis:** pXRD of both the remaining solid as well as the solidified filtrate was performed. Both solids consist of CsNa₂Hg₁₈, Cs₃Hg₂₀ and Na₁₁Hg₅₂ (see Fig. 7.110 and 7.111, p. 172).

K–Rb–Hg (TH008)

TH008: In a 100mL Schlenk flask, 11.23 g (56.0 mmol) Hg were added slowly in a dropwise manner to a mixture of 273.3 mg (7.0 mmol) K and 598.3 mg (7.0 mmol) Rb. The reaction mixture was homogenised by lightly shaking while melting with a hot air gun at 350 °C. Via pXRD the obtained solid was identified as Rb₇Hg₃₁ and most likely KHg₅ or KHg₄ (see Fig. 7.6, p. 154). The solid was thoroughly ground, further 23.54 g (117.4 mmol Hg were added and the mixture tempered at 105 °C for fourteen months. Afterwards, it was slowly cooled to RT inside a sand bath.

Analysis: The obtained product was identified as a solid solution of KHg₁₁ and RbHg₁₁ (see Fig. 7.7, p. 154). Further details on this compound are discussed in Chapter 4.3, p. 61.

K–Cs–Hg (TH009, TH044, TH070, TH071, TH085, TH088, TH089)

TH009: In a 100mL Schlenk flask, 11.23 g (56.0 mmol) Hg were added dropwise to a mixture of 273.7 mg (7.0 mmol) K and 930.3 mg (7.0 mmol) Cs. The reaction mixture was homogenised under light shaking while melting with a hot air gun at 350 °C and cooled off to RT. Via pXRD, the obtained solid was identified as a mixture of Cs₃Hg₂₀ and KHg₆ (see Fig. 7.8, p. 155). The solid was then thoroughly ground and further 25.06 g (124.9 mmol) Hg were added. The reaction mixture was tempered for 100 days at 105 °C. Afterwards, it was cooled to RT in a sand bath and excess mercury was removed with a Schlenk frit. The solid consisted of cuboid crystals.

Analysis: Via pXRD, the crystalline product was identified as KHg₁₁ (see Fig. 7.9, p. 155).

TH044: In a 100mL Schlenk flask, 36.03 g (179.6 mmol) Hg were slowly added dropwise to a mixture of 273.7 mg (7.0 mmol) K and 930.3 mg (7.0 mmol) Cs. The reaction mixture was then homogenised under light shaking while melting with a hot air gun at 350 °C and allowed to cool to RT. The product was then divided into equal parts (TH070 and TH071).

Analysis: The obtained product was identified as a mixture of KHg_{11} and $\text{Cs}_3\text{Hg}_{20}$ (see Fig. 7.44, p. 161).

TH070: Half of TH044 were transferred into a quartz flask and stored at 105 °C for three months. Afterwards, the reaction mixture was rapidly cooled off with an acetone/dry ice mixture.

Analysis: Via pXRD, the obtained product was identified as KHg_{11} (see Fig. 7.62, p. 164).

TH071: Half of TH044 were transferred into a quartz flask and stored at 105 °C for three months. Afterwards, the reaction mixture was rapidly cooled off with ice water.

Analysis: Via pXRD, the obtained product was identified as KHg_{11} (see Fig. 7.63, p. 164).

TH085: In a 20mL quartz flask, 41.454 g (206.7 mmol) Hg were slowly added to 277.6 mg (7.09 mmol) K and 929.5 mg (6.99 mmol) Cs. The reaction mixture was then homogenised under light shaking while melting with a hot air gun at 350 °C and allowed to cool to RT. It was then divided into two parts: TH088 and TH089.

Analysis: Via pXRD, the obtained product was identified as KHg_{11} (see Fig. 7.74, p. 166).

TH088: Half of TH085 was transferred into a Schlenk flask and Ostwald ripening performed (80 ± 5 °C, 15 min intervals, total time two weeks).

Analysis: Via pXRD, the obtained product was identified as KHg_{11} (see Fig. 7.77, p. 166).

TH089: Half of TH085 was transferred into a Schlenk flask and Ostwald ripening performed (50 ± 5 °C, 15 min intervals, total time two weeks).

Analysis: Via pXRD, the obtained product was identified as KHg_{11} (see Fig. 7.78, p. 166).

Rb–Cs–Hg (TH011, TH031, TH073, TH074, TH077, TH078, TH082, TH083)

TH011: In a 100mL Schlenk flask, 11.23 g (56.0 mmol) Hg were slowly added to a mixture of 598.3 mg (7.0 mmol) Rb and 930.3 mg (7.0 mmol) Cs. The reaction mixture was then homogenised under light shaking while melting with a hot air gun at 300 °C and allowed to cool to RT. Via pXRD, the obtained solid was identified as a solid solution of $\text{Cs}_5\text{Hg}_{19}$ and $\text{Rb}_5\text{Hg}_{19}$ (see Fig. 7.12, p. 155). The obtained solid was then ground thoroughly and further 31.23 g (155.7 mmol) Hg were added. It was then tempered for fourteen months at 105 °C. It was cooled to RT inside a sand bath and excess Hg was removed via Schlenk frit.

Analysis: Via pXRD, the obtained solid was identified as a mixture of $\text{Cs}_3\text{Hg}_{20}$ and RbHg_{11} (see Fig. 7.13, p. 155).

TH031: In a 100mL Schlenk flask, 9.245 g (46.1 mmol) Hg were dropwise added to a mixture of 295.4 mg (3.46 mmol) Rb and 459.42 mg (3.46 mmol) Cs. The reaction mixture was then homogenised under light shaking while melting with a hot air gun at 400 °C and allowed to cool to RT. It was subsequently tempered at 105 °C for four months. It was then cooled off to RT in a sand bath.

Analysis: Via pXRD, the obtained solid was identified as a mixture of $\text{Cs}_3\text{Hg}_{20}$ and RbHg_{11} (see Fig. 7.32, p. 159).

TH073: Because of the results of the DSC measurement of TH031, Ostwald ripening was performed at 140 °C.

Analysis: After reevaluation of the pXRD of TH031, it was discovered that the product only consisted of $\text{Cs}_3\text{Hg}_{20}$. It was then decided to stop the experiment, since further treatment did not seem promising.

TH074: In a 100mL Schlenk flask, 18.16 g (90.53 mmol Hg were slowly added to a mixture of 926.2 mg (10.84 mmol) Rb and 960.1 mg (7.22 mmol) Cs. The reaction mixture was then homogenised under light shaking while melting with a hot air gun at 400 °C and allowed to cool to RT. It was then thoroughly ground and tempered at 105 °C for four months.

Analysis: Via pXRD, the solid product was identified as a solid solution of Cs₃Hg₂₀ and Cs₃Hg₂₀ (see Fig. 7.65, p. 164) Unfortunately, Rietveld refinement of the obtained solid solution was not possible, since convergence could not be reached.

TH077: 9.7 g of a 1:1 mixture (volume) of TH075 and TH076 were thoroughly ground and tempered at 105 °C for three months. The reaction mixture was cooled to RT inside a sand bath. The originally silver-metallic solid appeared black and powderlike, with small droplets of mercury present. This indicated a decomposition due to leaky glass joints, and the reaction mixture was then discarded.

Analysis: Due to the aforementioned problem, further analysis was not done.

TH078: 10.0 g of a 1:1 mixture (volume) of TH075 and TH076 were thoroughly ground, 11.4 g (56.8 mmol) Hg were added and the reaction mixture was and tempered at 105 °C for three months. It was then cooled down to RT inside a sand bath.

Analysis: Via pXRD, the obtained product was identified as RbHg₁₁, a Cs-containing phase does not seem to be present (see Fig. 7.67, p. 164).

TH082: 4.2909 g (8.82 mmol) RbHg₂ (obtained in TH081) and 4.7091 g (8.82 mmol) CsHg₂ (obtained in TH080) were thoroughly ground and tempered at 105 °C for three months. Afterwards, the reaction mixture was cooled down to RT inside a sand bath.

Analysis: Via pXRD, the obtained product was identified as a mixture of RbHg₂ and Rb₅Hg₁₉, no Cs-containing phase was found (see Fig. 7.71, p. 165).

TH083: 4.2909 g (8.82 mmol) RbHg₂ (obtained in TH081) and 4.7091 g (8.82 mmol) CsHg₂ (obtained in TH080) were thoroughly ground and 3.540 g (17.64 mmol) Hg were added. The reaction mixture was ground again and tempered at 105 °C for three months. Afterwards, the reaction mixture was cooled down to RT inside a sand bath.

Analysis: Via pXRD, the product was identified as a mixture of RbHg₂ and a not-identifiable phase Rb_{1-x}Cs_xHg₁₉ (see Fig. 7.72, p. 165). Due to lack of crystallinity, analysis via SCXRD was not possible.

Na–Mg–Hg (TH023, TH027)

TH023: 29.4 mg (1.21 mmol) Mg, 27.8 mg (1.21 mmol) Na and 1.943 g (9.68 mmol) Hg were filled into a Ta crucible and welded shut. With 50 K h⁻¹, it was heated to 300 °C and tempered for four months. It was then cooled to RT by turning off the oven.

Analysis: Via pXRD, the product as identified as a mixture of Na₁₁Hg₅₂ and MgHg₂ (see Fig. 7.24, p. 157).

TH027: 14.9 mg (0.61 mmol) Mg, 14.1 mg (0.61 mmol) Na and 1.971 g (9.83 mmol) Hg were filled into a Ta crucible and welded shut. With 50 K h⁻¹, it was heated to 300 °C and tempered for three months. It was then cooled to RT by turning off the oven.

Analysis: Via pXRD, the product was identified as MgHg, MgHg₂ as well as a further, unidentified phase (see Fig. 7.28, p. 158).

Na–Ca–Hg (TH012, TH013, TH019, TH032, TH036, TH053, TH054)

TH012: 285.3 mg (7.0 mmol) Ca, 160.9 mg (7.0 mmol) Na and 11.230 g (56.0 mmol) Hg were weighed into a 100mL Schlenk flask. Since the Ca did not appear to melt after 30 min of heating at 350 °C with a hot air gun, the experiment was stopped.

Analysis: Further analysis was not performed.

TH013: 48.1 mg (1.2 mmol) Ca, 27.6 mg (1.2 mmol) Na and 1.924 g (9.6 mmol) Hg were filled into a Ta crucible and welded shut. With 50 K h^{-1} , it was heated to 300°C and tempered for eight weeks. It was then cooled to RT by turning off the oven.

Analysis: Via pXRD, the product was identified as a mixture of $\text{Na}_{11}\text{Hg}_{52}$ and $\text{Ca}_{141}\text{Hg}_{51}$ (see Fig. 7.14, p. 156).

TH019: 48.1 mg (1.2 mmol) Ca, 27.6 mg (1.2 mmol) Na and 3.848 g (19.2 mmol) Hg were filled into a Ta crucible and welded shut. With 50 K h^{-1} , it was heated to 300°C and tempered for eight weeks. It was then cooled to RT by turning off the oven.

Analysis: Via pXRD, the obtained product was identified as a mixture of $\text{Na}_{11}\text{Hg}_{52}$ and $\text{Ca}_{14}\text{Hg}_{51}$ (see Fig. 7.20, p. 157).

TH032: 48.1 mg (1.2 mmol) Ca, 27.6 mg (1.2 mmol) Na and 1.924 g (9.6 mmol) Hg were filled into a Ta crucible and welded shut. With 50 K h^{-1} , it was heated to 300°C and tempered for eight weeks. It was then cooled to RT by turning off the oven.

Analysis: Via pXRD, the product was identified as a mixture of $\text{Ca}_{11}\text{Hg}_{54}$ and $\text{Na}_{11}\text{Hg}_{52}$ (see Fig. 7.33, p. 159).

TH036: 24.5 mg (0.61 mmol) Ca, 14.1 mg (0.61 mmol) Na and 1.961 g (9.78 mmol) Hg were filled into a Ta crucible and welded shut. With 50 K h^{-1} , it was heated to 300°C and tempered for four months. It was then rapidly cooled with ice water.

Analysis: Via pXRD, the obtained product was identified as $\text{Ca}_{11}\text{Hg}_{54}$ with a slight shift towards higher diffraction angles (see Fig. 7.37, p. 159). Synchrotron powder diffraction analysis yielded a new ternary amalgam, $\text{Ca}_{6.9}\text{Na}_{4.1}\text{Hg}_{54}$ (for details, see Chapter 4.2, p. 42).

TH053: Due to the performed DSC measurement of TH013 (see Fig. 7.116, p. 173), the crystal quality was tried to improve at 140°C via Ostwald ripening. Since the reaction mixture solidified over night, further 2.132 g (10.6 mmol) Hg were added. In sum, 19 cycles of heating/cooling with 10 min intervals were performed.

Analysis: After analysis via pXRD, it was determined that the composition has not changed (see Fig. 7.51, p. 162). It was later determined to be the new ternary amalgam $\text{Ca}_{6.9}\text{Na}_{4.1}\text{Hg}_{54}$ (see Chapter 4.2, p. 42).

TH054: Due to the DSC measurement of TH019 (see Fig. 7.120, p. 173, crystal quality was tried to be improved at 180°C via Ostwald ripening (22 cycles, 10 min heating/cooling intervals).

Analysis: Via pXRD analysis, it was confirmed that the composition after Ostwald ripening did not change. Diffraction intensities were still between those of $\text{Na}_{11}\text{Hg}_{52}$ and $\text{Ca}_{14}\text{Hg}_{51}$ (see Fig. 7.52, p. 162).

Na–Sr–Hg (TH045, TH046)

TH045: 102.2 mg (1.17 mmol) Sr, 26.8 mg (1.17 mmol) Na and 1.864 g (9.29 mmol) were filled into a Ta crucible and welded shut. With 50 K h^{-1} , it was heated to 300°C and tempered for three months. It was then rapidly cooled with ice water.

Analysis: Via pXRD, the product was identified as a mixture of $\text{Sr}_{10.5}\text{Hg}_{54.5}$ and $\text{Na}_{11}\text{Hg}_{52}$ (see Fig. 7.45, p. 161).

TH046: 52.8 mg (0.60 mmol) Sr, 13.9 mg (0.60 mmol) Na and 1.964 g (9.79 mmol) Hg were filled into a Ta crucible and welded shut. With 50 K h^{-1} , it was heated to 300°C and tempered for three months. It was then rapidly cooled with ice water.

Analysis: As can be seen in the powder diffractogram, the obtained product show diffraction reflections between those of $\text{Sr}_{10.5}\text{Hg}_{54.5}$ and $\text{Na}_{11}\text{Hg}_{52}$, indicating a ternary variant (see Fig. 7.46, p. 161). Unfortunately, further attempts at Rietveld analysis based on synchrotron powder diffraction data did not reach convergence.

Na–Ba–Hg (TH062, TH066)

TH062: 155.6 mg (1.14 mmol) Ba, 26.1 mg (1.14 mmol) Na and 1.832 g (9.13 mmol) Hg were filled into a Ta crucible and welded shut. With 50 K h^{-1} , it was heated to 300°C and tempered for four months. It was then rapidly cooled with ice water.

Analysis: Via pXRD, the obtained product was identified as a mixture of $\text{Na}_{11}\text{Hg}_{52}$, $\text{Ba}_7\text{Hg}_{31}$ and BaHg_6 (see Fig. 7.59, p. 163).

TH066: 81.5 mg (0.59 mmol) Ba, 13.6 mg (0.59 mmol) Na and 1.890 g (9.42 mmol) Hg were filled into a Ta crucible and welded shut. With 50 K h^{-1} , it was heated to 300°C and tempered for four months. It was then rapidly cooled with ice water.

Analysis: Via pXRD, the obtained product was identified as a mixture of BaHg_{11} and $\text{Na}_{11}\text{Hg}_{52}$ (see Fig. 7.60, p. 163).

K–Mg–Hg (TH024, TH028)

TH024: 29.1 mg (1.20 mmol) Mg, 46.9 mg (1.20 mmol) K and 1.924 g (9.58 mmol) Hg were filled into a Ta crucible and welded shut. With 50 K h^{-1} , it was heated to 300°C and tempered for four months. It was then cooled to RT by turning off the oven.

Analysis: Via pXRD, the obtained product was identified as a mixture of MgHg_2 , KHg_6 and KHg_{11} (see Fig. 7.25, p. 157).

TH028: 14.9 mg (0.61 mmol) Mg, 23.9 mg (0.61 mmol) K and 1.961 g (9.78 mmol) Hg were filled into a Ta crucible and welded shut. With 50 K h^{-1} , it was heated to 300°C and tempered for three months. It was then cooled to RT by turning off the oven.

Analysis: Via pXRD, the product was identified as a mixture of KHg_{11} and MgHg_2 (see Fig. 7.29, p. 158).

K–Ca–Hg (TH014, TH020, TH033, TH037, TH055, TH056)

TH014: 47.6 mg (1.19 mmol) Ca, 46.4 mg (1.19 mmol) K and 1.906 g (9.5 mmol) Hg were filled into a Ta crucible and welded shut. With 50 K h^{-1} , it was heated to 300°C and tempered for eight weeks. It was then cooled to RT by turning off the oven.

Analysis: Via pXRD, the product was identified as a mixture of CaHg_3 , K_7Hg_{31} and KHg_5 (see Fig. 7.15, p. 156).

TH020: 47.6 mg (1.19 mmol) Ca, 46.4 mg (1.19 mmol) K and 3.812 g (19.0 mmol) Hg were filled into a Ta crucible and welded shut. With 50 K h^{-1} , it was heated to 300°C and tempered for eight weeks. It was then cooled to RT by turning off the oven.

Analysis: Via pXRD, the obtained product was identified as a mixture of CaHg_{11} , $\text{Ca}_{11}\text{Hg}_{54}$ and KHg_{11} (see Fig. 7.21, p. 157).

TH033: 47.6 mg (1.19 mmol) Ca, 46.4 mg (1.19 mmol) K and 1.906 g (9.50 mmol) Hg were filled into a Ta crucible and welded shut. With 50 K h^{-1} , it was heated to 300°C and tempered for four months. It was then rapidly cooled with ice water.

Analysis: Via pXRD, only CaHg_3 and $\text{Ca}_{11}\text{Hg}_{54}$ could be identified, a K-containing phase was not present (see Fig. 7.34, p. 159).

TH037: 24.4 mg (0.61 mmol) Ca, 23.8 mg (0.61 mmol) K and 1.952 g (9.73 mmol) Hg were filled into a Ta crucible and welded shut. With 50 K h^{-1} , it was heated to 300°C and tempered for four months. It was then rapidly cooled with ice water.

Analysis: Via pXRD, the product was identified as a mixture of $\text{Ca}_{11}\text{Hg}_{54}$ and KHg_{11} (see Fig. 7.38, p. 160).

TH055: Due to the DSC measurement of TH014 (see Fig. 7.117, p. 173), crystal quality was tried to improve by performing Ostwald ripening at 120°C . For this purpose, approx. 0.5 g (2.5 mmol) Hg were added and heating/cooling was done over 21 cycles with 10 min intervals.

Analysis: Via pXRD, the product was identified as a mixture of KHg_{11} , CaHg_{11} and $\text{Ca}_{11}\text{Hg}_{54}$ (see Fig. 7.53, p. 162).

TH056: Due to the DSC measurement of TH020, crystal quality was tried to improved by Ostwald ripening at 190 °C. For this purpose, 2.279 g (11.4 mmol) Hg were added and heating/cooling was performed over 22 cycles with 10 min intervals.

Analysis: Via pXRD, it was confirmed that the composition of the sample has not changed (see Fig. 7.54, p. 162).

K–Sr–Hg (TH047, TH048)

TH047: 101.2 mg (1.16 mmol) Sr, 45.2 mg (1.16 mmol) K and 1.847 g (9.21 mmol) Hg were filled into a Ta crucible and welded shut. With 50 K h⁻¹, it was heated to 300 °C and tempered for three months. It was then rapidly cooled with ice water.

Analysis: Upon opening the crucible, it was discovered that the sealing was incomplete. Further analysis was not performed.

TH048: 52.5 mg (0.60 mmol) Sr, 23.4 mg (0.60 mmol) K and 1.915 g (9.55 mmol) Hg were filled into a Ta crucible and welded shut. With 50 K h⁻¹, it was heated to 300 °C and tempered for three months. It was then rapidly cooled with ice water.

Analysis: Via pXRD, the obtained product was identified as a mixture of KHg₁₁ and Sr_{10.5}Hg_{54.5} (see Fig. 7.47, p. 161).

K–Ba–Hg (TH063, TH067)

TH063: 154.2 mg (1.12 mmol) Ba, 43.9 mg (1.12 mmol) K and 1.778 g (8.86 mmol) Hg were filled into a Ta crucible and welded shut. With 50 K h⁻¹, it was heated to 300 °C and tempered for four months. It was then rapidly cooled with ice water.

Analysis: Upon opening the crucible, it was discovered that the sealing was incomplete. Further analysis was not performed.

TH067: 81.1 mg (0.59 mmol) Ba, 23.1 mg (0.59 mmol) K and 1.875 g (9.35 mmol) Hg were filled into a Ta crucible and welded shut. With 50 K h⁻¹, it was heated to 300 °C and tempered for four months. It was then rapidly cooled with ice water.

Analysis: Via pXRD, the obtained product was identified as a mixture of KHg₁₁, Ba₂₀Hg₁₀₃ and BaHg₆ (see Fig. 7.61, p. 163).

Rb–Mg–Hg (TH025, TH029)

TH025: 28.4 mg (1.17 mmol) Mg, 85.5 mg (1.00 mmol) Rb and 1.872 g (9.33 mmol) Hg were filled into a Ta crucible and welded shut. With 50 K h⁻¹, it was heated to 300 °C and tempered for four months. It was then cooled to RT by turning off the oven.

Analysis: Via pXRD, the product was identified as a mixture of RbHg₁₁ and Rb₃Hg₂₀, no Mg-containing phase seems to be present (see Fig. 7.26, p. 158).

TH029: 14.6 mg (0.60 mmol) Mg, 51.5 mg (0.60 mmol) Rb and 1.934 g (9.64 mmol) Hg were filled into a Ta crucible and welded shut. With 50 K h⁻¹, it was heated to 300 °C and tempered for four months. It was then cooled to RT by turning off the oven.

Analysis: Via pXRD, the product was identified as RbHg₁₁, no Mg-containing phase seems to be present (see Fig. 7.30, p. 158).

Rb–Ca–Hg (TH015, TH021, TH034, TH038, TH057, TH058)

TH015: 46.3 mg (1.13 mmol) Ca, 98.8 mg (1.13 mmol) Rb and 1.855 g (9.25 mmol) Hg were filled into a Ta crucible and welded shut. With 50 K h⁻¹, it was heated to 300 °C and tempered for eight weeks. It was then cooled to RT by turning off the oven.

Analysis: Via pXRD, the obtained product was identified as Rb₃Hg₂₀, other phases, especially Ca-containing ones, are not present (see Fig. 7.16, p. 156).

TH021: 48.3 mg (1.13 mmol) Ca, 98.8 mg (1.13 mmol) Rb and 3.71 g (18.5 mmol) Hg were filled into a Ta crucible and welded shut. With 50 K h^{-1} , it was heated to $300\text{ }^{\circ}\text{C}$ and tempered for eight weeks. It was then cooled to RT by turning off the oven.

Analysis: Via pXRD, the obtained product was identified as a mixture of RbHg_{11} , $\text{Ca}_{11}\text{Hg}_{54}$ and CaHg_{11} (see Fig. 7.22, p. 157).

TH034: 46.3 mg (1.13 mmol) Ca, 98.8 mg (1.13 mmol) Rb and 1.855 g (9.25 mmol) Hg were filled into a Ta crucible and welded shut. With 50 K h^{-1} , it was heated to $300\text{ }^{\circ}\text{C}$ and tempered for four months. It was then rapidly cooled with ice water.

Analysis: Via pXRD, the obtained product was identified as a mixture of CaHg_3 , Rb_2Hg_7 and $\text{Rb}_3\text{Hg}_{20}$ (see Fig. 7.35, p. 159).

TH038: 24.0 mg (0.60 mmol) Ca, 51.2 mg (0.60 mmol) Rb and 1.925 g (9.60 mmol) Hg were filled into a Ta crucible and welded shut. With 50 K h^{-1} , it was heated to $300\text{ }^{\circ}\text{C}$ and tempered for four months. It was then rapidly cooled with ice water.

Analysis: Via pXRD, the obtained product was identified as a mixture of RbHg_{11} and $\text{Ca}_{14}\text{Hg}_{51}$ (see Fig. 7.39, p. 160).

TH057: Due to the DSC measurement of TH015 (see Fig. 7.118, p. 173), the crystal quality was tried to improve via Ostwald ripening. For this purpose, 1.666 g (8.31 mmol) Hg were added and 21 heating/cooling cycles of 10 min intervals were performed.

Analysis: Via pXRD, the obtained product was identified as only $\text{Ca}_{11}\text{Hg}_{54}$ (see Fig. 7.55, p. 162).

TH058: Due to the DSC measurement of TH021 (see Fig. 7.122, p. 174), the crystal quality was tried to improve via Ostwald ripening. For this purpose, 2.033 g (10.13 mmol) Hg were added and 22 heating/cooling cycles of 10 min intervals were performed.

Analysis: After analysis via pXRD, it was determined that the composition has not changed, the product still consisted of CaHg_{11} , $\text{Ca}_{11}\text{Hg}_{54}$ and RbHg_{11} (see Fig. 7.56, p. 163).

Rb–Sr–Hg (TH049, TH050)

TH049: 98.6 mg (1.12 mmol) Sr, 96.1 mg (1.12 mmol) Rb and 1.808 g (9.01 mmol) Hg were filled into a Ta crucible and welded shut. With 50 K h^{-1} , it was heated to $300\text{ }^{\circ}\text{C}$ and tempered for three months. It was then rapidly cooled with ice water.

Analysis: Via pXRD, the obtained product was identified as a mixture of $\text{Rb}_5\text{Hg}_{19}$ and $\text{Sr}_{10.5}\text{Hg}_{54.5}$ (see Fig. 7.48, p. 161).

TH050: 51.8 mg (0.59 mmol) Sr, 50.5 mg (0.59 mmol) Rb and 1.885 g (9.40 mmol) Hg were filled into a Ta crucible and welded shut. With 50 K h^{-1} , it was heated to $300\text{ }^{\circ}\text{C}$ and tempered for three months. It was then rapidly cooled with ice water.

Analysis: Via pXRD, the product was identified as a mixture of $\text{Rb}_3\text{Hg}_{20}$, RbHg_{11} and $\text{Sr}_{10.5}\text{Hg}_{54.5}$ (see Fig. 7.49, p. 161).

Rb–Ba–Hg (TH064, TH068)

TH064: 130.3 mg (1.09 mmol) Ba, 93.5 mg (1.09 mmol) Rb and 1.772 g (8.83 mmol) Hg were filled into a Ta crucible and welded shut. With 50 K h^{-1} , it was heated to $300\text{ }^{\circ}\text{C}$ and tempered for four months. It was then rapidly cooled with ice water.

Analysis: Upon opening the crucible, it was discovered that the sealing was incomplete. Further analysis was not performed.

TH068: 80.0 mg (0.59 mmol) Ba, 49.8 mg (0.59 mmol) Rb and 1.8745 g (9.34 mmol) Hg were filled into a Ta crucible and welded shut. With 50 K h^{-1} , it was heated to $300\text{ }^{\circ}\text{C}$ and tempered for four months. It was then rapidly cooled with ice water.

Analysis: Upon opening the crucible, it was discovered that the sealing was incomplete. Further analysis was not performed.

Cs–Mg–Hg (TH026, TH030)

TH026: 29.4 mg (1.21 mmol) Mg, 150.9 mg (1.21 mmol) Cs and 1.822 g (9.08 mmol) Hg were filled into a Ta crucible and welded shut. With 50 K h^{-1} , it was heated to $300\text{ }^{\circ}\text{C}$ and tempered for three months. It was cooled to RT by turning off the oven.

Analysis: Via pXRD, the obtained product was identified as a mixture of $\text{Cs}_3\text{Hg}_{20}$ and MgHg_2 (see Fig. 7.27, p. 158).

TH030: 14.4 mg (0.59 mmol) Mg, 78.9 mg (0.59 mmol) Cs and 1.91 g (9.52 mmol) Hg were filled into a Ta crucible and welded shut. With 50 K h^{-1} , it was heated to $300\text{ }^{\circ}\text{C}$ and tempered for three months. It was cooled to RT by turning off the oven.

Analysis: Via pXRD, only $\text{Cs}_3\text{Hg}_{20}$ was found, no Mg-containing phase was present (see Fig. 7.31, p. 158).

Cs–Ca–Hg (TH016, TH022, TH035, TH039, TH059, TH060)

TH016: 45.1 mg (1.13 mmol) Ca, 149.5 mg (1.13 mmol) Cs and 1.805 g (9.30 mmol) Hg were filled into a Ta crucible and welded shut. With 50 K h^{-1} , it was heated to $300\text{ }^{\circ}\text{C}$ and tempered for eight weeks. It was cooled to RT by turning off the oven.

Analysis: Via pXRD Analysis, the diffraction pattern of $\text{Cs}_3\text{Hg}_{20}$ with a shift towards higher diffraction angles was found (see Fig. 7.17, p. 156). On this basis, Rietveld refinement was performed, yielding a mixed occupation of Cs/Ca (for further details see Ch. 4.3, p.61).

TH022: 45.1 mg (1.13 mmol) Ca, 149.5 mg (1.13 mmol) Cs and 3.61 g (18.0 mmol) Hg were filled into a Ta crucible and welded shut. With 50 K h^{-1} , it was heated to $300\text{ }^{\circ}\text{C}$ and tempered for eight weeks. It was cooled to RT by turning off the oven.

Analysis: Via pXRD, only $\text{Ca}_{14}\text{Hg}_{51}$ was identified, no Cs-containing phase seemed present (see Fig. 7.23, p. 157).

TH035: 45.1 mg (1.13 mmol) Ca, 149.5 mg (1.13 mmol) Cs and 1.805 g (9.30 mmol) Hg were filled into a Ta crucible and welded shut. With 50 K h^{-1} , it was heated to $300\text{ }^{\circ}\text{C}$ and tempered for four months. It was then rapidly cooled with ice water.

Analysis: Via pXRD, the obtained product was identified as a mixture of $\text{Ca}_{11}\text{Hg}_{54}$, CaHg_2 and $\text{Cs}_3\text{Hg}_{20}$ (see Fig. 7.36, p. 159).

TH039: 23.7 mg (0.59 mmol) Ca, 78.6 mg (0.59 mmol) Cs und 1.898 g (9.46 mmol) Hg were filled into a Ta crucible and welded shut. With 50 K h^{-1} , it was heated to $300\text{ }^{\circ}\text{C}$ and tempered for four months. It was then rapidly cooled with ice water.

Analysis: Via pXRD, the obtained product was identified as a mixture of $\text{Ca}_{11}\text{Hg}_{54}$ and $\text{Cs}_3\text{Hg}_{20}$ (see Fig. 7.40, p. 160).

TH059: Due to the results of the DSC measurement of TH016 (see Fig. 7.119, p. 173), crystal quality was tried to be improved via Ostwald ripening at $120\text{ }^{\circ}\text{C}$. For this purpose, 1.448 g (7.22 mmol) Hg were added and 22 cycles of heating/cooling with 10 min intervals were performed.

Analysis: pXRD Analysis showed that during Ostwald ripening, the composition has changed. In addition to $\text{Cs}_3\text{Hg}_{20}$, $\text{Ca}_{11}\text{Hg}_{54}$ and $\text{Ca}_{14}\text{Hg}_{51}$ were identified (see Fig. 7.57, p. 163).

TH060: Due to the results of the DSC measurement of TH016 (see Fig. 7.123, p. 174), crystal quality was tried to be improved via Ostwald added and 8 cycles of heating/cooling with 10 min intervals were performed. Afterwards, the temperature was increased to $130\text{ }^{\circ}\text{C}$ and further 20 cycles of heating/cooling were performed.

Analysis: Via pXRD it was confirmed that the composition of the product has not changed, it still consists only of $\text{Ca}_{14}\text{Hg}_{51}$ (see Fig. 7.58, p. 163).

Cs–Sr–Hg (TH051, TH052)

TH051: 96.0 mg (1.10 mmol) Sr, 145.6 mg (1.10 mmol) Cs and 1.731 g (8.63 mmol) Hg were filled into a Ta crucible and welded shut. With 50 K h^{-1} , it was heated to 300°C and tempered for three months. It was then rapidly cooled with ice water.

Analysis: Via pXRD, the obtained product was identified as a mixture of $\text{Cs}_3\text{Hg}_{20}$, $\text{Cs}_5\text{Hg}_{19}$, $\text{Sr}_{13}\text{Hg}_{58}$ and SrHg_{11} (see Fig. 7.50, p. 162).

TH052: 51.1 mg (0.58 mmol) Sr, 77.5 mg (0.58 mmol) Cs and 1.874 g (9.34 mmol) Hg were filled into a Ta crucible and welded shut. With 50 K h^{-1} , it was heated to 300°C and tempered for three months. It was then rapidly cooled with ice water.

Analysis: Upon opening the crucible, it was discovered that the sealing was incomplete. Further analysis was not performed.

Cs–Ba–Hg (TH065, TH069)

TH065: 146.5 mg (1.07 mmol) Ba, 141.8 mg (1.07 mmol) Cs and 1.729 g (8.62 mmol) Hg were filled into a Ta crucible and welded shut. With 50 K h^{-1} , it was heated to 300°C and tempered for four months. It was then rapidly cooled with ice water.

Analysis: Upon opening the crucible, it was discovered that the sealing was incomplete. Further analysis was not performed.

TH069: 79.0 mg (0.57 mmol) Ba, 76.4 mg (0.57 mmol) Cs and 1.827 g (9.11 mmol) Hg were filled into a Ta crucible and welded shut. With 50 K h^{-1} , it was heated to 300°C and tempered for one week. It was then rapidly cooled with ice water.

Analysis: Upon opening the crucible, it was discovered that the sealing was incomplete. Further analysis was not performed.

Eu–Mg–Hg (TH090, TH094)

TH090: 22.6 mg (0.93 mmol) Mg, 140.7 mg (0.93 mmol) Eu and 1.8303 g (9.12 mmol) Hg were filled into a Ta crucible and welded shut. With 100 K h^{-1} it was heated to 800°C , kept at this temperature for 24 h, cooled with 100 K h^{-1} to 350°C and then cooled with 0.5 K h^{-1} to 250°C . After further 123 456 h, it was rapidly cooled with ice water inside the quartz tube, since the welding was not complete.

Analysis: Via pXRD, only EuHg_2 and MgHg_2 could be identified. Another, unknown phase seems to be present as the majority compound (see Fig. 7.79, p. 166)

TH094: 22.5 mg (0.93 mmol) Mg, 140.3 mg (0.92 mmol) Eu and 1.8385 g (9.13 mmol) Hg were filled into a Ta crucible and welded shut. With 100 K h^{-1} it was heated to 800°C kept at this temperature for 24 h, cooled with 100 K h^{-1} to 350°C and then cooled with 0.5 K h^{-1} to 250°C . After further 123 456 h, it was rapidly cooled with ice water

Analysis: Upon opening the crucible, it was discovered that the sealing was incomplete. Further analysis was not performed.

Eu–Ca–Hg (TH091)

TH091: 37.5 mg (0.94 mmol) Ca, 136.7 mg (0.90 mmol) Eu and 1.8470 g (9.21 mmol) Hg were filled into a Ta crucible and welded shut. With 100 K h^{-1} it was heated to 800°C kept at this temperature for 24 h, cooled with 0.5 K h^{-1} to 650°C and then rapidly cooled to RT with ice water.

Analysis: Analysis via pXRD showed that the diffraction pattern was directly between the ones of $\text{Ca}_{11}\text{Hg}_{54}$ and $\text{Eu}_{10}\text{Hg}_{54}$ (see Fig. 7.80, p. 167). Single crystal analysis as well as Rietveld refinement yielded the new ternary Amalgam $\text{Ca}_{4.5}\text{Eu}_{6.5}\text{Hg}_{54}$ (see Ch. 4.2, p. 42).

Eu–Ba–Hg (TH092)

TH092: 119.3 mg (0.87 mmol) Ba, 136.1 mg (0.90 mmol) Eu and 1.7346 g (8.65 mmol) Hg were filled into a Ta crucible and welded shut. With 100 K h^{-1} it was heated to 800°C kept at this temperature for 24 h, cooled with 100 K h^{-1} to 200°C and then cooled to 100°C with 0.5 K h^{-1} . Finally, it was rapidly cooled to RT with ice water.

Analysis: Via pXRD, the product was identified as a mixture of BaHg_{11} , EuHg_2 and $\text{Eu}_{10}\text{Hg}_{55}$ (see Fig. 7.82, p. 167).

Yb–Na–Hg (TH093, TH095)

TH093: 21.0 mg (0.91 mmol) Na, 154.3 mg (0.89 mmol) Yb and 1.8137 g (9.04 mmol) Hg were filled into a Ta crucible and welded shut. With 100 K h^{-1} it was heated to 800°C , kept at this temperature for 24 h, cooled with 100 K h^{-1} to 300°C and then cooled to 200°C with 0.5 K h^{-1} . Finally, it was rapidly cooled to RT with ice water inside the quartz tube.

Analysis: Via pXRD, the obtained product was identified as a mixture of $\text{Na}_{11}\text{Hg}_{52}$, YbHg_3 and NaHg_2 (see Fig. 7.82, p. 167).

TH095: 20.9 mg (0.91 mmol) Na, 178.8 mg (1.03 mmol) Yb and 1.8147 g (9.05 mmol) Hg were filled into a Ta crucible and welded shut. With 100 K h^{-1} , it was heated to 800°C , kept at this temperature for 24 h belassen, cooled with 100 K h^{-1} to 300°C and then cooled with 0.5 K h^{-1} to 200°C . After further 24 h it was rapidly cooled to RT with ice water.

Analysis: Via pXRD, the product was identified as a mixture of $\text{Na}_{11}\text{Hg}_{52}$, $\text{Yb}_{11}\text{Hg}_{54}$ and YbHg_3 (see Fig. 7.83, p. 167).

7.3 Powder diffractograms

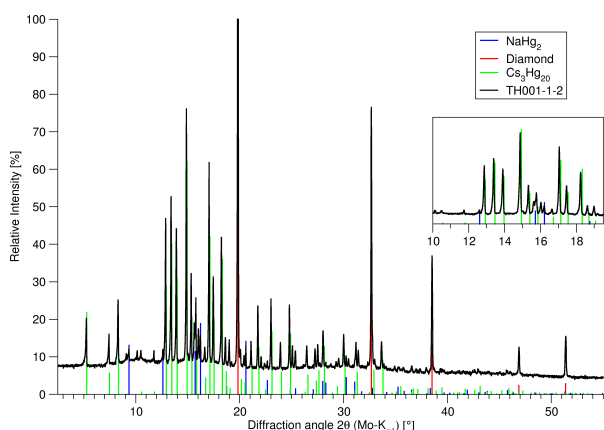


Fig. 7.2: Powder diffractogram of TH001 after quenching (black). Diamond^[4] (red) was used for optical dilution. Only NaHg₂^[5] (blue) and Cs₃Hg₂₀^[6] (green) were obtained.

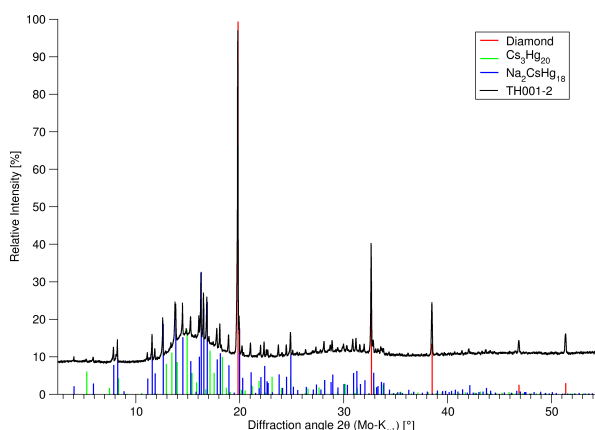


Fig. 7.3: Powder diffractogram of TH001-2 (black). Diamond^[4] (red) was used for optical dilution. The obtained solid consist of CsNa₂Hg₁₈ (blue, generated from single crystal data) and Cs₃Hg₂₀^[6] (green).

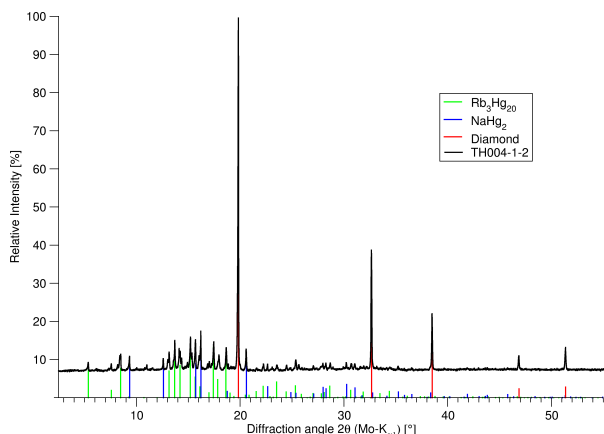


Fig. 7.4: Powder diffractogram of TH004-1 (black). Diamond^[4] (red) was used for optical dilution. The obtained solid was identified as a mixture of NaHg₂^[5] (blue) and Rb₃Hg₂₀^[6] (green).

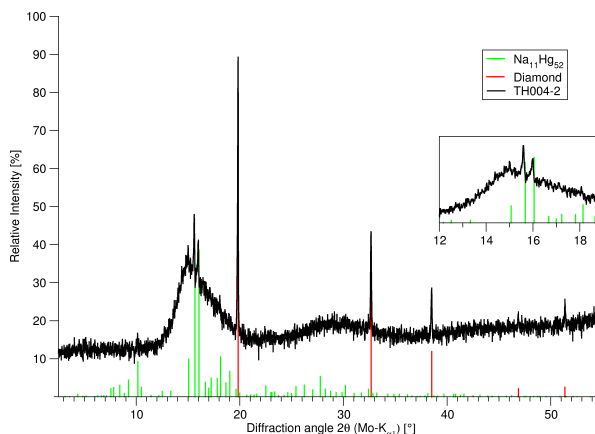


Fig. 7.5: Powder diffractogram of TH004-2 (black). Diamond^[4] (red) was used for optical dilution. The obtained product consists only of Na₁₁Hg₅₂^[2] (green).

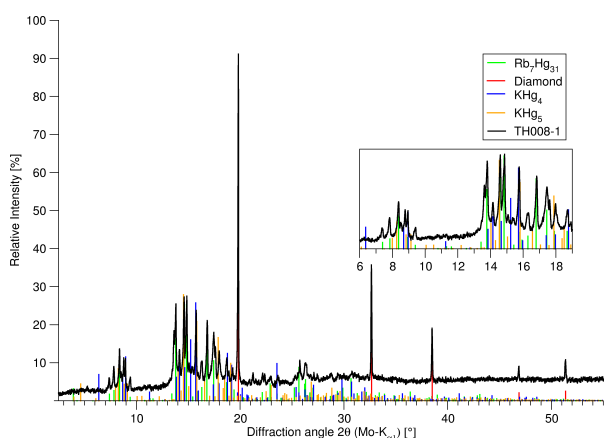


Fig. 7.6: Powder diffractogram of TH008-1 (black). Diamond^[4] (red) was used for optical dilution. Rb₇Hg₃₁^[6] (green) was obtained. The remaining reflexes cannot be assigned unequivocally, but KHg₄ (blue) or KHg₅ (red, both generated from single crystal data) seem most fitting.

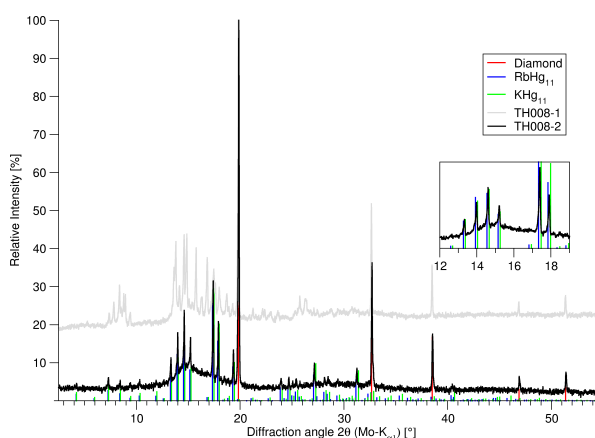


Fig. 7.7: Powder diffractogram of TH008-2 (black) with TH008-1 (gray) in comparison. Diamond^[4] (red) was used for optical dilution. As can be seen, the obtained product is a solid solution of KHg₁₁^[3] (green) and RbHg₁₁^[3] (blue). For further details, see Chapter 4.3, p. 61).

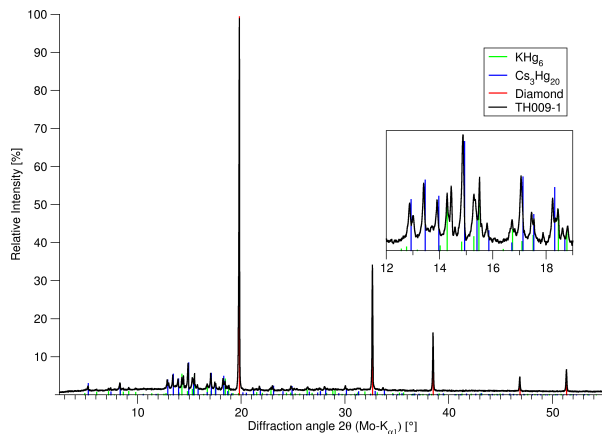


Fig. 7.8: Powder diffractogram of TH009-1 (black). Diamond^[4] (red) was used for optical dilution. The obtained product consists of KHg_6 ^[7] (green) and $\text{Cs}_3\text{Hg}_{20}$ ^[6] (blue).

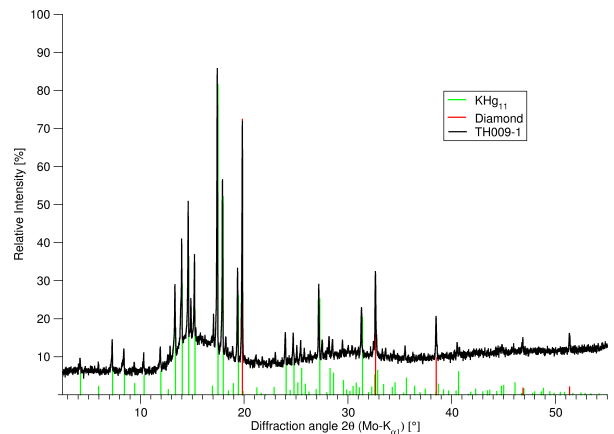


Fig. 7.9: Powder diffractogram of TH009-2 (black). Diamond^[4] (red) was used for optical dilution. The obtained product contains only KHg_{11} ^[3] (green).

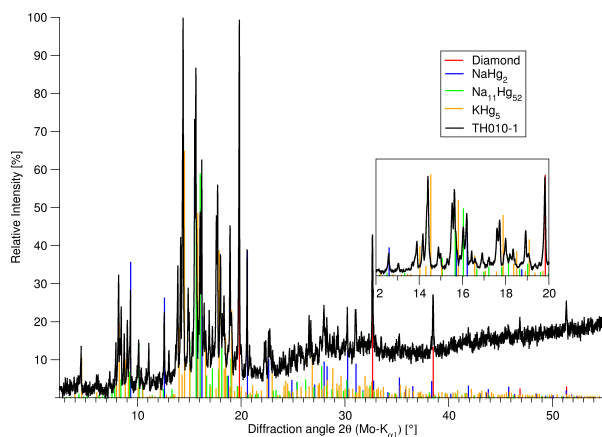


Fig. 7.10: Powder diffractogram of TH010-1 (black). Diamond^[4] (red) was used for optical dilution. The obtained product consists NaHg_2 ^[5] (blue), $\text{Na}_{11}\text{Hg}_{52}$ ^[2] (green) and KHg_5 (orange, generated from single crystal data).

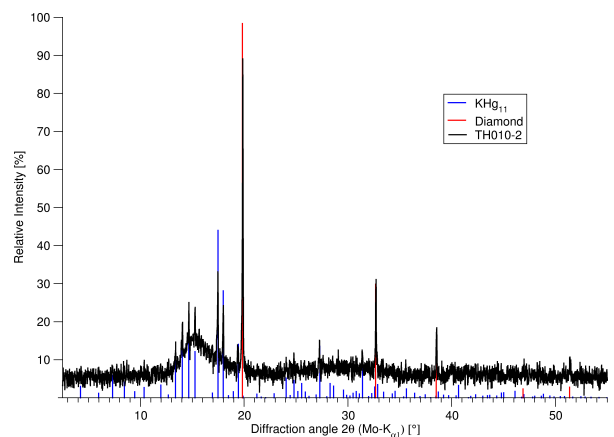


Fig. 7.11: Powder diffractogram of TH010-2 (black). Diamond^[4] (red) was used for optical dilution. The obtained product consists only of KHg_{11} ^[3] (blue).

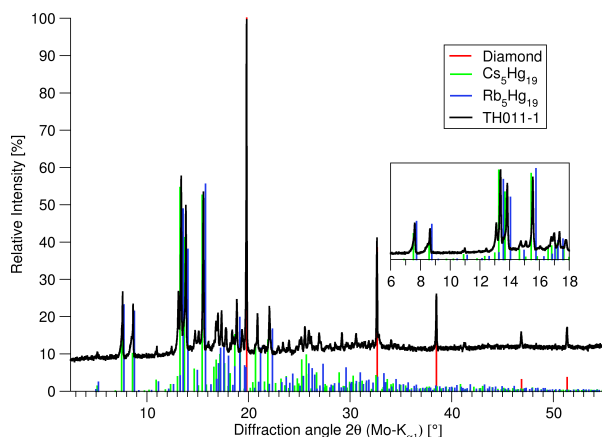


Fig. 7.12: Powder diffractogram of TH011-1 (black). Diamond^[4] (red) was used for optical dilution. The diffraction pattern of the obtained product is exactly between the ones of $\text{Cs}_5\text{Hg}_{19}$ ^[6] (green) and $\text{Rb}_5\text{Hg}_{19}$ ^[8] (blue).

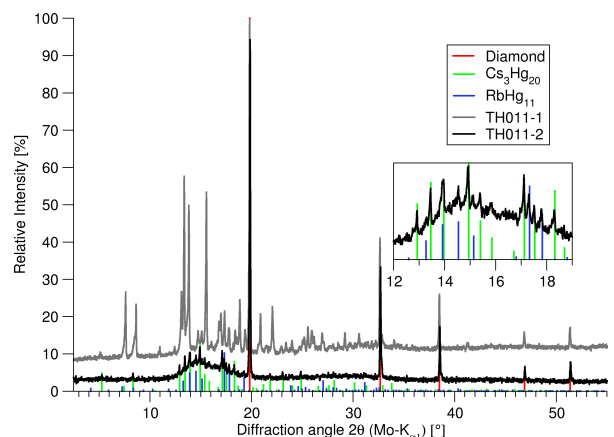


Fig. 7.13: Powder diffractogram of TH011-2 (black) and TH011-1 in comparison (grey). Diamond^[4] (red) was used for optical dilution. The obtained product consists of $\text{Cs}_3\text{Hg}_{20}$ (green)^[6] and RbHg_{11} (blue).^[3]

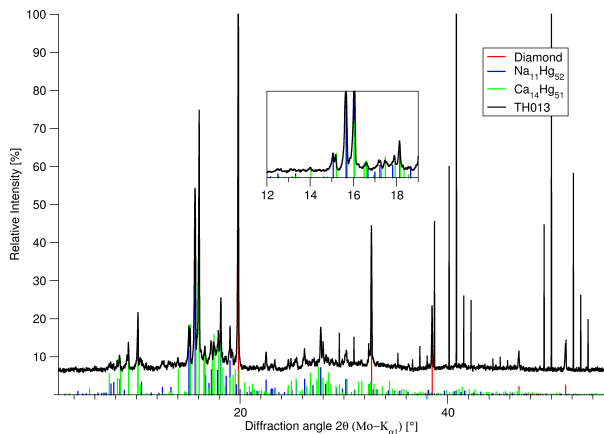


Fig. 7.14: Powder diffractogram of TH013 (black). Diamond^[4] (red) was used for optical dilution. The product only contained Na₁₁Hg₅₂^[2] (blue) and Ca₁₄Hg₅₁^[9] (green). Sharp intensities at angles $\geq 29.5^\circ 2\theta$ originate from a detector malfunction.

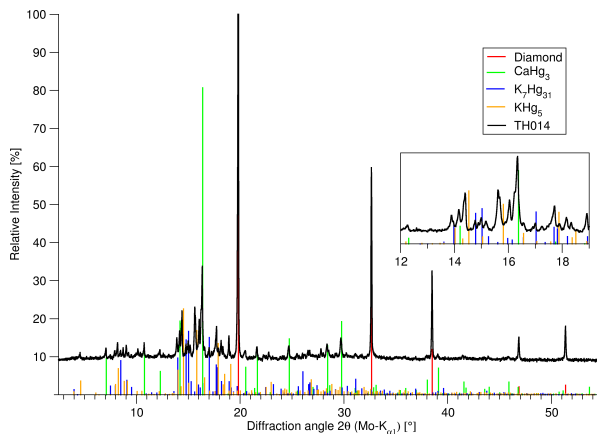


Fig. 7.15: Powder diffractogram of TH014 (black). Diamond^[4] (red) was used for optical dilution. The obtained product consists of CaHg₃^[10] (green), K₇Hg₃₁^[6] (blue) as well as KHg₅ (orange, generated from single crystal data).

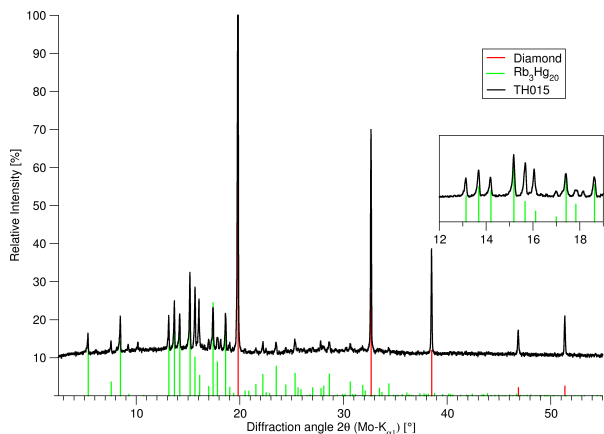


Fig. 7.16: Powder diffractogram of TH015 (black). Diamond^[4] (red) was used for optical dilution. Only Rb₃Hg₂₀^[6] (green) is present, no other phases can be seen.

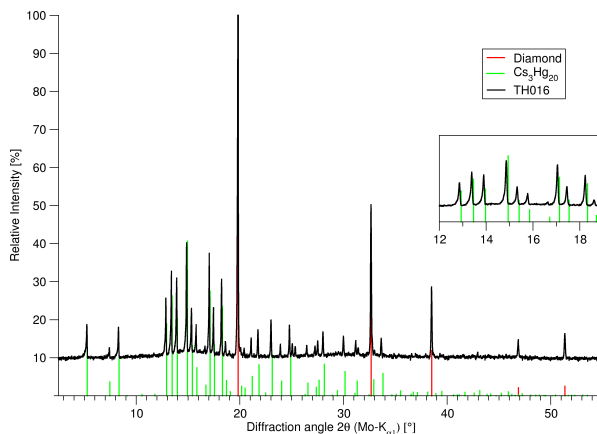


Fig. 7.17: Powder diffractogram of TH016 (black). The diffraction pattern indicates Cs₃Hg₂₀^[6] (green), but a shift towards higher diffraction angles can be seen. Thus, Rietveld refinement was performed, yielding a mixed occupation of the Cs site with Ca (further details see Ch. 4.3, p. 61).

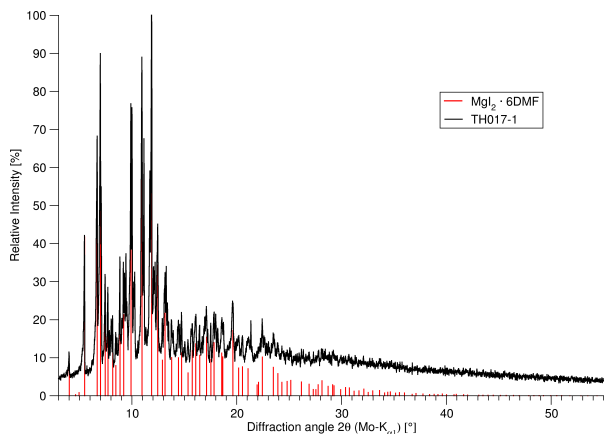


Fig. 7.18: Powder diffractogram of TH017 (black) with simulated intensities of MgI₂ · 6DMF^[11] (red).

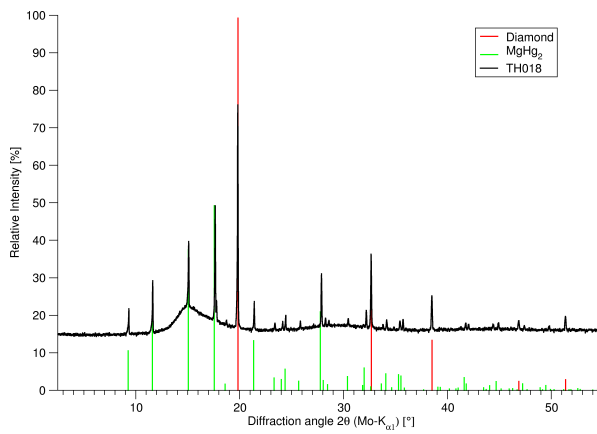


Fig. 7.19: Powder diffractogram of TH018 (black). Diamond^[4] (red) was used to optically dilute the sample. The obtained solid can be identified as MgHg₂^[12] (green).

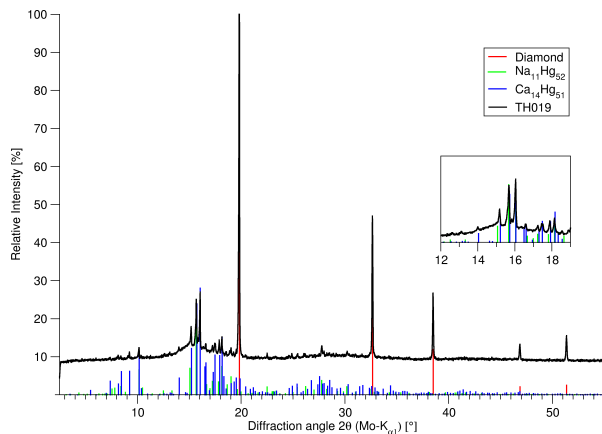


Fig. 7.20: Powder diffractogram of TH019 (black). Diamond^[4] (red) was used for optical dilution. The obtained product is a mixture of Na₁₁Hg₅₂^[2] (green) and Ca₁₄Hg₅₁^[13] (blue).

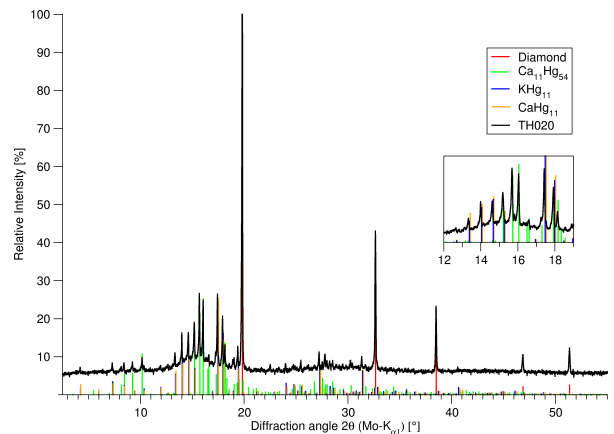


Fig. 7.21: Powder diffractogram of TH020 (black). Diamond^[4] (red) was used for optical dilution. The obtained product consists of Ca₁₁Hg₅₄^[9] (green), CaHg₁₁^[14] (orange) and KHg₁₁^[3] (blue).

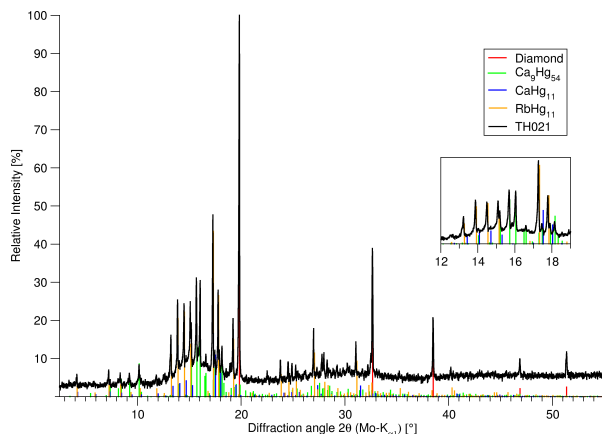


Fig. 7.22: Powder diffractogram of TH021 (black). Diamond^[4] (red) was used for optical dilution. The product consists of Ca₁₁Hg₅₄^[9] (green), CaHg₁₁^[14] (blue) and RbHg₁₁^[3] (orange).

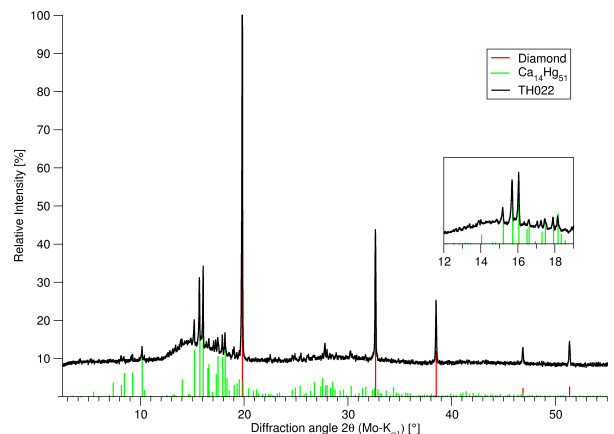


Fig. 7.23: Powder diffractogram of TH022 (black). Diamond^[4] (red) was used for optical dilution. Only Ca₁₄Hg₅₁^[13] (green) was found, no Cs-containing phase seemed present.

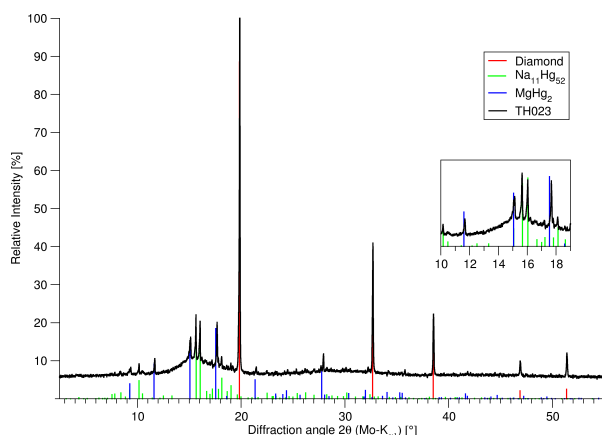


Fig. 7.24: Powder diffractogram of TH023 (black). Diamond^[4] (red) was used for optical dilution. The obtained product is a mixture of Na₁₁Hg₅₂ (green)^[2] and MgHg₂ (blue).^[12]

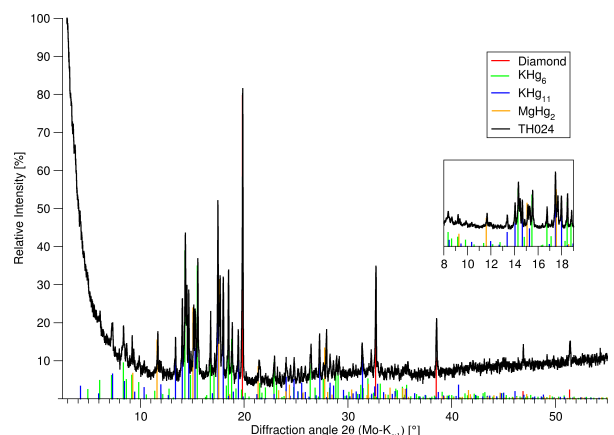


Fig. 7.25: Powder diffractogram of TH024 (black). Diamond^[4] (red) was used for optical dilution. The obtained product consists of MgHg₂^[12] (orange), KHg₆^[7] (green) and KHg₁₁^[3] (blue).

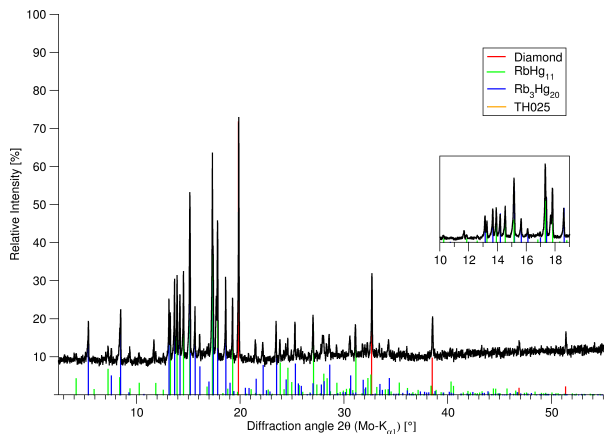


Fig. 7.26: Powder diffractogram of TH025 (black). Diamond^[4] (red) was used for optical dilution. The product consists of RbHg₁₁^[3] (green) and Rb₃Hg₂₀^[6] (blue), no Mg-containing phase seems to be present.

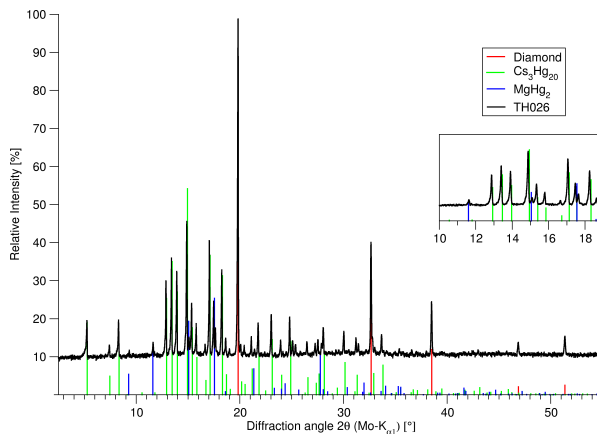


Fig. 7.27: Powder diffractogram of TH026 (black). Diamond^[4] (red) was used for optical dilution. The obtained product consists of Cs₃Hg₂₀^[6] (green) and MgHg₂^[12] (blue).

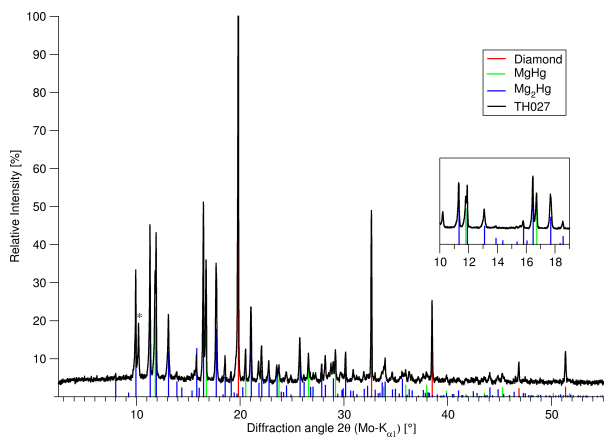


Fig. 7.28: Powder diffractogram of TH027 (black). Diamond^[4] (red) was used for optical dilution. The obtained products are MgHg^[15] (green), Mg₂Hg^[15] (blue) and an unknown phase (marked with *).

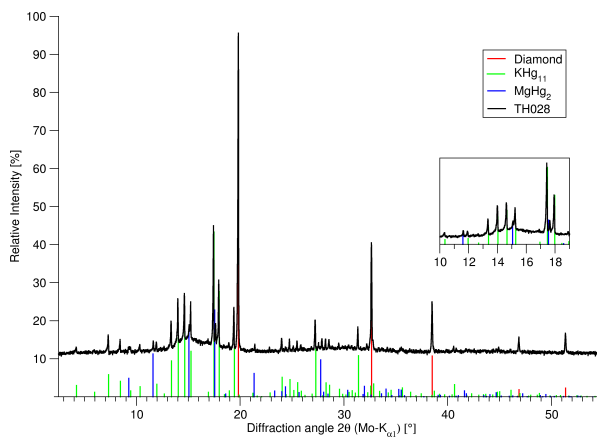


Fig. 7.29: Powder diffractogram of TH028 (black). Diamond^[4] (red) was used for optical dilution. The product consists of KHg₁₁^[3] (green) and MgHg₂^[12] (blue).

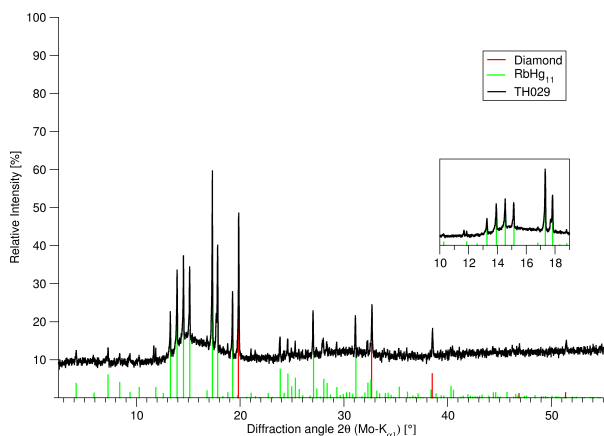


Fig. 7.30: Powder diffractogram of TH029 (black). The product consist only of RbHg₁₁^[3] (green), no Mg-containing phase seems to be present.

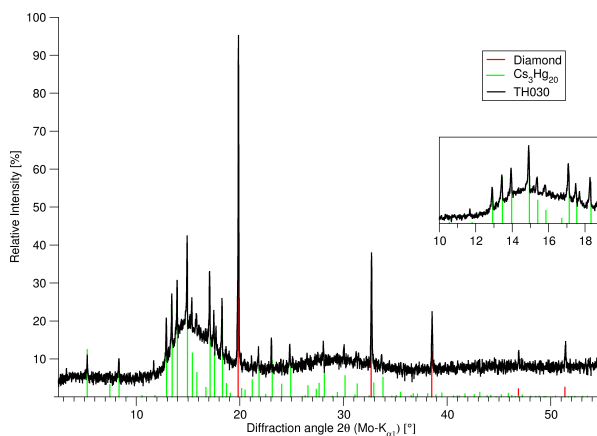


Fig. 7.31: Powder diffractogram of TH030 (black). Diamond^[4] (red) was used for optical dilution. Only Cs₃Hg₂₀^[6] (green) can be identified, a Mg-containing phase is not present.

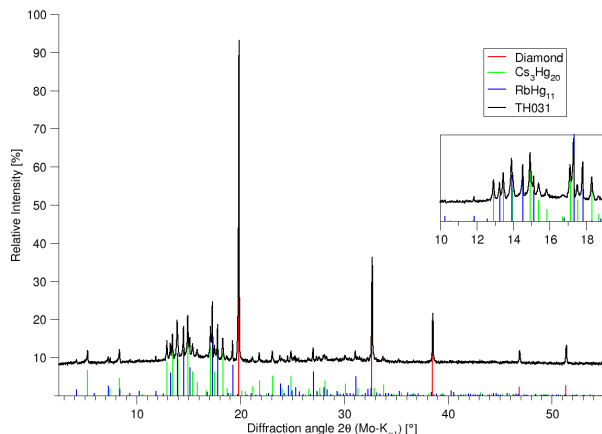


Fig. 7.32: Powder diffractogram of TH031 (black). Diamond^[4] (red) was used for optical dilution. The obtained product contains only RbHg₁₁^[3] (blue) and Cs₃Hg₂₀^[6] (green).

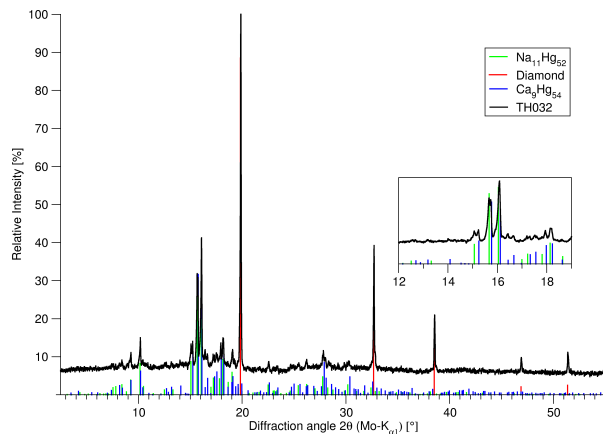


Fig. 7.33: Powder diffractogram of TH032 (black). Diamond^[4] (red) was used for optical dilution. The obtained product consists of Na₁₁Hg₅₂^[2] (green) and Ca₁₁Hg₅₄^[9] (blue).

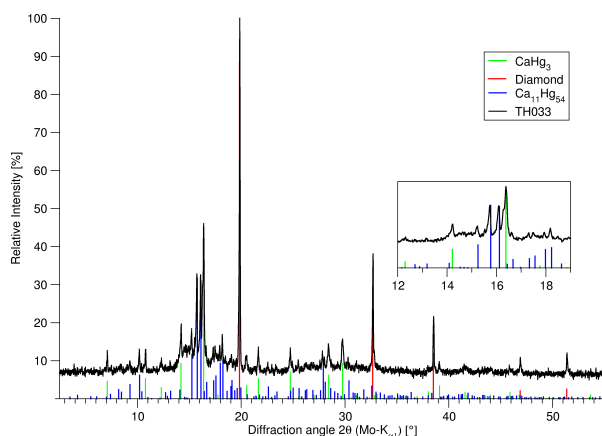


Fig. 7.34: Powder diffractogram of TH033 (black). Diamond^[4] (red) was used for optical dilution. The product contains only CaHg₃^[10] (green) and Ca₁₁Hg₅₄^[9] (blue), a K-containing phase does not seem to be present.

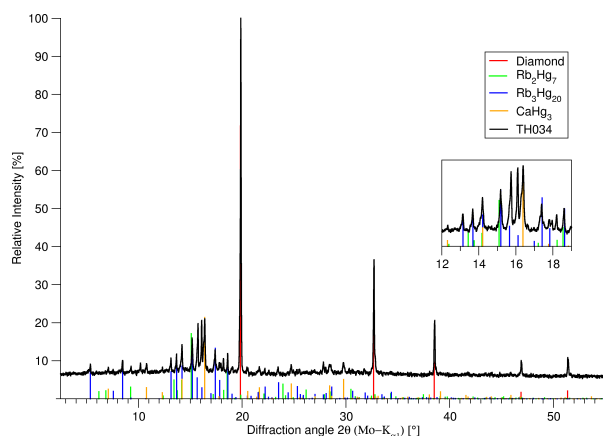


Fig. 7.35: Powder diffractogram of TH034 (black). Diamond^[4] (red) was used for optical dilution. The obtained product consists of CaHg₃^[10] (orange), Rb₂Hg₇^[16] (green) and Rb₃Hg₂₀^[6] (blue).

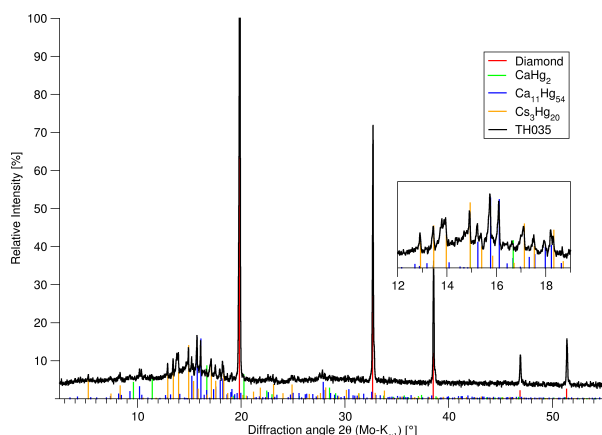


Fig. 7.36: Powder diffractogram of TH035 (black). Diamond^[4] (red) was used for optical dilution. The obtained product consists of CaHg₂^[17] (green), Ca₁₁Hg₅₄^[9] (blue) and Cs₃Hg₂₀^[6] (orange).

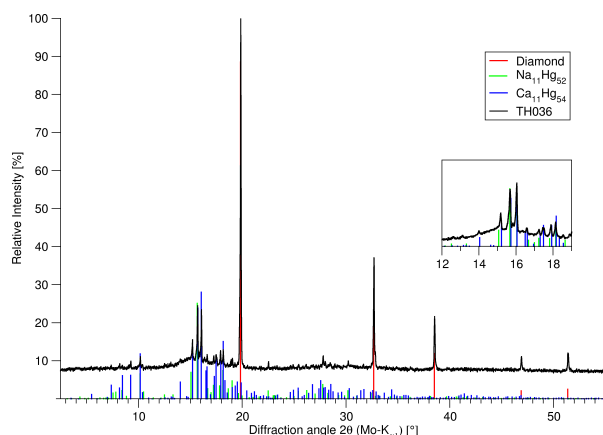


Fig. 7.37: Powder diffractogram of TH036 (black). Diamond^[4] (red) was used for optical dilution. The obtained product was identified as Ca₁₁Hg₅₄^[9] (blue) with a slight shift towards higher diffraction angles.

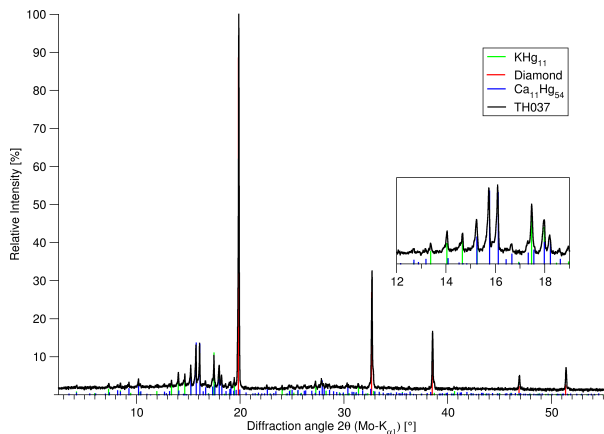


Fig. 7.38: Powder diffractogram of TH037 (black). Diamond^[4] (red) was used for optical dilution. The obtained product consists of Ca₁₁Hg₅₄^[9] (blue) and KHg₁₁^[3] (green).

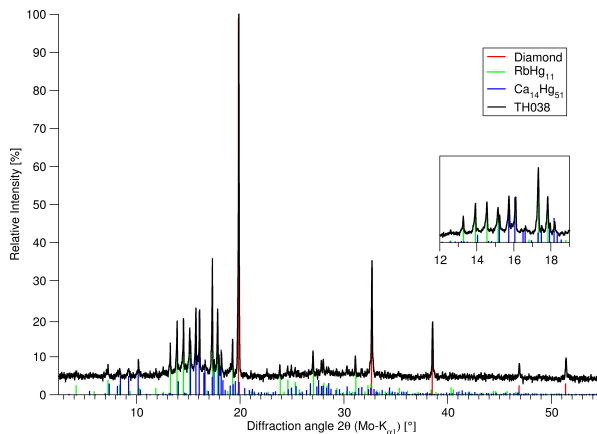


Fig. 7.39: Powder diffractogram of TH038 (black). Diamond^[4] (red) was used for optical dilution. The product consists of Ca₁₄Hg₅₁^[13] (blue) and RbHg₁₁^[3] (green).

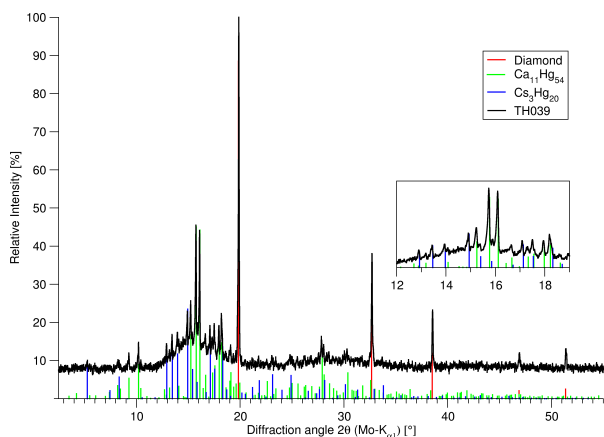


Fig. 7.40: Powder diffractogram of TH039 (black). Diamond^[4] (red) was used for optical dilution. The obtained product consists of Ca₁₁Hg₅₄^[9] (green) and Cs₃Hg₂₀^[6] (blue).

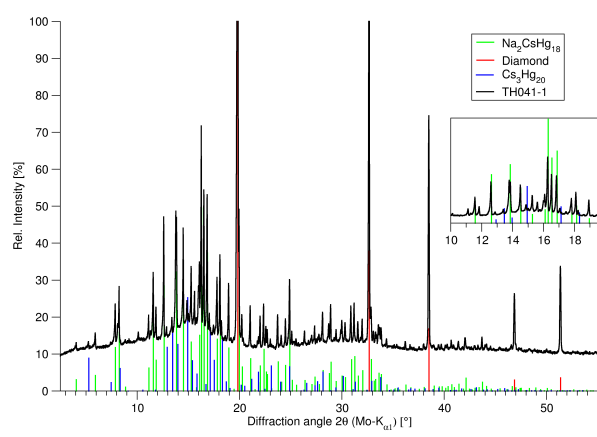


Fig. 7.41: Powder diffractogram of TH041 (black) after two weeks of tempering. Diamond^[4] (red) was used for optical dilution. CsNa₂Hg₁₈ (green, generated from single crystal data) was obtained as main product, with Cs₃Hg₂₀^[6] (blue) as byphase.

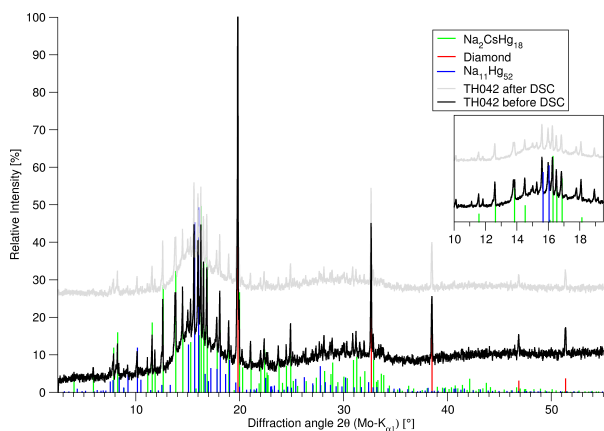


Fig. 7.42: Powder diffractogram of TH042 before (black) and after DSC measurement (grey). The obtained product consists of CsNa₂Hg₁₈ (green) and after DSC additionally Na₁₁Hg₅₂^[2] (blue).

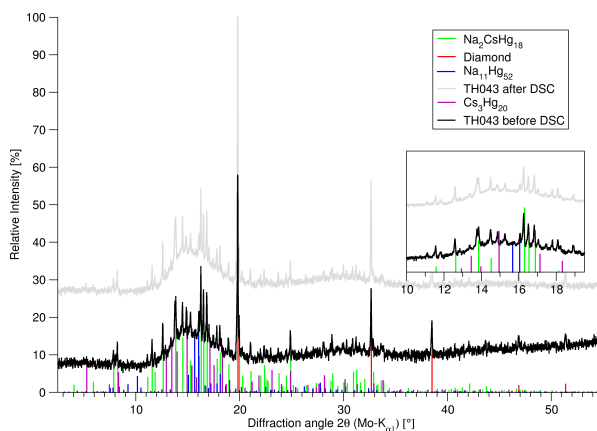


Fig. 7.43: Powder diffractogram of TH043 before (black) and after DSC (grey). Diamond^[4] (red) was used for optical dilution. The obtained product consists of CsNa₂Hg₁₈ (green) as well as Na₁₁Hg₅₂^[2] (green) and Cs₃Hg₂₀^[6] (purple).

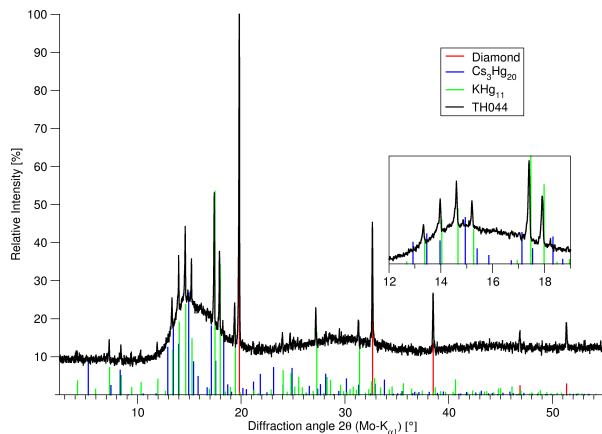


Fig. 7.44: Powder diffractogram of TH044 (black). The obtained product consists of $\text{Cs}_3\text{Hg}_{20}$ ^[6] (green) and KHg_{11} ^[3] (blue).

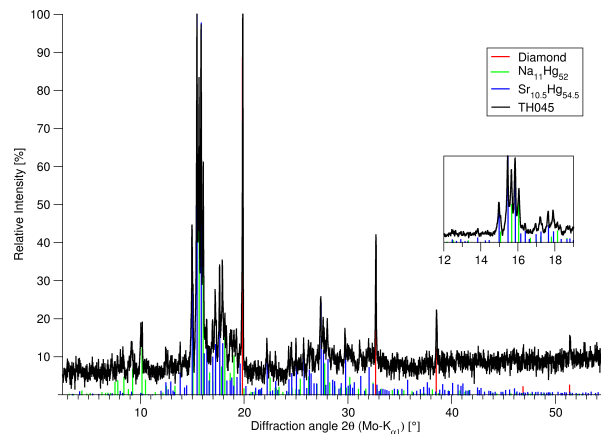


Fig. 7.45: Powder diffractogram of TH045 (black). Diamond^[4] (red) was used for optical dilution. The obtained product consists of $\text{Na}_{11}\text{Hg}_{52}$ ^[2] (green) and $\text{Sr}_{10.5}\text{Hg}_{54.5}$ ^[9] (blue).

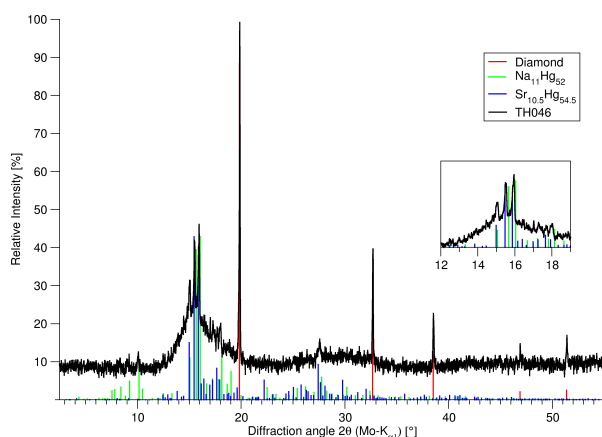


Fig. 7.46: Powder diffractogram of TH046 (black). Diamond^[4] (red) was used for optical dilution. The diffraction reflections are between those of $\text{Na}_{11}\text{Hg}_{52}$ ^[2] (green) and $\text{Sr}_{10.5}\text{Hg}_{54.5}$ ^[9] (blue), indicating a new ternary amalgam with the structural motif of the $\text{Gd}_{14}\text{Ag}_{51}$ family.

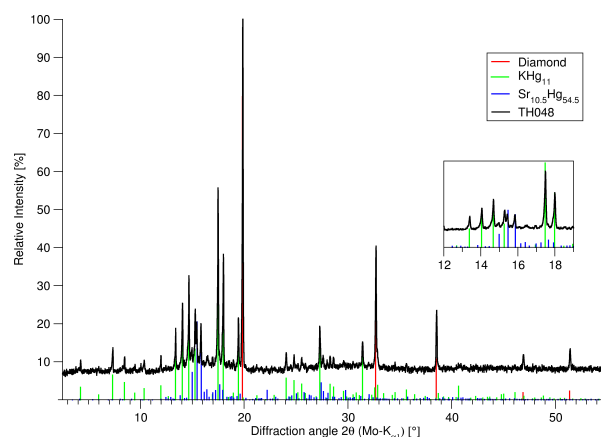


Fig. 7.47: Powder diffractogram of TH048 (black). Diamond^[4] (red) was used for optical dilution. The product consists of KHg_{11} ^[3] (green) and $\text{Sr}_{10.5}\text{Hg}_{54.5}$ ^[9] (blue).

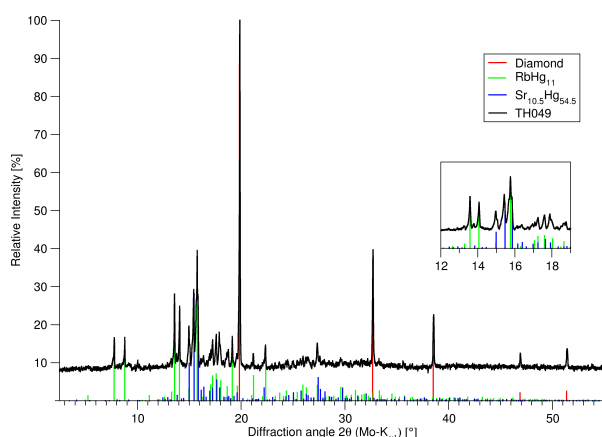


Fig. 7.48: Powder diffractogram of TH049 (black). Diamond^[4] (red) was used for optical dilution. The product consists of $\text{Rb}_3\text{Hg}_{20}$ ^[8] (green) and $\text{Sr}_{10.5}\text{Hg}_{54.5}$ ^[9] (blue).

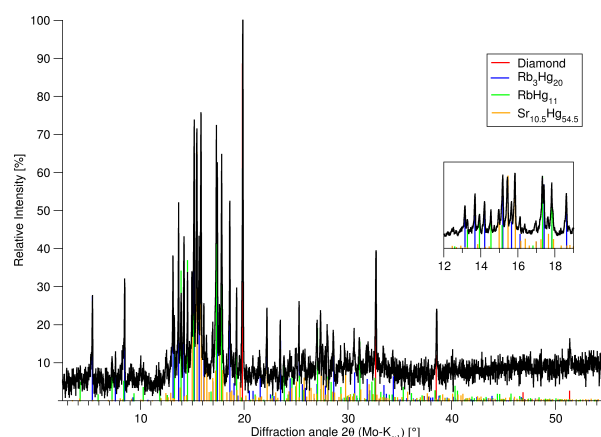


Fig. 7.49: Powder diffractogram of TH050 (black). Diamond^[4] (red) was used for optical dilution. The product consists of $\text{Rb}_3\text{Hg}_{20}$ ^[6] (blue), RbHg_{11} ^[3] (green) and $\text{Sr}_{10.5}\text{Hg}_{54.5}$ ^[9] (orange).

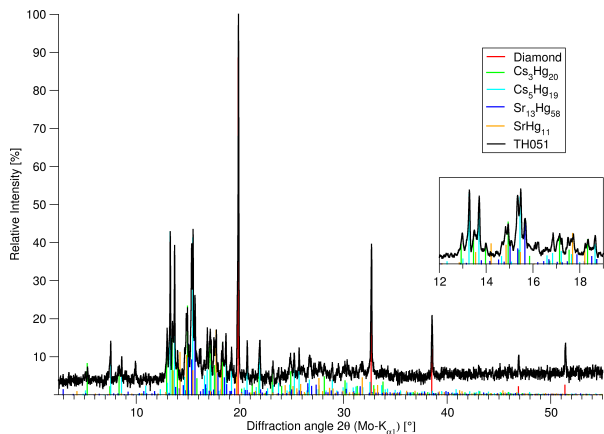


Fig. 7.50: Powder diffractogram of TH051 (black). Diamond^[4] (red) was used for optical dilution. The obtained product consists of Cs₃Hg₂₀^[6] (green), Cs₅Hg₁₉^[6] (cyan), Sr₁₃Hg₅₈^[18] (blue) and SrHg₁₁^[3] (orange).

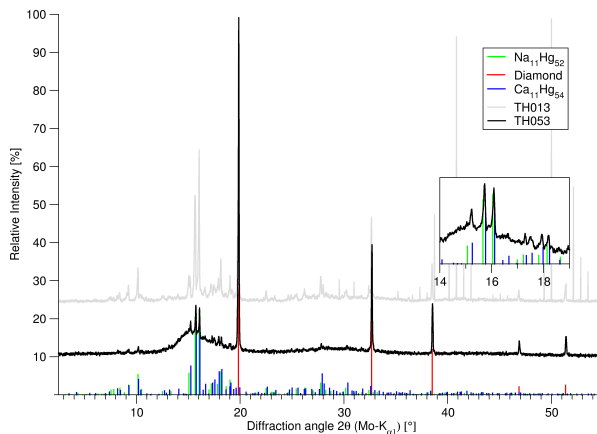


Fig. 7.51: Powder diffractogram of TH053 (black) and before Ostwald ripening (TH013, gray). Diamond^[4] (red) was used for optical dilution. The diffraction intensities exactly between Na₁₁Hg₅₂^[2] (green) and Ca₁₁Hg₅₄^[9] (blue). It was later identified as the new ternary amalgam Ca_{6.9}Na_{4.1}Hg₅₄. Sharp intensities at higher angles result from a detector malfunction.

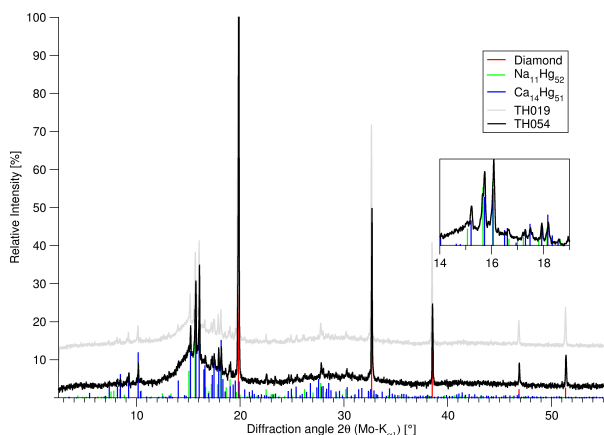


Fig. 7.52: Powder diffractogram of TH054 (black) in comparison to before Ostwald ripening (TH019, gray). Diamond^[4] (red) was used for optical dilution. The product consists of Na₁₁Hg₅₂^[2] (green) and Ca₁₄Hg₅₁^[13] (blue).

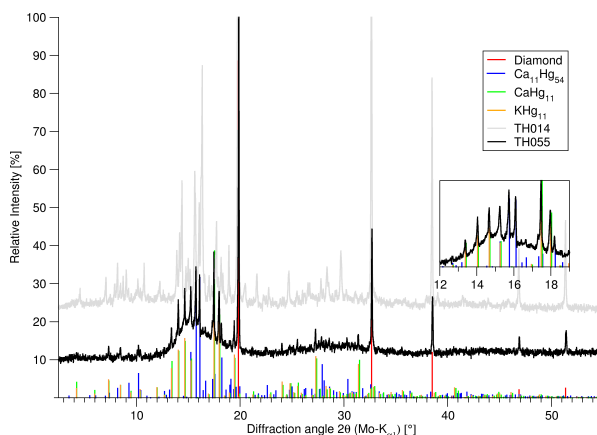


Fig. 7.53: Powder diffractogram of TH055 (black) in comparison to before Ostwald ripening (TH014, gray). Diamond^[4] (red) was used for optical dilution. The product only contains KHg₁₁^[3] (orange), CaHg₁₁^[14] (green) and Ca₁₁Hg₅₄^[9] (blue).

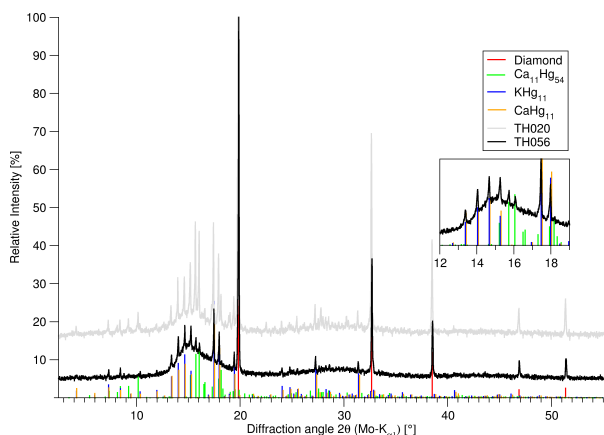


Fig. 7.54: Powder diffractogram of TH056 (black) in comparison to before Ostwald ripening (TH020, gray). Diamond^[4] (red) was used for optical dilution. The sample still consists of KHg₁₁^[3] (blue), CaHg₁₁^[14] (orange) and Ca₁₁Hg₅₄^[9] (green).

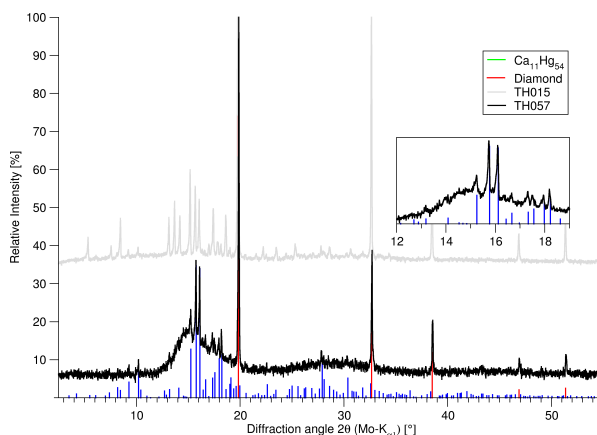


Fig. 7.55: Powder diffractogram of TH05 (black) in comparison to before Ostwald ripening (TH015, gray). Only Ca₁₁Hg₅₄^[9] (green) was found, Rb₃Hg₂₀ is not present anymore.

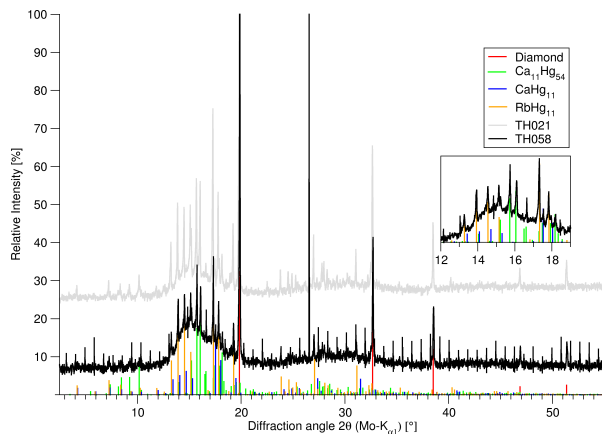


Fig. 7.56: Powder diffractogram of TH058 (black) as well as before Ostwald ripening (TH021, gray). The composition of the product has not changed, it still consists of $\text{Ca}_{11}\text{Hg}_{54}$ ^[9] (green), CaHg_{11} ^[14] (blue) and RbHg_{11} ^[3] (orange). Sharp, regular intensities originate from a detector malfunction.

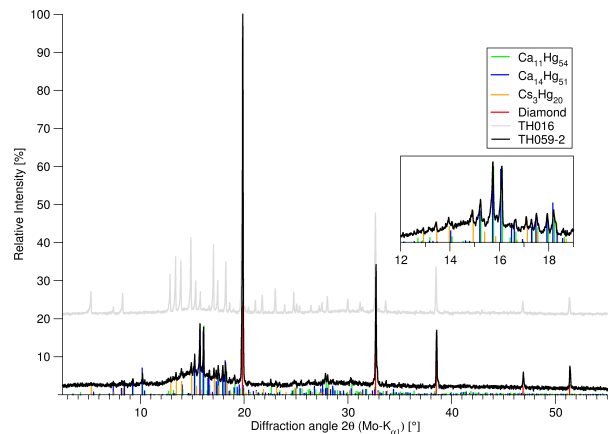


Fig. 7.57: Powder diffractogram of TH059 (black) in comparison to before Ostwald ripening (TH016, gray). Diamond^[4] (red) was used for optical dilution. The product was identified as a mixture of $\text{Ca}_{11}\text{Hg}_{54}$ ^[9] (green), $\text{Ca}_{14}\text{Hg}_{51}$ ^[9] (blue) and $\text{Cs}_3\text{Hg}_{20}$ ^[6] (orange).

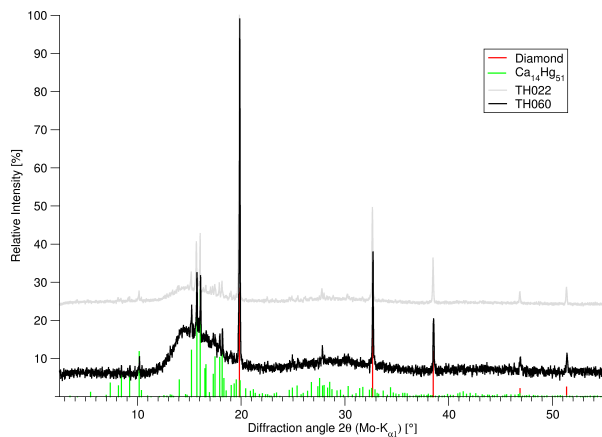


Fig. 7.58: Powder diffractogram of TH060 (black) in comparison to before Ostwald ripening (TH022, gray). Diamond^[4] (red) was used for optical dilution. The product still only consists of $\text{Ca}_{14}\text{Hg}_{51}$ ^[9] (blue), a Cs-containing phase seems not to be present.

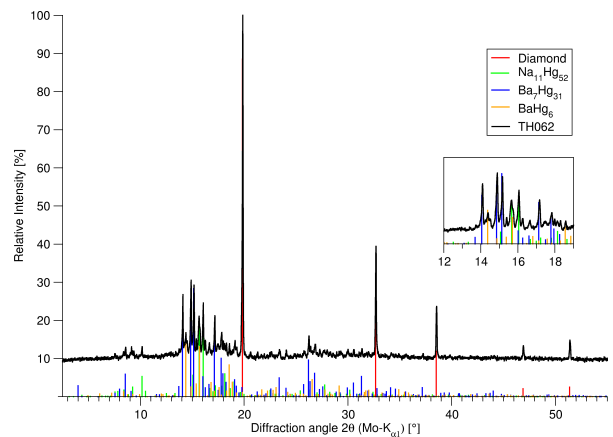


Fig. 7.59: Powder diffractogram of TH062 (black). Diamond^[4] (red) was used for optical dilution. The product obtained consists of $\text{Na}_{11}\text{Hg}_{52}$ ^[2] (green), $\text{Ba}_7\text{Hg}_{31}$ ^[19] (blue) and BaHg_6 ^[20] (orange).

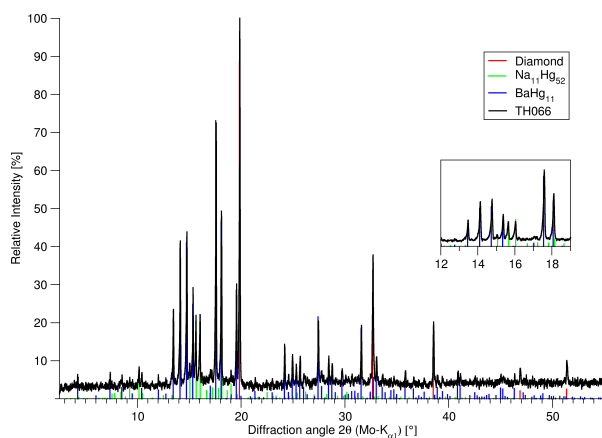


Fig. 7.60: Powder diffractogram of TH066 (black). Diamond^[4] (red) was used for optical dilution. The product consists of BaHg_{11} ^[3] (blue) and $\text{Na}_{11}\text{Hg}_{52}$ ^[2] (green).

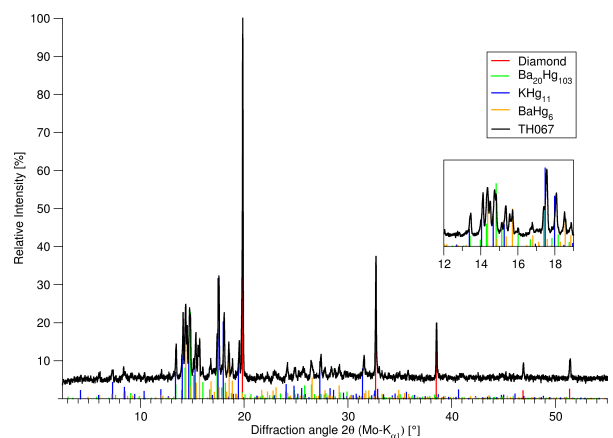


Fig. 7.61: Powder diffractogram of TH067 (black). Diamond^[4] (red) was used for optical dilution. The obtained product consists of $\text{Ba}_{20}\text{Hg}_{103}$ ^[21] (green), KHg_{11} ^[3] (blue) and BaHg_6 ^[20] (orange).

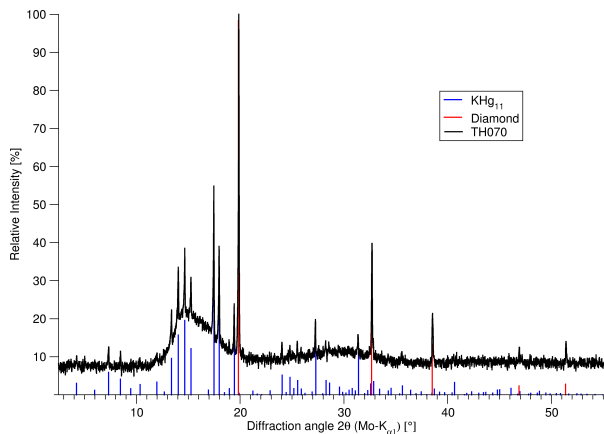


Fig. 7.62: Powder diffractogram of TH070 (black). Diamond^[4] (red) was used for optical dilution. The obtained product contains only KHg₁₁^[3] (blue).

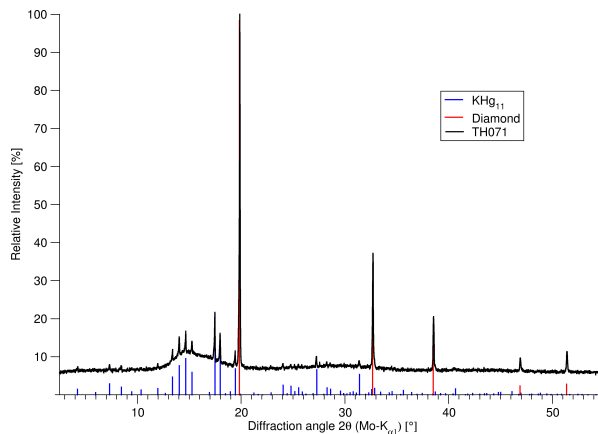


Fig. 7.63: Powder diffractogram of TH071 (black). Diamond^[4] (red) was used for optical dilution. The obtained product contains only KHg₁₁^[3] (blue).

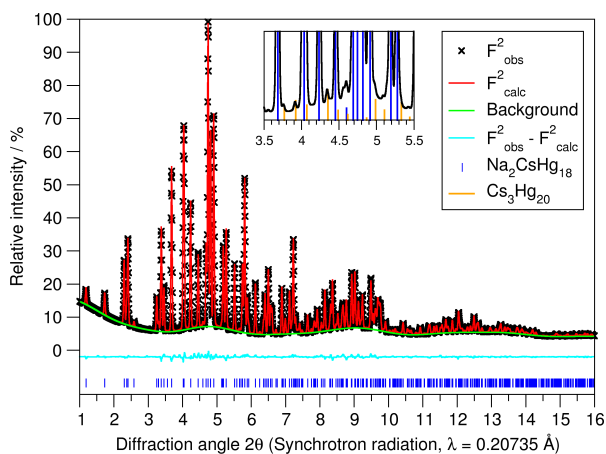


Fig. 7.64: Rietveld refinement of TH072 (black). Background is shown in green, calculated intensities in red. Difference plot is cyan, CsNa₂Hg₁₈ (blue, generated from single crystal data) is the main product obtained, with small (≤ 3 wt.% impurities of Cs₃Hg₂₀^[6] (orange). The refinement was performed with the GSAS-II^[22] software.

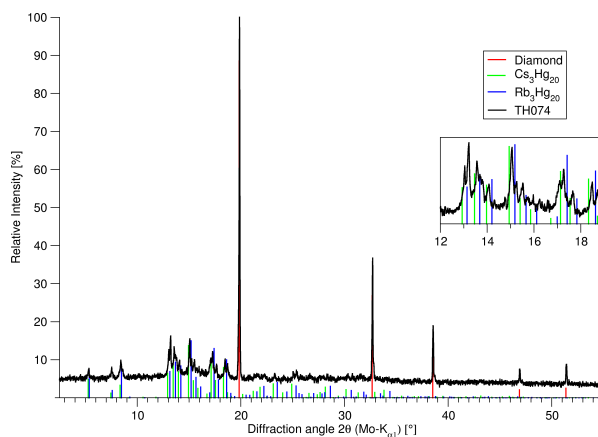


Fig. 7.65: Powder diffractogram of TH074 (black). Diamond^[4] (red) was used for optical dilution. The observed intensities are in between those of Cs₃Hg₂₀^[6] (green) and Rb₃Hg₂₀^[6] (blue).

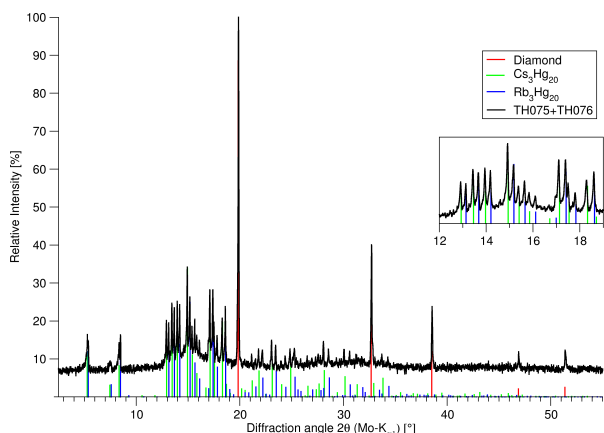


Fig. 7.66: Powder diffractogram of TH075 together with TH076 (black). Diamond^[4] (red) was used for optical dilution. The mixture contains only Cs₃Hg₂₀^[6] (green) and Rb₃Hg₂₀^[6] (blue).

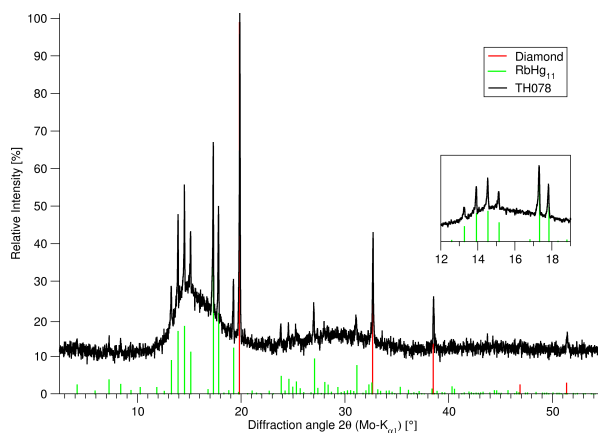


Fig. 7.67: Powder diffractogram of TH078 (black). Diamond^[4] (red)^[4] was used for optical dilution. Only RbHg₁₁^[3] (green) is identifiable, a Cs-containing phase does not seem to be present.

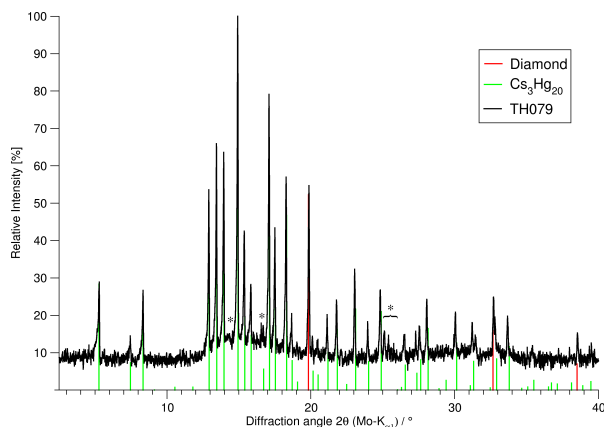


Fig. 7.68: Powder diffractogram of TH079 (black). Diamond^[4] (red)^[4] was used for optical dilution. The obtained product was identified as Cs₃Hg₂₀^[6] (green) with minimal amounts of Cs₅Hg₁₉^[6] (marked with *).

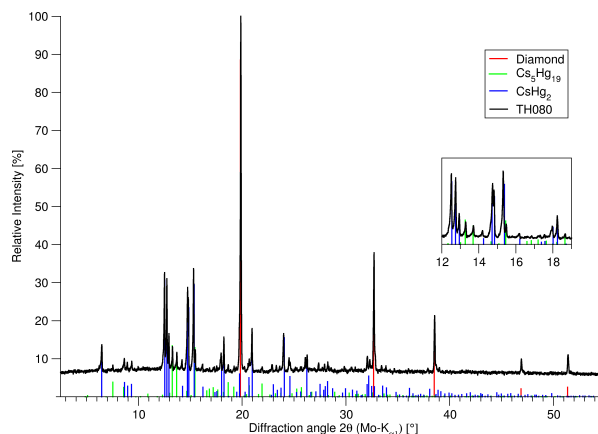


Fig. 7.69: Powder diffractogram of TH080 (black). Diamond^[4] (red) was used for optical dilution. The obtained product contains CsHg₂^[23] (blue) and Cs₅Hg₁₉^[6] (green).

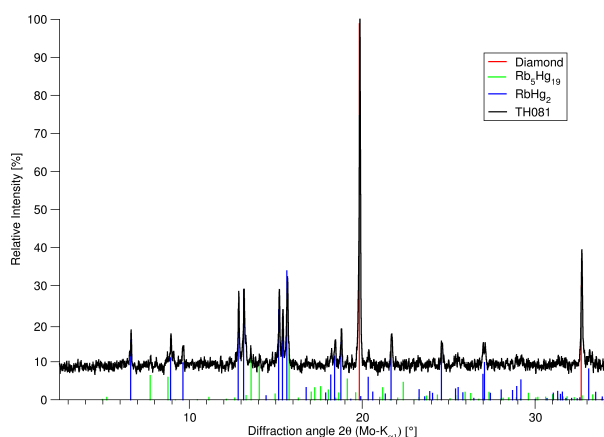


Fig. 7.70: Powder diffractogram of TH081 (black). Diamond^[4] (red) was used for optical dilution. The obtained product contains RbHg₂^[23] (blue) and small impurities of Rb₅Hg₁₉^[8] (green).

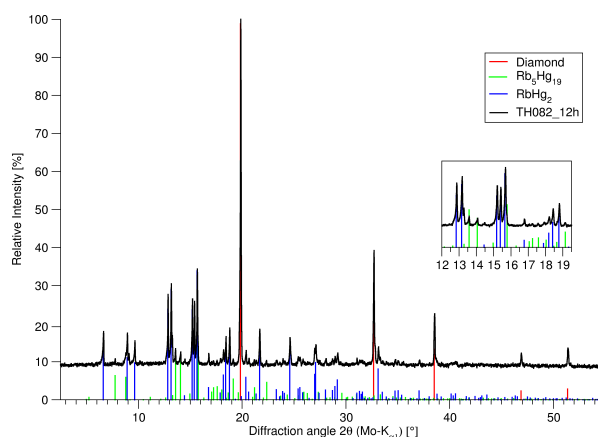


Fig. 7.71: Powder diffractogram of TH082 (black). Diamond^[4] (red) was used for optical dilution. The product contains only RbHg₂^[23] (blue) and Rb₅Hg₁₉^[8] (green), no Cs-containing phase can be seen.

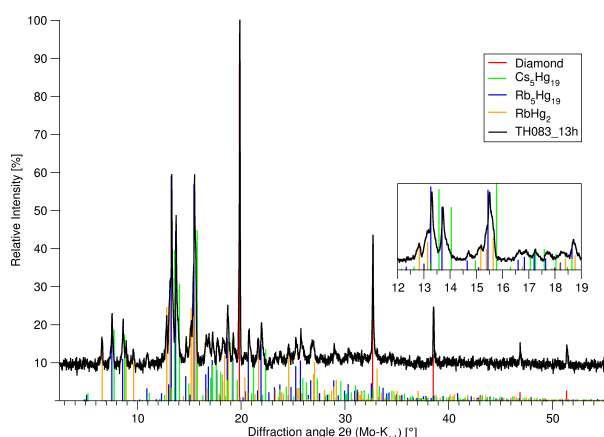


Fig. 7.72: Powder diffractogram of TH083 (black). Diamond^[4] (red) was used for optical dilution. The product contains RbHg₂^[23] (orange) and a solid solution of Rb₅Hg₁₉^[8] (blue) and Cs₅Hg₁₉^[6] (green).

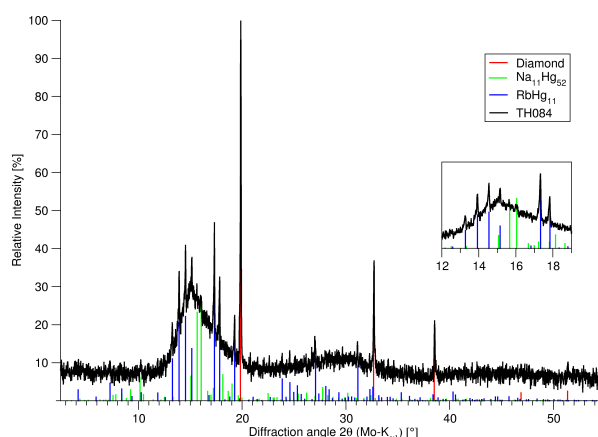


Fig. 7.73: Powder diffractogram of TH084 (black). Diamond^[4] (red) was used for optical dilution. The obtained products consists of Na₁₁Hg₅₂^[2] (green) and RbHg₁₁^[3] (blue).

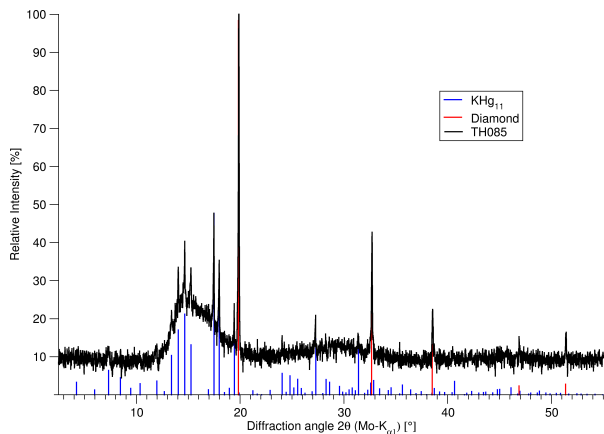


Fig. 7.74: Powder diffractogram of TH085 (black). Diamond^[4] (red) was used for optical dilution. The product contains only KHg₁₁^[3] (blue).

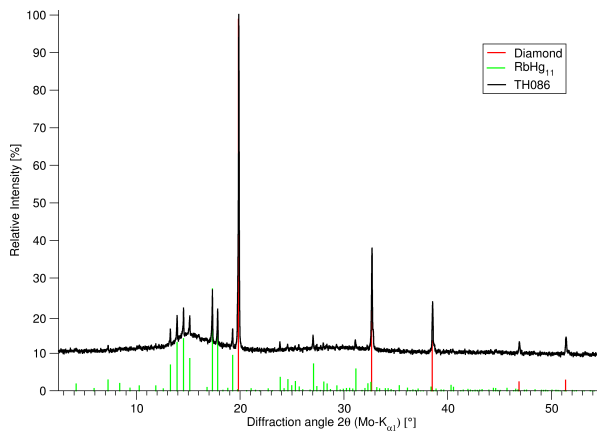


Fig. 7.75: Powder diffractogram of TH086 (black). Diamond^[4] (red) was used for optical dilution. The product contains only RbHg₁₁^[3] (green).

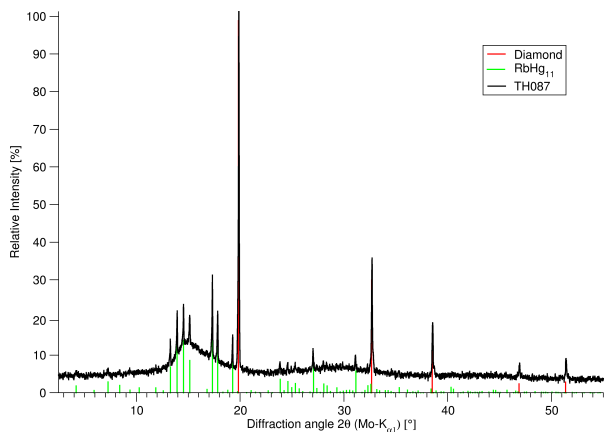


Fig. 7.76: Powder diffractogram of TH087 (black). Diamond^[4] (red) was used for optical dilution. The product contains only RbHg₁₁^[3] (green).

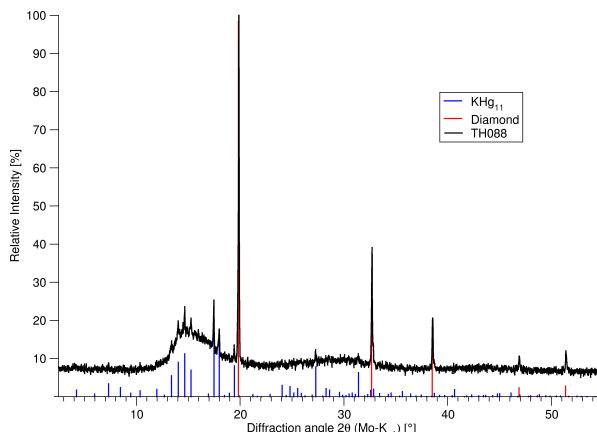


Fig. 7.77: Powder diffractogram of TH088 (black). Diamond^[4] (red) was used for optical dilution. The product contains only KHg₁₁^[3] (blue).

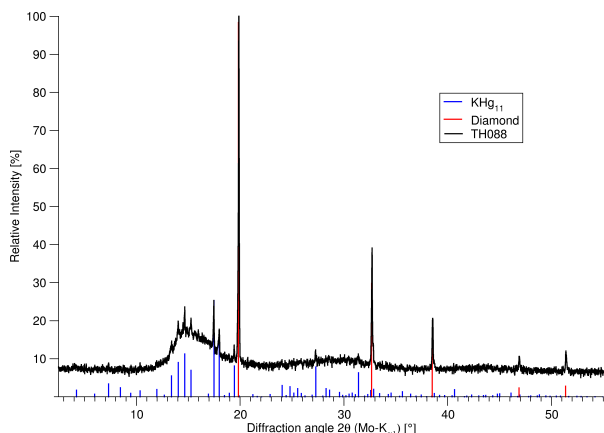


Fig. 7.78: Powder diffractogram of TH089 (black). Diamond^[4] (red) was used for optical dilution. The product contains only KHg₁₁^[3] (blue).

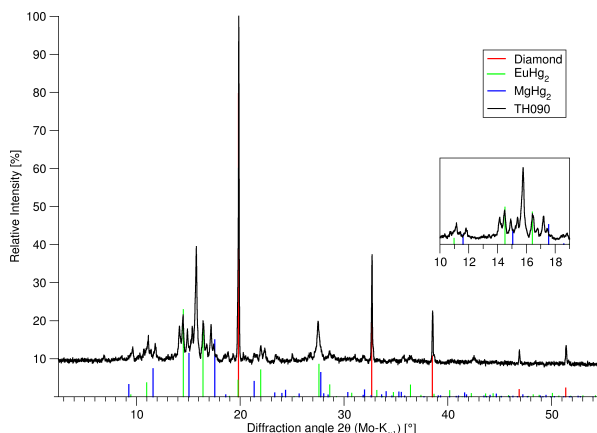


Fig. 7.79: Powder diffractogram of TH090 (black). Diamond^[4] (red) was used for optical dilution. The product contains EuHg₂^[24] (green), MgHg₂^[12] (blue) and a yet unknown phase.

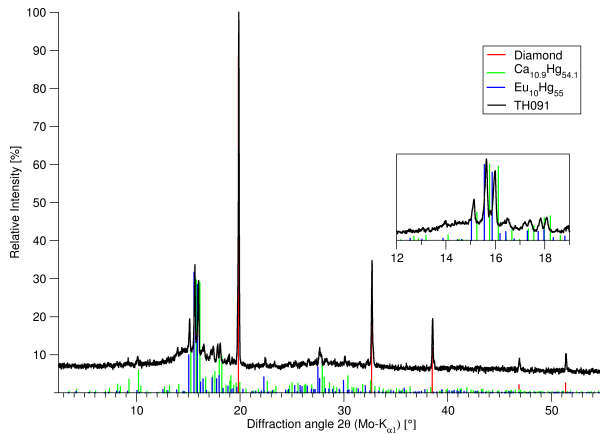


Fig. 7.80: Powder diffractogram of TH091 (black). Diamond^[4] (red) was used for optical dilution. The diffraction pattern of the obtained product is exactly between those of $\text{Ca}_{11}\text{Hg}_{54}$ ^[9] (green) and $\text{Eu}_{10}\text{Hg}_{54}$ ^[25] (blue).

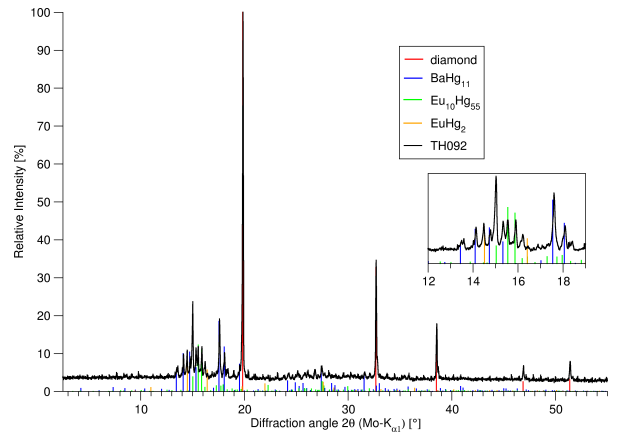


Fig. 7.81: Powder diffractogram of TH092 (black). Diamond^[4] (red) was used for optical dilution. The obtained product consists of BaHg_{11} ^[3] (blue), EuHg_2 ^[24] (orange) and $\text{Eu}_{10}\text{Hg}_{55}$ ^[26] (green).

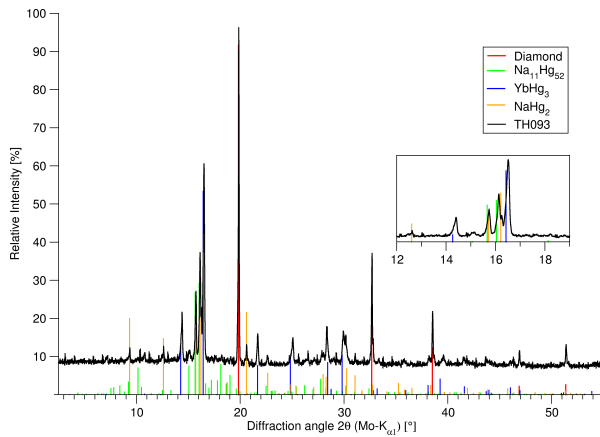


Fig. 7.82: Powder diffractogram of TH093 (black). Diamond^[4] (red) was used for optical dilution. The product consists of $\text{Na}_{11}\text{Hg}_{52}$ ^[2] (green), YbHg_3 ^[27] (blue) and NaHg_2 ^[5] (orange).

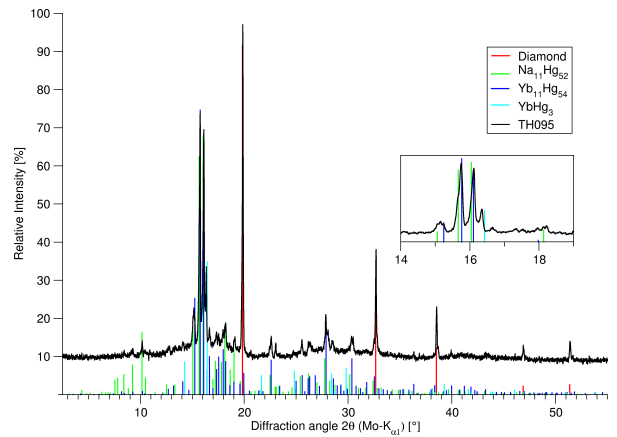


Fig. 7.83: Powder diffractogram of TH095 (black). Diamond^[4] (red) was used for optical dilution. The obtained product consists of $\text{Na}_{11}\text{Hg}_{52}$ ^[2] (green), $\text{Yb}_{11}\text{Hg}_{54}$ ^[28] (dark blue) and YbHg_3 ^[27] (cyan).

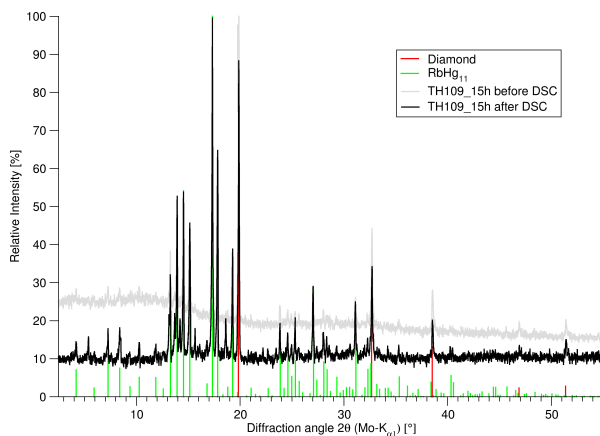


Fig. 7.84: Powder diffractogram of TH109 before DSC (gray) and after DSC (black). Diamond^[4] (red) was used for optical dilution. As can be seen, the crystalline solid contains only RbHg_{11} ^[3] (green).

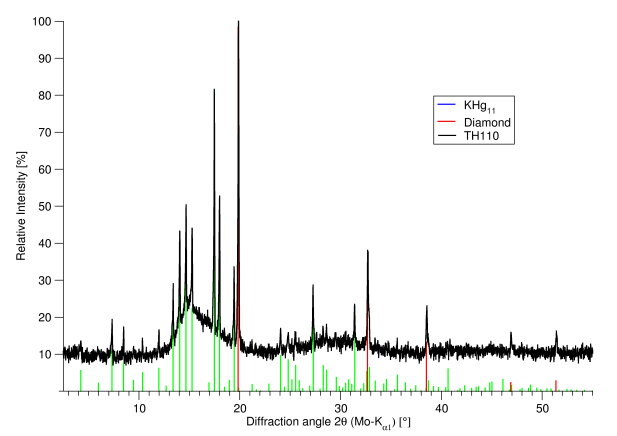


Fig. 7.85: Powder diffractogram of TH110 (black). Diamond^[4] (red) was used for optical dilution. The obtained product contains only KHg_{11} ^[3] (green).

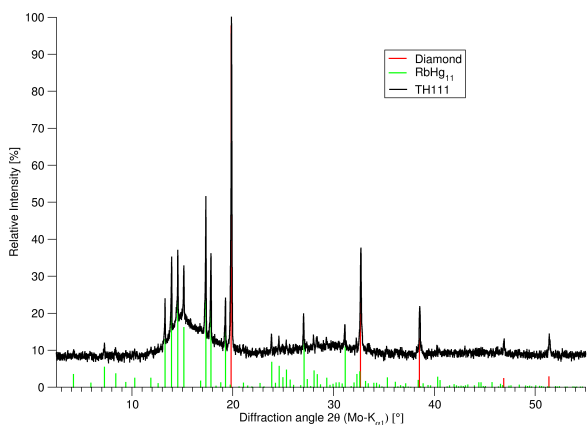


Fig. 7.86: Powder diffractogram of TH111 (black). Diamond^[4] (red) was used for optical dilution. The obtained product contains only RbHg₁₁^[3] (green).

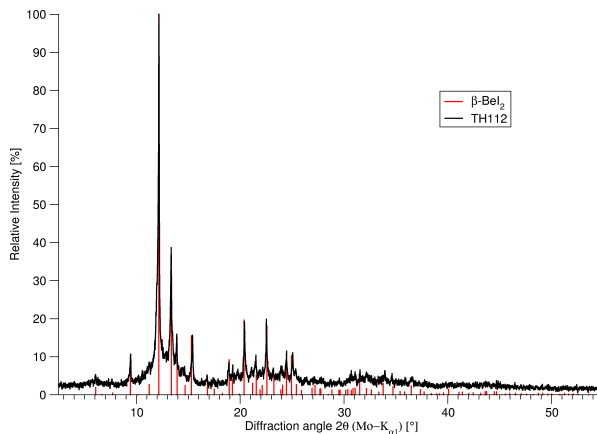


Fig. 7.87: Powder diffractogram of TH112 (black) with simulated intensities of β -BeI₂^[29] (red) as reference.

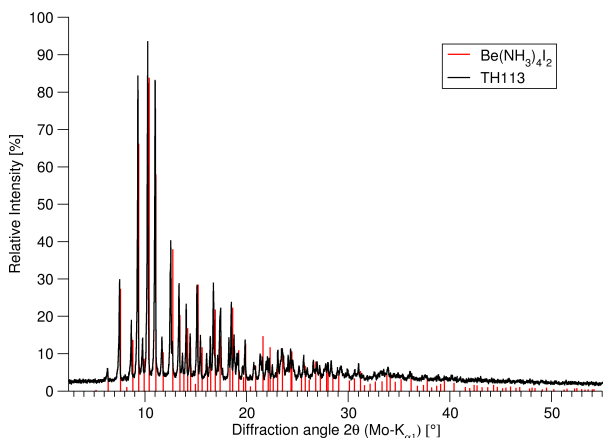


Fig. 7.88: Powder diffractogram of TH113 (black) with simulated intensities of Be(NH₃)₄I₂^[30] (red) as reference.

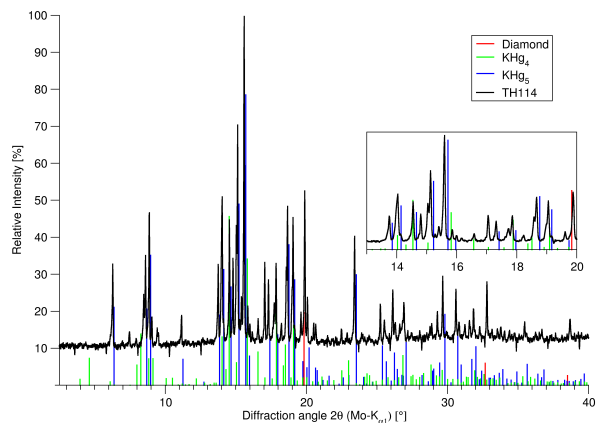


Fig. 7.89: Powder diffractogram of TH114 (black). Diamond^[4] (red) was used for optical dilution. The obtained crystalline solid was identified as a mixture of KHg₄ (green) and KHg₅ (blue), both generated from single crystal data.

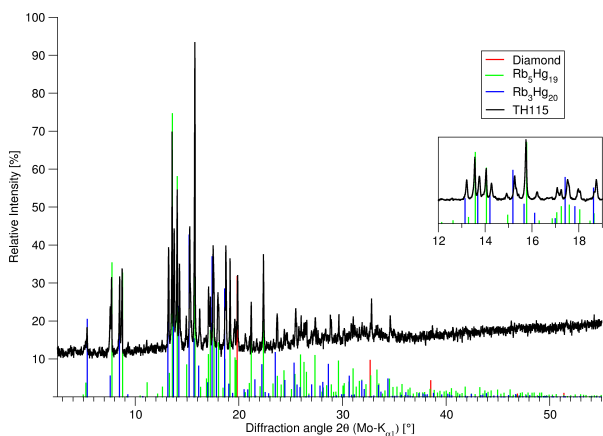


Fig. 7.90: Powder diffractogram of TH115 (black). Diamond^[4] (red) was used for optical dilution. The obtained product consists of Rb₃Hg₂₀^[6] (blue) and Rb₃Hg₁₉^[8] (green).

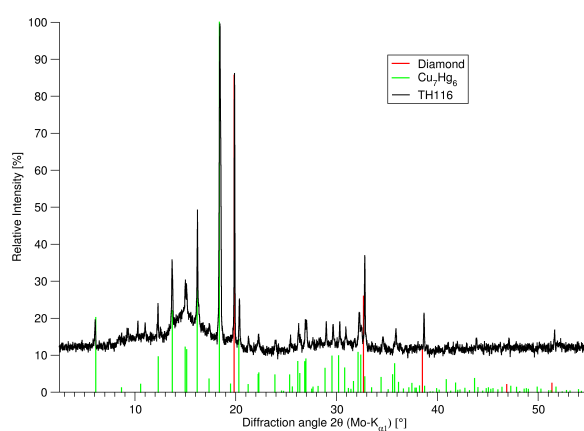


Fig. 7.91: Powder diffractogram of TH116 (black). Diamond^[4] (red) was used for optical dilution. The obtained crystalline solid was identified as Cu₇Hg₆^[31] (green).

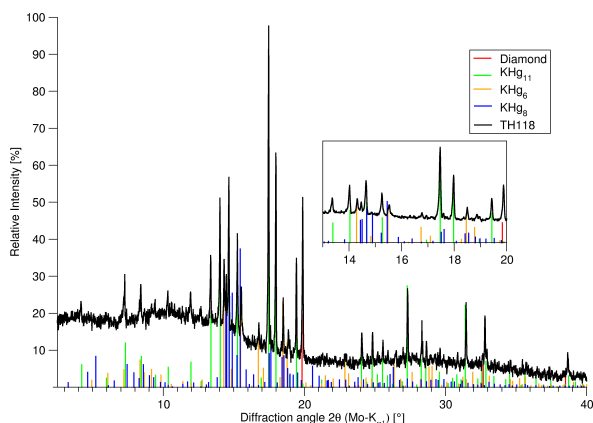


Fig. 7.92: Powder diffractogram of TH118 (black). Diamond^[4] (red) was used for optical dilution. The obtained solid contains KHg₆^[7] (orange), KHg₁₁^[3] (green) and small amounts of KHg₈ (blue, generated from single crystal data).

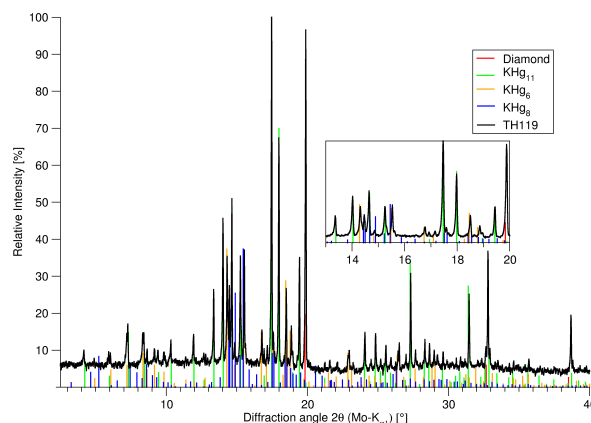


Fig. 7.93: Powder diffractogram of TH119 (black). Diamond^[4] (red) was used for optical dilution. The obtained solid contains KHg₆^[7] (orange), KHg₁₁^[3] (green) and small amounts of KHg₈ (blue, generated from single crystal data).

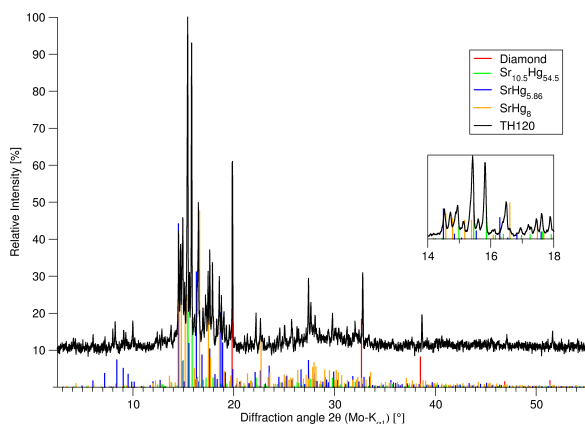


Fig. 7.94: Powder diffractogram of TH120 (black). Diamond^[4] (red) was used to dilute the sample. The obtained product is a mixture of SrHg_{5.86} (blue, generated from single crystal data), Sr_{10.5}Hg_{54.5}^[9] (green) and SrHg₈^[32] (orange).

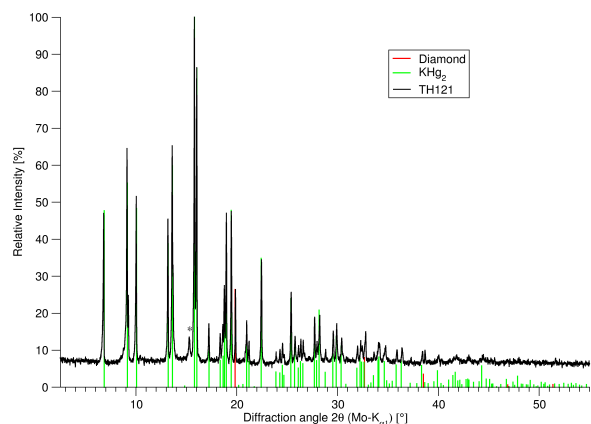


Fig. 7.95: Powder diffractogram of TH121 (black). Diamond^[4] (red) was used for optical dilution. The obtained product contains KHg₂^[33] (green) as well as trace amounts of a yet unknown phase (marked with *).

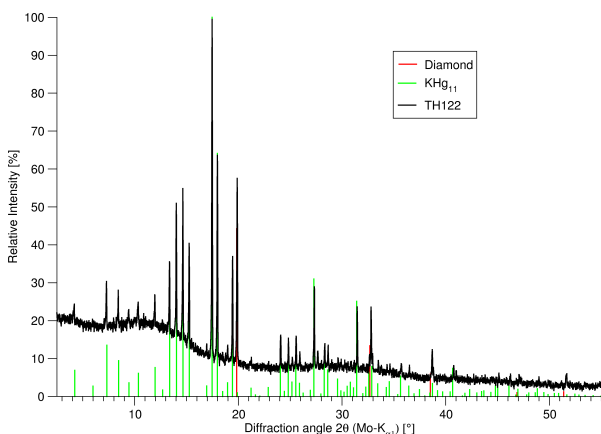


Fig. 7.96: Powder diffractogram of TH122 (black). Diamond^[4] (red) was used for optical dilution. The obtained product was identified as phase-pure KHg₁₁^[3] (green).

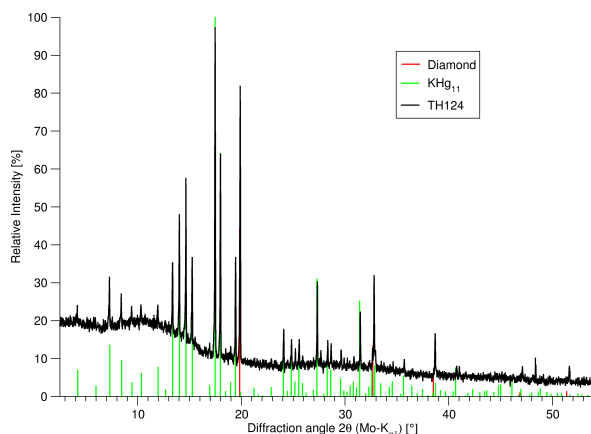


Fig. 7.97: Powder diffractogram of TH124 (black). Diamond^[4] was used for optical dilution. The product was identified as KHg₁₁^[3] (green).

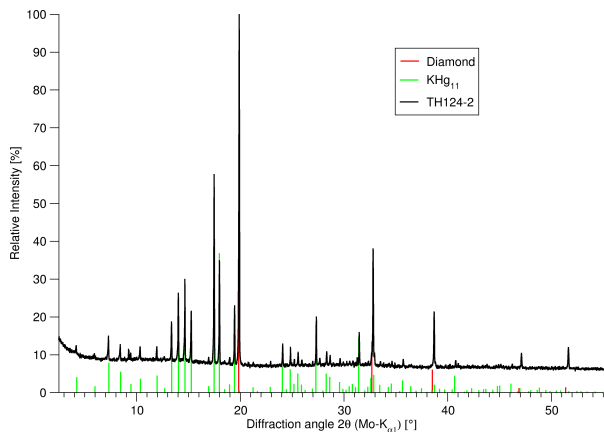


Fig. 7.98: Powder diffractogram of TH124-2 (black). Diamond^[4] was used for optical dilution. The product was identified as KHg₁₁^[3] (green).

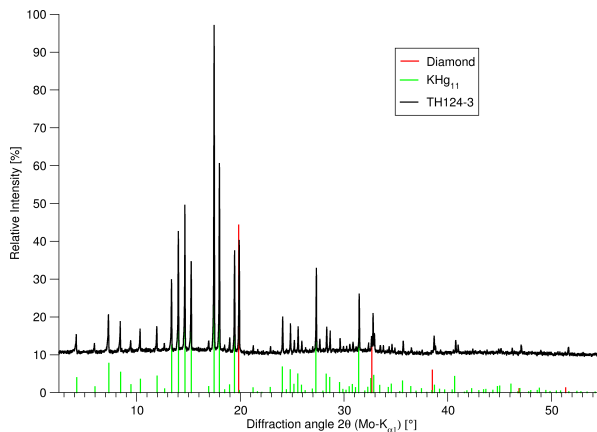


Fig. 7.99: Powder diffractogram of TH124-3 (black). Diamond^[4] was used for optical dilution. The product was identified as KHg₁₁^[3] (green).

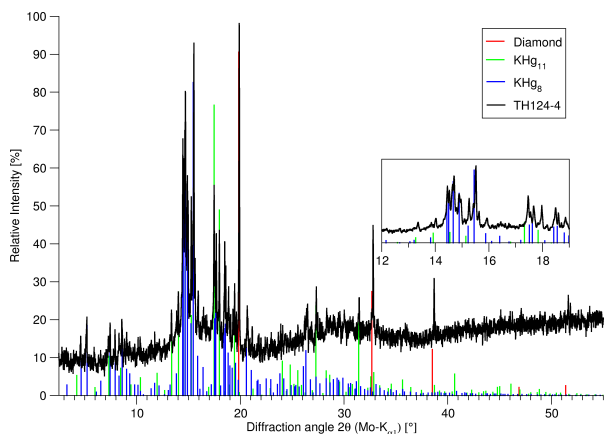


Fig. 7.100: Powder diffractogram of TH124-4 (black). Diamond^[4] was used for optical dilution. The product was identified as a mixture of KHg₁₁^[3] (green) and KHg₈ (blue, generated from single crystal data).

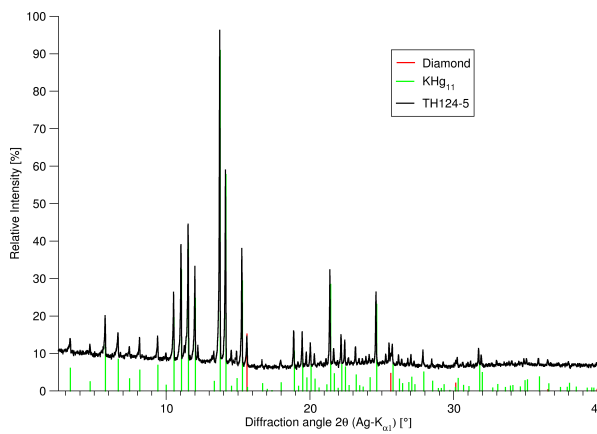


Fig. 7.101: Powder diffractogram of TH124-5 (black). Diamond^[4] was used for optical dilution. The product was identified as KHg₁₁^[3] (green).

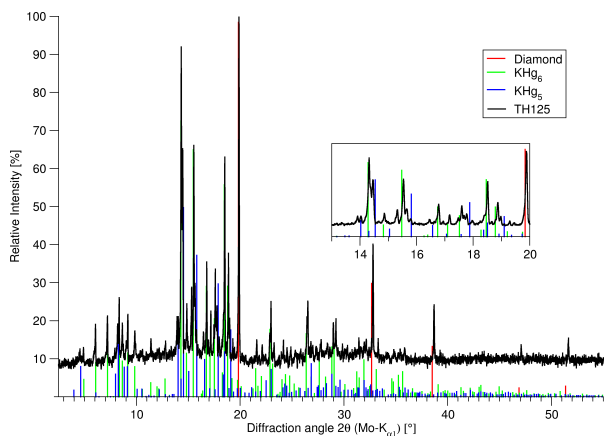


Fig. 7.102: Powder diffractogram of TH125 (black). Diamond^[4] was used for optical dilution. The product contains KHg₆^[7] (green) and KHg₅ (blue, generated from single crystal data).

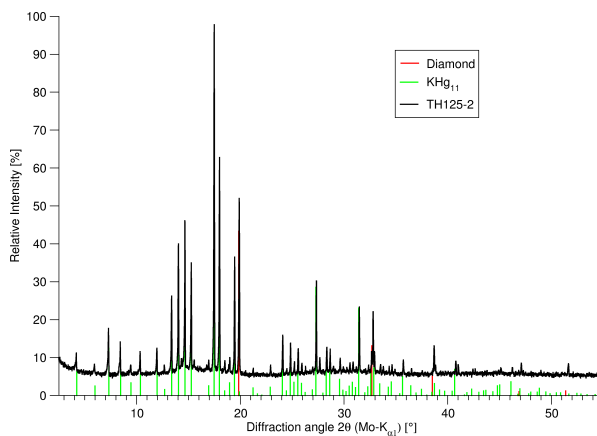


Fig. 7.103: Powder diffractogram of TH125-2 (black). Diamond^[4] was used for optical dilution. The product was identified as KHg₁₁^[3] (green).

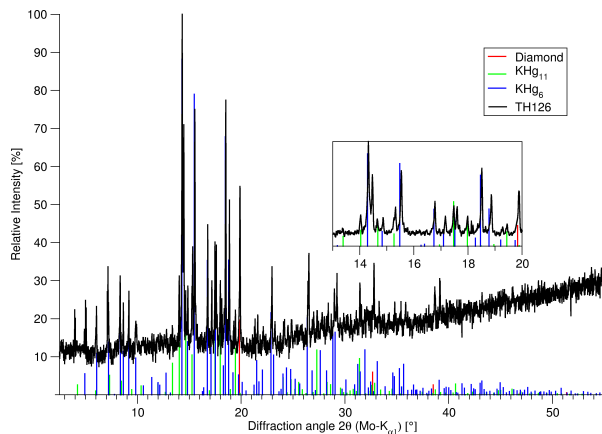


Fig. 7.104: Powder diffractogram of TH126 (black). Diamond^[4] was used for optical dilution. The product was identified as a mixture of KHg₁₁^[3] (green) and KHg₆^[7] (blue).

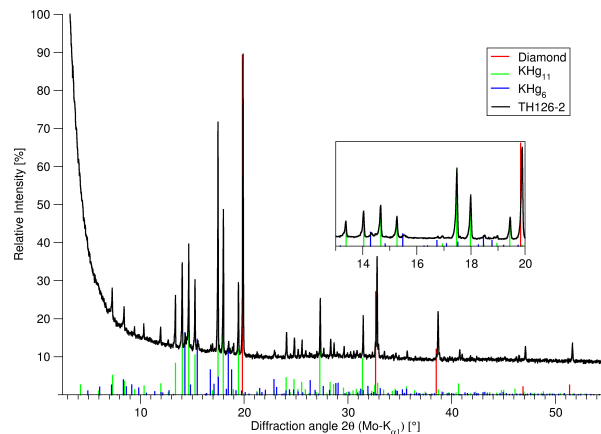


Fig. 7.105: Powder diffractogram of TH126 (black). Diamond^[4] was used for optical dilution. The product was identified as a mixture of KHg₁₁^[3] (green) and minor amounts of KHg₆^[7] (blue).

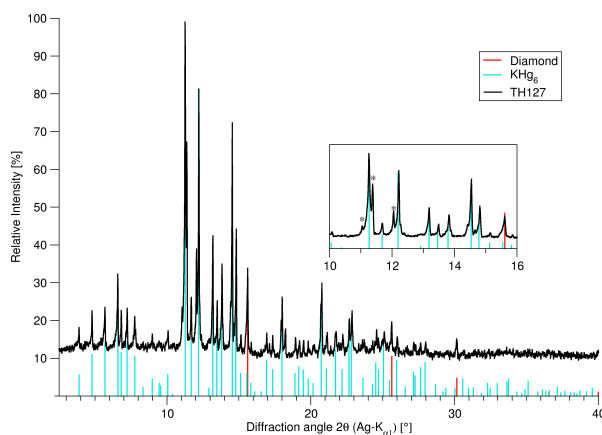


Fig. 7.106: Powder diffractogram of TH127 (black). Diamond^[4] (red) was used for optical dilution. The obtained product was identified as KHg₆^[7] (blue), while some reflexes could not be identified (marked with *).

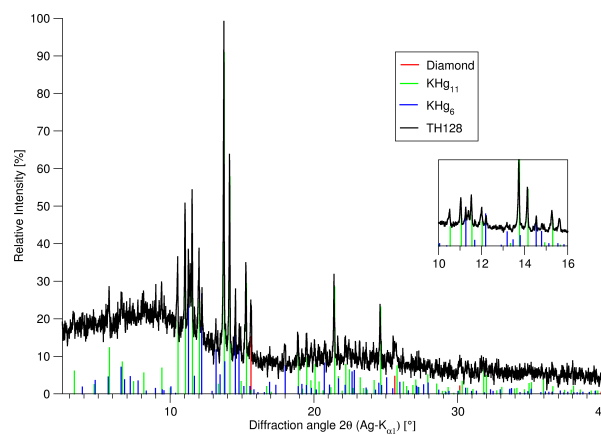


Fig. 7.107: Powder diffractogram of TH128 (black). Diamond^[4] was used for optical dilution. The product was identified as a mixture of KHg₁₁^[3] (green) and minor amounts of KHg₆^[7] (blue).

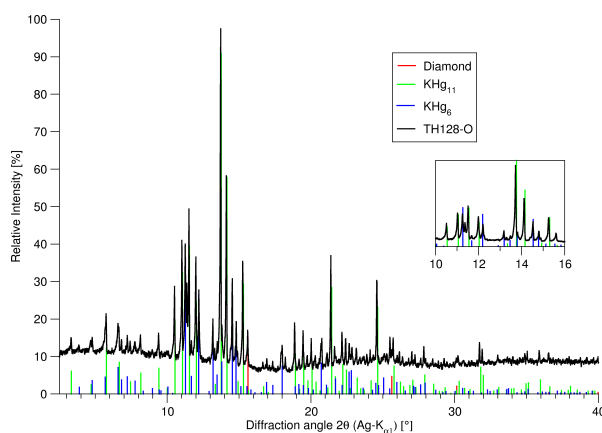


Fig. 7.108: Powder diffractogram of TH128-O (black). Diamond^[4] was used for optical dilution. The product was identified as a mixture of KHg₁₁^[3] (green) and minor amounts of KHg₆^[7] (blue).

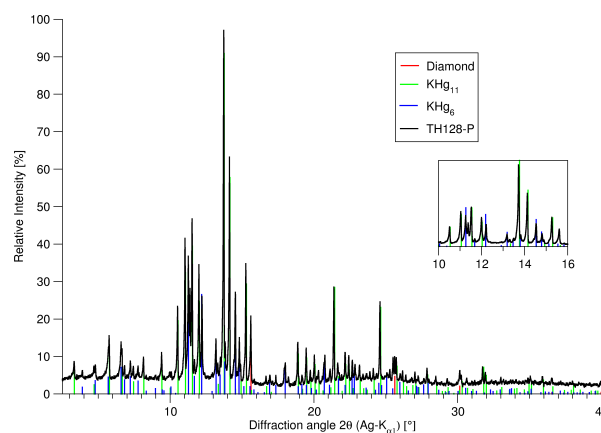


Fig. 7.109: Powder diffractogram of TH128-P (black). Diamond^[4] was used for optical dilution. The product was identified as a mixture of KHg₁₁^[3] (green) and minor amounts of KHg₆^[7] (blue).

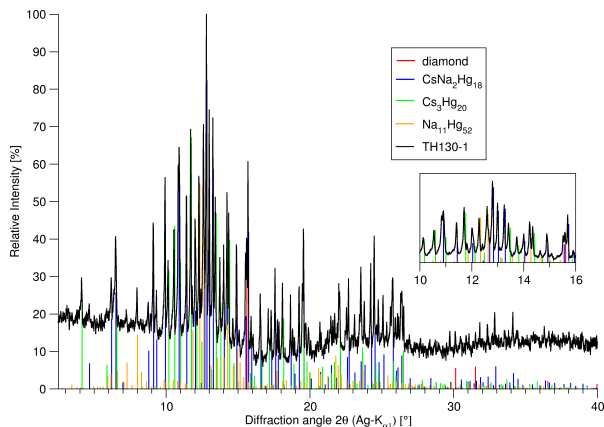


Fig. 7.110: Powder diffractogram of the remaining solid of TH130 (black). Diamond^[4] (red) was used for optical dilution. The solid consists of CsNa₂Hg₁₈ (blue, generated from single crystal data) as well as Cs₃Hg₂₀^[6] (green) and Na₁₁Hg₅₂^[2] (orange).

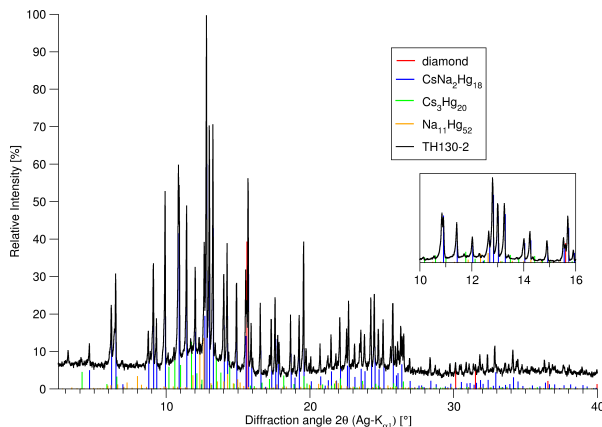


Fig. 7.111: Powder diffractogram of the solidified filtrate of TH130 (black). Diamond^[4] (red) was used for optical dilution. The solid consists of CsNa₂Hg₁₈ (blue, generated from single crystal data) as well as Cs₃Hg₂₀^[6] (green) and Na₁₁Hg₅₂^[2] (orange).

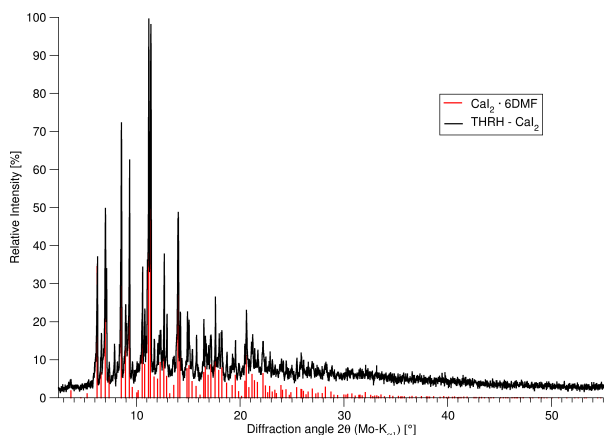


Fig. 7.112: Powder diffractogram of THRH-CaI₂*6DMF (black), with simulated intensities of CaI₂ · 6DMF^[11] (red).

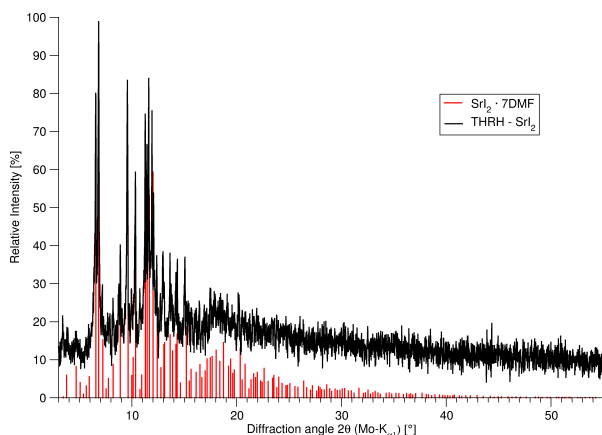


Fig. 7.113: Powder diffractogram of THRH-SrI₂*6DMF (black), with simulated intensities of SrI₂ · 7DMF^[11] (red).

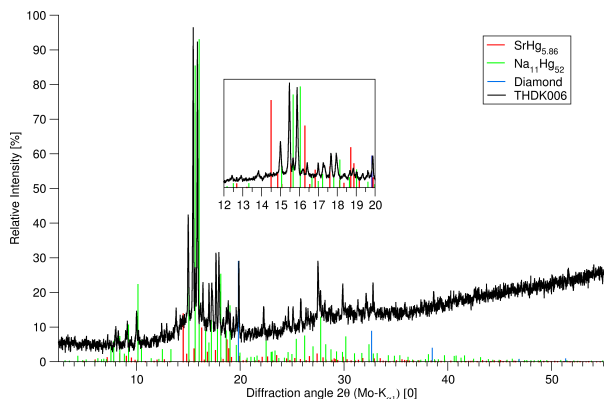


Fig. 7.114: Powder diffractogram of THDK006 (black). Diamond^[4] was used for optical dilution. The product was identified as a mixture of Na₁₁Hg₅₂^[2] (green) with a slight shift towards smaller diffraction angles. Comparison to the diffraction pattern generated from single crystal data yielded that the bulk sample did not contain major amounts of SrHg_{5.86}.

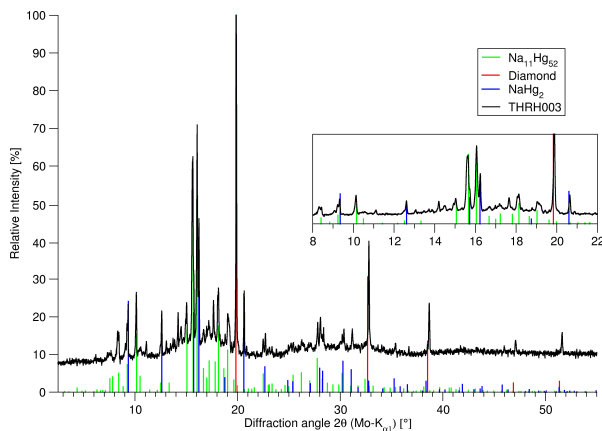


Fig. 7.115: Powder diffractogram of THRH003 (black) with diamond^[4] (red) used for optical dilution. The product contains NaHg₂^[5] (blue) as a byproduct, while the overall diffraction pattern shows a high overlap with Na₁₁Hg₅₂^[2] (green).

7.4 DSC measurements

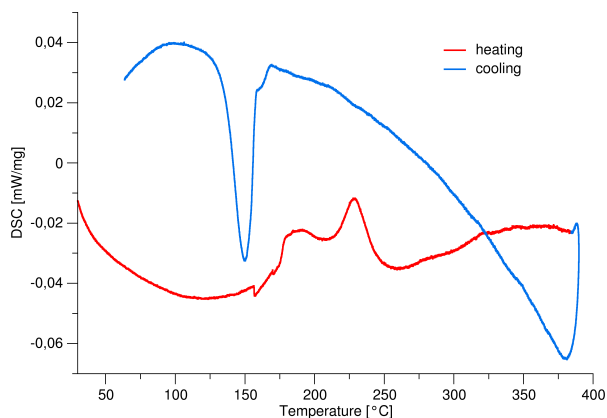


Fig. 7.116: DSC measurement of TH013. Heating/cooling segments are represented in red/blue.

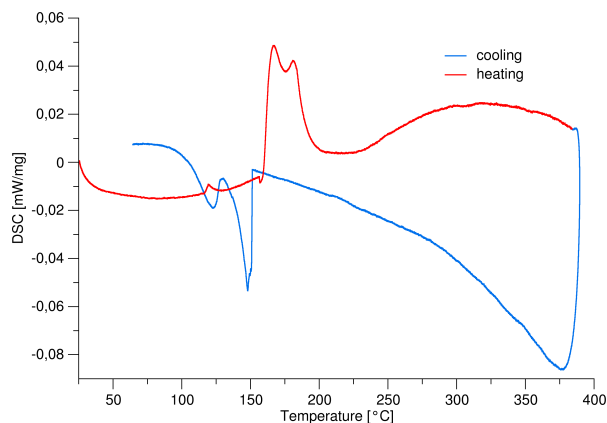


Fig. 7.117: DSC measurement of TH014. Heating and cooling segments are represented in red/blue, respectively.

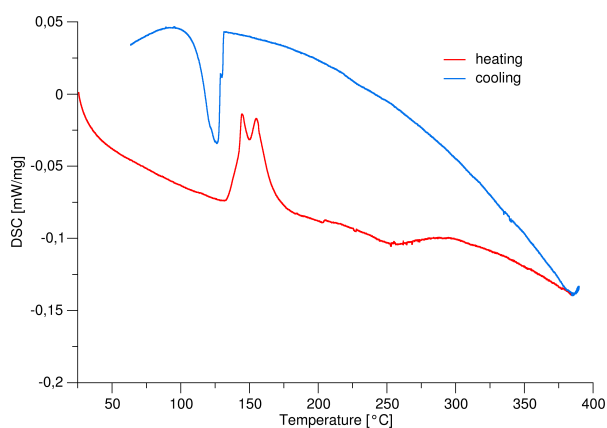


Fig. 7.118: DSC measurement of TH015. Heating and cooling segments are represented in red/blue, respectively.

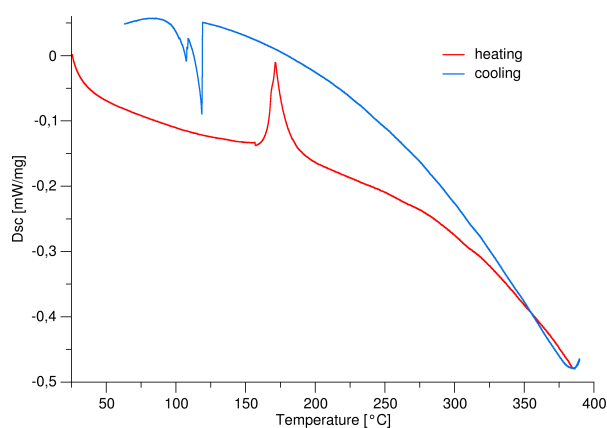


Fig. 7.119: DSC measurement of TH016. Heating and cooling segments are represented in red/blue, respectively.

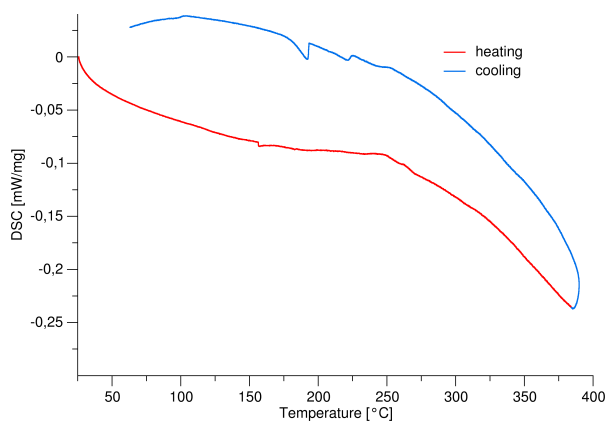


Fig. 7.120: DSC measurement of TH019. Heating and cooling segments are represented in red/blue, respectively.

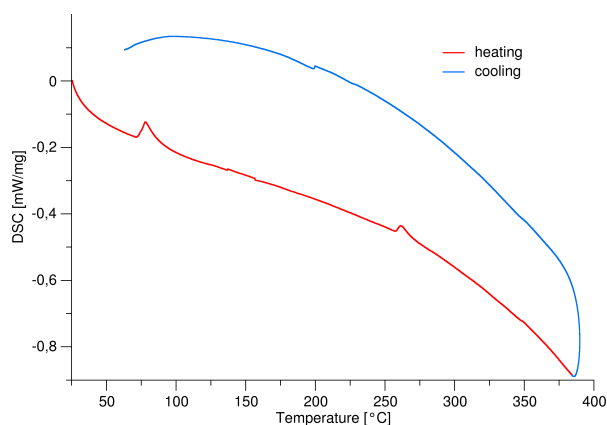


Fig. 7.121: DSC measurement of TH020. Heating and cooling segments are represented in red/blue, respectively.

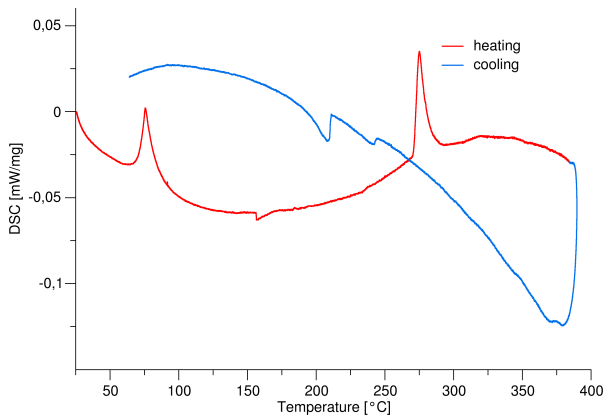


Fig. 7.122: DSC measurement of TH021. Heating and cooling segments are represented in red/blue, respectively.

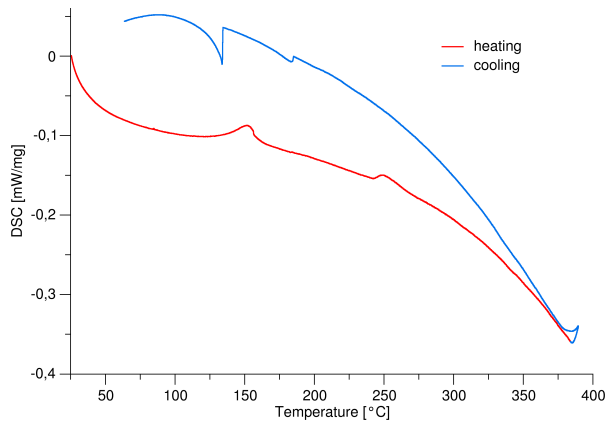


Fig. 7.123: DSC measurement of TH022. Heating and cooling segments are represented in red/blue, respectively.

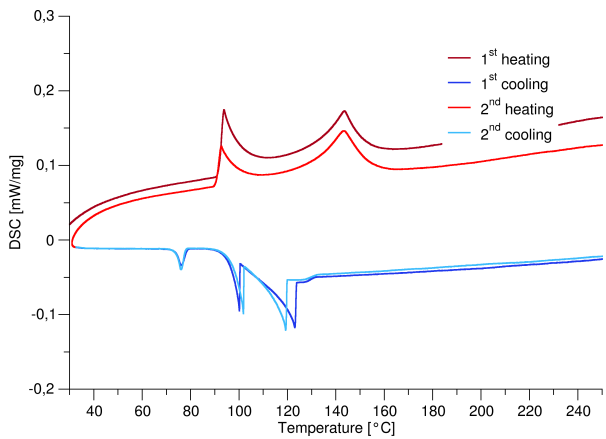


Fig. 7.124: DSC measurement of TH041. Heating and cooling segments are represented in red/blue, respectively.

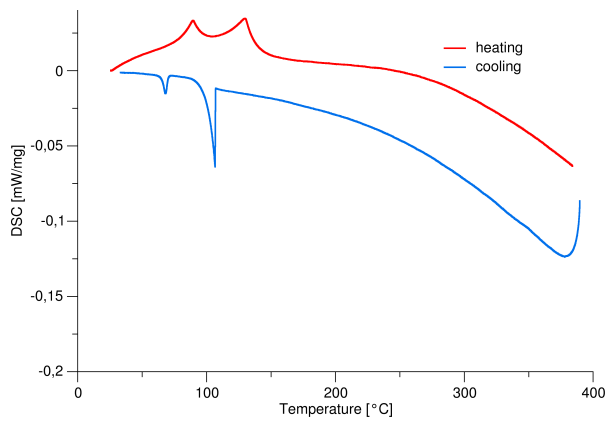


Fig. 7.125: DSC measurement of TH042. Heating and cooling segments are represented in red/blue with decreasing darkness, respectively.

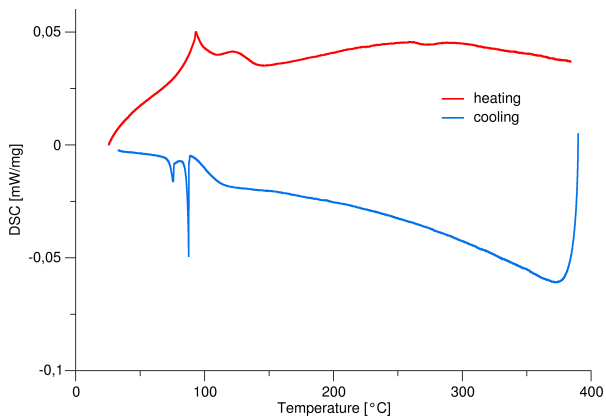


Fig. 7.126: DSC measurement of TH043. Heating and cooling segments are represented in red/blue with decreasing darkness, respectively.

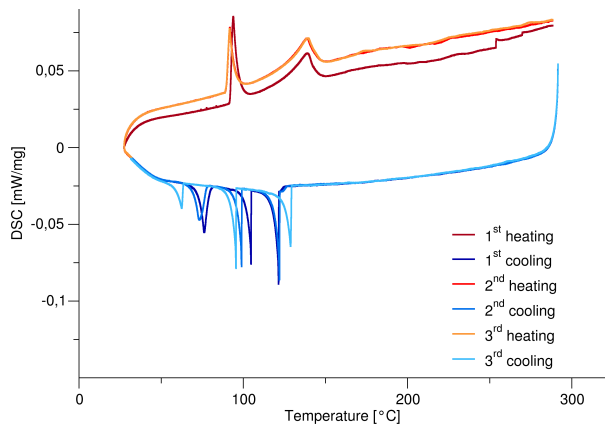


Fig. 7.127: DSC measurement of TH096. Heating and cooling segments are represented in red/blue with decreasing darkness, respectively.

7.5 Rietveld refinements

7.5.1 BeI₂

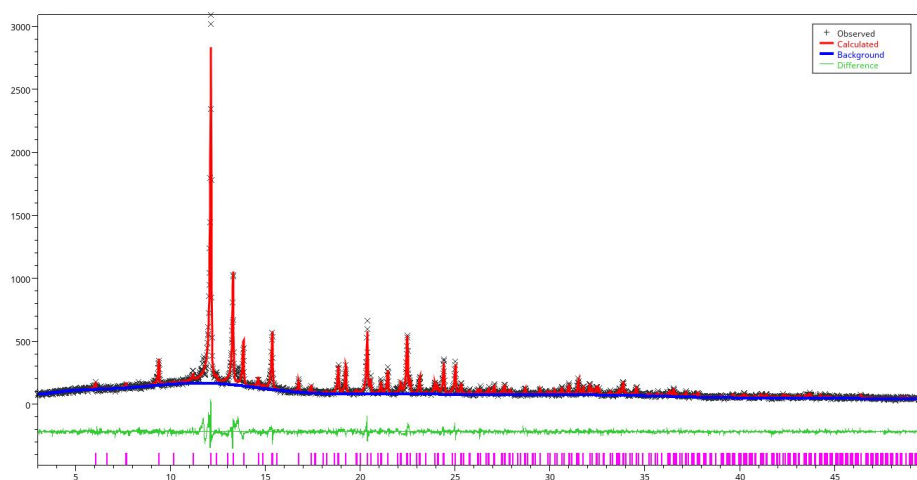


Fig. 7.128: Graphical representation of the result of the Rietveld refinement of BeI₂ synthesized from the elements (Mo-K_α1 radiation, program EXPO^[34]). Starting values for the refinement were taken from the literature model of β-BeI₂.^[29] For further information on the refinement see Table 7.9 (below).

Table 7.9: Results of the Rietveld refinement of BeI₂ prepared from the elements, see also Fig. 7.128 (above).

Composition	BeI ₂				
Structure type	ZnBr ₂				
Crystal system	tetragonal				
Space group	<i>I</i> 4 ₁ / <i>acd</i> , No. 142				
Formula units	<i>Z</i>	32			
Lattice parameters [Å, Å ³]	<i>a</i>	12.24804(3)			
	<i>c</i>	21.24267(13)			
	<i>V</i>	3186.8(2)			
Radiation	Mo-K _α 1				
Wavelength [Å]	<i>λ</i>	0.709317			
Data range [°]	2 <i>θ</i>	3.0 – 53.0			
Step size [°]	Δ2 <i>θ</i>	0.015			
Calculated density [g·cm ⁻³]	<i>ρ</i>	4.38			
Data points	3334				
Resolution [Å]	0.7946				
<i>h</i> _{max} , <i>k</i> _{max} , <i>l</i> _{max}	15, 15, 26				
Background function	shifted Chebyshev				
Background parameters	18				
Profile function	Pearson VII				
<i>R</i> values [%]	<i>R</i> _{<i>P</i>}	7.547			
	<i>R</i> _{<i>wP</i>}	9.840			
	<i>R</i> _{<i>exp</i>}	9.317			
	<i>R</i> _{<i>I</i>}	11.046			
GooF	1.115				
Atom	Wyck.	<i>x</i>	<i>y</i>	<i>z</i>	<i>U</i> _{<i>iso</i>}
Be1	32 <i>g</i>	0.144(10)	0.162(9)	0.931(6)	2.0(2)
I1	32 <i>g</i>	0.2288(5)	0.2798(7)	0.8733(6)	2.7(2)
I2	16 <i>d</i>	1/4	0.0454(10)	0	3.0(3)
I3	16 <i>e</i>	0	1/4	0.0103(4)	4.0(4)

7.6 List of performed Experiments

Table 7.10: Experiments performed by Timotheus Hohl (E = electrolysis, O = Ostwald-ripening, T = thermochemical synthesis). Experiments labelled with † were partly performed by Lucas Balzat, labelled with ‡ partly by Jessica Wulfes.

No.	page	Type	short description	result
TH001	143	T	CsNaHg ₈	CsNa ₂ Hg ₁₈ (see Chapter 4.1, p. 27)
TH002	140	E	NaI/KI	Na ₁₁ Hg ₅₂
TH003	140	E	KI in Na/Hg-mixture	KHg ₁₁
TH004-1	143	T	NaRbHg ₈	NaHg ₂ , Rb ₃ Hg ₂₀
TH004-2	143	T	NaRbHg ₁₆	Na ₁₁ Hg ₅₂
TH005	140	E	CsI in Na/Hg-mixture	no product obtained
TH006	140	E	CsI in Na/Hg-mixture	no product obtained
TH007	140	E	CsI in Na/Hg-mixture	no product obtained
TH008	144	T	KRbHg ₈	Rb ₇ Hg ₃₁ + unknown K-amalgam
TH008-2	144	T	TH008 + Hg	K _{0.53} Rb _{0.47} Hg ₁₁ (see Ch. 4.3, p. 61)
TH009	144	T	CsKHg ₈	KHg ₆ , Cs ₃ Hg ₂₀
TH009-1	144	T	CsKHg ₂₆	KHg ₁₁
TH010-1	142	T	KNaHg ₁₆	NaHg ₂ , Na ₁₁ Hg ₅₂ , KHg ₅
TH010-2	142	T	KNaHg ₈	KHg ₁₁
TH011-1	145	T	CsRbHg ₈	Cs ₅ Hg ₁₉ , Rb ₅ Hg ₁₉
TH011-2	145	T	TH011-1 + Hg	Cs ₃ Hg ₂₀ + RbHg ₁₁
TH012	146	T	CaNaHg ₈	disposed
TH013 [†]	147	T	CaNaHg ₈	Na ₁₁ Hg ₅₂ , Ca ₁₄ Hg ₅₁
TH014 [†]	148	T	CaKHg ₈	CaHg ₃ , K ₇ Hg ₃₁ , KHg ₅
TH015 [†]	149	T	CaRbHg ₈	Rb ₃ Hg ₂₀
TH016 [†]	151	T	CaCsHg ₈	Cs _{2.80} Ca _{0.20} Hg ₂₀ (see Ch. 4.3, p. 61)
TH017 [†]	137	T	MgI ₂ · 6 DMF	MgI ₂ · 6 DMF
TH018 [†]	140	E	Electrolysis of MgI ₂	MgHg ₂
TH019 [†]	147	T	CaNaHg ₁₆	Na ₁₁ Hg ₅₂ , Ca ₁₄ Hg ₅₁
TH020 [†]	148	T	CaKHg ₁₆	Ca ₁₁ Hg ₅₄ , CaHg ₁₁ , KHg ₁₁
TH021	150	T	CaRbHg ₁₆	Ca ₁₁ Hg ₅₄ , CaHg ₁₁ , RbHg ₁₁
TH022	151	T	CaCsHg ₁₆	Ca ₁₄ Hg ₅₁
TH023 [†]	146	T	MgNaHg ₁₆	Na ₁₁ Hg ₅₂ , MgHg ₂
TH024 [†]	148	T	MgKHg ₈	MgHg ₂ , KHg ₆ , KHg ₁₁
TH025 [†]	149	T	MgRbHg ₈	RbHg ₁₁ , Rb ₃ Hg ₂₀
TH026 [†]	151	T	MgCsHg ₈	Cs ₃ Hg ₂₀ , MgHg ₂
TH027 [†]	146	T	MgNaHg ₈	MgHg, Mg ₂ Hg + unknown compd.
TH028 [†]	148	T	MgKHg ₁₆	KHg ₁₁ , MgHg ₂
TH029 [†]	149	T	MgRbHg ₁₆	RbHg ₁₁
TH030 [†]	151	T	MgCsHg ₁₆	Cs ₃ Hg ₂₀
TH031	145	T	Rb _{1.5} Cs _{1.5} Hg ₂₀	RbHg ₁₁ , Cs ₃ Hg ₂₀
TH032	147	T	CaNaHg ₈	Ca ₁₁ Hg ₅₄ , Na ₁₁ Hg ₅₂
TH033	148	T	CaKHg ₈	CaHg ₃ , Ca ₁₁ Hg ₅₄
TH034	150	T	CaRbHg ₈	CaHg ₃ , Rb ₂ Hg ₇ , Rb ₃ Hg ₂₀
TH035	151	T	CaCsHg ₈	CaHg ₂ , Ca ₁₁ Hg ₅₄ , Cs ₃ Hg ₂₀
TH036	147	T	CaNaHg ₁₆	Ca ₁₁ Hg ₅₄
TH037	148	T	CaKHg ₁₆	Ca ₁₁ Hg ₅₄ , KHg ₁₁
TH038	150	T	CaRbHg ₁₆	Ca ₁₄ Hg ₅₁ , RbHg ₁₁
TH039	151	T	CaCsHg ₁₆	Ca ₁₁ Hg ₅₄ , Cs ₃ Hg ₂₀
TH040	143	T	CsNa ₂ Hg ₁₈	disposed
TH041	143	T	CsNa ₂ Hg ₁₈	CsNa ₂ Hg ₁₈ , Cs ₃ Hg ₂₀
TH042	144	T	CsNa ₂ Hg ₁₈ (DSC)	CsNa ₂ Hg ₁₈ , Na ₁₁ Hg ₅₂
TH043	144	T	CsNa ₂ Hg ₁₈ (DSC)	CsNa ₂ Hg ₁₈ , Cs ₃ Hg ₂₀
TH044	145	T	KCsHg _{25.7}	KHg ₁₁ , Cs ₃ Hg ₂₀
TH045 ^{†,‡}	147	T	SrNaHg ₈	Na ₁₁ Hg ₅₂ , Sr _{10.5} Hg _{54.5}
TH046 ^{†,‡}	147	T	SrNaHg ₁₆	ternary Sr variant of Na ₁₁ Hg ₅₂
TH047 ^{†,‡}	149	T	SrKHg ₈	no product obtained
TH048 ^{†,‡}	149	T	SrKHg ₁₆	KHg ₁₁ , Sr _{10.5} Hg _{54.5}
TH049 ^{†,‡}	150	T	SrRbHg ₈	Rb ₅ Hg ₁₉ , Sr _{10.5} Hg _{54.5}
TH050 ^{†,‡}	150	T	SrRbHg ₁₆	Rb ₃ Hg ₂₀ , RbHg ₁₁ , Sr _{10.5} Hg _{54.5}
TH051 ^{†,‡}	152	T	SrCsHg ₈	Cs ₃ Hg ₂₀ , Cs ₅ Hg ₁₉ , Sr ₁₃ Hg ₅₈ , SrHg ₁₁ + unknown.
TH052 ^{†,‡}	152	T	SrCsHg ₁₆	no product obtained
TH053 [†]	147	O	TH013	Ca _{6.9} Na _{4.1} Hg ₅₄ (see Ch. 4.2, p. 42)
TH054 [†]	147	O	TH019	Na ₁₁ Hg ₅₂ , Ca ₁₄ Hg ₅₁

continued on the next page

No.	page	Type	short description	result
TH055 [†]	148	O	TH014	KHg ₁₁ , CaHg ₁₁ , Ca ₁₁ Hg ₅₄
TH056 [†]	149	O	TH020	KHg ₁₁ , CaHg ₁₁ , Ca ₁₁ Hg ₅₄
TH057 [†]	150	O	TH015	Ca ₁₁ Hg ₅₄
TH058 [†]	150	O	TH021	Ca ₁₁ Hg ₅₄ , CaHg ₁₁ , RbHg ₁₁
TH059 [†]	151	O	TH016	Ca ₁₁ Hg ₅₄ , Ca ₁₄ Hg ₅₁ , Cs ₃ Hg ₂₀
TH060 [†]	151	O	TH022	Ca ₁₄ Hg ₅₁
TH061	143	O	TH004	Na ₁₁ Hg ₅₂
TH062 [†]	148	T	BaNaHg ₈	Ba ₇ Hg ₃₁ , BaHg ₆ , Na ₁₁ Hg ₅₂
TH063 [†]	149	T	BaKHg ₈	no product obtained
TH064 [†]	150	T	BaRbHg ₈	no product obtained
TH065 [†]	152	T	BaCsHg ₈	no product obtained
TH066 [†]	148	T	BaNaHg ₁₆	Na ₁₁ Hg ₅₂ , BaHg ₁₁
TH067 [†]	149	T	BaKHg ₁₆	Ba ₂₀ Hg ₁₀₃ , BaHg ₆ , KHg ₁₁
TH068 [†]	150	T	BaRbHg ₁₆	no product obtained
TH069 [†]	152	T	BaCsHg ₁₆	no product obtained
TH070	145	T	TH044	KHg ₁₁
TH071	145	T	TH044	KHg ₁₁
TH072	144	O	TH041	CsNa ₂ Hg ₁₈ + Cs ₃ Hg ₂₀
TH073	145	O	TH031	no product obtained
TH074	146	T	Rb ₃ Cs ₂ Hg ₁₉	Cs _x Rb _{3-x} Hg ₂₀
TH075	139	T	Rb ₃ Hg ₂₀	Rb ₃ Hg ₂₀
TH076	138	T	Cs ₃ Hg ₂₀	Cs ₃ Hg ₂₀
TH077	146	T	Cs ₃ Hg ₂₀ + Rb ₃ Hg ₂₀	discarded
TH078	146	T	Cs ₃ Hg ₂₀ + Rb ₃ Hg ₂₀ + Hg	RbHg ₁₁
TH079	138	T	Cs ₃ Hg ₂₀	Cs ₃ Hg ₂₀ (traces of Cs ₅ Hg ₁₉)
TH080	138	T	CsHg ₂	CsHg ₂ , Cs ₅ Hg ₁₉
TH081	139	T	RbHg ₂	RbHg ₂ + Rb impurities by Rb ₅ Hg ₁₉ (TH082, TH083)
TH082	146	T	CsHg ₂ + RbHg ₂	RbHg ₂ , Rb ₅ Hg ₁₉
TH083	146	T	CsHg ₂ + RbHg ₂ + 2 Hg	RbHg ₂ , (Rb/Cs) ₅ Hg ₁₉
TH084	143	T	NaRbHg ₂₈	Hg, Na ₁₁ Hg ₅₂ , RbHg ₁₁
TH085	145	T	CsKHg ₂₉	KHg ₁₁
TH086	143	T	TH084 (50 °C)	RbHg ₁₁
TH087	143	T	TH084 (80 °C)	RbHg ₁₁
TH088	145	T	TH085 (50 °C)	KHg ₁₁
TH089	145	T	TH085 (80 °C)	KHg ₁₁
TH090	152	T	EuMgHg ₁₀	EuHg ₂ , MgHg ₂ , unknown phase
TH091	152	T	EuCaHg ₁₀	Ca _{4.5} Eu _{6.5} Hg ₅₄ (see Ch. 4.2, p. 42)
TH092	153	T	EuBaHg ₁₀	BaHg ₁₁ , EuHg ₂ , Eu ₁₀ Hg ₅₅
TH093	153	T	YbNaHg ₁₀	Na ₁₁ Hg ₅₂ , YbHg ₃ , NaHg ₂
TH094	152	T	EuMgHg ₁₀	no product obtained
TH095	153	T	YbNaHg ₁₀	Na ₁₁ Hg ₅₂ , Yb ₁₁ Hg ₅₄ , YbHg ₃
TH096	144	T	CsNa ₂ Hg ₁₈	phase-pure CsNa ₂ Hg ₁₈
TH097–108				– not performed –
TH109	139	DSC	RbHg ₈	RbHg ₁₁
TH110	139	T	KHg ₁₁	phase-pure KHg ₁₁
TH111	140	T	RbHg ₁₁	phase-pure RbHg ₁₁
TH112	15	T	BeI ₂	β-BeI ₂
TH113	140	—	Diss. of BeI ₂ in liq. NH ₃	successful, formation of Be(NH ₃) ₄ I ₂
TH114	141	T	K ₇ Hg ₃₁	KHg ₄ , KHg ₅ , KHg ₈
TH115	139	T	Rb ₇ Hg ₃₁	Rb ₃ Hg ₂₀ , Rb ₅ Hg ₁₉
TH116	22	E	BeI ₂ in liq. NH ₃	Cu ₇ Hg ₆
TH117	15	T	BeI ₂	β-BeI ₂
TH118	141	T	KHg ₈	KHg ₆ , KHg ₈ , KHg ₁₁
TH119	141	T	KHg ₈	KHg ₆ , KHg ₈ , KHg ₁₁
TH120	142	T	SrHg _{5.86}	SrHg _{5.86} , Sr _{10.5} Hg _{54.5} , SrHg ₈
TH121	139	T	KHg ₂	KHg ₂ + traces of unknown phase
TH122	139	T	KHg ₁₁	KHg ₁₁
TH123	23	E	BeI ₂ in liq. NH ₃	unidentified
TH124	141	T	KHg ₈	KHg ₁₁ + KHg ₈
TH125	142	T	KHg ₈	KHg ₆ + KHg ₁₁
TH126	142	T	KHg ₈	KHg ₆ + KHg ₁₁
TH127	141	E	KI in DMF (75 °C)	KHg ₆ + unidentified
TH128	142	T	KHg ₈	KHg ₆ + KHg ₁₁
TH129	15	T	BeI ₂	β-BeI ₂

Table 7.11: Performed experiments by Lukas Nusser (F-Praktikum) (T = thermochemical synthesis).

No.	type	short description	result
THLN-001	DSC	ScSrHg	no new phases
THLN-002	DSC	TiSrHg	SrHg, SrHg ₂
THLN-003	DSC	VSrHg	unknown
THLN-004	DSC	CrSrHg	SrHg ₂ + unknown
THLN-005	DSC	MnSrHg	TaMn ₂
THLN-006	DSC	FeSrHg	SrHg ₂
THLN-007	DSC	CoSrHg	unknown
THLN-008	DSC	NiSrHg	SrHg ₂
THLN-009	DSC	CuSrHg	no product obtained
THLN-010	DSC	ZnSrHg	unknown
THLN-011	T	TiSrHg	SrHg
THLN-012	T	FeSrHg	SrHg, SrHg ₂
THLN-013	T	CoSrHg	SrHg, SrHg ₂
THLN-014	T	NiSrHg	SrHg ₂
THLN-015	T	MnSrHg	SrHg, SrHg ₂ , β-Mn
THLN-016-1	DSC	Yb ₁₀ SrHg	Sr _{0.5} Yb _{10.5} Hg ₅₄
THLN-017	T	Yb ₁₀ SrHg	Sr _{0.5} Yb _{10.5} Hg ₅₄ (see Ch. 4.2, p. 42)

Table 7.12: Performed experiments by Jessica Wulfes (F-Praktikum) (T = thermochemical experiment, D = distillation).

No.	type	short description	result
THJW001	T	Cs ₁₀ Hg ₈	CsHg
THJW002	T	SrEuHg ₁₀	unidentified
THJW003	T	MgYbHg ₁₀	MgHg ₂ , Yb ₁₁ Hg ₅₄
THJW004	T	CaYbHg ₁₀	unclear
THJW005	T	BaYbHg ₁₀	Yb ₁₁ Hg ₅₄ /Yb ₁₄ Hg ₅₁ , YbHg ₃ , BaHg ₃ , BaHg ₆ , BaHg ₁₁
THJW006	T	CaYbHg ₁₀	Ca ₁₁ Hg ₅₄ , Yb ₁₁ Hg ₅₄ /Yb ₁₄ Hg ₅₁
THJW007	T	Cs ₁₀ O ₂ Hg	disposed
THJW008	T	MgEuHg ₁₀	MgHg, EuHg ₂ , Eu ₁₀ Hg ₅₅
THJW009	T	CaEuHg ₁₀	disposed
THJW010	T	BaEuHg ₁₀	BaHg ₁₁ , Eu ₁₀ Hg ₅₅
THJW011	D	Cs ₂ O	disposed
THJW012	T	NaMgHg ₈	Na ₁₁ Hg ₅₂
THJW013	T	NaMgHg ₁₆	MgHg ₂ , Na ₃ Hg/Na ₁₁ Hg ₅₂
THJW014	T	KMgHg ₈	KHg ₁₁
THJW015	T	KMgHg ₁₆	KHg ₁₁
THJW016	T	RbMgHg ₈	unclear
THJW017	T	RbMgHg ₁₆	RbHg ₁₁
THJW018	T	CsMgHg ₈	unclear
THJW019	T	CsMgHg ₁₆	Cs ₃ Hg ₂₀
THJW020	T	CaEuHg ₁₀	EuHg ₂ , Eu ₁₀ Hg ₅₅
THJW021	T	NaYbHg ₁₀	Yb ₁₁ Hg ₅₄
THJW022	T	KYbHg ₁₀	disposed
THJW023	T	CsYbHg ₁₀	disposed
THJW024	T	RbYbHg ₁₀	Yb ₁₄ Hg ₅₁ /Yb ₁₁ Hg ₅₄ , Rb ₃ Hg ₂₀ , YbHg ₃
THJW025	T	CsYbHg ₁₀	Yb ₁₄ Hg ₅₁ /Yb ₁₁ Hg ₅₄ , Cs ₃ Hg ₂₀ , YbHg ₃
THJW026	T	Cs ₃ Hg ₂₀	disposed
THJW027	T	NaEuHg ₁₀	Eu ₁₄ Hg ₅₁ /Eu _{10.1} Hg _{54.9}
THJW028	T	KEuHg ₁₀	Eu ₁₄ Hg ₅₁
THJW029	T	RbEuHg ₁₀	disposed
THJW030	T	CsEuHg ₁₀	Eu ₁₄ Hg ₅₁ /Eu _{10.1} Hg _{54.9} , Cs ₂ Hg ₂₇
THJW031	T	SrEuHg ₁₀	Sr _{10.5} Hg _{54.5}
THJW025-031	T	solid material inside the quartz tube	Cs ₃ Hg ₂₀ , RbHg ₁₁
THJW032	T	KYbHg ₁₀	Yb ₁₄ Hg ₅₁ /Yb ₁₁ Hg ₅₄
THJW033	T	BaKHg ₈	Ba ₇ Hg ₃₁ , K ₂ Hg ₇
THJW034	T	BaRbHg ₈	BaHg ₆
THJW035	T	BaCsHg ₈	Ba ₇ Hg ₃₁ , Cs ₅ Hg ₁₉
THJW036	T	BaRbHg ₁₆	Ba ₇ Hg ₃₁ , Rb ₅ Hg ₁₉
THJW037	T	BaCsHg ₁₆	Cs ₃ Hg ₂₀ , BaHg ₁₁
THJW038	T	KSrHg ₈	disposed
THJW039	T	CsSrHg ₁₆	Sr _{10.5} Hg _{54.5} , SrHg ₈ , Cs ₃ Hg ₂₀
THJW040	T	RbYbHg ₁₀	Rb ₃ Hg ₂₉ , YbHg ₃ , Yb ₁₄ Hg ₅₁ /Yb ₁₁ Hg ₅₄

continued on the next page

No.	type	short description	result
THJW041	T	SrEuHg ₁₀	Sr _{10.5} Hg _{54.5}
THJW042	T	CsEuHg ₁₀	Cs ₃ Hg ₂₀ , Eu ₁₄ Hg ₅₁ /Eu _{10.1} Hg _{54.9}
THJW043	T	Cs ₁₀ Hg ₈	CsHg
THJW044	T	Cs ₁₀ Hg ₈	CsHg
THJW045	T	BaYbHg ₁₀	BaHg ₁₁ , YbHg ₂ , YbHg ₃ , Yb ₁₄ Hg ₅₁ /Yb ₁₁ Hg ₅₄

Table 7.13: Performed experiments by Robert Hübsch (F-Praktikum) (SM = Starting material synthesis, ES = electrolysis).

No.	type	short description	result
THRH - CaI ₂	SM	CaI ₂ · 6 DMF	CaI ₂ · 6 DMF
THRH - Sr ₂	SM	SrI ₂ · 7 DMF	SrI ₂ · 7 DMF
THRH - BaI ₂	SM	BaI ₂ · 8 DMF	BaI ₂ · 8 DMF
THRH003	ES	NaI + KI	ternary Na-K-amalgam (see Chapter 4.6, p. 98)

Table 7.14: Performed experiments by Daniel Kraut (F-Praktikum) (ES = electrolysis, T = thermochemical experiment).

No.	type	short description	result
THDK001	T	Na + K + 22 Hg (105 °C)	Na ₁₁ Hg ₅₂ , KHg ₁₁
THDK002	T	Na + Rb + 22 Hg (105 °C)	Na ₁₁ Hg ₅₂ , RbHg ₁₁
THDK003	T	Na + Cs + 22 Hg (105 °C)	Na ₁₁ Hg ₅₂
THDK004	T	Na + Mg + 22 Hg (105 °C)	MgHg ₂
THDK005	T	Na + Ca + 22 Hg (200 °C)	Na ₁₁ Hg ₅₂ , Ca ₁₁ Hg ₅₄
THDK006	T	Na + Ca + 22 Hg (200 °C)	Na ₁₁ Hg ₅₂ , SrHg _{5.86} (see Ch. 4.5, p. 91)
THDK007	T	Na + Ba + 22 Hg (200 °C)	BaHg ₁₁
THDK008	T	K + Rb + 22 Hg (200 °C)	KHg ₁₁ , RbHg ₁₁
THDK009	T	K + Cs + 22 Hg (200 °C)	KHg ₁₁
THDK010	T	K + Mg + 22 Hg (200 °C)	KHg ₁₁ , MgHg ₂
THDK011	T	K + Ca + 22 Hg (200 °C)	KHg ₁₁ , CaHg ₁₁ , Ca ₁₄ Hg ₅₁
THDK012	T	K + Sr + 22 Hg (200 °C)	KHg ₁₁ , Sr _{10.5} Hg _{54.5} , Sr ₁₄ Hg ₅₁
THDK013	T	K + Ba + 22 Hg (200 °C)	KHg ₁₁ , BaHg ₁₁
THDK014	T	Ca + Mg + 22 Hg (200 °C)	Ca ₁₁ Hg ₅₄ , Ca ₁₄ Hg ₅₁
THDK015	T	Ca + Sr + 22 Hg (200 °C)	Ca ₁₁ Hg ₅₄ , Ca ₁₄ Hg ₅₁ , Sr _{10.5} Hg _{54.5}
THDK016	T	Ca + Ba + 22 Hg (200 °C)	CaHg ₁₁ , BaHg ₁₁
THDK017	T	Sr + 3.5 Hg (-78 °C)	Sr _{10.5} Hg _{54.5} , Sr ₁₄ Hg ₅₁ , SrHg ₃
THDK017	DSC	Sr + 3.5 Hg (650 °C)	Sr ₁₄ Hg ₅₁
THDK018	T	Sr + 5 Hg (-78 °C)	Sr ₁₄ Hg ₅₁ , SrHg ₈
THDK018	DSC	Sr + 5 Hg (500 °C)	Sr ₁₄ Hg ₅₁
THDK019	T	Sr + 5.86 Hg (-78 °C)	Sr _{10.5} Hg _{54.5} , SrHg ₈
THDK019	DSC	Sr + 5.86 Hg (500 °C)	SrHg ₈
THDK020	T	Sr + 6.5 Hg (-78 °C)	SrHg ₈
THDK020	DSC	Sr + 6.5 Hg (500 °C)	SrHg ₈
THDK021	T	Sr + 8 Hg (-78 °C)	SrHg ₈ , SrHg ₁₁
THDK021	DSC	Sr + 8 Hg (500 °C)	SrHg ₈ , Sr _{10.5} Hg _{54.5}
THDK022	ES	NaI · 3 DMF + 2.8 SrI	Na ₁₁ Hg ₅₂ , KHg ₁₁
THDK023	ES	NaI · 3 DMF + 4.8 SrI	Na ₁₁ Hg ₅₂ , KHg ₁₁

References

- [1] L. M. Gelato, E. Parthé, Structure Tidy – a computer program to standardize crystal structure data, *J. Appl. Crystallogr.* **1987**, *20*, 139–143, DOI: [10.1107/S0021889887086965](https://doi.org/10.1107/S0021889887086965).
- [2] C. Hoch, A. Simon, Na₁₁Hg₅₂: Complexity in a Polar Metal, *Angew. Chem. Int. Ed.* **2012**, *51*, 3262–3265, DOI: [10.1002/anie.201108064](https://doi.org/10.1002/anie.201108064).
- [3] E. Biehl, H.-J. Deiseroth, Darstellung, Strukturchemie und Magnetismus der Amalgame MHg₁₁ (M: K, Rb, Ba, Sr), *Z. Anorg. Allg. Chem.* **1999**, *625*, 1073–1080, DOI: [10.1002/\(SICI\)1521-3749\(199907\)625:7<1073::AID-ZAAC1073>3.0.CO;2-V](https://doi.org/10.1002/(SICI)1521-3749(199907)625:7<1073::AID-ZAAC1073>3.0.CO;2-V).
- [4] W. H. Bragg, W. L. Bragg, The structure of the diamond, *Proc. Royal Soc. London* **1913**, *89*, 277–291, DOI: [10.1098/rspa.1913.0084](https://doi.org/10.1098/rspa.1913.0084).
- [5] J. W. Nielsen, N. C. Baenziger, The Crystal Structures of NaHg₂, NaHg and Na₃Hg₂, *Acta Crystallogr.* **1954**, *7*, 277–282, DOI: [10.1107/S0365110X54000783](https://doi.org/10.1107/S0365110X54000783).
- [6] E. Todorov, S. C. Sevov, *J. Solid State Chem.* **2000**, *149*, 419–427, DOI: [10.1006/jssc.1999.8569](https://doi.org/10.1006/jssc.1999.8569).
- [7] F. Tambornino, C. Hoch, Bad metal behaviour in the new Hg-rich amalgam KHg₆ with polar metallic bonding, *J. Alloys Compd.* **2015**, *618*, 299–304, DOI: [10.1016/j.jallcom.2014.08.173](https://doi.org/10.1016/j.jallcom.2014.08.173).
- [8] E. Biehl, H.-J. Deiseroth, Rb₅Hg₁₉: Eine neue, geordnete Defektvariante des BaAl₄-Strukturtyps, *Z. Anorg. Allg. Chem.* **1999**, *625*, 389–394, DOI: [10.1002/\(SICI\)1521-3749\(199903\)625:3<389::AID-ZAAC389>3.0.CO;2-9](https://doi.org/10.1002/(SICI)1521-3749(199903)625:3<389::AID-ZAAC389>3.0.CO;2-9).
- [9] A. V. Tkachuk, A. Mar, Alkaline-Earth Metal Mercury Intermetallics, A_{11-x}Hg_{54+x} (A = Ca, Sr), *Inorg. Chem.* **2008**, *47*, 1313–1318, DOI: [10.1021/ic7015148](https://doi.org/10.1021/ic7015148).
- [10] M. Wendorff, C. Röhr, Alkaline-earth tri-mercurides A^{II}Hg₃ (A^{II} = Ca, Sr, Ba): Binary intermetallic compounds with a common and a new structure type, *Z. Kristallogr.* **2018**, *233*, 515–529, DOI: [10.1515/zkri-2018-2054](https://doi.org/10.1515/zkri-2018-2054).
- [11] C. Hoch, Syntheses and crystal structures of solvate complexes of alkaline earth and lanthanoid metal iodides with N,N-dimethylformamide, *Z. Kristallogr. - Cryst. Mater.* **2020**, *235*, 401–411, DOI: [10.1515/zkri-2020-0071](https://doi.org/10.1515/zkri-2020-0071).
- [12] G. Brauer, R. Rudolph, Röntgenuntersuchungen an Magnesiumamalgamen. I., *Z. Allg. Anorg. Chem.* **1941**, *248*, 405–424, DOI: [10.1002/zaac.19412480412](https://doi.org/10.1002/zaac.19412480412).
- [13] G. Bruzzone, F. Merlo, The Calcium-Mercury System, *J. Less-Common Met.* **1973**, *32*, 237–241, DOI: [10.1016/0022-5088\(73\)90091-X](https://doi.org/10.1016/0022-5088(73)90091-X).
- [14] M. Pušelj, Z. Ban, Beitrag zur Kenntnis des Systems Quecksilber-Calcium, *Croat. Chem. Acta* **1978**, *51*, 75–79.
- [15] J. L. C. Daams, J. H. N. Van Vucht, Contribution to the system Mg-Au-Hg, *Philips J. Res.* **1984**, *39*, 275–292.
- [16] E. Biehl, H.-J. Deiseroth, K₂Hg₇ und Rb₂Hg₇, zwei Vertreter eines neuen Strukturtyps binärer intermetallischer Verbindungen, *Z. Anorg. Allg. Chem.* **1999**, *625*, 1337–1342, DOI: [10.1002/\(SICI\)1521-3749\(199908\)625:8<1337::AID-ZAAC1337>3.0.CO;2-W](https://doi.org/10.1002/(SICI)1521-3749(199908)625:8<1337::AID-ZAAC1337>3.0.CO;2-W).
- [17] W. F. Harms, Polare intermetallische Phasen AM und AM₂ (A = Ca, Sr, Ba; M = Ga, In, Zn, Cd, Hg, Cu, Ag, Au) - Kristallchemie, chemische Bindung und Eigenschaften, Dissertation, Albert-Ludwigs-Universität Freiburg im Breisgau, **2008**.
- [18] G. Bruzzone, F. Merlo, The Strontium-Mercury System, *J. Less-Common Met.* **1974**, *35*, 153–157, DOI: [10.1016/0022-5088\(74\)90154-4](https://doi.org/10.1016/0022-5088(74)90154-4).
- [19] G. Bruzzone, F. Merlo, The Barium-Mercury System, *J. Less-Common Met.* **1975**, *39*, 271–276, DOI: [10.1016/0022-5088\(75\)90201-5](https://doi.org/10.1016/0022-5088(75)90201-5).
- [20] M. Wendorff, C. Röhr, The new barium mercuride BaHg₆ and ternary indium and gallium derivatives, *J. Alloys Compd.* **2013**, *546*, 320–328, DOI: [10.1016/j.jallcom.2012.07.101](https://doi.org/10.1016/j.jallcom.2012.07.101).
- [21] M. Wendorff, C. Röhr, The new complex barium mercuride Ba₂₀Hg₁₀₃ and its ternary zinc and cadmium variants, *Z. Naturforsch. B.* **2012**, *67*, 893–906, DOI: [10.5560/znb.2012-0186](https://doi.org/10.5560/znb.2012-0186).

- [22] B. H. Toby, R. B. Von Dreele, GSAS-II: the genesis of a modern open-source all purpose crystallography software package, *J. Appl. Crystallogr.* **2013**, *46*, 544–549, DOI: [10.1107/S0021889813003531](https://doi.org/10.1107/S0021889813003531).
- [23] H.-J. Deiseroth, A. Strunck, W. Bauhofer, RbHg₂ und CsHg₂, Darstellung, Kristallstruktur, elektrische Leitfähigkeit, *Z. Anorg. Allg. Chem.* **1988**, *558*, 128–136, DOI: [10.1002/zaac.19885580112](https://doi.org/10.1002/zaac.19885580112).
- [24] A. Iandelli, A. Palenzona, Su alcuni composti intermetallici dell'eurobio con zinco, cadmio e mercurio, *Atti Accad. Naz. Lincei Rend. Cl. Sci. Fis. Mater. Nat.* **1964**, *37*, 165–168.
- [25] F. Merlo, M. L. Fornasini, Crystal Structure of the R₁₁Hg₄₅ compounds (R = La, Ce, Pr, Nd, Sm, Gd, U), *J. Alloys Compd.* **1979**, *64*, 221–231, DOI: [10.1016/0022-5088\(79\)90173-5](https://doi.org/10.1016/0022-5088(79)90173-5).
- [26] F. Tambornino, C. Hoch, The Mercury-richest Europium Amalgam Eu₁₀Hg₅₅, *Z. Anorg. Allg. Chem.* **2015**, *641*, 537–542, DOI: [10.1002/zaac.201400561](https://doi.org/10.1002/zaac.201400561).
- [27] A. Palenzona, MX₃ intermetallic phase of the rare earths with Hg, In, Tl, Pb, *J. Less-Common Met.* **1966**, *10*, 290–292, DOI: [10.1016/0022-5088\(66\)90031-2](https://doi.org/10.1016/0022-5088(66)90031-2).
- [28] F. Tambornino, C. Hoch, The simplest representative of a complex series: the Hg-rich amalgam Yb₁₁Hg₅₄, *Z. Kristallogr.* **2017**, *232*, 557–565, DOI: [10.1515/zkri-2016-2036](https://doi.org/10.1515/zkri-2016-2036).
- [29] S. I. Troyanov, Crystal modifications of beryllium dihalides BeCl₂, BeBr₂ and BeI₂, *Zh. Neorg. Khim.* **2000**, *45*, 1619–1624.
- [30] M. Müller, M. R. Buchner, Preparation and crystal structures of the beryllium ammines [Be(NH₃)₄]X₂ (X = Br, I, CN, SCN, N₃) and Be(NH₃)₂X'₂ (X' = Cl, Br), *Chem. Commun.* **2019**, *55*, 13649–13652, DOI: [10.1039/C9CC07712J](https://doi.org/10.1039/C9CC07712J).
- [31] H. J. Bernhardt, K. Schmetzer, Belendorffite, a new copper amalgam dimorphous with kolymite, *M. Jb. Miner. Mh.* **1992**, *1*, 21–28.
- [32] A. V. Tkachuk, A. Mar, In search of the elusive amalgam SrHg₈: a mercury-rich intermetallic compound with augmented pentagonal prisms, *Dalton Trans.* **2010**, *39*, 7132–7135, DOI: [10.1039/C0DT00304B](https://doi.org/10.1039/C0DT00304B).
- [33] E. J. Duwell, N. C. Baenziger, The crystal structures of KHg and KHg₂, *Acta Crystallogr.* **1955**, *8*, 705–710, DOI: [10.1107/S0365110X55002168](https://doi.org/10.1107/S0365110X55002168).
- [34] A. Altomare, C. Cuocci, C. Giacovazzo, A. Moliterni, R. Rizzi, N. Corriero, A. Falcicchio, EXPO2013: a kit of tools for phasing crystal structures from powder data, *J. Appl. Crystallogr.* **2013**, *46*, 1231–1235, DOI: [10.1107/S0021889813013113](https://doi.org/10.1107/S0021889813013113).

8

Miscellaneous

8.1 List of Publications

The following list contains all publications of this thesis in reversed chronological order, including all authors, citations and author contributions.

1. Ternary Amalgams: Expanding the structural variety of the $Gd_{14}Ag_{51}$ family

Timotheus Hohl, Lukas Nusser, Jessica Wulfes and Constantin Hoch

Published in : *Z. Kristallogr.* **2023**, in print.

DOI: [10.1515/zkri-2023-0007](https://doi.org/10.1515/zkri-2023-0007)

Practical work was performed by T. Hohl, L. Nusser and J. Wulfes. T. Hohl performed the crystallographic analyses. The manuscript was conceptualised and written by T. Hohl, with supervision from C. Hoch.

2. Influence of Disorder on the Bad Metal Behaviour in Polar Amalgams

Timotheus Hohl, Reinhard K. Kremer, Stefan G. Ebbinghaus, Saleem A. Khan, Ján Minár and Constantin Hoch

Published in: *Inorg. Chem.* **2023**, *62*(9), 3965–3975.

DOI: [10.1021/acs.inorgchem.2c04430](https://doi.org/10.1021/acs.inorgchem.2c04430)

T. Hohl performed the practical work and all Rietveld analyses. Conductivity measurements were performed by R. K. Kremer. Susceptibility Measurements were performed by S. G. Ebbinghaus, while electronic calculations of the disordered materials were done by S. A. Khan and J. Minár. The manuscript was conceptualised and written by T. Hohl and C. Hoch, which also supervised the project.

3. Structure and bonding in $CsNa_2Hg_{18}$, a new ternary amalgam with strong Coulombic bonding contributions

Timotheus Hohl, Frank Tambornino and Constantin Hoch

Published in: *Crystals* **2022**, *12*, 1679.

DOI: [10.3390/cryst12111679](https://doi.org/10.3390/cryst12111679)

C. H. conceptualised the studies and wrote the manuscript, T. H. performed the practical work, prepared the single crystal samples and performed all analyses, F. T. performed the DFT calculations., and conductivity measurements were conducted by R. K. Kremer.

4. Synthesis and Crystal Structures of β -[Be(DMF) $_4$]I $_2$, [Be(Pyr) $_4$]I $_2$, [Be(NMP) $_4$]I $_2$ and [BeI $_2$ (Lut) $_2$] Timotheus Hohl, Torben Sinn and Constantin Hoch

Published in: *Z. Naturforsch.* **2020**, *75b*, 509–516.

DOI: [10.1515/znb-2020-0035](https://doi.org/10.1515/znb-2020-0035)

T. Hohl and T. Sinn performed the experiments, single crystal analysis, structure solution and refinements were performed in collaboration with C. Hoch. The manuscript was written by T. Hohl and C. Hoch, with the latter supervising the project.

8.2 Publications beyond this thesis

The following list contains publications beyond this thesis in reversed chronological order.

5. The Cesium Oxide Mercuride $C_{18}Hg_8O_6$

Lukas Nusser, Timotheus Hohl, Frank Tambornino and Dr. Constantin Hoch

Published in: *Z. Anorg. Allg. Chem.* **2022**, *648*, e202100389.

DOI: [10.1002/zaac.202100389](https://doi.org/10.1002/zaac.202100389)

6. Electrochemical Synthesis and Crystal Structure of the organic ion intercalated superconductor $TMA_{0.5}Fe_2Se_2$ with $T_C = 43$ K

Bettina Rendenbach, Timotheus Hohl, Sascha Harm, Constantin Hoch and Dirk Johrendt

Published in: *J. Am. Chem. Soc.* **2020**, *32*, 866-873.

DOI: [10.1021/jacs.0c13396](https://doi.org/10.1021/jacs.0c13396)

7. New Solvate Complexes $[Be(Solv_4)]I_2$ of Beryllium Iodide with polar aprotic solvents

Timotheus Hohl, Torben Sinn, Constantin Hoch

Published in: *Z. Kristallogr. Suppl.* **2019**, *39*, 91.

DOI: [10.1515/9783110657272-003](https://doi.org/10.1515/9783110657272-003)

8.3 Conference Contributions and Presentations

In reversed chronological order

The Hg-rich part of the binary system K–Hg revised: Synthesis, crystal and electronic structures of KHg_4 , KHg_5 and KHg_8

Timotheus Hohl, Constantin Hoch, Marco Wendorff and Caroline Röhr

Poster Presentation, 33rd European Crystallographic Meeting, **2022**, Versailles (France)

Elektrokristallisation ternärer Amalgame

Timotheus Hohl

Oral Presentation, 49th Hirschegg Seminar, **2022**, Hirschegg (Austria)

From binary to ternary amalgams: expanding the structural variety of the $\text{Gd}_{14}\text{Ag}_{51}$ structure family

Timotheus Hohl, Lukas Nusser, Jessica Wulfes and Constantin Hoch

Oral Presentation (Online), 31st Meeting of the German Crystallographic Society (DGK), **2022**, Munich (Germany)

... it's complicated

Timotheus Hohl

Oral Presentation, Schnick Group Seminar, **2022**, Munich (Germany)

Flotter Dreier mit Quecksilber

Timotheus Hohl

Oral Presentation, Schnick Group Seminar, **2020**, Munich (Germany)

(K)ein Berylliumamalgam

Timotheus Hohl

Oral Presentation, Schnick Group Seminar, **2019**, Munich (Germany)

Solvatkomplexe des Berylliums vom Typ $[\text{Be}(\text{Sol}_4)]\text{I}_2$ mit polaren, aprotischen Lösungsmitteln

Timotheus Hohl, Torben Sinn and Constantin Hoch

Poster Presentation, 15th Meeting of coordination chemists (KCT), **2019**, Munich (Germany)

Beryllium Amalgams from Thermolysis of Precursor Complexes

Timotheus Hohl, Constantin Hoch

Poster Presentation, Undergraduate Research Conference on Molecular Sciences, **2016**, Kloster Irsee (Germany)

8.4 Deposited Crystallographic data

Crystallographic Information Files (CIFs) of selected compounds presented in this thesis can be obtained free of charge from The Cambridge Crystallographic Data Center (CCDC) via www.ccdc.cam.ac.uk/data_request/cif

Table 8.1: List of compounds presented in this thesis with their corresponding deposition numbers.

Compound	CCDC deposition number
$[(\text{Hg}(\text{en}))_2\text{I}_3][\text{HgI}_3]$	2244888
$(\text{Gdn})[\text{HgCl}_3]$	2244875
$[\text{NH}_4]_2[\text{Be}(\text{C}_2\text{O}_4)_2]$	2245578
$\beta\text{-}[\text{Be}(\text{DMF})_4]\text{I}_2$	1983410
$[\text{Be}(\text{NMP})_4]\text{I}_2$	1983411
$[\text{BeI}_2(\text{Lut})_2]$	1983412
$[\text{Be}(\text{Pyr})_4]\text{I}_2$	1983413
$\text{CsNa}_2\text{Hg}_{18}$	2031829
$\text{K}_{1-x}\text{Rb}_x\text{Hg}_{11}$ ($x = 0.472(7)$)	2229881
$\text{Cs}_{3-x}\text{Ca}_x\text{Hg}_{20}$ ($x = 0.20(3)$)	2229888
$\text{Yb}_{10.7}\text{Sr}_{0.3}\text{Hg}_{54}$	2240995
$\text{Ca}_{6.9}\text{Na}_{4.1}\text{Hg}_{54}$	2240996
$\text{Ca}_{4.5}\text{Eu}_{6.5}\text{Hg}_{54}$	2240997